Lecture Notes in Electrical Engineering 863

Sanjeet Dwivedi
Sanjeev Singh
Manish Tiwari
Ashish Shrivastava *Editors*

Flexible Electronics for Electric Vehicles

Select Proceedings of FlexEV—2021

Springer

Lecture Notes in Electrical Engineering

Volume 863

The book series *Lecture Notes in Electrical Engineering* (LNEE) publishes the latest developments in Electrical Engineering—quickly, informally and in high quality. While original research reported in proceedings and monographs has traditionally formed the core of LNEE, we also encourage authors to submit books devoted to supporting student education and professional training in the various fields and applications areas of electrical engineering. The series cover classical and emerging topics concerning:

- Communication Engineering, Information Theory and Networks
- Electronics Engineering and Microelectronics
- Signal, Image and Speech Processing
- Wireless and Mobile Communication
- Circuits and Systems
- Energy Systems, Power Electronics and Electrical Machines
- Electro-optical Engineering
- Instrumentation Engineering
- Avionics Engineering
- Control Systems
- Internet-of-Things and Cybersecurity
- Biomedical Devices, MEMS and NEMS

For general information about this book series, comments or suggestions, please contact leontina.dicecco@springer.com.

To submit a proposal or request further information, please contact the Publishing Editor in your country:

China

Jasmine Dou, Editor (jasmine.dou@springer.com)

India, Japan, Rest of Asia

Swati Meherishi, Editorial Director (Swati.Meherishi@springer.com)

Southeast Asia, Australia, New Zealand

Ramesh Nath Premnath, Editor (ramesh.premnath@springernature.com)

USA, Canada

Michael Luby, Senior Editor (michael.luby@springer.com)

All other Countries

Leontina Di Cecco, Senior Editor (leontina.dicecco@springer.com)

**** This series is indexed by EI Compendex and Scopus databases. ****

Sanjeet Dwivedi · Sanjeev Singh · Manish Tiwari · Ashish Shrivastava
Editors

Flexible Electronics for Electric Vehicles

Select Proceedings of FlexEV—2021

Springer

Editors
Sanjeet Dwivedi
Application Control
Danfoss Power Electronics A/S Denmark
Nordborg, Denmark

Manish Tiwari
Department of Electronics
and Communication Engineering
Manipal University Jaipur
Jaipur, Rajasthan, India

Sanjeev Singh
Department of Electrical Engineering
Maulana Azad National Institute
of Technology
Bhopal, Madhya Pradesh, India

Ashish Shrivastava
Skill Faculty of Engineering
and Technology
Shri Vishwakarma Skill University Haryana
Gurugram, India

ISSN 1876-1100 ISSN 1876-1119 (electronic)
Lecture Notes in Electrical Engineering
ISBN 978-981-19-0587-2 ISBN 978-981-19-0588-9 (eBook)
https://doi.org/10.1007/978-981-19-0588-9

Preface

It is a great privilege for us to present the proceedings of 2nd Conference on Flexible Electronics for Electric Vehicles 2021, held at Manipal University, Jaipur, Rajasthan, India, on 18–19 March 2021. FlexEV-2021 aims to provide a platform for discussing the issues, challenges, opportunities and findings in the field of flexible electronics. The conference proceedings presents the diligent work of the research community where flexible electronics application in different allied fields of engineering ranging from engineering materials to electrical engineering to electronics and communication engineering is discussed. The theoretical research concepts are supported with extensive reviews highlighting the trends in the possible and real-life applications of electric vehicles. The high-quality content with broad range of the topics pertaining to the book series is thoroughly peer reviewed and published on suitable approvals. This book compiles the refereed papers, and we hope that readers will find it helpful, exciting and motivating.

The responses to the call-for-papers had been overwhelming. We appreciate that the authors of FlexEV-2021 desire to maximize the popularity of their papers, and we have tried our best to support them in their efforts.

We would like to express our gratefulness and admiration for all the reviewers who assisted us retain the high excellence of manuscripts included in the proceedings published by Springer. We would also like to extend our thanks to the members of the organizing team for their hard work.

We are now optimistic and hope that this book will be mainly useful for research scholars, electric vehicles professionals, driving system designers and postgraduates from allied domains, as this incorporates economical and efficient electric vehicle driving and the latest innovations in the field of electric vehicles technology with their paradigms and methods that employ knowledge in the research community. This book is having its scope ranging from flexible electronics and electric vehicle which are having inbuilt capabilities of handling the technical issues and challenges such as energy-efficient systems, flexible electronics aspects involved in various domains of engineering such as storage devices, flexible photovoltaics, flexible electronics for robotics and EV standards: policy, education and market. The ongoing success of this conference series means that planning can now continue with confidence of our

team for the next event of this series (FlexEV-2022) to be held in Manipal University, Jaipur, in 2022.

Nordborg, Denmark — Sanjeet Dwivedi
Bhopal, India — Sanjeev Singh
Jaipur, India — Manish Tiwari
Jaipur, India — Ashish Shrivastava

Acknowledgements

The organizing committee of 2nd Conference on Flexible Electronics for Electric Vehicles 2021, held at Manipal University, Jaipur, would like to acknowledge all supporters and organizers of this conference. Gratitude is also extended to our distinguished plenary speakers and to our session chairs.

Dr. Rudolf Frycek, CEO-AMIRES, Switzerland
Dr. Sanjeet Kumar Dwivedi, Danfoss Power Electronics, Denmark
Dr. Leonardo Israel F. Cabrera, Professor, EIC, Campus Puebla, Tecnológico de Monterrey
Dr. Srinivas Gunti, Mahindra Research Valley, Tamil Nadu, India
Dr. Matt Dyson, Technology Analyst at IDTechEx, UK
Dr. Siddhartha Panda, Professor, IIT Kanpur, India

We would like to recognize the support and help of Manipal University Jaipur, and we take this opportunity to sincerely thank **Prof. K. Ramnarayan** Chairperson, MUJ, **Prof. G. K. Prabhu**, President, MUJ, **Prof. N. N. Sharma**, Pro-President, MUJ, **Prof. Jagannath Korody**, Dean, FoE-MUJ, **Prof. H. R. Kamath**, Registrar, MUJ, **Prof. Jamil Akhtar**, Director, SEEC, MUJ, for their inspiring mentorship besides providing us with all possible support towards organizing this event.

We would also like to acknowledge the important role of the conference convenors **Dr. Tarun Kumar Dubey** and **Dr. Vishnu Goyal** for their contributions to manage the event with many very interesting presentations. We also express our thanks to the conference participants and reviewers. All these contributions have been instrumental in maintaining this highly successful event.

Finally, we thank books production division of Springer for the kind permission to publish the book proceedings of Flex-EV2021.

Sanjeet Dwivedi
Sanjeev Singh
Manish Tiwari
Ashish Shrivastava

Invited Speakers

Dr. Leonardo Israel Farfan Cabrera

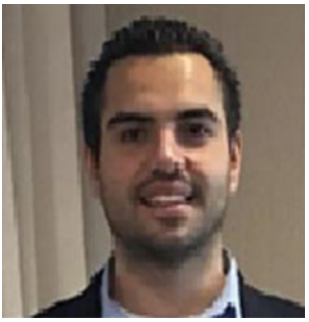

Dr. Leonardo Israel Farfan Cabrera is Professor/Researcher at the Escuela de Ingeniería y Ciencias, Campus Puebla, Tecnológico de Monterrey. He is also Member of the Nanomaterials Research Group at School of Engineering and Sciences. He obtained his Doctor of Science in Mechanical Engineering from ESIME—Unidad Culhuacan (IPN). He has published more than 30 research papers in various International journals. He has expertise in subjects related to automotive engineering project, materials applications, materials technology and mechanical engineering capstone project. His research domain includes the current state and future trends of critical technology of electric vehicles producing energy consumption by friction losses. He has been awarded with the Mexican Researcher Certification—Level 1

Dr. Srinivas Gunti

Dr. Srinivas Gunti completed his Ph.D. from IISc Bangalore and postgraduation from IIT Kharagpur. In the past, he worked for various automotive and tractor industries and has over 20 years of Research and Product Development experience. His research areas include computer-aided engineering (CAE) in product design, data science in product design (automotive product development), multidisciplinary design optimization (MDO), automotive safety and impact engineering, IC engines electric vehicles and bio-medical implants. His work resulted in 10 international conference publications, 32 peer-reviewed journal/technical papers (in SAE, Taylor and Francis, Elsevier and Begell House publications) and one US Patent. He received more than seven best performance awards and one patent award for his contribution in the areas of new product design and development. In his previous roles, he was responsible for developing various vehicle and powertrain systems and sub-systems. Presently, he is responsible for developing the frameworks, technical case studies on product development and processes for technical capability building (automotive product development) and technical assessments (auto, farm and powertrain) of MRV engineering leaders. He is active as a judge in various SAE competitions and a reviewer of manuscripts pertaining to international automotive conferences and journals.

Dr. Matt Dyson

Dr. Matt Dyson is Technology Analyst at IDTechEx, specializing in printed, organic, flexible and hybrid electronics. He has previously been involved in research across a wide range of printed/flexible electronics areas, contributing to 15 scientific papers and presenting his work in a variety of international conferences. At IDTechEx, he analyses companies and technologies in the printed/flexible sector, assessing innovations from a technical and commercial perspective.

Dr. Siddhartha Panda

Dr. Siddhartha Panda is Professor of Chemical Engineering, and a participating faculty in the Materials Science Programme, and is currently Coordinator (i.e. Head) of the National Centre for Flexible Electronics (NCFlexE), at IIT Kanpur. His research focuses on chemical sensors for healthcare applications and the accompanying transport, reactions, transductions materials processing and intelligence utilizing flexible printable platforms. Prior to joining IIT Kanpur in 2006, he was Staff/Advisory Engineer at the IBM Semiconductor R&D Center, New York, for over six years. He obtained a Ph.D. from the University of Houston in 1999, an M.S. from the University of Cincinnati in 1995 and a B.Tech. from IIT Kharagpur in 1992, all in chemical engineering.

Dr. Rudolf Fryček

Dr. Rudolf Fryček is CEO of AMIRES, and he has more than 15 years' experience in the European project management and consultancy. He was a consultant to several SMEs in the field of production, innovation and company development, including preparation of project for governmental incentive and for several business-oriented bank loans. In 2006, he was nominated as Seconded National Expert to the European Commission, DG Research and Innovation's Directorate for Industrial Technologies. Beside his technological expertise and daily project officer work (more than 13 projects under his responsibility), he has been active in the policy structuring for exploitation and commercialization of EU framework projects. He helped to analyse the overall nanotechnology unit project portfolio in terms of generated IPR and also co-organized the workshop with European Patent Office and US Patent and Trade Office on IPR in nanotechnology—lessons from experiences worldwide, held in Brussels. He was Scientific Coordinator of the Euro Nano Forum 2009, the bi-annual conference financed by the European Commission. Since 2011, he is an accredited coach of Innovation Platform—PLATINN, which provides hands-on coaching to SMEs. Rudolf is a cooperation coach, which helps companies to increase their innovation capacity. He founded AMIRES company in 2009, runs the Swiss branch and was responsible for FP7 projects Implantable Organic Nano-Electronics (iONE-FP7) and universal scanning electron microscope as a multi-nano-analytical tool (UnivSEM).

Dr. Sanjeet Dwivedi

Dr. Sanjeet Dwivedi is working as Senior R&D Motor and Application Control Engineer in Danfoss Power Electronics A/S Denmark. He is Adjunct Professor in Power Electronics at Curtin University Perth. He obtained 1st Masters M.E. in power electronics and drive (with Gold Medal) from IIT-R & 2nd Masters M.Sc. Engineering in Innovation and Business from DK, Ph.D. degree from IIT-D. He got Man on the Moon Award of Danfoss and IETE-Bimal Bose Award-2017. He is Associate Editor of IEEE Transactions on Industrial Electronics.

List of Session Chair

Mr. Rajkumar Gupta, Assistant Professor, Amity University, Rajasthan, e-mail: rkgupta1@jpr.amity.edu, area: VLSI
Dr. Amandeep Gill, Assistant Professor, JECRC University, e-mail: amandeep.gill@jecrcu.edu.in, area: electrical engineering
Mr. Amit Chaurasia, Assistant Professor, Amity University, Rajasthan, e-mail: achaurasia@jpr.amity.edu, area: material science and microelectronics
Mrs. Parul Pathak, Assistant Professor, JECRC University, e-mail: parul.pathak@jecrcu.edu.in, area: antennas
Dr. Ashwani Kumar Yadav, Assistant Professor, Amity University, Rajasthan, e-mail: akyadav@jpr.amity.edu, area: image processing
Mr. Sakar Gupta, Assistant Professor, Poornima College of Engineering, e-mail: sakar.gupta@poornima.org, area: image processing
Mr. Vinod Kumar Sharma, Assistant Professor, Amity University, Rajasthan, e-mail: vksharma1@jpr.amity.edu, area: antennas, instrumentation
Dr. Ashok Kumar, Assistant Professor, GWEC, Ajmer, e-mail: kumarashoksaini@gmail.com, area: antennas, instrumentation
Mr. Mahipal Bukya, Assistant Professor (Senior-Scale), Electrical Engineering Department, MUJ, area of research: electric vehicle protection, high-voltage engineering, e-mail: mahipal.bukya@jaipur.manipal.edu
Mr. Mohit Kumar Sharma, Assistant Professor, ECE, SEEC, area of research: system and control, e-mail: mohitkumar.sharma@jaipur.manipal.edu
Mr. Vishal Das, Assistant Professor, ECE, SEEC, area: industrial engineering, e-mail: vishal.das@jaipur.manipal.edu
Dr. Lokesh Vijayvargy, Associate Professor, area: industrial engineering, e-mail: lokesh.vijayvargy@jaipuria.ac.in
Dr. Amit Shrivastava, Professor and Dean, IQAC, Poornima University, Jaipur, e-mail: apasjpr@gmail.com
Dr. Cheruku Sandesh Kumar, Assistant Professor, Amity University, Rajasthan, Jaipur, e-mail: cskumar@jpr.amity.edu

Conference Schedule

Day 1 Thursday, 18 March 2021	2:15 PM to 3:45 PM	Paper Presentations Parallel Sessions 1
1. Mr. Rajkumar Gupta, Assistant Professor, Amity University, Rajasthan, e-mail: rkgupta1@jpr.amity.edu, area: VLSI 2. Dr. Amandeep Gill, Assistant Professor, JECRC University, e-mail: amandeep.gill@jecrcu.edu.in, area: electrical engineering		

Day 1 Thursday, 18 March 2021	2:15 PM to 3:45 PM	Paper Presentations Parallel Sessions 2
3. Mr. Amit Chaurasia, Assistant Professor, Amity University, Rajasthan, e-mail: achaurasia@jpr.amity.edu, area: material science and microelectronics 4. Mrs. Parul Pathak, Assistant Professor, JECRC University, e-mail: parul.pathak@jecrcu.edu.in, area: antennas		

Day 1 Thursday, 18 March 2021	4:00 PM to 5:30 PM	Paper Presentations Parallel Sessions 3
5. Dr. Ashwani Kumar Yadav, Assistant Professor, Amity University, Rajasthan, e-mail: akyadav@jpr.amity.edu, area: image processing 6. Mr. Sakar Gupta, Assistant Professor, Poornima College of Engineering, e-mail: sakar.gupta@poornima.org, area: image processing		

Day 1 Thursday, 18 March 2021	4:00 PM to 5:30 PM	Paper Presentations Parallel Sessions 4
7. Mr. Vinod Kumar Sharma, Assistant Professor, Amity University, Rajasthan, e-mail: vksharma1@jpr.amity.edu, area: antennas, instrumentation 8. Dr. Ashok Kumar, Assistant Professor, GWEC, Ajmer, e-mail: kumarashoksaini@gmail.com, area: antennas, instrumentation		

Day 2 Friday, 19 March 2021	12:00 Noon to 1:30 PM	Paper Presentations Parallel Sessions 5
9. Mr. Mahipal Bukya, Assistant Professor (Senior-Scale), Electrical Engineering Department, MUJ, area of research: electric vehicle protection, high-voltage engineering, e-mail: mahipal.bukya@jaipur.manipal.edu 10. Mr. Mohit Kumar Sharma, Assistant Professor, ECE, SEEC, area of research: system and control, e-mail: mohitkumar.sharma@jaipur.manipal.edu		

Day 2 Friday, 19 March 2021	12:00 Noon to 1:30 PM	Paper Presentations Parallel Sessions 6

11. Mr. Vishal Das, Assistant Professor, ECE, SEEC, area of research: system and control, e-mail: vishal.das@jaipur.manipal.edu
12. Dr. Lokesh Vijayvargy, Associate Professor, area: industrial engineering, e-mail: lokesh.vijayvargy@jaipuria.ac.in
13. Dr. Amit Shrivastava, Professor and Dean, IQAC, Poornima University, Jaipur, e-mail: apasjpr@gmail.com

List of Reviewers

Mr. Satya Narayan Agarwal, e-mail: ssnagarwal@gmail.com
Dr. Deepika Bansal, e-mail: deepika.bansal386@gmail.com
Dr. Shilpi Birla, e-mail: shilpi.birla@jaipur.manipal.edu
Mr. Vikash Kumar Boradak, e-mail: vikaskumar.boradak@jaipur.manipal.edu
Mr. Mahipal Bukya Bukya, e-mail: mahipalbhukya@gmail.com
Dr. Dhanraj Chitara Chitara, e-mail: dhanraj.chitara@gmail.com
Dr. Himanshu Choudhary, e-mail: himan.74@gmail.com
Mr. Chusen Duari, e-mail: chusen.duari@gmail.com
Dr. T. K. Dubey, e-mail: tarunkumar.dubey@jaipur.manipal.edu
Dr. Prashant Povel Dwivedi, e-mail: ppovel28@gmail.com
Dr. Lokesh Garg, e-mail: lokesh.engg07@gmail.com
Mr. Peeyush Garg, e-mail: peeyush01garg@gmail.com
Dr. Sunil Kumar Goyal, e-mail: sunilkumar.goyal@jaipur.manipal.edu
Dr. Vishnu Goyal, e-mail: vishnu.goyal@jaipur.manipal.edu
Dr. Abhilash Kumar Gupta, e-mail: abhidec91@gmail.com
Dr. C. P. Gupta, e-mail: cp106@rediffmail.com
Dr. Pranda Prasanta Gupta, e-mail: prandaprasantagupta@gmail.com
Mr. Vinay Gupta, e-mail: vinra_20@rediff.com
Dr. J. Tejpal, e-mail: tejpal4u@gmail.com
Dr. Vinay Kumar Jadoun, e-mail: vjadounmnit@gmail.com
Dr. Sushil Kumar Jain, e-mail: sushilkumar.jain@jaipur.manipal.edu
Ms. Smriti Jain, e-mail: smriti.agr@gmail.com
Col. Sanjiv Jaswal, e-mail: sanjiv.jaswal@jaipur.manipal.edu
Dr. Neeraj Kanwar, e-mail: nk12.mnit@gmail.com
Mr. Abhishek Kumar, e-mail: abhishekkumr@gmail.com
Dr. Renu Kumawat, e-mail: renukumawat@gmail.com
Dr. S. Das Mahapatra, e-mail: suddm.kgp@gmail.com
Dr. Neetu Marwah, e-mail: neetu03@rediffmail.com
Mr. Himanshu Priyadarshi, e-mail: himanshu.priyadarshi@jaipur.manipal.edu

Prof. Amit Rathi, e-mail: amitrathi1978@gmail.com
Mrs. Madhuri Sahal, e-mail: madhuri.sahal@jaipur.manipal.edu
Dr. Amit Saraswat, e-mail: amitsaras@gmail.com
Dr. Naveen Sharma, e-mail: naveen31.sharma@gmail.com
Mr. Mohit Kumar Sharma, e-mail: mohitkumar.sharma@jaipur.manipal.edu
Mrs. Suman Sharma Sharma, e-mail: 2015ree9012@mnit.ac.in
Mr. Divya Rishi Shrivastava, e-mail: divyarishi.shrivastava@jaipur.manipal.edu
Dr. Ajeet Singh, e-mail: ajeetksingh@yahoo.com
Dr. Amit Kumar Singh, e-mail: amitkumarsingh89@gmail.com
Dr. Kulwant Singh, e-mail: eckulwant@gmail.com
Dr. Neha Singh, e-mail: drnnehasingh@gmail.com
Dr. Satyendra Singh Singh, e-mail: satyendagur@gmail.com
Mr. Ritesh Singh, e-mail: ritesh.singh23@gmail.com
Ms. Jyotsna Singh Singh, e-mail: sjyotsna04@gmail.com
Samarendra Pratap Singh, e-mail: samarendra.singh@jaipur.manipal.edu
Dr. Abhishek Srivastava, e-mail: dr.ashrivastava2007@gmail.com
Dr. Manish Thukral, e-mail: manishkumarthukral1984@gmail.com
Dr. Dinesh Yadav, e-mail: dinesh.yadav@jaipur.manipal.edu
Dr. Pallavi Yarde, e-mail: pallavi.yarde@gmail.com

Contents

About the Editors

Sanjeet Dwivedi is working as Senior R&D Motor and Application Control Engineer in Danfoss Power Electronics A/S Denmark. He is an Adjunct Professor in Power Electronics at Curtin University, Perth, Australia. He obtained his M.E. in power electronics and drive from IIT Roorkee M.Sc. Engineering in Innovation and Business from DK, and a Ph.D. degree from IIT Delhi. He was awarded the 9th Man on the Moon Global Innovation Award of Danfoss (2015) and IETE-Bimal Base Award (2017) for outstanding contribution in power electronics and drive.

Sanjeev Singh is a Professor of Electrical Engineering at Maulana Azad National Institute of Technology (MANIT) Bhopal. He received his M.Tech. degree from Devi Ahilya Vishwa Vidyalaya, Indore, India, and a Ph.D. degree from the Indian Institute of Technology Delhi, in 2010. He was a post-doctoral researcher at Department of Electrical Engineering, École de Technologie Supérieure (ÉTS), Université du Québec, Montréal, QC, Canada. His areas of interest include power electronics, electrical machines and drives, electric vehicles, energy management, optimization in electrical systems, power quality, microgrids, and renewable energy integration.

Manish Tiwari received his Ph.D. in Electronics and Communication Engineering (ECE) in Photonics from Malaviya National Institute of Technology (MNIT), Jaipur. He is currently a Professor and Head of the ECE department at Manipal University, Jaipur. He was a visiting researcher at City University, London in 2010 and 2011, and Tsinghua University, Beijing, China, in 2016. His current research interests include micro/nano-structured photonic devices, fiber optics, numerical modeling, nonlinear optics, and photonic crystal fibers. He has published over 100 research papers in reputed journals and conferences. He has also authored/edited over 10 books and got 15 book chapters published to his credit.

Ashish Shrivastava earned his B.E. and M.Tech. degrees with honors in Electrical Engineering from the Govt. Engineering College, Rewa, and MANIT, Bhopal (MP), respectively. He is awarded a Ph.D. degree from IIT Delhi. He has been conferred with prestigious POSOCO Power System Award 2014 (PPSA-2014), under the Doctoral category for his outstanding research work focusing on "Low-cost energy-efficient electronic ballast/LED driver for low power lighting applications with power factor correction". Dr. Srivastava is currently a Professor and Head of the Department of Electrical Engineering at Manipal University Jaipur. He has 21 years of experience in academics and has published over 60 research papers in international journals. He is presently supervising six research scholars from different universities. His areas of interest include power quality, power electronics, and drives, electric vehicles, high-speed energy storage devices, artificial intelligence, deep learning, machine learning, solar PV, SMPS, custom power devices, PFC electronic ballast, PFC LED driver, and PFC DC/DC converters, etc.

New Text Detection Technique Using Machine Learning Architecture

Samriddhi Agarwal, Perepi Rahul, and Neetu

Abstract There has been a wide advancement in technology over the past two decades and the extensively usage of camera-embedded mobile phones all around the world has raised the demand of PC vision tasks and offers rise to incalculable open entryways in the field. A hot emerging area of research in this field is the extraction of text embedded in natural scene images. Natural scene images are the photos taken from a camera, where the establishment is self-assertive, and the arrangement of tones used in the image is classy and unique. Exactly when text is accessible in such sort of pictures, it is typically difficult for a machine to recognize and eliminate this due to different limits. This paper deals with a method that uses a blend of the Open Source Computer Vision Library (OpenCV) and the architectures of Machine Learning (ML), to separate English text from images. This paper provides the result by using two Machine Learning architectures, namely, Multi Layer Perceptron (MLP) and TensorFlow (TF). The data is predicted by using both the architectures, to compare their model accuracies and analyze their problems in text detection. The proposed OpenCV execution accomplished a precision rate of 95.2% and a recall rate of 70.6%, proving the efficacy of approach utilized.

Keywords Deep learning · Machine learning · MLP · Natural scene images · OpenCV · Text extraction TensorFlow

1 Introduction

In the past few decades, the technology has grown at an exponential rate which brings the importance of computer vision tasks such as extracting the text from the natural images or a video frame which might be exposed to different light situations [1]. Identification of text in pictures, instead of outputs obtained in printed form, letter heads and business cards, is a significant advance for various Computer Vision applications, like computerized rulebook for visually impaired people, programmed

S. Agarwal · P. Rahul · Neetu (✉)
Department of Electronics and Communication Engineering, Manipal University, Jaipur, India
e-mail: neetu03@rediffmail.com

S. Dwivedi et al. (eds.), *Flexible Electronics for Electric Vehicles*, Lecture Notes in Electrical Engineering 863, https://doi.org/10.1007/978-981-19-0588-9_1

geo-coding of organizations, and automated route in metropolitan conditions. Recovering writings in both indoor and open air conditions gives logical insights for a wide assortment of vision errands. Also, it has been shown that the presentation of picture recovery calculations relies basically upon the exhibition of their content recognition modules [2].

In early days, text detection was allotted from pictures captured through cameras. Optical Character Recognition (OCR) was the technology to detect text from scanned images and written images. However, it faces difficulties like quality backgrounds, diversity of scene text and interference factors etcetera, therefore, to beat the difficulties, researchers came up with other techniques like Adaboost, SVM, Fuzzy Logic, and Convolutional Neural Networks (CNN) etc. which are currently high acting capability text detection techniques available. The recent text detection can be performed through machine learning techniques which instinctively detect the text from advanced backgrounds. Machine learning is a technique that incorporates the usage of artificial intelligence (AI), which in turn has the capability to learn without any prior experience and programming skills. This novel learning interaction of machine begins with observing, direct insight, or direction to discover instances of examples dependent on better choices so that all can be performed again later on [3].

Both AI calculation and example recognition assumes an imperative part in extricating data from normal scenes [4]. Learning through machines permits investigating a lot of information. By and large, quick and more precise outcomes are gotten for pattern identification. A pattern may be anything from identification of picture to finger impression. A cycle of utilizing AI calculations for the recognition of configuration patterns is known as pattern recognition [5].

Natural Image processing is a type of signal processing. Image processing deals with a set of elements associated with an input image like pixel density, height, width, color, etc. One of the methods by which image processing can be carried out is with the OpenCV Library which is an open source software initially developed as research by Intel. OpenCV library consists of tools which help in solving computer detection problems. It contains low level picture preparing capacities and undeniable level calculations for face, text or item identification, highlight coordinating and following. Extraction of text from natural pictures is an important errand because of the wide assortment of text structures, for example, textual style, arrangement, shape, size, style, light conditions, shading, and a gathering of different boundaries. Natural text alludes to the content existing in pictures and recordings normally and generally caught by camera. Contrasted and fake content in motion pictures, normal scene text shows the varieties in size, textual style, shading and arrangement. Text extraction from normal scene pictures generally involves three stages: (I) text detection and localization, (ii) enhancement and segmentation of text and (iii) optical character recognition (OCR). Because of changes in varieties in the text dimension and shading, text arrangement, enlightenment change leads to pullout from extracting text from natural environment [6].

Additionally, natural photography situations regularly experience the ill effects of low goal and bad quality, mutilation of point of view, lighting changeability, and complex foundation. Also, there is an absence of earlier information on text images

and area of text areas. These components add to the trouble of picturing text from those pictures. There might be circumstances in which we need to duplicate certain data as text in a troublesome archive, photograph, or video. Moreover, light and shooting point can create twisted situation text in pictures. In this way, scene text extraction turns into a difficult and requesting research issue [7].

Conventional approach and deep neural network based approach are the two kinds of approaches to this tasks of text detection. The state of art techniques based on either approach are tedious and not ideal because of the utilization of different stages and parts all the while. Maximally Stable Extremal Regions (MSER) [8, 9] and Stroke Width Transform (SWT) comes under the category of conventional method [10]. These strategies for the most part use extremal district detection or edge detection to look for competitor characters in an image. The authors in [11] proposed a methodology that was focused on clustering method and strictly dependent on density values for the division of candidate characters by consolidating shading highlights of character pixels and spatial network. Authors in [12] proposed three content extraction procedures for normal scene pictures that depended on the force data of the info picture. The first method is "Gray Value Stretching" that includes binarization of the picture by computing the normal force of the relative multitude of pixels. The subsequent procedure presents the "Split and Merge" approach, which is a famous calculation for picture division. The third procedure is designed from the combination of the initial two strategies.

Further to tackle the "dubious" example of scene text [13] proposed a text detection strategy consolidating a few highlights like tone, spatial layout, texture and insights on OCR results. Similarly, [11] used edge detection and color enhancement technique to identify text regions. However, the machine learning model would provide us with more accurate results as the learning through machine centers around creating PC calculations, which can get to information and learn on their own. Significant results have been delivered by the researchers, however the best result accomplished till date is as yet not so extraordinary and still there is a scope of improvement.

The principle purpose behind accomplishing this work is to compare the accuracies of the Machine Learning models, particularly, MLP and TensorFlow architectures. The machine learning model uses pre-data to predict the outcomes, in this case, to predict the characters. By increasing the capacity of the dataset, it can increase the efficiency of prediction from troublesome photographs. Text detection is a widely researched domain, many researchers have worked on it by implementing newer technologies ever since. The paper is coordinated as follows. Section 1 sums up the issues and the advancement made during the previous decade. Section 2 gives a brief description of the problem that is going to be discussed through this research paper. Various tools used by the authors are highlighted in Sect. 3, and how these tools are implemented are discussed under Sect. 4. In Sects. 5, 6 and 7 results, limitations and applications are discussed. In Sect. 7, conclusion of the research paper has been summarized.

2 Problem Statement

Albeit the recognition of text can be utilized in abundant applications, the principal target is to make a decision on text embedded in a given picture. On confirmation, the other tasks are localization and recognition of the text. In the writing, different phases of these crucial assignments are alluded to by various names including text localization [14], which plans to decide the picture places of candidate text, text detection, which decides if there is text utilizing localization and verification techniques, and text information extraction [15, 16], which centers around both localization and binarization. Tasks, for example, enhancement of text are utilized to correct misshaped message or improve goal preceding recognition. Different references incorporate scene text recognition [17] and text recognition in the wild [18], which limit examination of pictures to text in regular scenes. At the very least the essential objectives of text detection, localization and recognition are fundamental for a "start to finish" framework.

3 Description of Tools

The authors have used various tools to pre-train the machine learning model and a synopsis of each tool is presented below:

Anaconda: Anaconda is an open-source distribution of the Python and R programming languages for logical processing that intends to improve on bundle the executives and sending.
Jupyter Notebook: The Jupyter Notebook is an open-source web application that licenses you to make and share records that contain live code, conditions, portrayals and story text.
OpenCV: OpenCV (*Open Source Computer Vision Library*) is a library of programming capacities primarily focused on constant PC vision.

3.3.1 **Imagio**: Imageio is a Python library that gives a basic interface to examine and make a wide extension out of picture data, including breathed life into pictures, volumetric data, and consistent courses of action.
findcontours(): This function helps in extracting the contours areas from the input image.
IDX: The motivation behind this capacity is to streamline removing properties from a chain of possibly composed properties.
TensorFlow: TensorFlow is a free and open-source programming library for machine learning. It might be used over an extent of endeavors yet has a particular focus on getting ready and acceptance of significant neural associations. TensorFlow is an agent numerical library reliant upon dataflow and differentiable programming.

4 Implementation

The research work has been done in the Anaconda environment under Jupyter Notebook interface. There are basically three sections by which the machine learning models predict the characters. Figure 1 depicts the flowchart of the complete work. First step is about creating a dataset in IDX file format from raw photographs or video frame. The image used in this work is a page from a novel "Percy Jackson". Second step is about creating train and test data from the dataset. Step 3 deals with predicting the characters by applying machine learning models on the dataset. Figure 1 represents the flowchart indicating the process used in text prediction technique.

Dataset creation is an important step in machine learning and Fig. 2 represents the process to create dataset.

Figure 3 gives the overview of result obtained for step "how to binarize the image". Firstly, the detection starts with converting the image from 'RBG' i.e., Red Blue Green to 'GREY' color. This is done by using the CV.color() function. CV. adaptiveThreshold() function is also used to get the threshold value and change the color to 255. The pictures below depict how the image is transformed to grey and then binarized. Secondly, the extraction of a character is done by using findcontours() function which analyzes the image to find contour colors.

The contour of boundaries of characters are not so efficient that the findcontours() does not recognize them. To avoid this, adjusting all the non-zero pixels to the highest possible contour, which is black color (255), provides more accurate results. The next step is to save the extracted character as a separate image in any image format. After all the characters have been saved in a folder, clustering should be done. Clustering can be done either manually or by using K-means clustering method. Once the grouping is completed, the created data should be converted into a compatible format for use in machine learning models. The IDX tool module converts the data into IDX format dataset wherein a list of file's name is created alongside with their file.

Fig. 1 Flowchart for text prediction process using machine learning model

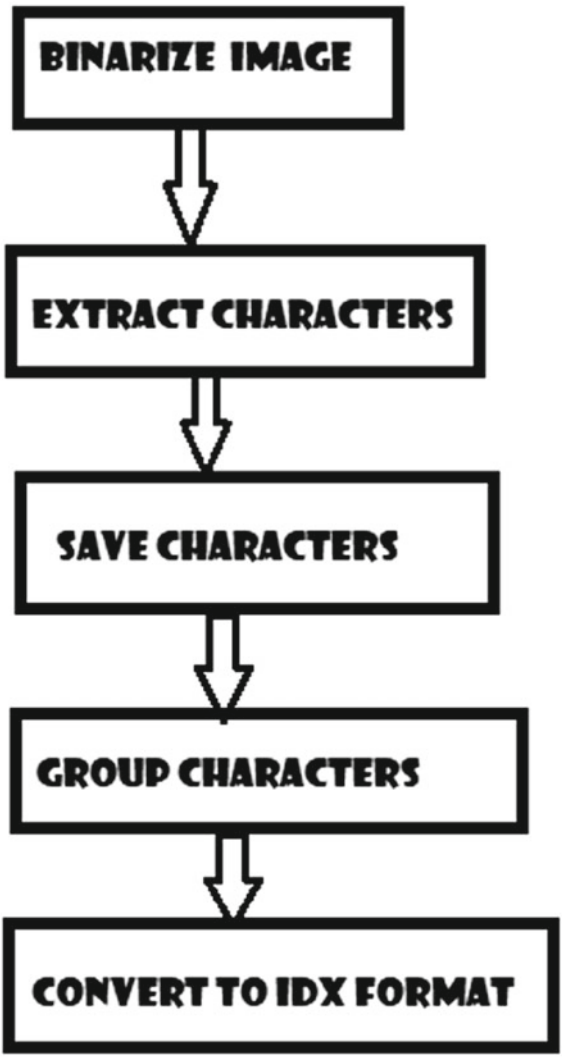

Fig. 2 Flowchart that depicts the process to create the dataset

Once the dataset is available in a usable format, it is divided into train and test data with 0.7 ratio. It means that out of 10 images from a file, the model trains on 7 images and predicts the result on the remaining 3 images. Finally, by using the MLP architecture and TensorFlow architecture, models have been created to predict the characters.

Fig. 3 Sample image chosen to create dataset

5 Results and Analysis

Precision Rate and Recall Rate are the two factors which broadly find their usage to quantify the execution of the calculation in the assignment of text extraction. Whereas precision rate is the ratio of the quantity of accurately identifiable words to the amount of the quantity of effectively recognized words and false positives, on the other hand, the recall rate represents the quantity of effectively recognized words to the amount of the quantity of accurately distinguished words and false negatives.

False positive can be defined as the locales of the picture that don't contain any text yet at the same time have been perceived by the calculation, on the contrary false negatives are the districts of the picture that do really contain text yet haven't been perceived by the calculation.

This methodology can likewise be utilized for singular characters instead of words, if the picture doesn't contain total words. These amounts are determined to decide the effectiveness of the calculation.

The proposed OpenCV execution has been turned out to provide precision rate of 95.2% with recall rate of 70.6%. This suggests that the model is equipped with providing less false positives.

From Figs. 4 and 5, it has been shown that MLP architecture scored 100% accuracy whereas TensorFlow architecture scored 99.8% accuracy respectively. From the image, the number '9' was faulty detected or was confused thinking it as an alphabet 'g' wherein, both the characters look similar in this particular font style. The same difficulty arrives with the number '6' and the alphabet 'b' which are also similar to each other.

Some of the pictures that the calculation created are shown in Fig. 6. The bounding boxes around the content are precisely created, and the calculation likewise performed well on noisy/disturbed pictures.

```
print('Test accuracy:', test_acc)
53/53 [==============================] - 1s 9ms/step - loss: 1.2349e-07 - accuracy: 1.0000
Epoch 193/200
53/53 [==============================] - 1s 10ms/step - loss: 1.1807e-07 - accuracy: 1.0000
Epoch 194/200
53/53 [==============================] - 0s 9ms/step - loss: 1.1742e-07 - accuracy: 1.0000
Epoch 195/200
53/53 [==============================] - 0s 9ms/step - loss: 1.1535e-07 - accuracy: 1.0000
Epoch 196/200
53/53 [==============================] - 1s 9ms/step - loss: 1.1050e-07 - accuracy: 1.0000
Epoch 197/200
53/53 [==============================] - 0s 9ms/step - loss: 1.0793e-07 - accuracy: 1.0000
Epoch 198/200
53/53 [==============================] - 0s 9ms/step - loss: 1.0500e-07 - accuracy: 1.0000
Epoch 199/200
53/53 [==============================] - 0s 9ms/step - loss: 1.0265e-07 - accuracy: 1.0000
Epoch 200/200
53/53 [==============================] - 0s 9ms/step - loss: 9.8865e-08 - accuracy: 1.0000
23/23 [==============================] - 0s 4ms/step - loss: 4.2086e-07 - accuracy: 1.0000
Test accuracy: 1.0
```

Fig. 4 Result obtained using MLP architecture

```
print(score)
Epoch 195/200
14/14 [==============================] - 38s 3s/step - loss: 0.0439 - accuracy: 0.9928 - val_loss: 0.0094 - val_accuracy: 0.9
986
Epoch 196/200
14/14 [==============================] - 38s 3s/step - loss: 0.0361 - accuracy: 0.9940 - val_loss: 0.0092 - val_accuracy: 0.9
986
Epoch 197/200
14/14 [==============================] - 38s 3s/step - loss: 0.0354 - accuracy: 0.9982 - val_loss: 0.0092 - val_accuracy: 0.9
986
Epoch 198/200
14/14 [==============================] - 39s 3s/step - loss: 0.0326 - accuracy: 0.9928 - val_loss: 0.0091 - val_accuracy: 0.9
986
Epoch 199/200
14/14 [==============================] - 39s 3s/step - loss: 0.0349 - accuracy: 0.9946 - val_loss: 0.0088 - val_accuracy: 0.9
986
Epoch 200/200
14/14 [==============================] - 38s 3s/step - loss: 0.0331 - accuracy: 0.9952 - val_loss: 0.0087 - val_accuracy: 0.9
986
[0.00866128783673048, 0.9985994100570679]
```

Fig. 5 Result obtained using TensorFlow architecture

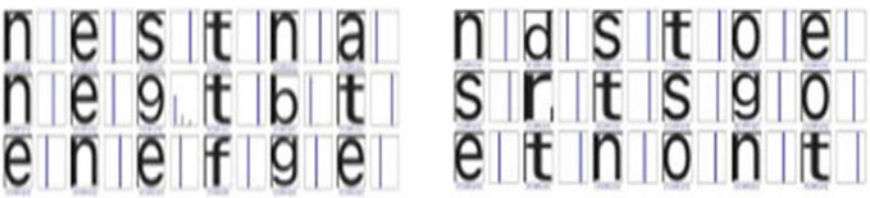

Fig. 6 Transformation of images into useful dataset

6 Limitations

After extracting the character images, the alphabets (small L) ‘l’ and (Capital i) ‘I’ are almost similar, in fact same, where the problem arises to distinguish between them.

While Extracting the characters, findcontours() function could not properly detect a few alphabets, particularly, 'i' (small i) and 'j' (small J). This is because of the gap between the dot and body part of the alphabet. The findcontours() function detects those alphabets as a separate body and separate dot rather than detecting them combined. There are two ways to solve this difficulty.

A. Firstly, the dimensions of the dot must be known. Whenever a rectangle with a 'dot' dimension occurs, add the y-axis dimensions to the body rectangle, so that an extra area will be detected. Obviously, the dot rectangle will be ignored and will not be extracted. The image, hence, detected will be a combined image.
B. By detecting adjacent contours in y-axis direction and combining both the bounding areas into one box which then gets extracted as a whole. Thus, solving the problem.

Both the models are limited to a particular font type. Applying the model on other fonts, fails it completely.

7 Conclusion

This paper has portrayed issues identified with programmed text discovery and image recognition. It begins with literature survey, comprises of various approaches and problems in the past ten years and shown execution for the most representative approaches as per the problem identified. In a decade ago, research in this field has advanced hugely as novel and improved strategies arise. Nonetheless, the end-to-end encryption execution shows that sufficient room stays for future research, which raises the further analysis for future scope. Here, the essential interface of OpenCV is written in python. The coding part has been performed using the Jupyter notebook interface. Python is a simple and user-friendly programming language which contains many in-built library functions. In this paper, a Machine Learning model along with OpenCV, matplotlib, IDX, TensorFlow, and imagio libraries have been used to detect, extract, save and learn the characters and achieve desired output. We have presented an enhanced way to increase the efficiency of findcontours () function by individually detecting the pixel's color and adjusting it to either complete white or black color. The IDX module has been used to convert the dataset into a usable dataset for machine learning models. The complete accuracy was achieved from MLP architecture whereas close to complete accuracy was achieved from TensorFlow architecture wherein the alphabets "I" and "l" were excluded from the initial dataset.

References

1. Goel V, Kumar V, Jaggi AS, Nagrath P (2019) Text extraction from natural scene images using OpenCV and CNN. Int J Inf Technol Comput Sci (IJITCS) 11(9):48–54. https://doi.org/10.5815/ijitcs.2019.09.06
2. Epshtein B, Ofek E, Wexler Y (2010) Detecting text in natural scenes with stroke width transform. In: Proceedings of 2010 IEEE conference on computer vision and pattern recognition, pp 2963–2970
3. Baydin AG, Pearlmutter BA, Radul AA, Siskind JM (2018) Automatic differentiation in machine learning: a survey. J Mach Learn Res 18:1–43
4. Sahare P, Dhok SB (2017) Review of text extraction algorithms for scene- text and document images. IETE Tech Rev 34(2):144–164. https://doi.org/10.1080/02564602.2016.1160805
5. Panhwar MA, Memon KA, Abro A, Zhongliang D, Khuhro SA, Memon S (2019) Signboard detection and text recognition using artificial neural networks. In: 2019 IEEE 9th International conference on electronics information and emergency communication (ICEIEC), Beijing, China, pp 16–19. https://doi.org/10.1109/ICEIEC.2019.8784625
6. Zhang H, Zhao K, Song YZ, Guo J (2013) Text extraction from natural scene image: a survey. Neurocomputing 122:310323
7. Liu X, Lu K, Wang W (2012) Effectively localize text in natural scene images. In: 21st International conference on pattern recognition (ICPR), November 11–15, 2012, Tsukuba, Japan
8. Matas J, Chum O, Urban M, Pajdla T (2002) Robust wide baseline stereo from maximally stable extremal regions. British Mach Vis Conf 1:384–393
9. Mikolajczyk K, Tuytelaars T, Schmid C, Zisserman A, Matas J, Schaffalitzky F et al (2005) A comparison of affine region detectors. Int J Comput Vis 65:43–72
10. Epshtein B, Ofek E, Wexler Y (2010) Detecting text in natural scenes with stroke width transform. In: CVPR
11. Yi C (2010) Text locating in scene images for reading and navigation aids for visually impaired persons. In: Proceedings of ASSETS, USA, pp 325–326, Oct. 25–27, 2010
12. Kim J, Park S, Kim S (2005) Text locating from natural scene images using image intensities. IEEE
13. Ye Q, Jiao J, Huang J, Yu H (2007) Text detection and restoration in natural scene images. J Vis Commun Image Represent 18(6):504–513
14. Lienhart R, Wernicke A (2002) Localizing and segmenting text in images and videos. IEEE Trans Circuits Syst Video Technol 12(4):256–268
15. Jung K, Kim KI, Jain AK (2004) Text information extraction in images and video: a survey. Pattern Recogn 37:977–997
16. Zang J, Kasturi R (2008) Extraction of text objects in video documents: recent progress. In: Proceedings of IAPR international workshop on document analysis systems, pp 5–17
17. Weinman JJ, Learned-Miller E, Hanson A (2009) Scene text recognition using similarity and a lexicon with sparse belief propagation. IEEE Trans Pattern Anal Mach Intell 31(10):1733–1746
18. Wang T, Wu DJ, Coates A, Ng AY (2012) End-to-end text recognition with convolution neural networks. In: Proceedings of IEEE international conference on pattern recognition, pp 3304–3308

Enhanced WSN-Based Automatic Temperature-Controlled and Data Storing Fan System with LabVIEW

T. H. Mujawar, J. Akhtar, and L. P. Deshmukh

Abstract The standard instruments have promising insufficiency and momentously needs to be sophisticated today. The present system uses wireless sensor networks, virtual instrumentation and control of temperature for exact set point temperature. The aim of this paper is to shove and refurbish the old speed control system by wirelessly automatic controlled temperature. This paper narrates a wireless temperature monitoring and control system which persistently examines the temperature within room and pedals the similar by triggering a fan. This paper depicts the devise and expansion of an impartial automatic fan speed controller that reins the speed of electric fan according to the temperature read by a LM35 sensor. This premeditated and developed system wields two motes and one sink node which makes the feedback control system proficient and unswerving. The major aspire of the device is to automatically read and regulate the temperature within the room and send this information to the sensor node to display it on LCD. Lastly, all this information is sent to the gateway node and displayed on the front panel of LabVIEW. The graphical temperature chart is displayed on the PC, and data acquirement consequences are stored in PC for export into Microsoft Excel. This system is portable to use with a superior quality GUI and operates automatically for short distance.

Keywords Wireless sensor networks · LabVIEW · Automatic control · Data storage

T. H. Mujawar (✉)
Department of Electronic Science, School of Physical Sciences, Punyashlok Ahilyadevi Holkar Solapur University, Solapur, Maharashtra 413255, India
e-mail: thmujawar@sus.ac.in

L. P. Deshmukh
Department of Electronic Science, Savitribai Phule Pune University, Pune, Maharashtra 416007, India

J. Akhtar
Department of Electronics & Communication Engineering, School of Electrical, Electronics & Communication Engineering, Manipal University, Jaipur, Rajasthan 302034, India

S. Dwivedi et al. (eds.), *Flexible Electronics for Electric Vehicles*, Lecture Notes in Electrical Engineering 863, https://doi.org/10.1007/978-981-19-0588-9_2

1 Introduction

An encroachment in the technology leads to the development of intelligent systems. All is being paid more sophisticated and comprehensible and therefore needs to be developing a cost-effective and highly efficient method. The proposed method is also an extremely efficient and applicable due to the use of wireless sensor networks.

Wireless sensor network has been revolutionized in the pasture of monitoring and remote sensing. It can gather information from different sensors from inaccessible destinations and considerately pass this through the sensor node to the coordinator node [1]. Consequently, monitoring of data from long distance is smoothly possible using wireless sensor networks [2, 3]. The proposed WSN-based system consists of two sensor nodes (motes) and one coordinator node. The sensor node uses XBee for wireless communication, Arduino microcontroller for computing and taking logical decisions, LM-35 temperature sensor and 9 V power supply subsystem. XBee is a feature-rich RF module that holds up a variety of communication protocols and superior resolution for WSN; the IEEE 802.15.4 protocols on the modules can extensively ease the effort taken by the programmer for ensuring data communication. Moreover, this module provides the facility of UART serial communication to communicate with Microcontroller; some additional pins in it help to create XBee standalone applications, e.g. a router node can be developed exclusively of a microcontroller.

Microcontroller plays a significant role to expand the elegant electronic gadgets. It is a single chip used for control and computerization purpose of technology and processors. This paper presents imitation of fan speed control using LM-35 sensor. The LM-35 has been used to measure the temperature, and rate of fan varies with respect to the temperature reading using PWM technique. The microcontroller compares the current temperature with set temperature based on in-built algorithm of an Arduino. The result obtained from the process is given through the output port of an Arduino board to LCD display and finally to the front panel of LabVIEW [4]. Owing to the sophisticated technologies, all the electronic systems are becoming with compact extent and an elegant effective. Old fan speed is determined manually and requires energy to manage its speed. Therefore, it needs to be improved. Accordingly to reduce the user's energy and time consumption in controlling the speed of fan, an automatic temperature-controlled fan using WSN is designed. This application can be used in home and industry. It can also be implemented for several applications together with air conditioners, water heaters, ovens, incubators, thermal baths, etc. This system will help to save energy/electricity. In this technique, the temperature can amend the speed of fan apart from varying the speed of fan by manually. Subsequently, it is needed to build wireless automatic temperature-controlled fan system. The WSN with a star topology is chosen here because the sensor nodes are powerfully grouped mutually and they communicate individually with coordinator node. This topology ensures the individual motes to save the battery power. Therefore, star topology helps to save the energy amongst the sensor nodes. The mining of the data gathered from WSN is important because this data is extensive in a real-life

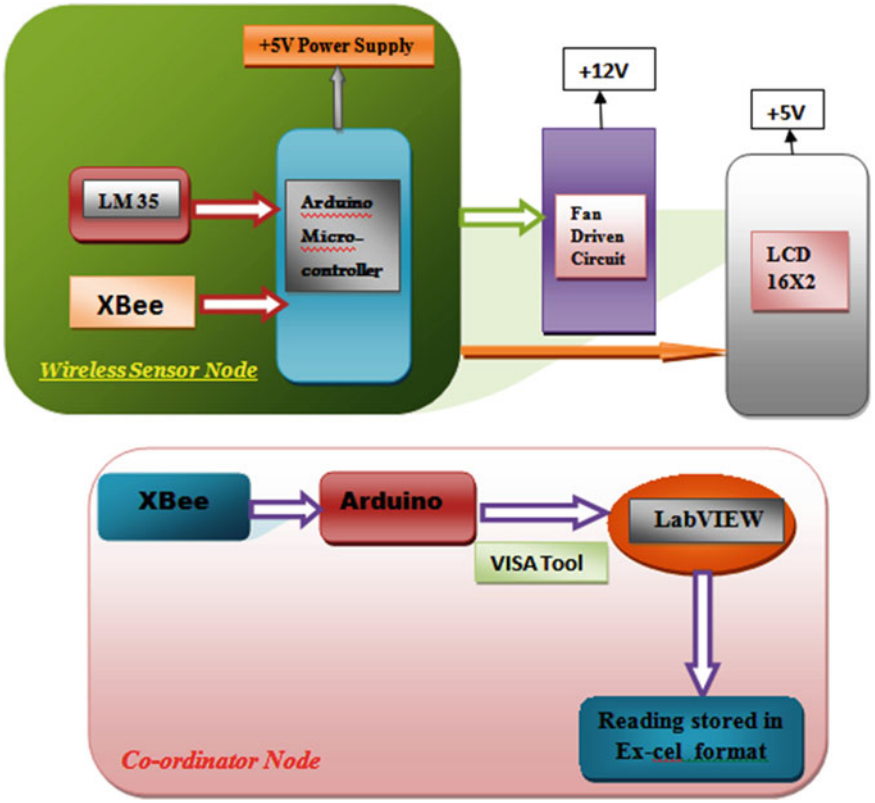

Fig. 1 Block diagram of the system

situation. Our endeavour is to design and develop a wireless automatic temperature-controlled fan system, an application that would be developed and experienced in order to monitor and control the temperature within the room using WSNs. The block diagram and circuit diagram of the system are shown in Figs. 1 and 2.

2 Working of the Proposed System

We developed a LabVIEW and WSN-based temperature measurement and monitoring system. The block diagram of the proposed system is as shown in Fig. 1. The sensor node of the present system intended with following subsystem.

- Sensing subsystem—LM-35 sensor
- Computing subsystem—Arduino microcontroller
- Communication subsystem—XBee
- Power supply subsystem—+5 and +12 V power supply.

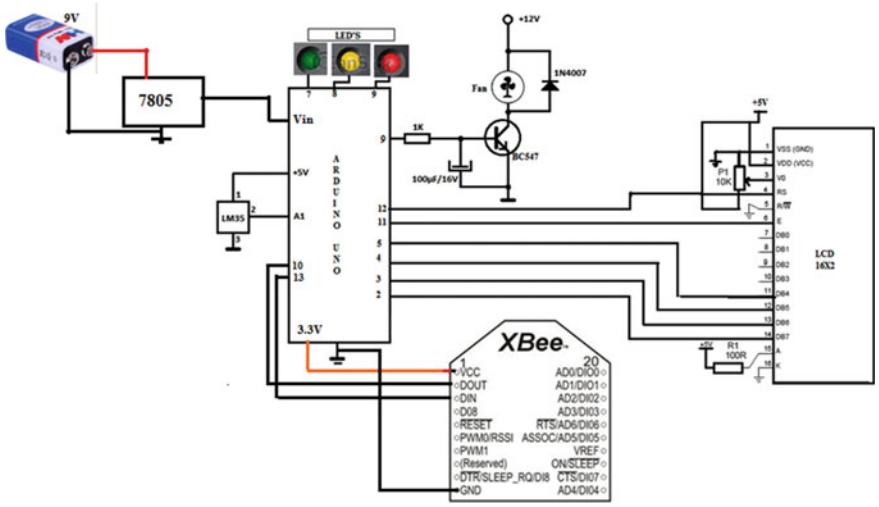

Fig. 2 Circuit diagram of the sensor node

All these subsystems are described individually. This system intended with XBee, microcontroller, fan, temperature sensor, LCD and a DC motor [5]. The LM-35 is used as temperature sensor. This LM-35 produced voltage in terms of mV range (10 mV/°C).

The augmented output of the LM-35 is given to the analog input A1 of the Arduino microcontroller. Arduino will interpret the analog signal from this LM-35 sensor. By the use of in-built analog to digital converter (ADC), it will convert it to digital form.

Consequently, the comparison between current temperature and set temperature is performed by microcontroller as per the logic of the program. The outcome getting from this is given through the pins 5, 4, 3, 2 of an Arduino microcontroller to the LCD display of an appropriate data and resulting pulses fed to the driver circuit to obtain the desired output to fan (Fig. 3).

All these results are wirelessly sent to the gateway node through XBee. The Arduino linked to the gateway node that runs the LabVIEW program. This LabVIEW code converts the binary equivalent signals to algebraic value legible by the users. The LabVIEW acts as the user interface between PC and gateway node to monitor the temperature continuously [6]. When the precise temperature is above or below the preferred temperature, according to that fan speed changes shown by interactive GUI developed in LabVIEW. Three conditions are displayed on front panel of LabVIEW and also LCD. There are three LEDs that are used for indicating the result. Green LED indicates that the temperature level is COOL and fan will be in off condition. When temperature level goes to NORMAL, i.e. between 26° and 30°, the yellow LED is turned on, other two will be in off condition, and fan speed will be 60. When temperature goes above 35°, then it will consider as a HOT temperature, red LED

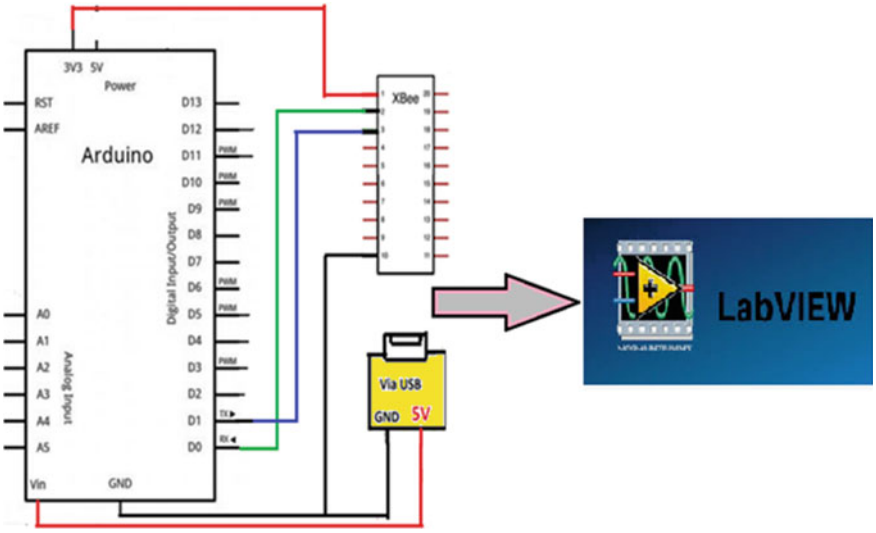

Fig. 3 Circuit diagram of the coordinator node

is turned on, and fan speed will be 90. The pictorial representation of the proposed system for displaying data on LCD is described in Fig. 4.

3 Hardware Implementation of the System

The hardware interface is an important aspect that will manage the input and output of a system. The hardware implementation of a system is represented in Fig. 5.

3.1 LM-35

LM-35 is an analog temperature sensor. According to the circuit diagram, we have connected V_{out} of LM-35 to A1 of arduino (Fig. 6).

Fundamentally, LM-35 is pre-calibrated in degree Celsius to be used for temperature sensor IC. It is approximately linear in characteristics. It does not require any external calibration and gives +10-mV/°C scale aspect [7]. According to that, Arduino programming is done, and its consequences are displayed on Arduino serial monitor window (Fig. 7).

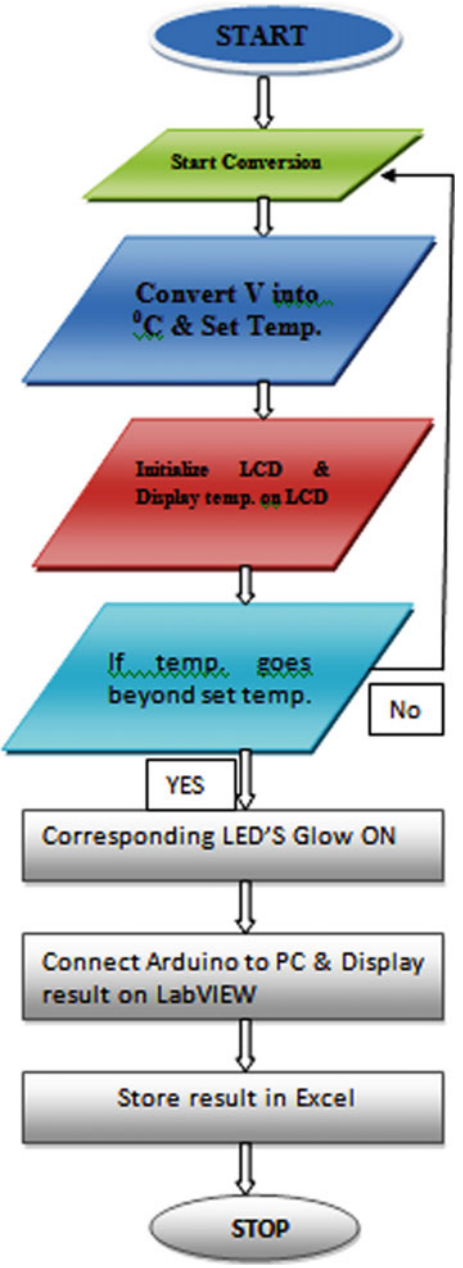

Fig. 4 Flowchart representation of a system

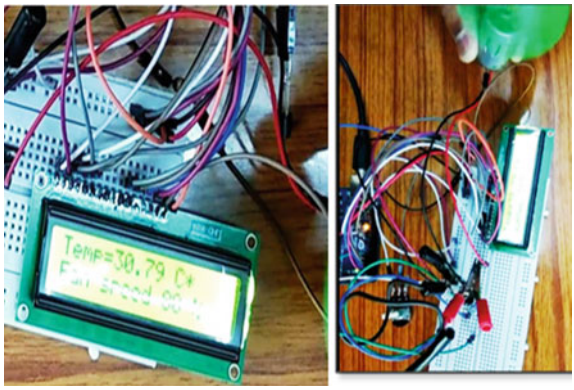

Fig. 5 Hardware implementation of the system

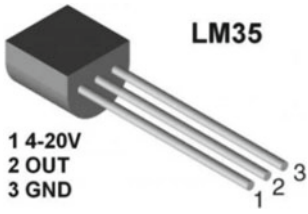

Fig. 6 LM-35

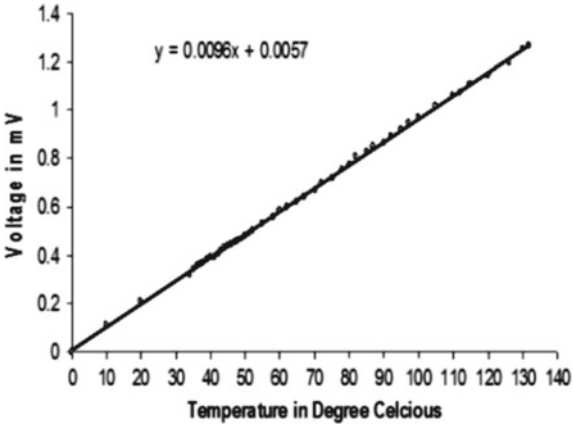

Fig. 7 Characteristics curve of LM-35

3.2 Fan Drive Circuit

The proposed system uses the following fan with operating temp—10 to 75 °C. Its rated speed and voltage is 1000 RPM and 2–12 V. The maximum air flow capacity of this fan is 45 CFM. The fan drive circuitry is explained in Fig. 8. This system uses the transistor BC547 to drive the fan. Depending upon the type of fan, the transistor

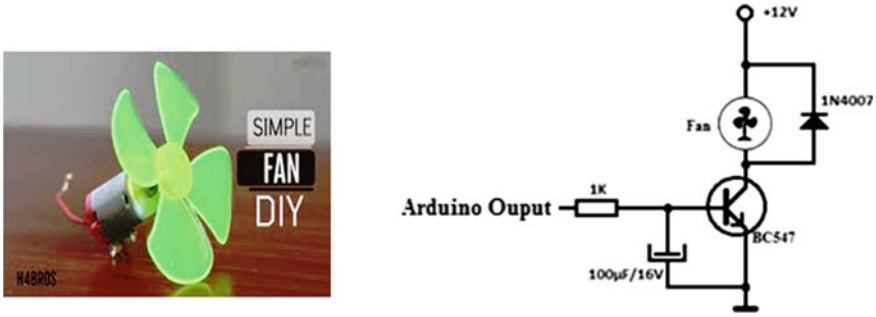

Fig. 8 Fan drive circuit

may vary. The system uses a 12 V battery to provide power to the fan and transistor. The LM35 sensor and led are powered with 5 V from the Arduino board.

3.3 Arduino

Microcontroller is a preeminent ingredient of the hardware interface which can read sensor's value and makes the logical decision for further action. There are copious microcontroller existing in marketplace resembling Arduino, ARM, PIC, Raspberry Pi and so forth. Nevertheless, Arduino is a most excellent alternative because of its open-source platform, user friendly and companionable to LabVIEW via an apt driver. *Arduino boards* are able to read inputs—light on a sensor, a finger on a button, or a Twitter message—and turn it into an output—activating a motor, turning on a LED and publishing something online. All this is defined by a set of instructions programmed through *the Arduino software (IDE)*. The software of Arduino platform is the Arduino Integrated development environment (IDE) [8] (Fig. 9).

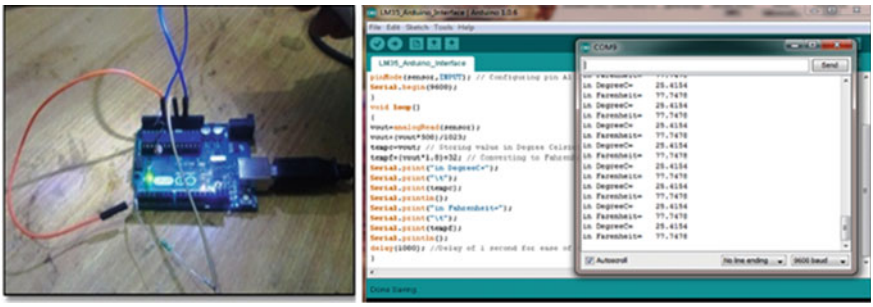

Fig. 9 LM-35 interfacing to Arduino UNO and its result on serial monitor window

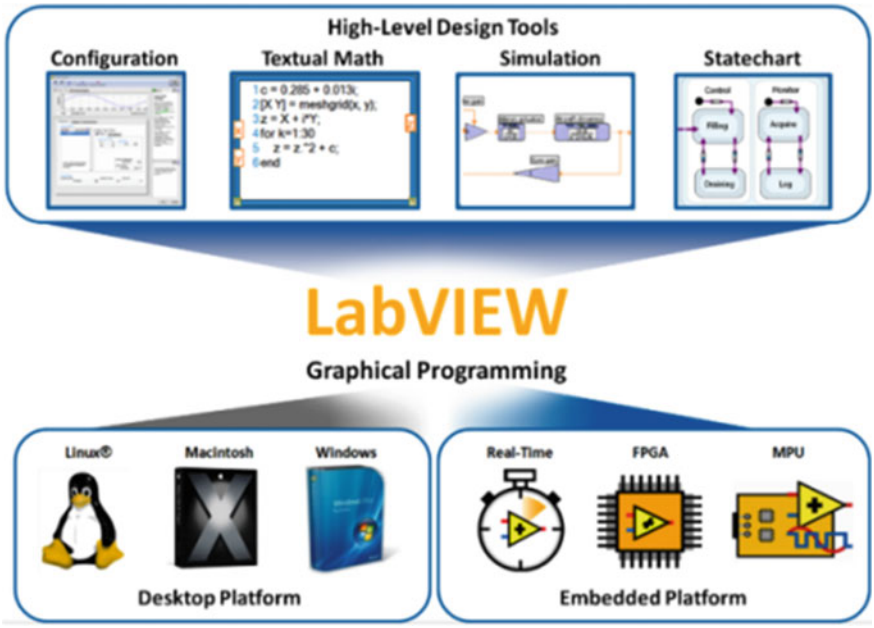

Fig. 10 LabVIEW [https://www.lcm.at/en/project/labview-ni-software/]

3.4 LabVIEW

Monitoring of all the hardware components is done through LabVIEW. LabVIEW is a dataflow model that uses graphical encoding language to inscribe an efficient code using a various tools available in it (Fig. 10).

The G-code formed by LabVIEW is more insightful to use than further programming languages [8, 9]. For execution of G-code in LabVIEW, compact time is required. Any mathematical difficulty can be solved rapidly without performing any complex matrix and calculations. Any multifunction code for carrying out on multicore processors can be done using NI's LabVIEW tool [10, 11]. Without knowing this multi-threaded language, anyone can do this programming using tools existing in LabVIEW.

For interfacing Arduino to LabVIEW, VISA function tool is used. There are three levels available for the VISA interface in LabVIEW, which are configured as serial port, VISA read and VISA closed. VISA configured serial port is the preliminary stage for initializing the serial ports specified by VISA resources. COM 22 has been chosen as the port, and baud rate of 9600 is elected. Final stage of VISA programming is to read the data from Arduino microcontroller. After the whole process is finished, then VISA is closed. VISA programming is shown in Fig. 11.

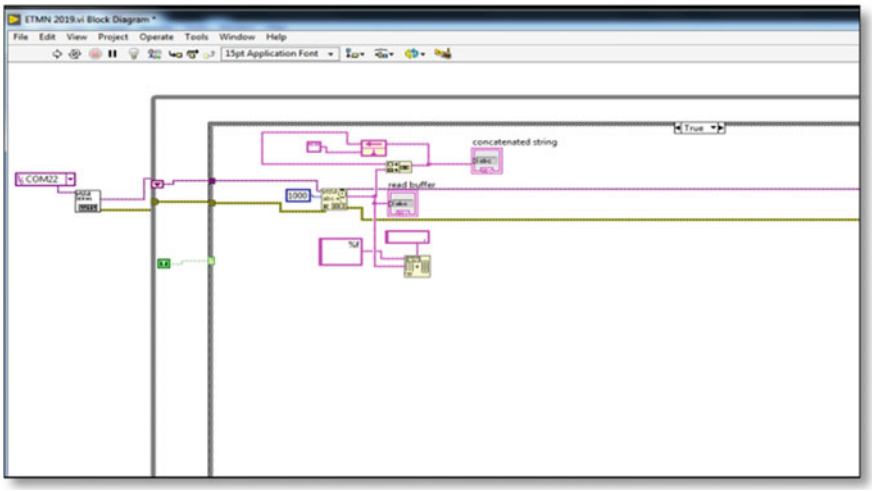

Fig. 11 VISA programming

4 Results

The Arduino programming for the proposed system is publicized in Fig. 12.

The results of this algorithm are depicted in serial monitor window and are revealed in Fig. 13.

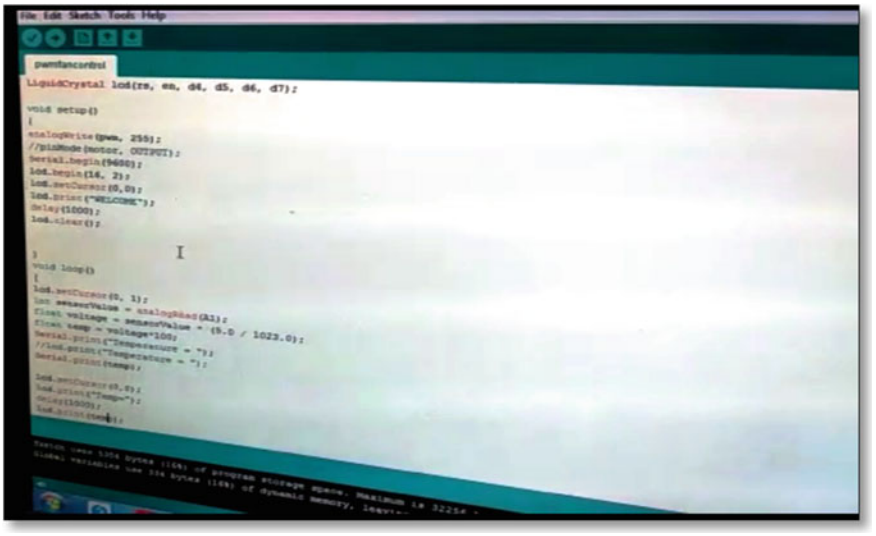

Fig. 12 Arduino programming for the proposed system

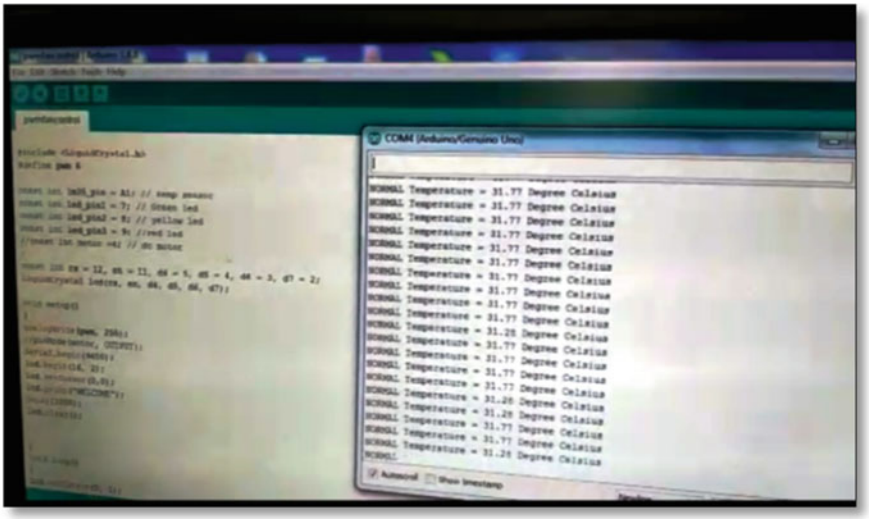

Fig. 13 Arduino programming result

An interactive and facile graphical user interface (GUI) is developed in LabVIEW to display the changes in temperature using a graph. The LabVIEW programming for the proposed system is shown in Fig. 14. The graphical user interface of the proposed system is shown in the following figures. It consists of LEDs, graphical

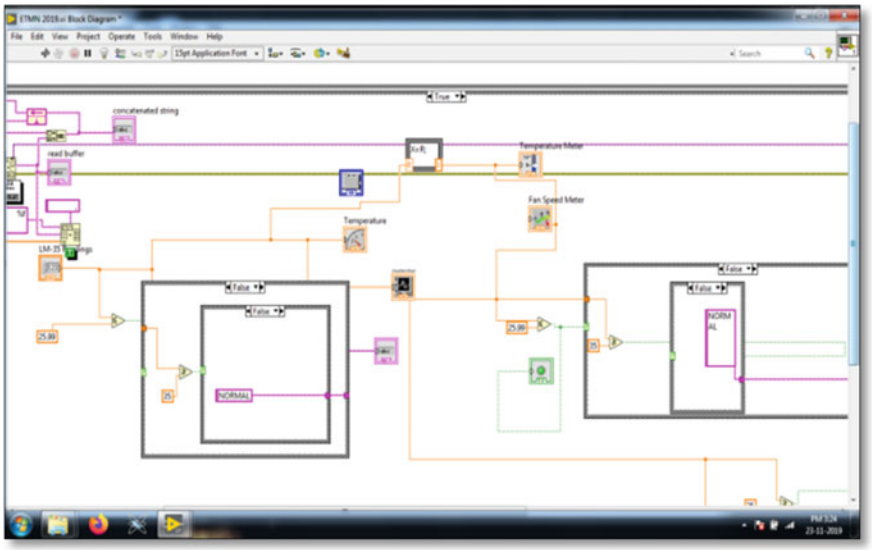

Fig. 14 LabVIEW programming

chart, VISA function tool, etc. As shown in Figs. 14, 15and 16, green colour LED indicates COOL level, and fan will be in OFF condition; whereas yellow colour indicates normal temperature level, and fan speed will be 60. While, red-coloured LED indicates a HOT temperature range, and fan speed will be increased up to 90.

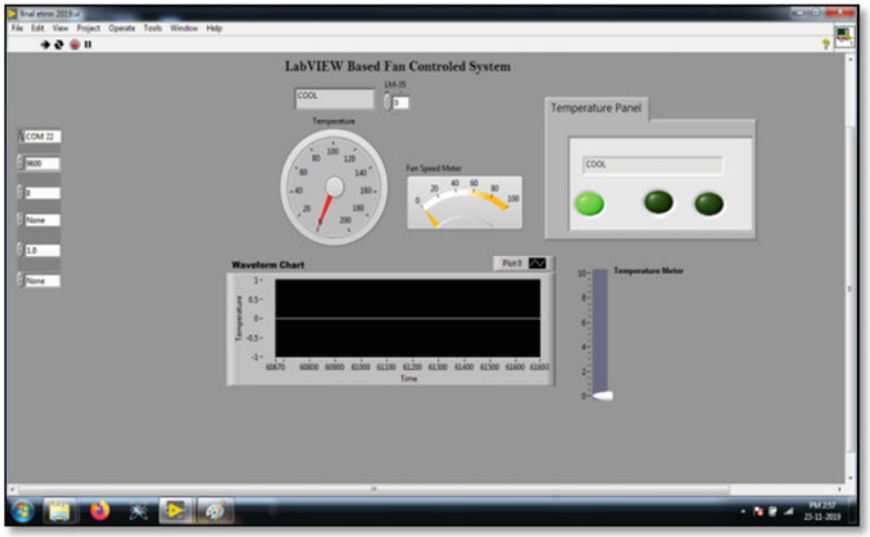

Fig. 15 COOL level measurement using LabVIEW

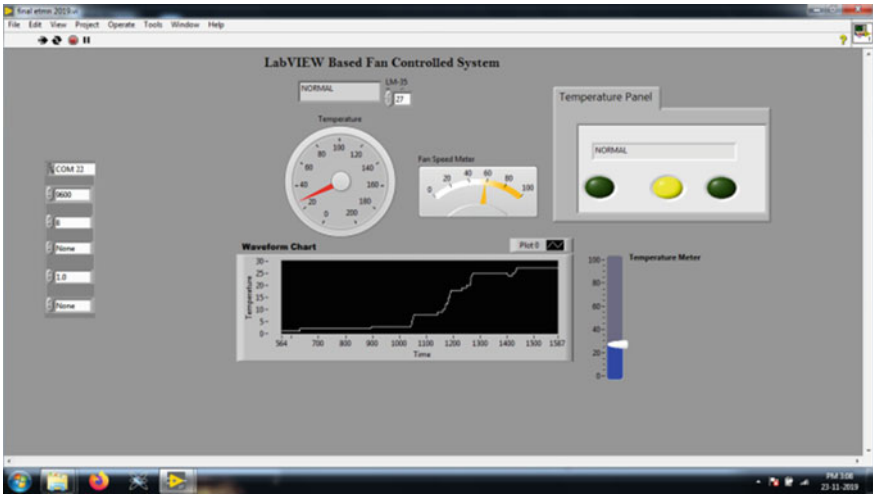

Fig. 16 NORMAL level measurement using LabVIEW

Table 1 Observations carried out during experiment

Time	Date	Temperature in 0 °C
8:05	01/01/2019	20
8:05	01/01/2019	21
8:05	01/01/2019	21
8:05	01/01/2019	21
8:07	01/01/2019	22
8:08	01/01/2019	20
8:08	01/01/2019	22
8:10	01/01/2019	21
8:11	01/01/2019	21
8:12	01/01/2019	22
8:14	01/01/2019	22
8:15	01/01/2019	22

The fan speed controls the temperature of the room. The virtual speed regulation of the fan is also depicted in Figs. 14, 15 and 16 (Fig. 17).

Table 1 and graph depict the temperature monitoring in 0 °C versus time, which was formed via a Microsoft Excel from the LabVIEW built-in export function. Testing was carried out from 8:05 am to 8:15 am by deploying this WSN-based sensor node and coordinator within a room, and corresponding readings were carried out as follows.

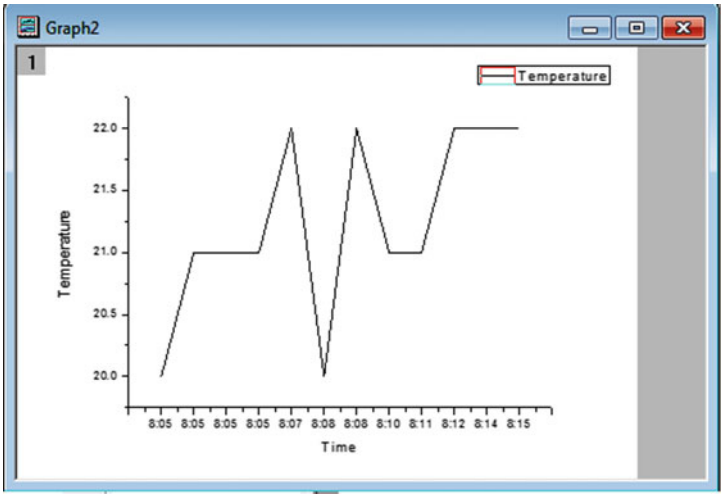

After exporting the LabVIEW data into the Excel sheet, we get results as shown in Fig. 18.

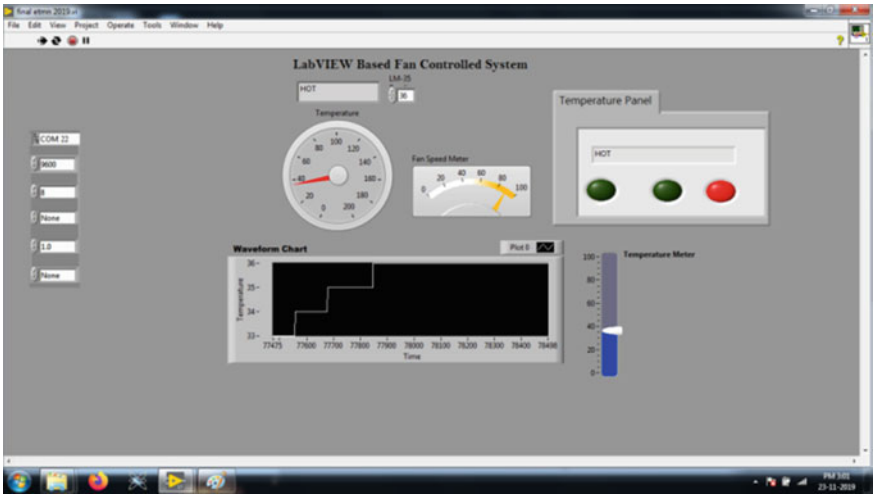

Fig. 17 HOT level measurement using LabVIEW

5 Conclusions

This system performs the virtual programming as well as Arduino programming for automatic temperature-controlled fan system. We have developed WSN and Arduino-based system successfully. The main aim of the system is to wireless automatic read and regulates the temperature within room by controlling the speed of the fan. The VISA tool in LabVIEW helps to reduce the extra hardware required for serial communication between Arduino and LabVIEW. The use of XBee protocol in motes offers an instantaneous monitoring with low data rate and least power consumption wireless communication technology. This system encompasses an immense acceptance in the industrial sectors and will accomplish an efficient amalgamation between WSN and fan drive system. Finally, all this data is displayed on front panel of the LabVIEW and stored it in Excel format.

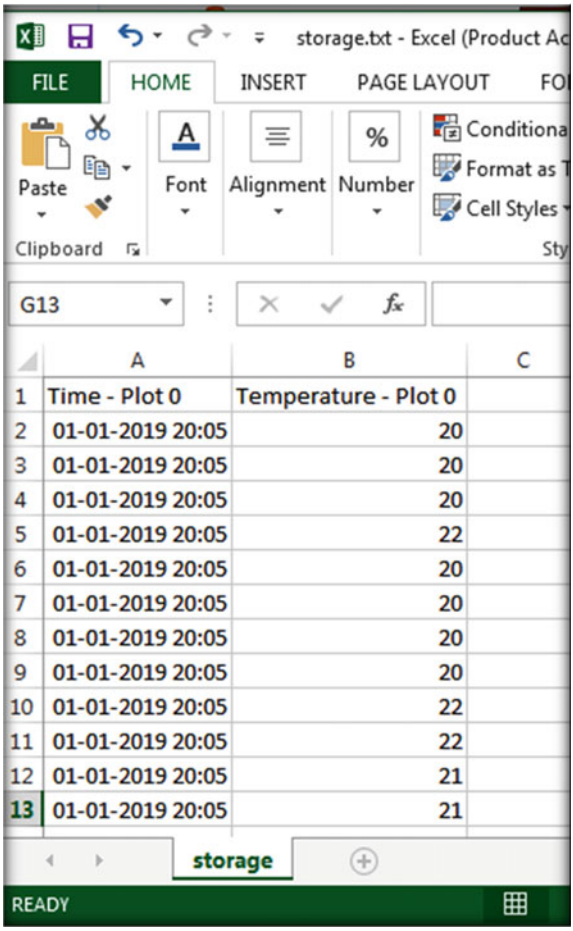

Fig. 18 Data storage in Excel

References

1. Xu H, Li F, Chen C, Dong X (2004) NOKIA mobile phone LCD module LPH7366 principle and its application. Foreign Electron Compon, pp 55–57
2. Dong W et al (2015) Mosaic: towards city scale sensing with mobile sensor networks. In: 2015 IEEE 21st International conference on parallel and distributed systems (ICPADS). IEEE, New York
3. Patel HR, Desai A, Upadhyaya T (2015) A discussion on electrically small antenna property. Microwave Opt Technol Lett 57(10):2386–2388
4. Ayuba Y (2016) Temperature control and data acquisition method for factory using LabVIEW. Int J Comput Eng Technol 7(2):1–14
5. Kumaran M et al (2018) Design of an automatic fan speed controlling system using arduino UNO. Int J Int Adv Res Eng Comp 06(02):2039–2042
6. Khan AA, D'Souza D, Auctioneering temperature control using LabVIEW. Int J Sci Eng Technol Res 6(11):1427–1429

7. Datasheets, “LM 35 Sensors”
8. Bitter R, Mohiuddin T, Narocki M (2001) LabVIEW advanced programming techniques. CRC Press LLC, Boca Raton
9. Mujawar TH (2014) Development of wireless sensor network for hazardous gas detection and alert system. http://www.shodhgang.inflibnet.ac.in
10. http://www.ni.com/labview
11. Mujawar TH, Kasbe MS, Mule SS, Deshmukh LP (1989) Online monitoring of WSN based air quality monitoring system. In: Emerging technologies: micro to nano (ETMN-2017), AIP Conference Proceedings 1989, pp 020030-1–020030-9

Resistive Random Access Memory: Materials, Filament Mechanism, Performance Parameters and Application

Neeraj Jain, Renu Kumawat, and Shashi Kant Sharma

Abstract Till today, we are using conventional technologies for memory-related applications. However, as the size of the electronic devices are shrinking day by day, such conventional memory devices will not be compatible with emerging applications like artificial intelligence, cloud storage, data mining, Internet of Things, etc. After the coronavirus outburst, these technologies are more needed as now all work is online. Henceforth, high data storage and fast information processing is one of the vital requirements which is to be researched. So, the researchers are now approaching the new memory technologies such as resistive random access memory (RRAM) which is superior than conventional memory devices in terms of scalability, speed, power consumption, design structure and many more other advantages. With all the pros, RRAM also has some cons like higher level of variability and reliability issues. So, to discuss all these issues, we present the basics of RRAM, their advantages, applications and technological trends in this manuscript.

Keywords RRAM · NVMs · Resistive switching mechanism · COVID-19

N. Jain
Department of Electronics and Communication Engineering, Manipal University Jaipur, Jaipur, Rajasthan 303007, India

Department of Electronics and Communication Engineering, Swami Keshvanand Institute of Technology, Management & Gramothan, Jaipur, Rajasthan 302017, India

R. Kumawat (✉)
Department of Computer and Communication Engineering, Manipal University Jaipur, Jaipur, Rajasthan 303007, India
e-mail: renu.kumawat@jaipur.manipal.edu

S. K. Sharma
Department of Electronics and Communication Engineering, Indian Institute of Information Technology, Ranchi, Jharkhand 834010, India

S. Dwivedi et al. (eds.), *Flexible Electronics for Electric Vehicles*, Lecture Notes in Electrical Engineering 863, https://doi.org/10.1007/978-981-19-0588-9_3

1 Introduction

After the COVID-19 pandemic, it is observed that the memory requirements for the applications like cloud computing, data mining, big data, Internet of Things, Artificial Intelligence, etc., have exponentially increased. Almost all the work is now online, and need for storage is increasing day by day. This cannot be fulfilled by the existing memory technology that is CMOS-based memories like Static Random Access Memory (SRAM), Dynamic Random Access Memory (DRAM), flash memory, etc. [1–5]. As these technologies have their own merits and demerits like DRAM type has high capacity and density but it is volatile in nature. On the other hand, SRAM has faster speed but it is volatile and has lower density. Flash memories are employed for large capacity and have non-volatile nature. These are slower than SRAM-based memories [6].

The information storage in memories has different approaches like a SRAM stores information on the nodes of cross-coupled inverters, a DRAM stores information by charging a capacitor, and a flash memory uses floating gates of transistor. As we see all these memory devices use charge-based approach to store the data which is limited by down scaling of transistors. Hence, the search for non-charge-based memories come in pace, and many researchers are working on it [2–5, 7].

Figure 1 shows the different type of charge and non-charge-based memories [6]. The Fig. 1 also depicts different type of non-volatile memories like Resistive Random Access Memory (RRAM), Ferroelectric Random Access Memory (FeRAM), Phase Change Random Access Memory (PCRAM), Magnetic Random Access Memory (MRAM) and Conductive Bridging Random Access Memory (CBRAM) [2–5, 8,

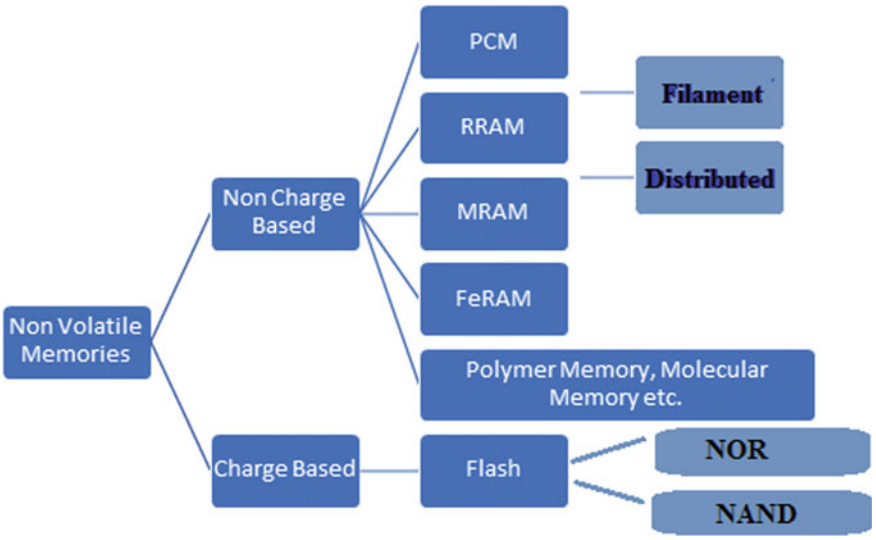

Fig. 1 Different type of charge and non-charge-based memories

9]. Among all these non-volatile memories, RRAM shows its great capabilities in memory sector as it is compatible with existing CMOS technology, consumes low power, scalable and has faster operating speed [10, 11]. So, because of all these advantages, there is extensive research going on RRAM with the focus of improving their performance and removing the limitation such as variability in material and circuit level. Table 1 lists down the performance comparison between different resistive switching memories [6]. With respect to the performance parameters listed in Table 1, the RRAM proves to be a better choice as compared to the other emerging memory devices like PCRAM, MRAM, FeRAM, CBRAM etc. Table 2 lists the comparison of existing and emerging memory technologies based on memory parameters.

In this manuscript, we present the recent research on RRAM with focus on the following aspects: materials used, operating performance/mechanism, performance parameters and their application prospects. This will be helpful for the new researchers as well as those who are already working in the area of RRAM. The

Table 1 Performance comparison between different resistive switching memories (Table BC2.6 in [6])

Parameter	FeRAM	PCRAM	MRAM	CBRAM	RRAM
Scalability	P	E	G	E	E
Multibit computing	P	E	P	E	G
Retention	G	G	G	G	E
Endurance	E	G	E	G	G
Power	E	P	G	E	G
3D Integration	P	E	G	G	E
Speed/latency	E	G	E	G	G
Variability	E	G	P	G	P

E *excellent*, G *good*, P *poor*

Table 2 Comparison of existing and emerging memory technologies

Parameter	Hard disk	DRAM	NAND flash	PCRAM	STTRAM	RRAM
Data retention	✔	X	✔	✔	✔	✔
Cell size (F = Feature Size)	Not applicable	6–10 F^2	4–6 F^2	4–12 F^2	6–50 F^2	4–10 F^2
Endurance	$>10^{15}$	$>10^{15}$	10^4–10^5	10^8–10^9	$>10^{15}$	10^{11}
Write/Read	5 ms/5 ms	50 ns/50 ns	500 us/25us	500 ns/50 ns	50 ns/10 ns	50 ns/10 ns
Standby power	Disk access mechanism	Refresh	X	X	X	X
Access granularity (B)	512	64	4192	64	64	64

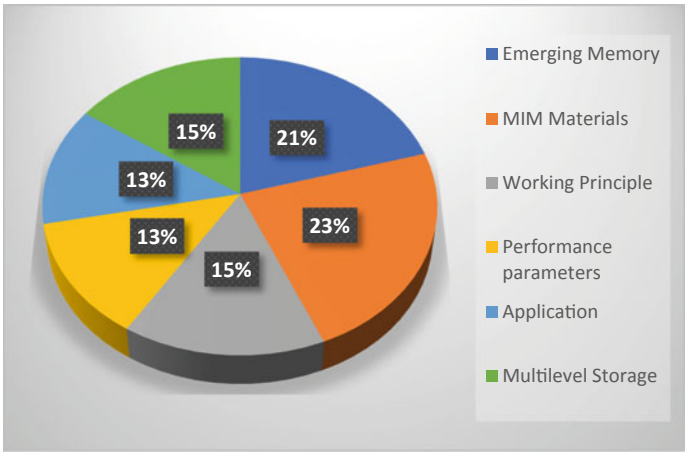

Fig. 2 Category-wise distribution of papers considered for preparation of the manuscript on RRAM

paper is organized as follows: In the Sect. 2, we have discussed the state-of-the-art work related to the materials used in constructing RRAM in past and recent years. In the next section, we have explained the operating principle of RRAM. In Sect. 4, we have discussed the performance parameters and listed different application of RRAM in Sect. 5. At last conclusion with future scope is presented Sect. 6. Figure 2 depicts the category-wise distribution of papers considered for preparation of the manuscript.

2 Material Used in RRAM

RRAM is based on the materials which show resistance change under electric field or current stimulus. These materials are divided into two types: organic and inorganic materials. Organic materials are mainly inspired by biology for example Parylene [12], albumen [13] etc., and there are others which are polymer-based organic materials like P3HT [14], "PVDR" (nano aggregated dispersed red 1-grafted poly (N-vinyl carbazole)) [15] etc. These materials have found application in wearable electronics and in monitoring devices for health diagnosis.

The search for inorganic materials started in early 1960s and the first such negative resistance change in material was demonstrated by Hickmott's [16] using thin oxide films such as SiO_2, Al_2O_3, Ta_2O_5, ZrO_2 and TiO_2 in a Metal-Insulator-Metal (MIM) structure. After his demonstration, the search for new materials by researchers came in pace, and in 1990s, materials like perovskite oxides such as Cr-doped $SrTi(Zr)O_3$, $PbZr_{0.52}Ti_{0.48}$ etc., were explored. But these were not found to be stable for memory applications. After that, in 2004, the oxide RAM based on binary transition metal

oxides [17] was developed. These were fully compatible with existing Complementary Metal Oxide Semiconductor (CMOS) technology, stable at 300 °C and voltage level below 3 V. This development filled the researchers with enthusiasm, and after 2004, other new materials were explored which include binary and ternary metal oxides, chalcogenides, nitrides, polymers and 2-D layered materials. The binary metal oxides like CuO_x, HfO_x, ZrO_x, etc., are mainly used because of their good compatibility with CMOS processes. Excellent endurance, high speed, low power and multi-level properties have been demonstrated in ZrO_2-based RRAM. For dielectric, in MIM structure, mainly transition materials are used. Complex oxides like $SrTiO_3$, $BiFeO_3$ etc. which have higher dielectric constants are also used, and they have improved the switching properties like ON/OFF ratio and voltage.

Now at present, as the device size is shrinking day by day, so low-dimensional material which has small size and excellent properties is now becoming a hotspot for research. The 2-D materials such as hexagonal boron nitride (h-BN) [18], graphene oxide (GO) [19], etc., are used. As compared to the traditional TMO-based resistive switching devices, these materials have low power consumption, reduced operating voltage, high endurance, a switching ratio of up to 10^9 etc. Table 3 shows the comparison of different MIM materials with performance parameters used for RRAM. This brief summery shows currently used materials for constructing RRAM. It is observed that further exploration as well as optimization is required in this field, so that we can replace the existing memory technologies with RRAM. The RRAM has potential to serve for the applications like cloud computing, neuromorphic logic, etc.

Table 3 Comparing performance parameters of MIM materials used for RRAM

Reference No.	MIM material	Resistance (OFF/ON)	V_{set}/V_{reset}	Endurance (Cycles)	Retention (S)	Compliance current (mA)
[20]	TiN/Hf/HfO_x/TiN	10^4	0.5/0.5	5×10^7	10^4	–
[21]	Ti/AlO_x/Ti	10^3	0.65/−1.1.5	75	10^3	50
[22]	ITO/aTiO_2/Pt	>10	0.6/−0.5	~NS	$<10^3$	0.2
[23]	Pd/HFO_x/Ag NP/TIN	10^3	5.25/2.2	$>1 \times 10^8$	$>10^4$	0.1
[24]	Al/V-doped SZO/$LaNiO_3$	10^7	7/2	50	10^6	1
[25]	Pt/parylene-C/W	–	3/−0.6	130	10^5	1
[26]	rGO/MoS_2 /ITO/SiO_2	10^4	−0.47 to − 1.04/1.91 to 3.932/−2	–	10^3	–
[27]	Ti/W/Ag NPs TiOx/MgO/Ru	<32	1.4/−1.8	$>10^3$ Cycles $>10^9$ Cycles	~NS	8
[28]	Au/NiO/Ni/NiO/Au	–	3.05/3.55	–	10^5	–
[29]	Ti/ZrO_2/Pt Ti/ZnO/ZrO_2/Pt	10^4	–	10^4	10^5	–

3 Operating Performance of RRAM

RRAM is a device which is based on resistance change in materials, and its structure is Metal-Insulator-Metal (MIM) [1]. The insulator between the metal electrodes such as Pt and Ti can be binary or ternary oxide like hafnium, tantalum, chalconides and low-dimensional materials like h-BN. The structure can be single or multi-layer as shown below in Fig. 3 in which multi-layer has advantages of better SET and RESET voltages, multibit storage, etc. [30].

RRAM will show resistance switching between two levels, namely high resistance state (HRS) and low resistance state (LRS) which is the storage levels for "1" and "0" bit. The switching between HRS and LRS is carried out by SET and RESET process. The conductive filament (CF) between two states is formed in insulator after an appropriate bias is applied to the device. The CF is formed by a forming process in which a high voltage is applied to the device and because of that there is a soft breakdown of insulator. This results in defects (oxygen vacancies) which is required for high current during regular operation.

The operating principle is as follows: During the ON/SET process, a CF is formed, and device resistance is low (LRS), and the current flows. When the CF is broken, the device resistance is increased (HRS), and current stops. Now, the device is in OFF/RESET stage. In the SET process, a compliance current is applied which avoids uncontrolled CF formation and protects device from permanent failure. Figure 4 shows the illustration of SET and RESET process of metal oxide-based RRAM.

Now, on the basis of working principle of RRAM cells, there are three filament mechanism, i.e., (i) thermochemical, (ii) electrochemical and (iii) valence change mechanism [31]. The thermochemical mechanism of filament is based on the resistance change because of electric field and joule heat. In the electrochemical mechanism, the change is based on electric field which induces the movement of metallic ions, and the valance change is based on movement of oxygen ions in the insulator. Electrochemical and valence change mechanisms are mostly same, but mainly

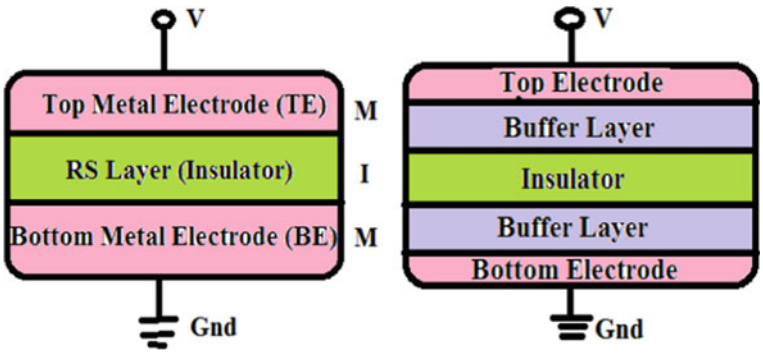

Fig. 3 Single layer and multi-layer RRAM structure

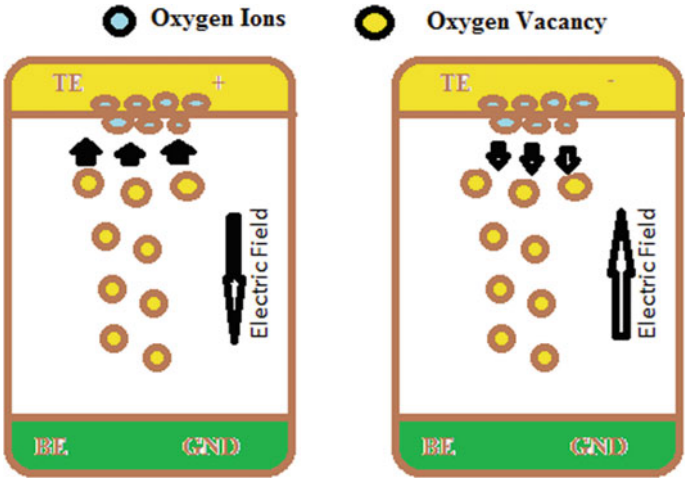

Fig. 4 Illustration of **a** Set, and **b** Reset process of metal oxide-based RRAM

valance change mechanism type is more explored. In addition to the filament mechanism, different bias schemes of resistance switching are also employed in different RRAM's like unipolar (Al_2O_3/HfO_2) [32], bipolar ($Cu/HfO_2/Pt/Si$) [33] and non-polar. Unipolar deals with SET/RESET process employed by voltage impulses of same polarity as compared to bipolar in which opposite polarity pulses are utilized and in non-polar any polarity pulse is used. The bipolar one is more superior as compared to others in terms of endurance, ON/OFF voltage, power consumption and variability. Figure 5 shows the I-V curves of metal-oxide RRAM showing unipolar and bipolar switching mechanism.

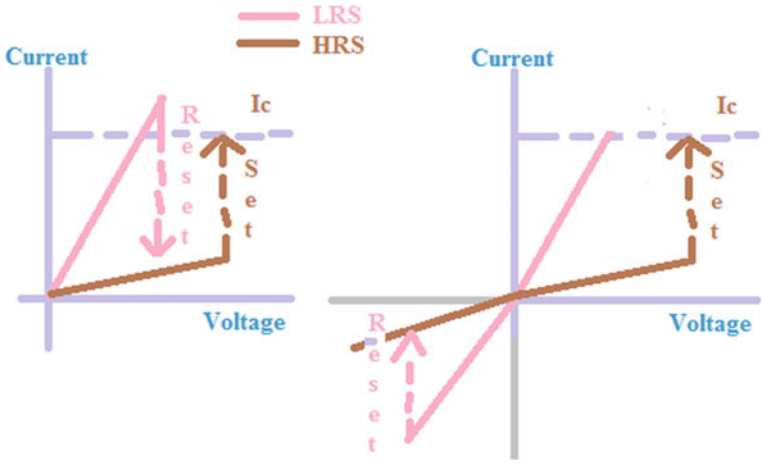

Fig. 5 I-V curves of metal-oxide RRAM **a** Unipolar **b** Bipolar

In addition to this, the conductive path can be filament type or distributed type [1]. Filament is area-specific and consumes more power, but it is faster and distributed on entire area range, consumes less power. It is worth to point that RRAM with all combination of filament mechanism is superior like as employed in Ti/ZrO_2/N^+-si structure.

4 Performance Parameters of RRAM

When we are dealing with RRAM, then there are several FOM on which RRAM performance depends. Thus, here in this manuscript we have presented some of the parameters, and the best results quoted:

(1) **Endurance**—It is defined as the number of SET/RESET cycles undergoes while maintaining a distinct resistance level. The ideal memory must have long cycling endurance. As with the increasing program/erase cycle, the resistance ratio degrades, and the device is said to be failed when ON/OFF current reaches below threshold level. The RRAMs employing tantalum oxides as switching medium have been reported for endurance higher than 10^{12} cycles [31].

(2) **Data retention**—It is the investigation of time for which the low and high resistance stages (LRS and HRS) are stable after the SET/RESET process. The Ti/HfO_2/TiN memory has showed a retention of 10 years and at 85 °C [31].

(3) **Variability**—RRAM is deployed by variability issues which is similar to CMOS variability. The variability includes cell to cell and cycle to cycle. The cycle-to-cycle variability is because of the random nature of CF, and it became worse with reducing compliance current [31]. The cell-to-cell variability is attributed to the defects in fabrication process, surface roughness, etching damages etc. Variability issues are more viable in multi-level RRAM.

(4) **Scalability**—Scalability is the reduction of the dimensions without degradation of the other parameters. As compared to different existing memories (Table 1), it shows that RRAM is highly scalable. Many works suggest that it can scale down to nanometers (<10 nm) [31].

(5) **Power consumption**—As discussed earlier the material and filament mechanism are responsible for power consumption. Filamentary type has high power consumption as compared to distributed type. It is desirable to have low power consumption, and from [34], it is seen that power consumption as low as 0.1 pj/bit is achieved in a TiN/Hf/HfO_x/TiN structure.

5 Application of RRAM

As discussed in this manuscript, RRAM has superior characteristics over current existing memories like simple design, faster operation, low power consumption, low

cost, 3D integration, and most importantly, it is scalable so because of all these advantages, it can find its application in

(1) **Multi-level resistance switching:** For ultra-high storage density, multi-level switching is the efficient way, and it can be realized in RRAM by coupling two or more mechanisms as discussed earlier.
(2) **Crossbar selector**—RRAM can be implemented as 1T-1R structure. The selector is a Front-End-of-Line (FEoL) device employing CMOS transistor, BJT, etc., but it consumes large area, has high cost, so structure which has back-end-of-line (BEoL) is preferred and called cross point arrays. In the cross point arrays, RRAM is employed, and they consume less area, have low cost, etc. The von Neumann architecture [35] proposed by John von Neumann in 1946 suffers from the speed and bandwidth constraint as memory is not the part of processing unit. So, in neuromorphic computing [36], the memory is the part of processing unit, and RRAM makes it possible as it can be embedded in processing unit.
(3) **Security application**: Security circuits based on RRAM are more robust as compared to CMOS-based memories as RRAM has complete random switching mechanism. The RRAM parameters like random telegraph noise, resistance variation, etc., are desirable for security application [37].

6 Conclusion

Here, We presented an overview of RRAM devices starting from basics to applications prospects. We have also discussed the material used, its RS mechanism and performance parameters. RRAM has shown several advantages like high speed, low power consumption, 3D integration, scalability, non-volatility etc., and can be considered as a potential candidate for future memory devices in electronic systems. It finds application in Internet of thing (IoT) devices, neuromorphic computing, cloud computing, etc. However, with all these pros, there is still a lot of research needed to make RRAM commercialized and further development in regard of low cost, high density. RRAM technologies will likely pave the way for the future.

References

1. Philip Wong H-S et al (2012, June) Metal oxide RRAM. Proc IEEE 100(6):1951–970. https://doi.org/10.1109/JPROC.2012.2190369
2. Gupta V, Kapur S, Saurabh S, Grover A, Resistive random access memory: a review of device challenges. IETE Tech Rev. https://doi.org/10.1080/02564602.2019.1629341
3. Wang H, Yan X (2019) Overview of resistive random access memory (RRAM): materials, filament mechanisms, performance optimization, and prospects. Phys Status Solidi RRL 1900073. https://doi.org/10.1002/pssr.201900073
4. Shen Z et al (2020) Advances of RRAM devices: resistive switching mechanisms, materials and bionic synaptic application. Nanomaterials 10:1437. https://doi.org/10.3390/nano10081437

5. Zahoor et al (2020) Resistive random access memory (RRAM): an overview of materials, switching mechanism, performance, multilevel cell (MLC) storage, modeling, and applications. Nanoscale Res Lett 15(90). https://doi.org/10.1186/s11671-020-03299-9
6. International Roadmap for Devices and Systems (2020) "Beyond CMOS
7. Akinaga H, Shima H (2010) Resistive random access memory (ReRAM) based on metal oxides. Proc IEEE 98:2237e51. https://doi.org/10.1109/JPROC.2010.2070830
8. Han ST, Zhou Y, Roy VAL (2013) Towards the development of flexible non-volatile memories. Adv Mater 25:5425e49. https://doi.org/10.1002/adma.201301361
9. Cagli C et al (2017, April) About the intrinsic resistance variability in HfO_2-based RRAM devices. In: 2017 Joint international EUROSOI workshop and international conference on ultimate integration on silicon (EUROSOI-ULIS), Athens, April 2017, pp 31–4. https://doi.org/10.1109/ULIS.2017.7962593
10. Chen S, Lou Z, Chen D, Shen G (2018) An artificial flexible visual memory system based on an UV-motivated memristor. Adv Mater 30:1705400. https://doi.org/10.1002/adma.201705400
11. Chen A (2016) A review of emerging non-volatile memory (NVM) technologies and applications. Solid State Electron 125:25–38. https://doi.org/10.1016/j.sse.2016.07.006
12. Cai Y, Tan J, YeFan L, Lin M, Huang R (2016) A flexible organic resistance memory device for wearable biomedical applications. Nanotechnology 27(27):275206. https://doi.org/10.1088/0957-4484/27/27/275206
13. Chen YC, Yu HC, Huang CY, Chung WL, Wu SL, Su YK (2015) Nonvolatile bio-memristor fabricated with egg albumen film. Sci Rep 5:10022. https://doi.org/10.1038/srep10022
14. Jin Z, Liu G, Wang J, Jin Z, Liu G, Wang J (2013) Organic nonvolatile resistive memory devices based on thermally deposited Au nanoparticle. AIP Adv 3(5):052113. https://doi.org/10.1063/1.4804948
15. Liu G, Chen Y, Gao S, Zhang B, Li R-W, Zhuang X (2018) Recent advances in resistive switching materials and devices: from memories to memristors. Eng Sci 4. https://doi.org/10.30919/es8d779
16. Hickmott TW (1962) Low frequency negative resistance in thin anodic oxide films. J Appl Phys 33(9):2669–2682. https://doi.org/10.1063/1.1702530
17. Baek IG et al (2004) Highly scalable non-volatile resistive memory using simple binary oxide driven by asymmetric unipolar voltage pulses. In: IEDM technical digest. IEEE international electron devices meeting, San Francisco, CA, 2004, pp 587–90. https://doi.org/10.1109/IEDM.2004.1419228
18. Siddiqui GU, Rehman MM, Yang YJ, Choi KH (2017) A two-dimensional hexagonal boron nitride/polymer nanocomposite for flexible resistive switching devices. J Mater Chem C 5:862. https://doi.org/10.1039/c6tc04345c
19. Jang J, Pan F, Braam K, Subramanian V (2012) Resistance switching characteristics of solid electrolyte chalcogenide Ag_2Se nanoparticles for flexible nonvolatile memory applications. Adv Mater 24:3573. https://doi.org/10.1002/adma.201200671
20. Wei Z et al (2008) Highly reliable TaO_x ReRAM and direct evidence of redox reaction mechanism. In: 2008 IEEE international electron devices meeting, 2008, pp 1–4. https://doi.org/10.1109/IEDM.2008.4796676
21. Varun I, Bharti D, Raghuwanshi V, Tiwari SP (2017, October) Multi-temperature deposition scheme for improved resistive switching behavior of Ti/AlO_x/Ti MIM structure. Solid State Ionics 309:86–91. https://doi.org/10.1016/j.ssi.2017.07.013
22. Yang L et al (2009) The influence of copper top electrodes on the resistive switching effect in TiO_2 thin films studied by conductive atomic force microscopy. Appl Phys Lett 95(1). https://doi.org/10.1063/1.3167810
23. Wu Q et al (2018) Improvement of durability and switching speed by incorporating nanocrystals in the HfO_x based resistive random access memory devices. Appl Phys Lett 113:023105. https://doi.org/10.1063/1.5030780
24. Lin C-C, Lin C-Y, Lin M-H, Lin C-H, Tseng T-Y (2007) Voltage-polarity-independent and high-speed resistive switching properties of V-doped $SrZrO_3$ thin films. IEEE Trans Electron Devices 54:3146–51. https://doi.org/10.1109/TED.2007.908867

25. Kuang Y, Huang R, Tang Y, Ding W, Zhang L, Wang Y (2010) Flexible single-component-polymer resistive memory for ultrafast and highly compatible nonvolatile memory applications. IEEE Electron Device Lett 31(7):758–60. https://doi.org/10.1109/LED.2010.2048297
26. Xu X-Y, Yin Z-Y, Xu C-X, Dai J, Hu J-G (2014) Resistive switching memories in MoS_2 nanosphere assemblies. Appl Phys Lett 104(3): 033504. https://doi.org/10.1063/1.4862755
27. Menzel S, von Witzleben M, Havel V, Böttger U (2019) The ultimate switching speed limit of redox-based resistive switching devices. Faraday Discuss 213:197–213. https://doi.org/10.1039/C8FD00117K
28. Ting YH, Chen JY, Huang CW, Huang TK, Hsieh CY, Wu WW (2018) Observation of resistive switching behavior in crossbar core-shell Ni/NiO nanowires memristor. Small 14:1703153. https://doi.org/10.1002/smll.201703153
29. Chand U et al (2014) Mechanism of high temperature retention property (up to 200 °C) in ZrO_2-based memory device with inserting a ZnO thin layer. IEEE Electron Device Lett 35(10). https://doi.org/10.1109/LED.2014.2345782
30. Chen Z et al (2019) Ultrafast multilevel switching in Au/YIG/nSi RRAM. Adv Electron Mater 5(2):1800418. https://doi.org/10.1002/aelm.v5.2
31. Lanza M et al (2019) Recommended methods to study resistive switching devices. Adv Electron Mater 5(1):1800143. https://doi.org/10.1002/aelm.v5.1
32. Maestro-Izquierdo M et al, Unipolar resistive switching behavior in Al_2O_3/HfO_2 multilayer dielectric stacks: fabrication, characterization and simulation. Nanotechnology 31(13):1–35. https://doi.org/10.1088/1361-6528/ab5f9a
33. Lata LK et al (2020) Resistive switching characteristics of HfO_2 based bipolar nonvolatile RRAM cell. Mat Today Proc 30. https://doi.org/10.1016/j.matpr.2020.06.209
34. Govoreanu B et al (2011, December) 10×10 nm^2 Hf/HfO_x crossbar resistive RAM with excellent performance, reliability and low-energy operation. In: 2011 International electron devices meeting, Dec 2011, pp 31.6.1 4. https://doi.org/10.1109/IEDM.2011.6131652
35. Li H et al (2015) A learnable parallel processing architecture towards unity of memory and computing. Sci Rep 5:13330. https://doi.org/10.1038/srep13330
36. Chen Z et al, Optimized learning scheme for grayscale image recognition in a RRAM based analog neuromorphic system. In: IEEE international electron devices meeting (IEDM). IEEE, New York, pp 17–7. https://doi.org/10.1109/IEDM.2015.7409722
37. Chen A, Comprehensive assessment of RRAM-based PUF for hardware security applications. In: IEEE international electron devices meeting (IEDM). IEEE, New York. https://doi.org/10.1109/iedm.2015.7409672

Survey of Microstrip Antenna in Nanotechnology Using Different Nanostructures

Sonam Gour, Priya Chaudhary, and Amit Rathi

Abstract The nanoscale science area is increasing over the last two decades. The ability to control and restructure matter at the atomic and molecular levels is referred to as nanotechnology. It has a large surface-to-volume ratio for equipment development and molecular discovery in the atomic level for increasing development and product manufacturing. In the field of communication engineering, the many solutions are found by the help of nanotechnology. It provides the solution for the power-efficient device, more sensing elements, builds up memory, and human-to-machine interaction. This paper is focused on the different types of structures of the nanomaterial and later that it also provides a brief idea about the potential application in various fields of nanotechnology. It discussed the type of application of nanotechnology and nanosensor techniques in nano communication. Nanoantennas are used as the sensing part for the ability of effectively broadcasting, and spatial optical fields. Nanoparticles are highly used in the field of nanoantennas. The paper represents the application of nanomaterial in the field of wireless communications using antenna design. This paper provides an overview and analyzes the microstrip antenna design in nanotechnology using different nanostructures, and it also discusses about the performance of the microstrip antenna under different subtract configurations.

Keywords Nanosensor · Nanomaterial · Communications · Microstrip antenna

1 Introduction

Nanotechnology is the control process for reconstructing the matter in the nanoscale. Physicist Richard Feyman gave the idea and concept of nanotechnology at the American Physical Society meeting of California Institute of Technology that was held

S. Gour · P. Chaudhary · A. Rathi (✉)
Department of Electronics and Communication Engineering, Manipal University Jaipur, Jaipur, Rajasthan, India
e-mail: amitrathi1978@gmail.com

S. Gour · P. Chaudhary
Department of Electronics and Communication Engineering, Arya College of Engineering and Research Center, Jaipur, Rajasthan, India

S. Dwivedi et al. (eds.), *Flexible Electronics for Electric Vehicles*, Lecture Notes in Electrical Engineering 863, https://doi.org/10.1007/978-981-19-0588-9_4

in 1959. But, practicing of modern nanotechnology began only in the year of 1981, when the scanning tunneling microscope process was able to see individual atoms or molecules [1]. The application in nanotechnology has been developed as a revolutionary field in science, technology, and electricity [2]. From the past one decade, the development and growth in the experiment in nanotechnology is increasing rapidly. Nanotechnology's main aim is to create small structures by the use of devices, materials, and systems with new properties. The technique changes the economical material properties and length for smaller designs. It also shows the transition from the single atoms to molecules and analyzing the behavior of molecular and atomic togetherness is monitored in nature. The research area in nanotechnology is very vast. The one branch of nanotechnology is nano electronics and is seen as a solution to the problems of silicon-based CMOS devices. Thus, the issue of scaling in the device with continued scaling process is not so much technical as economic. Thus, provides benefits in the manufacturing level and increased functionality through the process of miniaturization. Further miniaturization with the help of the process of nanotechnology would allow the designer to put millions of currently available electronic devices over an area that is less than a few millimeters over a few millimeters. The one term that directly reflects the term miniaturization is surface-to-volume ratio. Nanotechnology works under the range from 1 to 100 nanometers range, also called nanoscale. In the field of mobile communication, the use ability of nano science is for controlling the process in nanometer scale. Nanotechnology is highly demanding in mobile impact field and core network. The better use of the sensor makes this technique more significant. These tiny size particles are controlling the individual atoms as well as molecules. The material shows better functionality of the cell in comparison to the micro or macro scale [3]. The quantum size effect changes the behavior of the matter [4]. The use of carbon nanotubes has come also in nanotechnology. In all the generations of mobile phones, the cells count as nano devices because they are equipped with the help of nanotechnology. Nano intelligent technologies are used for betterment of the person. In a nano communication network, the network device and mobile are embedded in the human environment to create a new platform. Electromagnetic waves are the highly responsible for the communication. These waves can propagate with or without the wire. For design a bidirectional wireless communication in the nano communication, a frequency range or the radio frequency must be interrelate with the Nano Machine. It requires a development in the antenna design for the very high frequency. Many types of antennas are designed under the nano communication and they provide very good bandwidth. Optimization in the size of the antenna provides lower ultra-wideband (UWB) application and also able to perform the work in the modern wireless communication systems such as Wi-Fi, WiMax bands, and WLAN [5]. Electronic components today are all-pervasive and are progressing toward flexible structures. Increasing demand of technologies, the use of electronic components, and ease of use is increasing [6].

2 Types of Nanostructures

Nanotechnology has three types of structure techniques: 0-D, 1-D, and 2-D structures. This is done by the dimensions of the material which are outside from the nanoscale. When all dimensions are measured within the nanoscale, it is known as 0-D, for example, nanoparticles. Nanoparticles and quantum dots are the examples of 0-D structure. Figure 1 shows about the different types of nanostructures.

It allows much higher absorption in the form of solar radiation. This radiation is used in photovoltaic cells with the composition of nanoparticles or thin films of continuous sheets. It is composed from the same materials. Whereas in one-dimensional (1-D) nanomaterials design (1D), one dimension is outside from the nanoscale. Nanotubes, nanorods, and nanowires are the examples of 1-D nanomaterial. Carbon nanotubes are also very usable for designing the nanomaterials. It has a long whole structure, surrounding formed walls by one thick sheet of atom. The sheet is formed by the carbon. It is also known as the grapheme. The nanotube properties are decided by the rolling angle and the radius of the sheet. They are rolled at specific and discreet chiral angles. If two dimensions are outside from the nanoscale it is known as two-dimensional (2-D) nanomaterials. It includes nanofilms, nanolayers, nanocoatings, plate-like shapes, and includes graphene. The spectrum given by the material becomes discrete in the nanostructure; the first subcategory is defined by the crystalline material. In crystalline, the molecules or ions, which make a material, are arranged in the regular pattern. In some crystalline cases, the regular ordering of the molecules can continue unbroken and attachable over a large scale. For example, the diamond structure has a single crystal [7]. Polycrystalline materials belong to the second subcategory. They are not connected in the form of a single crystal. For example, salt objects are large enough to see and to handle in a single crystal form. Amorphous materials are known as the third category of the crystal. It is called nanocrystalline solid. Table 1 shows about the different types of nanostructure with their example.

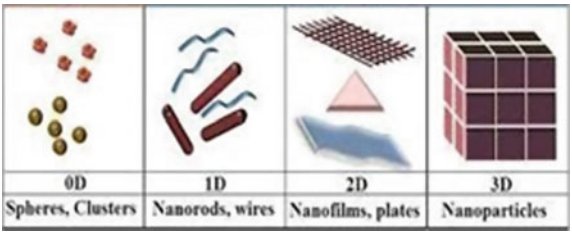

Fig. 1 Types of nanostructures [1]

Table 1 Type of nanostructure

Dımension of nanomaterial	Scales	Movement of electron	Key representative	Examples
0-D	All are confined in one direction	In all three direction	Quantum dots	Molecules, metal carbides, rings cluster
1-D	Two direction are confined	Only in X direction	Quantum wire	Nanotube spirals, fiber
2-D	One dimension is confined	Moves in X–Y planes	Thin films	Graphene
3-D	All direction is confined	Moves in all three direction	Nonconstructed material	Small nanocluster membranes

3 Nanotechnology Applications

With the help of nanotechnology, the designer creates sensor and computer chips which are comparatively very small, fast, energy efficient, and cheap. In everyday environments, people use embedded sensors. The component used for the designing of robot is very close to the microscopic range of a nanometer or from 9 to 10 m. In communication, nanotechnology makes a great revolution and builds up many features. It reflects the telecommunication industry in many ways [8].

Wireless Technology

The telecommunication is designed by the cellular and the core network. It keeps changing with new nanotechnology. It makes a direct impact on the cellular and the core networks. New development in the wireless technology rebuilds the new promises for the intelligent operation in the computation and the implementation [9]. The main objective of the wireless industries is to gain the most nano intelligent technologies in a smart way.

Body Area Network

This device can be attached with a person by as a dress or as some part of the body. As per the very busy and improper routine of the human being, the use of these techniques increase day by day. Very much innovation has been done by the many researchers. The uses of the stents and pacemaker are increasing. In the heart failure patients, many sensors are planted in the body and communicated in the form of nano communication. The grain of rice size of particles can be used to sensing the blood flow rate, arteries in the body, and much more complexity [10].

Nano Communication and Networks

Nano machines take place in the modern communication for transmit a message to a carrier by the use of a receiver. The information is encoded by the transmitter side and decoded at the receiver side. In the molecular transmission, the information is passing through as per the molecules and provides easy recognition of the message at receiver

size. Nano machines are done by considering of the molecules. The molecules are used as an information carrier in biological systems. Nano techniques can also be used as next-generation microcontroller because some computers uses silicon nano crystal as the storing device for the charge particles [11].

4 Nano Communication Approach

As per above application, nanotechnology has various advantages over the field of communications. Nanoantennas and carbon nano tubes are designed for the increasing demand of nanoantennas.

Sensing Elements Design

An integration of antenna with the RF sensor is required for designing the RF wireless sensor. Carbon nanotubes (CNTs) are very much useful for designing the biological sensor due to the many applications of its like sensitivity, selectivity, and very fast response time [12]. Carbon nanotubes are also used in the biosensor and used as a sensing element in wireless antenna. The sensor is used for collecting and integrating data. The nanonetwork data can be collected from various parts and analysis as per the data applied [13]. In the field of nanoscale, designers used two antennas for radiation and propagation of enhanced and coherent fields, for example nanoantennas and microwave antennas. Nanoantennas are used in the sensing part of the antenna due to the capability to efficiently link the broadcasting and spatially confined optical fields [14].

Microstrip Antenna Design

Nanoscale technology is used for designing the patch of the antenna. The size reduction of any antenna is highly desirable. Different types of patches have been designed for analyzing the antenna performance. The patch characteristics directly affected the bandwidth and the directivity of the antenna. Microstrip antenna is useful for GPS tracking system, medical implant service, and easy communication system. The side lobe suppression for 4 * 4 array design provides the 9% fractional bandwidth. Capacitive patch feeding and coaxial timeline are used for reducing the excessive inductance [15]. The feeding technique of the microstrip antenna directly affected the characteristics of the antenna. Microstrip antenna can be designed by four different types of feeding techniques. Two different types of substrate are used in aperture coupled and proximity type of feeding techniques. These techniques increase the bandwidth and the gain of the antenna, but the spurious radiation is present in the technique. High impedance matching is required. In microstrip feed line technique, a conducting strip is connected directly to the edge of the microstrip patch. It can be etched in the different substrate structures. In coaxial feeding technique, the feed can be placed in any desired location of the feed. The MWT also known as microstrip-to-waveguide transition is one type of feeding technique. These techniques increase the bandwidth and the gain of the antenna, but the spurious radiation is present in

the techniques. High impedance matching is required. In microstrip feed line technique, a conducting strip is connected directly to the edge of the microstrip patch. It can be etched in the different substrate structures. In coaxial feeding technique, the feed can be placed in any desired location of the feed. The MWT also known as microstrip-to-waveguide transition is one type of feeding technique. It is widely used for feeding the microstrip array antenna. By blocking the direct radiation of the antenna the spurious radiation can be reduced [16]. The patch of antenna is designed by connecting two patches in serial connecting form that analyze the behavior of the circuitary. Adding two slots can enhance the bandwidth and return loss of the antenna [17]. Designed by the H-type slot coupling provided the wider bandwidth and the spurious radiation pattern. This design also increases the bandwidth and reduces the radiation losses in the antenna. The effect of the radiating element is also reduced [18]. The aperture coupled antenna by using the U-shaped and M-shaped microstrip feed line provided the good impedance matching and provided stable performance [19]. The circularly polarized technique in the cross-shaped microstrip antenna is proposed in three shapes which are circular, square, and cross shaped. Each design is analyzed by varying the rotation angle, arm width, and the structure of the ground plane structure. The cross-shaped structured desired to achieve large perimeter [20]. Reconfigurable antenna is used for the frequency reconfiguration, vast radiation patterns, and pattern reconfiguration. It can be changed by using PIN and varacter diode in the feed line structures. It provides the solution in the network congestion [21]. The nanoscale heterostructure is used the InGaAs/GaAsSb for the quantum well material. It provides the effiecient optical gain [22].

5 Conclusion

This paper discusses the development with the help of nanotechnology. Development in nanotechnology is still in the early phase with the help of fundamental understanding and tools. Research areas and innovation are increasing in the field of nano techniques in the last decade. This paper discusses the various approaches of nanotechnology. The development in the nanoscale can also be used in the sensing element of any antenna. It represents the use of nanoantennas and carbon nanotubes as sensing elements. The opportunities and challenges in the field of nanotechnology, nano communication, and biomedical fields. It represents the effect of nanotechnology in the field of telecommunication. It discussed the uses of nanotechnology in the telecommunication field. The paper presents different types of techniques used for the designing of the microstrip antenna design. Along with this, we have studied how the bandwidth and the radiation pattern of the microstrip antenna can be changed by the different substrates.

References

1. Coursera Education for everyone : Nanotechnology and Nanosensor Part 1, Technion Israel Institute of Technology. https://www.coursera.org/learn/nanotechnology1
2. Roco MC, Mirkin CA, Hersam MC (2011) Nanotechnology research directions for societal needs in 2020: summary of international study. J Nanoparticle Res, pp 897–919
3. Rehman HYFU, Zhao C, Liu B, He N (2016) Recent advances in nano scaffolds for bone repair. Bone Res 4
4. Berger ML (2009) Nano-Society pushing the boundaries of technology. RSC Publishing, Cambridge
5. Singh H, Soni GK, Suryawanshi P, Shankar G (2020) Performance analysis and BER comparison of OFDM system for 4 × 4 MIMO fading channel in different modulation scheme. In: IEEE third international conference on smart systems and inventive technology (ICSSIT), pp 255–259
6. Sharma A, Saini Y, Singh AK, Rathi A (2020) Recent advancements and technological challenges in flexible electronics: mm wave wearable array for 5G networks. In: AIP conference proceedings, vol 2294 (1). AIP Publishing LLC, p 020007
7. Naishadham K, Bayat A, Savi P (2017) Antenna integration with nanotechnology-based thick film circuit for Sensor applications. In: International conference on electromagnetics in advanced application. IEEE, New York, pp 1711–1714
8. Ahmed ESA, Sohel HS (2017) Nanotechnology in communication engineering: issues, applications, and future possibilities. World Scientific News, pp 134–148
9. Padmavathi G, Shanmugapriya D, Valliammal N, Geetha G, Kandhasamy CJK (2016) 1–315. UGC sponsored two day national conference on internet of things. World Scientific News 41
10. Dressler F, Fischerb S (2014) Connecting in-body nano communication with body area networks challenges and opportunities of the internet of nano things. Elsevier
11. Roco M, Mirkin C (2011) Nanotechnology research directions for societel needs in 2020: summary of international study, pp 897–99
12. Pierobon M (2013) A routing framework for energy harvesting wireless nano sensor networks in the Terahertz Band, vol 20, Issue 5. Wireless Networks Springer
13. Naishadham K, Bayat A, Savi P (2017) Antenna integration with nanotechnology-based thick film circuit for sensor applications, pp 1711–1714
14. Pramanik PKD, Solanki A, Debnath A, Nayyar A, El-Sappagh S, Supkwak K (2020) Advancing modern health care with nanotechnology, nanobiosensors, and internet of nano things: taxonomies, applications, architecture, and challenges, vol 8. IEEE Access, pp 65230–65266
15. Shinde KS, Shah SN, Patel PN (2019) A review on opportunities and challenges of nano antenna for terahertz communications. In: 5th International conference on computing, communication, control and automation
16. Nguyen DH, Ala-Laurinaho J, Moll J, Krozer V, Zimmer G (2020) Improved sidelobe suppression microstrip patch antenna array by uniform feeding networks. IEEE Trans Antenna Propag 68(11):7339–7347
17. Luzon MA, Geresta OJ (2018) Slotted circular polarized rectangular microstrip patch antenna with enhanced bandwidth for wireless communication in 2.45 GHz. IEEE, New York
18. Noh E, Kim K (2019) Effects of MWT radiation on sidelobe levels in mm-wave microstrip array antenna. In: IEEE international symposium on antennas and propagation, pp 873–874
19. Chen Z, Dai X, Luo G (2018) A new H-slot coupled microstrip filter-antenna for modern wireless communication systems. In: IEEE International workshop on antenna technology
20. Li H, Kang L, Wei F, Cai YM, Yin YZ (2017) A low-profile dual-polarized microstrip antenna array for dual-Mode OAM applications. IEEE Antenna Wireless Propag 16:3022–3025
21. Sharma A, Rathi A (2020) Analysing reconfigurable slot antenna for cognitive radio applications. In: International conference on reliability, Infocom technologies and optimization (trends and future directions) (ICRITO), Amity University, Noida India, pp 744–747

22. Jayprakash V, Yadav RK, Alvi PA, Singh K, Rathi A (2020) Design and modeling of InGaAs/GaAsSb nanoscale heterostructure for application of optical fiber communication system. Mater Today: Proc 30:128–131

Design and Modeling of the Ring Resonator-Based Microwave Sensor for Skin Cancer Detection

Madan Kumar Sharma, Ranjana Kumari, Akshat Mittal, Manish Kumar Upadhyay, Amit Mittal, and Komal Singh

Abstract This research proposed a novel microwave sensor and detection of skin cancer is carried out using this sensor. The sensor is fabricated on Rogers RT 5880 substrate with thickness of 0.508 mm and has dielectric constant value of 2.2. In terms of the S-parameters, radiation pattern, surface current density, gain, and directivity versus frequency, the sensor output is tested. The resonating frequency of the proposed design is 2–18 GHz. The computer simulation tool (CST) is used to create normal and malignant skin models. The sensor is integrated over the skin to perform analysis of the skin models, and S-parameters are calculated. Measured sensor S-parameters are different from each other for normal and malignant phantoms. The magnitude and phase angle of the sensor are monitored for normal and malignant case. The signal radiated in 2–18 GHz range is more capable to penetrate in the human skin. This illustrates the ability of this approach to differentiate between cancerous and normal tissues.

Keywords CSRR · Skin cancer · Resonator · Microwave sensor · Dielectric contrast

1 Introduction

The largest organ that protects the human inner components is the body skin. Skin cancer is the most common form of cancer, among others. The high percentage of cancer-induced annual mortality rates indicates the importance of carrying out more research in this field in order to achieve an effective early-stage cancer detection technique. It is of three types-basal cell carcinoma (BCC), squamous cell carcinoma

M. K. Sharma · R. Kumari · A. Mittal (✉) · M. K. Upadhyay · A. Mittal · K. Singh
Galgotias College of Engineering & Technology, Greater Noida, India
e-mail: akshatmittal2402@gmail.com

M. K. Sharma
e-mail: madan.kumarsharma@galgotiacollege.edu

R. Kumari
e-mail: ranjana.kumari@galgotiacollege.edu

S. Dwivedi et al. (eds.), *Flexible Electronics for Electric Vehicles*, Lecture Notes in Electrical Engineering 863, https://doi.org/10.1007/978-981-19-0588-9_5

(SCC), and melanoma. Skin cancers are curable in most cases if they are diagnosed at an early stage. In order to detect a tumor in the early stages, a wide variety of similar research work has been carried out [1, 2]. Where a higher resolution is required at the microscopic level, biopsy samples are used to assess the form and stage of skin cancer [3]. Other diagnostic alternatives include bioelectrical methods where electrical properties of the skin are used to distinguish between malignant and benign skin lesions, e.g., conductivity and permittivity, but research on these approaches is still in progress. The calculated reflection properties are directly affected by the dielectric properties of the questioned material [4]. The dielectric properties of human tissues may be used for diagnostic purposes as an important and precise indicator [5].

The dielectric properties of the skin are directly related to parameters such as the content of water, sodium, and protein, which vary considerably between normal skin and benign and malignant lesions. For normal skin, the water content is about 60.9% and 81.7% for malignant lesions [6]. Early studies have shown that the tumor has a major dielectric contrast in the microwave frequency spectrum with regard to healthy tissues. Microwave imaging (MI) and microwave detection techniques promise a highly efficient complementary technology because it is possible to manufacture the associated systems cost-effectively allowing more widespread availability. Electromagnetic waves are scattered through cancer cells due to higher allowability compared to normal cells. Microwave detection for frequent skin monitoring, in particular, would provide a safe, comfortable technique that could help increase tumor detection rates in the early stage. The antenna is considered to be the main sensing feature in the proposed microwave detection system's RF front-end [7, 8].

In [9], a microwave sensor-based SRR for precise detection of the actual component of dielectric constant in composite magnetodielectric was proposed. Dual SRRs are coupled with a line microstrip, and the sensitivity of the structure has been improved. A series of complementary split ring resonators was used in [10] to reduce the impact of the air gaps between the sample and the ground of the sensor.

CSRRs are sub-lambda structures, i.e., their measurements are electrically small at the resonant frequency. Hence, the use of these particles is required to provide a high degree of miniaturization [11]. Usage of electrically small resonators or quasistatic resonators is implemented and demonstrated as a near-field probe. More precisely, the behavior of the CSRR as a material characterization sensor is analyzed. The sensor requires a simple preparation of the sample as observed in [12, 13].

The production of new advanced sensors with small sizes and better sensitivity has been made possible by the improvement of metamaterial technology in the microwave region [14]. The concept of the SRR-based microwave sensor is a traditional one. Techniques can have a high degree of sensitivity and resolution. Due to its low-radiative losses and very high-efficiency factor, the sensing capability of the device can be improved by using metamaterial particles such as SRRs and CSRRs [15]. In the case of a CSRR, the behavior of magnetic and electrical fields is interchangeable. As a result of the authorization characterization, a CSRR is required to become a stronger sensor.

Khor et al., for example, performed an experimental study that was able to detect the presence and locate an object of high-permittivity accurately positioned in a cylinder using a Vivaldi style antenna inside a low-permittivity plastic (modeling healthy fat tissue) [16].

Caratelli et al. suggest a non-invasive micro-sensor approach based on concept of effective material parameters and sufficient standardization of magnitudes specific to the electromagnetic field, which has been expanded using a local finite difference time domain technique [17].

The objective of this research is to develop a method for properties of microwave reflection calculation and simulation of skin and to demonstrate the ability of properties of reflection. It serves as the base for the diagnosis of skin cancer [18]. A new imaging modality is needed due to lack of a convenient, reliable, affordable, and real-time system for skin cancer detection.

The sensor is developed and simulated using a computer simulation tool (CST). It has a high-gain directional radiation property and is operated within the 2–18 GHz frequency range. The proposed sensor is designed for a more compatible Rogers RT5880 substrate that is conveniently embedded over human skin. Initially, the output review is conducted for the verification of S-parameter, gain, and radiation patterns. When further analyzed, the sensor output is incorporated in the stable and malignant model of the human skin layer.

The findings of the sensor are evaluated in terms of magnitude and phase, and the difference between the findings for healthy and malignant skin layers was observed. The proposed approach to skin cancer detection is contrasted with current sensor designs. However, comparative research indicates that the proposed method is an alternative technique for the detection of skin cancer. In addition, the proposed method is quick, fast, accurate, non-invasive, readily available, patient-friendly, inexpensive, and real-time skin cancer detection system.

2 Proposed Ring Resonator Sensor Development

The proposed sensor consists of complementary split ring resonators and a microstrip transmission line that operates in the 2–18 GHz frequency range. The structure is fabricated on the Rogers RT5880 substrate with thickness of 0.508 mm and dielectric constant value of 2.2 with metallic ground plane. The proposed ring resonator sensor is shown in Fig. 1. Table 1 collects and displays all of the sensor's dimensions.

2.1 Evolution Process of the Proposed Sensor

The designing procedure of the proposed sensor shown in Fig. 2 consists of three major steps, the structure is modified to getting multiple resonance, and the following steps are discussed below.

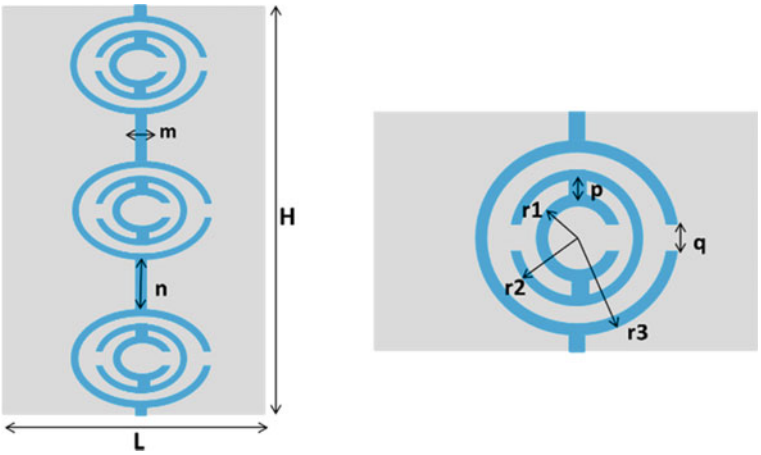

Fig. 1 Sensor structure with all dimensions nomenclature

Table 1 Sensor's dimensional values

Parameters	H	L	m	n	p	Q	r1	r2	r3
Values (in mm)	30	16	0.5	5	0.5	0.5	1.4	2.2	3

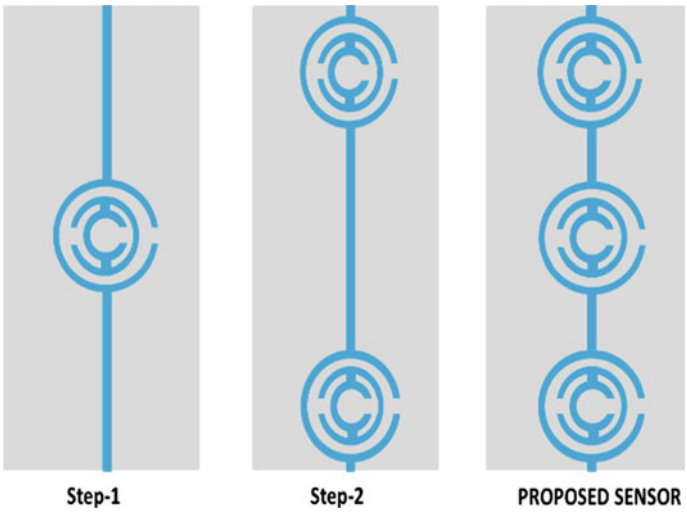

Fig. 2 Designing procedure of the proposed sensor

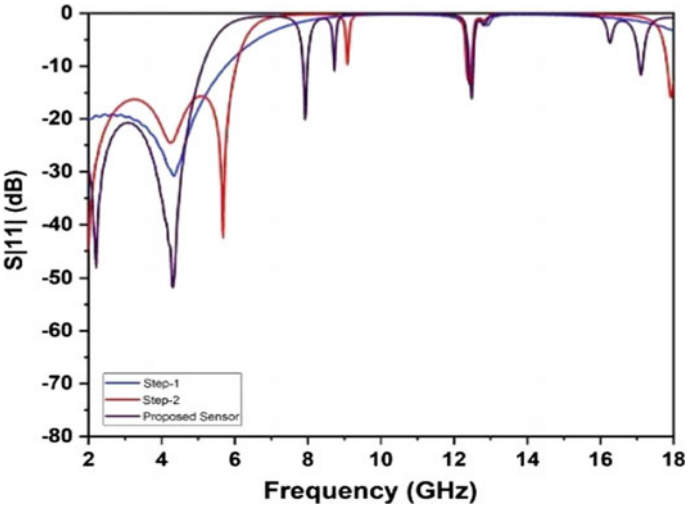

Fig. 3 Reflection coefficient (S11) of the evolution steps of the sensor

Three evolutionary iterations are discussed, and their S-parameters are compared in order to understand design process of proposed sensor. First, in step-1, a single resonator and a microstrip transmission line are designed. In the modification step, the number of resonators increases and the suggested sensor consists of three complementary split ring resonators with a transmission line as a feedline connecting ports to all the three resonators.

S-parameters are the most important parameters for analyzing the resonance behavior of the sensor. Figure 3 shows reflection coefficient of three different steps, and Fig. 4 shows the transmission coefficient. These results are then compared for better understanding the performance of proposed sensor. S-parameters show that proposed sensor with multiple resonators shows more resonance and provides good parameters and excels multi-band frequencies in final step by exciting higher modes of current distribution.

3 Result and Discussion

3.1 Performance Analysis of the Sensor

Simulated results of the S-parameters for the sensor are shown in Fig. 5. The senor exhibits multiple resonances at frequencies 8.5, 9, 12, and 16 GHz. However, transmission coefficients have two wide dip for the frequency range 10 GHz–12 GHz and 13 GHz–17 GHz, respectively. Multiresonance behavior of the ring resonator sensor is most desirable to differentiate the healthy and malignant skin.

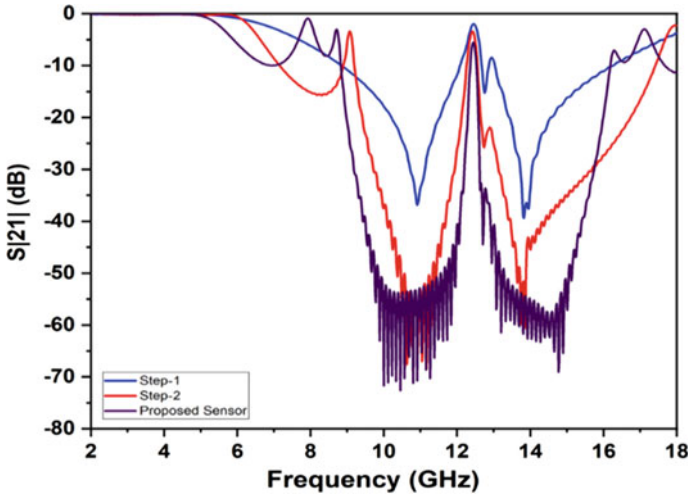

Fig. 4 Transmission coefficient (S21) of the evolution steps of the sensor

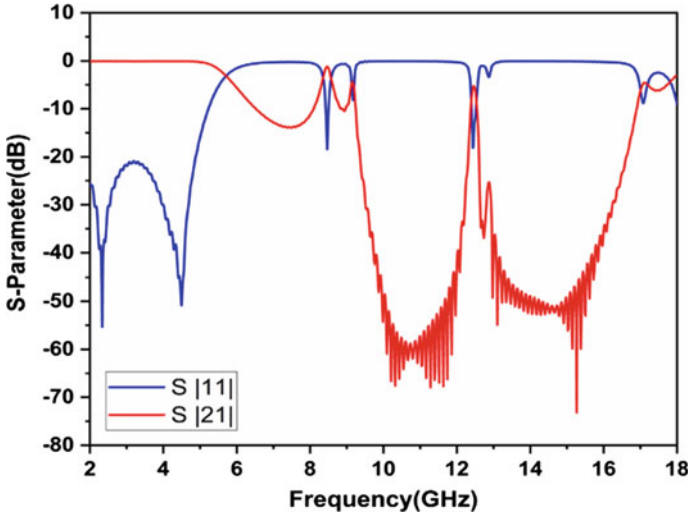

Fig. 5 S-parameters of the proposed sensor

Figure 6 depicts the proposed sensor's simulated gain and directivity over the target frequency spectrum. The sensor has stable gain more than 5 dB, and directivity also varies from −15 to 4 dBi within the interested frequency 2–18 GHz range.

To determine the pattern stability and orientation of the radiation, the simulated radiation patterns of the microwave sensor are analyzed and shown in Fig. 7a, b.

Here, obtained results are depicted at 2.3, 8.4, and 9.5 GHz frequency for the (phi = 0°) and (phi = 90°). These results are stable and directional at all frequencies.

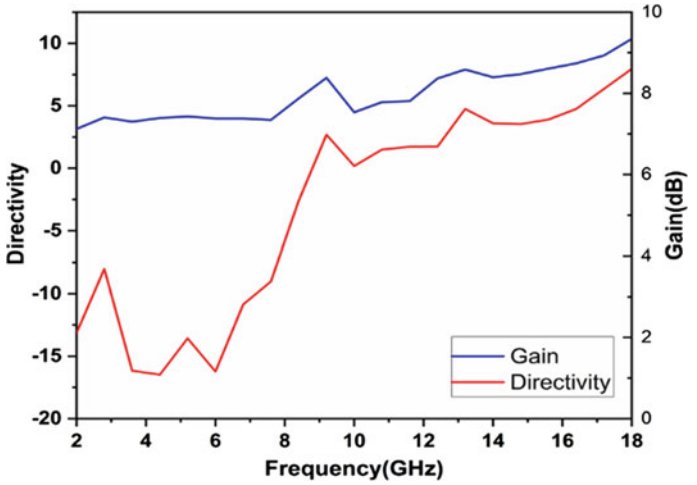

Fig. 6 Directivity and gain versus frequency results of the sensor

For microwave sensing radiation patterns should be more directional, here obtained results of the proposed antenna are acceptable for skin sensing applications.

The surface current density is shown in Fig. 8. The surface current is caught inside the near loop of the CSRR structure as it resonates, resulting in a high-current rate.

3.2 Development of Skin Model and Result of the Sensor with Skin

The engineered three layers of the skin phantom modeled in computer simulation technology (CST) microwave studio are shown in Fig. 9a, c. Human skin is divided into three layers, i.e., epidermis, dermis, and hypodermis. The upper layer comprises dead cells with a thickness of 15–35 μm. The epidermis average thickness of 25 μm is used in this work to build a skin model. The water content of this layer is about 55–75%. Dermis is a dense membrane between the epidermis and the subcutaneous tissues that protects the body from stress and pressure. However, hypodermis is a fat collection site composed of adipose tissue. Malignant tissues have a higher water content than healthy tissues. Both types of cancer cells have a bound water content in the epidermis layer. Usually, the water content of all types of cancerous skin tissues is about 80–85%.

It is obvious that higher water content of malignant tissues would create more reflections of the pulse transmitted. This is illustrated in Fig. 10 where a comparative S-parameter (S11 and S21) plot is seen for two cases of proposed sensor radiating with and without a cancer cell parallel to the skin phantom model. The upward shifted S11 and S21 parameter plots (solid red plot with cancer cell in the skin phantom model)

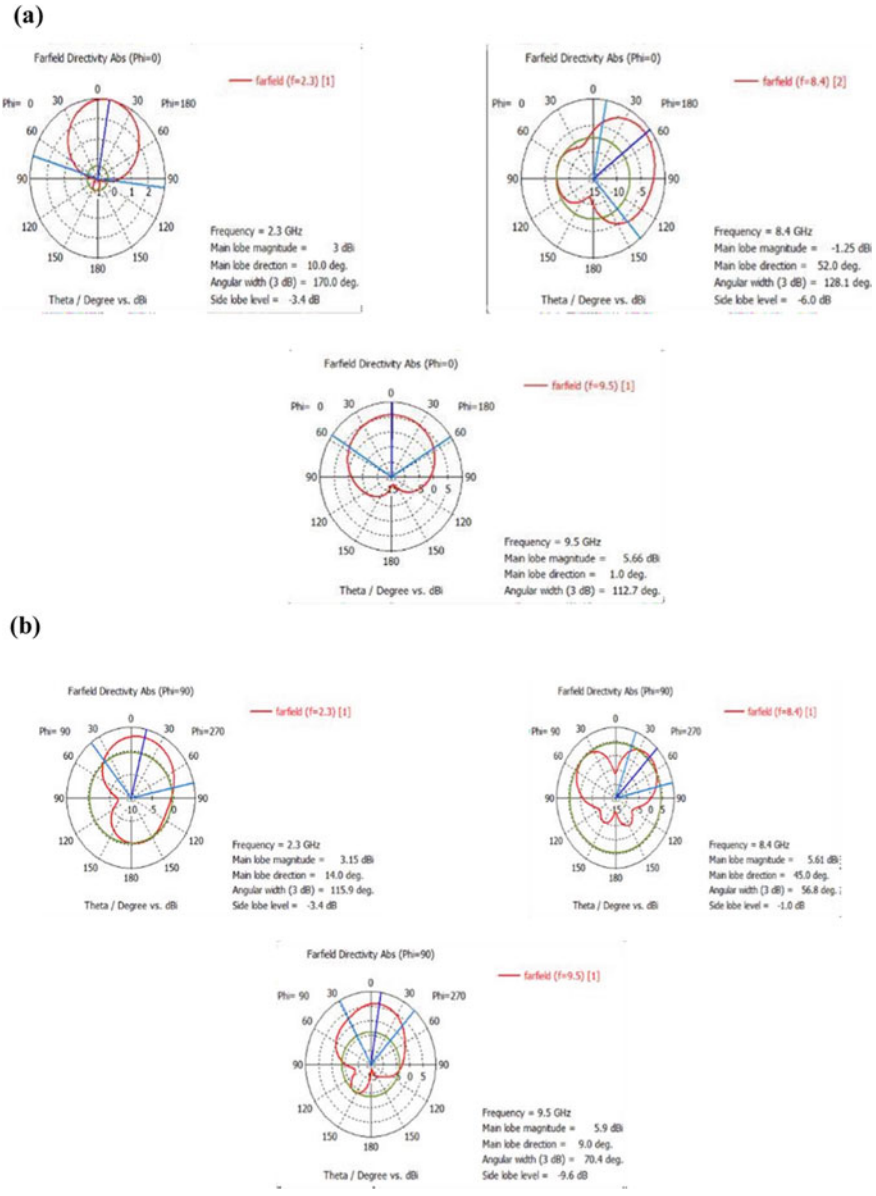

Fig. 7 **a** Radiation pattern at (Phi = 0°). **b** Radiation pattern at (Phi = 90°)

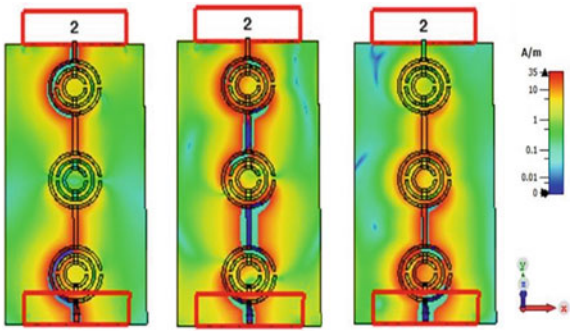

Fig. 8 Surface current density of the sensor

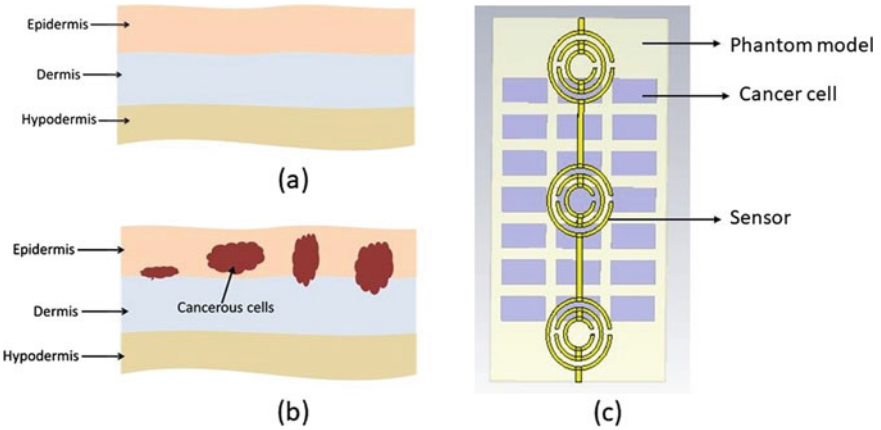

Fig. 9 **a** Skin equivalent model without cancer cells, **b** skin model with cancer cells, and **c** skin phantom model with embedded proposed sensor

are shown in Fig. 10 compared to the standard S11 and S21 parameter response plots (solid blue line plot without cancer cell in the skin phantom model). It is noted that the 2–4.5, 10–12, 14–15, 16–16.5 GHz frequency bands display more reflection in the skin phantom model in the presence of a cancer cell and thus allows the detection of tumor very visible in the phantom. On the basis of the difference in outcomes obtained between the parameters of S11 and S21 of a cancer cell impacted phantom of the skin to that of a healthy skin phantom; it is concluded that a CSRR sensor attached to the skin tissues infected by cancer may be used to identify a malignant cell in the affected skin tissues at an early stage.

The S-parameter (phase) in the presence and absence of cancer cell in the skin phantom depicts in Fig. 11a, b, respectively. From the obtained results, the following conclusion is taken: In the presence of the cancerous phase, difference has been noticed as normal skin phantom.

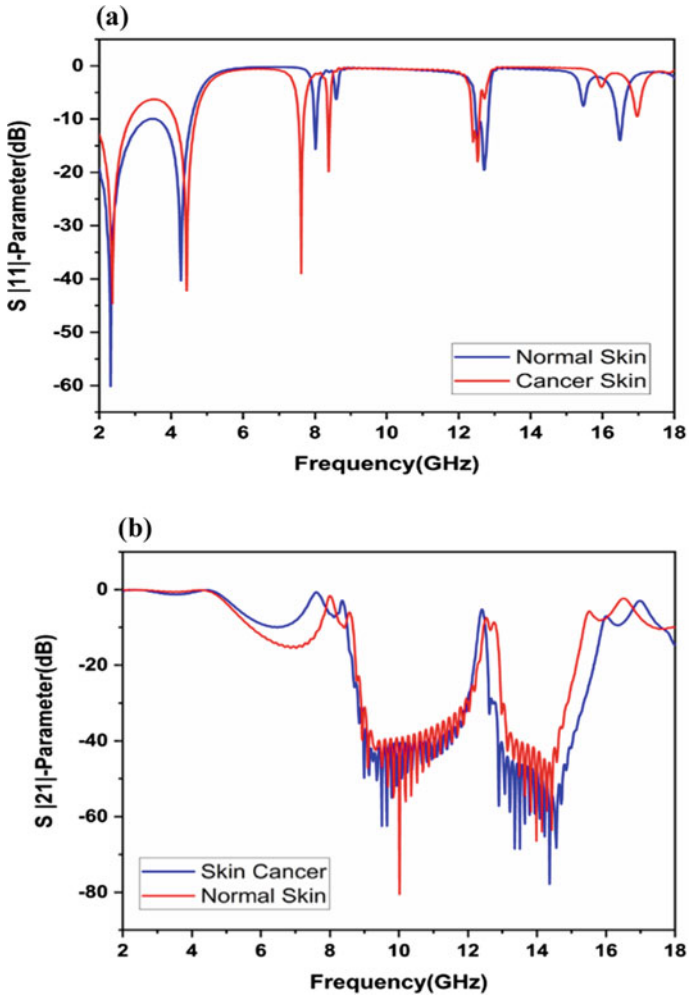

Fig. 10 **a** S11 parameter with and without cancer cell. **b** S21 parameter with and without cancer cell

4 Conclusion

This paper introduced a ring resonator microwave sensor and design approach focused on the CSRR to detect skin cancer, and the sensor performance is verified by using computer simulation tool (CST). The proposed resonator has multiple resonances. The sensor has radiation patterns aimed at 2.3, 8.4, and 9.5 GHz with stable directional patterns. Achieved performance standards are well suited for the identification of skin cancer in this frequency range. In this study, normal and cancerous skin models were selected for skin cancer research. The developed sensor is exposed

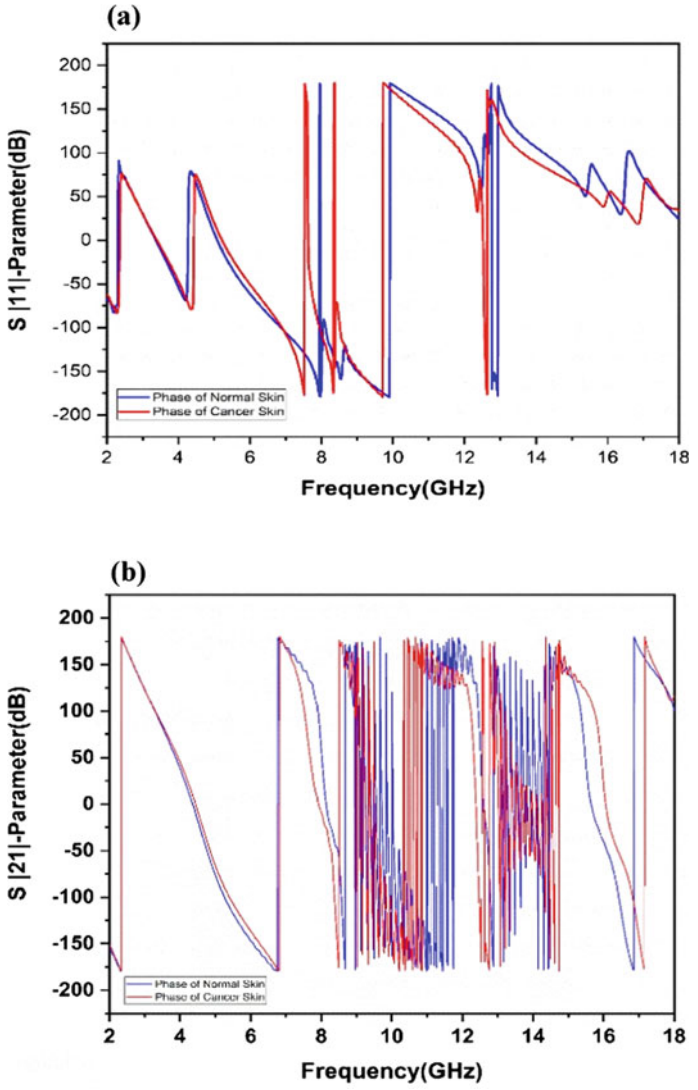

Fig. 11 **a** S11 parameter (phase) with and without cancer cell. **b** S21 parameter (phase) with and without cancer cell

to both types of models, and their S-parameter results are analyzed for the identification of cancerous cells. Compared to the case of a phantom without cancer cells, a difference in the S-parameter results between a skin phantom with cancer cells helps in the identification of any malignant cells. The magnitude and phase angle parameters of reflection clearly separated healthy and malignant skin cells. The proposed method of identification of skin cancer is also contrasted with the current method. In

contrast, the non-invasive, swift, and premature modality for skin cancer detection are low cost and effective.

References

1. Khalesi B et al (2018) Skin cancer detection through microwaves: validation on phantom measurements. In: 2018 IEEE international conference on imaging systems and techniques (IST). IEEE, New York
2. Singh SP et al (2020) Shallow 3D CNN for detecting acute brain hemorrhage from medical imaging sensors. IEEE Sensors J
3. Arab H et al (2020) Early-stage detection of melanoma skin cancer using contactless millimeter-wave sensors. IEEE Sensors J 20(13):7310–7317
4. Zoughi R (2000) Microwave non-destructive testing and evaluation principles, vol 4. Springer Science & Business Media
5. Beetner DG et al (2003) Differentiation among basal cell carcinoma, benign lesions, and normal skin using electric impedance. IEEE Trans Biomed Eng 50(8):1020–1025
6. Suntzeff V, Carruthers C (1946) The water content in the epidermis of mice undergoing carcinogenesis by methylcholanthrene. Cancer Res 6(10):574–577
7. Katbay Z et al (2018) From narrow-band to ultra-wide-band microwave sensors in direct skin contact for breast cancer detection. Analog Integr Circuits Sign Process 96(2):221–234
8. Muhammed Shafi KT et al (2017) Design of SRR-based microwave sensor for characterization of magnetodielectric substrates. IEEE Microwave Wireless Components Lett 27(5):524–526
9. Sharma MK, Kumar M, Saini JP (2015) UWB-MIMO antenna with enhanced isolation for breast cancer detection. In: 2015 2nd International conference on computing for sustainable global development (INDIACom). IEEE, New York
10. Yang C-L et al (2015) Noncontact measurement of complex permittivity and thickness by using planar resonators. IEEE Trans Microwave Theory Tech 64(1):247–257
11. Falcone F et al (2004) Effective negative-/spl epsiv/stopband microstrip lines based on complementary split ring resonators. IEEE Microwave Wireless Compon Lett 14(6):280–282
12. Boybay MS, Ramahi OM (2012) Material characterization using complementary split-ring resonators. IEEE Trans Instrum Meas 61(11):3039–3046
13. Sharma MK et al (2020) Experimental investigation of the breast phantom for tumor detection using ultra-wide band–MIMO antenna sensor (UMAS) probe. IEEE Sensors J 20(12):6745–6752
14. Nahata H, Singh SP (2020) Deep learning solutions for skin cancer detection and diagnosis. In: Machine learning with health care perspective. Springer, Cham, pp 159–182
15. Mukherjee S et al (2019) Enhancement of microwave imaging using a metamaterial lens. IEEE Sensors J 19(13):4962–4971
16. Khor WC et al (2006) An ultra wideband microwave imaging system for breast cancer detection, pp 1–5
17. Caratelli D et al (2011) Accurate time-domain modeling of reconfigurable antenna sensors for non-invasive melanoma skin cancer detection. IEEE Sensors J 12(3):635–643
18. Mehta P et al (2006) Microwave reflectometry as a novel diagnostic tool for detection of skin cancers. IEEE Trans Instrum Meas 55(4):1309–1316

Model-Based Hardware-in-the-Loop Closed-Loop Control of Brushless Direct Current Motor in Electric Vehicle Applications

Ramachandran Ramaraj, Ganeshaperumal Dharmaraj, Subathra Balasubramanian, and Renu Kumawat

Abstract Electric vehicles (EVs) widely use brushless direct current (BLDC) motor with trapezoidal commutation due to its high-power efficiency, ability to operate at high speeds, acceleration, and less maintenance. However, load torque ripples due to trapezoidal commutation and load torque variations due to terrain conditions affect the BLDC motor speed and performance significantly. Furthermore, load torque fluctuations reduce the lifetime of driver components and the battery significantly. Therefore, efficient driver design for BLDC motors that can handle load torque variations and maintains a set-speed for BLDC motors are emerging as an urgent need in the EVs. This investigation presents a hardware-in-the-loop (HIL)-based closed-loop control of BLDC motor for electric vehicle applications. The hardware to be tested which is the proportional integral controller that adjusts the pulse-width modulation applied to the BLDC motor. The motor parameters are obtained from experiments, and their values are used in the simulations. Then the electronic control unit is developed with Arduino and is tested with the MATLAB/Simulink model. Our results demonstrate the ability of HIL to provide a controller design that matches the electric vehicle requirements.

Keywords BLDC · HIL · Arduino

R. Ramaraj (✉) · G. Dharmaraj · S. Balasubramanian
Department of Instrumentation and Control Engineering, School of Electronics and Electrical Technology, Kalasalingam Academy of Research and Education, Virudhunagar District, Krishnankoil, Tamil Nadu, India
e-mail: ramachandran@klu.ac.in

G. Dharmaraj
e-mail: d.ganeshaperumal@klu.ac.in

S. Balasubramanian
e-mail: b.subathra@klu.ac.in

R. Kumawat
Department of Electronics and Communication Engineering, School of Electrical, Electronics and Communication Engineering, Manipal University, Jaipur, Rajasthan, India
e-mail: renu.kumawat@jaipur.manipal.edu

S. Dwivedi et al. (eds.), *Flexible Electronics for Electric Vehicles*, Lecture Notes in Electrical Engineering 863, https://doi.org/10.1007/978-981-19-0588-9_6

1 Introduction

Electric vehicles (EV) are emerging as a promising solution to reduce the vehicular emissions that are caused by internal combustion engines. The typical propulsion system for an EV comprises a motor, driver hardware, and a battery system. As the advancement in battery technology is limited, researchers focus on the selection and design of the motor and the driver hardware to extend the driving range of the EV. In recent years, the brushless direct current (BLDC) motor is prevalent in EV due to its high-power efficiency, high torque, lightweight, and less maintenance requirements [1]. However, improper selection and design of the driver hardware lead to vibrations and torque ripples in the BLDC motor, consequently affecting its performance, battery life, and driving comfort considerably. Although these effects can be eliminated by adding additional components to the driver, they are expensive and energy-consuming. Also, the BLDC motor experiences constant load torque disturbances due to the terrain conditions. This affects the performance of the BLDC motor and prevents the motor from operating at a set-speed. Therefore, suitable control algorithms need to be developed to handle load torque variations. However, the choice of the control algorithm is determined by the control unit used.

One method to design an efficient driver is installing a DC-DC converter in front of the inverter to regulate its voltage during the commutation period. Widely used converters are (i) buck converter [2], (ii) Cuk converter [3], (iii) boost converter [4], (iv) SEPIC converter [5, 6], and (v) multi-stage DC-link inverters [7]. Another approach is to use a multilevel inverter to reduce the torque ripple [5]. However, these modifications increase the number of components, cost, and power consumption. A half-bridge inverter design to commutate the BLDC is studied in [8] to reduce the cost. But their real-time deployment and performance are not studied. As an alternative, software modifications such as developing an effective control algorithm are preferred to handle the load torque variations, torque ripples and maintain set-speed.

Several control algorithms are proposed in the literature to control speed and minimize the load torque ripples. The fundamental approach is pulse-width modulation (PWM), wherein the ON/OFF time of the MOSFET switches is varied based on the error signal [9, 10]. However, it cannot handle load torque fluctuations. The proportional, integral, and derivative (PID) controller, with its simple design, is a widely preferred choice for speed control. Further, these controllers can be deployed in low-cost control units. But they require proper tuning to handle the load disturbance. Fractional-order PID controllers that retain the simple design of PID yet provide additional tuning parameters are proposed in [11–14]. However, it requires proper control parameter tuning for robust performance. Soft computing techniques such as fuzzy logic controllers [15] and artificial neural networks [16] are investigated for speed control. Though these techniques provide human-like reasoning and can handle nonlinear behaviors, they consume more memory.

Optimization-based control algorithms, such as model predictive control (MPC), are investigated for torque ripple minimization and speed control in [17]. Similarly,

model reference adaptive control (MRAC) coupled with a sliding mode controller is used for speed control in [18, 19]. Also, an adaptive load torque observer is studied in [20] to analyze the load torque disturbances. While the optimization-based control algorithms address the load torque variations and commutation ripples, their implementation requires dedicated hardware with powerful processors and memory.

In literature, widely used control hardware for BLDC control are: (i) microcontroller unit (MCU) [21], (ii) digital signal processors (DSP) [22], and (iii) field-programmable gate arrays (FPGA) [23]. Among these devices, the DSP and FPGA devices have powerful processors. They can host sophisticated control algorithms such as MPC and MRAC. However, they require high development cost, lacks programming flexibility, and consume energy due to their powerful processors. On the other hand, MCU, with its low cost and simplicity to program the control algorithm, is a suitable choice for BLDC speed control. However, the MCUs have limited processing speed and memory. Therefore, the control algorithm must be selected in such a way that the MCU is not overloaded. The review of the literature reveals that the PID controller is a suitable choice due to its simple design and minimum memory requirements.

A detailed review of the literature reveals that an efficient driver for BLDC motor requires optimal selection of control algorithm and hardware components due to their implications on cost and energy consumption. From a controller perspective, the PID controller stands out due to its simple design, yet deployable in a low-cost MCU.

The main contributions of this investigation are:

1. Experiments to study the parameters of the BLDC motor for EV applications.
2. A HIL-based approach for the design of BLDC controller and its validation for different load profiles.
3. Validation of the design on real-time embedded hardware.

The rest of the paper is organized as follows: Section 2 problem formulation, Sect. 3 mathematical model of BLDC motor, Sect. 4 presents the BLDC motor parameter identification. In Sect. 5, hardware-in-the-loop (HIL) implementation is presented. In Sect. 6, results and discussions are presented and concluded in Sect. 7.

2 Problem Formulation

The problem is to design a controller for BLDC motor for EV applications considering various loading patterns. Offline design of the BLDC motor without understanding the loading effects may lead to a controller design that does not replicate the requirements and exploring the entire design space is a costly option. Therefore, approaches to synthesize controllers for BLDC drives using model-based approaches emerge as a promising solution. The model-based approaches have the following steps: (1) requirement elicitation, (2) model generation, (3) preliminary design using simulation, (4) HIL-based design, (5) validation and verification of the performance.

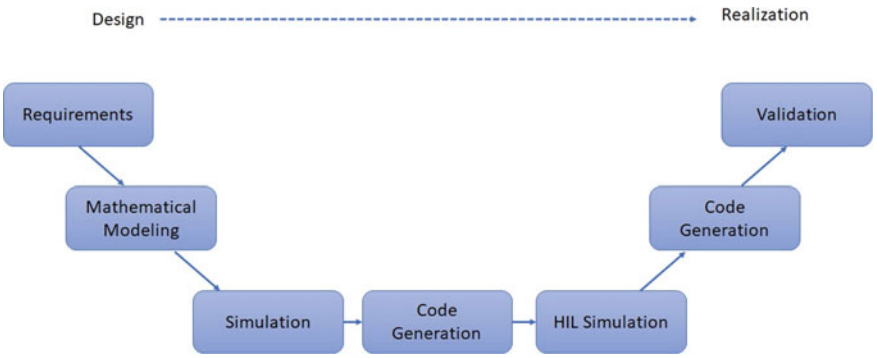

Fig. 1 Model-based design methodology

This paper illustrates the procedure to run the workflow from the start and tries to build the BLDC controller that suits the EV applications. To design the controller, a V-model is adapted as shown in Fig. 1. In the closed-loop control configuration of the BLDC, the main drive consists of an inverter that is controlled using a PWM technique whose firing angle is adjusted by a PI controller which acts on the error to command the firing angle to meet the set-speed. The feedback is taken from the hall-sensors and provided as a feedback input to the controller. The difference between the set-speed and the feedback signal is the error and the input to the controller which modifies the PWM rate to control the speed of the motor. One of the major concerns in the design of the BLDC drive is the effect of torque ripple which is caused to the commutation that occurs during switching instants. The load influences are another major challenge. The BLDC motor should meet the requirements in the presence of load variations and torque ripples.

Exhaustively verifying all load conditions and studying the effect of torque ripple to tweak the controller parameters is a daunting task. Therefore, to perform this design space exploration, this investigation will go through the different steps of the model-based design and each of them will be discussed in great detail.

3 BLDC Motor Mathematical Model

We construct two kinds of BLDC motor models to analyze its dynamic behavior and to design control algorithms for speed control, respectively. To capture the dynamics of the BLDC motor, we construct a detailed model that includes asymmetric three-phase currents, trapezoidal back emf generation, and electromagnetic torque generated from the phase currents. While designing control algorithms, we modify the detailed BLDC motor configuration to a simple DC motor model.

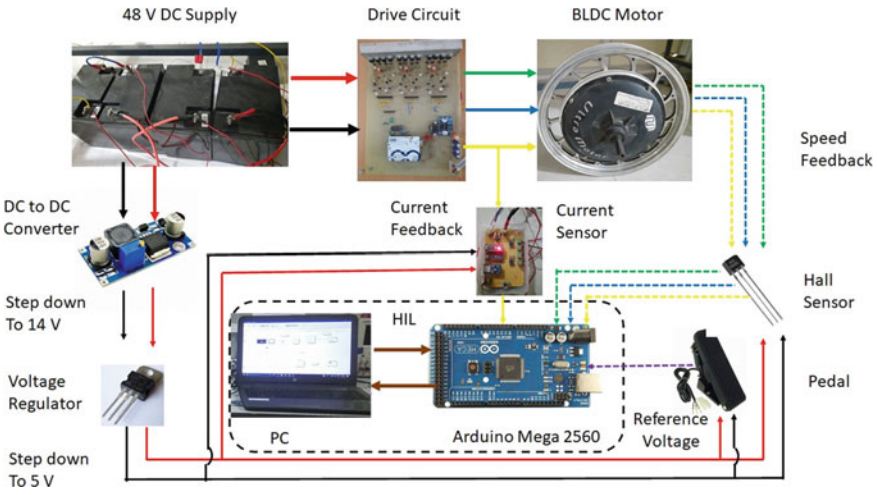

Fig. 2 HIL deployment

3.1 Detailed Model

We derive a detailed mathematical model of the BLDC motor considering the following assumptions.

1. The BLDC motor taken for the study is three-phase and star-connected
2. The resistance and inductance for all three phases are identical
3. The mutual inductance of each phase is negligible.

Now, consider a in-wheel BLDC motor with stator windings *a*, *b,* and *c*, denoting three phases. If I_a, $I_{b,}$ and I_c denote the current through the coils, then the voltage across each phase of BLDC is given by,

$$V_p(t) = R_p i_p(t) + L_p \frac{di_p(t)}{dt} + e_p(t), \quad \forall p \in a, b, c, \forall t \in \mathcal{R}^+ \tag{1}$$

$$i_a(t) + i_b(t) + i_c(t) = 0, \quad \forall t \in \mathcal{R}^+ \tag{2}$$

where V_p, R_p, $L_{p,}$ and e_p are phase voltage, resistance, inductance, and back emf of *k*th phase, respectively. The back emf for each phase is given by,

$$\begin{aligned} e_a(t) &= K_b \omega_m(t) f(\theta_e), \\ e_b(t) &= K_b \omega_m(t) f\left(\theta_e - \frac{2\pi}{3}\right) \\ e_c(t) &= K_b \omega_m(t) f\left(\theta_e - \frac{4\pi}{3}\right), \forall t \in \mathcal{R}^+ \end{aligned} \tag{3}$$

where K_b is the back emf constant in Vs rad^{-1}, θ_e is electrical displacement in rad, ω_m is the motor shaft angular velocity in rad s^{-1}. The function $f(\theta_e)$ depends on the rotor position and trapezoidal back emf waveform.

The total electromagnetic torque T_e is given by,

$$T_e(t) = K_t\left[f(\theta)i_a(t) + f\left(\theta_e - \frac{2\pi}{3}\right)i_b(t) + f\left(\theta_e - \frac{4\pi}{3}\right)i_c(t)\right] \tag{4}$$

where K_t is the torque constant. The electromagnetic torque is related to motor's angular velocity as,

$$T_e(t) - T_l(t) = J\frac{d\omega_m(t)}{dt} + B\omega_m(t), \tag{5}$$

where J and B are moment of inertia and damping coefficient, respectively. Note that T_l is the load torque in Nm. Equations (1)–(5) provide the dynamics of the BLDC motor.

3.2 Control Model

To design the speed control algorithm, we model the BLDC motor as a simple DC motor. We derive a transfer function relating the BLDC's angular velocity and the stator voltage as follows.

The stator excitation voltage of the BLDC motor is an output from the inverter module given by,

$$V_s(t) = \delta V_{DC}, \quad 0 \le \delta \le 1 \tag{6}$$

where V_s is the BLDC stator excitation voltage, V_{DC} is the battery voltage, and δ is the duty cycle of the inverter switches. Then, the voltage drop across the stator coil is given by,

$$V_s(t) = i(t) \cdot R + L \cdot \frac{di(t)}{dt} - E(t), \tag{7}$$

where i is the stator current, R and L are the resistances and inductances of the stator coil, respectively. E is the back emf generated by the BLDC motor. The back emf is given by

$$E(t) = K_b \cdot \omega_m(t) \tag{8}$$

Then the electromagnetic torque generated by the BLDC motor is

$$T_e(t) = K_t \cdot i(t) \tag{9}$$

We retain Eq. (5) to obtain the angular velocity of the BLDC motor. Combining Eqs. (5) and (7) and taking Laplace transformation yield a control model for BLDC motor as,

$$\frac{\omega_m(s)}{V_s(s)} = \frac{K_t \cdot K_b}{(Ls + R)(Js + B) + K_t \cdot K_b}, \tag{10}$$

where $\omega_m(s)$, $V_s(s)$ are the Laplace of the angular velocity and stator voltage, respectively.

4 BLDC Parameter Identification for Control Design

The accurate BLDC parameters are required to design the speed control algorithm. The key parameters of the BLDC motors are

4.1 Phase Resistance R_p

For a star-connected BLDC motor, the line-to-line resistance R_L is measured using an ohm meter, and the corresponding phase resistance is calculated as,

$$R_p = \frac{R_L}{2} \quad \forall p \in \{a, b, c\} \tag{11}$$

4.2 Electrical Time Constant τ_e

The electrical time constant is the time taken for a BLDC motor to reach 63.2% of the final value of phase current I_p for a step-change in the phase voltage V_p, and it is given by,

$$\tau_e = \frac{L_p}{R_p} \tag{12}$$

Though a straightforward expression is available to calculate τ_e, experiments are required to have an accurate measurement that accounts for losses. Therefore, we split the entire voltage range (0–48 V) into three regions, namely low range (0–16 V), medium-range (16–32 V), and high range (32–48 V). In each range, we provide

a step-change in the voltage and record the corresponding current profile. The time taken to reach 63.2 % of the final current is noted for all the ranges, and its average is calculated to provide an electrical time constant τ_e. Then, the phase inductance can be obtained straightforward from (12).

4.3 Back emf Constant K_b

The back emf generated by the BLDC motor is related to its operating speed. To measure the back emf constant K_b, we operate our BLDC motor as a generator by coupling it with another motor that is rotating at a known angular velocity ω_m. We measure the line-to-line voltage V_L from the BLDC and convert it to phase voltage V_p. Then using the following expression, the back emf constant is calculated as,

4.4 Torque Constant K_t

$$K_b = \frac{V_p}{\omega_m} \tag{13}$$

The motor torque constant is given by,

$$K_t = \eta K_b, \tag{14}$$

where η is the efficiency of BLDC motor, which is the ratio between the mechanical power P_m and the electrical power P_e,

$$\eta = \frac{P_m}{P_e} \tag{15}$$

where $P_m = T_m.\omega_m$ and $P_e = V_p.I_p$.

4.5 Moment of Inertia J

To determine rotor inertia J, we increase the BLDC's angular velocity from ω_1 to ω_2 and measured the corresponding time elapsed Δt. Then multiplying it with torque T, we get,

$$J = \frac{\omega_1 \omega_2}{\Delta t} \cdot T \tag{16}$$

Table 1 BLDC motor parameters [24]

Parameters	Value
Phase resistance R_p	0.3 Ω
Phase inductance L_p	0.35 mH
Electrical time constant τ_e	1.2 ms
Back emf constant K_b	0.5 Vs/rad
Torque constant K_t	0.4 Nm/A
Moment of inertia J	0.0099 kg m^2
Damping coefficient B	0.12 Nm s
Mechanical time constant τ_m	80 ms

4.6 Damping Coefficient B

Under equilibrium condition, the damping coefficient is the ratio of motor torque T_m and the angular velocity ω_m, and it is given by,

$$B = \frac{T_m}{\omega_m} \tag{17}$$

4.7 Mechanical Time Constant τ_m

The mechanical time constant is the 63.2% of the time taken to reach from angular velocity ω_1 to ω_2. A straightforward expression to obtain τ_m is,

$$\tau_m = \frac{J}{B} \tag{18}$$

The BLDC parameters obtained using the above procedures are listed in Table. 1.

5 Hardware-in-the-Loop Implementation

This section deals with HIL implementation for the BLDC motor model mentioned in the previous section. The system consists of three main parts,

(i) PC—it is used to do PID controller part in MATLAB for the system.
(ii) ATMega2560—microcontroller used for interface between hardware and MATLAB, which is used to generate PWM for the BLDC motor.
(iii) BLDC motor—it responds for the reference speed and gives the hall sensor feedback to the microcontroller.

There are two inputs and one output for the HIL in the Simulink. The very first task for the HIL is accepting input from the reference generator, which is coming from the pedal of the electric vehicle as an analog value (0–5 V). The second input is from the hall sensor of the BLDC motor, and it is used to find the speed of the BLDC motor using the speed algorithm. The output from HIL is PWM for the motor.

The analog input is 0–5 V, and this real-time value is given to ATMega2560 microcontroller to the analog input of 'A5'. Since it is a 10-bit microcontroller, the resolution is '1024' values. Hence, the maximum value is '1023' and the minimum value is '0'. In Simulink first, it is given as analog values; however, this is converted into 0–5 V through the help of a quantizer. Then this analog input is converted to desired reference speed using a reference generator. Hall sensor from the real motor will give the position of the rotor, this is fed-back through ATMega328P, and a speed algorithm is applied to get the actual speed. The hall sensor signal is a square wave, and it is a digital signal, wherein speed algorithm the time difference between two successive rising edges are noted and converted to speed. For this motor, the frequency of the hall sensor varies between 10 and 145 Hz. An ACS712 current sensor is used to record the current measurement, and it is an analog sensor with a resolution of 4.88mV per count. It can measure up to 30 A both AC and DC current. It has been chosen because can be easily interfaced with the Arduino microcontroller and measurement can be recorded and waveform can be drawn. PWM generator block is used to create PWM value to the Arduino microcontroller. This controller PWM value is 8-bit, and it varies between 0 and 255, where '0' is zero percentage and '255' is hundred percentage PWM accordingly.

6 Results and Discussion

In this section, the simulation results and HIL results are compared. For the simulation study, the input voltage frequency is derived from the speed of the BLDC motor. A number of revolutions for one minute are first converted to revolutions for one second, and the reciprocal will give us the time duration for one revolution. This is known as one mechanical cycle to achieve one full rotation which is 360°. This BLDC motor has 46 poles, from the relation between electrical and mechanical degrees one electrical cycle is given by,

$$\theta_e = \frac{P}{2}\theta_m \tag{19}$$

where θ_e is electrical degree in rad, P is total number of poles, θ_m is mechanical degree.

The reference speed here is 200 rpm, and hence, the input voltage frequency is 76.9 Hz; the generated input voltage amplitude is equal to DC input voltage 48 V, and load torque set commands are: (i) No-load for 0–100 ms, (ii) 3 Nm for 100–200 ms as shown in Fig. 1. The proportional gain is found from the relation between

error and frequency of the generated input voltage. The slope is 0.3879. Further, the integration time is calculated from the load torque profile to achieve the desired response in motor during load conditions.

Figure 3a shows the speed response for various load torque applied at every 100 ms. The first command is no-load till 100 ms, so the steady state of actual speed maintains at 200 rpm. Second load torque command given at time 100 ms is 3 Nm, so the speed is suddenly decreased to 190 rpm and rises back to 200 rpm at 108 ms.

The torque variations are illustrated in Fig. 4. At no-load the electromagnetic torque is maintained around 0.5 Nm for the 100 ms duration. Then it is increased for sudden load applied at 100 ms. The phase current variations are shown in Fig. 5, at no-load the current maintains at 5 A. When the 3 Nm load is applied at 100 ms, the phase current increases to 10 A. This control is named as optimal PID control, and this is compared with the auto-tuned PID for verification. Finally, verified with the HIL results.

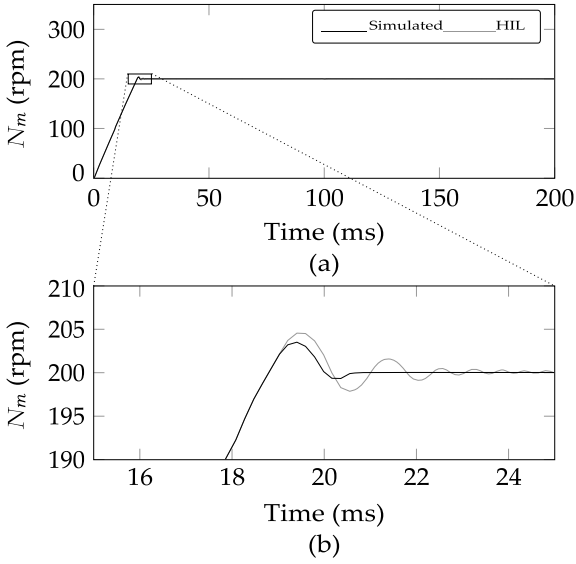

Fig. 3 Simulated versus HIL results: speed tracking

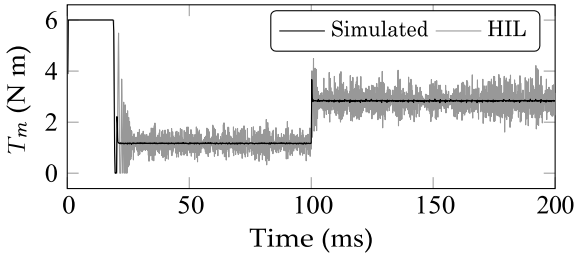

Fig. 4 Simulated versus HIL results: torque variations

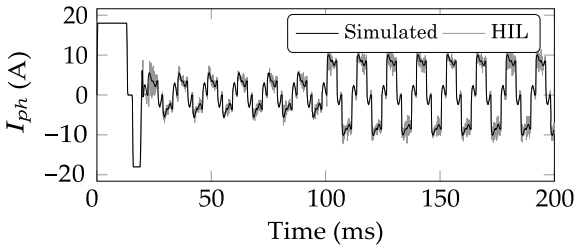

Fig. 5 Simulated versus HIL results: phase current variations

Table 2 Simulated versus HIL performance indices

Performance metrics	MSE			RMSD		
	ω_{m}	T_{m}	I_{ph}	ω_{m}	T_{m}	I_{ph}
Auto-tuned versus optimal	0.3	0.035	0.01	0.54	0.115	0.012
Optimal versus HIL	0.2	0.012	0.0099	0.44	0.1136	0.099

The HIL results are recorded as mentioned earlier, the motor speed is measured using the hall sensor feedback, and the phase current is measured using the current sensor. The simulated speed tracking, torque variations, and phase current variations are compared with the HIL results. The performance metrics are illustrated in Table 2. MSE is the mean square error, and RMSD is the root mean square deviation. The main advantage of using the HIL approach is that the design validations were performed during each step of the design process that enabled faithful replication of the design objectives.

7 Conclusion

This paper presented a HIL-based approach for designing a controller for BLDC motor used in EV applications. The HIL approach had the following steps: (1) requirements, (2) model-based parameter identification, (3) simulation study, (4) implementation, (5) testing and validation. The main advantage of using the HIL approach is that the design validations were performed during each step of the design process that enabled faithful replication of the design objectives. In the first step of the HIL, the requirements were described in text-based language, and then the modeling of the motor was performed using experiments. Once the model was obtained, the controller design ensued with the selection of the components, sampling frequency, and protection equipment such as fuses. Then the SIL tests were performed wherein both the motor and the controller were tested using simulations and then the actual design was performed with Arduino, a driver circuit, FET, and the associated components. Our results demonstrated that HIL is a good approach to design controllers for BLDC motors intended for EV applications.

References

1. Safi S, Acarnley P, Jack A (1995) Analysis and simulation of the high-speed torque performance of brushless DC motor drives. IEE Proc Electr Power Appl 142(3):191–200. https://doi.org/10.1049/ip-epa:19951808
2. Xiaofeng Z, Zhengyu L (2006) A new BLDC motor drives method based on BUCK converter for torque ripple reduction. In: 2006 CES/IEEE 5th international power electronics and motion control conference, vol 3, pp 1–4. IEEE. https://doi.org/10.1109/IPEMC.2006.4778275
3. Bist V, Singh B (2014) A unity power factor bridgeless isolated CUK converter-fed brushless dc motor drive. IEEE Trans Industr Electron 62(7):4118–4129. https://doi.org/10.1109/TIE.2014.2384001
4. Chen W, Xia C, Xue M (2008) A torque ripple suppression circuit for brushless DC motors based on power dc/dc converters. In: 2008 3rd IEEE conference on industrial electronics and applications, pp 1453–1457. IEEE. https://doi.org/10.1109/ICIEA.2008.4582760
5. Viswanathan V, Jeevananthan S (2014) Approach for torque ripple reduction for brushless DC motor based on three-level neutral-point-clamped inverter with DC–DC converter. IET Power Electron 8(1):47–55. https://doi.org/10.1049/iet-pel.2013.0471
6. Shi T, Guo Y, Song P, Xia C (2009) A new approach of minimizing commutation torque ripple for brushless DC motor based on DC–DC converter. IEEE Trans Industr Electron 57(10):3483–3490. https://doi.org/10.1109/TIE.2009.2038335
7. Su GJ, Adams DJ (2001) Multilevel DC link inverter for brushless permanent magnet motors with very low inductance. In: Conference record of the 2001 IEEE Industry Applications Conference. 36th IAS Annual Meeting (Cat. No. 01CH37248). vol 2, pp 829–834. IEEE. https://doi.org/10.1109/IAS.2001.955549
8. Lu M, Li Y (2010) New design for sensorless BLDC motor using half-bridge driver circuit. In: 2010 International Conference on E-Product E-Service and E-Entertainment, pp 1–4. IEEE. https://doi.org/10.1109/ICEEE.2010.5661498
9. Zhou X, Zhou Y, Peng C, Zeng F, Song X (2018) Sensorless BLDC motor commutation point detection and phase deviation correction method. IEEE Trans Power Electron 34(6):5880–5892. https://doi.org/10.1109/TPEL.2018.2867615
10. Ramachandran R, Ganeshaperumal D, Subathra B (2019) Closed-loop control of BLDC motor in electric vehicle applications. In: 2019 IEEE international conference on clean energy and energy efficient electronics circuit for sustainable development (INCCES). pp 1–5. IEEE. https://doi.org/10.1109/INCCES47820.2019.9167730
11. Ganeshaperumal D, Muthukumar N, Ramkumar K, Srinivasan S, Subathra B (2016) Optimal fractional controller design methodology for electric drive train. Int J Electr Hybrid Veh 8(4):335–350. https://doi.org/10.1504/IJEHV.2016.080731
12. Perumal DG, Saravanakumar G, Subathra B, Srinivasan S, Ramaswamy S (2014) Nonlinear state estimation based predictive path planning algorithm using infrastructure-to-vehicle (i2v) communication for intelligent vehicle. In: Proceedings of the second international conference on emerging research in computing, information, communication and applications (ERCICA 2014). https://doi.org/10.1016/j.ifacol.2016.03.130
13. Perumal DG, Srinivasan S, Subathra B, Saravanakumar G, Ayyagari R (2016) MILP based autonomous vehicle path-planning controller for unknown environments with dynamic obstacles. Int J Heavy Veh Syst 23(4):350–369. https://doi.org/10.1504/IJHVS.2016.079272
14. Perumal DG, Subathra B, Saravanakumar G, Srinivasan S (2016) Extended kalman filter-based path-planning algorithm for autonomous vehicles with I2V communication. IFAC-PapersOnLine 49(1):652–657. https://doi.org/10.1016/j.ifacol.2016.03.130
15. Kahveci H, Okumuş H, Ekici M (2014) Improved brushless DC motor speed controller with digital signal processor. Electron Lett 50(12):864–866. https://doi.org/10.1049/el.2014.0609
16. Colak I, Sahin M, Esen Z (2013) Artificial neural networks controller algorithm developed for a brushless DC motor. In: 2013 12th international conference on machine learning and applications, vol 2, pp 238–242. IEEE. https://doi.org/10.1109/ICMLA.2013.129

17. de Castro AG, Pereira WCA, de Almeida TEP, de Oliveira CMR, de Almeida Monteiro JRB, de Oliveira AA (2018) Improved finite control-set model-based direct power control of BLDC motor with reduced torque ripple. IEEE Trans Indus Appl 54(5):4476–4484. https://doi.org/10.1109/TIA.2018.2835394
18. Zhang D, Liu G, Zhou H, Zhao W (2018) Adaptive sliding mode fault-tolerant coordination control for four-wheel independently driven electric vehicles. IEEE Trans Industr Electron 65(11):9090–9100. https://doi.org/10.1109/TIE.2018.2798571
19. Chen S, Zhou X, Bai G, Wang K, Zhu L (2017) Adaptive commutation error compensation strategy based on a flux linkage function for sensorless brushless DC motor drives in a wide speed range. IEEE Trans Power Electron 33(5):3752–3764. https://doi.org/10.1109/TPEL.2017.2765355
20. Ko JS (1998) Asymptotically stable adaptive load torque observer for precision position control of BLDC motor. IEE Proc Electric Power Appl 145(4):383–386. https://doi.org/10.1049/ip-epa:19982010
21. Ganeshaperumal D, Sreram B, Ramachandran R (2019) ECU design for BLDC motor using truetime. In: 2019 IEEE international conference on clean energy and energy efficient electronics circuit for sustainable development (INCCES), pp 1–5. IEEE. https://doi.org/10.1109/INCCES47820.2019.9167690
22. Carey KD, Zimmerman N, Ababei C (2018) Hybrid field oriented and direct torque control for sensorless BLDC motors used in aerial drones. IET Power Electron 12(3):438–449. https://doi.org/10.1049/iet-pel.2018.5231
23. Darba A, De Belie F, D'haese P, Melkebeek JA (2015) Improved dynamic behavior in BLDC drives using model predictive speed and current control. IEEE Trans Indus Electron 63(2):728–740. https://doi.org/10.1109/TIE.2015.2477262
24. Ramaraj R, Dharmaraj G, Srinivasan S, Balasubramanian S, Periyasamy M, Bekiroglu K (2020) Real-time extremum seeking controller for brushless dc hub motors in electric vehicles. IET Electr Power Appl 14(12):2438–2449. https://doi.org/10.1049/iet-epa.2020.0117

Comparative Study of Shortest Distance Calculation Techniques in IoT-Based Wireless Sensor Networks

Ramandeep Gill and Tarun Kumar Dubey

Abstract The Internet of Things (IoT) includes the network of physical things installed with sensors, software application, and various other modern technologies to attaching and exchanging information with various other tools and systems over the Internet (Lee et al., in Int J Appl Sci MDPI 7:1072–1097, 2017). With the introduction of the IoT, communication capacity will certainly not be restricted to only smartphones. Instead, it will increase to all points which exist side-by-side. In this paper, a wireless sensor network (WSN) is designed using IoT nodes. A comparative study of two techniques is carried out to calculate the shortest distance between the source and destination node. The techniques are simulated using CupCarbon IoT 5.0 simulator.

Keywords Internet of Things · Wireless sensor network · CupCarbon IoT 5.0

1 Introduction

WSN includes spatially distributed independent devices using sensors to cooperatively keep track of physical or environmental conditions, such as temperature level, audio, vibration, stress, motion, or toxins, at various locations [1]. It consists of many sensor nodes/IoT nodes that are randomly deployed in an environment. There are four main stages in an IoT architecture shown in Fig. 1.

R. Gill (✉) · T. K. Dubey
Department of Electronics and Communication Engineering, Manipal University Jaipur, Dahmi Kalan, Jaipur, Rajasthan 303007, India
e-mail: raman89gill@gmail.com

T. K. Dubey
e-mail: tarunkumar.dubey@jaipur.manipal.edu

S. Dwivedi et al. (eds.), *Flexible Electronics for Electric Vehicles*, Lecture Notes in Electrical Engineering 863, https://doi.org/10.1007/978-981-19-0588-9_7

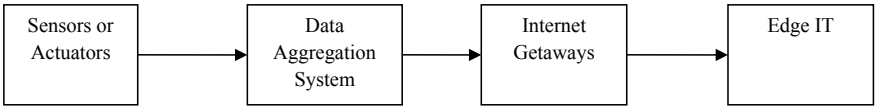

Fig. 1 Different stages in IoT architecture

Sensors or actuators to collect the data from the surrounding environment, data aggregation system to aggregate and assess incoming data, Internet getaways connects through Wi-Fi, wired LANs for further processing, and edge IT systems perform improved analytics as well as preprocessing. For instance, it refers to artificial intelligence and visualization of modern technologies. Simultaneously, some added processing might happen here, before the stage of entering the data center.

In metropolitan locations, the combination of the IoT and "sensing as a service" ideas with traditional WSN-based systems leads to the change of conventional city services in the direction of smart cities [2]. This paper is working on the same concept where a WSN of IoT node is designed, and a comparative study of two techniques is carried out to calculate the shortest distance between the source and destination node. The techniques are simulated using CupCarbon IoT 5.0 simulator [3].

2 System Model

There are various techniques to calculate the shortest distance between the source and destination node [4]. In this paper, two main techniques named Bellman–Ford algorithm and Dijkstra's algorithm are discussed. These two techniques are simulated to compute the end-to-end delay [5], for each case, it is calculated using the mathematical formula as listed in Eq. (1)

$$\frac{N \times L}{R} \times P \tag{1}$$

Here, P denotes the number of packets sent over a network, N denotes the number of links between the nodes, L denotes the packet's length, and R is the transmission rate. The end-to-end delay for every simulation is computed by the simulator and represented as execution time.

A network of five IoT nodes is designed (see Fig. 2).

In the network (see Fig. 2), IoT1[0] is considered as the source node and IoT5[0] is considered as the destination node. Distance between every two nodes is enabled by using the "Distance" option in the simulator. To reach the destination node from source node, there exist three possible paths (see Fig. 3).

Two techniques are used to calculate the shortest distance that is discussed below.

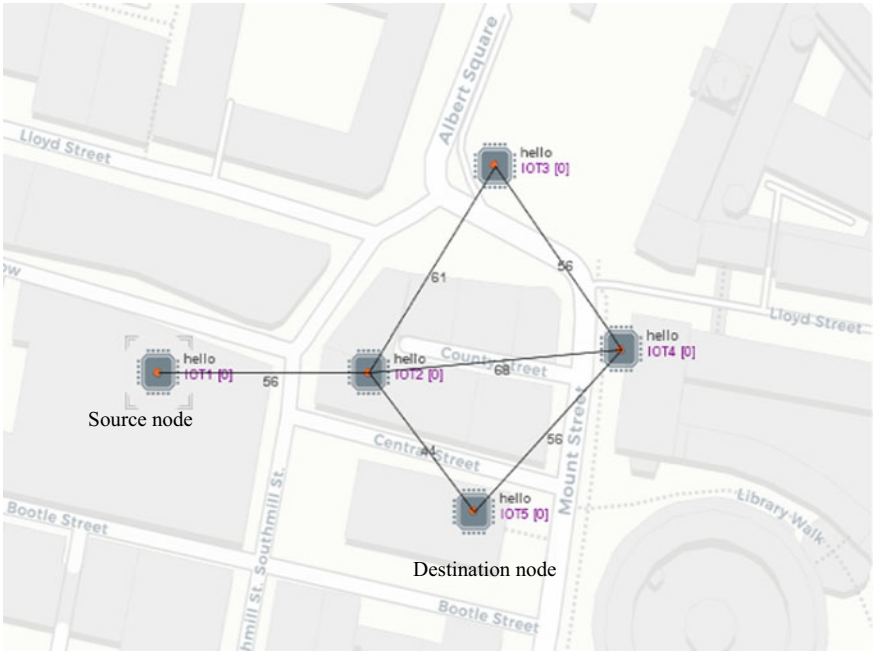

Fig. 2 Network of five IoT nodes in CupCarbon IoT 5.0 simulator

IDs of IoT nodes

No. of paths	1	2	3	4	5	Distances in metres
1	IoT1[0]	IoT2[0]	IoT3[0]	IoT4[0]	IoT5[0]	229
2	IoT1[0]	IoT2[0]	IoT3[0]	IoT5[0]	-	180
3	IoT1[0]	IoT2[0]	IoT5[0]	-	-	100

Fig. 3 Number of possible paths from the source node to destination node

2.1 Bellman–Ford's Algorithm

Bellman–Ford's algorithm is a single-source shortest path algorithm, i.e., in a directed weighted network, one node is selected as the source node, and the shortest path from the source node to all other nodes is calculated [6]. The weights of the network can be negative numbers. It follows a dynamic programming strategy in which all the possible solutions are tested, and the best solution is selected [7]. In this algorithm, the entire network edges are relaxed n-1 times where n is the number of nodes, and the distance of each edge is calculated in every repetition [6] (see Fig. 4).

The algorithm is simulated in CupCarbon IoT 5.0 simulator (see Fig. 5).

The results obtained after simulation are obtained (see Fig. 6).

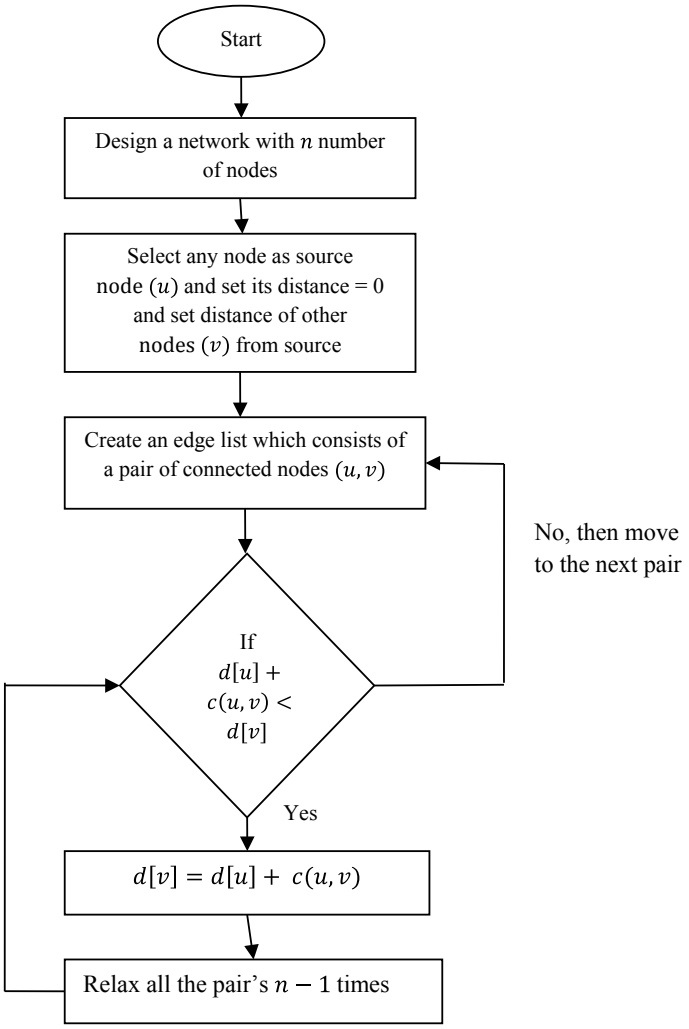

Fig. 4 Flow chart of Bellman–Ford's algorithm

Figure 6 shows that algorithm calculated the distance of all the nodes from the source node, and it is observed that the distance from the source node, i.e., IoT1[0] to IoT5[0] is the shortest, i.e., 100 m. Execution time to calculate all the distances is 0.1419999599456787s.

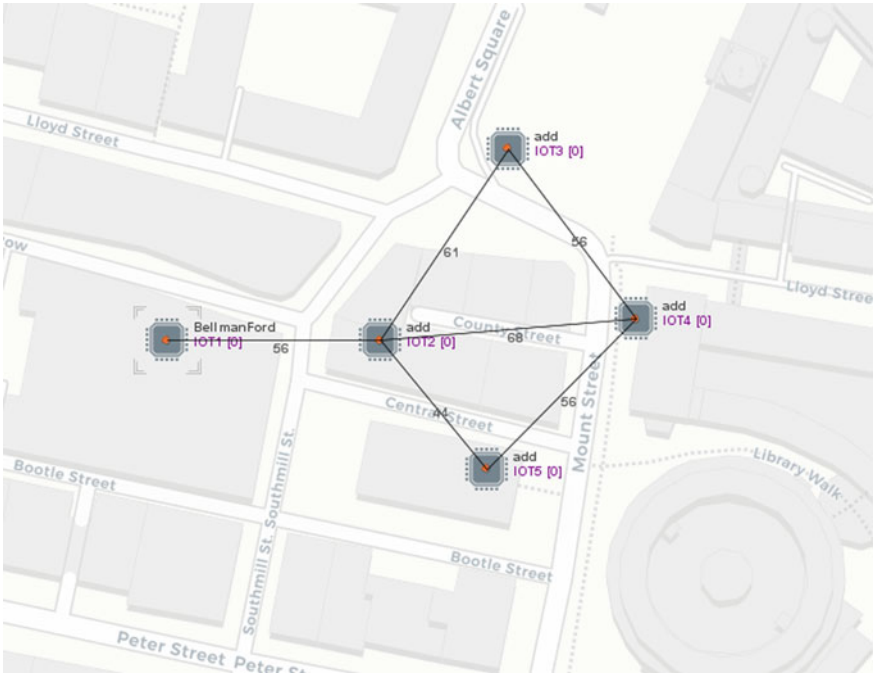

Fig. 5 Simulation of Bellman–Ford algorithm in CupCarbon IoT 5.0

2.2 Dijkstra's Algorithm

Dijkstra's algorithm is also a single-source shortest path algorithm and follows the Greedy method in which the problem is solved in stages considering one input at a time [7]. It does not work for networks with negative weights which is not an issue in maps as there is no negative distance between two nodes [7]. This algorithm is faster than the Bellman–Ford algorithm because it uses a priority queue that greedily selects the closest node that has not been visited and calculates the distance of selected nodes only. There is a predefined procedure to get an optimal solution which is described with the help of the following flow chart (see Fig. 7).

The algorithm is simulated in CupCarbon IoT 5.0 simulator (see Fig. 8).

The results for Dijkstra's algorithm are obtained (see Fig. 9).

Figure 9 shows the results obtained for Dijkstra's algorithm, and it is observed that it calculated the shortest distance, i.e., path 3 of 100 m. Also, the route to min distance is "1" which represents IoT2[0] node and "3" which represents IoT5[0] node in the code. The execution time is calculated as 0.04399991035461426 s which is 0.09800004959 s lesser and 69.01% faster than the Bellman–Ford algorithm.

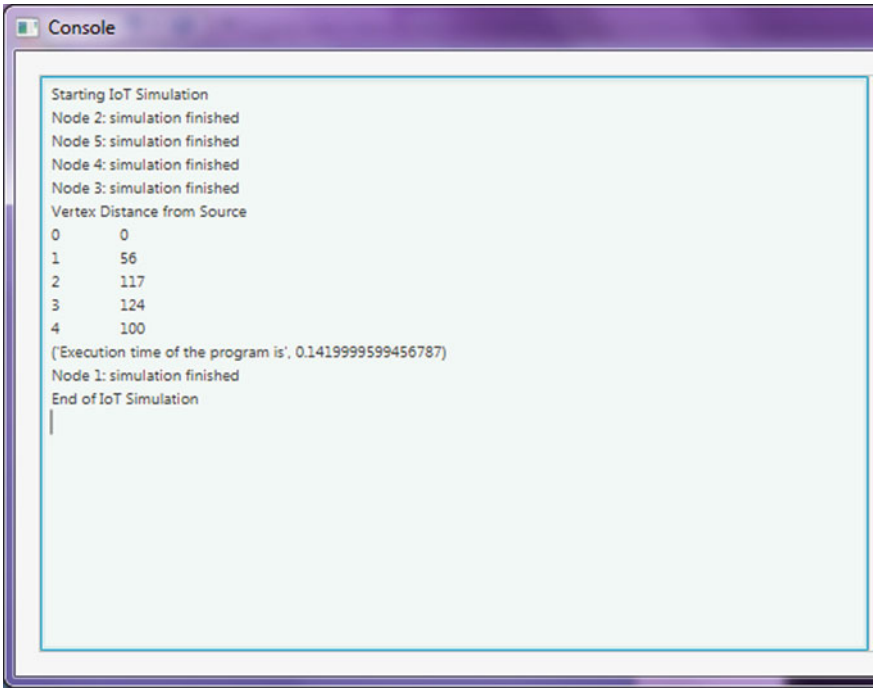

Fig. 6 Results obtained for Bellman–Ford algorithm

3 Result Analysis

Table 1 shows the comparative study of the two techniques discussed in the paper.

4 Conclusion and Future Work

In this paper, features of two techniques named Bellman–Ford algorithm and Dijkstra's algorithm used to calculate the shortest distance are studied, and comparison is drawn to gain knowledge about their advantages and disadvantages for IoT-based WSN. A network of five IoT nodes is developed in the CupCarbon IoT 5.0 simulator, and both the algorithms are simulated. The efficiency of both algorithms is compared based on their execution time. The execution time obtained in the Bellman–Ford algorithm is 0.1419999599456787 s, and for Dijkstra's algorithm is 0.04399991035461426 s. The results obtained show that Dijkstra's algorithm is 69.01% faster than the Bellman–Ford algorithm for computation of the shortest path between the source and destination node. For future work, two algorithms' efficiency can be compared to a more extensive network or other techniques.

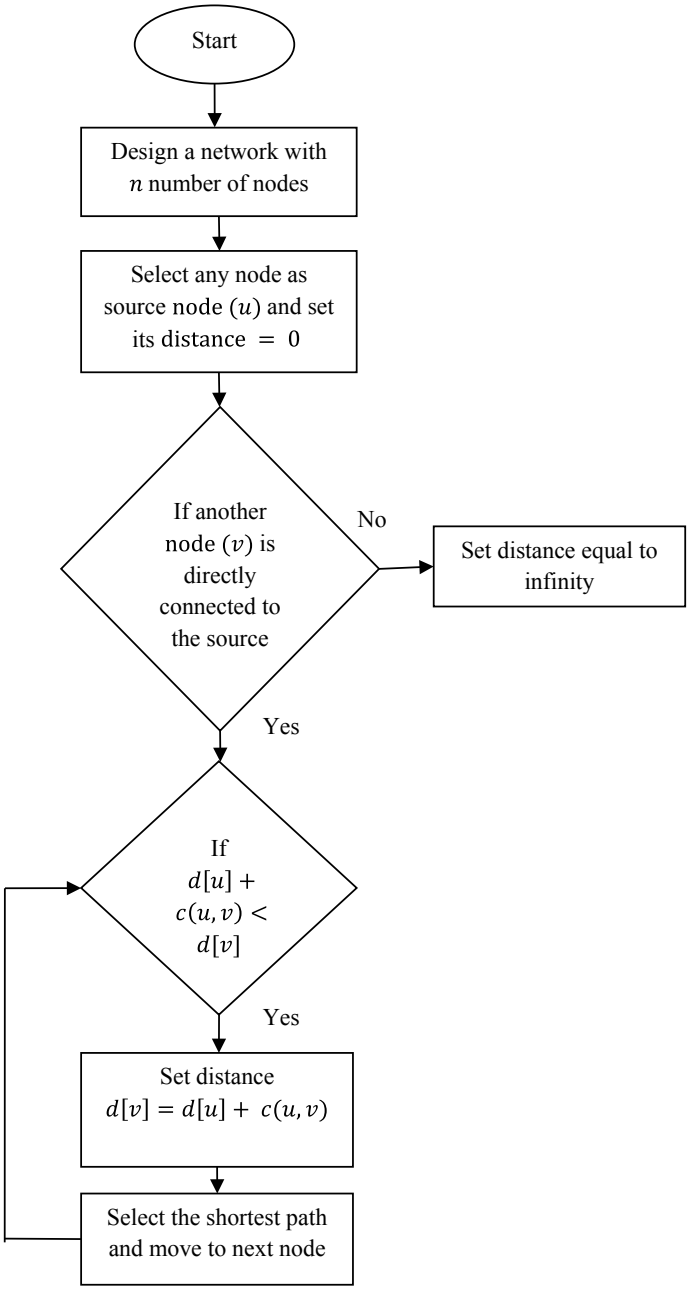

Fig. 7 Flow chart of Dijkstra's algorithm

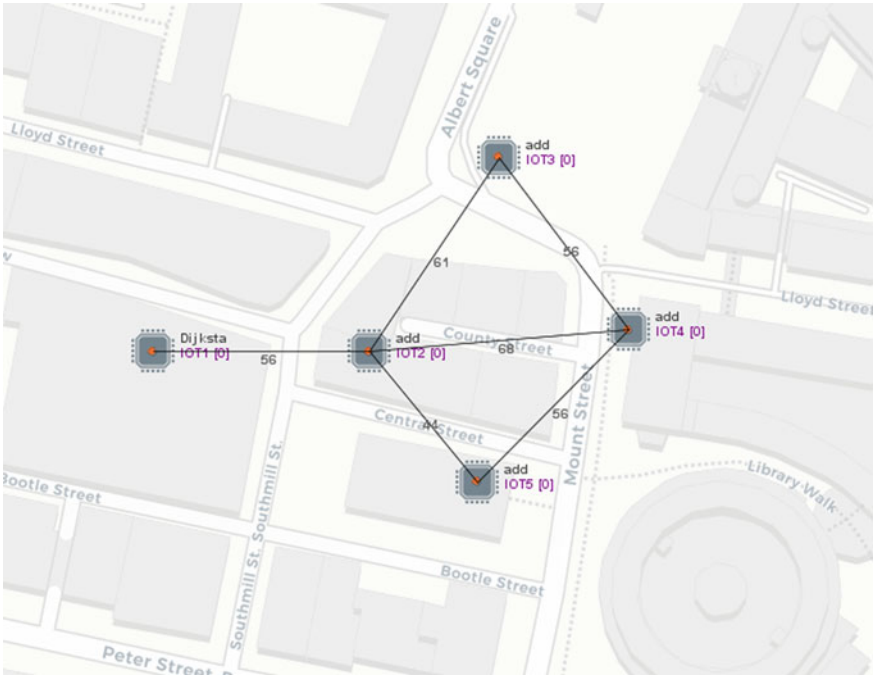

Fig. 8 Simulation of Dijkstra's algorithm in CupCarbon IoT 5.0

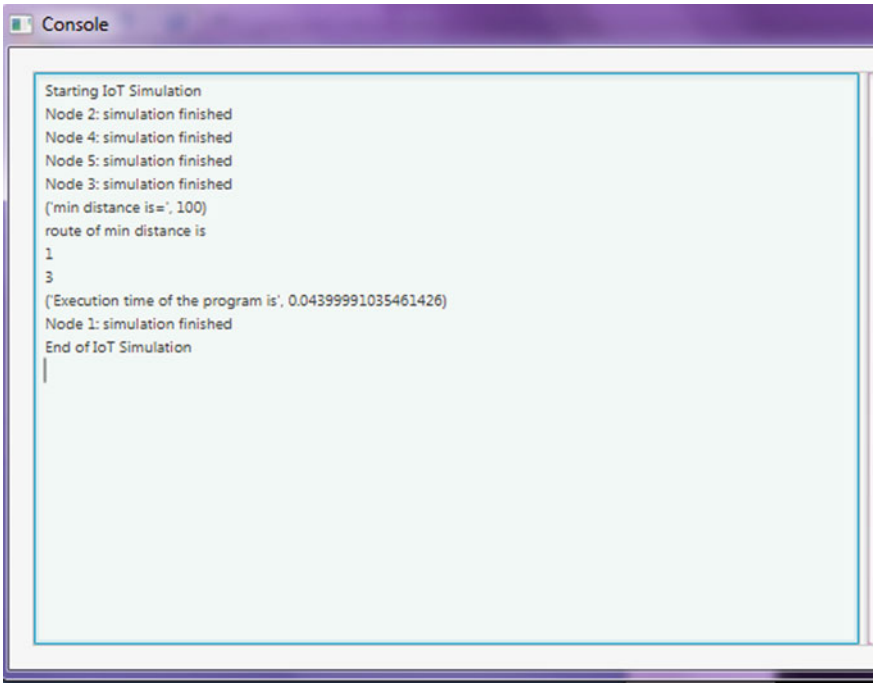

Fig. 9 Results obtained for Dijkstra's Algorithm

Table 1 Comparison of the techniques discussed to calculate the shortest distance in IoT-based WSN

S. No.	Technique	Features	Advantages	Disadvantages	Execution time
1	Bellman–Ford's algorithm [7]	Dynamic programming strategy, single-source shortest path algorithm, time complexity for the complete network is θ(n3)	Can be used for complex networks	If the algorithm fails to update the weights in case of cyclic network then it becomes slow and time consuming	0.1419999599456787 s

(continued)

Table 1 (continued)

S. No.	Technique	Features	Advantages	Disadvantages	Execution time
2	Dijkstra's algorithm [3]	Single-source shortest path algorithm, Greedy method, time complexity for a complete network is $\theta(n^2)$	Works for both directed and undirected networks, faster as compared to the Bellman–Ford algorithm	Less surety to work for networks with negative weights	0.04399991035461426 s

References

1. Zhao F, Guibas L (2004) Wireless sensor networks, an information processing approach. Morgan Kaufmann Publishers is an Imprint of Elsevier
2. Kantarci B, Oktug S (2018) Special issue: wireless sensor and actuator networks for smart cities. J Sens Actuat Netw 7:71–75
3. Cup Carbon User Guide. Available at: http://www.cupcarbon.com/cupcarbon_ug.html
4. Magray A, Younis M, Sharma C (2019) Wireless sensor networks based on shortest path algorithms. Int J Adv Sci Res Manage 4(1):106–110
5. Giner VC, Navas TI, Flórez DS, Hernández TRV (2019) End to end delay and energy consumption in a two tier cluster hierarchical wireless sensor networks. Inform MDPI 10(4):135–164
6. Mummoorthy A, Bhasker B, Kumar T (2018) Using of Bellman Fords Algorithm in WSN to identify the shortest path and improve the battery power & control the DDOS attackers and monitor the system environment. Bonfring Int J Netw Technol Appl 5(1):9–11
7. Goyal M, Kumar V, Dahiya A (2015) Performance measurement of wireless sensor network using Dijkstra's algorithm. Int J Comput Sci Manage Stud 18(1):2231–5268
8. Lee S, Bae M, Kim H (2017) Future of IoT networks: a survey. Int J Appl Sci MDPI 7(10):1072–1097

Review of Energy Management Strategies in Plug-in Hybrid-Electric Vehicles

J. Rohith and G. T. Mahesha

Abstract As a step toward a pollution-free environment, governments and regulatory bodies worldwide are moving toward cleaner means of transportation. A lot of tailpipe emissions occur in a conventional internal combustion engine. One solution to these hazardous emissions is the use of hybrid-electric vehicles (HEVs) or fully electric vehicles (EVs). The HEVs, especially plug-in HEVs (PHEVs), are soon expected to have more significant commercial applications, as the EVs may take more time for their larger part of the share. A hybrid-electric vehicle employs an IC engine combined with a smaller battery and an electric motor. On the other hand, a PHEV consists of a much larger capacity battery storage known as a rechargeable energy storage system (RESS). It is equally important to apply a stable drivetrain topology for greater efficiency. PHEV blends power from battery and engine using an energy management system, which always tries to impart the best driving conditions, least emissions, and maximum mileage and range. In the paper, an overview of all the control strategies is reviewed with few simulation results.

Keywords Energy management · Control strategies · PHEV · SOC · Vehicle to the grid

1 Introduction

The transportation sector consumes 49% of the world's oil resources worldwide and is one of the most rapidly growing consumers of available global energy. It is predicted that, at this rate of consumption, total oil reserves will be depleted by 2038 [1]. Researchers are developing various alternative power trains, which are gaining much attention lately. A hybrid-electric vehicle (HEV) is one among them and can reduce exhaust gases, saves fuel, and paves the way for a greener environment. An HEV can reduce the consumption of fossil fuels by 70% [2, 3].

J. Rohith · G. T. Mahesha (✉)
Department of Aeronautical and Automobile Engineering, Manipal Institute of Technology, Manipal Academy of Higher Education, Manipal 576104, India
e-mail: mahesh.gt@manipal.edu

S. Dwivedi et al. (eds.), *Flexible Electronics for Electric Vehicles*, Lecture Notes in Electrical Engineering 863, https://doi.org/10.1007/978-981-19-0588-9_8

A hybrid vehicle consists of an IC engine combined with a battery storage system that supplies energy to an electric motor. For HEV, there are two types of propulsion systems, mainly an ICE and battery supply with a rechargeable energy storage system (RESS). Superior range and versatility in the modules' scale are the most important benefits that an HEV has over a pure EV.

An efficient drivetrain design is essential for an HEV as it impacts mechanical efficiency, fuel consumption, and price. A drivetrain is the collection of parts that supply power to the vehicle's wheels from the engine or motor. The drivetrain's configuration defines how the electric motor functions combined with the traditional engine in hybrid-electric vehicles. Series, parallel, and series–parallel hybrids are the necessary powertrains available in an HEV.

Series Hybrid: Only the engine, which in turn charges the batteries, can drive the motor. The transmission operates by an electric motor, which is entirely battery powered. It is an effortless but not the most powerful method.

Parallel Hybrid: The engine and the battery run the motor, which in turn powers the transmission. Only the engine spins the rotor when the battery is exhausted.

Series–Parallel Hybrid: It is a blend of series and parallel systems. With a power-split unit, the engine may selectively drive the wheels or the generator, or both based on driving conditions. This arrangement is deemed the most successful and was assimilated by Toyota.

Figure 1 shows a pictorial view of all the drivetrains, the red line indicating the engine line and the blue being the electrical supply.

Enormous versatility is available in choosing the structures for power splitting. Based on the hybridization, i.e., the engine's size and the battery source, an HEV classification is done. Figure 2 illustrates the different types of HEV's based on the size of the battery and IC engine.

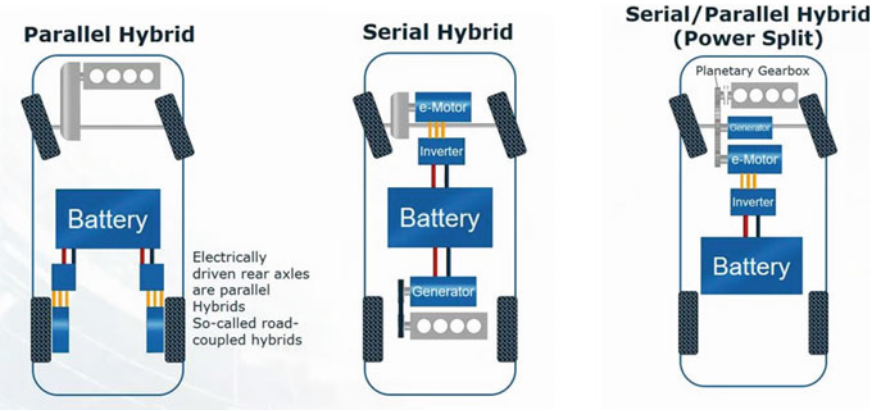

Fig. 1 Classification of drivetrain designs [4]

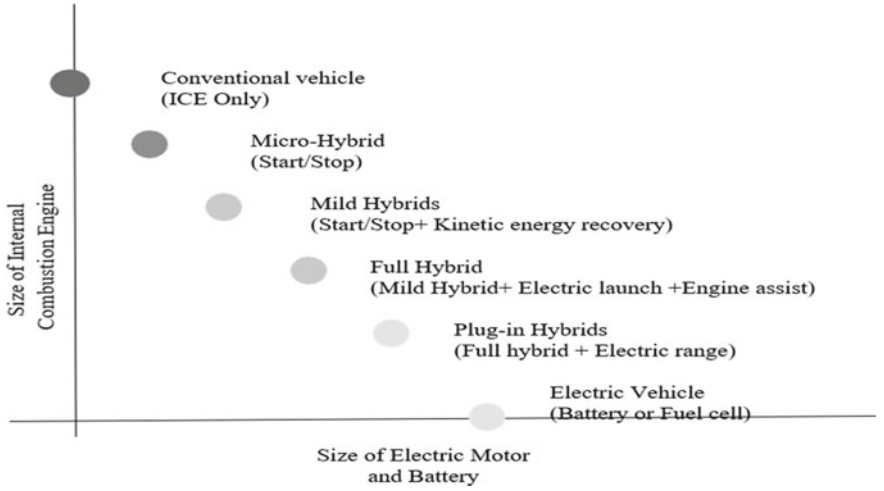

Fig. 2 Hybrid-electric vehicles based on the size of the IC engine and battery [5]

Much of the research is focused recently on plug-in hybrid-electric vehicles (PHEVs) that store and draw power from a renewable energy source. The concepts from a basic HEV can be implemented in developing a PHEV. Also, the primary source of power can be changed from fossil fuel to multiple sources like solar and wind to make the transportation sector even cleaner. PHEVs can all-electric mode, or pure engine mode or both combined based on the charge region. The main features of PHEVs are as follows.

(a) Recovering regenerative energy from brakes instead of dissipating as heat.
(b) Optimizing the splitting of power between various sources.
(c) Downsizing the engine while attaining the maximum requirement of the vehicle [6].

With their all-electric range in cities and an extensive cruising range and battery charging capabilities, PHEVs give a wide range and function as a range extender. Many pollutants are released when the engine runs in a transient mixture and is fixed by a PHEV. With its vehicle to grid technology (V2G), it can even power back the house if needed [7].

1.1 Terminology in Plug-In Hybrid Vehicle (PHEV)

State of Charge (SOC): It is relative to the initial charge of the battery to the current level of charge, also known as the remaining energy fraction present in the battery [8, 9].

Charge sustaining mode: Batteries state of charge (SOC) may increase or decrease in a driving profile, but by the end, it should come to an equivalent state.

Charge-depletion mode: The SOC of the battery on a driving profile shows a net drop in stowed energy.

All-electric range (AER): The vehicle's complete distance is in an electric mode until the engine turns ON [10].

The overall consumption advantages of today's HEVs are developed purely from developments in charge sustaining mode, as they have no charge-depleting mode. A PHEV that does not use petroleum (all-electric) in a charge-depletion mode and with a fuel economy in a charge-sustaining mode is equal to a traditional vehicle consuming 50% less petroleum as the first 40 miles will be electrically powered ex. PHEV40 [8]. A blended strategy is employed to maximize the charge-depletion time and even less fuel consumption in some cases.

1.2 Overview of Control Strategies in Plug-in Hybrid-Electric Vehicles

It is essential to maximize powertrain efficiency and increase the driving range. There are many challenges in employing the perfect control strategies in multi-source systems like plug-in HEV. The energy management system is an essential part in the control of HEVs. It plays a major role between the IC engine and the battery storage system is maintained and keeping the proper state of charge (SOC). Energy management can instantaneously identify and control the actuators in the system. By altering the input signals, various outputs can be formed, gaining maximum efficiency. A fixed control strategy cannot be adopted as there will be a change in the driving parameters and patterns, leading to poor fuel economy in HEV.

Compared with an HEV, the AER in a PHEV is helpful in refining mileage, efficiency, and emissions. Still, it may increase the intricacy by increasing the challenges for the control system design. Electric drive trains are more efficient and considerably cheaper. Most ICEs are very ineffective in transients as they consume a lot of energy, Hence, it is useful to run the vehicle in AER wherever feasible [11].

The energy is consumed significantly when the vehicle is idling. A PHEV control strategy is devised to turn off the engine when not in use, and the start-up efficiency is increased by converting to EV mode. The topology of the vehicles determines the engine turn-off and turn-on process. This is true for all parallel PHEVs. There is no necessity to operate the engine in an EV-start and propulsion until the traction battery is exhausted. Although the engine does not lead to acceleration, its load can be applied gradually and in a controlled manner, irrespective of the driver's requirement.

The engine logics are based on three criteria such as (1) threshold power required, (2) SOC of the battery, and (3) the capacity of the electric motor to provide the necessary power [11].

Several papers have been addressed based on the control strategies' overview in recent years [12–14].

The next section consists of the main control strategies such as rule-based and optimization-based and its subdivisions and the latest technological advancements in a plug-in HEV with some simulation results in real time.

2 General Classification of Control Strategies

Control strategies are mathematical models based on descriptive methods. They are broadly divided into two types, such as rule-based control strategy and optimization-based control strategy. These approaches are subdivided further on the way they are employed, which is shown in Fig. 3.

Control strategies focusing on rules help achieve fuel economy, productivity, optimal output, and lower pollution for a particular drive cycle. They are described by a series of parameters that are pre-programmed using specific mathematical models into the framework. Due to their simplicity, researchers have turned toward optimization-based strategies, involving an optimal method by minimizing the cost function.

Using the past as well as future information, regarding the trip controllers are designed. Most advanced control techniques involve a real-time data collection through sources such as on-board sensors and encoders.

2.1 Rule-Based Control Strategy

In a PHEV, the key goal of a rule-based strategy is to obtain optimum effectiveness. Moving the electric machine and the engine at its highest efficiency utilizing the

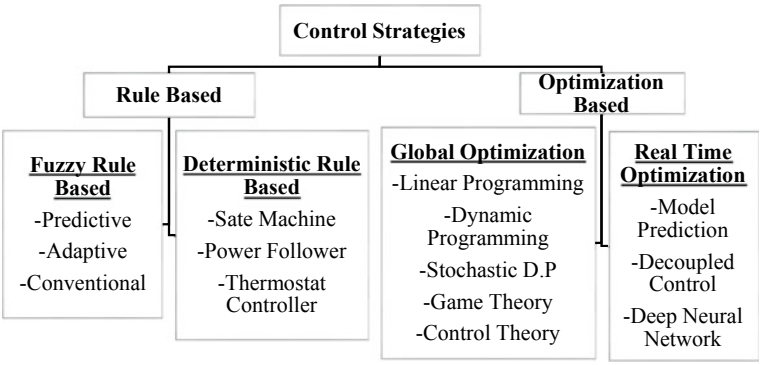

Fig. 3 PHEV control strategies [11]

all-electric range (AER) and maximum energy regeneration. There will not be any knowledge of the trip as the rules are predefined to get the desired output. It works on wide range of conditions without the knowledge of the trip beforehand. Changing of modes between one and the other depends on the acceleration and deceleration needed, engine and motor power demands, vehicle speed, and the SOC of batteries.

The following are the real-life rule-based strategies applied in Prius, a bend of both series and parallel topology (a) full EV mode of operation: If there is sufficient SOC in the battery, vehicle running at low speed and adequate coolant temperature. (b) Engine and motor sharing the power: When the engine is ON and the battery SOC is over the required SOC. (c) The engine only operation and charging of battery: When the battery's SOC dropped below the required SOC, (d) when the energy demanded is negative and the engine is OFF, the negative power needed is retained in the batteries utilizing the regenerative braking.

A simple rule-based simulation run by bavait and anwar, proposed a rule-based controller compared with the simple rule-based model in ADVISOR software, using several drive cycles for Toyota Prius with a planetary gear train acting as a speed coupler. They proposed a set of new rule-based strategies. "(a) When the battery SOC falls below the aim level and the vehicle requires a positive power condition, the engine must be switched on. (b) When the battery's SOC reaches its intended capacity and the vehicle's power output is less than the full power that the engine will produce but is optimistic, the engine will be switched off. (c) When the battery SOC reaches its intended cap and the power needed by the vehicle exceeds the available power supplied by the engine but is optimistic, the engine shall be turned on. (d) When the vehicle's power requirement is negative and the battery's SOC is below its upper limit, the engine must be turned off" [15]. It is observed that Toyota Prius's basic rule strategy for a PHEV gave a 74.8 MPG mileage while PHEV's alternative or proposed rule-based control strategy produced an 87.6 MPG mileage for the 37.2-mile drive loop. The engine's function output improved 6 percent from 29 percent using the Prius approach to 35 percent using the RBS approach suggested.

Rule-based strategies are also known as a mode selector type system where a set of modes is shifted based on the battery's SOC characteristics. A simple mode selector energy consumption strategy is shown in the Fig. 4.

2.1.1 Deterministic Control Strategy

A deterministic strategy is based on certainty since there is no randomness. All the rules are based on certain predefined formulations. Rule-based controller operates on a bunch of rules set before the actual operation [17], and inputs are made instantaneously from the decision-making models. The undeveloped determined rule-based control strategy is the ON and OFF of ICE that is thermostat supervisor. It runs on the simple principle that the vehicle engine will be turned ON and OFF based on the ESS SOC values and the required torque.

A power follower system is used in this method, normally employed at minimum vehicle speeds. The motor is used to produce excess power when there is a greater

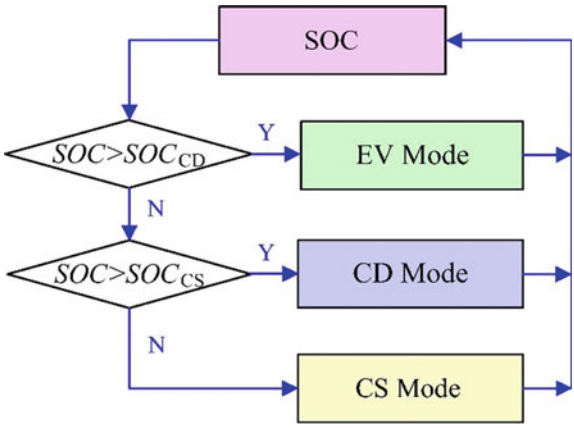

Fig. 4 Energy utilization mode switch control strategy [16]

demand of power. The motor charges the battery by regenerative braking. Hmidi, Salem et al. carried out a simulation [18] using a deterministic rule by the start/stop of the engine, electric assistance, i.e., boost function, regenerative braking with on-board charging at low speeds, is developed in an HEV. With 15–20 kmph speed and varying SOC values, it is observed that hybridization can significantly reduce fuel consumption by 10–15% on urban road and highway conditions. Applying it to a PHEV can increase efficiency even better.

Following these CS models, Toyota (Prius) and Honda (Insight) HEVs run on charging sustaining mode in ESS following a parallel topology of the drivetrain.

2.1.2 Fuzzy Logic Rule-Based Control Strategy

Fuzzy logic can be named as an extension of the deterministic rule-based approach. It is an ideal strategy for non-linear, time-varying systems as they are robust and adaptable to any situation. It gave a profound notion to the controller developed by Hmidi et al. [18] and gave a higher fuel economy. These are built on fixed rules that mainly run on CS rule-based model. These logics evaluate the driver's normal behavior, and they function accordingly. A controller that can pick the points of action by the lowest effect on fuel's economy, as instigated by Johnson [19], gave a better fuel economy compared to simple controls based on rules. It is impossible to optimize a system of more than two variables, which makes it a device constraint. The difficulty of the simulation makes it challenging to implement in real life. The system designed to use the depletion mode of charge instead of the maintaining mode of charge would have the highest fuel output [20]. Figure 5 shows the different modes AE mode, CS mode, CD mode based on SOC and time profile.

Logical relations AND and NOT (even OR) are used in the fuzzy laws of Table 1. The Boolean logic which is a traditional one was generalized to fuzzy alternatives for this purpose. These fuzzy equivalents can be implemented in many ways but in

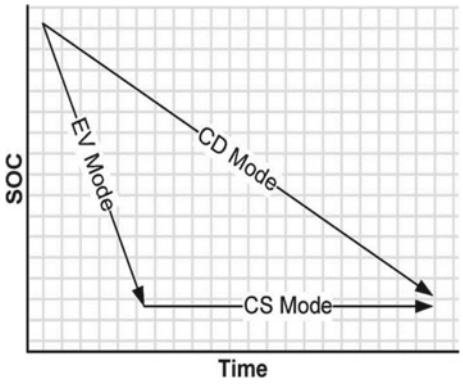

Fig. 5 SOC profile with time [11]

Table 1 Sample rules for fuzzy logic control of a PHEV [21]

Rule base of the fuzzy logic controller
1. **If** SOC is too high, **then** P_{gen} is 0 kW
2. **If** SOC is normal **and** P_{driver} is normal **and** ω_{em} is optimal, **then** P_{gen} 10 kW
3. **If** SOC is normal **and** ω_{em} is **not** optimal, **then** P_{gen} is 0 kW
4. **If** SOC is low **and** P_{driver} is normal **and** ω_{em} is low, **then** P_{gen} is 5 kW
5. **If** SOC is low **and** P_{driver} is normal **and** ω_{em} is **not** low, **then** P_{gen} is 15 kW
6. **If** SOC is too low, **then** p gen is P_{gen}, max
7. **If** SOC is too low, **then** scale factor is 0
8. **If** SOC is **not** too **and** P_{driver} is high, **then** P_{gen} is 0 kW
9. **If** SOC is **not** too low, **then** scale factor is 1

general, AND is the minimum operator used, NOT is for simple compliment, and OR is the maximum operator. Using these fuzzy set, a fuzzy controller can be built.

The perceptive mechanism used in fuzzy logic can be explained in four key steps [21]

- Fuzzification: Using the membership functions, the three input values of the degree membership of a fuzzy logic controller are computed.
- Degree of Fulfillment: This is the degree to which the rules are valid, when the precursor of every rule from Table 1 is figured using fuzzy logic operator.
- Inference: If–then the operation constitutes implication. The degree of the enforcement standard is used to alter the rules accordingly. It is done by multiplying the amount of fulfillment of the precedent by the resulting rule. Table 1, rule 2 is an example.
- Aggregation: For every output of a controller, the outcomes are combined into a specific value from the inference step. By taking the average of the inference results, this is done.

For the default controller, all components' performance is lower, except for the ICE where the default controller's optimization is more efficient. There is no trade-off between the performance of the other PHEV modules and the ICE engines' performance. Therefore, the ICE's operating points are closer to the default controller's optimum curve than for the FLC [21].

Results of simulation applying the different drive cycles suggest possible changes utilizing the fuzzy reasoning defined in the SAE J1711 standard compared to other techniques that only maximize ICE efficiency [22].

2.2 Optimization-Based Control Strategy

Local optimization is the significant limitation of a rule-based CS as we cannot optimize the PHEV as a unit. Two primary standards are present for a global strategy, one focused on past evidence, and the other focused on the compilation of real-time data. In a set of rules, optimization takes place with the learning system while responding to the situation. They were considering maximum performance requirements from the powertrain configuration. It also allows two factors, i.e., mileage levels and pollution expectations, to be combined into a minimized cost function. The fuel efficiency depends mainly on the controller's capacity to maximize, and the controller can forecast the potential condition of the trip correctly. A lot of effort to enhance the performance is noticed, but the right balance of application is difficult in optimization.

2.2.1 Global Optimization System

Optimization-based management methods, as they refer to HEVs and PHEVs, are typically divided into two groups. Technical developments such as the global positioning system (GPS), global information system (GIS), traffic data collection in real-time, and Internet maps have rendered it simpler to schedule a trip [23, 24]. Linear programming is one of the commonly used optimization methods. When a PHEV is designed and a controller is installed, it should match the global optimization model. "Together, an engine and an electrical machine power a PHEV, and parallel topologies directly relate to the two elements torques and speeds. The control theory method exploits this relationship to define a cost function using only two decision variables" [25]. The Bellman principle [26] taking the engine torque as the criteria of command, a real-time control strategy using MATLAB Simulink is developed. During the cycle, the energy loss is minimized. A generic algorithm is also one of the non-linear optimization methods [27]. Such strategies rely on the direction, road profile, congestion level, atmospheric conditions, and further details taken from the global position system (GPS), intelligent transport systems (ITSs), geographic information systems (GIS), and traffic modeling [28, 29].

2.2.2 Real-Time Optimization

Real-time optimization majorly uses past data in analyzing and optimizing a trip. Various techniques have been used for programming the techniques, and dynamic programming (DP) is one among them [28]. A DP is a closed-loop form of optimization strategy. In general control questions, DP is an algorithm capable of evaluating the best possible global solutions. Taking into consideration the current and potential consequences of management choices, the desired approach is accomplished by reducing undesirable outcomes [29–31]. It is used in any problem to which the findings are to be made in steps to find a minimal decision pathway [32–34]. A dynamic programming algorithm consists of the engine's battery level and speed, which influences the rate of fuel and is regarded as regulated or controlled variables are induced. This gives very high-computational cost—however, two degrees of freedom of optimization. The flowchart shows steps involved in DP in Fig. 6.

The motor constraints, the battery, and the engine, should be considered correct, and the engine fuel rate should be calculated using different battery currents. Simultaneously, it is possible to build up the cost to go matrix, then an optimal SOC curve and maximum battery current with various starting SOC can be determined.

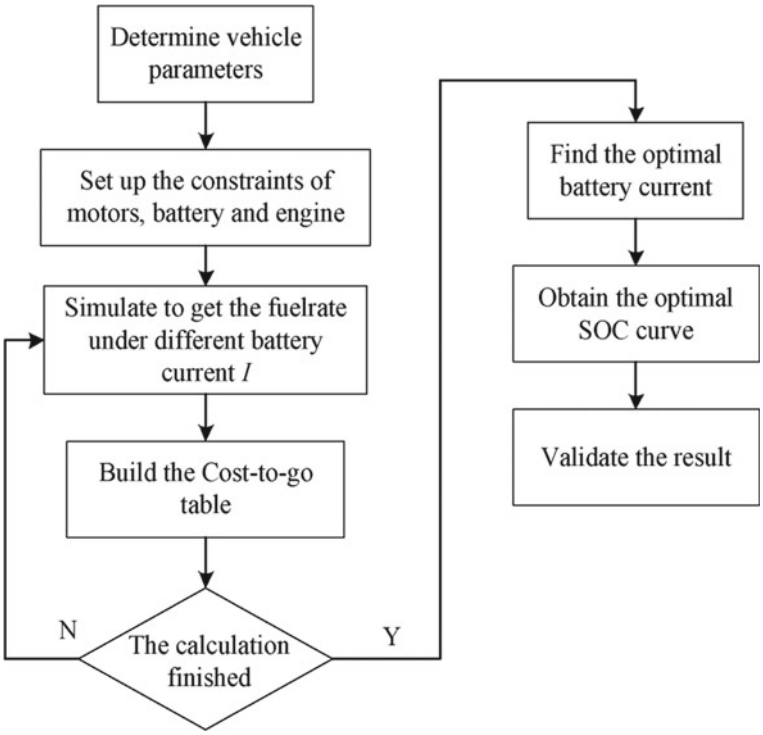

Fig. 6 Procedure of dynamic programming method [35]

Table 2 Vehicle parameters [35]

Vehicle type	Plug-in split HEV
Vehicle mass	1641.3 kg
Engine power	57 kW
Motor power	25 kW, peak power 50 kW
Generator power	15 kW, peak power 30 kW
Planetary gear set	Sun gear 30 teeth Ring gear 78 teeth
Battery	Lithium-ion battery Rated capacity 20 Ah Rated voltage 356 V

With the number of drive cycles simulated by Chen and Xu using dynamic programming taking Table 2 of the vehicle parameters, it is observed that the default algorithm discharges the battery quicker than the DP method. The level of engine efficiency based on various algorithms are being compared. The average engine efficiency is observed to be higher when the DP method is applied compared with the default algorithm. The contrasts will illustrate to some degree how the DP system will minimize fuel consumption.

(a) *Deep Neural Networking*

Neural networks offer brain-like activity inspired by biological brain behavior. Depending on the input characteristics, the signals are sent to other neurons like in the brain as it sends to other neurons through dendrite. These processes are usually expressed with transfer functions [36]. Layers are built combining the neuron network. Based on complexity, desired fidelity, and model nonlinearity, the density of neurons may change. Training data are required to determine the neuron parameter calculation [37].

The error backpropagation is used for enhancing error convergence in NN, which optimizes the training data error. A least-squares regression process is used in training, where the initial values of dendrites weights are assigned randomly [36, 38]. The NN performance is influenced directly by the quality of training, e.g., overfitting risk. However, an optimal amount of training data exists, and therefore, there will not be any improvement in performance with excess training data. The construction of a typical neural network is shown in Fig. 7.

A power-split hybrid-EV EM system cantered on machine learning by Murphey, which is trained by dynamic programming that combines terrain knowledge with the jamming level forecast, and applied NNs concept to enhance battery performance and speed of the engine [39].

Khayyam and Bab-Hadiashar [40] projected a neural network application in hybrid multilayer adaptive fuzzy neuron interpretation, to increase and adapt the application range, the fuzzy logic controller is given learning characteristics with the help of NN. They have designed a controller that can spontaneously tune the values

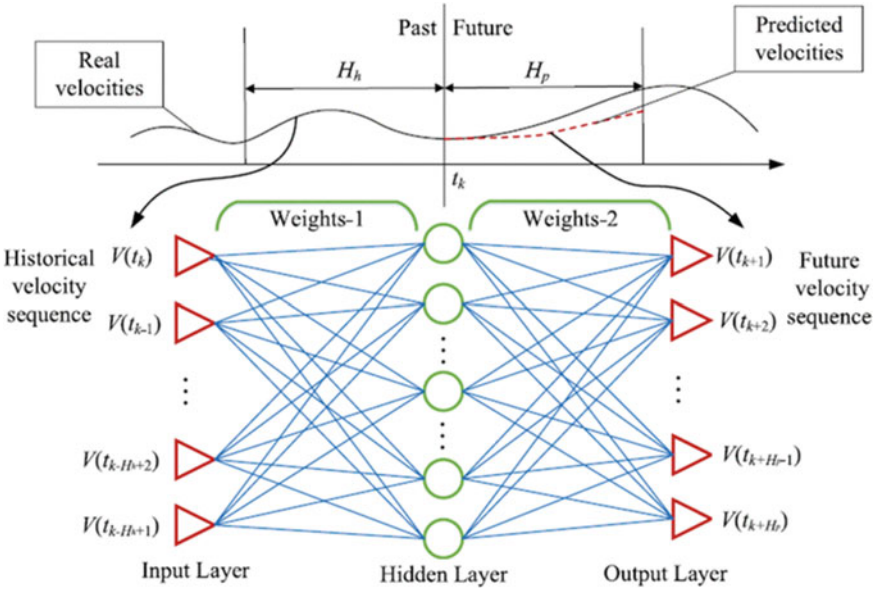

Fig. 7 Neural network strategy in real versus predicted velocities [36]

themselves, according to the influence of roads, driver's behavior, and environmental conditions.

Chen et al. [35] give intelligent controllers the need for a wide range of use and follow a good trade-off between computational effort and algorithm robustness. To lessen the fuel consumption of a PHEV, the author employs NN, which takes training data from wide-ranging driving conditions. Working with different levels of trip information, the NN consists of modules N1 and N2.

Incorporating neural network into a model predictive control in the short term by Sun et al. also presented a machine learning-based NN algorithm and claimed to have a 92% fuel optimality compared to a DP algorithm [41, 42].

Game theory, sliding mode controller, convex programming, and analytical solution are some of the futuristic control strategies.

(b) *Energy management using a vehicle-to-vehicle interaction with intelligent transport.*

The increase in the advance driving assistance system and intelligent EMS makes possible shifts toward predictive EMS. Optimum productivity needs to take the most useful trip data, mainly from Google services. Such data gathered were used in combination with predictive model control by Sun et al., he also built a two-stage EMS controller for a power-split PHEV. For an optimized SOC reference path, real-time traffic information is collected for running a long term with the supervised control system. Over the last few years, connected and intelligent vehicle technology has surfaced to catalyze the optimal fuel economy in an eco-driving system developed by

Ko et al. considering traffic signals and leading vehicles the power demand assumed [43–45].

Vehicles run mostly on random and transients and majorly depend on traffic, road type, weather, driver style. Thus, random and biased errors are observed in vehicles [46].

3 Moderns Control Strategies for HEVs

In providing an efficient power system, the current power demand and the future power requirement have to be determined. This gives a real-time distribution of the total decision variable. In an **extreme learning machine algorithm (ELM)** developed by Zhang et al. [47] considering traffic and urban driving conditions, with vehicle-to-vehicle (V2V), a one-step model is designed. A multi-step optimal algorithm with many single steps is built for driver torque demand prediction.

Consumption of fuel and environmental pollution is drastically reduced with the application of advanced control strategies. Based on the driving conditions like urban environment and traffic conditions, the SOC values' variation plays a major role in planning a CS. In a study by Erfan et al. [48], a new rule-based CS with SOC parameters and teaching learning-based optimal CS is employed. It is observed that an **optimal charge-depletion strategy (OCDS)** can significantly improve fuel consumption than an AER-focused CS. An OCDS is used in a long trip, whereas an AER is more efficient for a shorter trip.

Sometimes, there may be a condition where prior knowledge of the trip is not present, and a **deep-reinforced learning (DRL)** can be used. "It observed that original DRL-based EMS achieves an average 3.5% gap from benchmark compared to model predictive EMS" [49].

Table 3 illustrates the pros and cons of various energy management strategies that are used in PHEVs.

4 Conclusions

The following inferences are drawn from the review of the technical papers published on hybrid-electric vehicle energy management strategies.

Plug-in hybrid-electric vehicle (PHEV) configuration is a promising transportation mode because of its range extender ability. Energy management strategies adapted in PHEVs can be broadly categorized as rule-based (RB), optimization-based (OB), and learning-based (LB) strategies. Rule-based strategies are easy to program and cost-effective. However, no on-board prediction capabilities make them insignificant.

Adaptive control algorithms like fuzzy logic, dynamic programming, and deep neural networks increase the fuel economy and reduce emissions. Most of these

Table 3 Main EMS strategies and their application summary

Strategy	Main advantage	Main disadvantage	Simulation result (if any)	References
General rule-based	Balanced SOC	Not optimal	NA	[14, 15, 17, 50]
Predicted rule or new rule-based (anwar and bavait)	Increased SOC	Lacks real-time data	The mileage of the PHEV increased by 16%	[15, 17]
Deterministic	Computational simplicity	Only applicable for series hybrid powertrain	NA	[17, 50]
Fuzzy logic	Can be Easily tuned	Very complex	The drive cycle by SAE J1711 gives optimal efficiency	[8, 19–21, 23]
Global optimization system	Optimal solution	Cannot be implemented in real-time system	NA	[24–29]
Real-time optimization	Instantaneous minimization of the cost function, does not need proper knowledge of the drive cycle	Values of equivalence factor are difficult to obtain for different DC	The average efficiency of the engine is higher	[30–33]
Deep neural network	Very adaptive	Difficult to program	NA	[35–40]
Vehicle-to-vehicle interaction/intelligent transport	Trip-based online system	Random and biased errors	NA	[44–46]

algorithms require the drive cycle information beforehand, or a training system is necessary in neural networks. Versatile energy management strategies in hybrid-electric vehicles can include a blend of various techniques (RB, OB, and LB), forming an integrated EMS (iEMS) toward improved fuel economy and performance.

References

1. Ehsani M, Gao Y, Longo S (2018) Modern electric, hybrid electric, and fuel cell vehicles, 3rd edn. CRC Press, Boca Raton
2. Sioshansi R, Denholm P (2009) Emissions impacts and benefits of plug-in hybrid electric vehicles and vehicle-to-grid services. Environ Sci Technol 43(4):1199–1204. https://doi.org/10.1021/es802324j

3. Karbowski D, Rousseau A, Pagerit S, Sharer P (2006) Plug-IN vehicle control strategy: from global optimization to real-time application. In: 22nd International Battery, Hybrid and Fuel Cell Electric Vehicle Symposium and Exposition, EVS 2006, pp 274–286
4. Evehicles.info (2019) xEVs-difference between battery electric vehicle (BEVs), Plug-in hybrid (PHEVs) and hybrid vehicle (HEVs). https://bijliwaligaadi.com/2019/08/xevs-difference-between-battery-electric-vehicle-bevs-plug-in-hybrid-phevs-and-hybrid-vehicle-hevs.html
5. Onori S, Serrao L, Rizzoni G (2016) Hybrid electric vehicles: energy management strategies
6. Guzzella L, Sciarretta A, Guzzella L, Sciarretta A (2013) Electric and hybrid-electric propulsion systems. Veh Propuls Syst 67–162. https://doi.org/10.1007/978-3-642-35913-2_4
7. Berthold F, Blunier B, Bouquain D, Williamson S, Miraoui A (2011) PHEV control strategy including vehicle to home (V2H) and home to vehicle (H2V) functionalities. In: 2011 IEEE Vehicle Power and Propulsion Conference, VPPC 2011. https://doi.org/10.1109/VPPC.2011.6043120
8. Markel T, Simpson A (2006) Plug-in hybrid electric vehicle energy storage system design. In: 6th International Adv. Automot. Batter. Ultracapacitor Conference. AABC
9. Williamson SS (2013) Energy management strategies for electric and plug-in hybrid electric vehicles. Springer
10. Sun L, Liang R, Wang Q (2008) The control strategy and system preferences of Plug-in HEV. In: 2008 IEEE Vehicle Power and Propulsion Conference VPPC 2008, pp 1–5. https://doi.org/10.1109/VPPC.2008.4677573
11. Wirasingha SG, Emadi A (2011) Classification and review of control strategies for plug-in hybrid electric vehicles. IEEE Trans Veh Technol 60(1):111–122. https://doi.org/10.1109/TVT.2010.2090178
12. Guo F, Inoa E, Choi W, Wang J (2012) Study on global optimization and control strategy development for a PHEV charging facility. IEEE Trans Veh Technol 61(6):2431–2441. https://doi.org/10.1109/TVT.2012.2195787
13. Mets K, Verschueren T, Haerick W, Develder C, De Turck F (2010) Optimizing smart energy control strategies for plug-in hybrid electric vehicle charging. IEEE/IFIP Netw Oper. Manag Symp Work NOMS 2010:293–299. https://doi.org/10.1109/NOMSW.2010.5486561
14. Li Y, Lu X, Kar NC (2014) Rule-based control strategy with novel parameters optimization using NSGA-II for power-split PHEV operation cost minimization. IEEE Trans Veh Technol 63(7):3051–3061. https://doi.org/10.1109/TVT.2014.2316644
15. Banvait H, Anwar S, Chen Y (2009) A rule-based energy management strategy for plugin hybrid electric vehicle (PHEV). In: Proceedings of the American Control Conference, pp 3938–3943. https://doi.org/10.1109/ACC.2009.5160242
16. Peng J, He H, Xiong R (2017) Rule based energy management strategy for a series–parallel plug-in hybrid electric bus optimized by dynamic programming. Appl Energy 185:1633–1643. https://doi.org/10.1016/j.apenergy.2015.12.031
17. Phillips AM, Jankovic M, Bailey KE (2000) Vehicle system controller design for a hybrid electric vehicle. IEEE Conf Control Appl Proc 1:297–302. https://doi.org/10.1109/cca.2000.897440
18. Hmidi ME, Ben Salem I, El Amraoui L (2019) Analysis of rule-based parameterized control strategy for a HEV Hybrid Electric Vehicle. In: The 19th international conference on sciences and techniques of automatic control and computer engineering, STA 2019, pp 112–117. https://doi.org/10.1109/STA.2019.8717250
19. Johnson VH, Wipke KB, Rausen DJ (2000) HEV control strategy for real-time optimization of fuel economy and emissions. SAE Tech Pap 724. https://doi.org/10.4271/2000-01-1543
20. Surmann H (1996) Genetic optimization of a fuzzy system for charging batteries. IEEE Trans Ind Electron 43(5):541–548. https://doi.org/10.1109/41.538611
21. Schouten NJ, Salman MA, Kheir NA (2002) Fuzzy logic control for parallel hybrid vehicles. IEEE Trans Control Syst Technol 10(3):460–468. https://doi.org/10.1109/87.998036
22. Duoba M, Lohse-Busch H, Rask E (2012) Evaluating plug-in vehicles (plug-in hybrid and battery electric vehicles) using standard dynamometer protocols. World Electr Veh J 5(1):196–209. https://doi.org/10.3390/wevj5010196

23. Gong Q, Li Y, Peng ZR (2007) Optimal power management of plug-in HEV with intelligent transportation system. IEEE/ASME international conference on advanced intelligent mechatronics, AIM, pp 1–6. https://doi.org/10.1109/AIM.2007.4412579
24. Ichikawa S et al (2004) Novel energy management system for hybrid electric vehicles utilizing car navigation over a commuting route. IEEE intelligent vehicles symposium, proceedings, pp 161–166. https://doi.org/10.1109/ivs.2004.1336374
25. Delprat S, Lauber J, Guerra TM, Rimaux J (2004) Control of a parallel hybrid powertrain: optimal control. IEEE Trans Veh Technol 53(3):872–881. https://doi.org/10.1109/TVT.2004.827161
26. "Barney" Carlson R, Michael Duoba JW (2009) Test procedure development for 'blended type' plug-in hybrid vehicles. SAE Tech Pap 1(1):13 [Online]. Available https://www.jstor.org/stable/26308287?seq=1
27. Piccolo A, Ippolito L, Zo Galdi V, Vaccaro A (2001) Optimisation of energy flow management in hybrid electric vehicles via genetic algorithms. IEEE/ASME Int Conf Adv Intell Mechatron AIM 1:434–439. https://doi.org/10.1109/aim.2001.936493
28. Tianheng F, Lin Y, Qing G, Yanqing H, Ting Y, Bin Y (2015) A supervisory control strategy for plug-in hybrid electric vehicles based on energy demand prediction and route preview. IEEE Trans Veh Technol 64(5):1691–1700. https://doi.org/10.1109/TVT.2014.2336378
29. Li L, Yang C, Zhang Y, Zhang L, Song J (2015) Correctional DP-based energy management strategy of plug-in hybrid electric bus for city-bus route. IEEE Trans Veh Technol 64(7):2792–2803. https://doi.org/10.1109/TVT.2014.2352357
30. O'Keefe MP, Markel T (2006) Dynamic programming applied to investigate energy management strategies for a plug-In HEV1. In: 22nd international battery, hybrid and fuel cell electric vehicle symposium expo, EVS 2006, pp 1035–1046
31. Sciarretta LG, Vehicle propulsion systems. Springer, Berlin
32. Murphey YL, Park J, Chen Z, Kuang ML, Masrur MA, Phillips AM (2012) Intelligent hybrid vehicle power control part I: machine learning of optimal vehicle power. IEEE Trans Veh Technol 61(8):3519–3530. https://doi.org/10.1109/TVT.2012.2206064
33. Chen Z, Mi CC (2009) An adaptive online energy management controller for power-split HEV based on dynamic programming and fuzzy logic. In: 5th IEEE vehicle power and propulsion conference VPPC'09, pp 335–339. https://doi.org/10.1109/VPPC.2009.5289831
34. Mi XZC (2011) Vehicle power management modeling, control and optimization. Springer, Berlin
35. Chen Z, Mi CC, Xu J, Gong X, You C (2014) Energy management for a power-split plug-in hybrid electric vehicle based on dynamic programming and neural networks. IEEE Trans Veh Technol 63(4):1567–1580. https://doi.org/10.1109/TVT.2013.2287102
36. Martinez CM, Hu X, Cao D, Velenis E, Gao B, Wellers M (2017) Energy management in plug-in hybrid electric vehicles: recent progress and a connected vehicles perspective. IEEE Trans Veh Technol 66(6):4534–4549. https://doi.org/10.1109/TVT.2016.2582721
37. Yang X, Koziel S (2011) Computational optimization, methods and algorithms. Springer, Berlin
38. Karrenberg U (2007) Signals, processes, and systems an interactive multimedia introduction to signal processing, 3rd edn. Springer, Berlin
39. Murphey YL et al (2013) Intelligent hybrid vehicle power control—Part II: online intelligent energy management. IEEE Trans Veh Technol 62(1):69–79. https://doi.org/10.1109/TVT.2012.2217362
40. Khayyam H, Bab-Hadiashar A (2014) Adaptive intelligent energy management system of plug-in hybrid electric vehicle. Energy 69:319–335. https://doi.org/10.1016/j.energy.2014.03.020
41. Sun C, Hu X, Moura SJ, Sun F (2015) Velocity predictors for predictive energy management in hybrid electric vehicles. IEEE Trans Control Syst Technol 23(3):1197–1204. https://doi.org/10.1109/TCST.2014.2359176
42. Sun C, Moura SJ, Hu X, Hedrick JK, Sun F (2015) Management in plug-in hybrid electric vehicles 23(3):1075–1086
43. Ko B, Cui L, Choi S, Park BB, Ryu S (2018) Field evaluation of vehicle to infrastructure communication-based eco-driving guidance and eco-signal system. Transp Res Rec 2672(25):123–138. https://doi.org/10.1177/0361198118797456

44. Lin Q, Du X, Li SE, Ye Z (2016) Vehicle-to-infrastructure communication based eco-driving operation at multiple signalized intersections. In: 2016 IEEE vehicle power and propulsion conference, VPPC 2016—Proceedings. https://doi.org/10.1109/VPPC.2016.7791809
45. Yu H, Kuang M, McGee R (2014) Trip-oriented energy management control strategy for plug-in hybrid electric vehicles. IEEE Trans Control Syst Technol 22(4):1323–1336. https://doi.org/10.1109/TCST.2013.2278684
46. Baker D, Asher ZD (2018) Integration of advanced, pp 1–11. https://doi.org/10.4271/2018-01-1000.Abstract
47. Zhang J, Xu F, Zhang Y, Shen T (2020) ELM-based driver torque demand prediction and real-time optimal energy management strategy for HEVs. Neural Comput Appl 32(18):14411–14429. https://doi.org/10.1007/s00521-019-04240-7
48. Taherzadeh E, Dabbaghjamanesh M, Gitizadeh M, Rahideh A (2018) A new efficient fuel optimization in blended charge depletion/charge sustenance control strategy for plug-in hybrid electric vehicles. IEEE Trans Intell Veh 3(3):374–383. https://doi.org/10.1109/TIV.2018.2843173
49. Li Y, He H, Peng J, Wang H (2019) Deep reinforcement learning-based energy management for a series hybrid electric vehicle enabled by history cumulative trip information. IEEE Trans Veh Technol 68(8):7416–7430. https://doi.org/10.1109/tvt.2019.2926472
50. Lee HD, Koo ES, Sul SK, Kim JS (2000) Torque control strategy for a parallel-hybrid vehicle using fuzzy logic. IEEE Ind Appl Mag 6(6):33–38. https://doi.org/10.1109/2943.877839

Three-Level Inverters with Volt Per Hz Control for Induction Motor Driven Electric Vehicles

Paramjeet Singh Jamwal, Sanjeev Singh, and Shailendra Jain

Abstract This paper presents comparative study of three-level (3L) inverters fed induction motor (IM) drive operated with closed loop volt per hertz (V/f) control scheme. The performance of 3L inverter topology, namely cascaded H-bridge (CHB) and neutral point clamped (NPC) is compared with two-level (2L) inverter topology for IM drive (IMD) operated with closed loop V/f control scheme for electric vehicle (EV) application. The performance of 2L inverter and 3L inverters fed IMD is analyzed with Simulink model created in R2017b version of MATLAB at variable torque and speed. Performance of all the three inverters for IMD is compared with various common parameters. It is observed that with the application of V/f control scheme, wide variation in speed is obtained for EV application along with improvement in various performance parameters of complete system.

Keywords Electric vehicle (EV) · Induction motor drive (IMD) · Loss reduction · Three-level cascaded H-bridge (3L-CHB) inverter · Three-level neutral point clamped (3L-NPC) inverter · Two-level voltage source inverter (2L-VSI) · Volt per hertz (V/f) control

1 Introduction

According to International Federation of Automobiles (FIA) report, only transport sector contributes 22% of CO_2 emission but due to sharp increase in traffic it is a fastest growing sector. In this emission, 73% emission comes from road transport in which 47% emission is from heavy-duty vehicles (HDV) while 53% emission is from light-duty vehicles (LDV) [1]. As per the report of United Nations Environment Programme (UNEP), there are 1 billion global LDV on the road and expected to be

P. S. Jamwal (✉) · S. Jain
Sant Longowal Institute of Engineering and Technology, Longowal, Punjab, India
e-mail: paramjeet_pei1803@sliet.ac.in

S. Singh
Maulana Azad National Institute of Technology, Bhopal, Madhya Pradesh, India
e-mail: sschauhan@manit.ac.in

S. Dwivedi et al. (eds.), *Flexible Electronics for Electric Vehicles*, Lecture Notes in Electrical Engineering 863, https://doi.org/10.1007/978-981-19-0588-9_9

more than 2.5 billion global LDV by 2050. Therefore, to reduce and control the CO_2 emission from LDV, battery electric vehicles (BEVs) are playing important role and it is expected that there should be 300 million electric LDV up to 2030 [2]. Recently, low-cost autonomous BEV to maximize the traffic flow is reported by Cecotti et al. in [3]. Low-cost induction motor (IM) with aluminum cage rotor and totally enclosed fan-cooled (TEFC) technology for city BEV application is reported by Tran et al. in [4].

IM is a low-cost motor because of its magnet less construction. With the high-performance power semiconductor devices, its smooth control is also possible which put it among the popular choice for electric vehicle (EV) application [5]. There are two most common scheme to control the IM, i.e., scalar and vector control. Scalar control also known as volts per hertz (V/f) control is a low-cost, simple, and easy to implement control scheme with open and closed loop. The design and implementation of closed loop V/f control scheme for IM with simulation and dSPACE are reported in [6]. Closed loop V/f control scheme for Z-source inverter (ZSI) fed IM is discussed in [7]. Open loop and closed loop V/f control scheme for two-level voltage source inverter (2L-VSI) fed IM is discussed in [8]. This 2L-VSI fed IM drive has high voltage total harmonic distortion (THD), voltage stress across the switch, and current stress through the switch which can be reduced with the use of three-level (3L) inverters [9]. Ivanov et al. applied rising edge (RE) sawtooth, falling edge (FE) sawtooth, level shifted (LS) triangular, and phase shifted (PS) triangular carrier wave in 3L neutral point clamped (NPC) inverter to analyze its effects on voltage THD (THDv) [10].

In this paper, closed loop V/f control scheme is implemented for two topologies of three-level (3L) inverters named as cascaded H-bridge (CHB) and NPC inverter for IM, and the obtained performance is compared with two-level (2L) inverter fed IM. With V/f control scheme wide variation in speed can be achieved which is desired for EV application.

After the introduction in this section, inverter topologies are given in second section, closed loop volt per hertz control scheme is discussed in third section, performance simulation results are discussed in fourth section, conclusions from the work are described in fifth section and parameters used for this work are provided in appendix.

2 Inverter Topology

Schematic diagram of 2L-VSI fed IM with closed loop V/f control scheme is shown in Fig. 1. The control scheme begins with, slip speed (ω_{sl}) obtained from slip speed generator using speed error. On addition of slip speed in measured speed (ω_m), mechanical synchronous speed (ω_s) is obtained. This ω_s is fed to modulated signal generator to generate modulated signal. PWM controller compares modulated signal with high frequency signal to generate switching sequence for IGBT switch of voltage source inverter [9]. Schematic diagram of 3L-CHB and 3L-NPC inverter fed IM drive is shown in Figs. 2 and 3, respectively.

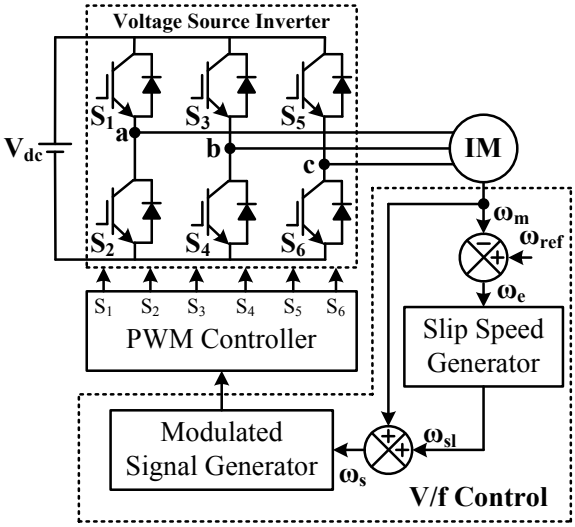

Fig. 1 Schematic diagram of a 2L-VSI fed IM with V/f control

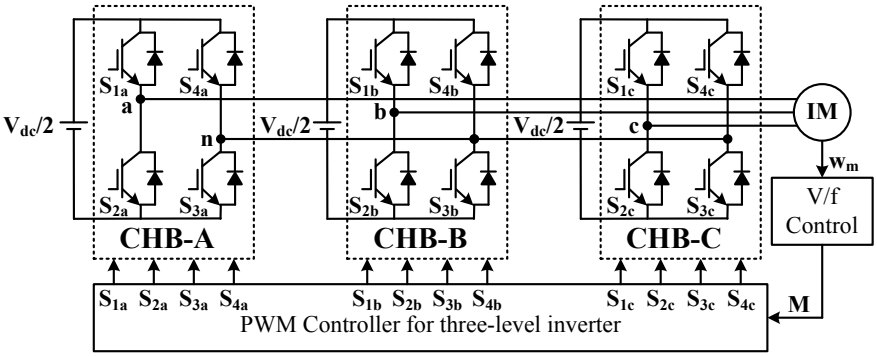

Fig. 2 Schematic diagram of a 3L-CHB inverter fed IM drive

With same control scheme as discussed in Fig. 1, modulated signal (M) is generated from the sensed speed of the IM. This modulated signal is processed through pulse width modulation (PWM) controller to generate the switching sequence for IGBT switches of three-phase three-level CHB and NPC inverters [9]. Volt per Hertz (V/f) control scheme is discussed with detail in next section.

3 Volt Per Hz Control

The closed loop V/f control scheme to generate the modulated signal (M) from sensed speed (ω_m) of IM is shown in Fig. 4.

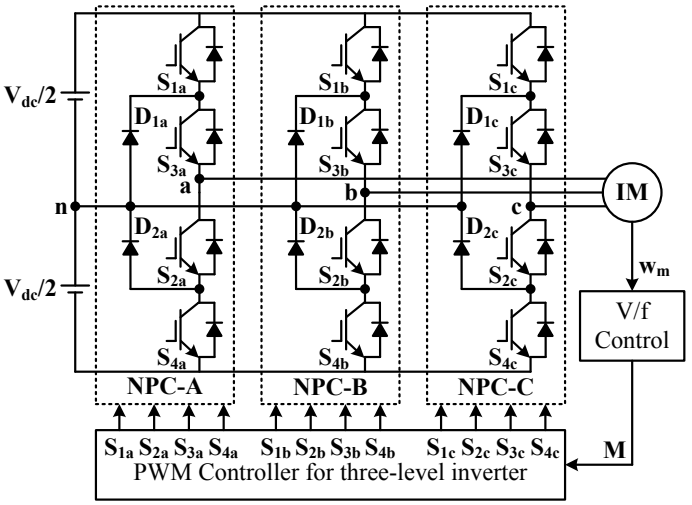

Fig. 3 Schematic diagram of a 3L-NPC inverter fed IM drive

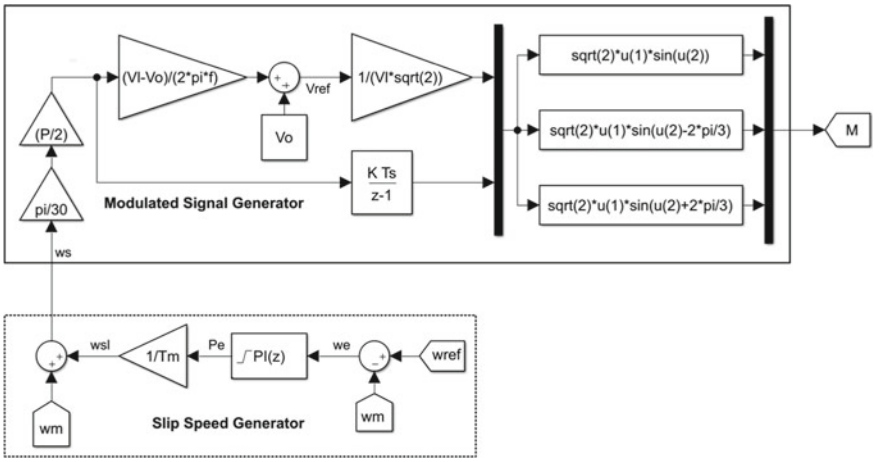

Fig. 4 Modulated signal generation with closed loop V/f control scheme

Control action begins with the comparison of sensed speed (ω_m) with reference speed (ω_{ref}) to generate speed error (ω_e). This speed error is processed through proportional-integral (PI) controller to generate slip power (P_{sl}). This slip power is divided by rated torque (T_m) of IM to generate the slip speed (ω_{sl}). This slip speed is added with sensed speed of IM to generate synchronous speed (ω_s). This synchronous speed is in revolution per minute (rpm), hence multiplied with $\pi/30$ to transform it into radian per second (rad/s). Thereafter, it is multiplied with poles/2 to convert it from mechanical rad/s to electrical rad/s. This electrical synchronous speed (ω_{se}) is

integrated to generate the angular position (u(2)) of modulated signal. This electrical synchronous speed is also multiplied with the difference of rated rms line voltage (Vl) and offset voltage which is further divided with rated angular frequency (ω_{rated}) to generate the corresponding voltage. An offset voltage (V_{o}) is added with voltage to operate the IM at starting [11]. This reference voltage is divided with peak amplitude of the voltage to generate amplitude ($u(1)$) of modulated signal. After obtaining angular position and amplitude, three phases (M_{a}, M_{b}, and M_{c}) of modulated signals are generated by using Eqs. (1)–(3).

$$M_{\text{a}} = \sqrt{2}\, u(1)\ \sin(u(2)) \tag{1}$$

$$M_{\text{b}} = \sqrt{2}\, u(1)\ \sin(u(2) - 2\pi/3) \tag{2}$$

$$M_{\text{c}} = \sqrt{2}\, u(1)\ \sin(u(2) + 2\pi/3) \tag{2}$$

This three-phase modulated signal (M) is passed through the PWM controller of 10 and 5 kHz switching frequency to operate the two-level (VSI) and three-level (CHB and NPC) inverters, respectively [9].

4 Performance Simulation

Performance of IMD, operated with V/f controlled 2L-VSI, 3L-CHB inverter, and 3L-NPC inverter is analyzed at different speed on different torque. Considering the EV application, speed is taken at 25, 50, 75, and 100% on 85, 100, and 105% torque of rated torque to analyze the different performance parameters. On these variations, THDv, power factor (PF), voltage stress on the switch, current stress through the switch, and efficiency of IM are analyzed. Voltage stress across the switch of 2L-VSI, 3L-CHB inverter, and 3L-NPC inverter fed V/f controlled IMD is shown in Fig. 5.

There is 6450 kV/s voltage stress across the switch of 2L-VSI while the switch of 3L-CHB and 3L-NPC inverter has 1613 and 1617 kV/s voltage stress across the switch, respectively. It means that with the use of 3L inverter in place of 2L inverter, switch voltage stress can be reduced by 75%. THDv of 2L-VSI, 3L-CHB inverter, and 3L-NPC inverter fed V/f controlled IMD on 85% torque, 100% torque, and 105% torque is shown in Fig. 6a–c, respectively.

There is THDv reduction of 42.11–50% on 85% torque, 44.44–51.11% on 100% torque, and 41.18–51.11% on 105% torque with 3L-CHB inverter and 3L-NPC inverter as compared with 2L-VSI fed V/f controlled IMD. THDi of 2L-VSI, 3L-CHB inverter, and 3L-NPC inverter fed V/f controlled IMD on 85% torque, 100% torque, and 105% torque is shown in Fig. 7a–c, respectively.

There is THDi reduction of 9.09% on 85% torque, 14.53% on 100% torque, and 13.64% on 105% torque with 3L-CHB inverter as compared with 2L-VSI fed V/f

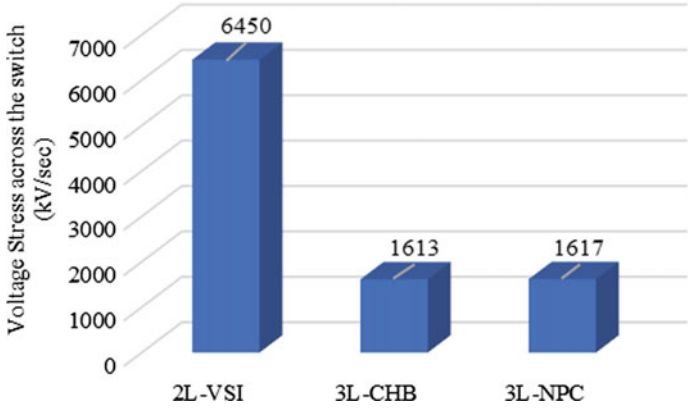

Fig. 5 Voltage stress through the switch of 2L-VSI, 3L-CHB, and 3L-NPC inverter fed IMD

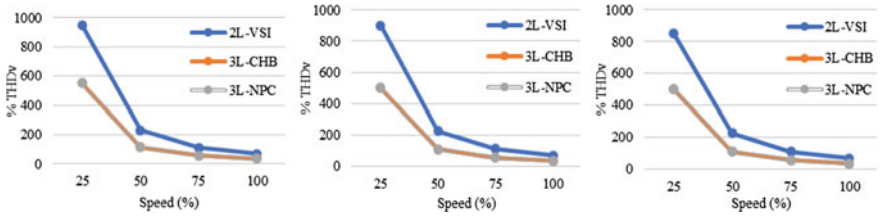

(a) 85% torque (b) 100% torque (c) 105% torque

Fig. 6 Voltage THD at different speeds

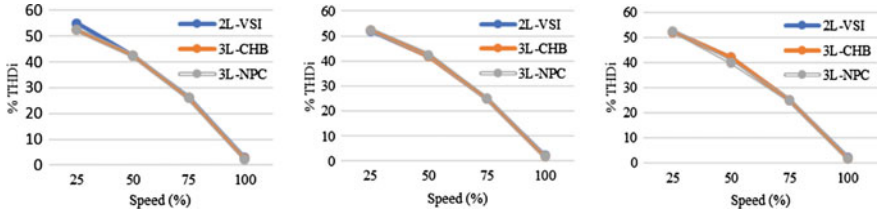

(a) 85% torque (b) 100% torque (c) 105% torque

Fig. 7 Current THD at different speeds

controlled IMD. There is THDi reduction of 16.36% on 85% torque, 15.43% on 100% torque, and 15.91% on 105% torque with 3L-NPC inverter as compared with 2L-VSI fed V/f controlled IMD. Efficiency of IM with 2L-VSI, 3L-CHB inverter, and 3L-NPC inverter on 85% torque, 100% torque, and 105% torque is shown in Fig. 8a–c, respectively.

There is efficiency improvement of 1.1–8.84% on 85% torque, 4.51–14.29% on 100% torque, and 4.05–15.94% on 105% torque with 3L-CHB inverter as compared

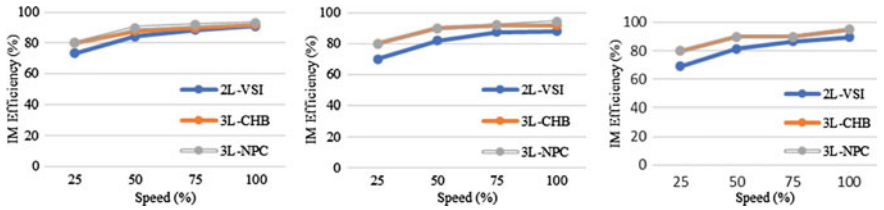

(a) 85% torque (b) 100% torque (c) 105% torque

Fig. 8 Efficiency of IM at different speeds

with 2L-VSI fed V/f controlled IMD. There is efficiency improvement of 2.2–8.84% on 85% torque, 5.14–14.29% on 100% torque, and 4.05–15.94% on 105% torque with 3L-NPC inverter as compared with 2L-VSI fed V/f controlled IMD. PF of 2L-VSI, 3L-CHB inverter, and 3L-NPC inverter fed V/f controlled IMD on 85% torque, 100% torque, and 105% torque is shown in Fig. 9a–c, respectively.

There is PF improvement of 14.50–47.88% on 85% torque, 10.21–47.73% on 100% torque, and 17.39–44.44% on 105% torque with 3L-CHB inverter as compared with 2L-VSI fed V/f controlled IMD. There is PF improvement of 14.50–47.88% on 85% torque, 12.31–54.55% on 100% torque, and 15.94–51.11% on 105% torque with 3L-NPC inverter as compared with 2L-VSI fed V/f controlled IMD. Switch current stress of 2L-VSI, 3L-CHB inverter, and 3L-NPC inverter fed V/f controlled IMD on 85% torque, 100% torque, and 105% torque is shown in Fig. 10a–c, respectively.

There is switch current stress reduction of 49.50–50.95% on 85% torque, 50–50.85% on 100% torque, and 50–51.46% on 105% torque with 3L-CHB inverter as compared with 2L-VSI fed V/f controlled IMD. There is switch current stress reduction of 49.50–50.73% on 85% torque, 50–50.85% on 100% torque, and 50.21–50.82% on 105% torque with 3L-NPC inverter as compared with 2L-VSI fed V/f controlled IMD. Waveform and harmonic order of line voltage with 2L-VSI, 3L-CHB inverter, and 3L-NPC inverter are shown in Fig. 11.

The 2L-VSI has three levels in output line voltage and 68.85% THD at rated torque and speed. The 3L-CHB inverter has five levels in output line voltage and 35.38%

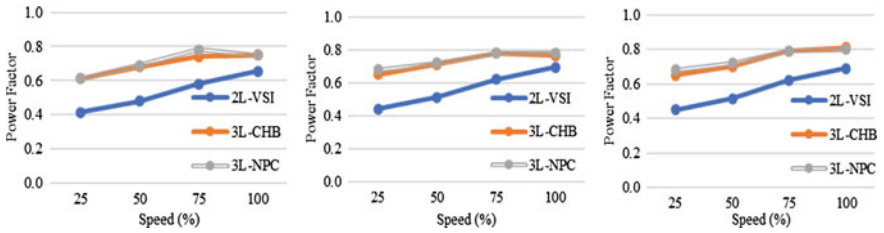

(a) 85% torque (b) 100% torque (c) 105% torque

Fig. 9 Power factor at different speeds

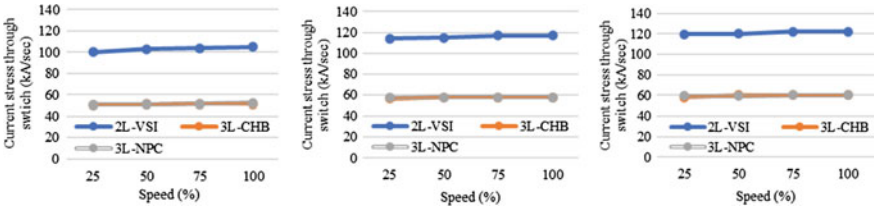

(a) 85% torque (b) 100% torque (c) 105% torque

Fig. 10 Current stress through switch at different speeds

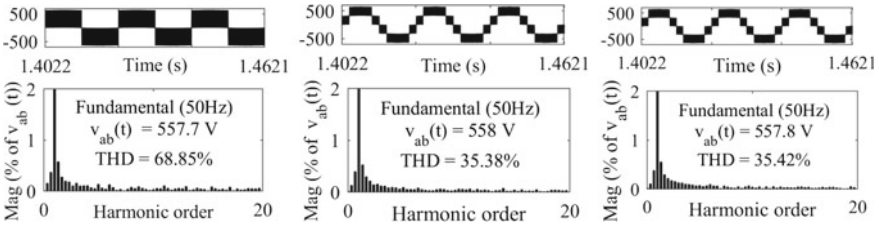

(a) 2L-VSI (b) 3L-CHB inverter (c) 3L-NPC inverter

Fig. 11 Line voltage and its harmonic spectrum with inverter fed V/f controlled IMD at rated torque and rated speed

THD at rated torque and speed. The 3L-NPC inverter has five levels in output line voltage and 35.42% THD at rated torque and speed.

The line current with 2L-VSI, 3L-CHB inverter, and 3L-NPC inverter has THD within specified limit at rated torque and speed. Stator current, speed, torque of 2L-VSI, 3L-CHB inverter, and 3L-NPC inverter fed IMD at rated torque are shown in Fig. 12. Speed variation is considered from 100–75%, 75–50%, 50–25%, 25–50%, 50–75%, and 75–100% with all three inverters fed IMD. Performance parameters comparison of 3L inverter with respect to 2L inverter are given in Table 1.

5 Conclusions

In this paper, performance of volt per hertz controlled three-level (3L) inverters and two-level (2L) inverter fed induction motor drive for electric vehicle application is compared and other advantage of 3L inverters over 2L inverter is obtained as wide variation in speed with volt per hertz control scheme. Performance simulation results are presented to show the best possible topology. Both 3L-CHB and 3L-NPC inverters topology have equal reduction in voltage stress across the switch and THD_v. While reduction in THD_i, improvement in efficiency of IM, and improvement in power factor are better with 3L-NPC inverter as compare to 3L-CHB inverter. Reduction in current stress through switch is better with 3L-CHB inverter as compared to 3L-NPC

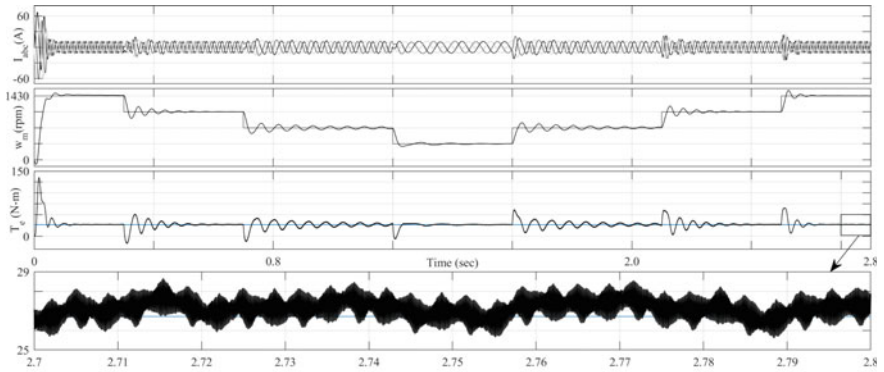

(a) With 2L-VSI fed IMD

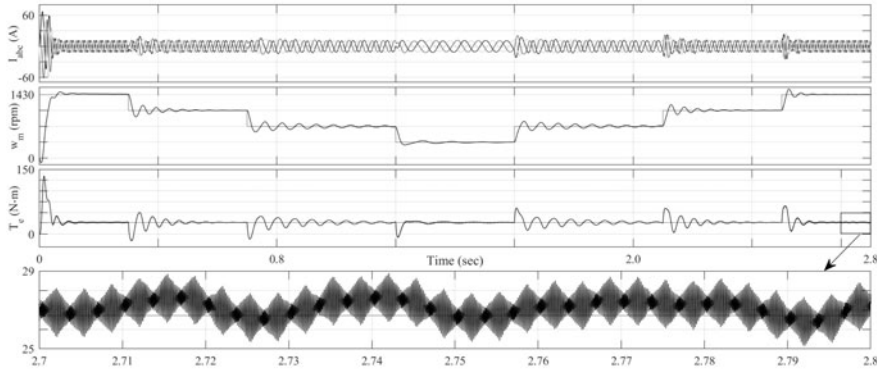

(b) With 3L-CHB inverter fed IMD

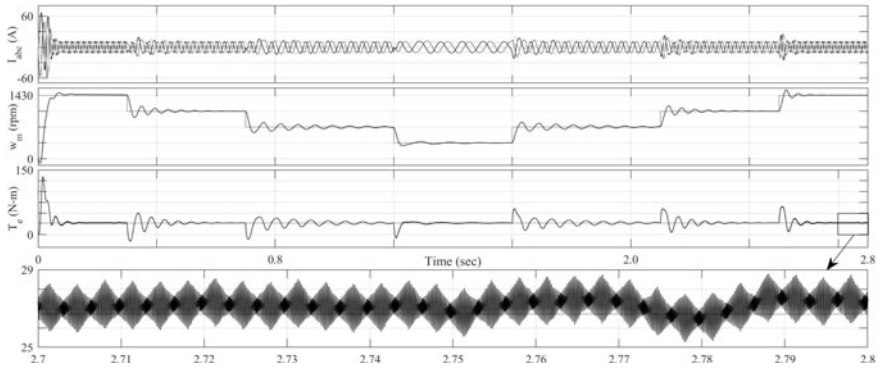

(c) With 3L-NPC inverter fed IMD

Fig. 12 Stator current, speed, torque, and steady state torque at rated torque

Table 1 Comparison of obtained parameters

S. No.	Parameters	3L-CHB (%)	3L-NPC (%)
1	Voltage stress reduction	75	75
2	THDv reduction	41.18–51.11	41.18–51.11
3	THDi reduction	14.53	16.36
4	IM efficiency improvement	1.1–15.94	2.2–15.94
5	PF improvement	10.21–47.88	12.31–54.55
6	Current stress reduction	49.5–51.46	

inverter. Therefore, it is concluded that the 3L-NPC inverter topology is better for EV application using V/f control.

Appendix

Motor Power: 4 kW, Motor Speed: 1430 rpm or 149.75 rad/s, Motor Torque: 26.71 Nm, Battery Voltage (Vdc): 645 V, Line Voltage: 400 V, Frequency: 50 Hz, Stator Resistance: 1.405 Ω, Rotor Resistance: 1.395 Ω, Stator and Rotor Inductance: 0.005839 H, Friction Factor: 0.002985 N-m-s, Inertia: 0.0131 kg-m^2, Mutual Inductance: 0.1722 H, Pole: 4, Proportional gain (Kp) of PI controller: 18.90867, Integral gain (Ki) of PI controller: 66.73151.

References

1. FIA Mobility (2015) Global reduction in CO_2 emissions from cars: a consumer's perspective, Paris
2. Electric Light Duty Vehicles, UN Environment Programme. https://www.unenvironment.org/explore-topics/transport/what-we-do/electric-mobility/electric-light-duty-vehicles. Last accessed 14 Jan 2021
3. Cecotti M, Larmine J, Fellows N, Hayatleh K (2019) Development of an autonomous battery electric vehicle, SAE Technical Paper, pp 1–9
4. Tran TV, Negre E, Mikati K, Pellerey P (2019) Optimal design of TEFC induction machine and experimental prototype testing for city battery electric vehicle. IEEE Trans Indus Appl
5. Zeraoulia M, Benbouzid MEH, Diallo D (2006) Electric motor drive selection issues for HEV propulsion systems: a comparative study. IEEE Trans Veh Technol 55(6):1756–1764
6. Srilad S, Tunyasrirut S, Suksri T (2006) Implementation of a scalar controlled induction motor drives. In: SICE-ICASE international joint conference, Busan, South Korea
7. Ellabban O, Mierlo JV, Lataire P (2011) A comparative study of different control techniques for an induction motor fed by a Z-source inverter for electric vehicles. In: International conference on power engineering, energy and electrical drives, Malaga, Spain

8. Goda SM, Elkoteshy YS, Ouda AN, Elawa AE (2018) Scalar control technique for three-phase induction motor for electric vehicle application. In: Twentieth international middle east power systems conference (MEPCON), Cairo, Egypt
9. Jamwal PS, Singh S, Jain S (2021) Three-level inverters for induction motor driven electric vehicles. In: 3rd IEEE International conference on energy, power and environment towards clean energy technologies, in press, Meghalaya, India
10. Ivanov S, Mandache L, Ivanov V, Radu A, Roman M, Prejbeanu R (2019) Comparison of PWM strategies for three level inverters. IEEE international conference on electromechanical and energy systems (SIELMEN), Craiova, Romania. https://doi.org/10.1109/SIELMEN.2019.8905789
11. Krishnan R (2001) Electric motor drives modeling, analysis, and control. Prentice Hall

Interval Type-2 Fuzzy Logic Image Process Technology in Flexible Electronics to Analyze Defects in TFT-LCD

Mohit Kumar Sharma, Ashish Vijay, and Vishal Das

Abstract Manufacturing process of TFT-LCD from TFT substrate leads to visual defects. These defects have direct impact on reliability, accuracy, and resolution of TFT-LCD panel. Inspection of these defects is a complicated procedure as it depends on characteristics of defects. So it is necessary to design a highly accurate model for defect detection. This paper is dealing with the design of system for defect detection based on the concept of interval type-2 fuzzy logic. This system is more suitable for inspection of extremely small defects.

1 Introduction

Nowadays, in flexible electronics, a lot of features such as high resolution, viewing angle, contrast, brightness, etc., are main important domains of research in TFT-LCD. About hundreds of working procedures are involved in manufacturing process of TFT-LCD. The process of making thin film TFT-LCD involves the process of determining its size by cutting TFT glass substrate at first. Next step forward is to grind the edges. Since circuits on terminals are part of edges of TFT glass substrate, edges will fracture, during grinding process, if there is a positional deviation, pollutants between respective laminates [1]. As large number of procedures are involved, TFT-LCD may also exhibit visual defects as a result [2]. Due to complexity and uncertainties of such defects, it is equally important to develop a defect detection method.

M. K. Sharma (✉) · A. Vijay · V. Das
Manipal University Jaipur, Jaipur, India
e-mail: mohitkumar.sharma@jaipur.manipal.edu

A. Vijay
e-mail: ashish.vijay@jaipur.manipal.edu

V. Das
e-mail: vishal.das@jaipur.manipal.edu

S. Dwivedi et al. (eds.), *Flexible Electronics for Electric Vehicles*, Lecture Notes in Electrical Engineering 863, https://doi.org/10.1007/978-981-19-0588-9_10

Section 2 of this paper deals with features extraction for defect detection. Section 3 of this paper envisages designing of IT2FLES system to recognize defects on TFT-LCD panel screen. In the last section, experimental results for two samples are provided.

2 Features Extraction for Defect Detection

To detect any defect on TFT-LCD panel, first attempt is to categorize all the possible defects on the basis of their attributes. Each attribute plays an important role as they have direct impact on reliability and accuracy of defect detection. On the basis of shape and size of defect, there are mainly three defects namely point defect, line defect, and MURA (Japanese term for blemish) defect as shown in Fig. 1. In point defect, if defective pixel is darker or brighter than background then "Dark Point" or "Brighter Point" will result [2]. Point defect appears as either dark or bright point whose area is almost one pixel. So selection features are contrast, area, and location in case of point defect. Similarly, complete line will be defective when the color of line is darker than surrounding color or vice-versa. Line defects can be further categorized namely horizontal, vertical, and slanted line defects as "Direction" is considered as an attribute. So direction is now important for judgment of line defects [2]. Hence, selection features of line defects will cover all the attributes of point defect with one more attribute namely "Direction". This paper deals with these two defects only.

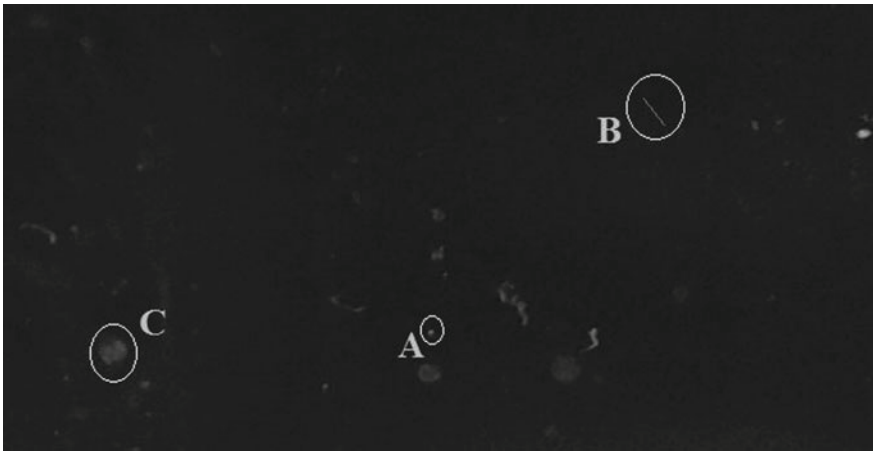

Fig. 1 TFT-LCD screen defects of which encircled points A, B, and C are representing point defect, line defect, and MURA defect, respectively

3 Designing of Interval Type-2 Fuzzy Logic Expert System (IT2FLES)

Point defects and line defects are very common among all defects appearing during manufacturing process of TFT-LCD panel. There are different reasons behind these defects such as defective transistors used in the manufacturing process, open or shorted signals. Point defects appear as a dark point or bright point of about one pixel. So limited numbers of point defects can be tolerated if they are not clustered together. Defect testing challenge lie in identification and quantification of line defects as they are considered fatal.

Defects of TFT-LCD are complex in nature, and degree of vagueness is also high. So accurate mathematical model is designed for the judgement of such defects by using IT2FLES system. Building blocks of IT2FLES system is shown in Fig. 2. In type-1 fuzzy system, uncertainties may lie in antecedent, consequent parts of rule bases, and different tuning parameters of the system [3, 4].

Due to complex and fuzzy behavior of defects of TFT-LCD, each attribute value is distributed and their information is not centric [2, 5]. So at the first stage of fuzzifier block, original crisp data are mapped on membership function. The original crisp data are values derived from image segmentation process of color (RGB) samples of different contrasts that are shown in Figs. 4 and 5. As the complexity and degree of vagueness are high, Gaussian function is selected as membership function as shown in Fig. 3. In IT2FLES, behavior of membership function is fuzzy in itself. As per attributes extracted from scanned image of TFT-LCD panel, following rule bases are formed.

Rule Base 1: If "CONTRAST" attribute of image is high (most important)
AND "AREA" attribute of image is small (most important)
AND "LOCATION" attribute of image is central (important)
AND "DIRECTION" attribute of image is vague (common)
THEN the TFT-LCD PANEL has serious POINT DEFECT.

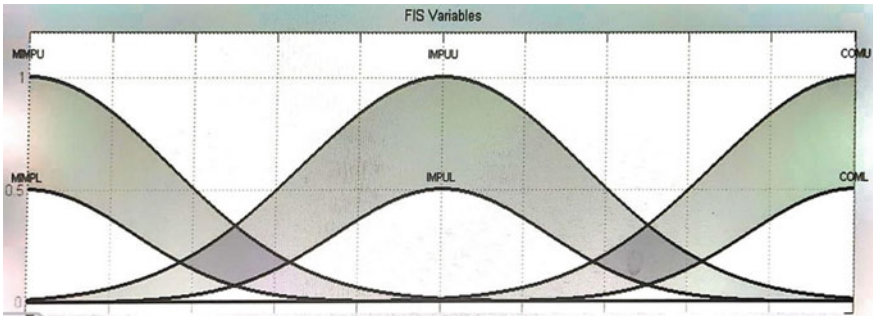

Fig. 2 Gaussian membership function used in proposed IT2FLES system

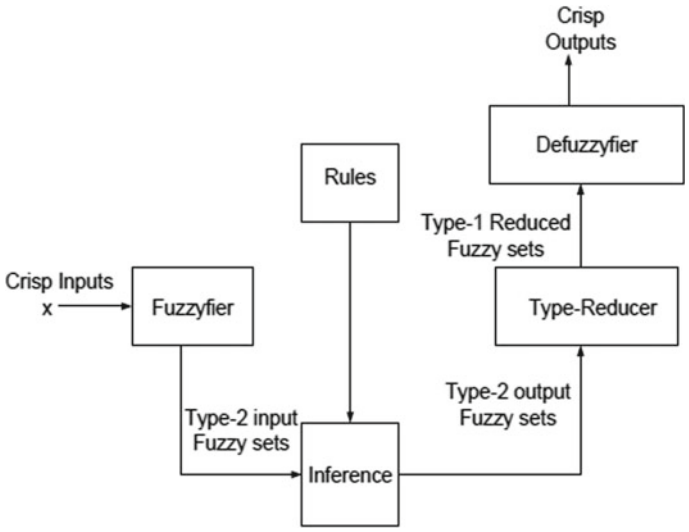

Fig. 3 Block diagram of proposed IT2FLES system

Rule Base 2: If "CONTRAST" attribute of image is high (most important)
AND "AREA" attribute of image is big (most important)
AND "LOCATION" attribute of image is central (important)
AND "DIRECTION" attribute of image is not vague (common)
THEN the TFT-LCD PANEL has serious LINE DEFECT.

As per importance of each antecedent part of rule bases, grading is done by "most important," "important," and "common". This grading decides the weight coefficient of each antecedent part. For example, if grading is 3, 2, and 1 for "most important," "important," and "common," respectively, then weight coefficient of "LOCATION attribute of image is central" is

$$w = 2/(3 + 2 + 1) = 1/3 \tag{1}$$

Similarly, weight coefficient of "AREA attribute of image is big" is

$$w = 3/(3 + 2 + 1) = 1/2 \tag{2}$$

After inference process, de-fuzzification followed by type-reducer is accomplished to obtain crisp data output for judgement of defects on TFT-LCD panel.

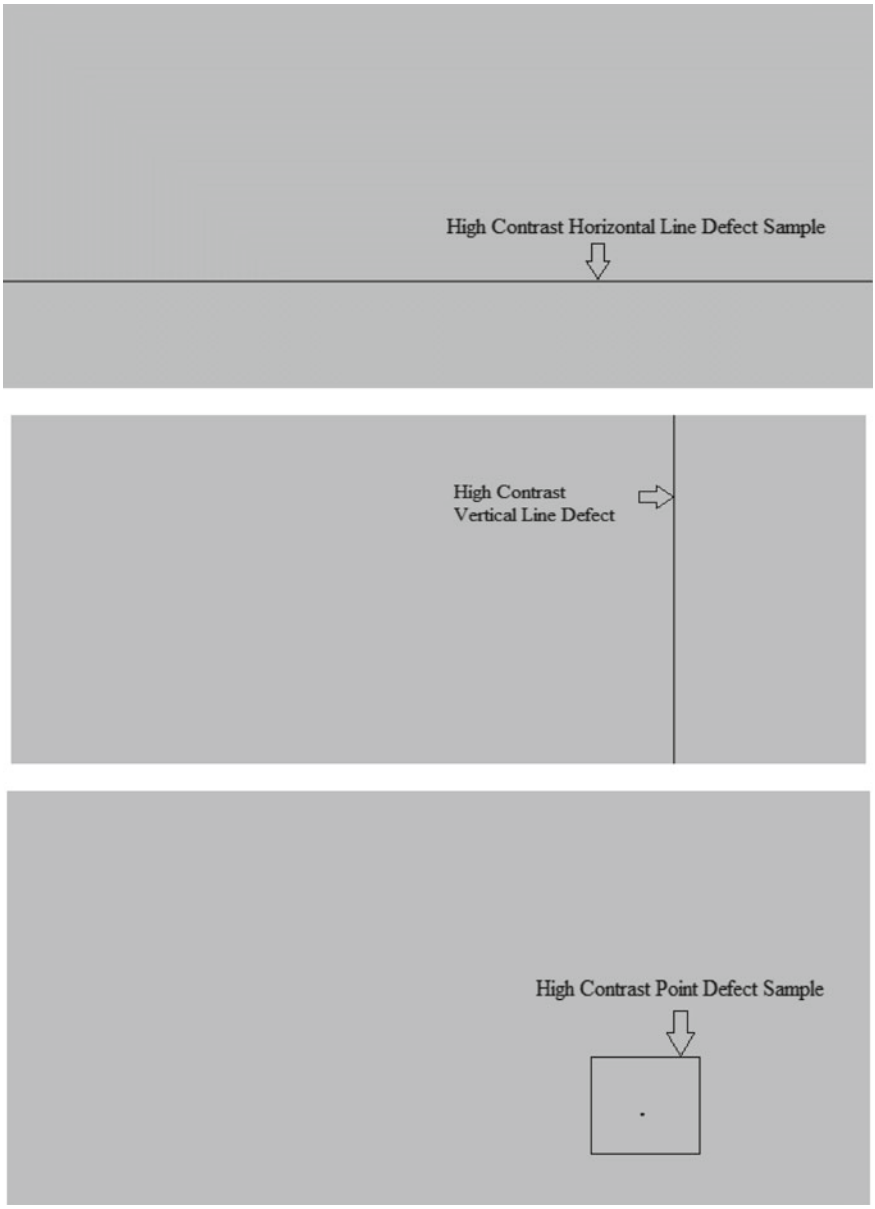

Fig. 4 "High Contrast" samples for defect detection

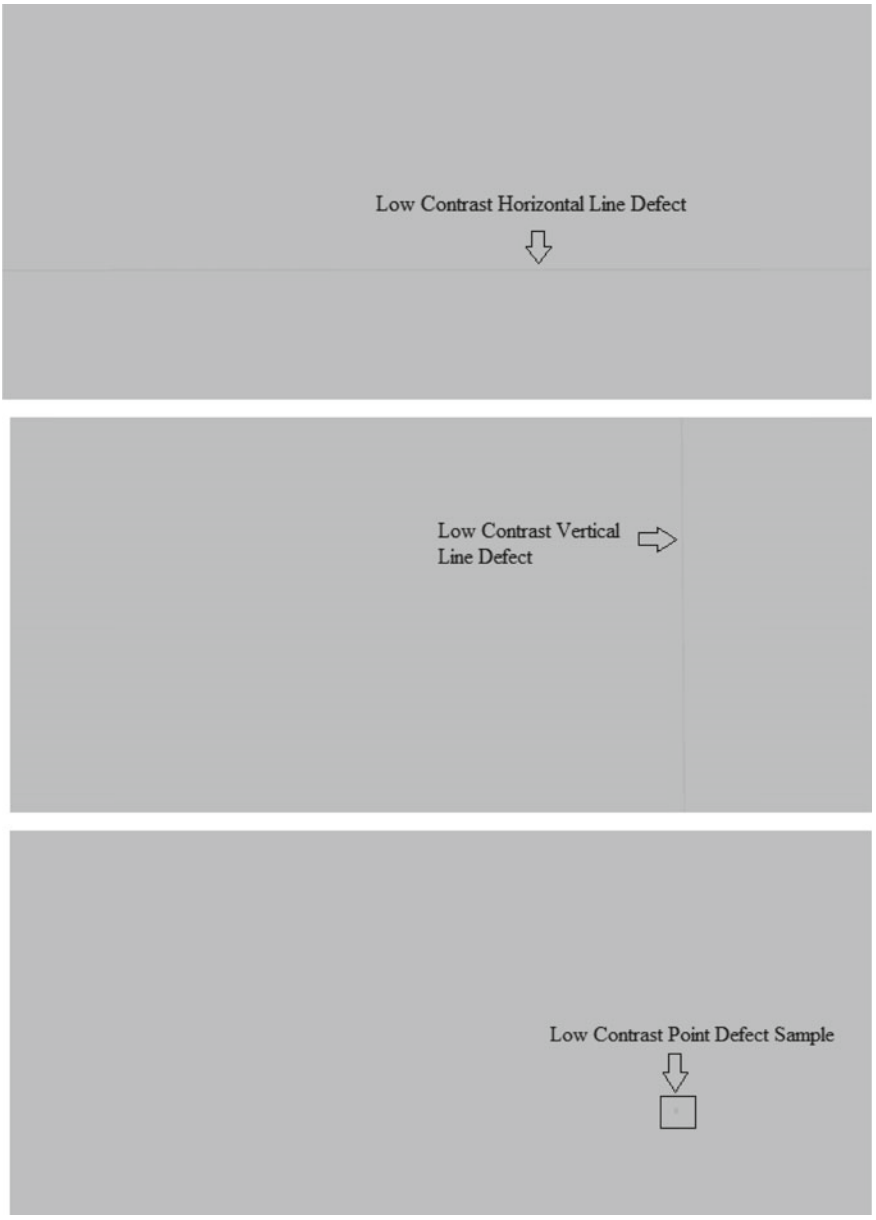

Fig. 5 "Low Contrast" samples for defect detection

Table 1 Defects in "High Contrast" samples detected by IT2FLES system

Samples	*X*-axis (pixels)	*Y*-axis (pixels)	Width (mm)	Height (mm)	Area (Sq. mm)	Result
1	2710	1221	717.020	1.322	947.900	Horizontal line defect
2	2710	1221	1.058	323.056	341.793	Vertical line defect
3	2710	1221	5.820	3.968	23.093	Dot/point defect

Table 2 Defects in "Low Contrast" samples detected by IT2FLES system

Samples	*X*-axis (pixels)	*Y*-axis (pixels)	Width (mm)	Height (mm)	Area (Sq. mm)	Result
1	2710	1221	717.020	1.322	947.900	Horizontal line defect
2	2710	1221	1.058	323.056	341.793	Vertical line defect
3	2710	1221	3.175	6.350	20.161	Dot/point defect

4 Experimental Results

The proposed fuzzy-based system in this paper is applied on various examples of different contrasts to recognize defects. In this paper, proposed expert fuzzy system is applied on two different samples as shown in Fig. 4. As per features extracted from the samples of "High Contrast" as shown in Fig. 4, three defects came out. Table 1 is providing the details of the reports of the samples of "High Contrast" processed by proposed expert fuzzy system.

Similarly, for "Low Contrast" samples as shown in Fig. 5, three defects came out and Table 2 is providing details of the reports of the "Low Contrast" samples processed by proposed expert fuzzy system.

5 Conclusion

To detect defects in TFT-LCD, interval type-2 fuzzy logic is giving results better and faster. To mitigate uncertainties associated with pixels (if noise is non stationary also), this IT2FLES method is playing key role. Three major defects with less number of rule bases in IT2FLES are easily identified for two different samples of different contrasts.

References

1. Jeffrey Kuo C-F, Chiu C-H, Su T-Y, Peng K-C (2011) Applying fuzzy image processing technology to inspect defects of thin film transistor-liquid crystal display
2. Yu Z, Jian Z (2005) Fuzzy recognition of the defect of TFT-LCD. In: Li C-S, Yeung MM (eds) Electronic imaging and multimedia technology IV, Proceedings of SPIE, vol 5637, SPIE, Bellingham
3. Mendel JM (2001) Uncertainty rule-based fuzzy logic systems. In: Introduction and new directions. Prentice- Hall, Upper Saddle River
4. Mendel JM (2007) Advances in type-2 fuzzy sets and systems. Inform Sci 177:84–110
5. Russo F (1993) A new class of fuzzy operators for image processing: design and implementation. In: IEEE International Conference on Fuzzy Systems, FUZZ-IEEE 93, pp 815–820

A Survey on Wearable Antenna Used for Defense Applications

Tapan Nahar and Sanyog Rawat

Abstract This paper consists of the survey of different types of wearable antennas used for military and defense applications. Wearable antennas can be directly integrated on clothing or can be made using textile materials. These unconventional antennas fulfill the requirement of robust, light weight, ease of integration, low cost, and multiband communication. These are required in various applications such as military, defense, remote health monitoring, portable handheld communication, security packaging, radio communication, positioning system, radar, remote sensing, off body communication, body to body communication, radio frequency identification (RFID), and consumer wearable electronics. Wearable antennas can be designed by combining flexible electronics with antenna technology which may be employed in any materials such as jackets, helmet, clothing, buttons, backpacks, tags, belt, wrist, briefcases, and labeling to enable efficient communication in a digital world.

Keywords Wearable antenna · Flexible antennas · Microstrip patch antenna · Defense · Textile antennas

1 Introduction

Rapid development of the flexible electronics and wireless communication has made possible to design and implement wearable textile antennas on the different fabrics. These antennas can be directly integrated or made on the clothing of human being [1]. Low cost microstrip antenna can be designed on flexible dielectric substrates made of the textile materials. Radiating elements are made of metallic coted threads, copper tape, conducting inks, and conducting fabric. These antennas can be used in the variety of applications such as telemedicine, navigation, public safety, defense, police, telemetry, and tracking [2–33]. Their major benefits are real time and "on-the-go" communication power with no need to use additional antenna hardware.

T. Nahar · S. Rawat (✉)
Department of Electronics and Communication Engineering, Manipal University Jaipur, Jaipur, India
e-mail: sanyog.rawat@jaipur.manipal.edu

S. Dwivedi et al. (eds.), *Flexible Electronics for Electric Vehicles*, Lecture Notes in Electrical Engineering 863, https://doi.org/10.1007/978-981-19-0588-9_11

For military and defense applications, there are various requirements such as enhancing the currently used cell phone coverage by up to 200%, increment in uploading and downloading rates, omnidirectional radiation pattern, enabling communication capabilities at 800–3000 MHz with environment friendly, washable, durable, non-corrosive, and flexible characteristics of system. Battery life extension with optimization of operating power is also a big issue [34].

Major issue of wearable antennas is lack of availability of electrical and dielectric characteristics of textile materials [7]. There are many reported works [8–10] regarding the study of dielectric behaviors of textile fibers, but measurement techniques and the measuring conditions are different in different cases. The performance of wearable antenna is affected by human body like shift in resonant frequency, reduction in gain, and distortion in radiation pattern because human body is lossy material [11, 12]. Some techniques are required to adopt to improve isolation between antenna and human body and minimize the effect of body on antennas. Isolations can be improved by reducing the backward radiations by employing conductive surface between antenna and user body [13]. Specific absorption rate (SAR) can be reduced by addition of conducting surface [14]. Radiation pattern of antenna should have opposite orientation with respect to human body [11]. Efficiency of antenna can also be increased by adding felt layer between antenna and human body because it enhances the distance between them [15–18]. Antenna using electro-magnetic band gap material and substrate integrated waveguide technique can reduce SAR [9, 19–22, 27]. Absorption of moisture and liquid material in textile-based antenna also affects antenna characteristics because dielectric constant is varied due to absorption and which can shift the resonant frequency [19]. This issue can be reduced by selecting proper textile material with shielding. Material used for wearable antennas should have capabilities like the temperature tolerance, non-corrosive, durable, invariance in the electrical properties due to physical abrasion, stress, compression, expansion, banding, and miniaturization other environmental effects [21]. Textile superstrate may be stacked to prevent antenna from these effects. To fulfill the requirement of high gain and omnidirectional coverage, multi antenna system may be employed. Reconfigurable antennas and tunable circuits may also be used in wearable antenna to reducing detuning effect [22].

2 Different Types of Wearable Antennas

2.1 Substrate Integrated Waveguide (SIW)-Based Wearable Antenna

SIW-based antenna is preferred because of small back radiations toward the human body. It is cost-effective technique where electric field is confined inside the cavity made using number of shorting vias at the edges of patch and backside antennas full

ground plane. It enhances the isolation between human body and antenna. It is also used to reduce the mutual coupling when antenna array is used in wearable systems [9].

2.2 *Fractal Antenna on Jeans Cloth*

Compact geometries are required in wearable antenna. Fractal geometries or self-similarity of this structure are used for size miniaturization and multiband operation [3, 4, 22, 28]. Small antenna structure affects the antenna performance and increases the quality factor and reduces the bandwidth. Koch fractal geometry has characteristics of filling a plane which eliminates the limitations of performance of Euclidean geometry. Koch fractal dipole antennas are designed in [3] with 0th, 1st, and 2nd iteration on textile material denim having dielectric constant and loss tangent 1.71 and 0.085, respectively, at 0.915 GHz. Bandwidth was increased from 43.9 to 72.5 MHz and size is reduced from 149.28 to 132.48 mm using 2nd iteration in comparison with 0th iteration. Resonant frequency is shifted to lower range by increasing iterations. Gain and efficiency of antenna are increased by increasing iterations in geometries. Specific absorption rate is minimum at geometries with 1st iteration in both horizontal and vertical employments [3]. Koch fractal geometry-based dipole antenna is designed in [4] by pasting designed shaped copper sheet on jeans fabric by fabric glue. Geometry of proposed antenna is shown in Fig. 1. Presented antenna with 2nd iteration in geometry provides 32% reduction in the length and improvement in the return loss. SAR level of fractal geometry is much below safety level of 0.119 W/kg which indicates its applicability for wearable applications [4].

Flexible material affects the antenna performance when soldier is bent because effective length and effective area of antenna changes. Performance deterioration is big challenge for the antenna designers under bending and crumpling conditions.

Fig. 1 Geometry of Koch fractal antenna ([4], reproduced courtesy of The Electromagnetics Academy)

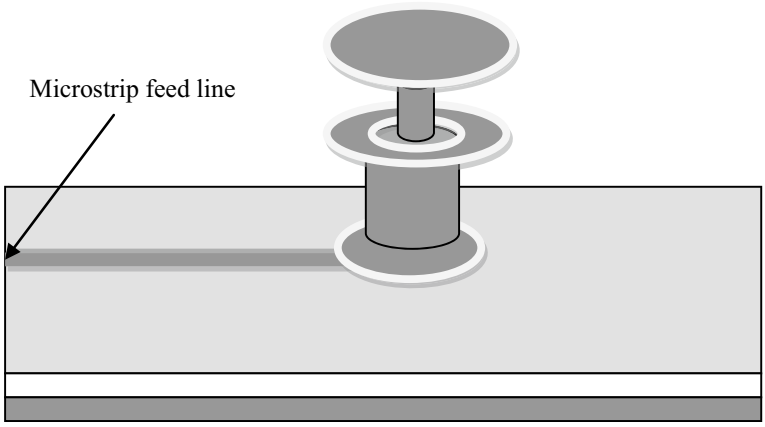

Fig. 2 Geometry of dual band metallic button antenna [5]

2.3 Metallic Button Antenna

Major challenges of wearable antenna are the variation in the performance parameters due to banding and human skin characteristics. Button antenna which consists of three disks and a coaxial post, solve this problem because its shape is not changing. Its shape is inspired from the button used in denim jeans. It does not require large ground plane which is required in flexible patch antennas. Feeding is provided by microstrip line at the side of bottom, and impedance is 50 ohms at both the operating frequencies. Flexible plastic layer is used as dielectric between lower disk and ground plane. Vacro is used in [5] as dielectric. Geometry of proposed antenna is shown in Fig. 2. Coaxial feeding can also be used. Lower and higher resonant frequencies can be controlled by changing the diameters of upper and lower disks, respectively. Bandwidth is controlled by the gap between both the disks. Bandwidth at higher band can be controlled by changing antenna height. Numerous Wearable devices and systems have been developed with the aim of simplifying the human computer interface, reducing size, and removing the need for physical connection. Proposed geometry provides good omnidirectional radiation pattern with gain around 2.4 dBi. There is also less effect of moisture on antenna parameters [5].

2.4 Adhesive-Bandage-Like Antenna

Adhesive-bandage-like antenna consists of metallic patch surrounded by metal ring on the top layer of dielectric substrate and back side with full ground plane. Since its structures like bandage, it is known as adhesive-bandage-like antenna. Thick substrate can be used in order to reduce the losses. As patch antenna is put close to ground, quality factor of antenna increases which increases the stored energy and

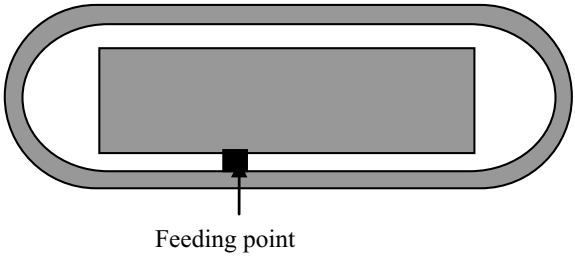

Fig. 3
Adhesive-bandage-like antenna [11]

reduces the radiating energy. Textile materials like thick jeans can be used as dielectric substrate. It also provides flexibility due to elastic behavior of cotton. Thick materiel prevents the variation in properties due to stretching and compression. Wash cotton, curtain cotton, poly cotton, jeans cotton, etc., may be used as substrate material. To provide excitation to the patch, feeding is provided at the gap between metal ring which acts as virtual ground and patch. Similar geometry can be used in the coplanar waveguide fed antenna in which large coplanar ground is surrounded by the patch which increases overall size. When metallic ring is connected to ground using shorting vias across the ring, bandwidth and gain of antenna are increased by 2.1 MHz and 0.39 dBi, respectively. To improve the gain and front to back ratio of antenna and reduce the back radiation, the shielded ground plane is increased at two radiating slots. Geometry of proposed antenna is shown in Fig. 3. When banding is performed, resonant frequency is almost unchanged but gain, efficiency, and bandwidth are decreased. With extension at the edges, reduction in gain during banding is very small [11].

2.5 Embroidered Antenna

Previously designing materials of textile antenna material did not allow washing and reusing of wearable suits. Nowadays, new embroidery-based wearable antenna allows washing and reusing and fabricated using textile materials [16]. No glues, mask, and etching are required to design antenna. Polymer fibers plated with conductive material is generally known as E-textile which is used to fabricate wearable antenna and used as replacement of copper foil [16]. High price and finite conductivity issues limit its use for commercial applications. Mixed conductive textile threads are cost efficient materials in place of fully conductive fabrics Nora, Shieldit, Flec-Tron, etc. Conductive thread of a silver plated nylon thread provides good strength and conductivity with resistance to multiple deformations. Additionally, it allows washing and has ability to resist temperature up to 150 °C [29]. Woven conductive textile material has good electrical properties but issues arise at the edges where it is cut. Embroidery conductive thread may be used to design any planer conductive geometries. Conducting properties can be varied by using different mesh densities. When embroidery is done using yarn in fabric, straight line could not be designed

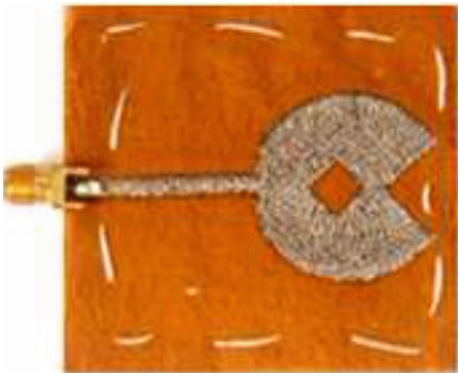

Fig. 4 Geometry of embroidered wearable antenna ([17] reproduced courtesy of The Electromagnetics Academy)

properly and some zig-zag appears at the edges which increase the current paths and antenna becomes electrically larger than normal metallic antenna. Resonant frequency is also reduced due to this property. To provide feeding to antenna, direct soldering is impossible in textile material. Small piece of copper tape, conductive epoxy, etc., can be used to allow soldering. Metallic part of fabric like button and rivets may be used to achieve stable transition between antenna and outer circuitry. Button can be also hand sewn using conductive yarn to provide proper connections [23–26]. Influences of metallic button on scattering parameters are less than 1 dB and lower [26]. Metallic button allows removing the connection of circuit during washing. Gain of the antenna depends on stitch spacing. By reducing stitch spacing from 0.8 to 0.4 mm, efficiency and gain are increased by 8% and 1.2 dBi, respectively [27]. Gain of embroidered antenna is less than similar shaped antenna made by copper because of discontinuous structure of embroidery and losses in current flow between adjacent thread [27]. Computer controlled embroidery machinery is used to design the ultra-wide band wearable antenna geometry on flannel substrate fabric [17]. Geometry is shown in Fig. 4. Flanner fabric has smooth surface with property of fluffy surface. Three layers of flannel fabric is used in which top layer consists of patch geometry, middle layer is isolation layer, and bottom layer is ground plane. Conducting area was created using the stitching conducting thread on the surface of fabric. Direct soldering is used to connect the SMA connector. Proposed antenna provides 17 GHz bandwidth with omnidirectional radiation pattern and adequate gain.

2.6 RFID Textile Tags

RFID textile tag antennas are very popular because it can be wearied at any part of body like arm, wrist, chest, back, etc., these antennas are fabricated using regular textile processing, electrically conductive textiles, embroidery with conductive yarn

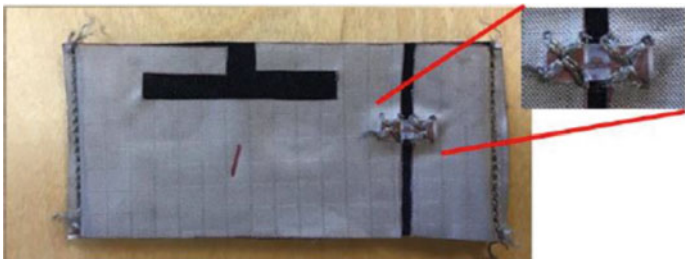

Fig. 5 Geometry of RFID tag antenna [30]

and sewing. Challenges associated with tag antenna are to achieve required performance at placement of closed to body. Biological conductivity and polarizability may alter the antenna performance. Slot-based tag antenna is used in [30]. Geometry of proposed antenna is shown in Fig. 5. Antenna conductor is fabricated using nickel- and copper-plated less EMF Shieldit super fabric. Ethylene-propylene-diene-monomer cell rubber foam (thickness of 4 mm) is used as dielectric substrate which have dielectric constant and loss tangents of 1.26 and 0.007, respectively. Conductive walls are used to provide interconnection between patch and ground which is formed by sewing with conductive yarn. Proposed antenna provides good RFID read range of 3–4 m at resonant frequency.

2.7 Helmet and Vest Antenna

To enable comfortable "hands free operation" of wireless device for soldier, fire technician, police officer, forest officer, etc., antennas may be placed or implemented on outer or inner layers of top portion of helmet so it is also known as helmet antenna or vest antenna. Major challenges associated with these antennas are to achieve broad bandwidth, low specific absorption rate, compact size, light weight, cost efficiency, and radiation safety [31]. Broadband design of helmet antenna is proposed in [31]. Antenna is mounted at inner layer of top section of helmet. Geometry of proposed antenna is shown in Fig. 6. Antenna consists of thermochemical composite which have light foam, thin sheet of copper, and printed circuit board. Excitation cable is integrated in the head protection layer which is made using energy absorbing material for safety of head from helmet. Conductive shield is also used to prevent human head from the RF radiations. Impedance bandwidth of 160% was obtained at 4 GHz. Gain of antenna is small at frequencies below 600 MHz but radiation pattern presented good coverage at all frequencies. Bandwidth and gain can be enhanced using broadband balun structure and low loss magneto-dielectric material, respectively. These antennas may be used as good replacement option of whip antenna. Wearable antenna on military beret is designed using conductive thread, felt substrate, and conductive

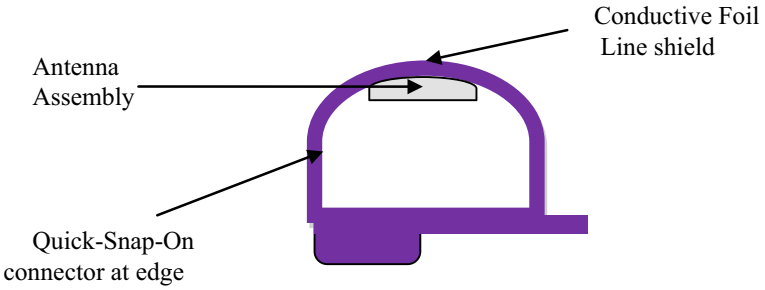

Fig. 6 Helmet and vest antenna [31]

textile in [32] to for positioning system. Proposed antenna performance is not affected with head phantom, and SAR level is below safety values.

2.8 Monopole Zip-Based Antenna

Wearable antennas which can be designed on already installed accessories like button, tag, belt, zip, etc., are popularly used because there is no need of additional metallization. Zip, which is available in pockets and garments, can be used to design monopole antenna [33]. It can be easily hide inside the cloth materials. Zip antenna has been designed using felt fabric as dielectric material and electro-textile material as conducting material in [33]. Geometry of proposed antenna is shown in Fig. 7. Dielectric constant and loss tangent of felt fabric were 1.22 and 0.016, respectively. Resonant frequency of antenna can be calculated using length of connected Zip which is chosen as 25% of guided wavelength (λg). Ground plane can be designed at back side of felt fabric using Shieldit electro-textile. Partial ground plane was used in [33].

Fig. 7 Wearable monopole Zip antenna [33]

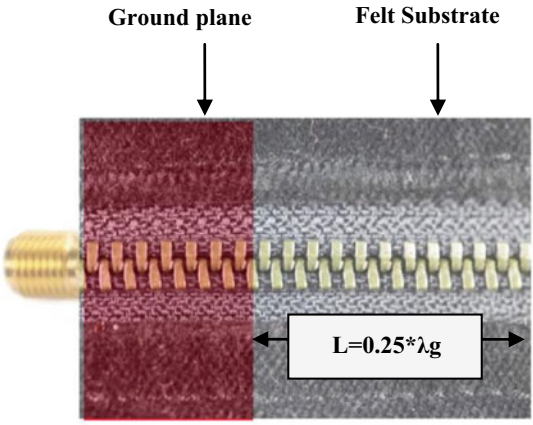

Presented geometry is shown in Fig. 7. Proposed antenna provides 40% bandwidth and approximately 0 dB gain at 2.5 GHz and can be used for Wi-Fi communication. Gain can be increased by optimizing the ground plane length, its radiation pattern similar to monopole antenna.

3 Conclusion

In this paper, various types of wearable antennas used for defense applications are presented with the merits and demerits. Wearable antenna offers number of benefits like bulky structure, low profile, small size, non-corrosive, flexible, un-obstructive, and rugged. Antenna design techniques should be selected and combined in order to resolve multiple issues like mechanical deformation, human body movement and posture, effects of human body on antenna parameters, effects of antenna on human body, and many more.

References

1. Sankaralingam S, Gupta B (2010) Development of textile antennas for body wearable applications and investigations on their performance under bent conditions. Progr Electromagn Res B 22:5371
2. Raad HK, Al-Rizzo HM, Isaac A, Hammoodi AI (2016) A compact dual band polyimide based antenna for wearable and flexible telemedicine devices. Progr Electromagn Res C 63:153–161
3. Jalil ME, Rahim MKA, Samsuri NA, Murad NA, Bala B (2013) Evaluation Koch Fractal textile antenna using different iteration toward human body. In: 2013 proceedings of the international symposium on antennas & propagation, Nanjing, China, pp 1017–1020
4. Poonkuzhali R, Alex Z, Balakrishnan T (2016) Miniaturized wearable fractal antenna for military applications at VHF band. Progr Electromagn Res C 62:179–190
5. Sanz-Izquierdo B et al (2006) Covert dual-band wearable button antenna. Electron Lett 42:668–670
6. Shekina Jessie Jennifer R, Balakrishnan K (2016) Wearable eight cross shaped antenna using eight different dielectric substrates. Imperial J Interdiscip Res (IJIR) 5(2)
7. Sheeba R, Jayanthy T (2016) Design and analysis of a low cost, flexible soft wear antenna for an ISM band working in different bending environment. Springer India
8. Patel T, Sahoo M (2016) A technical review: design issues of wearable antennas. IJARIIE 3(2)
9. Paracha KN, Abdul Rahim SK, Soh PJ, Khalily M (2019) Wearable antennas: a review of materials, structures, and innovative features for autonomous communication and sensing. IEEE Access 7:56694–56712. https://doi.org/10.1109/ACCESS.2019.2909146
10. Daya Murali S, Narada Maha Muni B, Dilip Varma Y, Chaitanya SVSK (2014) Development of wearable antennas with different cotton textiles. Int J Eng Res Appl 7(4)
11. Chi Y, Chen F (2014) On-body adhesive-bandage-like antenna for wireless medical telemetry service. IEEE Trans Antennas Propag 5(62):2472–2480. https://doi.org/10.1109/TAP.2014.2308918
12. Lim EG, Wang Z, Chen Wang J, Leach M, Zhou R, Lei C-U, Man KL (2014) Wearable textile substrate patch antennas. Eng Lett
13. Khaleel Raad H, White C, Ayman Isaac HA-R, Hammoodi A (2016) A compact dual-band antenna for wearable e-health devices. eTELEMED

14. Chauraya A, Whittow WG, Yiannis J, Vardaxoglou C, Li Y, Torah R, Yang K, Beeby S, Tudor J (2013) Inkjet printed dipole antennas on textiles for wearable communications. IET Microw Anten Propag 9(7)
15. Singh J, Brar GS, Sidhu E (2016) High gain textile microstrip patch antenna for radio navigation applications. Int J Adv Res Comput Eng Technol (IJARCET) 6(5)
16. Ouyang Y, Chappell WJ (2008) High frequency properties of electro-textiles for wearable antenna applications. IEEE Trans Antennas Propag 2(56):381–389
17. Rahman Osman MA, Abd Rahim MK, Samsuri NA, Salim HAM, Ali MF (2011) Embroidered fully textile wearable antenna for medical monitoring application. Progr Electromagn Res 117:321–337. https://doi.org/10.2528/PIER11041208, http://www.jpier.org/PIER/pier.php?paper=11041208
18. Wang JC, Lim EG, Leach M, Wang Z, Manand KL, Huang Y (2016) Conformal wearable antennas for WBAN applications. In: Proceedings of the international multiconference of engineers and computer scientists, vol. II, IMECS 2016
19. Kuhjani, Neshati MH (2014) Design investigation of a dual-band circularly-polarized wearable antenna. In: The second Iranian conference on engineering electromagnetics (ICEEM 2014)
20. Kiourti A, Volakis JL (2016) Wearable antennas, sensors and a novel class of textiles. Forum Electromagn Res Method Appl Technol (FERMAT)
21. Patel T, Sahoo M (2013) Design issues of wearable antennas. Int J Sci Res (IJSR)
22. Puente C, Claret J, Sagues F, Romeu J, Lopez-Salvans MQ, Pous R (1996) Multiband properties of a fractal tree antenna generated by electrochemical deposition. Electron Lett 25(32):2298–2299
23. Paraskevopoulos A, de Sousa Fonseca D, Seager RD, Whittow WG, Vardaxoglou JC, Alexandridis AA (2016) Higher-mode textile patch antenna with embroidered vias for on-body communication. IET Microw Antennas Propag 7(10):802–807
24. Prasad Gupta N, Maheshwari R, Kumar M (2013) Advancement in ultra wideband antennas for wearable applications. Int J Sci &Eng Res 8(4)
25. Loss C, Gonçalves R, Lopes C, Pinho P, Salvado R (2016) Smart coat with a fully-embedded textile antenna for IoT applications. MDPI J Sens
26. Ivsic B, Bonefacic D, Bartolic J (2013) Considerations on embroidered textile antennas for wearable applications. IEEE Antennas Wirel Propag Lett 12:1708–1711. https://doi.org/10.1109/LAWP.2013.2297698
27. Zhang S et al (2012) Embroidered wearable antennas using conductive threads with different stitch spacing. In: 2012 Loughborough Antennas & Propagation Conference (LAPC), Loughborough, UK, pp 1–4. https://doi.org/10.1109/LAPC.2012.6403059
28. Hatem GM, College T, Najaf, Iraq Ali JS (2016) Wunderlich fractal-based printed dual-band dipole antenna for wearable RFID applications. University of Technology, Iraq
29. Vejasegaran R, Jusoh M, Kamarudin MR, Rahim HA, Malek F, Sabapathy T, Shakhirul MS (2016) Embroidered dual band textile antenna for ISM band application on bending performance. ARPN J Eng Appl Sci 10(11)
30. Virkki J, Wei Z, Liu A, Ukkonen L, Björninen T (2017) Wearable passive E-Textile UHF RFID tag based on a slotted patch antenna with sewn ground and microchip interconnections. Int J Anten Propagation. https://doi.org/10.1155/2017/3476017
31. Wang JJH, Triplett DJ (2007) Multioctave broadband body-wearable helmet and vest antennas. In 2007 IEEE antennas and propagation society international symposium, Honolulu, HI, USA, pp 4172–4175. https://doi.org/10.1109/APS.2007.4396460
32. Lee H, Tak J, Choi J (2017) Wearable antenna integrated into military berets for indoor/outdoor positioning system. IEEE Antennas Wirel Propag Lett 16:1919–1922. https://doi.org/10.1109/LAWP.2017.2688400
33. Mantash M, Tarot A, Collardey S, Mahdjoubi K, Zip based monopole antenna for wearable communication systems. In: 6th European conference on antennas and propagation (EUCAP), Prague, Czech Republic, pp 762–764. https://doi.org/10.1109/EuCAP.2012.6206237
34. GlobeNewswire Homepage, https://www.globenewswire.com/news-release/2016/10/04/1207969/0/en/Advanced-Wearable-Antennas-for-Military-and-Defense-Exhibited-by-Bluewater-Defense-and-Vorbeck-at-AUSA-2016.html. Last accessed 12 Mar 2021

Analyzing the Different EV Policy and Strategy Components Essential in Deploying the Electric Mobility in India

Abhishek Shrivastava

Abstract In India, electric vehicles (EVs) policy framework certifies that India's electric mobility mission keeps tempo with the worldwide scale. India's development projections create capability for emerging scopes for EV in certain segments. In India, a particular set of circumstances such as presence of useable renewable energy resources, readiness of expert work force and knowledge, an infrastructure and consumer conversion for applying technology, and cultural that promotes sharing, are encouraging to an ecological mobility concept have created a prospect for accelerated adoption of EVs over internal combustion engine vehicles.

Keywords Electric vehicles · Policy framework · Electric mobility · Renewable energy

1 Introduction

Electric vehicles (EV) as compare to internal combustion engine vehicles (ICEV) or ICE now considered as environment friendly mobility choice. It means, EV as compare to ICEV has more potential to reduce the greenhouse emissions (GHEs). As EVs are driven completely or partly by batteries, they help in reducing dependency on fossil fuels (FFs) as well. As per a report in 2019, India's GHG discharges have risen by 150% (1990–2016) and the government's environment aims to reduce its discharge amount by 33–35% by 2030 are not yet in line with a 1.5 °C path [1]. Considering these facts and keeping EVs as an alternative to bring down GHEs percentage, promotes clean, connected, shared, sustainable, and holistic mobility, an effective and robust EVs policy framework is very much required, keeping in view the complete electric mobility ecosystem and its various aspects.

There are studies that have been carried out about electric mobility segment in many countries like Austria [2], Brazil [3, 4], China [5], Denmark [6], Ireland [7],

A. Shrivastava (✉)
Manipal University Jaipur, Jaipur, Rajasthan 303007, India
e-mail: abhishek.shrivastava@jaipur.manipal.edu

S. Dwivedi et al. (eds.), *Flexible Electronics for Electric Vehicles*, Lecture Notes in Electrical Engineering 863, https://doi.org/10.1007/978-981-19-0588-9_12

Germany [8], Latvia [9], Lithuania [10], Norway [11, 12], Portugal [13], Spain [14–16], Sweden [17], the USA [18], Nordic countries [19], etc.

In India, there are investigation findings that have been done on electric vehicle regulations, procedures, decent methods, drivers and hurdles, tasks, and prospects. Luthra performed study on need assessment of the growth of the electric vehicles in India resulted by challenges in the EV development and on the power concerns and power need [20]. Khurana et al. examined the different factors that effects a consumer's adoption of EVs [21]. Kumar et al. investigated the challenges before India to adopt EV by 2030 and the actions taken by Government of India to boost exploration and advancement in EV sector [22]. Vidhi et al. reviewed different stages in the lifespan of an EV, their influence on ecological discharges, and endorses strategies appropriate for diverse socio-economic assembly that are applicable to the Indian bazaar, rise trade of EVs, intensification fraction of renewable energy, and stop air contamination triggered from battery-operated manufacturing [23]. Sriram et al. explored the overall scenario of the EV and areas for further growth [24]. Mokariya et al. presented various aspects in terms of challenges and issues related to impact of EVs on Indian power grid, potential services, and applications [25].

However, no study has yet been presented linked to various characteristics of plans and approaches for the amalgamation of electric movement, RE, and ICT in India.

1.1 Electric Mobility Ecology

Electric mobility holds jointly two separate sectors—transport and power. The integration of these two sectors decides the successful implementation of electric mobility. The electric mobility ecology includes following stakeholders [26] as shown in Fig. 1.

Government, which makes the policy, suppliers, which design and makes the electric vehicle, electricity suppliers, charging infrastructure, and end consumer are

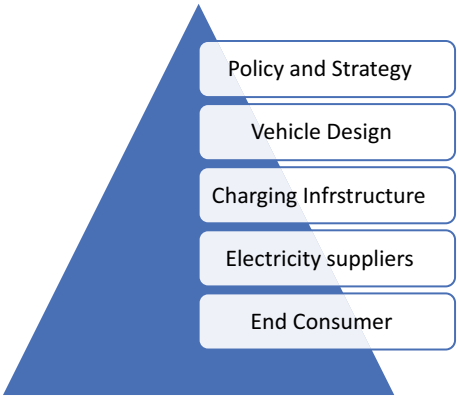

Fig. 1 Different EVs ecology stakeholders

the distinct stakeholders of the electric mobility. The end user could be a truck or bus driver, personal vehicle owner, who would ought to charge batteries in a small time or would like the charging to occur fast for numerous EVs at the same time.

1.2 Drivers of Electric Mobility

For the proper functioning of the electric mobility, following are factors could be the key drivers [27]

- Battery cost
- Government support
- Action by cities.

Battery cost is one the main obstacles for the application of the EVs. With encouraging administration procedures and decline in battery rates, a substantial progress in the EV sell is anticipated.

Governments around the world have been enthusiastic on embracing environment friendly modes of transport.

The growth of EVs apart from national and state policy framework also requires aggressive act headed by cities. Air quality advantages that EVs deal are turn out to be a significant driver of such act around cities, worldwide.

EV acceptance in different international geographics, as illustrated in Fig. 2, comprises nearly 40% of the globe's entire EV trades [29].

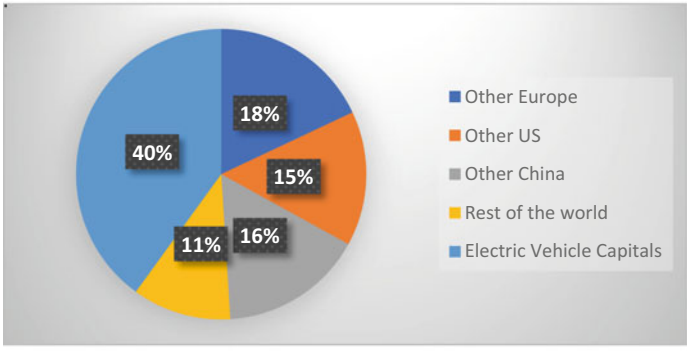

Fig. 2 Estimated cumulative EV stock in market, in different geographies [29]

2 Electric Mobility in India

Though several nations have adopted EVs as a part of conveyance strategy, their reactions have diverged corresponding to their phase of financial growth, energy reserve abilities, industrial resources, and diplomatic ordering of replies to environment shift. In India, a specific set of conditions such as presence of useable renewable energy resources, readiness of trained work force and knowledge, an infrastructure and consumer conversion for applying technology, and cultural that promotes sharing, are encouraging to an ecological mobility concept have created a prospect for accelerated adoption of EVs over ICE [26].

India has initiated its EV promotional program in 2013 through implementing the NEMMP 2020. The plan aims at state power safety measures, alleviation of harmful effects of road transportation development on environment and development of domestic industrial resources. The project aims on providing direct and sustained assistance for supporting electric vehicle knowledge in the country by 2020 [27].

Progressing the NEMMP 2020, the administration has proclaimed that it will offer fiscal support as aid to smart cities for the buying of electric vehicles for majority civic transport for executing model projects in the Faster Adoption and Manufacturing of Electric vehicle (FAME-I & II) plan. Cities with inhabitants more than 10 lakhs can avail this grant [27].

With an objective at speed up advancement of charging base in the country, the government in recent times delicensed setting up of charging bases for EVs [27]

Other initiatives are taken up by the Government of India and State governments to promote EVs are reduced GST on the purchase of EVs, the National E-Mobility Programme (MoP), and the Zero-emission corridor, Agra [27].

There are private initiatives offered like deployment of e-cars, Mahindra Electric is offering rapid charging assistance to electric cars, and the launch of a pilot EV fleet [27].

Several bus pilots' schemes have also been started in many Indian cities [27].

There are well-known disputes cum challenges for EV sector in India like absence of robust EV policies at national and state levels, such uncertainty discourages the EV manufacture, and investing in the EV production. India is also technologically dependent especially in the fabrication of batteries—import of lithium-ion batteries, semiconductor, etc. Lack of clarity over charging infrastructure related to charging stations, grid stability are other issues that hamper the development of EV business [28].

3 Context of the Study

The back-and-forth of technology and mobility is expected to transform India's electric mobility models. The dynamic shift to electric mobility underpins the critical role of policy. In India, EV policy framework certifies that India's electric mobility

mission holds tempo with the worldwide scale. India's development options create possibility for emerging scopes for EV in certain segments. In that sense, national and state levels conducive EV policy support will promote a direction which begins with Indian particular attributes and programs for its auto-segment, constructing for worldwide significance, and applications [26].

4 Various Identified Components for Drafting EV Policies and Strategies

Facilitate awareness to consumer regarding EVs benefits The promotion of electric vehicle markets is essentially depending on the consumers' consciousness and awareness regarding the possible advantages of electric vehicles. Governments both at national and state levels, and city level, private auto-sectors dealing with EV manufacturing, regulatory authorities and private NGOs are involved in many endeavors to help surmount hurdles to consumer consciousness about electric vehicles. These exchange attempts include reports, workshops, technology demonstration projects, conducting campaigns using public platforms, etc. These actions are essential because many prospective consumers are not aware about the green technology behind EVs, benefits EV is offering and also about the other associated incentives [27].

Necessary steps to address the challenges for EV industries Government initiated technical skill enhancement schemes should be modernized to match the obligations of the sectors. Providing tax and other non-monetary incentives can address the prevailing uncertainty of demand and supply cycle. EVs are speedily flourishing dawn sector which can provide momentum to 'Aatma Nirbhar Bharat Abhiyaan' and 'Make in India'. Doing memorandum of understanding (MoU) with countries for filling the technological gaps. Development of coordination among national and state level EV related policies and strategies, this will assist in logical adoption of this sustainable mode of transport.

Policy framework where renewable energy and electric mobility work together Electrification of street transportation has become a primary inclination for maintainable electric mobility, and two of the greatest, noteworthy movements which are achieving drive in cities are power-driven automobiles and renewable energies. Therefore, it is vital to co-build on a framework of systems and approaches where energy and electric movement will work mutually and not perform as distinct units.

Facilitate employment growth in sector Electrification of vehicles can lead to job losses especially in oil industry but can at the same time drive job creation in a host industry. Electrified efficient vehicles require more automation and such design and production require more manpower. Moreover, EVs are much cheaper to operate as

compare to the traditional vehicle, and this would help get more disposable income to spend in other sector of economy.

Promotion of EV related technological advancements Funding from administration and changing mindsets toward EVs has caused in an intensified need for these automobiles at slashed costs. Also, matters such as enhanced vehicle variety and charging structure have fueled the requirement beyond. Here are some of the most encouraging scientific inventions and developments such as charging machinery, battery technology, and autonomous driving.

Clarity over charging infrastructure The energy infrastructure will be the front for the effective expansion of a viable electric mobility environment in India. However, the growth in electricity need from EVs presents a chance for the services with increased revenue, the additional investments required for strengthening or augmenting the present charging base to provide to the alternating demand refers to a financial challenge.

Other identified considerations while promoting electric mobility in policy Government at national and state levels should try to make efforts to utilize renewable resources to get clean electricity. Availability of public charging infrastructure requires availability of approachable and affordable locations. Government is taking several measures in linking the broad gap in EV investment costs.

5 Conclusion

India would considerably reduce its fossil fuel import bill by adopting electric vehicles at the earliest to get improved air quality index especially, in the cities with dense road transportation. On considering the efforts put by the government both at national and state levels in promoting the EV vehicles sales, it seems that in next few years, if the things go in the same pace, we can have clean and green air. This would, however, require more cohesive policies, and strategies which includes amicable solutions to all alarming and favorable circumstances, includes climate shift, innovations in renewable energy, rapid expansion, data recording and assessment, battery technology and infrastructure.

References

1. Climate Transparency homepage. https://www.climate-transparency.org/g20-climateperformance/g20report2019. Last accessed 8 Feb 2021
2. Priessner A, Sposato R, Hampl N (2018) Predictors of electric vehicle adoption: an analysis of potential electric vehicle drivers in Austria. Energy Policy 122:701–714

3. Luna TF, Uriona-Maldonado M, Silva ME, Vaz CR (2020) The influence of e-carsharing schemes on electric vehicle adoption and carbon emissions: an emerging economy study. Transp Res Part D 79:102226
4. Benvenutti LM, Ribeiro AB, Forcellini FA, Maldonado MU (2016) The effectiveness of tax incentive policies in the diffusion of electric and hybrid cars in Brazil. In: Proceedings of the XIV Congresso Latinoamericano de Dinamica de Sistemas, São Paulo, Brasil, 20–21 October 2016
5. Li Y (2016) Infrastructure to facilitate usage of electric vehicles and its impact. Transp Res Procedia 14:2537–2543
6. Christensen L, Klauenberg J, Kveiborg O, Rudolph C (2017) Suitability of commercial transport for a shift to electric mobility with Denmark and Germany as use cases. Res Transp Econ 64:48–60
7. O'Neill E, Moore D, Kelleher L, Brereton F (2019) Barriers to electric vehicle uptake in Ireland: perspectives of car-dealers and policymakers. Case Stud Transp Policy 7:118–127
8. Bubeck S, Tomaschek J, Fahl U (2016) Perspectives of electric mobility: total cost of ownership of electric vehicles in Germany. Transp Policy 50:63–77
9. Barisa A, Rosa M, Kisele A (2016) Introducing electric mobility in Latvian municipalities: results of a survey. Energy Procedia 95:50–57
10. Raslavi˘cius L, Azzopardi B, Keršys A, Starevi˘cius M, Bazaras Ž, Makaras R (2015) Electric vehicles challenges and opportunities: Lithuanian review. Renew Sustain Energy Rev 42:786–800
11. Mersky AC, Sprei F, Samaras C, Qian ZS (2016) Effectiveness of incentives on electric vehicle adoption in Norway. Transp Res Part D Transp Environ 46:56–68
12. Ingeborgrud L, Ryghaug M (2019) The role of practical, cognitive, and symbolic factors in the successful implementation of battery electric vehicles in Norway. Transp Res Part A 130:507–516
13. Camus C, Farias T, Esteves J (2011) Potential impacts assessment of plug-in electric vehicles on the Portuguese energy market. Energy Policy 39:5883–5897
14. Cansino JM, Yñiguez R (2018) Promoting electro mobility in Spain. Public measures and main data (2007–2012). Transp Res Part D 59:325–345
15. Ampudia-Renuncio M, Guirao B, Molina-Sanchez R (2018) The impact of free-floating carsharing on sustainable cities: analysis of first experiences in Madrid with the university campus. Sustain Cities Soc 43:462–475
16. Ampudia-Renuncio M, Guirao B, Molina-Sanchez R, Bragança L (2020) Electric free-floating Carsharing for sustainable cities: characterization of frequent trip profiles using acquired rental data. Sustainability 12:1248
17. Egnér F, Trosvik L (2018) Electric vehicle adoption in Sweden and the impact of local policy instruments. Energy Policy 121:584–596
18. Wee S, Coman M, La Croix S (2018) Do electric vehicle incentives matter? Evidence from the 50 U.S. States. Res Policy 47:1601–1610
19. Kester J, Noel L, de Rubens GZ, Sovacool BK (2018) Policy mechanisms to accelerate electric vehicle adoption: a qualitative review from the Nordic region. Renew Sustain Energy Rev 94:719–731
20. Luthra G (2017) Struggles faced in the research and development of electric vehicles in India: present. Scenario 5:34–37
21. Kurana A, Kumar RVV, Sidhpuria M (2019) A study of adoption of electric vehicles in India: the mediating role of attitude. Vision: J Bus Perspect. https://doi.org/10.1177/0972262919875548
22. Kumar R, Jha A, Damodaran A, Bangwal D, Dwivedi A (2020) Addressing the challenges to electric vehicle adoption via sharing economy: an Indian perspective. Manag Environ Qual 32(1):82–99. https://doi.org/10.1108/MEQ-03-2020-0058
23. Vidhi R, Shrivastava P (2018) A review of electric vehicle lifecycle emissions and policy recommendations to increase EV penetration in India. 11:483. https://doi.org/10.3390/en11030483

24. Sreeram K, Pretha PK, Poornachandran P (2019) Electric vehicle scenario in India: roadmap, challenges and opportunities. IEEE. 978-1-5386-8158
25. Mokaraiya KL, Shah VA, Lokhande MM (2015) Impact of penetration of electric vehicles on Indian power grid. EVS28 KINTEX, Korea, May 3–6
26. NITI Aayog, World Energy Council (2018) Zero Emission Vehicles (ZEVs): towards a policy framework
27. Ministry of Housing and Urban Affairs (MoHUA), Rocky Mountain Institute (RMI) (2019) Electric mobility: policy framework
28. Drishti homepage. https://www.drishtiias.com/to-the-points/paper3/electric-vehicles-evs. Last accessed 8 Feb 2021
29. International Council on Clean Transportation (ICCT) (2017) Zero emission buses are worth reaching for, but emission performance standards are the low-hanging fruit. Retrieved from https://www.theicct.org/blog/staff/zero-emission-buses-are-worth-reaching-for

New Flexible Printed Circuit Electronic Devices and Their IoTs Applications

Jai Prakash Mishra, Kulwant Singh, and Himanshu Chaudhary

Abstract The Internet of Things (IoT) as an emergent technology provides the ability to link objects every day in the real-life physical world to cyberspace, creating smart sensing, control, and administration network. Due to the flexibility, bendability, and deformability of the flexible electronics has found a unique position for smart things, and it becomes a core-technology that bridges real-world things to cloud. In this paper, we review progress and recent developments in flexible electronics devices, which cover equipment for printed thin-film transistors (TFT), memory and flexible sensors, etc., and integrated IoT circuits and systems such as fully metallic printed RFID tags and antennas and smart packages for food protection. There are also discussed about future challenges and issues for flexible electronics in the preparation of components, the manufacturing of instruments and system integration, etc.

Keywords Internet of Things · Flexible electronics · Printed electronics · RFID · System integration

1 Introduction

Flexible and stretchable devices are a fast-growing class of technology that revolutionize life in human beings by pioneering digital healthcare applications, personal health care, the interaction between humans and machines, and the Internet of Things, among many other things [1]. The "Internet of Things" (IoT) is a core idea, to adopt a series of technologies and scientific research (including smart sensors, low-power signal processing, smart sensing nodes and gateways, new generation broadband networks, cloud computing, big data information processing, information services, information security, etc.), making Internet technology extending to the identification and intelligent management of objects in the physical world [2].

The Internet of Things technology involves the perception layer, access layer, network layer, and data processing. The physical layer and the application layer,

J. P. Mishra · K. Singh · H. Chaudhary (✉)
Department of Electronics and Communication Engineering, Manipal University Jaipur, Jaipur, Rajasthan, India
e-mail: himanshu.chaudhary@jaipur.manipal.edu

S. Dwivedi et al. (eds.), *Flexible Electronics for Electric Vehicles*, Lecture Notes in Electrical Engineering 863, https://doi.org/10.1007/978-981-19-0588-9_13

etc., are the impact of the existing IT technology in the industrialization and comprehensive application and sublimation in daily life. Through the "Internet of Things" technology is able to achieve more thorough perception and measurement, more comprehensive interconnection, and interoperability in-depth information and intelligence in industry and daily life [3]. Applied to key electronic systems of the Internet of Things and seamless integration with "things," embedded chip, and large-area flexible components, including sensors, electronic tags, wireless smart terminals, and various access devices, etc., are in the field of "Internet of Things" important core technologies, but also insurmountable intellectual property barriers and international competition the commanding heights of the competition. Besides, as a standards based and interactive communication protocol for the establishment of a global dynamic network facility with self-configuration capabilities, the Internet of Things is the virtual and real "things" on the Internet have their own logos, and their physical properties and virtual personality, and use intelligent interfaces and information networks for the seamless link. Therefore, the identification and coding system of items, the configuration protocol of the network such standardization is the basis of IoT applications [4]. At the service and application level, things networking involves comprehensive integration across departments and fields. Therefore, at the technical level improves the IoT support platform based on cloud computing technology to build an open cooperative application platform can greatly accelerate the promotion and application of the Internet of Things. Item in the past, the Internet of Things was considered to be the next step among computers, the Internet, and mobile communication networks. The third wave of the post-world information industry is a new round of information technology revolution. Life, countries around the world will upgrade it to the strategic level of national development [5].

The flexible wearable electronic system is the basic element of the Internet of Things. The traditional semiconductor chips represented by materials are complicated in processing technology and equipment investment. Inherent limitations such as high input cost, large environmental pollution, and inability to bend the chip nature, limiting its large-scale application on the Internet of Things, because of this, based on flexible large-area electronics such as organic semiconductor materials and nanomaterials (flexible wide area electronics) technology has been developed rapidly in recent years. Compared with traditional electronic devices, flexible electronic technology has many advantages: (1) The device can be bent and stretched, which can give birth to many new application areas; (2) Large-scale printing technology can be used for processing on flexible and large-area substrates; now, the production cost is low; (3) The processing equipment is simple, and the initial investment cost low; (4) The processing process is a low-temperature process, the process is simple, and will not create pollution. Therefore, in a sense, due to its association with various "things" good integration and combination can form smart packages such as food new IoT products such as flexible and wearable healthcare terminals, flexible electronic technology has become the core of the real popularization and large-scale application of the Internet of Things heart technology [6]. The Internet of Things and smart technology application together with large-area display as printed electronics as the future direction of technology. However, the research of flexible printed electronic

technology and development involves the integration of multiple disciplines and multiple technologies. This paradigm, which is constantly changed from rigid electronics to flexible electronics, must be smaller, lighter, and greater, but also consists of biocompatible materials, especially in implantable uses. Applied to implantable sensors and energy harvesters, advanced 2D technologies, as well as biodegradable materials, fulfill these needs. The evolutionary advances in such flexible electronics have opened a new age and can be amplified in combination with the Internet of Things (IoT) [7–9].

This article is based on the author's own review work, based on the Internet of Things and intelligence flexible device technology starting with flexible materials and devices, focusing on discussion large-area flexible electronic devices, systems, integrated applications, etc.

2 Flexible Material Selection

According to the different functions of materials in flexible electronic devices, they can be divided into basic substrate materials, conductive materials, semiconductor materials, and dielectric materials, etc. Flexible material in addition to considering the optimization of device performance, the selection of materials must also fully consider the requirements of the printing process on material performance to achieve low manufacturing costs.

2.1 Base Materials

In order to meet the requirements of flexible electronic devices, the base material requires heavy and light, bendable, not fragile, impact resistance, corrosion resistance, high insulation, features such as easy portability, and low cost. In addition, you can also use roll-to-roll printing technology to greatly increase productivity and reduce production costs. Because of the above considerations, high molecular polymers are mostly used for flexible substrates. The previously available flexible substrate materials include polyimide, polyethylene naphtholate (PEN), polymer organic polymers such as ethylene phthalate (PET) [10], these organic materials can meet the requirements of insulation, flexibility, and strength well, and Fig. 1 is a flexible electronic device prepared on a polyimide plastic substrate.

2.2 Conductive Materials

The conductive materials are mainly used for metal electrodes and interconnection lines. For printing workers in terms of art, the conductive material is a mainly

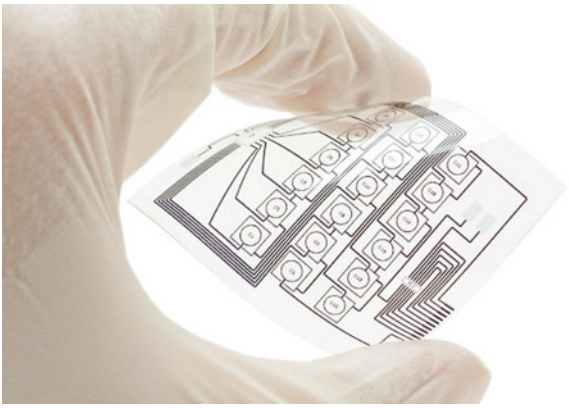

Fig. 1 Flexible electronic device prepared on polyimide plastic substrate

conductive ink, which is generally filled with conductor particles. It is composed of materials, solvents, and additives. At present, nano-level metals are mostly used for conductor particles, such as nanoparticles such as nanosilver, nanogold, and nano copper metal, in addition to the excellent electrical conductivity of nanoparticles, their small size effect can be greatly reduced their melting point. Below the glass transition temperature of the plastic substrate, guide the electro-ink can be sintered into a film or wire, which can be combined with other conductive materials in comparison, it shows unparalleled advantages, becoming one of the current conductive inks research focus [11].

2.3 Semiconductors Materials

Semiconductor materials are generally divided into p-type semiconductors and n-type semiconductors. For organic semiconductor materials, most of them are p-type, and currently the most widely used a wide range of organic semiconductor materials include conjugated conductive polymers, conjugated polymers, multi-π-electron aromatic organic molecules, etc. [12]. But organic semiconducting of the bulk material has low mobility, poor air stability, low life, and lack of weaknesses such as n-type conductive materials. In contrast, inorganic nano-semiconductors bulk materials, such as a metal oxide semiconductor ZnO/IGZO, carbon nanotubes, and graphene, which has greater performance, stability, and reliability advantages [13]. However, it is difficult to prepare solutions for inorganic semiconductor materials that easily form films and have problems with grain boundaries. A feasible solution is to adopt a chemical modification of organic semiconductor materials with inorganic nanomaterials to improve the performance and stability of organic semiconductor materials.

2.4 Medium Materials

In flexible electronic devices, dielectric materials are mainly used as insulating material against electrical conduction. So, the insulating material should have a large bandgap. But due to the poor flexibility and flexibility of inorganic dielectric materials, the dielectric materials in electronic devices are generally selected as organic materials, such as polyethylene alcohol (PVA), polyvinylpyrrolidone (PVP), and benzo-cyclobutene resin (BCB) [14]. These organic dielectric materials and semiconductor materials and the flexible substrate have good compatibility and is suitable for low-cost and low-temperature solution processing technology.

3 Flexible Electronics

3.1 Flexible Thin-Film Field-Effect Transistor

A field-effect transistor (FET) is the most widely used in modern electronics one of the devices in data storage, logic operations, signal amplification, and plane display, and other fields play an irreplaceable role. Different from conventional metals-oxide-semiconductor field-effect transistors (MOSFETs), flexible film field-effect transistors (TFT) are simple, low cost, and easy to prepare features such as bending have won widespread attention. It is like the chip itself in application fields that are not demanding, but it can be used flexibly in a large area, such as flat panel display driver, medical imaging, smart packaging, large-area sensors, and sensor arrays, as well as surface lighting present a broad application prospect. Since the 1980s, organic semiconductor materials have been used as the guide the TFT of the electric channel is very popular. These organic materials are lightweight, the film is thin, has good flexibility, and can be deposited on various flexible substrates. At the same time, they are very suitable for various liquid-phase processing technologies, such as new printing brush electronic technology, which can greatly reduce production costs. However, the purpose, the previously known organic materials have very low mobility (<1 cm^2/Vs), resulting in the device works slowly and is easily degraded in the air [14]. By modifying these organic materials has some extent, such as using doping with carbon nanotubes can significantly improve its electrical properties. Figure 2 shows the carbon nanotube composite thin-film transistor switching characteristic curve. As the concentration of carbon nanotubes increases, the organic composite film of the mobility can be increased from 10–4 cm^2/Vs to 10 cm^2/Vs, increasing it is about 4 orders of magnitude [15, 16], which is close to the current performance of polysilicon TFT. Besides, it was found that adding a small number of carbon nanotubes can increase the air stability of organic thin-film devices. After long air exposure, it is revealed that the performance of organic thin-film devices without doped carbon nanotubes degrades quickly, and the composite thin-film device doped with carbon nanotubes has not seen any performance change [17].

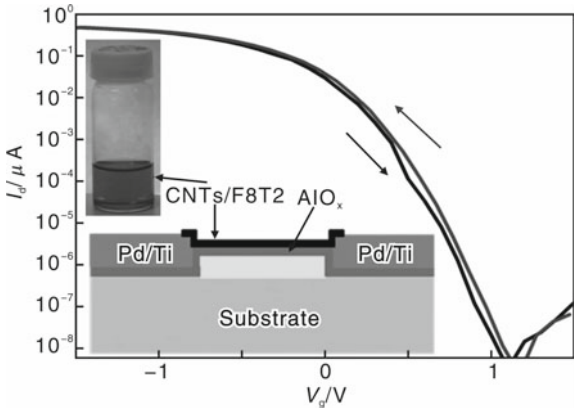

Fig. 2 Switching curve of CNT-modified polymer composite TFT. Inset: CNT-polymer composite ink and schematic structure of a back gate TFT

On this basis, the F8T2 composite film modified with carbon nanotubes field-effect transistors and prepares the most basic unit in logic circuits-reverse phase device. The maximum voltage gain of the inverter is about 4, in the channel of 20 μm the cut-off operating frequency under the length is 100 kHz. Theoretical calculations show that the device cut-off frequency still has a lot of room for improvement, but it can basically satisfy some requirements for low-frequency amplification applications. Besides, some basic logic operations have been prepared, i.e., calculating unit circuits, such as NAND gate and NOR gate circuit [16]. Due to organic, the conductive channel of the thin-film device is directly exposed to the air, so the water and oxygen molecules will react electrochemically with the organic film material, resulting in the film the threshold voltage in the device drifts, which affects the stability of the device. Therefore, a certain surface passivation protection must be performed on thin-film devices to isolate the influence of external environmental factors [18].

3.2 Flexible Thin-Film Memory

In addition to organic semiconductor materials that can be used in thin-film field-effect transistors, non-volatile memory devices based on organic materials have also received increasing attention. Depending on the theory, a single organic molecule can constitute a functional device, so this technology has the potential to achieve ultra-high density and ultra-large capacity storage. Organic polymerization of the thin-film memory is also suitable for the inkjet printing process to meet production requirements single, low-cost requirements. The advantages of flexible thin film memory include low cost, easy processing, variable & foldable structure, small size, quick response, low-power consumption and high storage density. Therefore, organic

non-volatile memory devices for information storage and logic circuits have more & more attention for rapid development.

Organic non-volatile memory device is also called organic bistable device (OBD), belongs to the resistance type memory (RRAM), it is shown as having two different conductivities under the same voltage states, namely the high and low conduction states, which are equivalent to the binary digits of the computer "1" and "0." These two conductivity states can be controlled by applying a certain electric field. The application changes to realize the "write" or "erase" of information. This kind of existence the reservoir has a simple structure, usually a layer of organic work is inserted between the upper and lower electrodes. The energy layer constitutes a simple sandwich structure, which greatly simplifies the fabrication process of the device art. In 2006, at the University of California at Los Angeles, the Yang research group incorporated metal nanoparticles into the organic layer and used the nanoparticle charge transfer effect (charge transfer) to realize the electrical resistance state transition [19]. Such devices can be used by spin coating and inkjet printing techniques. The technical film formation which has an important role in the application of future flexible smart devices application prospects.

So far, there have been many literature reports on different organic materials and organic semiconductor devices with different device structures for the memory effect of resistive transition characteristics [17]. At the same time, for organic electricity, various possible explanations for the bistable effect have also been proposed. In general, these possible mechanisms can be based on the difference in the resistance transition area of the device. The same is roughly divided into two categories: (1) The device resistance state transition occurs in the entire machine layer is a kind of overall transformation behavior; (2) The resistance state transformation of the device occurs in a local area of the device, which is a local microchannel conduction mechanism [20].

4 System and Integration

4.1 Chipless Fully Printed Radio Frequency Label Technology

After more than 60 years of development, radio frequency identification technology has greatly improved and changed in people's life and production methods. In its development process, electronic reduction of label production cost is one of the important factors for its widespread applications. The development of today's society requires cheaper electronic tags to achieve the low-end product automatic identification technology with the huge market potential to produce a real Internet of Things. However, the previously widely used silicon-based integration of the circuit

chip electronic label faces has limitation that it is difficult to continue to reduce the cost performance, which requires new production technology with low-cost manufacturing advantages appear.

In order to meet this demand, printing technology is introduced to produce ultra-low-cost electronic label of the book. Compared with the ordinary silicon process, the printing process does not need to use a mask, no contact manufacturing is required, and it is a full addition technology, so it can provide a more cost-effective production method [21]. At the same time, different chipless electronic label solutions began to appear. The traditional electronic tags are not the same as they use as a memory to store data, no chip power sub-tags mainly use in metal passive devices to achieve data storage and reading, such as using metal resonators, capacitors, or inductors pieces [22, 23]. Such electronic tags do not require more expensive integrated circuit cores film, but also suitable for large-scale full-printing process and reel production (reel-to-reel), so it has an unparalleled cost advantage. Among them paper-based fully printed chipless electronic tags are a hot topic of research. It is predicted that the cost of a fully printed chipless electronic label is expected to drop to several cents or less than one cent, which can be compared with the widely used cursor codes [24].

4.2 Thin-Film Sensor Applications

Sensors are an indispensable basic component of the Internet of Things [25], to interconnect items and obtain useful information. It must be the sensor senses and transmits status information of the surrounding environment or the addressed objects and the development and maturity of the Internet of Things technology also puts forward new requirements for sensors. Market demand for low cost, low power and printable flexible film sensors will increase sharply in the next 10 years.

4.2.1 Moisture Sensitive Film Materials

Humidity is closely related to human social activities, no matter in modern industrial production or daily life, but real-time humidity monitoring is often required. The traditional resistive humidity-sensitive materials are mainly oxide ceramics and polymers [26]. The Carbon nanotubes were discovered, due to their outstanding physical properties, such as large aspect ratio, high specific surface area, excellent thermal and electrical conductivity. It was found through experiments that after acidification processing, functionalized multi-walled carbon nanotube film to the environmental humidity shows significant sensitivity and fast response time [27].

4.2.2 Passive Wireless Sensing and Smart Packaging Applications

In order to realize the Internet of Things that can perceive anyone and things anytime, anywhere, flexible wearable wireless sensor technology has attracted much attention. In many application areas such as smart packaging for food and drug safety, a passive wireless sensor is more attractive. Passive sensors can externally get the energy to work, no need to equip and replace batteries, working longer life and lower cost. A commonly used flexible passive wireless sensor realization method of the device is to combine discrete sensing elements (such as resistive or capacitive type sensing element) and signal conditioning circuit, energy harvesting circuit and no line communication circuit is integrated on the flexible substrate. This solution can provide advanced wireless data link but requires higher design and manufacturing costs, energy supply, and its flexibility is also affected by the size and limitations of integration technology. Therefore, two kinds of integrated circuits without silicon are proposed [27–30], can be fully printed wireless sensor design: the first type is the resistive sensing element is used as the load resistance of the high-frequency antenna. By measuring, the energy of the backscattered signal of the antenna at a specific frequency is known to the physics under test amount of information. By integrating humidity-sensitive multi-wall carbon nanotube film resistors, a UHF passive humidity sensor that can work up to 2 GHz has been developed for the device [27].

The second kind of passive sensor design principle is to combine the frequency domain principle of backscattering is applied to the time domain. This sensor consists of a multi-segment flat surface type microwave transmission line and multiple resistance type sensor element strings with different functions jointly formed [31]. When the sensor receives the interrogation pulse signal through the antenna, this pulse will propagate on the transmission line and encounter various sensitive resistances component produces reflections, and by measuring the reflected pulses separated in the time domain impulse signal energy and apply specific algorithms to obtain multiple DUTs at the same time and manage the amount of information. These technologies have been successfully applied to food and medicine in the smart packaging [28–31].

5 Conclusion

The global flexible electronics and organic electronics industry are estimated to increase $73.43 billion by 2027, according to the world market research report. Flexible electronics continue to evolve every day, so the future of flexible electronics includes an infinity of new applications. The new research is driven by functional materials with incredible new methodologies of fabricating devices in the ruggedness, lightweight, low-cost production, and specific electronic and mechanical properties. The modular technology must, therefore, advance to increase the flexibility of the device, density, performance, and production. However, modular manufacturing

continues to evolve with the advancement of technology. As the core hardware technology that promotes the Internet of Things, flexible and wearable electronics in the field of sub-devices. The future of IoT will be powered mostly by versatile substrates with active components constructed on top of 2D materials typically based on silicone technologies. To develop flexible electronics integrated with Internet of Things (IoTs), we should concentrate on breakthrough key innovations, focus on developing independent potential for creativity and do a good job in application creation and standard formulation.

References

1. Luan H, Zhang Y (2021) Programmable stimulation and actuation in flexible and stretchable electronics. Adv Intell Syst. https://doi.org/10.1002/aisy.202000228
2. Zheng L, Zhang H, Han W, Zhou X (2011) Technologies, applications, and governance in the Internet of Things. Proc Internet Things-Global Technol Soc Trends 141–175
3. Sethi P, Sarangi SR (2017) Internet of Things: architectures, protocols, and applications. J Electr Comput Eng 2017:1–25. https://doi.org/10.1155/2017/9324035
4. Ray PP (2018) A survey on Internet of Things architectures. J King Saud Univ Comput Inf Sci 30:291–319. https://doi.org/10.1016/j.jksuci.2016.10.003
5. Botta A, De Donato W, Persico V, Pescapé A (2016) Integration of cloud computing and Internet of Things: a survey. Futur Gener Comput Syst 56:684–700. https://doi.org/10.1016/j.future.2015.09.021
6. Zhan Y, Mei Y, Zheng L (2014) Materials capability and device performance in flexible electronics for the Internet of Things. J Mater Chem C 2:1220–1232. https://doi.org/10.1039/c3tc31765j
7. Lacour SP, Courtine G, Guck J (2016) Materials and technologies for soft implantable neuroprostheses. Nat Rev Mater. https://doi.org/10.1038/natrevmats.2016.63
8. Choi S, Lee H, Ghaffari R et al (2016) Recent advances in flexible and stretchable bioelectronic devices integrated with nanomaterials. Adv Mater 28:4203–4218. https://doi.org/10.1002/adma.201504150
9. Yogeswaran N, Dang W, Navaraj WT et al (2015) New materials and advances in making electronic skin for interactive robots. Adv Robot 29:1359–1373. https://doi.org/10.1080/01691864.2015.1095653
10. MacDonald WA, Looney MK, MacKerron D et al (2007) Latest advances in substrates for flexible electronics. J Soc Inf Disp 15:1075. https://doi.org/10.1889/1.2825093
11. Cummins G, Desmulliez MPY (2012) Inkjet printing of conductive materials: a review. Circuit World 38:193–213. https://doi.org/10.1108/03056121211280413
12. Facchetti A (2011) π-Conjugated polymers for organic electronics and photovoltaic cell applications. Chem Mater 23:733–758. https://doi.org/10.1021/cm102419z
13. Sun JAR (2010) Semiconductor nanomaterials for flexible technologies
14. Ortiz RP, Facchetti A, Marks TJ (2010) High-k organic, inorganic, and hybrid dielectrics for low-voltage organic field-effect transistors. Chem Rev 110:205–239. https://doi.org/10.1021/cr9001275
15. Liu Z, Li H, Qiu Z et al (2012) SMALL-hysteresis thin-film transistors achieved by facile dip-coating of nanotube/polymer composite. Adv Mater 24:3633–3638. https://doi.org/10.1002/adma.201200906
16. Liu Z, Gao X, Zhu Z et al (2013) Solution-processed logic gates based on nanotube/polymer composite. IEEE Trans Electron Devices 60:2542–2547. https://doi.org/10.1109/TED.2013.2264969

17. Scott JC, Bozano LD (2007) Nonvolatile memory elements based on organic materials. Adv Mater 19:1452–1463. https://doi.org/10.1002/adma.200602564
18. Qu M, Li H, Liu R et al (2014) Interaction of bipolaron with the H2O/O2 redox couple causes current hysteresis in organic thin-film transistors. Nat Commun. https://doi.org/10.1038/ncomms4185
19. Yang BY, Ouyang J, Ma L et al (2006) Electrical switching and bistability in organic/polymeric thin films and memory devices. Adv Funct Mater. https://doi.org/10.1002/adfm.200500429
20. Tang W, Shi H, Xu G et al (2005) Memory effect and negative differential resistance by electrode-induced two-dimensional single-electron tunneling in molecular and organic electronic devices. Adv Mater 17:2307–2311. https://doi.org/10.1002/adma.200500232
21. Shao B, Chen Q, Amin Y et al (2010) An ultra-low-cost RFID tag with 1.67 Gbps data rate by ink-jet printing on paper substrate. In: 2010 IEEE Asian Solid-State Circuits Conf A-SSCC 2010, vol 1, pp 109–112. https://doi.org/10.1109/ASSCC.2010.5716569
22. Zheng L, Rodriguez S, Zhang L et al (2008) Design and implementation of a fully reconfigurable chipless RFID tag using inkjet printing technology. Proc IEEE Int Symp Circuits Syst. https://doi.org/10.1109/ISCAS.2008.4541720
23. Shao BC, Amin Q, Yasar Hållstedt J (2009) Process-dependence of inkjet printed folded dipole antenna for 2.45 GHZ RFID tags. In: 2009 3rd European conference on antennas and propagation, pp 1–6
24. Shao B, Amin Y, Chen Q et al (2013) Directly printed packaging-paper-based chipless RFID tag with coplanar LC resonator. IEEE Antennas Wirel Propag Lett 12:325–328. https://doi.org/10.1109/LAWP.2013.2247556
25. Kortuem G, Kawsar F, Sundramoorthy V, Fitton D (2010) Smart objects as building blocks for the internet of things. IEEE Internet Comput 14:44–51. https://doi.org/10.1109/MIC.2009.143
26. Chen Z, Lu C (2005) Humidity sensors: a review of materials and mechanisms. Sens Lett 3:274–295. https://doi.org/10.1166/sl.2005.045
27. Feng Y, Cabezas AL, Chen Q et al (2012) Flexible UHF resistive humidity sensors based on carbon nanotubes. IEEE Sens J 12:2844–2850. https://doi.org/10.1109/JSEN.2012.2202390
28. Xie L, Feng Y, Mantysalo M et al (2013) Integration of f-MWCNT sensor and printed circuits on paper substrate. IEEE Sens J 13:3948–3956. https://doi.org/10.1109/JSEN.2013.2260534
29. Mäntysalo M, Xie L, Jonsson F et al (2012) System integration of smart packages using printed electronics, pp 997–1002
30. Feng Y, Xie L, Mantysalo M et al (2013) Electrical and humidity-sensing characterization of inkjet-printed multi-walled carbon nanotubes for smart packaging. Proc IEEE Sensors. https://doi.org/10.1109/ICSENS.2013.6688306
31. Feng Y, Chen Q, Zheng LR (2011) Design of a printable multi-functional sensor for remote monitoring. Proc IEEE Sensors. https://doi.org/10.1109/ICSENS.2011.6127184

Performance Analysis and Simulation of MEMS Capacitive Pressure Sensor

S. Ananthi, Monica Lamba, Himanshu Chaudhary, and Kulwant Singh

Abstract MEMS capacitive pressure sensor has a wide application due to its less power dependency and less sensitive to temperature changes. It also has good over-pressure tolerance. This paper focuses on sensitivity analysis of capacitive pressure sensor by plotting graphs between diaphragm displacement versus applied pressure, change in capacitance versus applied pressure at different temperatures for different materials. Sensor working principle is based on electro-mechanics interface. In this paper, capacitive pressure sensor with different structure is designed, simulated and the results are analyzed using COMSOL Multiphysics 5.5.

Keywords MEMS capacitive pressure sensor · COMSOL multiphysics · Structure · And sensitivity

1 Introduction

1.1 MEMS Pressure Sensors

Sensors are used in modern devices for monitoring various physical parameters like temperature, pressure, humidity, etc., based on MEMS technology. Pressure sensors have wide range of applications in almost all possible areas like automobile industries, aerospace, biomedical, defense applications, etc. Pressure sensors are used to measure the applied pressure by a liquid or gas, and then the measured quantity is expressed as an electrical signal by a read circuit. Pressure sensors are based on piezoelectric, piezo-resistive, or capacitive technology. These types have their own advantages and disadvantages [1, 2]. Selection is based on application requirement like pressure range, accuracy, power consumption, and environmental condition like

S. Ananthi (✉) · M. Lamba · H. Chaudhary
Department of Electronics and Communication Engineering, MUJ, Jaipur, India
e-mail: ananthi232@gmail.com

K. Singh
FlexMEMS Research Centre, Department of Electronics and Communication Engineering, MUJ, Jaipur, India

S. Dwivedi et al. (eds.), *Flexible Electronics for Electric Vehicles*, Lecture Notes in Electrical Engineering 863, https://doi.org/10.1007/978-981-19-0588-9_14

temperature, etc. The piezo-resistive pressure sensors are the simplest to fabricate and provide electrical output directly [3]. In MEMS piezo-resistive pressure sensors, four resistors placed in Wheatstone bridge configuration are strained in proportion to the applied pressure [4, 5]. Change in their resistance value is a measure of applied pressure.

Capacitive pressure sensors have the capability to meet up the rising demand of specialized pressure sensors because of its high sensitivity, fast response time, less temperature dependency [6, 7], and low power requirement. They have a simple design and analysis due to the simple governing equation [8].

In MEMS capacitive pressure sensors [9], two parallel and electrically isolated conducting plates by a dielectric medium like vacuum are fabricated on a silicon substrate. The bottom plate is fixed and the top membrane bends according to the applied pressure, thereby creating a capacitance change. This change is then converted into an electrical signal as a measure of applied pressure.

1.2 Comparison of Capacitive with Piezo-Resistive MEMS Pressure Sensor

Capacitive sensors have high accuracy, low power consumption [8, 9], and long term stability. The main advantage of capacitive sensor is the over pressure tolerance. Touch mode sensors have higher burst pressures [10] commonly used in biomedical applications. It can withstand up to hundred times the rated pressure without breaking and with no plastic deformation. Sensor performance is unaffected after the release of the over pressure. Capacitive pressure sensors are more suitable for medical applications [11, 12] (where high accuracy and long term stability are required) and for industry, where the occurrence of over pressure [13] is common and sensor repair is not an option. MEMS capacitive technology can be applied in demanding environments such as absolute, gauge, and relative pressure measurement [14]. But it needs more complex signal conditioning circuit and production cost is high compared with piezo-resistive sensors. The readout circuit for the capacitive sensor can be monolithically integrated [15], based on a switched mode method using reference and sensing capacitors.

2 Mathematical Modeling of Capacitive Pressure Sensors

The equation for the capacitance of a parallel plate capacitor is given by the relation indicated as

$$c = \frac{\varepsilon_0 \varepsilon_r A}{d} \tag{1}$$

Here, C denotes capacitance, expressed in terms of A = area between the two plates, ε_r = dielectric constant, ε_0 = permittivity of free space, and d = distance between the two plates. The generalized equation for determining the maximum deflection of a square membrane whose thickness is uniform and all its edges are fixed, is given by [16] when external pressure is applied

$$w_{\max} = \frac{0.0138L^4P}{Eh^3} \tag{2}$$

In terms of poison's ratio, central maximum deflection of the square shaped diaphragm of MEMS sensor under the applied pressure is given by [17]

$$w_{\max} = \frac{0.01512(1-\mu^2)L^4P}{Eh^3} \tag{3}$$

Here, P = applied pressure, L = length of diaphragm, h = thickness of diaphragm, E = Young's Modulus of Elasticity, and μ = Poisson's ratio.

Now, since the spacing between the two plates of the capacitor changes due to the applied pressure, the change in capacitance is given by

$$\Delta C = \iint \frac{\varepsilon_0 \varepsilon_r}{d - w(x, y)} dx dy \tag{4}$$

3 Modeling MEMS Capacitive Sensor in COMSOL Multiphysics

The COMSOL Multiphysics software [18, 19] provides incorporated environment in which we can build the sensor model. The pressure sensor is part of the silicon die. One fourth of the model is considered due to the geometrical symmetry of the sensor as shown in Fig. 1. This will reduce the computational time and the memory required for computation. Using an in-build model, build-in physics structural mechanics with electro-mechanics interface and stationary study is performed. Pressure ranging from 0 to 25 kPa is applied, at $T_0 = 20$ °C and the sensor is considered to have a die bonding temperature of 70 °C.

The boundary conditions are applied to the right side (zx plane at $y = 0$) and left side (zy plane at $x = 0$) as indicated in Fig. 1. Simulation is carried out for three different materials defined for diaphragm (silicon, graphene, and SiC). Thickness of the diaphragm is 0.01 mm and has a square shape with length and breadth as 0.5 mm. The distance between the electrodes (the cavity blue in color) is 0.003 mm, as shown in Fig. 2. The thickness of lower electrode and substrate are 0.39 mm and 0.7 mm, respectively, relatively very low thickness of diaphragm and cavity are seen as a bold horizontal line as in Fig. 3. The cavity is sealed under high vacuum, and

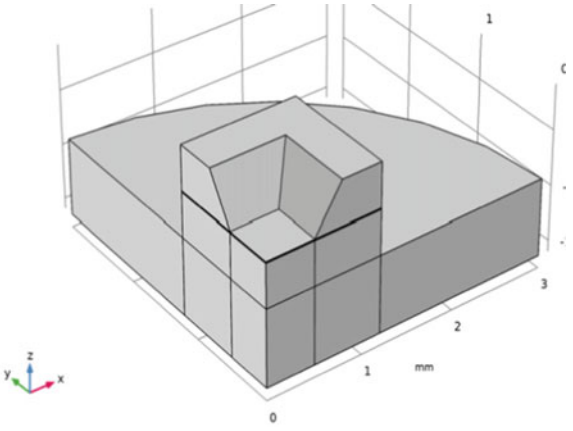

Fig. 1 Geometrical model of MEMS capacitive pressure sensor

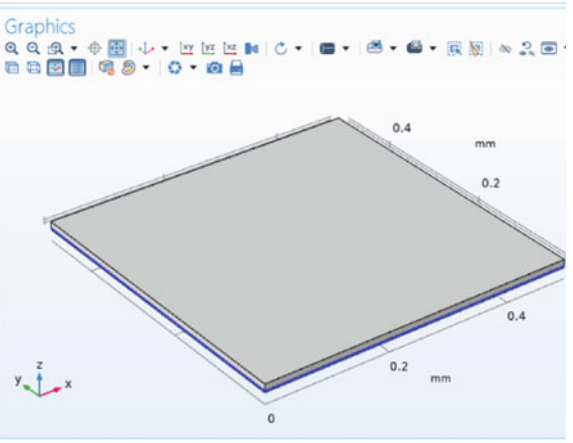

Fig. 2 Cavity between the two electrodes

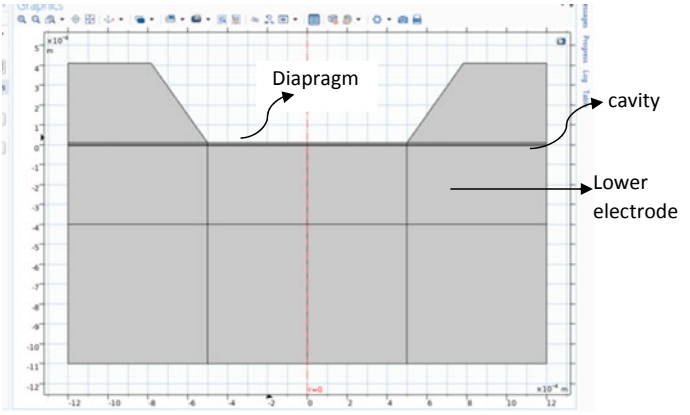

Fig. 3 Cross sectional view of MEMS capacitive pressure sensor

Table1 Material property of different materials used for diaphragm

Property	Silicon	Graphene	SiC
Young's modulus (TPa)	0.170	1	0.450
Poisson's ratio	0.06	0.17	0.22
Density (kg/cubic meter)	2330	2000	3200
Coefficient of thermal expansion (per Kelvin)	$2.6 * 10^{-6}$	$8 * 10^{-6}$	$3.8 * 10^{-6}$

the sides are insulated so that there is no connection between upper diaphragm and lower electrode. The boundary load is applied on upper boundary of the diaphragm. The diaphragm is allowed to move only in the z-direction to get the correct values of the capacitance change. The upper diaphragm (domain) is seized at a fixed potential of 1 V with respect to the ground at 0 V. The ground is applied to boundary of lower electrode.

In the physics part, solid mechanics and electrostatics are added. This automatically adds the electro-mechanical forces interface. To do the finite element analysis, over the whole capacitor MEMS structure moving mesh is applied. When pressure is applied, the center of the diaphragm is more compressed, and as a result, the applied mesh over the center of the diaphragm is also compressed. Hence, moving mesh is the appropriate to apply, instead of applying physics controlled mesh.

The material properties of different materials under consideration for simulation are as shown in Table.1.

Stationary study is computed with parametric sweep of different pressures ranging from 0 to 25 kPa and the t the corresponding displacement of diaphragm, capacitance is analyzed. An applied pressure originates deformation in diaphragm owing to that potential is not uniformly distributed in plane. Thus, plot for deformation of diaphragm versus pressure and plot of capacitance versus pressure are simulated separately. The analysis first carried out without any added stress due to sensor packaging stress and at a temperature of 20 °C. Then, it is analyzed with packaging stress and the operating temperature is varied from 290 to 300 K to find out the corresponding change in capacitance of the sensor.

4 Simulation Results

4.1 Diaphragm Displacement in Response to an Applied Pressure for Different Materials

Using switch mode simulation displacement of diaphragm as a function of pressure is simulated. Center of the diaphragm is more deflected, as shown in Fig. 4.

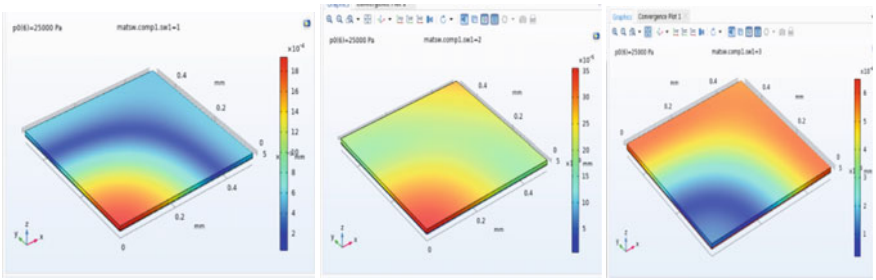

Silicon Graphene SiC

Fig. 4 Displacement of the diaphragm for an applied pressure of 25 kPa

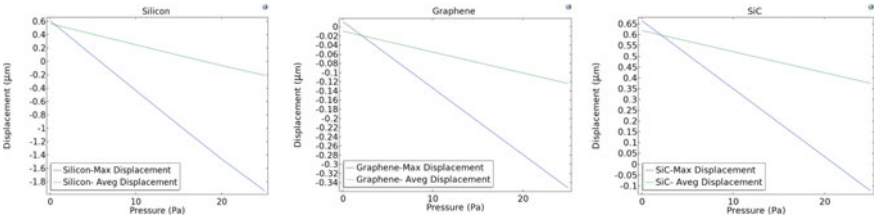

Fig. 5 Displacement of the diaphragm for an applied pressure range of 0–25 kPa

4.2 Displacement Versus Various Pressure for Square Diaphragm

The applied pressure is varied between 0 and 25 kPa. Deformation of diaphragm versus applied pressure is plotted as shown in Fig. 5.

4.3 Capacitance Versus Pressure for Square Diaphragm

Pressure range of 0–25 kPa is applied for which Si material shows a capacitance change from 0.75 to 1.2 pF, graphene from 0.74 to 0.77 pF, and in the case of SiC, it is 0.74–1.06 pF. Graphene material has more linear curve as compared with Si and SiC. Graphs are plotted as shown in Fig. 6.

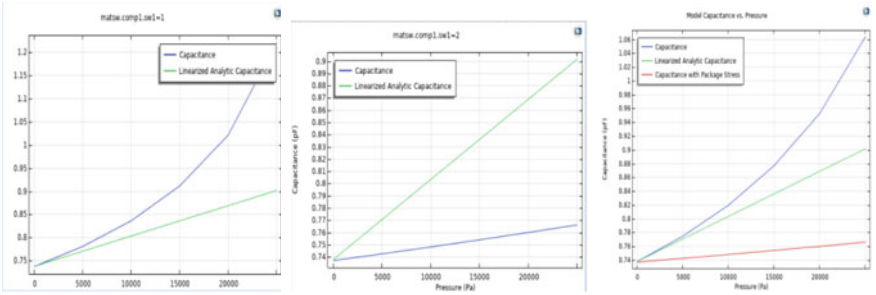

Silicon Graphene SiC

Fig. 6 Capacitance in pF versus applied pressure in P_a

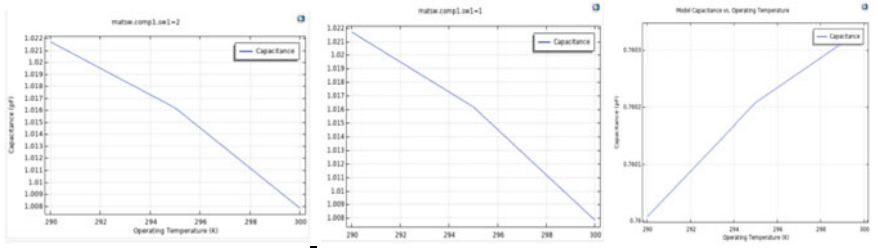

Silicon Graphene SiC

Fig. 7 Variation in capacitance with variation in operating temperature

4.4 Capacitance Versus Operating Temperature

To observe the effects of packaging stress on performance of device, thermal expansion is added in the model. The effect of thermal expansion is observed on entire structure as drawn in Fig. 7. The temperature is varied from 290 to 300 K.

4.5 Displacement of Structure with Packaging Stress

The designed structure is assumed to be operating at a temperature of 20 °C. And its bonding temperature is 70 °C. The displacement of the structure at operating temperature of 20 °C with a load of 25 kPa is simulated and plotted as shown in Fig. 8. There is an interaction between the thermal stress and stress due to applied load.

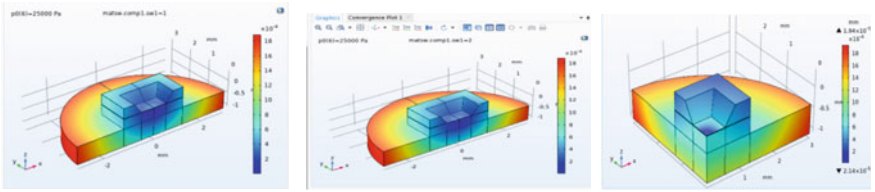

Silicon Graphene SiC

Fig. 8 Displacement of structure with packaging stress

Table 2 Simulation analysis

Property (for one quadrant of sensor)	Silicon	Graphene	SiC
Sensitivity (pF/Pa)	$18 * 10^{-6}$	$1.2 * 10^{-6}$	$12.8 * 10^{-6}$
Pressure sensitivity at 25 kPa	1.2 pF	0.77 pF	0.81 pF
Maximum displacement of diaphragm at 25 kPa	−2 μm	−0.35 μm	−0.12 μm
Change in capacitance due to change in operating temperature (290–300 K)	−0.014 pF	−0.014 pF	0.0003 pF

5 Simulation Analysis

The simulated results are compared, shown in Table 2. Silicon has the maximum sensitivity for the pressure range 0–25 kPa, and diaphragm thickness of 0.01 mm. Sensitivity of capacitor for a change in temperature, over a range of 290–300 K is not very significant for the given pressure range proving capacitive MEMS sensor is less sensitive to temperature changes. Negligible changes are observed in the case of SiC which is widely used in high temperature application [20].

6 Conclusion

With the help of COMSOL Multiphysics 5.5 simulation tool, analysis and simulation of capacitive MEMS pressure sensor are carried out. The capacitor model and the physics acting upon it is studied through the simulation. Mathematical modeling is done, and the analytical value of the capacitor is compared with the simulated value by COMSOL. Geometrical shapes and diaphragm material can be changed to optimize the sensitivity and linearity of the sensor depending upon the application requirement such as pressure range operating condition, etc. Since capacitive pressure sensor are capable of measuring absolute pressure (by comparing unknown low pressure with vacuum), gauge pressure (pressure higher than atmosphering pressure), and differential pressure they find application in medical and industrial field.

References

1. Balavalad K, Sheeparamatti B (2015) A critical review of mems capacitive pressure sensors. Sens Transducers 187:120–128
2. Eswaran P, Malarvizhi S (2013) Mems capacitive pressure sensors: a review on recent development and prospective
3. Bhat KN (2007) Silicon micromachined pressure sensor: reviews. J IISc 87:1. Jan–Mar 2007. journal.library.iisc.ernet.in
4. Akhtar J, Dixit BB, Pant BD, Deshwal VP (2003) Polysilicon piezoresistive pressuresensors based on MEMS technology. IETE J Res 49:365–377
5. Singh K, Joyce R, Varghese S, Akhtar J (2015) Fabrication of electron beam physical vapor deposited polysilicon piezoresistive MEMS pressure sensor. Sens and Actuat A: Phys 223:151–158
6. Samyuktha N, Maneesha P, Sreelakshmi B, Pattnaik P, Narayan K (2015) Application of mems based capacitive sensor for continuous monitoring of glucose. In: TENCON 2015–2015 IEEE Region 10 Conference, pp 1–4. IEEE
7. Bhol K (2017) Highly sensitive mems based capacitive pressure sensor design using comsol multiphysics its application in lubricating system. Eng Appl Sci 2:66. https://doi.org/10.11648/j.eas.20170204.12
8. Puers R (1993) Capacitive sensors: when and how to use them. Sens Actuat A 37–38:93–105
9. Hezarjaribi Y, Hamidon MN, Bahadorimehr AR, Keshmiri SH (2008) Capacitive pressure sensor technology and applications. In: ICSE 2008 Proceedings
10. De Hennis A, Chae J (2008) 2.04—pressure sensors. In: Gianchandani YB, Tabata O, Zappe H (2008) Comprehensive microsystems. Elsevier, pp 101–133
11. Lakhdari A, Mekkakia Maaza N, Maamar A, Boughenna A, Kichene M (2014) Modeling of silicon mems capacitive pressure sensor for biomedical applications. https://doi.org/10.1109/IDT.2014.7038625
12. Mishra RB, Kumar SS, Mukhiya R (2018) Analytical modelling and femsimulation of capacitive pressure sensor for intraocular pressure sensing. In: IOP conference series: materials science and engineering, vol 404, pp 012026. IOP Publishing
13. Sharma A, Singh J (2013) Design and analysis of high performance MEMS capacitive pressure sensor for TPMS. In: International conference on control, automation, robotics and embedded system
14. De Hennis A, Chae J, Baroutaji A (2016) Pressure sensors, reference module in materials science and materials engineering, Elsevier
15. Jang M, Yun KS (2017) MEMS capacitive pressure sensor monolithically integrated with CMOS readout circuit by using post CMOS processes. Micro and Nano Syst Lett 5:4
16. Hsu TR (2008) MEMS and micro systems: design, manufacture and nano scale engineering. Wiley, Hoboken
17. Anadkat N, Rangachar D (2015) Simulation based analysis of capacitive pressure sensor with comsol multiphysics. Int J Eng Res V4:4. https://doi.org/10.17577/IJERTV4IS041064
18. https://www.comsol.co.in/model/capacitive-pressure-sensor-476
19. Hatti G, Veerabhadraiah A et al (2016) Modelling simulation of capacitive pressure sensor using comsol multiphysics. https://doi.org/10.15680/IJIRSET.2016.0505284
20. Marsi N, Majlis B, Hamzah A, Mohd-Yasin F (2014) The mechanical and electrical effects of mems capacitive pressure sensor based 3c-sic for extreme temperature. J Eng 5:1–8. https://doi.org/10.1155/2014/715167

Antenna Performing Frequency Shift Operation for WiMAX Applications

Ishita Agarwal, Rashmi A. Pandhare, and Dinesh Yadav

Abstract This paper represents the transformation of frequency of the microstrip patch antenna from 5.2 to 3.5 GHz for use in WiMAX applications. For a frequency shift, a large varying change in dimensions is required to make it reach to a particular resonant frequency. It has been shown that an increase in the dimensions of the substrate, patch and ground as well as a decrease in the dimensions of feed line and a decrease in the gap between the patch and feed line causes a prefect jump in frequency from 5.2 to 3.5 GHz. In addition to varying the dimensions, a slot is added at the rear side of the antenna in the ground which helps to cancel another band arising at 7 GHz. This helps for a single resonant frequency at 3.5 GHz to exist instead of arising of the dual band feature.

Keywords Frequency shift · Microstrip · WiMAX

1 Introduction

Communication has been an important necessity to mankind since its development. The trends in the field of communication have changed over time, and this has led to the development of more advanced technology, i.e. wireless communication [1]. The frequencies in the ultra-wide band are suitable for use in wireless applications. Researchers are putting in a lot of hard work to construct new designs of antenna for their analyzation in the rising trends of wireless communication [2–4]. Extremely large data rates have become an important requirement. These high data rates are a necessity for transfer of large amount of information over long distances, and this is only possible if large data rates are an availability for the transmission. The application that implements this feature of high data rates is the WiMAX technology.

I. Agarwal (✉) · D. Yadav
Manipal University Jaipur, Jaipur, India
e-mail: ishitalko21@gmail.com

R. A. Pandhare
Indian Institute of Information Technology, Nagpur, India

S. Dwivedi et al. (eds.), *Flexible Electronics for Electric Vehicles*, Lecture Notes in Electrical Engineering 863, https://doi.org/10.1007/978-981-19-0588-9_15

WiMAX (also known as worldwide interoperability for microwave access) is a well-advanced technology that is used with the feature of enlarged data rates for large distance communications [5–7]. In this proposed antenna structure, a conversion plays a very important role for frequency shift operation so that the antenna can be used in WiMAX applications. Firstly, the antenna that is made to operate on a 5.2 GHz frequency is transformed into a new antenna structure using the same design to implement a frequency shift from 5.2 to 3.5 GHz [8, 9]. This frequency of the new antenna design, i.e. 3.5 GHz is an ideal frequency to work in WiMAX applications. The variation of the dimensions of the antenna becomes a necessity to make it shift in frequency operation from 5.2 to 3.5 GHz. Another feature taken into account is that a rectangular slot is constructed in the ground of the antenna which provides the feature of cancellation of a band and makes the antenna to operate on a particular resonant frequency of 3.5 GHz so that the antenna can successfully carry out the use of WiMAX applications.

2 Design Analysis of the Proposed Antenna Structure

The construction is based on the selection of substrate material as well as the substrate properties such as its relative permittivity [10]. The substrate material chosen for first constructing the antenna working at 5.2 GHz resonant frequency is the Rogers RT5880 substrate considering its standard thickness of 0.762 mm. The width and length of the substrate taken are 29 mm and 31.51 mm, respectively. The material copper (annealed) is used to construct the feed line which contains 2.45 mm width and 16.80 mm length as shown in Fig. 1. The patch constructed has dimensions with 24 mm width and 19 mm length which is separated from the feed line by a gap.

The back side of the design has a ground made of copper (annealed) with a width and length of 29 mm as shown in Fig. 2.

To convert this antenna functioning at 5.2 GHz into another antenna working at 3.5 GHz resonant frequency, there is a certain amount of change in the dimensions. The material of substrate remains the same, i.e. Rogers RT5880, but its dimensions change. The new dimensions of the substrate change to a width of 40.76 mm and a length resulting into 34 mm as shown in Fig. 3. There has to be an increase in the dimensioning of the patch changing its width to 26 mm and length to 28.50 mm, respectively, as shown in Fig. 3. The gap between the patch and the feed line reduces to 0.4 from 0.5 mm.

The back part of the structure results into an increase in the dimensions of the ground with its width resulting into 34 mm and its length resulting into 32.10 mm as shown in Fig. 4.

The difference also arises for the ground of structure functioning at 3.5 GHz as a slot also needs to be constructed which helps in the cancellation of a band of frequency 7 GHz which is not required for WiMAX applications. In comparison with the antenna operating at 5.2 GHz, it does not require slot to be removed from the ground structure. Antenna dimensions are shown in Table 1.

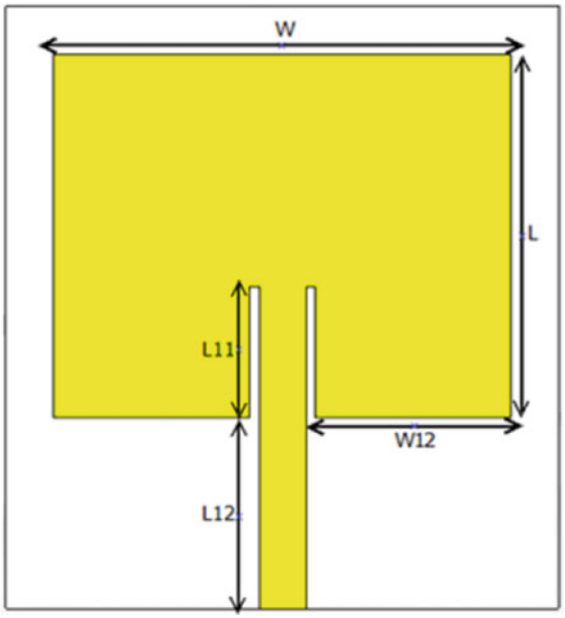

Fig. 1 Front part of structure functioning at 5.2 GHz

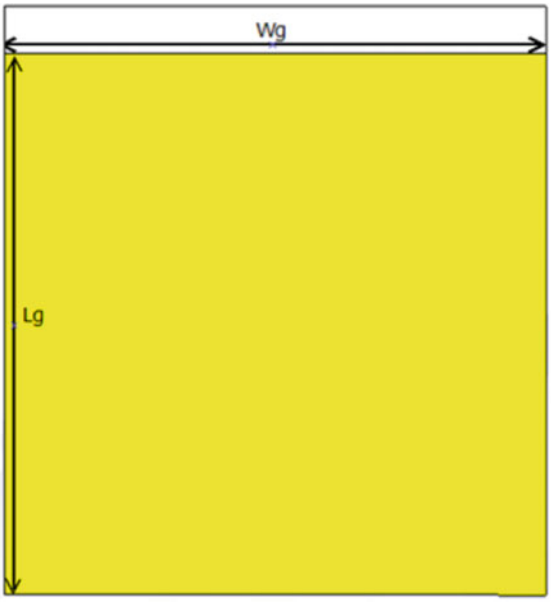

Fig. 2 Back part of structure operating at 5.2 GHz

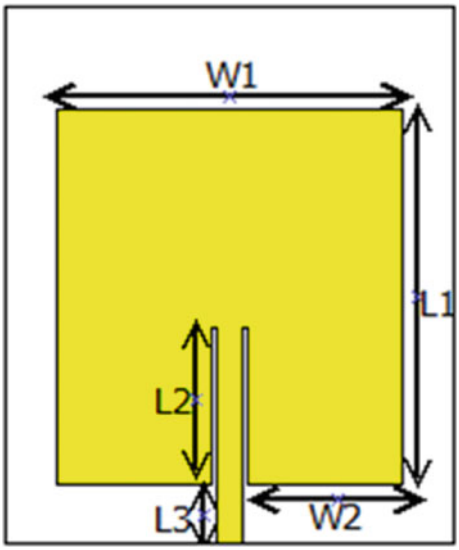

Fig. 3 Front part of structure functioning at 3.5 GHz

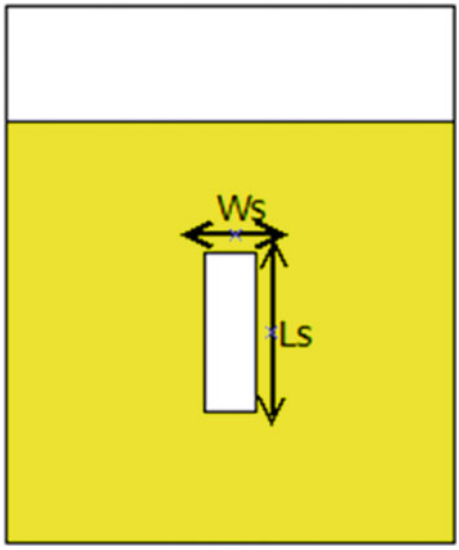

Fig. 4 Back part of structure functioning at 3.5 GHz

3 Result Discussions

The simulation of results using CST software shows that the antenna before transformation is working at 5.2 GHz resonant frequency with a dip of −25.127 dB. The bandwidth that this antenna covers is from 5.1827 to 5.2559 GHz. After the transformation stage, the resonant frequency shifts to 3.5 GHz with a dip of −24.45 dB.

Table 1 Proposed Antenna dimensions in mm

Width	Value (mm)	Length	Value (mm)
W	24	L	19
W12	10.28	L11	6.8
Wg	29	L12	10
W1	26	Lg	29
W2	11.70	L1	28.5
W3	4	L2	12.01
		L3	4.49
		Ls	12

The bandwidth covered by this antenna begins from 3.4927 GHz and reaches to 3.5193 GHz. In the 5.2 GHz antenna, the back side, i.e. the suitable dimensioning of the ground helped to make the S-parameters dip reach to −25.127 dB. In the 3.5 GHz transformation, a slot is added as an extra feature (Fig. 5).

The slot cut at the back of the antenna cancels the extra band occurring at 7 GHz. This extra band has to be suppressed because the frequency shift has to be shown only from 5.2 to 3.5 GHz for WiMAX applications. If this antenna contains dual band, then it cannot be used for WiMAX applications. It has to operate at single functioning frequency of 3.5 GHz.

The gain and directivity presented by the structure functioning at 5.2 GHz are 6.342 and 7.318 dBi. As the shift of frequency happens to a lower frequency, there is a large amount of change in gain and the gain becomes quite low, but the special aspect covered in this transform that the gain does not decrease by a large amount. The gain only decreases by only a small amount. The gain covered at the 3.5 GHz resonant frequency is 5.044 dBi, and the directivity amounts to 6.355 dBi (Fig. 6).

The magnitude of the main lobe represented by the structure functioning at 5.2 GHz resonant frequency is 7.22 dBi in the E-plane as well as 7.33 dBi in the H-plane. The difference lies in the magnitude of the main lobe with the antenna operating at the 3.5 GHz resonant frequency which is of value 6.04 dBi in the E-plane and 6.36 dBi in the H-plane (Fig. 7).

The antenna efficiencies for their working at 5.2 GHz implies a radiation efficiency of 80.2% and a total efficiency of 79.99%. After alteration of the dimensions of the antenna including the patch, ground, feed, the gap between the feed line and the patch as well as inclusion of the slot in the ground converts the radiation efficiency of the antenna from 80.2 to 77% with the antenna made to operate at resonant frequency 3.5 GHz.

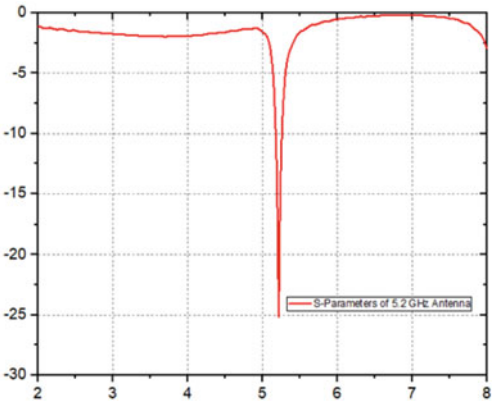

(a) S-Parameters of Structure functioning at 5.2 GHz

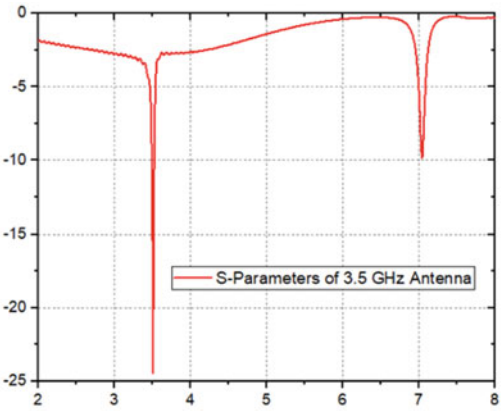

(b) S-Parameters of Structure functioning at 3.5 GHz

Fig. 5 S-parameter representations of the proposed antenna

4 Conclusion

The making of shift in frequencies is a very calculative procedure as many simulations have to be made to see how much increase or decrease in every dimension of the antenna has to be made to reach to a particular effective resonant frequency so that the antenna can work efficiently for a particular application. In this antenna, the alteration of a simple microstrip patch antenna structure functioning at 5.2 GHz resonant frequency is made to make the use of antenna possible in WiMAX applications. This transformation is achieved by varying the dimensions of the antenna components as seen through various simulations. The including of slot at the back side of the antenna in the ground adds another feature that shows that different bands occurring can be supressed so that the antenna can be used for only a particular application. In the proposed antenna, the 7 GHz frequency band is supressed by this slot so that the antenna can completely work for only WiMAX applications.

Fig. 6 Gain representations of the proposed antenna

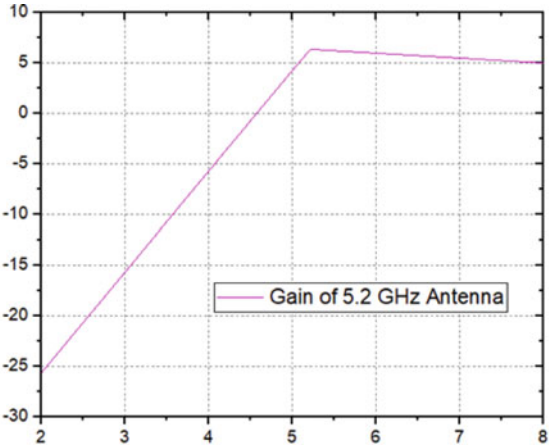

(a) Gain Representation of Antenna operating at 5.2 GHz

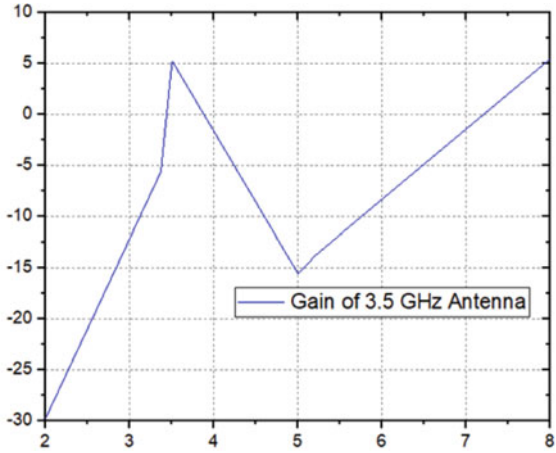

(b) Gain Representation of Antenna operating at 3.5 GHz

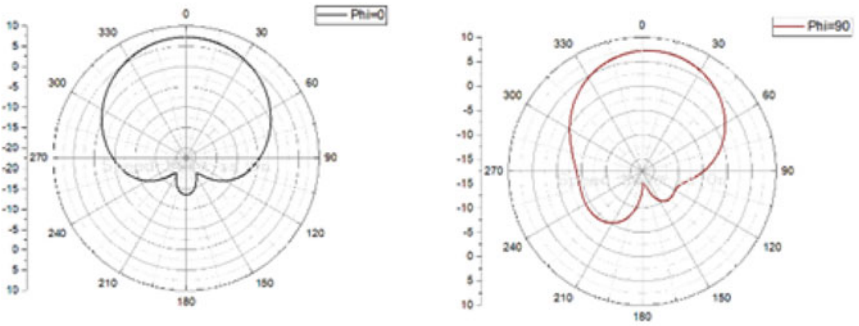

(a) Radiation Patterns of Structure functioning at 5.2 GHz

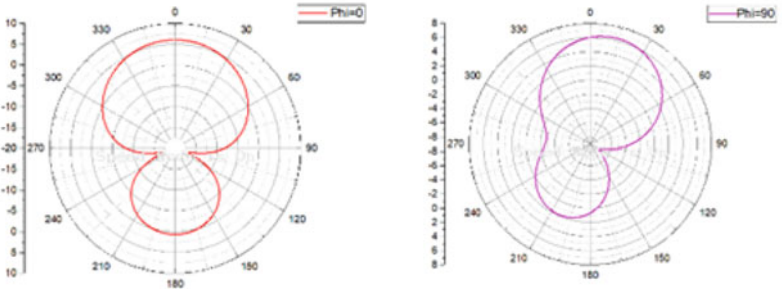

(b) Radiation Patterns of Structure functioning at 3.5 GHz

Fig. 7 Radiation pattern representations of the proposed antenna

References

1. Hazra R, Ghosh CK Frequency shifting to lower frequency side of a micro strip patch antenna. Int J Comput Commun Syst Eng (IJCCSE)
2. Liu Y, Si L, Wei M et al (2012) Some recent developments of microstrip antenna. Int J Antennas Propag 2012 p 10 Article ID 428284
3. Mobashsher AT, Abbosh A (2015) Utilizing symmetry of planar ultra-wideband antennas for size reduction and enhanced performance. 2nd edn. IEEE Antennas Propag Magazine 57(2):153–166
4. Cicchetti R, Faraone A, Caratelli D, Simeoni M (2015) Wideband, multiband, tunable, and smart antenna systems for mobile and UWB wireless applications 2014. Int J Antennas Propag 2015, 3 Article ID 536031
5. Rajpoot AS, Gadani N, Patel A, Pansinia P (2016) A review paper on WiMAX technology. Int J Adv Res Comput Eng Technol (IJARCET) 5(6)
6. Yeo J, Lee JI (2019,) Slot-loaded microstrip patch sensor antenna for high-sensitivity permittivity characterization. Electron Lics 8:502. https://doi.org/10.3390/electronics8050502
7. Maci S, Gentili G (1997) Dual-frequency patch antennas. IEEE Antennas Propag Mag 39:13–20
8. Wong KL, Chen WS (1997) Compact micro strip antenna with dual frequency operation. Electron Lett 33(8):646

9. Ferdous N, Hock GC, Hamid SHA, Raman MNA, Kiong TS, Ismail M (2018) Design of a small patch antenna at 3.5 GHz for 5G application. In: International conference on sustainable energy and green technology
10. Ramli N, Noor SK, Khalifa T, Abd Rahman NH (2020) Design and performance analysis of different dielectric substrate based microstrip patch antenna for 5G applications. Int J Adv Comput Sci Appl (IJACSA) 11(8)

A Charge-Based Capacitance Model for Tri-Gate FinFET

K. Jyndiang and N. Bora

Abstract A charge-based capacitance model of Tri-Gate Fin Field Effect Transistors (TG-FinFET) is revisited. and it elaborates the characteristics of the capacitance versus applied voltages. The tri-gate FinFETs considered here are undoped or lightly doped. By analyzing the inversion charge density and the equation of the drain current, trans-capacitances are derived. To predict the output and transfer characteristics of the transistor's different parameters of the capacitance model are used. The model is verified by using 3D GENIUS VTCAD simulations.

Keywords Capacitance modeling · Tri-Gate (TG) FinFETs · Undoped silicon

1 Introduction

Silicon-based integrated circuits have grown rapidly in the last 40 years. Its evolution had a great impact on the silicon technology and this is happening because of the continuous downscaling of the CMOS technology. This downscaling helps the IC technology to follow the Moore's predictions. This scaling was quite successful in the previous years, but then continued scaling to a certain gate length has added a lot of complexity to the CMOS fabrication process as well as the device doping profiles which led to the difficulties in controlling the short-channel effects (SCEs) [1, 2]. The IC industries are researching for new device structures to overcome scaling limits of the MOS devices. There were several device architectures and analytical models were proposed like Double Gate MOSFET [3–6], Gate all around MOSFET [7, 8], carbon nano tubes [9], and very recently the junctionless transistors [10–14]. But still due to the advantages of TG structures, industries are still going with the most promising TG-FinFET [15, 16].

FinFETs are multigate metal oxide semiconductor field-effect transistor and non-planar or 3D transistors. These devices use ultra-thin body which reduces the SCEs and also helps in higher packing density. When top part of the fin has a thick oxide,

K. Jyndiang · N. Bora (✉)
Department of Electronics and Communication Engineering, NEHU, Shillong, India
e-mail: nbora@nehu.ac.in

S. Dwivedi et al. (eds.), *Flexible Electronics for Electric Vehicles*, Lecture Notes in Electrical Engineering 863, https://doi.org/10.1007/978-981-19-0588-9_16

then the FinFETs are called double gate (DG) FinFETs, but if the oxide thickness is thin on the sides and on top of the fin then they are called TG-FinFETs [17]. The TG-FinFET is one of the most popular device structures in the scaling for sub-10 nm technology as they have excellent gate control which helps in the suppression of the short-channel effects [18, 19]. It is preferable to use undoped or lightly doped channels so as to reduce corner effects and random dopant fluctuation [20].

2 Model Formulation

Figure 1, shows the structure of the device, where W_{fin} is the fin width, H_{fin} is the fin height, L is the channel length and t_{ox} is the gate oxide thickness. The effective width of the channel is $W_{\text{eff}} = 2H_{\text{fin}} + W_{\text{fin}}$, and thermal voltage is $V_{\text{th}} = kT/q$. In the moderate to the strong inversion region, the device capacitance is mainly contributed by the inversion charges. Here, we have revisited the Fasarakis [21] analytical model. Q_i is the mobile charge sheet density, and if we integrate Q_i along L, we obtain the total gate charge Q_g, i.e.

$$Q_g = -W_{\text{eff}} \int_0^L Q_i(y)\mathrm{d}y \tag{1}$$

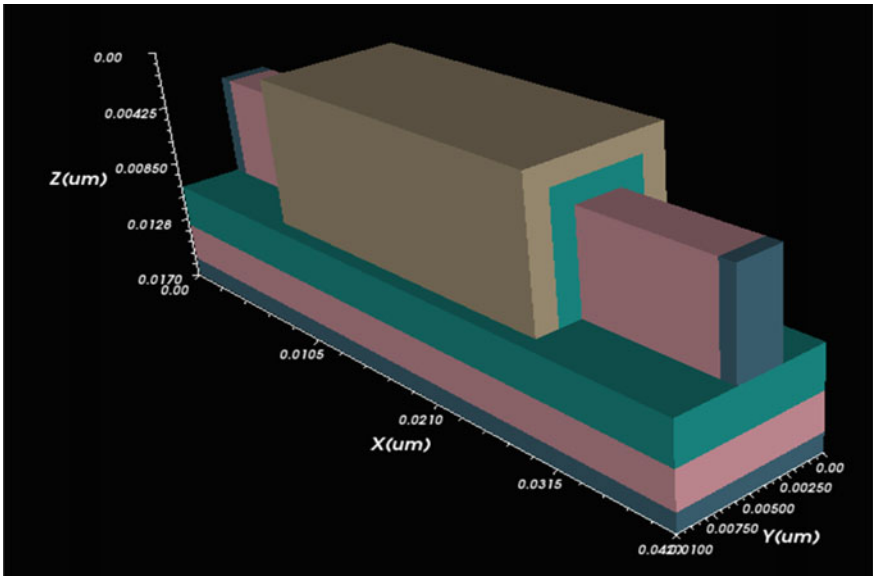

Fig. 1 The 3D simulation structure of Tri-Gate FinFET

The equation of charge density $Q_i(y)$ is [22]

$$Q_i(y) = 2C_{\text{ox}} V_{\text{th}} q_i(y) \tag{2}$$

where the capacitance of the gate oxide is C_{ox} and q_i is considered as the inversion charge density.

In strong inversion region, the inversion charge sheet density q_{is} is given by the relationship

$$q_{\text{is}}(\phi) = \text{Lambert}W\left[\exp\left(\frac{V_{\text{gs}} - \phi_{\text{th}} - \phi}{2V_{\text{th}}}\right)\right] \tag{3}$$

where V_{gs} represents the gate voltage, ϕ_{th} is the threshold voltage, and ϕ is the quasi-Fermi potential. From the continuity equation for the current, i.e.

$$\text{d}y = -\mu_0 W_{\text{eff}} Q_i(y) \frac{\text{d}\phi}{I_d(y)}$$

The drain current is [21],

$$I_d = \mu_0 \frac{W_{\text{eff}}}{L} C_{\text{ox}} (2V_{\text{th}})^2 \left[(q_{\text{is},s} - q_{\text{is,d}}) + \frac{1}{2}(q_{\text{is,s}}^2 - q_{\text{is,d}}^2)\right] \tag{4}$$

where ε_{ox} is the gate oxide permittivity, $q_{\text{is},s}$ and $q_{\text{is},d}$ are the normalized inversion sheet-charge densities values which are calculated, respectively, at the source and the drain.

The following analytic equation can elaborate the gate charge in all operational regions:

$$Q_{\text{g}} = \frac{V_{\text{th}}}{3} C_{\text{ox}} W_{\text{eff}} L \frac{q_{\text{is}}^2(3 + 2q_{\text{is}}) - q_{\text{id}}^2(3 + 2q_{\text{id}})}{q_{\text{is}}(1 - \frac{1}{2}q_{\text{is}}) - q_{\text{id}}(1 - \frac{1}{2}q_{\text{id}})} \tag{5}$$

where q_{i} is the inversion charge density valid in all region of operations [22, 23] i.e.,

$$q_i = \text{Lambert}W \times \left[\frac{\exp\left(V_{\text{gs}} - \phi_{\text{th}} - \phi\left(\frac{1}{2V\text{th}} + \frac{1}{2\eta'_{\text{TG}} V_{\text{th}}}\right)\right)}{M + \exp\left(\frac{V_{\text{gs}} - \phi_{\text{th}} - \phi}{2\eta'_{\text{TG}} V_{\text{th}}}\right)}\right] \tag{6}$$

where

$$M = \frac{\exp\left(\frac{\phi_{\text{th}} - V_{\text{fb}}}{V_n}\right)}{e^{f_0}}; \quad \eta'_{\text{TG}} = \frac{\eta_{\text{TG}}}{2 - \eta_{\text{TG}}}.$$

where f_0 represents a constant, V_{fb} is the flat-band voltage, the normalizing factor is represented by $V_n = 1$ V, and the coefficient for the subthreshold swing (tri-gate FinFET) is η_{TG}.

The equation for the drain charge Q_d is obtained as

$$Q_d = -\frac{V_{\text{th}}}{3} C_{\text{ox}} W_{\text{eff}} \alpha L \frac{b_1 + b_2 + b_3}{q_{\text{is}}(1 + \frac{1}{2}q_{\text{is}}) - q_{\text{id}}(1 + \frac{1}{2}q_{\text{id}})} \tag{7}$$

where

$$b_1 = \frac{1}{10 + 5q_{\text{is}} + 5q_{\text{id}}} \times \begin{bmatrix} 4q_{\text{is}}^2[q_{\text{is}}^2 - q_{\text{is}}q_{\text{id}} + (4q_{\text{id}}(2 + 3q_{\text{id}}))] \\ -2q_{\text{id}}^2[3q_{\text{id}}^2 + (q_{\text{id}}(4 + 3q_{\text{id}}))] \end{bmatrix},$$

$$b_2 = \left[\left[\frac{5q_{\text{is}}^2(q_{\text{is}} + 2q_{\text{id}} - q_{\text{id}})}{4 + 2q_{\text{is}} + 2q_{\text{id}}}\right] + \left[\frac{q_{\text{id}}^2(9q_{\text{is}} - 10q_{\text{is}} - 9q_{\text{id}})}{4 + 2q_{\text{is}} + 2q_{\text{id}}}\right]\right],$$

$$b_3 = \left[\frac{2q_{\text{is}}^2 - 4q_{\text{id}}^2 + 2q_{\text{is}}q_{\text{id}})}{8 + 4q_{\text{is}} + 4q_{\text{id}}}\right]$$

Then the charge at the source region is given by

$$Q_{\text{s}} = W \int_0^L \left(1 - \frac{y}{L}\right) Q_{\text{i}}(y)\text{d}y = -Q_{\text{g}} - Q_{\text{d}} \tag{8}$$

Substituting the values of Q_{g} and Q_{d}, we have

$$Q_{\text{s}} = -\left\{\frac{V_{\text{th}}}{3} C_{\text{ox}} W_{\text{eff}} L \times \left[\frac{\left[q_{\text{is}}^2(3 + 2q_{\text{is}}) - q_{\text{id}}^2(3 + 2q_{\text{id}})\right] - [\alpha(b_1 + b_2 + b_3)]}{q_{\text{is}}\left(1 + \frac{1}{2}q_{\text{is}}\right) - q_{\text{id}}\left(1 + \frac{1}{2}q_{\text{id}}\right)}\right]\right\} \tag{9}$$

From the charges at the all three terminals, the trans-capacitance of the device can be given as,

$$C_{ij} = \left.\frac{\partial Q_i}{\partial V_j}\right|_{i=j}, \quad C_{ij} = -\left.\frac{\partial Q_i}{\partial V_j}\right|_{i \neq j} \tag{10}$$

where i and j represent the gate, source, and drain.

Explicitly the expression of independent capacitances is obtained as follows:

$$\left.\begin{aligned} C_{gs} &= \frac{B_s}{2\eta'_{TG}V_{th}} \times \frac{1}{(q_{is}-q_{id})+\frac{1}{2}(q_{is}^2-q_{id}^2)}, \\ C_{gg} &= C_{gs} - \frac{B_s}{2\eta'_{TG}V_{th}} \times \frac{1}{(q_{is}-q_{id})+\frac{1}{2}(q_{is}^2-q_{id}^2)} \times (2V_{th}C_{ox}W_{eff}L_{eff}q_{id}^2 - Q_g q_{id}), \\ C_{ds} &= -\frac{B_s}{2\eta'_{TG}V_{th}} \times \frac{4V_{th}C_{ox}W_{eff}L_{eff}}{3} \times \frac{q_{is}(f_1-5q_{is}-15q_{id}+10)}{5(1+q_{is})(2+q_{is}+q_{id})^3}, \\ C_{dg} &= -\frac{B_d}{2\eta'_{TG}V_{th}} \times \frac{4V_{th}C_{ox}W_{eff}L_{eff}}{3} \times \frac{q_{id}(f_2-10q_{id}+20)}{5(1+q_{is})(2+q_{is}+q_{id})^3} - C_{ds}, \end{aligned}\right\} \quad (11)$$

where

$$B_s = \frac{A+\eta'_{TG}(A+\beta_s)}{A+\beta_s}, \quad B_d = \frac{A+\eta'_{TG}(A+\beta_d)}{A+\beta_d},$$

where,

$$\beta_s = \exp\left(\frac{V_{gs}-\phi_{th}}{2\eta'_{TG}V_{th}}\right), \quad \beta_d = \exp\left(\frac{V_{gs}-\phi_{th}-\phi}{2\eta'_{TG}V_{th}}\right),$$

$$f_1 = (2q_{is}^3+3q_{is}^2q_{id}+2q_{is}q_{id}^2+12q_{is}^2+2q_{is}^2+16q_{is}q_{id}+25q_{is}+25q_{id}),$$

$$f_2 = (3q_{id}^3+8q_{is}^2q_{id}+9q_{is}q_{id}^2+8q_{is}^2+18q_{id}^2+34q_{is}q_{id}+25q_{is}+45q_{id}), \quad (12)$$

and L_{eff} is the effective channel length.

3 Result and Discussions

The TCAD software [24] numerical results were used to compare and validate the capacitance model. The 3D TCAD simulation diagram of the TG-FinFET is shown in Fig. 1, which was designed at per with the SOI technology. The carrier trapping, Lombardi mobility model, and DIBL effects were included in simulations. The Shockley–Read–Hall (SRH) recombination model is included to study the leakage currents issues of the TG-FinFET. The F-D statistics with impact ionization model are also utilized throughout the simulations. The symbols represent the simulation results and the lines were used to represent the results obtained from our model in Figs. 2, 3, 4, 5, 6, 7, and 8.

The device parameters are $W_{fin} = 10$ nm, $H_{fin} = 20$ nm, $L = 20$ nm, the electron mobility $\mu_0 = 200$ cm^2/V, $t_{ox} = 1$ nm, $T = 300$ K, $V_{th} = 0.0259$ V, $f_0 = 2.2$, and $V_{gs} = 0.6$ V. The mid-gap work function is 4.71 eV, and the concentration of doping of channel and drain/source is $N_{siA} = 10^{16}$ cm^{-3} and $N_{siD} = 10^{21}$ cm^{-3}, respectively.

From the transfer characteristics graph shown in Fig. 2, we can see that as V_{gs} starts increasing from 0 to 0.5 V, I_d is almost equal to 0. This shows that the resistance between the source and drain terminal is quite high. But, when V_g reaches 0.5 V or

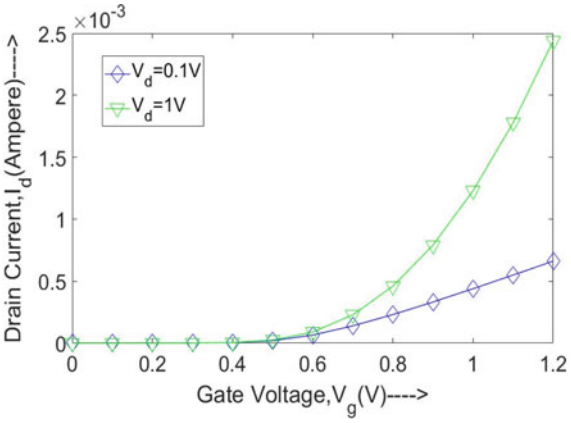

Fig. 2 Transfer characteristics (I_d–V_{gs}) in linear representation

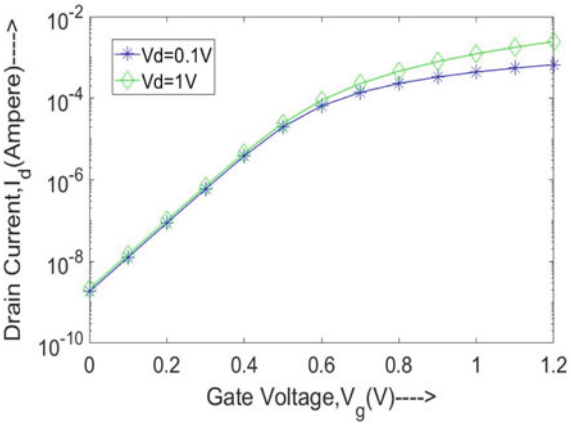

Fig. 3 Gate voltage versus drain current transfer characteristics in semi-log scale

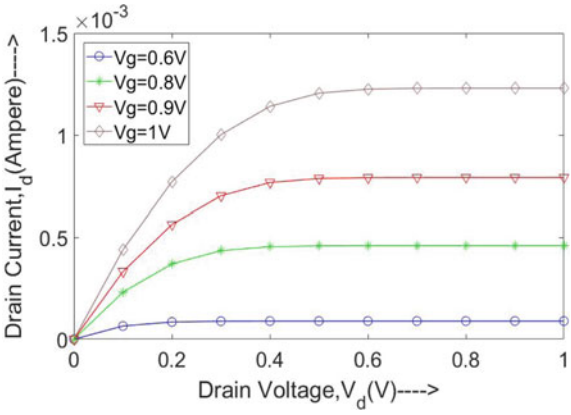

Fig. 4 Transfer characteristics (I_d–V_{ds}) in linear representation

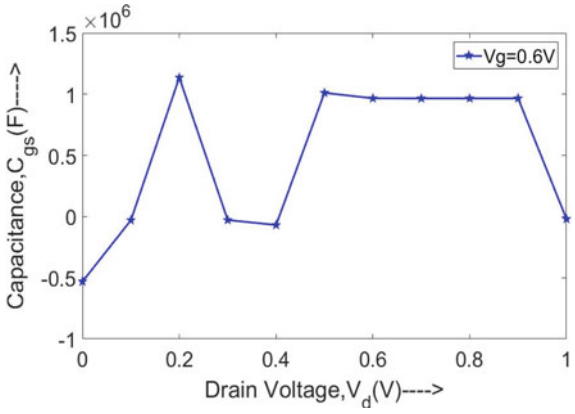

Fig. 5 Gate trans-capacitance, C_{gs} versus V_d of the device

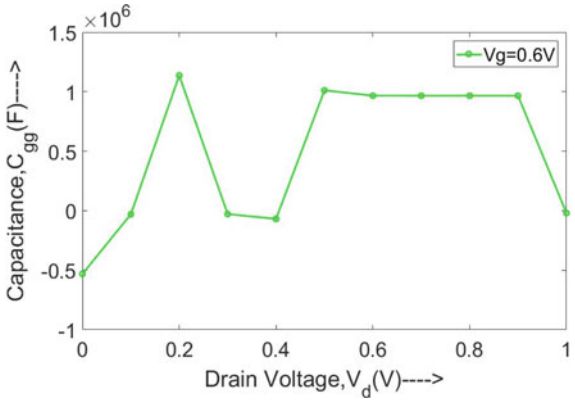

Fig. 6 Gate trans-capacitance, C_{gg} versus V_d of the device

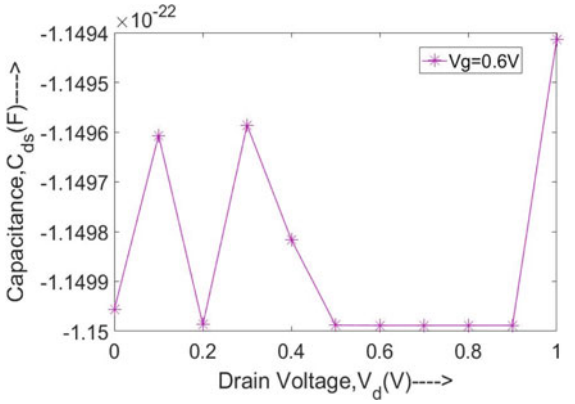

Fig. 7 Source trans-capacitance C_{ds} versus V_d of the device

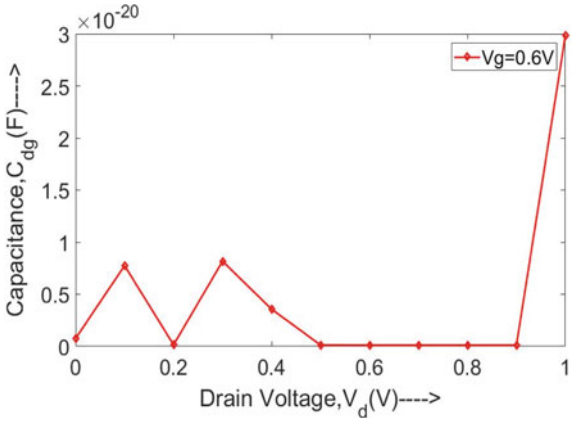

Fig. 8 Gate trans-capacitance C_{dg} versus V_d of the device

around the threshold voltage, the drain current increases rapidly which indicates that as V_{gs} increases the equivalent resistance at the drain decreases. For low drain voltage, the current will be lowered which is obvious. Figure 3 shows the same results in the semi-log scale.

The input–output results of the TG-FinFET are similar to that of the characteristics of a MOSFET. The characteristics mainly consist of the three regions from the cut-off to the saturation region. Figure 4 shows the drain current of TG-FinFET which is increasing with the drain voltage, but after a particular voltage, there is no effect of V_{ds} due to CLM.

Figure 5 shows the plot for gate trans-capacitance C_{gs} versus drain voltage. In Figs. 6 and 7, the plot is shown for gate trans-capacitances C_{gg} versus drain voltage and C_{dg} versus drain voltage. Figure 8 shows the source trans-capacitance C_{ds} versus drain voltage characteristics of the TG-FinFET for $V_g = 0.6$ V.

4 Conclusion

A capacitance model based on physics is revisited for a TG-FinFET taking into consideration for small geometry effects. The characteristics of capacitance-voltages operational in all regions are modeled and displayed. The capacitance model is helpful in analyzing the characteristics of the transistor. The results were verified by 3D GENIUS VTCAD simulations.

References

1. Chaudhry A, Kumar MJ (2004) Controlling short-channel effects in deep-submicron SOI MOSFETs for improved reliability: a review. IEEE Trans Device Mater Reliab. https://doi.org/10.1109/TDMR.2004.824359
2. Chen KL, Saller SA, Groves IA, Scott DB (1985) Reliability effects on MOS transistors due to hot-carrier injection. IEEE J Solid-State Circ 20:306–313. https://doi.org/10.1109/JSSC.1985.1052307
3. Ren Z, Taur Y (2020) Non-GCA modeling of near threshold I-V characteristics of DG MOSFETs. Solid State Electron 166. https://doi.org/10.1016/j.sse.2020.107766
4. Baruah RK, Bora N (2011) Analytic solution for symmetric DG MOSFETs with gate-oxide-thickness asymmetry. J Comput Theor Nanosci 8:2025–2028. https://doi.org/10.1166/jctn.2011.1920
5. Bora N, Baruah RK (2011) Quantum mechanical treatment on modeling of drain current, capacitances and transconductances for thin film undoped symmetric DG MOSFETs. In: IEEE international conference on nanoscience technology societal implications, NSTSI11. pp 1–6. https://doi.org/10.1109/NSTSI.2011.6111994
6. Hazarika MR, Bora N (2018) Performance analysis of 3-D asymmetric junctionless double gate MOSFET. In: IEEE international conference on energy, communication, data analytics and soft computing, ICECDS. pp 1391–1395. https://doi.org/10.1109/ICECDS.2017.8389672
7. Song JY, Choi WY, Park JH, Lee JD, Park BG (2006) Design optimization of gate-all-around (GAA) MOSFETs. IEEE Trans Nanotechnol. https://doi.org/10.1109/TNANO.2006.869952
8. Yilmaz K, Darbandy G, Reimbold G, Iniguez B, Lime F, Kloes A (2020) Equivalent DG dimensions concept for compact modeling of short-channel and thin body GAA MOSFETs including quantum confinement. IEEE Trans Electron Dev 67. https://doi.org/10.1109/TED.2020.3028336
9. Shulaker MM, Hills G, Patil N, Wei H, Chen HY, Wong HSP, Mitra S (2013) Carbon nanotube computer. Nature 501:526–530. https://doi.org/10.1038/nature12502
10. Colinge JP, Lee CW, Afzalian A, Akhavan ND, Yan R, Ferain I, Razavi P, O'Neill B, Blake A, White M, Kelleher AM, McCarthy B, Murphy R (2010) Nanowire transistors without junctions. Nat Nanotechnol 5:225–229. https://doi.org/10.1038/nnano.2010.15
11. Bora N, Das P, Subadar R (2016) An analytical universal model for symmetric double gate junctionless transistors. J Nano-Electron Phys 8. https://doi.org/10.21272/jnep.8(2).02003
12. Bora N, Subadar R (2019) A complete analytical model of surface potential and drain current for an ultra short channel double gate asymmetric junctionless transistor. J Nanoelectron Optoelectron 14:1283–1289. https://doi.org/10.1166/jno.2019.2643
13. Raibaruah AK, Sarma KCD (2021) A potential model for parallel gated junctionless field effect transistor. SILICON. https://doi.org/10.1007/s12633-020-00890-8
14. Bora N, Deka N, Subadar R (2020) Quantum mechanical analysis on modeling of surface potential and drain current for nanowire jlfet. J Nano Res 64. https://doi.org/10.4028/www.scientific.net/JNanoR.64.123
15. Bhor M Intel® 14 nm technology.
16. Stiffler SR, Ramachandran R, Henson WK, Zamdmer ND, McStay K, La Rosa G, Boyd KM, Lee S, Ortolland C, Parries PC (2018) Process technology for IBM 14-nm processor designs featuring silicon-on-insulator FinFETs. IBM J Res Dev 62. https://doi.org/10.1147/JRD.2018.2800518
17. Tang M, Pregaldiny F, Lallement C, Sallese JM (2009) Explicit compact model for ultranarrow body FinFETs. IEEE Trans Electron Dev 56. https://doi.org/10.1109/TED.2009.2020324
18. Weimin Z, Fossum JG, Mathew L, Yang D (2005) Physical insights regarding design and performance of independent-gate FinFETs. IEEE Trans Electron Dev 52. https://doi.org/10.1109/TED.2005.856184
19. Kranti A, Armstrong GA (2006) Performance assessment of nanoscale double-and triple-gate FinFETs. Semicond Sci Technol 21. https://doi.org/10.1088/0268-1242/21/4/002

20. Tang X, De VK, Meindl JD (1997) Intrinsic MOSFET parameter fluctuations due to random dopant placement. IEEE Trans Very Large Scale Integr Syst 5. https://doi.org/10.1109/92.645063
21. Fasarakis N, Tsormpatzoglou A, Tassis DH, Pappas I, Papathanasiou K, Bucher M, Ghibaudo G, Dimitriadis CA (2012) Compact capacitance model of undoped or lightly doped ultra-scaled triple-gate FinFETs. IEEE Trans Electron Dev 59:3306–3312. https://doi.org/10.1109/TED.2012.2223471
22. Fasarakis N, Tsormpatzoglou A, Tassis DH, Pappas I, Papathanasiou K, Bucher M, Ghibaudo G, Dimitriadis CA (2012) Compact model of drain current in short-channel triple-gate FinFETs. IEEE Trans Electron Dev 59. https://doi.org/10.1109/TED.2012.2195318
23. Papathanasiou K, Theodorou CG, Tsormpatzoglou A, Tassis DH, Dimitriadis CA, Bucher M, Ghibaudo G (2012) Symmetrical unified compact model of short-channel double-gate MOSFETs. Solid State Electron 69. https://doi.org/10.1016/j.sse.2011.10.002
24. Cogenda Pte Ltd. (2014) Genius, 3-D device simulator, Reference manual, Singapore

Prediction of Short-Term Solar Radiation Using Machine Learning Methods

Praveen Kumar Singh, Amit Saraswat, Yogesh Gupta, and Sunil Kumar Goyal

Abstract The renewable energy such as wind energy and solar energy has been established to offer benefits of sustainable energy sources and lowered environmental pollution levels. In addition to the benefits they offer, factors such as global warming and the growing energy crisis have led to a progressive increase in demand for renewable energy. To meet such a growing demand, there is a need for an efficient energy management system that promotes more accurate forecasting techniques. Forecasting to solar system output is mainly focused on the prediction of solar radiation. Numerous forecasting methods have been applied for achieving short-term solar radiation forecasting. This paper presents a comparative analysis of forecasting performance of three machine learning methods such as support vector machine, multiple linear regression, and artificial neural network. It is investigated that the prediction accuracy based on the multiple linear regression yields better results than that of the artificial neural network and support vector regression. Subsequent paragraphs, however, are indented.

Keywords Support vector machine · Multiple linear regression · Artificial neural network · Solar radiation · Solar power

1 Introduction

With the tremendous growth in the global world, requirements of energy have boomed remarkably, especially in emerging countries. The realization of resources like fossil fuel for the generation of energy is falling short, and due to this, energy saving and environmental protection have become the need of the hour. Change in climate due

P. K. Singh
Department of Computer Applications, Manipal University Jaipur, Jaipur, Rajasthan, India

A. Saraswat (✉) · S. K. Goyal
Department of Electrical Engineering, Manipal University Jaipur, Jaipur, Rajasthan, India
e-mail: amit.saraswat@jaipur.manipal.edu

Y. Gupta
Department of Computer Science, BML Munjal University, Gurugram, Haryana, India

S. Dwivedi et al. (eds.), *Flexible Electronics for Electric Vehicles*, Lecture Notes in Electrical Engineering 863, https://doi.org/10.1007/978-981-19-0588-9_17

to carbon emissions must be stopped to protect the atmosphere. Renewable energy sources come with many advantages, such as the outback in dependence on fossil fuel resources and to minimize the emissions of carbon into the atmosphere. Over the past decade, renewable energy sources have started to gain prominence in the power generation sector. Among different renewable energy sources, solar energy is one of the most significant sources of energy which is green in nature, and in different countries, it is currently under research.

An accurate forecasting of solar radiation is strongly associated with the accurate forecasting estimation of solar energy generation, and it depends upon various atmospheric variables. These variables are latitude, longitude, temperature, wind velocity, pressure, wind direction, daily global irradiation, and sunshine duration. The nature of solar radiation is intermittent and random; because of this, solar energy systems like photovoltaic have some technical issues like maintaining the balance between production and consumption patterns [1].

The forecasting horizons are an important factor and are generally divided into four sections including long term, medium term, short term, and very short term. Short-term forecasting is mainly done for decision-making activities, medium-term forecasting is for maintenance scheduling of power units, and long-term forecasting is done for planning the network operations [2].

The short-term time scale of forecast for solar radiation is essential for grid operators for grid maintenance and load balancing of solar power systems integrated with electricity grid. In the past few years, numerous works have been done to forecast solar radiation using different methods and atmospheric variables. Generally, the four different categories of techniques have been reported in different literature for short-term solar radiation forecasting physical, statistical, artificial intelligence machine learning, and hybrid [3]. The popular physical model reported in different literature is numerical weather prediction [4]. Statistical techniques use real-time data generated by numerical weather predictor and historical time series. The popular statistical methods for solar radiation forecasting are autoregressive moving average and autoregressive integrated moving average [5, 6]. Artificial neural network technique defines a nonlinear relationship between meteorological data and solar power output. Some researchers used a combined approach for prediction, a hybrid method which is a combination of statistical, physical, or artificial intelligence to provide better accuracy [7].

The selection of a forecasting model is commonly based on observed data, the selected model network mechanism, and energy planning operation. For the power grid operators, the forecasting of solar radiation must ensure a reliable supply of solar electricity, and because of this, it is a basic requirement for the future energy generation system [8]. Short-term solar radiation forecasting provides a good management operational schedule from minute to hour time frame. Solar radiation is the amount of solar energy per time per unit area on the earth. The equation for solar power prediction using solar radiation is represented as follows:

$$\mathrm{PE} = \mathrm{PA} \times r \times \mathrm{pr} \times H \tag{1}$$

Here, PE is the predication energy (kwh), PA is the total area of the panel, pr is the performance ratio, and H is the average solar radiation on the panel [9]. The solar irradiance is affected by different conditions like the location, time, and cloud cover. To predict solar radiation, most forecast techniques utilized available meteorological parameters like temperature, sunshine duration, and humidity as forecast model input. The remaining paper is organized as follows. In Sect. 2, introductions related to work in the area of solar radiation are explained. In sect. 3, forecasting methods for solar radiation are proposed. Section 4 has given experimental results and their discussion. Finally, conclusive remarks are there in Sect. 5.

2 Related Work

The worldwide demand for solar energy integration to the power grid creates a viable and sustainable future. The nature of solar energy is volatile, and because of this, it creates the significant challenges to the secure and reliable operation of power grid [4]. One of the important considerations for solar power system output is forecasting of the solar irradiance. Solar irradiance can be categorized into three, direct, diffuse, and global solar radiation. There are different categories for solar radiation forecasting methods: physical, statistical, artificial intelligence/machine learning, ensemble, and hybrid-based prediction models. The input for physical model is the metrological data, and for this category, numerical weather predictor is widely used for solar irradiance forecasting technique [10]. The statistical methods use historical time series data. Statistical techniques show better performance in short-term forecasting than physical models. Statistical techniques basically find a pattern and draw a mathematical equation using the past record. The main drawback of statistical model is its accuracy degraded as the time of prediction horizon increases. Statistical methods include autoregressive moving average (ARMA) [6] and autoregressive integrated moving average (ARIMA) [6] for solar radiation forecasting.

Over the years, artificial neural network-based methods, namely deep neural network methods, have been broadly reported by different researchers with better forecasting accuracy. On the basis of application, the machine learning techniques are broadly categorized into two, regression and classification. Prediction of solar radiation requires regression techniques. In most of the studies, support vector machine has been mainly used for classification problem but when they are applied to regression problems, they are known as support vector regression [11]. Lanre Olatomiwa suggested a model based on support vector machine for global solar radiation forecasting using metrological data like temperature, humidity, and wind speed as input [12]. For a global solar radiation forecast, a new prediction model suggested on support vector machine has been proposed by Meenal and Selva [13]. The global solar irradiance is the sum of direct irradiance and diffuse irradiance, and for this, a model based on support vector machine has been proposed by Jiang and Dong [14]. Lin develops a long-term solar power forecasting method using a hybrid approach and for this uses least square support vector regression [15]. Das has proposed a

support vector regression-based forecasting model using historical solar power and atmospheric data for solar power generation [16]. For probabilistic solar power forecasting, multiple linear regression model performs well [17]. A comparative analysis of multiple linear regression and support vector regression is presented for short-term solar power forecasting.

For short-term solar power prediction, there is always a nonlinear and complex relationship between input and output, and for this, artificial neural network is the most preferred techniques [18, 19]. A more complex structure of neural network multi-layer perceptron is used for better prediction accuracy [20]. Amrouche proposed artificial neural network-based model to predict global solar radiation [21]. A model based on artificial neural network is proposed for short-term global solar irradiance forecasting ranging from 1 to 6 h using satellite-generated metrological data as input [22]. In recent years, more focus is on ensemble methods for improved solar radiation forecasting accuracy [23]. A model was proposed for global solar radiation based on artificial neural network using different metrological data as input. A hybrid model was proposed based on artificial neural network for prediction of global solar radiation [24].

3 Methodology

In the paper, three different classes of machine learning models such as multiple linear regression, artificial neural network, and support vector machine are applied for determining dependencies and predicting solar radiation. These methods are compared in terms of the performance metrics such as RMSE, MAE, and MSE. In the next section, a brief descriptions about these three models and performance metrics are presented.

3.1 Multiple Linear Regression

Multiple linear regression is the extension of simple linear regression that predicts response using two or more independent features. It is basically the case where the dependent variable is predicted on the base of two or more independent features of the dataset. The model for multiple linear regression given p observation is

$$H(x_i) = b_0 + b_1 x_{i1} + b_2 x_{i2} + \ldots + b_p x_{ip} + e \tag{2}$$

Here, $H(x_i)$ is response output variable and x_i is the input variable, e is the term which represents model residual, and b_0, b_1, b_p are regression coefficient.

3.2 Support Vector Machine

Support vector machine is supervised machine learning algorithm that is based on kernel function mainly used to transform high dimensional space into required output space. For classification, the algorithm mainly finds an optimal hyperplane to divide different class of data. Support vector regression is an application of support vector machine which is used for regression task. *F*or support vector machine, different types of kernels are used to provide more accuracy and the names are linear, polynomial, and radial basis functions. The equation is:

$$F(\mathrm{x}) = (\mathrm{w} \times \mathrm{x}) + b \tag{3}$$

It is the general form of the model. The basic objective of the model is to achieve better prediction accuracy for all instances.

3.3 Artificial Neural Network

Artificial neural network is another section of artificial intelligence which works as tool to solve nonlinear complex problem, optimization, pattern detection, and regularization. The basic building blocks of artificial neural network are neuron, and the neurons are arranged at different layers in artificial neural network. There are three types of layers in artificial neural network, input layer, output layer, and hidden layer. The neural network weights and bias are optimally updated iteratively as shown in Fig. 1. The execution of artificial neural network is divided into two consecutive steps, learning and recalling. In training or learning steps, the artificial neural network adjust weights and bias recursively to reduce the error for to generate output. The Eq. (4) depicts the relationship between input and output layer in neural network.

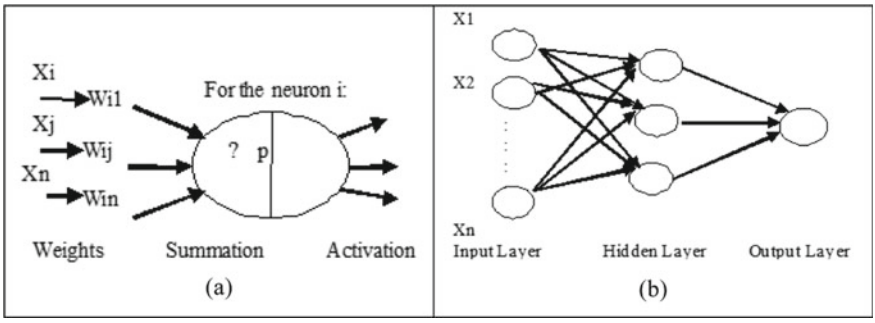

Fig. 1 Representation of artificial neural network: **a** single neuron representation, **b** layer structure of artificial neural network

$$p = \sum_{k=1}^{Ni-1} x_k^{i-1} W_{k,i} - \beta_k \tag{4}$$

where $W_{k,i}$ is the weight between neurons, x_k^{i-1} is the input from neuron k in the layer j, and β_k is the bias. The activation function for a neuron is crucial to decide the output from each node. Equation (5) shows activation function sigmoid [25].

$$F(\mathrm{x}) = \frac{1}{1 + \mathrm{e}^{-x}} \tag{5}$$

3.4 Performance Measures

To evaluate the forecasting performance of the machine learning method (i. support vector machine, multiple linear regression, and artificial neural network), different performance measures are used. In this paper, the used error metrics are MSE, RMSE, and MAE to evaluate the accuracy for forecasting performance. Mean square error is very similar to the mean absolute error but instead of using absolute values, square of the difference between the model predictors and the training dataset is being calculated.

$$\mathrm{MSE} = \frac{1}{N} \sum_{i=1}^{N} \left(y_i - \hat{y} \right)^2 \tag{6}$$

The root mean square represents the standard deviation of residuals. RMSE can be easily interpreted compared to MSE because RMSE units match the units of outputs:

$$\mathrm{RMSE} = \sqrt{\sum_{i=1}^{n} \frac{\left(\hat{y} - y \right)^2}{n}} \tag{7}$$

The mean absolute error is obtained by calculating the absolute difference between the model predictions and the true values. MAE is a measure of the average magnitude of error generated by the regression model.

$$\mathrm{MAE} = \frac{1}{n} \sum_{i=1}^{n} \left| y - \hat{y} \right| \tag{8}$$

4 Experimental Analyses

The main objective is to suggest solar radiation forecasting model with minimal error and have better forecast result in comparison to other reference models. The dataset used in the experiment has 11 features, and the names are humidity, temperature, date, time, radiation, sunrise, sunset, pressure, wind direction, wind speed, and unix time. The data is gathered over 5 min of interval with 327,000 observations. Here, in the dataset, the dependent variable is taken as radiation, whereas all other variables are considered as independent variables. Solar radiation variable is measured in watt per square meter (w/m^2), temperature in ($^{\circ}F$), humidity in percentage, and pressure in inch of mercury (Hg). Table 1 shows one row of dataset. For defining a forecasting model, it is always to get the analysis of dataset. The statistics of this dataset is presented in the Table 2. Here, the dependent variable in the dataset is taken as radiation, while all other variables are assumed as an independent variable.

The precision of the model generally depends on the selection of best features for the forecasting model; for this, correlation among the variables is determined; and on the basis of outcome, best features are selected as predictors for solar radiation. From Table 3 and Fig. 2, it is clearly demonstrated that solar radiation is highly correlated with temperature. There are some variables in the table that are negatively correlated with solar radiation which means their values do not play any significant role in solar irradiance prediction. Based on heat map correlation as shown in Fig. 2, other relevant features like pressure, wind speed, and time are also identified. The model accuracy is also dependent on the number of features involved in model prediction. To minimize the number of features, feature selection method is used which is based upon the value of determinant.

The summary and statistics of target variable radiation and all other independent variables are shown in Table 4. Here, R is a coefficient of correlation and its variant determines the dependency of the target variable to all other variables. From Table

Table 1 One row of dataset

Features	Font size and style
Date	09-01-2016 00:00
Time	00:05:10
Unix time	1,472,724,310
Pressure	30.43
Humidity	103
Radiation	2.83
Temperature	51
Speed	9.00
Sunrise time	06:07:00
Sunset time	18:38:00
Wind direction	153.44

Table 2 Statistics of used dataset

	Radiation	Temperature	Pressure	Humidity	Wind direction	Speed
Mean	207.1247	51.1033	30.4229	75.0163	143.4898	6.2439
Std. error	1.7474	0.0343	0.0003	0.1438	0.4600	0.0193
Median	2.6600	50.0000	30.4300	85.0000	147.7000	5.6200
Mode	1.2200	45.0000	30.4400	102.0000	0.1100	5.6200
Std. dev	315.9164	6.2012	0.0547	25.9902	83.1675	3.4905
Variance	99,803.16	38.4544	0.0030	675.4915	6916.8330	12.1834
Kurtosis	0.5111	−0.3161	2.1199	−0.7507	0.2311	6.6321
Skewness	1.3697	0.5221	−1.2270	−0.7763	0.5686	1.4698
Range	1600.1500	37.0000	0.3700	95.0000	359.8600	40.5000
Minimum	1.1100	34.0000	30.1900	8.0000	0.0900	0.0000
Maximum	1601.2600	71.0000	30.5600	103.0000	359.9500	40.5000
Sum	6,770,077.86	1,670,361.00	994,402.22	2,451,983.00	4,690,108.28	204,087.11
Count	32,686.00	32,686.00	32,686.00	32,686.0000	32,686.0000	32,686.0000

Table 3 Correlation matrix

Parameter	Radiation
Radiation	1
Temperature	0.734954755
Pressure	0.119015658
Humidity	−0.226170647
Wind direction (degrees)	−0.230323549
Speed	0.073626868
Time of sunrise	−0.092849977
Time of sunset	0.045688447
Time	0.00434807

3, it shows that the r^2 value from iteration 1–4 is maximum and it is approximately 0.95 in comparison to iteration 5 in which the value is 0.79. Therefore, the features in iteration 5 cannot be taken. Among all other iterations from 1 to 4, iteration 4 has a minimum number of features and its value is almost same as other iterations in the given table, so select the features temperature, time, and day only as it is a minimal combination for which the value is maximum. After selecting the best features for solar radiation forecasting, now the data is divided into two parts for training and testing purpose. 80% of the dataset is allocated for training purpose and another 20% for testing purpose. The selection of data for training and testing purposes is random in nature.

For electricity management decision-making, it is very important to predict a model with better accuracy. For this, I tried to compare the forecasting performance

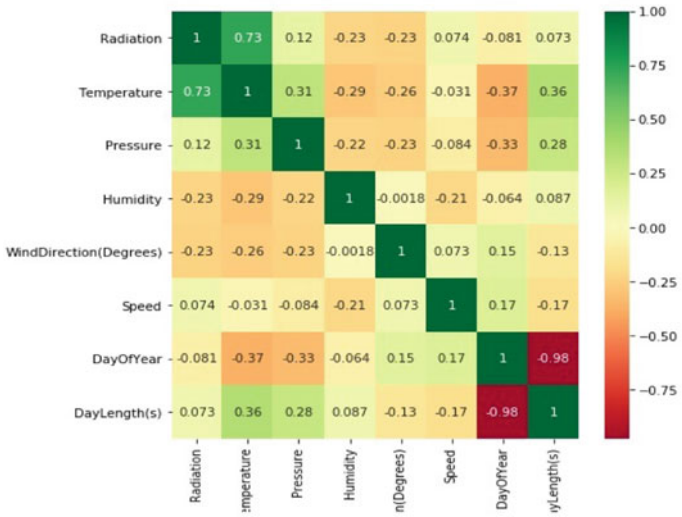

Fig. 2 Feature correlation heat map

Table 4 Value of r^2 with different feature combination

Iteration	Features	r^2 score
1	Humidity, wind direction, temperature, day of year, time of day	0.932594
2	Wind direction, humidity, temperature, day of year	0.931415
3	Day of year, temperature, time of day, humidity	0.933993
4	Time of day, humidity, day of year	0.932925
5	Time of day, temperature	0.799848

of multiple linear regression, support vector regression, and artificial neural network. Figure 3 shows the forecasting performance of these models. From the scatter plot, we

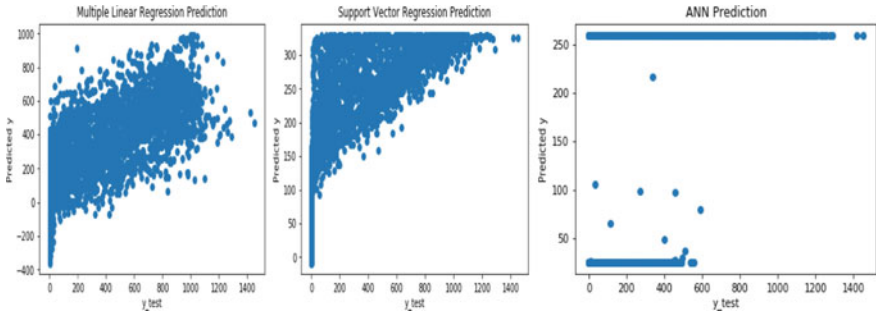

Fig. 3 Forecasting performance of different models

Table 5 Comparative analysis of different models

Performance metrics	Multiple linear regression	Support vector machine (RBF kernel)	Artificial neural network
r^2	0.61443109	0.417442811	0.16904260
RMSE	199.3601	245.0510242	287.763221
MSE	39,744.44949	60,050.00446	89,479.4662
MAE	151.2300811	151.2559992	216.585452

can see that multiple linear regression performs better than support vector machine and artificial neural network.

In order to compare the prediction accuracy of the applied machine learning method such as support vector machine, multiple linear regression, and artificial neural network, Table 4 summarizes RMSE, MAE, MSE, values for these three models. The coefficient of determination represents the proportion of variance that has been explained by independent variables in the model. As per the result, it is evident that for multiple linear regression the value is greater than support vector machine and artificial neural network, and this means that goodness of fit of multiple linear regression is much better than artificial neural network and support vector machine. The RSME provides an estimate of how large the residuals are being dispersed, and from the result, it is evident that artificial neural network is more dispersed than multiple linear regression and support vector machine. In MSE, error increases in quadratic fashion, while in MAE, error increases in proportional fashion. So from Table 5, it is observed that MSE value for multiple linear regression is almost half of artificial neural network and support vector machine.

5 Conclusion

In this study, prediction performance for solar radiation using three machine learning algorithms such as multiple linear regression, artificial neural network, and support vector machine, is compared. The study has used three variables such as temperature, day, and time for the prediction performance. The forecasting performance of these algorithms is compared using error metrics such as RMSE, MSE, and MAE. It is observed that the prediction accuracy of multiple linear regression is better than support vector machine and artificial neural network and based on the study observed that multiple linear regression machine learning approach is best for accurate prediction of solar radiation. However, the model is open for further improvement using the best possible combination of feature selection and ensemble model of machine learning.

References

1. Li J, Ward J, Tong J, Collins L, Platt G (2016) Machine learning for solar irradiance forecasting of photovoltaic system. Renew Energy 90:542–553
2. Jordehi A (2018) How to deal with uncertainties in electric power systems? A review. Renew Sustain Energy Rev 96:145–155
3. Voyant C, Notton G, Kalogirou S, Nivet M, Paoli C, Fouilloy F (2017) Machine learning methods for solar radiation forecasting: a review. Renew Energy 105:569–582
4. Paulescu M, Paulescu E, Gravila P, Badescu V (2013) Weather modeling and forecasting of PV systems operation. Springer, London
5. Rajesh G (2009) Day-ahead wind speed forecasting using f-ARIMA models. Renew Energy 34:1388–1393
6. Luis J, Garcia T (2019) Forecast of daily output energy of wind turbine using ARIMA and nonlinear autoregressive models. Adv Mech Eng 11:1–15
7. Troncoso A, Sanz SS, Mateo C, Riquelme J, Prieto L (2015) Local models-based regression trees for very short-term wind speed prediction. Renew Energy 81:589–598
8. Sharma A, Kakkar A (2018) Forecasting daily global solar irradiance generation using machine learning. Renew Sustain Energy Rev 83:2254–2269
9. Munawar U, Wang Z (2020) A framework of using machine learning approaches for short-term solar power forecasting. J Electr Eng Technol 15:561–569
10. Perez R, Kivalov S, Schlemmer J, Hemker K, Renn D, Hoff T (2010) Validation of short and medium term operational solar radiation forecasts in the US. Sol Energy 84:2161–2172
11. Lin G, Li L, Tseng M, Liu H, Yuan D, Raymond R (2020) An improved moth-flame optimization algorithm for support vector machine prediction of photovoltaic power generation. J Cleaner Prod 253
12. Olatomiwa L, Mekhile S, Shamshirband S, Sudheer K (2015) A support vector machine–firefly algorithm-based model for global solar radiation prediction. Solar Energy 115:632–644
13. Meenal R, Selvakumar A (2017) Assessment of SVM, empirical and ANN based solar radiation prediction models with most influencing input parameters. Renew Energy 121:324–343
14. Jiang H, Dong Y (2016) A nonlinear support vector machine model with hard penalty function based on glowworm swarm optimization for forecasting daily global solar radiation. Energy Convers Manage 126:991–1002
15. Fana J, Wangb X, Wuc L, Zhoud H, Zhanga H, Luc X, Xianga Y (2018) Comparison of support vector machine and extreme gradient boosting for predicting daily global solar radiation using temperature and precipitation in humid subtropical climates: a case study in China. Energy Convers Manage 164:102–111
16. Das U, Tey K, Seyedmahmoudian M, Idris M, Mekhilef S, Horan B, Stojcevsk A (2017) SVR-based model to forecast PV power generation under different weather conditions. Energies 10
17. Abuella M, Chowdhury B (2015) Solar power probabilistic forecasting by using multiple linear regression analysis. In: Proceedings of the IEEE south east con 2015, April, pp 9–12
18. Yesilbudak M, Çolak M, Bayindir R (2016) A review of data mining and solar power prediction. In: IEEE international conference on renewable energy research and applications
19. Marzouq M, El Fadili H, Lakhliai Z, Zenkouar K (2017) A review of solar radiation prediction using artificial neural networks. In: Interantional conference on wireless technologies, embedded and intelligent systems, pp 1–6
20. Hernández-Travieso JG, Travieso CM, Alonso JB, Dutta MK (2014) Solar radiation modeling for the estimation of the solar energy generation. In: Interantional conference on contemporary computing, pp 536–541
21. Amrouche B, Pivert X (2014) Artificial neural network based daily local forecasting for global solar radiation Appl Energy 130:333–341
22. Pereira L, David M, Diaz F, Lauret P (2015) Use of satellite data to improve solar radiation forecasting with bayesian artificial neural networks. Solar Energy 122:1309–1324

23. Percy SD, Aldeen M, Berry A (2018) Residential demand forecasting with solar-battery systems: a survey-less approach. IEEE Trans Sustain Energy 9:1499–1507
24. Assi A, Al-Shamisi M, Hejase M, Haddad A (2013) Prediction of global solar radiation in UAE using artificial neural networks. In: 2013 International conference on renewable energy research and applications (ICRERA), Madrid, pp 196–200
25. Gupta Y, Saraswat A (2021) Machine learning techniques for short-term forecasting of wind power generation. In: Hassanien A, Bhatnagar R, Darwish A (eds) Advanced machine learning technologies and applications. AMLTA 2020. Advances in intelligent systems and computing, vol 1141. Springer, Singapore

After Life Cost Modelling of 160 kW Grid Integrated Solar Photovoltaic Plant: BSDU Jaipur

Manisha Sheoran, Pancham Kumar, Susheela Sharma, and Mahipal Bukya

Abstract Modern times have involved surplus use of solar photovoltaic technology in energy sector. India is incredible in its energy source category be it renewable or non-renewable sources. Average solar insolation of India is 5000 T kWh per year (i.e. ~600 TW), and major insolation accounts for states like Gujarat, Telangana and Rajasthan, etc. Western side between North latitude (23° 30′ and 30° 11′) and East latitude (69° 29′ and 78° 17′) locates Rajasthan. Annually it receives 6–7 kWh/m^2 solar irradiance each day. 5109.96 MW of the total solar installation has been already done in Rajasthan, and further wider opportunity is available. End life recycling monetary aspects along with material recovery are also put forward. The current article focusses towards origin (2017) and retirement (2042) evaluation of 160 kW on grid rooftop solar PV plant installed in Bhartiya Skill Development University Jaipur Rajasthan. Objective of the paper is to lay down the complete cost analysis from set-up of the plant to its dismantling at the end life. Energy generated in the payback period also plays a key factor in deciding overall benefit from the installed plant. Such analysis will help in promoting the installation of rooftop solar panels at domestic and commercial level across the state. End life responsibilities should be taken care by the manufacturers to facilitate the steps for easy and economic recycling and also to eradicate the toxic components. This will be promoting the onset of independent and sustainable society in the crisis era of fossil fuels.

Keywords Photovoltaic · Cost analysis · Grid-connected payback

1 Introduction

In present century with the accelerating energy consumption, renewable sources of energy are being used. In India, most areas receive solar irradiance of approximately

M. Sheoran (✉) · P. Kumar · S. Sharma
Bhartiya Skill Development University, Jaipur, India
e-mail: manishasheoran480@gmail.com

M. Bukya
Manipal University, Jaipur, India

S. Dwivedi et al. (eds.), *Flexible Electronics for Electric Vehicles*, Lecture Notes in Electrical Engineering 863, https://doi.org/10.1007/978-981-19-0588-9_18

4.7 kWh/m^2/day, and its land mass is expected to receive approximately 5000 trillion kWh of solar energy per annum. With the promotion of Jawaharlal Nehru National Solar Mission from the year 2010, the installation of solar photovoltaic system in India received exponential upsurge [1]. In this paper, 160 kW grid-connected solar rooftop panel installed in Bhartiya Skill Development University Jaipur Rajasthan is studied. BSDU is a skill-based university established to achieve the principle of Aatma Nirbhar Bharat located in the Mahindra World City, off Ajmer highway Jaipur Rajasthan. Even though with aim of provision of electricity to every niche of India still the variation in the electricity bill is reported in areas of Rajasthan in terms of energy tariff. This particular issue can be pulled out by the usage and installation of grid-connected solar photovoltaic system. This grid connected solar photovoltaic system generates excess electricity rather than load requirement [2]. It feeds the extra electricity to grid, and when the same grid (on-grid) produces less electricity than the load requirement, it takes the surplus electricity from the grid to fulfil the load demand [3].

2 Methodology

A 160 kW grid-connected rooftop solar photovoltaic system based on monocrystalline silicon solar panels in BSDU is evaluated here. This system comprises solar panel, inverter, battery, mount structure and storage battery. In the rooftop grid-connected plant, the panels are anchored on 0° azimuth angle and 26° inclination leaning towards South [4]. During installation, panels are mounted in the shade-free area. 320 Wp rated anchor Panasonic crystalline silicon panels are utilized. The mechanical properties for solar panels of the proposed solar plant are mentioned underneath in Table 1. These panels are resistant to the harsh weather conditions like salt, mist, dust, corrosion and shadow [5].

Table 1 Mechanical properties of 320 W anchor Panasonic solar panel [6]

Solar cell	Polycrystalline silicon 156 × 156 mm (6 inches)
No. of cells	72
Dimensions	1956 × 992 × 40 mm (77.0 × 39.1 × 1.6 inches)
Weight	25.8 kg
Front glass	4 mm (0.16 inches) tempered glass
Frame	Anodised aluminium alloy
Junction box	IP67 rated (3 bypass diodes)
Connectors	MC4 compatible
Back sheet	High resistant polyester
Encapsulating material	Ethylene vinyl acetate (EVA)

Table 2 Input and output side—technical data of the ABB inverter [7]

Absolute maximum DC input voltage (V_{max})	1000 V
Start-up DC input voltage (V_{start})	300–500 V (default 360)
Rated DC input voltage V_{dcr}	715 rated DC input V_{dc}
Rated DC input power P_{dcr}	51,250 W
Number of independent MPPT	1
MPPT input DC voltage range	520–800 V_{dc}
Maximum DC input current (I_{dcmax})	100 A
Maximum input short circuit current	144 A
Number of DC inputs strings/pairs	12 or 16 string combiner version available
AC grid connection type	3-Phase, 440 V
Rated AC power	50,000 W
Maximum AC output power	50,000 W
AC voltage range	422–528 V
Maximum AC output current (I_{acmax})	61 A
Rated output frequency (f_r)	50 Hz

The mounted solar panels working efficiency is tested under standard conditions. Aluminium brackets and bolts of steel are utilized to anchor the panels on the roof. Three numbers of 50 kW capacities of ABB string inverter are used, and their specifications are mentioned as in Table 2.

The total number of solar panels used in 160 kW solar power plant upon reaching their end life will generate huge amount of waste. This can be tackled by either recycling through usage of thermal, mechanical or chemical process or by dismantling of the panels [9–11]. The material market price of recycled and dismantled product also accounts for profit making from the solar plant at its end life [12, 13]. D'Adamo et al. [8] estimated the mass fraction of 1 ton of crystalline Si PV modules. After the attainment of the end life of grid-connected solar plant, amount of revenue generated by recycling process of the solar panels is denoted as (B). The amount generated from the recycled materials is denoted as C.

3 Result and Discussion

The total panels in the 160 kW BSDU plant weigh 12,900 kg. Mass fraction of this is shown in Fig. 4.

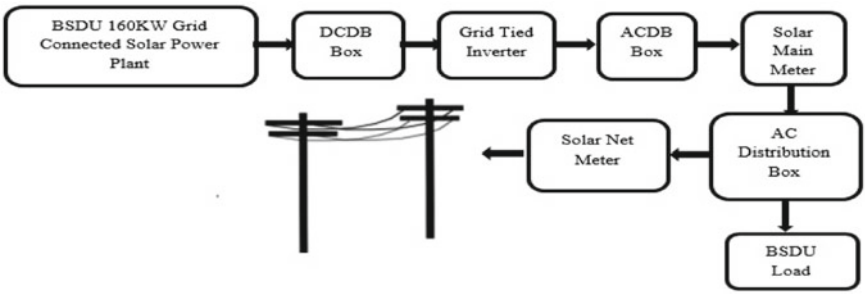

Fig. 1 BSDU 160 kW grid-connected solar power plant

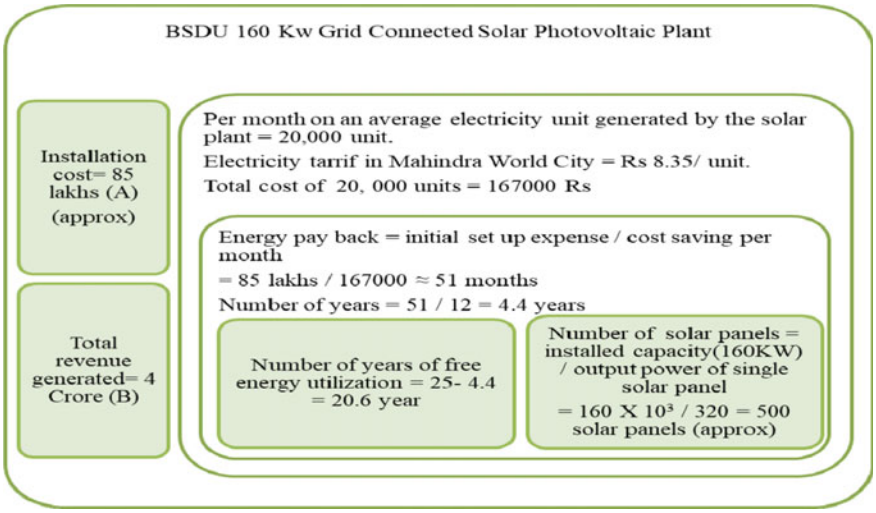

Fig. 2 End life cost analysis of 160 kW grid-connected solar power plant at BSDU

Recovery yield from the 160 KW plant for Al is 100%, glass is 97%, Si is 85%, Cu is 78%, and plastics include ethylene vinyl acetate layer which is not considered in the calculation part due to its fractional recovery compared to others [8, 14–17]. The market price of each recovered element is explored for [18]. Recovered amount is estimated to be approximately total Rs. 22,815. Recovered mass fraction and individual amount of the panel material through recycling are shown in Fig. 5.

$$\text{Henceforth the total savings in terms of profit} = B + C - A = D \qquad (1)$$

However, in this calculation, only the recycling recovery cost is taken, if the recovery of materials by dismantling is also added to it than further the cost benefit will be increased more [19, 20]. Overall profit is 31,522,815 Rs approximately (Thirty-One Million, five hundred twenty-two thousand, and eight hundred fifteen).

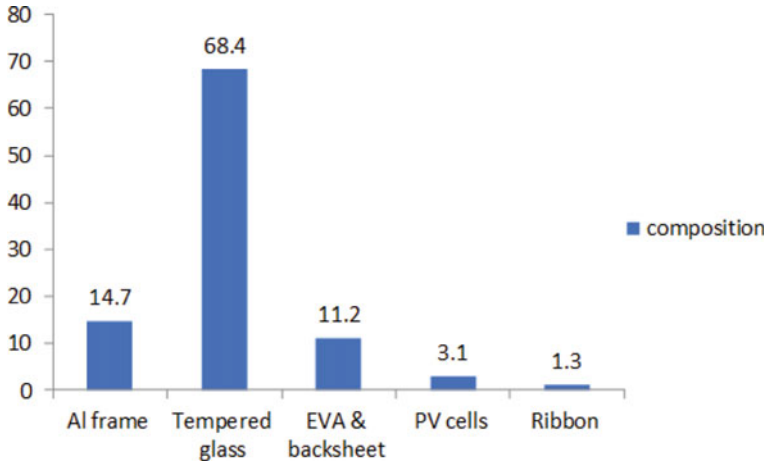

Fig. 3 Mass fraction of the PV modules in 1 ton of crystalline Si PV module [8]

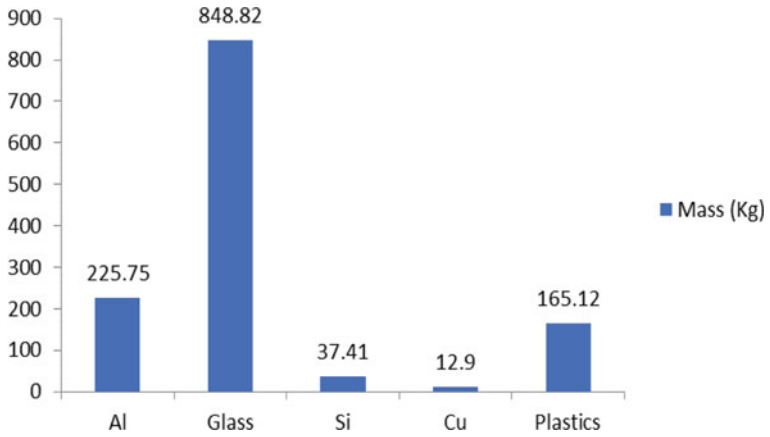

Fig. 4 Mass fraction in panels of BSDU 160 kW solar rooftop plant

Value can be generated from the solar photovoltaic waste by their recycling at end life. Recycling techniques need to be practiced at commercial scale so as to recover the valuable materials as it will boon the employment sector by establishing recycling industry, and further new industry will be set up to utilize the recycled materials. Construction industry can utilize the recovered aluminium in making doors, window panes and floor tiles. Automotive industry can utilize Al, Cu, glass, etc. Packaging industry can also utilize the recycled solar panel parts. Interior designing can be furnished by the recycled products.

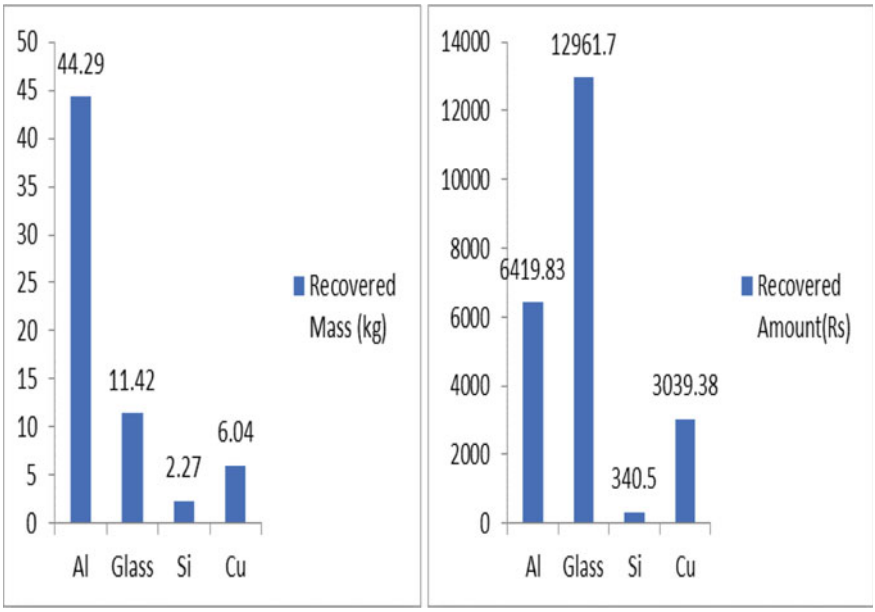

Fig. 5 Recovered mass and amount of material from panels of 160 kW grid-connected plant in BSDU

4 Conclusion

The overall analysis of the 160 kW grid-connected rooftop solar photovoltaic plant reveals beneficiary outcome. This includes major in terms of saving electricity bill as consumption from the grid increases financial load on any institute. Here, the complete reward is free electricity generated after energy payback time is attained. Further benefit is an added effect from the recycling of the silicon panels at the end life. However, the benefit discussed here is only from the recycling of the modules which is not greatly significant as crystalline silicon modules are devoid of economic elements. This study focused on the module and their parts which are recovered significantly.

References

1. Raina G, Sinha S (2019) Outlook on the Indian scenario of solar energy strategies: policies and challenges. Energy Strategy Rev 24:331–341. https://doi.org/10.1016/j.esr.2019.04.005
2. Baitule AS, Sudhakar K (2017) Solar powered green campus: a simulation study. Int J Low-Carbon Technol 12(4):400–410. https://doi.org/10.1093/ijlct/ctx011
3. Chakraborty S, Sadhu PK, Pal N (2015) Technical mapping of solar PV for ISM—an approach toward green campus. Energy Sci Eng 3(3):196–206. https://doi.org/10.1002/ese3.65

4. Khatri R (2016) Design and assessment of solar PV plant for girls hostel (GARGI) of MNIT University, Jaipur city: a case study. Energy Rep 10
5. Smith YR, Bogust P (2018) Review of solar silicon recycling. In: Energy technology. Springer International Publishing, Cham, pp 463–470
6. 310–315–320 W polycrystalline solar module. [Online]. Available: https://lsin.panasonic.com/media/brouchers/2017/3/310-315-320.pdf. Accessed: 10 Oct 2020
7. TRIO-50.0-TL-OUTD-US-480_Rev.G.pdf. [Online]. Available: https://library.e.abb.com/public/4d8140daa2b24c7c9ca4a37638e153bc/TRIO-50.0-TL-OUTD-US-480_Rev.G.pdf. Accessed: 10 Oct 2020
8. D'Adamo I, Miliacca M, Rosa P (2017) Economic feasibility for recycling of waste crystalline silicon photovoltaic modules. Int J Photoenergy 2017:1–6. https://doi.org/10.1155/2017/4184676
9. Domínguez A, Geyer R (2017) Photovoltaic waste assessment in Mexico. Resour Conserv Recycl 127:29–41. https://doi.org/10.1016/j.resconrec.2017.08.013
10. Li Y, Wang G, Shen B, Zhang Q, Liu B, Xu R (2021) Conception and policy implications of photovoltaic modules end-of-life management in China. WIREs Energy Environ 10(1). https://doi.org/10.1002/wene.387
11. Contreras Lisperguer R, Muñoz Cerón E, de la Casa Higueras J, Martín RD (2020) Environmental impact assessment of crystalline solar photovoltaic panels' end-of-life phase: open and closed-loop material flow scenarios. Sustain Prod Consum 23:157–173. https://doi.org/10.1016/j.spc.2020.05.008
12. Dias P, Veit H (2018) Recycling crystalline silicon photovoltaic modules. In: Kurinec SK (ed) Emerging photovoltaic materials, 1st edn. Wiley, pp 61–102
13. Kumar S, Soni A, Swarnkar NK, Lalwani M (2020) Performance characteristics of 6.124 MW solar power plant at military engineering service (Jodhpur, Rajasthan): a case study. Int J Adv Sci Technol 29(3):15
14. Celik I, Lunardi M, Frederickson A, Corkish R (2020) Sustainable end of life management of crystalline silicon and thin film solar photovoltaic waste: the impact of transportation. Appl Sci 10(16):5465. https://doi.org/10.3390/app10165465
15. Dias P et al (2021) Comprehensive recycling of silicon photovoltaic modules incorporating organic solvent delamination—technical, environmental and economic analyses. Resour Conserv Recycl 165:105241. https://doi.org/10.1016/j.resconrec.2020.105241
16. Yi YK, Kim HS, Tran T, Hong SK, Kim MJ (2014) Recovering valuable metals from recycled photovoltaic modules. J Air Waste Manag Assoc 64(7):797–807. https://doi.org/10.1080/10962247.2014.891540
17. Klugmann-Radziemska E, Kuczyńska-Łażewska A (2020) The use of recycled semiconductor material in crystalline silicon photovoltaic modules production—a life cycle assessment of environmental impacts. Sol Energy Mater Sol Cells 205:110259. https://doi.org/10.1016/j.solmat.2019.110259
18. Aluminium Price | MCX Aluminium—aluminium rate in India today live on the economic times. The economic times. https://economictimes.indiatimes.com/commoditysummary/symbol-ALUMINIUM.cms. Accessed 10 Oct 2020
19. Maani T, Celik I, Heben MJ, Ellingson RJ, Apul D (2020) Environmental impacts of recycling crystalline silicon (c-SI) and cadmium telluride (CDTE) solar panels. Sci Total Environ 735:138827. https://doi.org/10.1016/j.scitotenv.2020.138827
20. Markert E, Celik I, Apul D (2020) Private and externality costs and benefits of recycling crystalline silicon (c-Si) photovoltaic panels. Energies 13(14):3650. https://doi.org/10.3390/en13143650

Modeling of Drain Current for Degradation in Threshold Voltage and Mobility Due to Aging in a-Si:H TFTs

Ashish Vijay and Mohit Kumar Sharma

Abstract Amorphous silicon thin-film transistor (TFT) is used in different analog and digital applications. In analog applications due to DC stress voltage at gate terminal of TFT, there is a degradation in threshold voltage, mobility, etc., and these parameters are degraded with time. By making aging aware equivalent model of TFT, we can easily simulate the circuit and analyze the variation in output parameter due to degradation. In this work, we show that the aging aware equivalent model shows the same percentage variation in drain current as we can find out due to the variation in mobility and threshold voltage in different stress conditions.

Keywords TFT · Aging · a-Si:H

1 Introduction

Reliability is a major concern in today scenario. It became an adverse effect on circuit critical parameter if not handled properly. Degradation of parameters with respect to time under DC bias condition becomes more severe when TFT is used for analog device rather than its uses as digital applications [1]. In analog application, it would require providing constant stress voltage at gate and drain terminal which makes this variation or degradation in several parameter like threshold voltage, mobility, etc. more pronounce. So, to analyze or to simulate the impact of the variation, it is better to replace original transistor with aging equivalent model. In this paper, we are trying to make more compact model in which we take effect of degradation due to both mobility and threshold voltage simultaneously, and instead of using mathematical aging model, we can use this equivalent aging aware model to analyze the output. For make this compact model, we modeling the drain current in manner that it inculcate

A. Vijay (✉) · M. K. Sharma
Manipal University Jaipur, Jaipur, India
e-mail: ashish.vijay@jaipur.manipal.edu

M. K. Sharma
e-mail: mohitkumar.sharma@jaipur.manipal.edu

S. Dwivedi et al. (eds.), *Flexible Electronics for Electric Vehicles*, Lecture Notes in Electrical Engineering 863, https://doi.org/10.1007/978-981-19-0588-9_19

all the degradation effect in the form of change in voltage at gate end. This research focuses on developing the aging aware model for TFT.

2 Aging Effect on Threshold Voltage Due to Stress Voltage

There are several theories define the threshold voltage variation in TFT. And some mathematical relation to define the variation in threshold voltage with respect to time and stress voltage. In this paper, we also take the variation in mobility into account by taking a predefined mathematical function. So, in Fig. 1 a, aging aware equivalent model is presented where a DC source of Δv_{th} connected at gate terminal [2]. The physics behind the degradation in parameters AI almost similar. Due to contact of different crystalline structure, there is a crystallographic defect at interface state where charge trapping take place. These charge trapping becomes more severe for high stressed voltage at gate terminal and drain terminal. It also shown experimentally that aging phenomenon in several parameter is function of time, temperature, and electrical field across its channel length [3, 4].

The mathematical expression of degradation in threshold voltage found by experimentally data is given by [5, 6].

$$\Delta v_{\text{th}} = C\left(V_{\text{gs}}\right]^{\beta} t^{\nu} \exp\left(-\frac{E_a}{KT}\right) \tag{1}$$

C is a constant, E_a is the activation energy, and β and ν are constant. For different value of gate voltage and temperature, these constants have different value. In this paper, we measured the variation in threshold voltage at $\beta = 2$, $V_{\text{gs}} = 80$ V, $\nu = 0.4$, and at $T = 150$ °C.

The drain current for TFT can be defined by (Figs. 2 and 3).

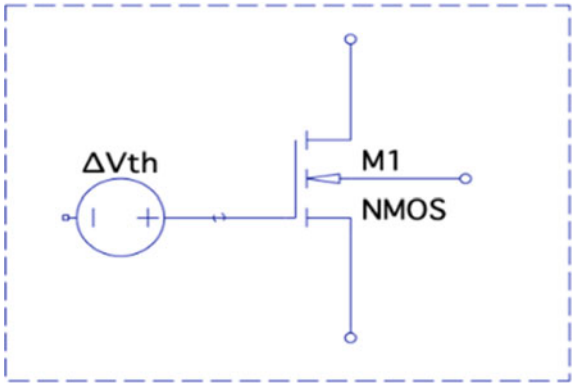

Fig. 1 Aging aware equivalent transistor model

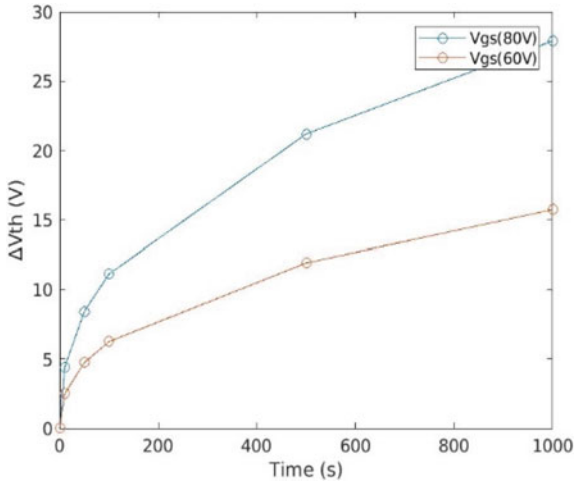

Fig. 2 Variation in threshold voltage of a-Si:H TFT with time for different stress condition

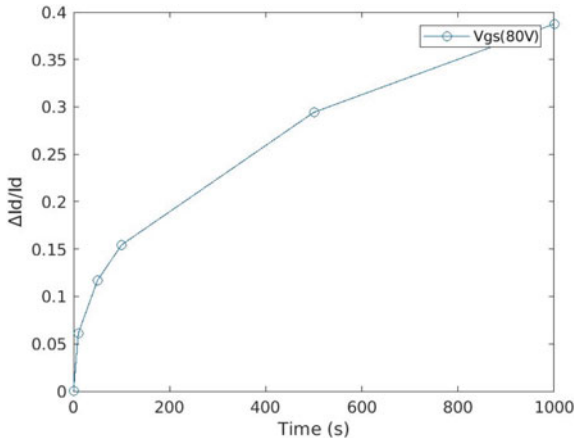

Fig. 3 Percentage change in drain current with time at $V_{\text{gs}} = 80$ V

$$I_d = 1/2 * \mu_0 C_{\text{ox}}\ W/L * \left(V_{\text{gs}} - V_t\right)^2 \tag{2}$$

If new, $V_{t\text{new}} = V_t + \Delta v_{\text{th}}$.
Then the equation of drain current becomes

$$I_d = 1/2 * \mu_0 C_{\text{ox}}\ W/L * \left(V_{\text{gs}} - V_t - \Delta v_{\text{th}}\right)^2 \tag{3}$$

By this equation, we easily identify that the effect. Then the equation of drain current becomes on drain current due to degradation in threshold voltage which can be inculcated in circuit by connecting a DC sources in series with gate voltage, the polarity should be opposite.

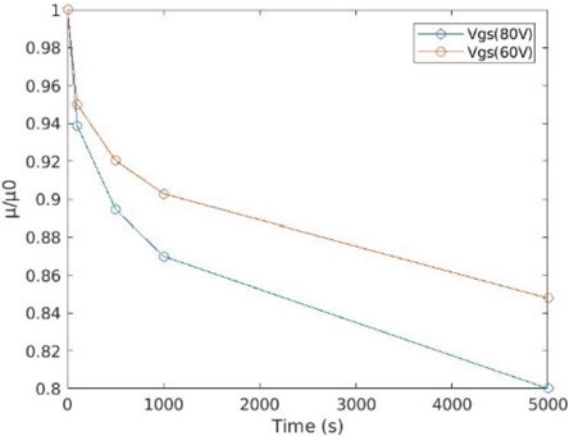

Fig. 4 Degradation in mobility of TFT with time for different stress condition

3 Aging Effect on Mobility

As we analyzed that threshold voltage degraded with respect to time, the rate of degradation is depending on stressed voltage already shown in Fig. 2. There is a variation in drain current due to this aging effect on threshold voltage. It has been observed that for different stress voltage, there is a degradation in mobility. Due to variation in mobility, the current through the TFT becomes change. The dependency of mobility degradation is shown by [5] (Fig. 4).

$$\frac{\mu_{\text{eff}}}{\mu_0} = \exp\left(-\frac{t}{\tau}\right)^{\alpha} \tag{4}$$

is approximately defined by relation $= \left(1 - \left(-\frac{t}{\tau}\right)^{\alpha}\right)$.

where α and τ are constant, it is found experimentally [5] that the value of τ is different for different stress voltage at gate side. The value of τ increases with decreases in gate voltage. It is found that the degradation in mobility is 20%, 15%, 10% at $V_{\text{gs}} =$ 80 V, $V_{\text{gs}} = 60$ V, and $V_{\text{gs}} = 40$ V at 5000 s. So the drain current again reduced due to decreasing in mobility.

4 Modeling of Drain Current for Aging Aware Equivalent TFT

$$I_d = 1/2 * \mu_0 C_{\text{ox}}\ W/L * \left(V_{\text{gs}} - V_t - \Delta v_{\text{th}} - kV_x\right)^2 \tag{5}$$

where K is fitting parameter and V_x is the amount of voltage which provides the same degradation in drain current as provide by degradation in mobility [7].

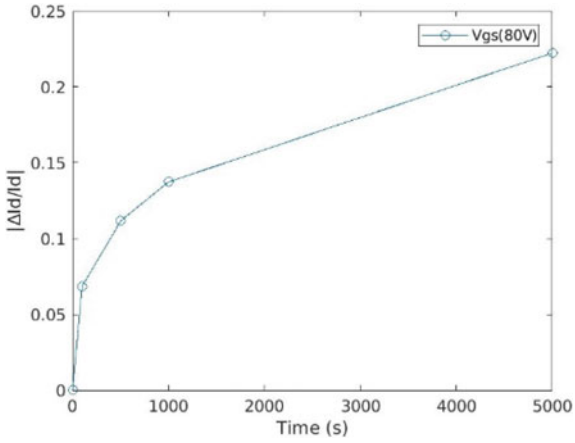

Fig. 5 Percentage variation in drain current due to aging effect on mobility

$$I_d = 1/2 * \mu_0 \exp\left(-\frac{t}{\tau}\right)^{\alpha} C_{\text{ox}}\ W/L * \left(V_{\text{gs}} - V_t\right)^2 \tag{6}$$

$$\Delta I_d/I_d = -\left(-\frac{t}{\tau}\right)^{\alpha} \tag{7}$$

$$I_d = 1/2 * \mu_0 C_{\text{ox}}\ W/L * \left(V_{\text{gs}} - V_t - V_x\right)^2 \tag{8}$$

$$\Delta I_d/I_d = -\frac{2(V_x)}{\left(V_{\text{gs}} - V_t\right)} \tag{9}$$

By using this relation, we easily define the mathematical behavior of V_x. So now the new aging equivalent model having two DC source connected in series having opposite polarity. So we can replace by this equivalent circuit in TFT module and can analyze the variation in output parameters like gain, bandwidth, etc. (Figs. 5 and 6).

5 Conclusions

We studied the reliability issue of a-Si:H TFTs at 150 °C and find out that due to DC biasing in analog TFT circuit, there is a variation in some critical parameters of TFT. By using the aging aware equivalent model of TFT, it becomes easy to analyze the output more correctly. And accordingly, we can know how much variation is required to get desired output. Parameters like mobility and threshold voltage get variation due to stress voltage which getting increase with time, so by inculcate this variation in TFT model, our circuit becomes more reliable. So earlier, we have mathematical model to analyze the degradation due to these parameters but it is difficult to analyze

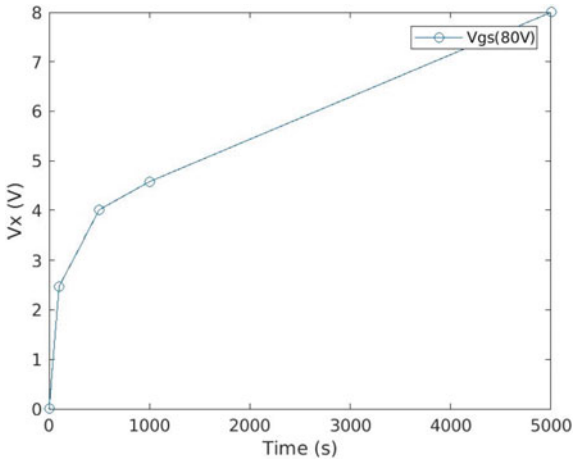

Fig. 6 Variation in voltage (V_x) for stress voltage 80 V

when the circuit is complex in nature, and there are different stress voltage at different end. So by using this aging aware model in which we inculcate all the degradation effect due to mobility and threshold voltage by doing modeling of drain current, we can easily analyze the variation in critical parameter of given circuit.

References

1. Karim KS, Nathan A, Hack M, Milne WI (2004) Drain-bias dependence of threshold voltage stability of amorphous silicon TFTs. IEEE Trans Electron Devices 25(4):188–190
2. Maricau E, Gielen G (2013) Analog IC reliability in nanometer CMOS. Springer Science & Business Media
3. Shen C-H, Li Y, Lo I-H, Lin P-J, Chung S-C (2011) Modeling temperature and bias stress effects on threshold voltage of a-Si:H TFTs for gate driver circuit simulation. IEEE
4. Ibaraki N, Kigoshi M, Fukuda K, Kobayashi J (1989) Threshold voltage instability of a-Si:H TFT' in liquid crystal displays. J Non-Cryst Solids 115(1–3):138–140
5. Gleskova H, Wagne S (2001) DC-gate-bias stressing of a-Si:H TFTs fabricated at 150 °C on polyimide foil. IEEE Trans Electron Devices 48(8)
6. Shringarpure R, Clark LT, Bawolek E (2007) Circuit simulation of threshold-voltage degradation in a-Si:H TFTs fabricated at 175 °C. IEEE Trans Electron Devices 54(7)
7. Allee DR, Clark LT, Vogt BD, Shringarpure R, Venugopal SM, Uppili SG, Kaftanoglu K, Shivalingaiah H, Li ZP, Ravindra Fernando JJ, Ba-wolek EJ, O'Rourke SM (2009) Circuit-level impact of a-Si:H thin-film-transistors degradation effects. IEEE Trans Electron Devices 56(6):1166–1176

Charging of Multiple Batteries Using Single-Stage Multi-source Converter with Bidirectional Power Flow

Siddhant Gudhe and Sanjeev Singh

Abstract This paper bestows a topology of inverter called as multi-source inverter (MSI) which is used to connect multiple batteries to a single source. A novel approach has been discussed where this inverter topology is used to charge batteries in electric vehicles (EV) through stator windings of the electrical machine. The same set of batteries can be used as a source to drive electrical machine through this inverter. A detailed analysis on simulated performance using MATLAB/Simulink is presented during charging and discharging with variable load conditions of electric vehicle to demonstrate the effectiveness of the proposed concepts.

Keywords Electrical vehicle (EV) · Multi-source inverter (MSI) · Modified multi-source inverters

1 Introduction

Technological advancements for electric vehicles (EV) are witnessing rapid change while having steady growth in the basic structures such as converters and electric motors. By using power electronics switches, various converters in the EV are controlled and operated. Power converters having re-configurable capability with more than one mode of operation are active research area [1]. The invention of new devices with wide band gap, power electronics devices uses high-frequency soft switching technology for controlling the drive parameters. EVs with two batteries backup are need of an hour, one supplying the motor and other battery supplying the auxiliary requirements of EV [1]. The use of battery for the reactive power compensation can also be obtained using EVs [2, 3]. One of the two batteries can satisfy this purpose using inverter. Boost inverter topology is used in single stage for both boosting and inverting. This minimizes the ripple components and increases

S. Gudhe (✉) · S. Singh
Maulana Azad National Institute of Technology, Bhopal, India
e-mail: sidgudhe007@gmail.com

S. Singh
e-mail: sschauhan@manit.ac.in

S. Dwivedi et al. (eds.), *Flexible Electronics for Electric Vehicles*, Lecture Notes in Electrical Engineering 863, https://doi.org/10.1007/978-981-19-0588-9_21

the battery life [2]. The batteries can be used to supply power to grid in case of demand deficit using vehicle-to-grid (V2G) mode of operation. In vehicle-to-grid (V2G) mode, total harmonic distortion (THD) and power factor are maintained within limits [4]. Also, coordinated smart charging along with smart metering is required as discussed in [4]. EV can act as load as well as source with bidirectional energy flow using inverter. The requirement of the reactive power of EV changes with the weather conditions. Less reactive power is required in summer as compared to winter [5]. In EVs, instead of using VSI or boost VSI using inductor, the bidirectional switched capacitor (SC) for boost conversion and AC to DC and DC-to-DC conversion is also discussed in [6]. In the same study, SiC MOSFET is presented for converter action using FPGA. This adds to the complexity of the controlling technology which can affect the speed of the overall control system. An inverter topology named as multi-source inverter (MSI) was patented in 2014 [7]. The MSI operates at different voltage levels using the same inverter connected to multiple DC sources.

This paper extends multi-source inverter for bidirectional power flow with the basic concept of multiple DC source charging through single phase AC supply using only single stage of conversion. The MSI can act as three-level inverter and supplies the electrical traction motor without any additional converter. This traction power is supplied from main battery which is called as primary battery. Other loads of EV such as electronic loads, lights, and fans can be supplied with secondary battery which is almost half capacity and size compared to main battery. This reduces the converter complications and its control algorithm. A study of MSI on hybrid electric powertrains has been presented in [8, 9]. The battery is charged through internal combustion engine (ICE) and during regenerative mode. The charging of the batteries through MSI has not been discussed. In general, batteries need to charge through grid using separate battery charger.

This paper proposes a neutral point clamped (NPC) three-level inverter topology with DC side having two batteries completely independent from each other. Use of motor windings for charging of batteries has been reported in 1990s [10–12] but has not been explored extensively. Power supply is applied to any two phases of the stator winding of induction motor connected to inverter. The charging of both batteries through MSI is done through stator winding of the electric motor through single-phase supply. Level 1 single-phase chargers are targeted using this topology of charging through IM.

The paper is organized as follows: Introduction, neutral point clamped topology for MSI performance simulation, and conclusion.

2 Neutral Point Clamped (NPC) Topology for MSI

Circuit topology of MSI for charging of multiple batteries is derived from a three-level inverter. Three-level inverter has reduced dV/dt across the switches, thereby reduction in EMI. Lower voltage rating devices can be used with better waveform quality of output voltage. Neutral point clamped (NPC) topology of three-level inverter is

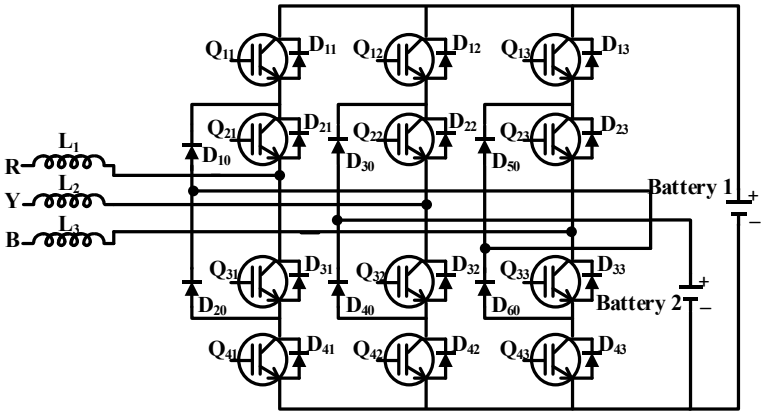

Fig. 1 Modified multi-source inverter with batteries connections

adapted for MSI [9], and circuit is modified further to meet the objectives of this paper. Neutral point in MSI connecting switches from the upper leg and lower leg is absent and does not have half DC voltage as in three-level inverter circuit; instead, voltage rating of the batteries determines the voltage at various nodes in the circuit. The battery voltages of MSI can be of different levels and are not dependent on each other. To meet the objectives of this paper, a modified topology of the MSI with battery connection is considered as shown in Fig. 1.

During positive half cycle, shown in Fig. 2a, battery 1 charges through Q_{21}-Q_{11}-Q_{42}-$Q_{32}$and battery 2 charges though Q_{31}-D_{20}-Q_{42}-Q_{32}. In Fig. 2b, during negative half cycle, battery 1 charges through Q_{22}-Q_{12}-Q_{41}-$Q_{31}$and battery 2 charges though Q_{32}-D_{40}-Q_{41}-Q_{31}. Figure 3 shows the circuit while discharging. The stator windings are connected in star to create rotating magnetic field in IM during starting. Output voltage can be obtained with three-level voltages like that in three-level inverter when only battery 1 discharges. So, the advantage of three-level inverter is retained along all the merits of MSI. Switching during charging are controlled using sine PWM (SPWM) control scheme which is implemented without any complex mathematical computation. Switching during discharging is obtained using SVPWM control to obtain good quality output voltage waveforms.

3 Performance Simulation

MATLAB/Simulink is used for the performance simulation and verification of the proposed topology. Electric vehicle with a multi-battery system has good option at least two batteries are sufficient to supply entire load. The charging of both the batteries can be done with single-phase level 1 charging. This paper uses two battery systems where battery 1 bears the rating of 400 V, 120 Ah and battery 2 bears the

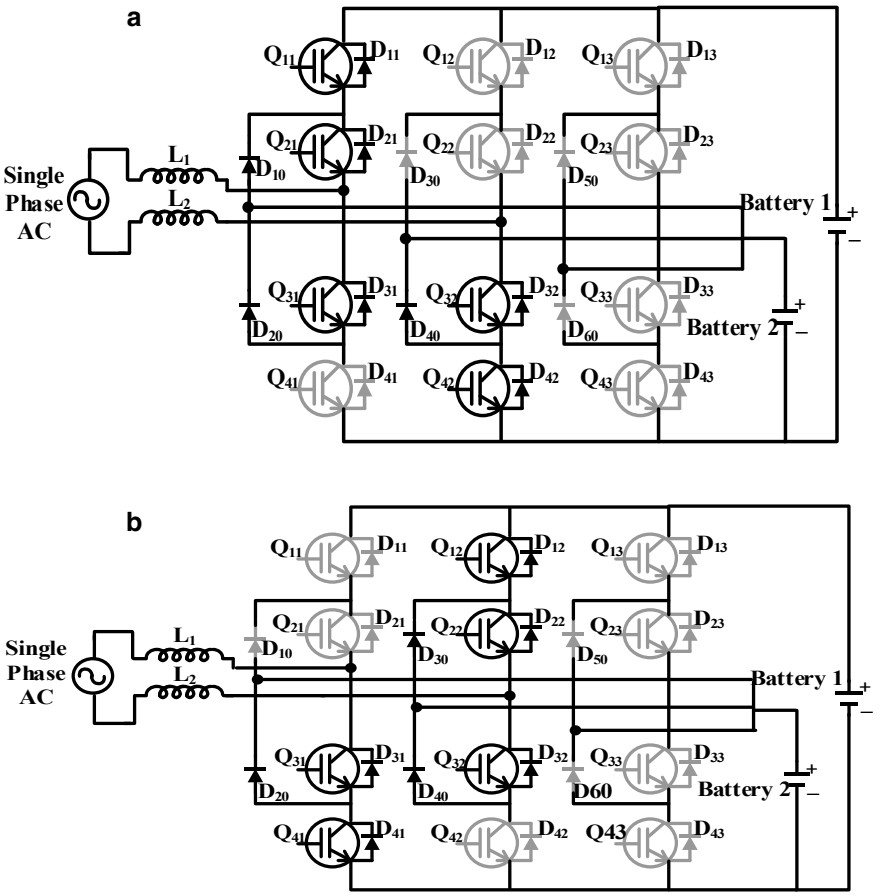

Fig. 2 **a** Operation of modified multi-source inverter during positive half cycle. **b** Operation of modified multi-source inverter during negative half cycle

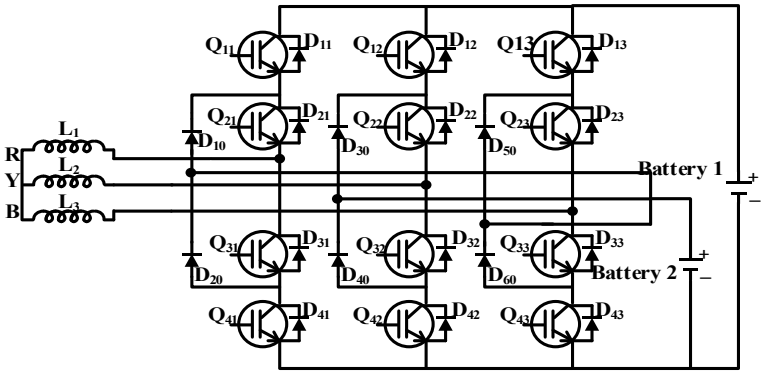

Fig. 3 Operation of modified multi-source inverter during discharging mode

rating of 200 V, 1.5 Ah and is induction motor specifications is shown in Table 1. Battery 1 has the voltage rating of approximately half the rating of battery 2 to obtain proper rectification of the input voltage. The main battery is charged till 80% and then the charging is disconnected. This is because, there may arise the condition for regenerative action during the motoring, the IM may act as generator. So, there is some buffer required for battery to charge beyond 80%. This may be special case for EVs. When EVs are started at the top of the slope, then the motor may get into regenerative mode. Figure 4 shows the charging of the battery 1 and battery 2. Battery 1 is charging faster compared to battery 2. Battery 2 is connected to the DC motor for validation purpose, and battery 1 is connected to the main motor of the EV.

The voltage and current waveforms during charging as well as discharging are shown in Fig. 5. The voltage waveform is obtained when only main battery 1 is used as a source for traction induction motor. During charging, the MSI acts as the rectifier and current in only two phases will flow in the stator windings out of three-phase stator windings. During discharging, all the three phases will be used for supplying current to the induction motor.

The current waveforms of each switch and diodes are shown in Fig. 6. It is observed for single cycle that the current across switch Q_{11} and Q_{21} is negative and current through Q_{31} is positive. No current will flow through Q_{41} during positive half cycle. The return path for the current is through Q_{32} and Q_{42}. During negative half cycle switch Q_{12} and Q_{22} have negative currents and switch Q_{31} and Q_{41} have negative current for return path. The current waveforms further depend upon the switching

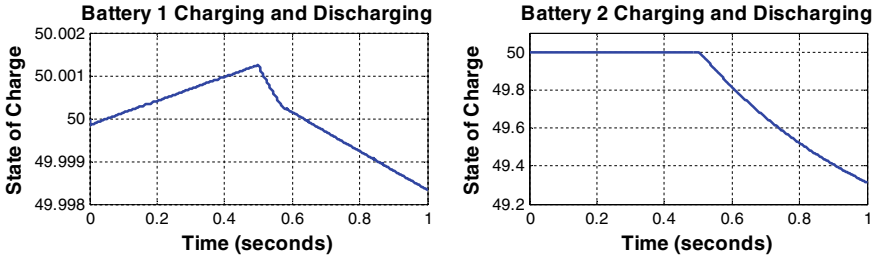

Fig. 4 Charging and discharging of battery 1 and battery 2

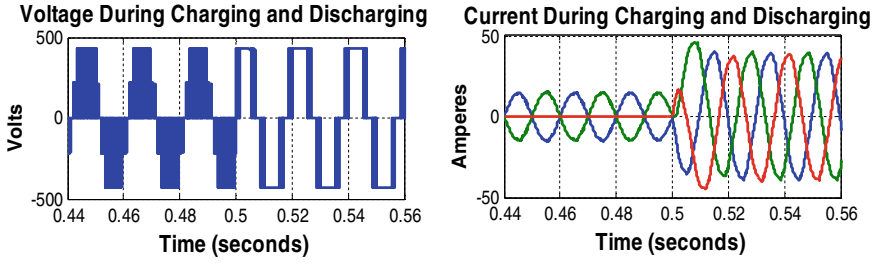

Fig. 5 Voltage and current during charging and discharging of batteries

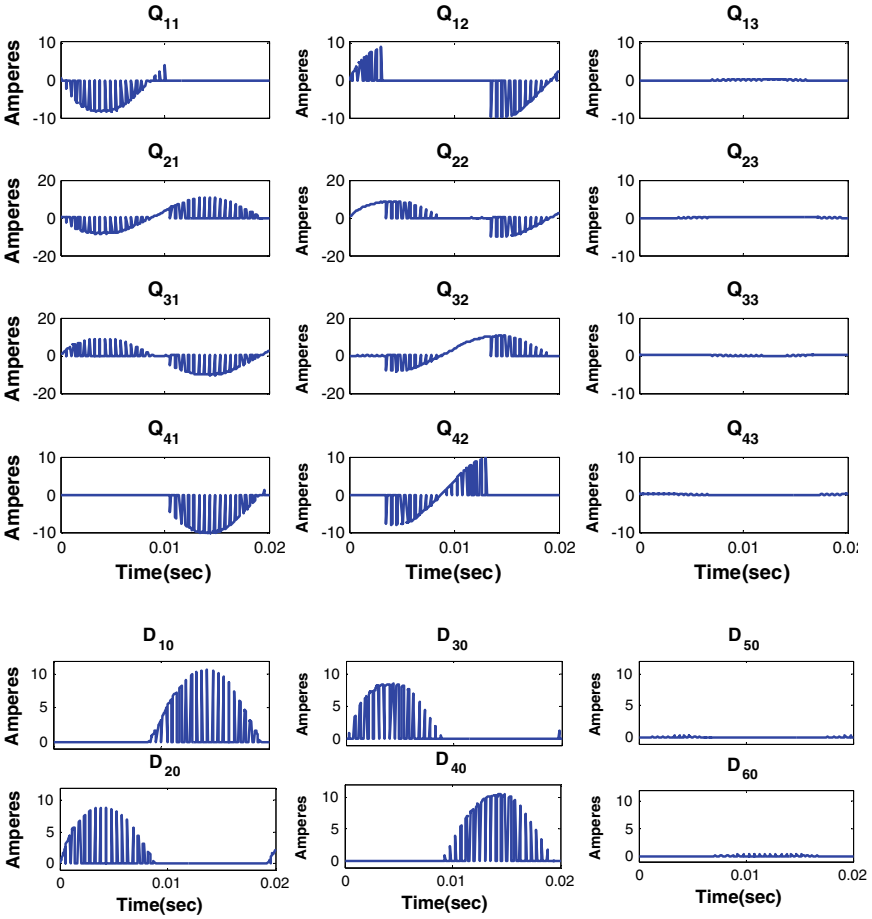

Fig. 6 Current waveforms across all the switches and diodes

method employed. During positive half cycle diode, D_{20} and D_{40} become forward biased and similarly during negative half cycle diode D_{20} and D_{30} becomes forward biased. Thus the battery is charging according to the proposed concept using single-phase level 1 supply. Third leg switches are not connected to the supply, so even though voltage appears across the switches, no current will flow through switch and the diode (Table 1).

$$m = (V_{\text{ref}})/((2/3) * V_{\text{dc}}) \tag{1}$$

$R_s = 0.435\ \Omega$, and $X_s = 1.25\ \Omega$, Angle $= 70.81°$.

During charging input power factor is 0.9755. During discharging, motor draws current with the power factor angle of 72.62° which is close to theoretical value of 70.81°. Figure 7 shows the currents and voltage waveforms during charging. To

Table 1 The specifications of the induction motor for validation are as follows

Parameter	Value
Power	33 HP
Voltage	400 V
Stator resistance	0.435 Ω
Stator inductor	4 mH
Rotor resistance	0.816 Ω
Rotor inductor	2 mH
Inertia	0.09 kg.m^2
Rated speed	2000 RPM

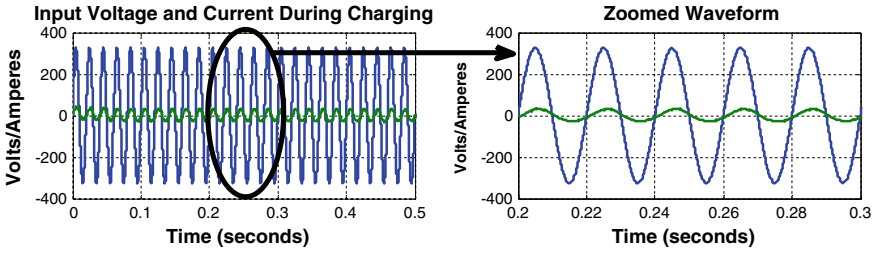

Fig. 7 Input voltage and current during charging

compare input voltage and current waveforms, current is increased to ten times than the actual value. THD for voltage and current during charging and discharging are summarized in Table 2 and is shown in Fig. 8.

The inverter efficiency comes out to be 88.97% at rated torque of 105 Nm. Figure 9 shows the running of the induction motor at 95 Nm torque, at 1900 rpm speed. By using single battery 1 no extra converter is required; the same MSI is used for running main traction motor. Figure 10 shows the variable torque operation of induction motor at constant speed. Figure 11 shows the variable speed for motor and motor tries to keep torque is constant. Command speed is kept at 1900 rpm and torque command is 70 Nm. Thus, a single battery directly used for controlling induction motor without using any other additional converter. The closed-loop control is obtained for SVPWM using Eq. 1 for the modulation index.

Table 2 THD for current and voltage is as shown below

Parameter	During changing (%)	During discharging (%)
Voltage	46.17	37.76
Current	2.33	2.68

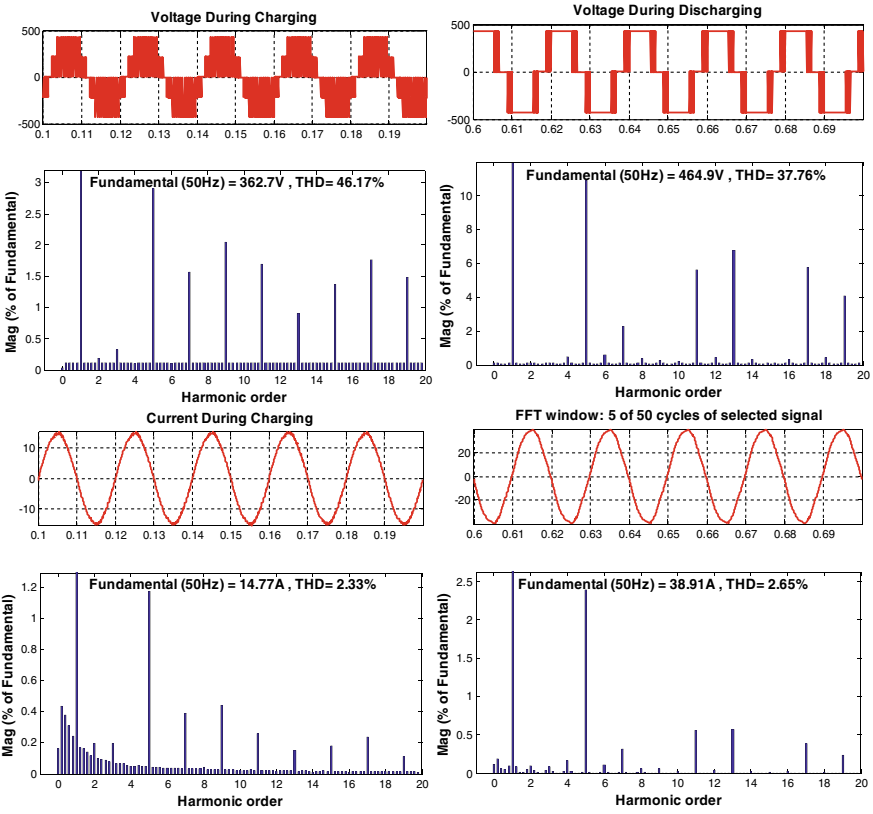

Fig. 8 Total harmonic distortion for voltage and current waveforms

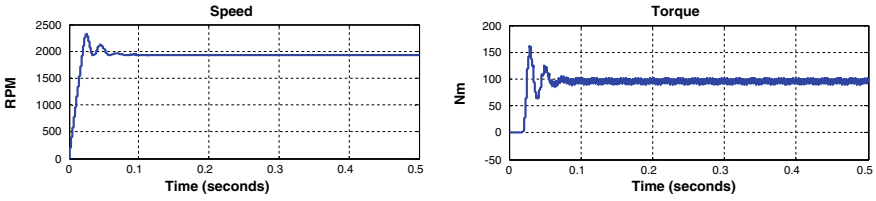

Fig. 9 Induction motor running at 95 Nm torque and at 1900 rpm

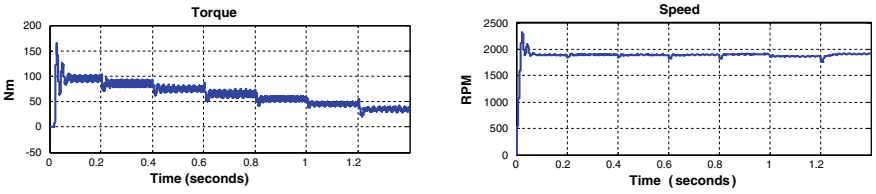

Fig. 10 Variable torque constant speed operation of induction motor

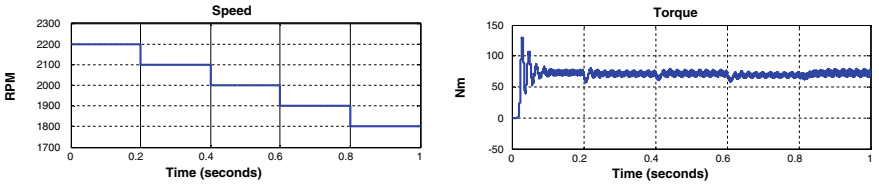

Fig. 11 Variable speed constant torque operation of induction motor

4 Conclusion

This paper discusses the novel multi-source inverter concept for the charging EVs having two batteries. The modified topology has been analyzed with the help of the voltage and current waveforms with neutral point clamped concept. The same charged batteries have been used to run induction motor under varied loading. Other battery has been used for applications in EVs.

The verification of this topology with the help of the MATLAB supports the hypothesis. The input charging current is obtained at nearly unity power factor. Then, the battery 1 is used directly to run induction motor of EV without extra DC–DC converters. The losses and control complexity is reduced as the number of converter is reduced. The traction motor is operated at various torque and speed operations. This concept has potential for further studies in fast charging using three-phase level 2 chargers as well as DC level 3 chargers for EV.

References

1. Majid P, Jain P (2020) Soft-switching power electronics technology for electric vehicles: a technology review. IEEE J Emerg Sel Top Ind Electron 1(1):80–90
2. Buddika D, Abeywardana W, Acuna P, Hredzak B, Aguilera R (2018) Single-phase boost inverter-based electric vehicle charger with integrated vehicle to grid reactive power compensation. IEEE Trans Power Electron 33(4):3462–3471
3. Sousa T, Hashemi S, Andersen P (2019) Raising the potential of a local market for the reactive power provision by electric vehicles in distribution grids. IET Gener Transm Distrib 13(12):2446–2454
4. Yilmaz M, Krein PT (2013) Review of the impact of vehicle-to-grid technologies on distribution systems and utility interfaces. IEEE Trans Power Electron 28(12):5673–5689
5. Sousa T, Hashemi S, Andersen PB (2019) Raising the potential of a local market for the reactive power provision by electric vehicles in distribution grids. IET Gener Transm Distrib 13(12):2446–2454
6. Janabi A, Wang B (2020) Switched-capacitor voltage boost converter for electric and hybrid electric vehicle drive. IEEE Trans Power Electron 35(6):5615–5624
7. Emadi A, Magne P (2014) Power converter. US Patent 0,117,770 A1 May 2014
8. Dorn-Gomba L, Magne P, Danen B, Emadi A (2018) On the concept of the multi-source inverter for hybrid electric vehicle powertrains. IEEE Trans Power Electron 33(9):7376–7386
9. Dorn-Gomba L, Guo J, Emadi A (2019) Multi-source inverter for power-split hybrid electric powertrains. IEEE Trans Veh Technol 68(7):6481–6494

10. Rippel WE (1990) Integrated traction inverter and battery charger apparatus. US Patent 4,920,475 April 1990
11. Rippel WE, Cocconi AG (1992) Integrated motor drive and recharge system. US Patent 5,099,186
12. Cocconi AG (1994) Combined motor drive and battery charger system. US Patent 5,341,075

Performance Analysis of a Transmission Network Under Wind Power and Load Demand Uncertainty Using Probabilistic Optimal Power Flow on DigSILENT Power Factory

Ravi Ucheniya, Amit Saraswat, Shahbaz Ahmed Siddiqui, and Sunil Kumar Goyal

Abstract With the continuous technical development in wind turbine technology, wind energy penetration and utilization have significantly increased. As a result, the uncertainty of wind energy is also rising in the power system. Under this situation, probabilistic optimal power flow plays a significant role to analyze uncertainties in power systems. In this paper, probabilistic analysis of the transmission networks under wind and load demand uncertainty has been prepared at the DigSILENT power factory. The total real power generation cost has been used as the target objective and solved using the interior point method. Results obtained during probabilistic analysis have been carried out.

Keywords Probabilistic optimal power flow · Quasi-Monte Carlo simulation · Interior point method · DigSILENT power factory

1 Introduction

The wind energy generated by the wind turbine depends directly on the wind speed. The variability in wind speed also makes wind energy production variable [1]. The ambiguity of wind energy generation affects the reliable and stable operation of the network [2]. By the way, effective and efficient optimization framework (optimal power flow) is available in the electricity market [3, 4] which are often used to optimize network operations as well as improve system reliability and stability. The primary goal of optimal power flow is to reduce the operational cost of the power grid by following all the limitations of the network. Due to the deterministic structure of the optimal power flow, it is unable to address the ambiguity of stochastic variables

R. Ucheniya · A. Saraswat (✉) · S. K. Goyal
Department of Electrical Engineering, Manipal University Jaipur, Jaipur, Rajasthan, India
e-mail: amit.saraswat@jaipur.manipal.edu

S. A. Siddiqui
Department of Mechatronics Engineering, Manipal University Jaipur, Jaipur, Rajasthan, India

S. Dwivedi et al. (eds.), *Flexible Electronics for Electric Vehicles*, Lecture Notes in Electrical Engineering 863, https://doi.org/10.1007/978-981-19-0588-9_22

directly. The probabilistic optimal power flow [5–8] is used to overcome the limitation of optimal power flow.

As a process of probabilistic analysis, specific experiments are often studied. In which, stochastic parameters are defined as random variables, and randomness follows a predefined probability distribution function. According to the random variable handling method, Monte Carlo simulation [5], Quasi-Monte Carlo simulation [6, 7], and the point estimate method [8] are well-known and frequently used procedures, which incorporate the uncertainty of the variables into the operation of the power system. Furthermore, power system modeling and simulation platforms play a significant role in the probabilistic analysis of power systems. The software industry has developed several modeling and simulation platforms to study the performance of power systems [9]. DigSILENT power factory is one of them. It is a software package for power system analysis covering a full range of standard and highly sophisticated applications [10].

In this paper, probabilistic analysis of transmission networks under wind and load demand uncertainty has been prepared at the DigSILENT power factory. The total real power generation cost has been used as the target objective and solved using the interior point method. The rest of the paper is as follows: modeling of uncertain parameters is presented in Sect. 2. Implementation of probabilistic optimal power flow at DigSILENT power factory is present in Sect. 3. Sections 4 and 5 consist of the simulation result and conclusion, respectively.

2 Modelling of Uncertain Parameters

In this study, wind speed and load demand have been considered uncertain parameters. The uncertainty of the uncertain parameters has expressed using the Weibull probability distribution function and the normal probability distribution function, respectively. The mathematical representation of both probability distribution function has adopted form [11]. The DigSILENT power factory has wide range of distribution function to incorporate uncertainty parameters, as shown in Fig. 1. Normal distribution function is select for load demand and Weibull distribution function (along with power curve of the wind turbine) is select for wind farm output.

3 Implementation of Probabilistic Optimal Power Flow

DigSILENT power factory has wide range of inbuilt functions to analyze the preformation of the power system network [10]. The popup window of probabilistic analysis is presented as shown in Fig. 2. The optimal power flow along with Quasi-Monte Carlo simulation is selected and set maximum number of samples on probabilistic analysis window. The execute button starts the probabilistic analysis and collect the samples.

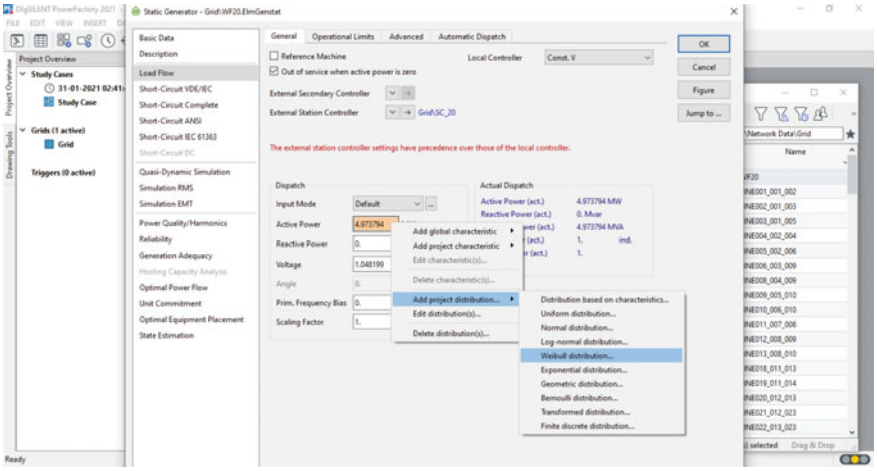

Fig. 1 Available probability distribution function on DigSILENT power factory

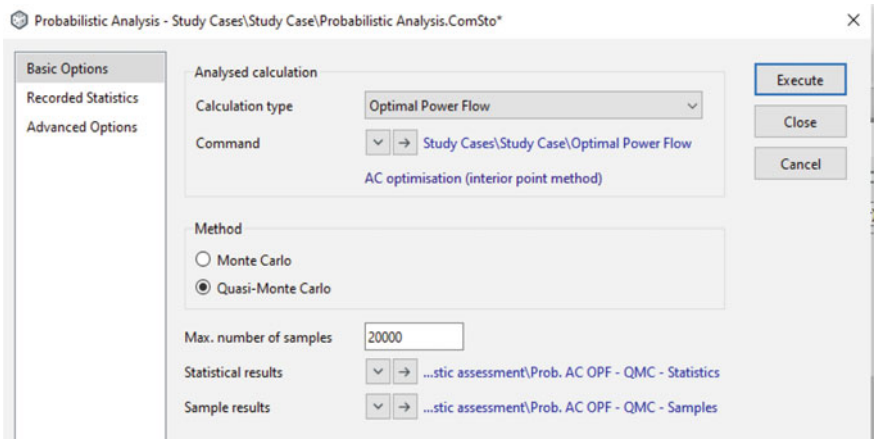

Fig. 2 The popup window of probabilistic analysis on DigSILENT power factory

4 Simulation Work

In this paper, IEEE 24 bus reliability test system along with 80 MW wind farm, has been used to simulate the probabilistic optimal power flow and Quasi-Monte Carlo Simulation is used to generate random samples. Total cost of the real power generation is considered as target objective. The realization process of both test system and wind farm is adopted from [12]. Under this study, total 20,000 samples are generated during process of probabilistic analysis out of which 11,016 samples are

successfully converge. The statistical analysis of the successfully converged samples has been carried out and is as follow.

The samples of load demand and wind speed generated during the probabilistic analysis are shown in Figs. 3 and 4, respectively. The effect of variation of both load demand and wind speed on the total cost of real power generation is shown in Fig. 5. Statistical analysis of the uncertain variables (load demand, wind speed, and wind power) and the target objective (total actual power generation costs) are presented in Table 1. Furthermore, statistical analysis of shunt compensation and transformer tap settings is presented in Table 2. Table 3 shows the real power output of the generators.

After observing the standard deviation (which is present in column 5 of Table 3), the generators are divided into two categories. Generators whose standard deviation is almost zero are placed in category one and generators whose standard deviation is greater than zero (as highlighted bold as shown in column 5 of Table 3) are placed in category two. From this bifurcation, it can be concluded that the operating point of the generators of category one is constant compared to the generators of category two and there is no effect of the variance of uncertain variables on their operating point. In other words, additional monitoring is needed on the operation of generators of category two.

Moreover, statistical analysis of the voltage profile of the network is presented in Table 4. According to the nature of the connecting element, the buses of the voltage profile are divided into two categories (see bottom of Table 4). The first category consists of the buses to which the generator is connected, and the remaining buses are placed in category two (as shown in column 1 of Table 4). Analysing the standard

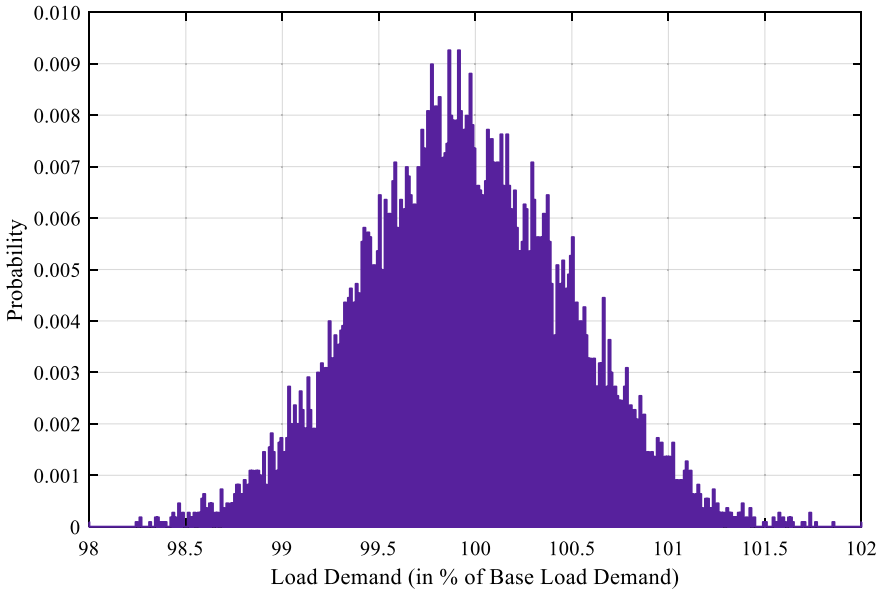

Fig. 3 Generated samples of the load demand

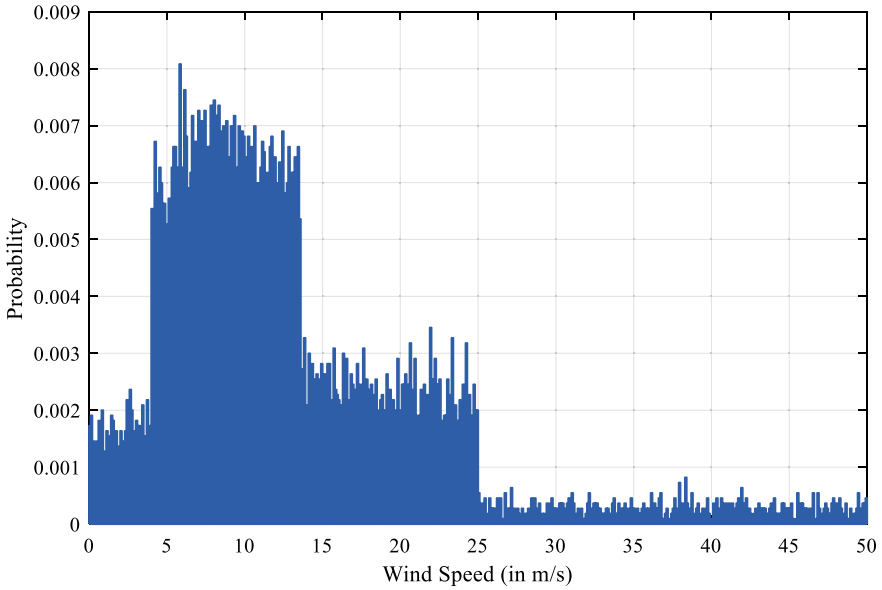

Fig. 4 Generated samples of the wind speed

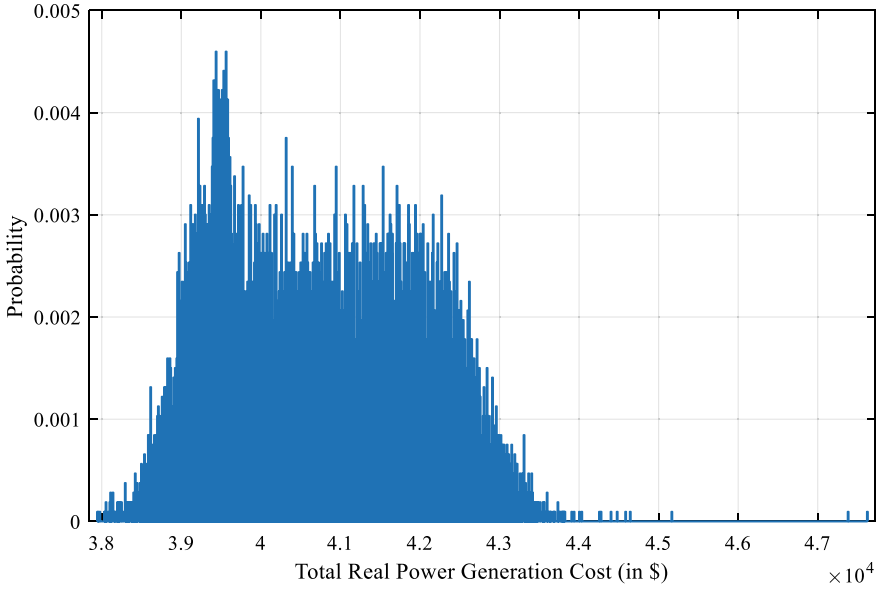

Fig. 5 Obtained value of total real power cost at generated samples of the load demand and wind speed

Table 1 Statistical analysis of uncertain variable and target objective

Variables	Mean	Minimum	Maximum	Standard deviation
Load demand (in %)	99.95	98.00	102.01	0.53
Wind speed (in m/s)	12.98	0.01	49.98	8.93
Wind power output (in %)	56.55	0.00	100.00	37.60
Real power cost generation (in $)	40,733.54	37,948.08	47,624.82	1236.05

Table 2 Statistical analysis of shunt compensation and transformer tap settings

Variables	Mean	Minimum	Maximum	Standard deviation
SH06 (in MVar)	−82.67	−200.00	0.00	14.41
TAP03_24	1.02	0.89	1.20	0.06
TAP09_11	1.08	0.82	1.12	0.04
TAP09_12	1.07	0.87	1.19	0.05
TAP10_11	1.03	0.89	1.20	0.04
TAP10_12	1.03	0.82	1.15	0.04

deviation of generator buses leads to the conclusion that the effect of variation on the voltage of bus 13 and bus 2 is minimum and maximum, respectively. Furthermore, analysing the standard deviation of the load buses leads to the conclusion that the effect of the variation on the voltage of bus 17 and bus 3 is minimal and maximum, respectively. Bus 2 (from generator bus range) and bus 3 (from load bus ranges) are highly sensitive to variations in uncertain variables.

5 Conclusion

The probabilistic analysis of transmission networks under wind and load demand uncertainty has efficiently done. The statistical result presented in Table 3 concludes that the variability of load demand and wind power affects the generators that belong to category two. Similarly, the statistical result of the voltage profile of the network presented in Table 4 concludes that bus 2 (from generator bus category) and bus 3 (from load bus category) are highly sensitive to the variability of uncertain variables. In light of the result analysis presented in Sect. 4, it can be said that probabilistic analysis proves to be very helpful in finding the units whose operation is most affected due to the uncertainty of uncertain parameters.

Table 3 Statistical analysis of real power output of the generators (in MW)

Variable	Mean	Minimum	Maximum	Standard deviation
PG01_01	0.00	0.00	0.00	0.00
PG01_02	0.00	0.00	0.00	0.00
PG01_03	76.00	75.98	76.00	0.00
PG01_04	76.00	75.98	76.00	0.00
PG02_01	0.00	0.00	0.00	0.00
PG02_02	0.00	0.00	0.00	0.00
PG02_03	**75.96**	**15.14**	**76.00**	**1.43**
PG02_04	**75.96**	**15.14**	**76.00**	**1.43**
PG07_01	**79.77**	**65.17**	**100.00**	**2.38**
PG07_02	**79.77**	**65.17**	**100.00**	**2.38**
PG07_03	**79.77**	**65.17**	**100.00**	**2.38**
PG13_01	**240.91**	**207.00**	**462.19**	**30.20**
PG14_01	0.00	0.00	0.00	0.00
PG15_01	0.00	0.00	0.00	0.00
PG15_02	0.00	0.00	0.00	0.00
PG15_03	0.00	0.00	0.00	0.00
PG15_04	0.00	0.00	0.00	0.00
PG15_05	0.00	0.00	0.00	0.00
PG15_06	155.00	155.00	155.00	0.00
PG16_01	155.00	155.00	155.00	0.00
PG18_01	400.00	399.99	400.00	0.00
PG21_01	**399.88**	**126.61**	**400.00**	**4.37**
PG22_01	50.00	50.00	50.00	0.00
PG22_02	50.00	50.00	50.00	0.00
PG22_03	50.00	50.00	50.00	0.00
PG22_04	50.00	50.00	50.00	0.00
PG22_05	50.00	50.00	50.00	0.00
PG22_06	50.00	50.00	50.00	0.00
PG23_01	155.00	154.99	155.00	0.00
PG23_02	155.00	154.99	155.00	0.00
PG23_03	**349.94**	**227.63**	**350.00**	**2.04**

Table 4 Statistical analysis of bus voltage (in p. u.)

Category	Bus	Mean	Minimum	Maximum	Standard deviation
Generator bus	V_{01}[a]	1.0348	0.9545	1.0500	0.0159
	V_{02}[a]	1.0348	0.9536	1.0500	0.0159
	V_{07}[a]	1.0420	0.9500	1.0500	0.0131
	V_{13}[a]	0.9813	0.9813	0.9813	0.0000
	V_{14}[a]	1.0193	0.9624	1.0500	0.0056
	V_{15}[a]	1.0321	0.9876	1.0466	0.0043
	V_{16}[a]	1.0343	0.9992	1.0481	0.0035
	V_{18}[a]	1.0499	1.0153	1.0500	0.0006
	V_{20}[a]	1.0324	0.9907	1.0478	0.0054
	V_{21}[a]	1.0500	1.0161	1.0500	0.0006
	V_{22}[a]	1.0500	1.0373	1.0500	0.0001
	V_{23}[a]	1.0343	0.9855	1.0500	0.0050
Load bus	V_{03}[b]	0.9991	0.9500	1.0487	0.0269
	V_{04}[b]	1.0072	0.9500	1.0318	0.0206
	V_{05}[b]	1.0194	0.9527	1.0378	0.0166
	V_{06}[b]	1.0222	0.9500	1.0500	0.0167
	V_{08}[b]	1.0068	0.9500	1.0232	0.0155
	V_{09}[b]	1.0180	0.9500	1.0500	0.0250
	V_{10}[b]	1.0300	0.9500	1.0500	0.0193
	V_{11}[b]	0.9847	0.9500	1.0248	0.0095
	V_{12}[b]	0.9785	0.9500	1.0238	0.0097
	V_{17}[b]	1.0443	1.0110	1.0493	0.0013
	V_{19}[b]	1.0280	0.9972	1.0408	0.0043
	V_{24}[b]	0.9977	0.9500	1.0429	0.0164

[a] Generator bus; [b] Load bus

References

1. Gupta Y, Saraswat A (2021) Machine learning techniques for short-term forecasting of wind power generation. In: Hassanien A, Bhatnagar R, Darwish A (eds) Advanced machine learning technologies and applications. AMLTA 2020. Advances in intelligent systems and computing, vol 1141. Springer, Singapore, pp 439–448
2. Saraswat A, Ucheniya R, Gupta Y (2020) Two-stage stochastic optimization for reactive power dispatch with wind power uncertainties. In: 2020 international conference on computation, automation and knowledge management (ICCAKM). IEEE, pp 332–337
3. Ferreira JS, de Oliveira EJ, de Paula AN, de Oliveira LW, Passos Filho JA (2021) Optimal power flow with security operation region. Int J Electr Power Energy Syst 124:106272
4. Naderi E, Pourakbari-Kasmaei M, Cerna FV, Lehtonen M (2021) A novel hybrid self-adaptive heuristic algorithm to handle single- and multi-objective optimal power flow problems. Int J Electr Power Energy Syst 125:106492

5. Pareek P, Nguyen HD (2021) Gaussian process learning-based probabilistic optimal power flow. IEEE Trans Power Syst 36:541–544
6. Sun W, Zamani M, Zhang H-T, Li Y (2019) Probabilistic optimal power flow with correlated wind power uncertainty via Markov chain quasi-monte-Carlo sampling. IEEE Trans Ind Inform 15:6058–6069
7. Xie ZQ, Ji TY, Li MS, Wu QH (2018) Quasi-monte Carlo based probabilistic optimal power flow considering the correlation of wind speeds using copula function. IEEE Trans Power Syst 33:2239–2247
8. Chen Y, Guo Z, Li H, Yang Y, Tadie AT, Wang G, Hou Y (2020) Probabilistic optimal power flow for day-ahead dispatching of power systems with high-proportion renewable power sources. Sustainability 12:518
9. Ringkjøb H-K, Haugan PM, Solbrekke IM (2018) A review of modelling tools for energy and electricity systems with large shares of variable renewables. Renew Sustain Energy Rev 96:440–459
10. GmbH, DIgSILENT (2021) DIgSILENT power factory V2021—user manual. DIgSILENT GmbH, Gomaringen, Germany
11. Ucheniya R, Saraswat A, Siddiqui SA (2020) Decision making under wind power generation and load demand uncertainties: a two-stage stochastic optimal reactive power dispatch problem. Int J Model Simul 1–16
12. Ucheniya R, Saraswat A, Siddiqui SA, Goyal SK, Kanwar N (2020) A wind farm modeling in IEEE-24 bus reliability test system on DIgSILENT power factory. In: 2020 international conference on intelligent engineering and management (ICIEM). IEEE, pp 477–483

Image Transliteration from Vernacular Languages

Yogesh Gupta, Amit Saraswat, and Ghanshyam Raghuwanshi

Abstract India is a multi-cultured and multi-language country, which has 23 official languages, and Hindi is known as the mother language as most of the people speak Hindi here. This paper implements a model which can extract text from images and then transliterates the text written from Indic language (Hindi) to English language. It presents distinctive issues of various text styles and patterns, comparability in structure. Therefore, it is essential to discover viable techniques for text extraction. It can be useful for a tourist to easily read the signboards or names of shops in North India as the focus of this work is to work on Hindi language. A great deal of enhancements has been made in the field deep learning and natural learning processing. This paper implements text extraction and transliteration in an efficient manner by using approaches which provide accurate results. Google Vision API and natural language processing have been used for text extraction and performing transliteration, respectively, in this paper.

Keywords Transliteration · Image · Text · Encoder · Decoder

Y. Gupta
Department of Computer Science, BML Munjal University, Gurugram, India

A. Saraswat (✉)
Department of Electrical Engineering, Manipal University Jaipur, Jaipur, Rajasthan, India
e-mail: amit.saraswat@jaipur.manipal.edu

G. Raghuwanshi
Department of Computer and Communication Engineering, Manipal University Jaipur, Jaipur, Rajasthan, India
e-mail: ghanshyam.raghuwanshi@jaipur.manipal.edu

S. Dwivedi et al. (eds.), *Flexible Electronics for Electric Vehicles*, Lecture Notes in Electrical Engineering 863, https://doi.org/10.1007/978-981-19-0588-9_23

1 Introduction

Every year approximately six million tourists visit India, and it is projected that it will be double in coming years. When they visit any place here, they usually face problems to understand the information presented in a vernacular language as printed on signboards, nameplates, hoarding boards, etc. Therefore, an image transliterator is needed which can help among tourists. Innovation and technology have always been there to ease human beings with their tasks and daily chores. In the connection of this problem, this paper provides a solution which helps tourists in reading the signboards and the menu at the restaurant with the use of technology.

An object detection is a major challenge in the field of computer vision, and it has gotten extraordinary consideration as of late. With regard to computer vision, object detection focuses on detecting the various instances considering as visual objects belonging to specific classes. These classes are humans, animals and texts of different languages in digital images. Problem when considered as object detection is for the most part taken care of in two steps. First is the recognition of word, and second is the process to get the characters. In computer vision, for an example of a given image as shown in Fig. 1, the system should be able to cull-out the regions with text and use them for further processing. There are a wide range of techniques for text detection like stroke width transform (SWT) and maximally stable extremal regions (MSER). A way to deal with the problem of text extraction from the digital image is integrated using Google Vision API, which provides strong pre-trained models through REST and RPC APIs. It classifies the images into lots of already defined groups. This API can help in detecting faces, text, and build valuable metadata.

Now, the extracted text will be used for transliteration. Transliteration is little bit different from translation. In translation, script of one language is converted into the script of second language. While transliteration converts text from one script to another script, it involves swapping of letters. Transliteration is primarily concerned with representing the characters, ideally accurately and unambiguously. To deal with transliteration tasks, a traditional natural language processing (NLP)-based solution is used that includes deep learning sequential models like RNN. Google presented

Fig. 1 Text detected from an image

sequence model for the very first time in 2014. It represents input of fixed length into output of fixed length, where length of input and output may differ. Sequence models have a wide range of applications like machine translation, speech recognition and video captioning.

2 Literature Review

The existing work reported in literature is described in this section. Mathew et al. [1] demonstrated the recognition of scene text in three different languages such as Devanagari, Malayalam and Telugu. Authors used deep neural network, i.e., CNN–RNN for transliterating the word images to the corresponding texts. First, cropped word images are segmented into the sub-word units, and the network is trained using CTC loss. They evaluated the performance on various parameters like character recognition rate and word recognition rate. Rosca and Breuel worked on Arabic and English language using Epsilon insertion method and attention sequence-to-sequence model [2]. Busta et al. [3] presented an approach for scene text localization and recognition using CNN. Shi et al. explored the challenges for text recognition from scenes [4]. They applied neural network model to incorporate feature extraction process, transcription process and sequence modeling process. Wang et al. [5] presented an approach for representing the scene text with the help of end-to-end learning scheme. They used instance transformation network to train the representation of scene text instances based on transformation embedding.

Deng et al. [6] proposed a method to detect scene text via instance segmentation as text instances in scene images. They used PixelLink as scene text detection algorithm in their work. In this work, authors only worked on English script. Tounsi et al. [7] used bag of features (BoF) to recognize scene characters. They applied deep learning to represent features for accurate SCR of different languages. Bhunia et al. [8] demonstrated a method for text recognition using color channel selection based on hidden Markov model. The proposed approach analyzed the image properties from the sliding window of a color channel, and then they applied improved version of support vector machine to select the color channel.

3 Methodology

The detailed methodology used in this work is shown in Fig. 2. First the image is captured and classified into text and no-text classes. Then after, detection is done to locate bounding box. Further, extraction is performed, which extracts the text from the image followed by the recognition process. The recognition process identifies the written text and translated into English.

To perform all above-mentioned steps, a transliteration corpus is collected from GitHub. This data contained English sentences along with its Hindi transliterated text.

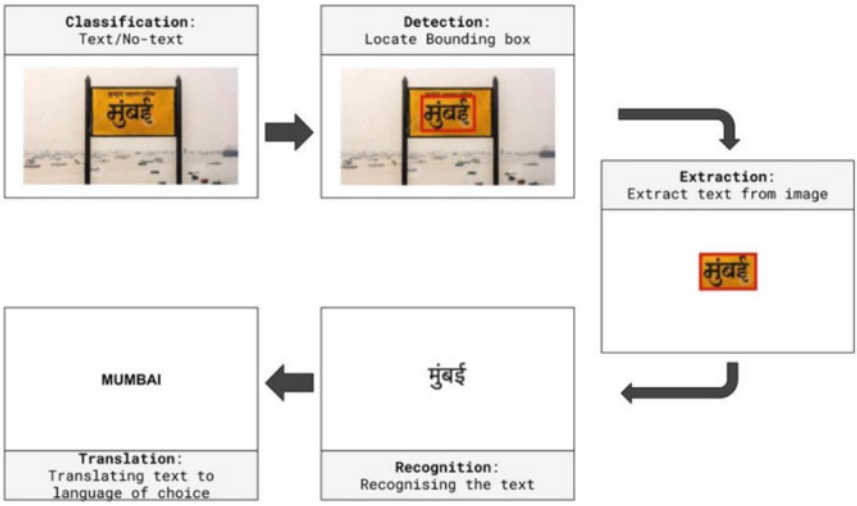

Fig. 2 Methodology used in the work

There was some noisy data where the length of English word list was not equal to the Hindi word list. Then, Seq2Seq model or encoder–decoder model is implemented. The working of encoder–decoder is explained in Fig. 3.

The encoder–decoder sequence model consists of following three essential parts:

1. Encoder: A stack of several RNNs, in which each RNN takes one sequence as input element, processes it and proliferates it further.
2. Encoder vector: Encoder produces the encoder vector as final state of the model. It comprises all knowledge related to input sequence. This is used as the initial hidden state for decoder.
3. Decoder: The output of hidden state is fed to decoder, and it produces an output.

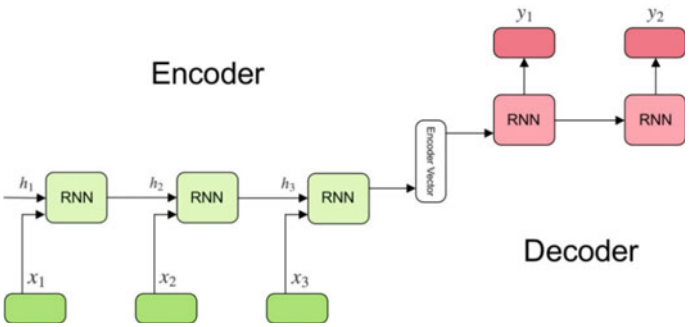

Fig. 3 Encoder–decoder model

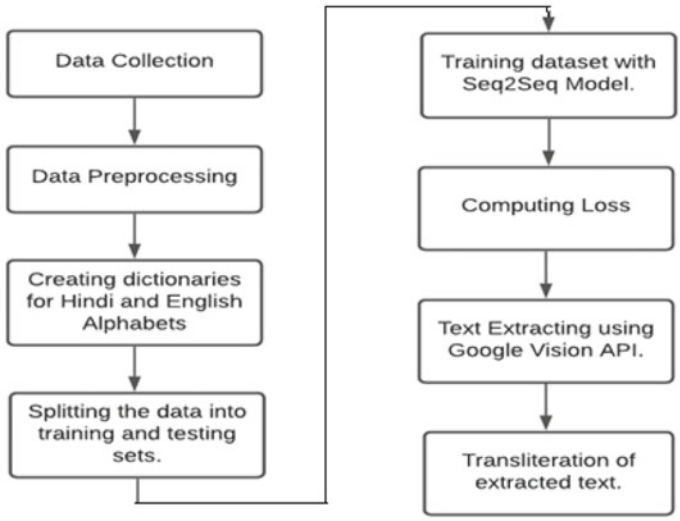

Fig. 4 Block diagram of used methodology

The encoder reads the input sequence and gives a single vector as output, and the decoder reads that single vector and generates the sequence. The methodology used in this work can be understood from Fig. 4, which contains the following steps:

a. Extract the Hindi text from the photo using Google Vision API.
b. Import all the required libraries.
c. Extract the data by the xml file using ReadXml data set function.
d. Remove the noisy data.
e. Make a dictionary of Hindi and English alphabets to assign them an index.
f. Splitting the data into training and testing sets.
g. Applying the model on the training data and computing the loss.
h. Generating the transliterated text of test data, text extracted using Google Vision API, and some custom user's input.

4 Experimental Results and Analysis

In this work, Python, Google, Google Colaboratory and Google Vision API have been used for experiments. For example, the image given in Fig. 5 is supplied to Google Vision API, and text is extracted from it as shown in Fig. 6. Then after, data is preprocessed, and the results are presented in Fig. 7. This data is used for transliterations. The experimental results are shown in Fig. 8.

Fig. 5 Input image to extract text from

```
for i in range(len(w)):
  # print(len(w[i]))
  if translator.detect(w[i]).lang == 'hi':
    print(w[i])
```

जनपथ
मार्केट

Fig. 6 Output obtained by extracting the text from image

5 Conclusion

A new methodology is used in this paper, which proposed to utilize Google Vision API for text extraction because of its favorable circumstances. We have used it to settle the genuine issue of tourists to read the signboards in real time. As a future work, we have planned to integrate this into an app for better usability. The tourists will be able to visit more places and explore them more in a better way using our app. This work can be further scaled by including more languages so that it could be used worldwide.

```
Skipping:  BARHARWA JUNCTION  -  बरहरवा
Skipping:  STATE BNK TR  -  स्टेट बैंक ऑफ त्रावणकोर
Skipping:  SOUTH ARLINGTON CHURCH OF CHRIST  -  साउथ अर्लिंग्टन
Skipping:  KING EDWARD VII  -  किंग एडवर्ड
Skipping:  DIBANG VALLEY  -  दिबंगवैली
Skipping:  ORDER OF VASA  -  ऑडर ऑफ़ द वासा
Skipping:  AZAMNAGAR ROAD  -  आज़मनगर
Skipping:  CAPE TOWN  -  केपटाउन
Skipping:  NEW ZEALAND  -  न्यूज़ीलैंड
Skipping:  SEA OF THE HEBRIDES  -  सी ऑफ हरब्रिड्स
Skipping:  RAMCOIND  -  राम्को इंड
Skipping:  KELVINGROVE ART GALLERY AND MUSEUM  -  केल्विनग्रोव आर्ट एण्ड म्युज़ियम
Skipping:  AUSTRALIAN NATIONAL UNIVERSITY  -  ऑस्ट्रेलियननेशनल यूनिवर्सिटी
Skipping:  JAHAN AARA  -  जहाँआरा
Skipping:  NAVABHARAT FERRO ALLOYS  -  नव भारत फ़ेरो अलॉय
Skipping:  RAMA LINGESHWARA  -  रामालिंगेश्वर
Skipping:  FAKHRUN NISA  -  फखरुन्निसा
Skipping:  REDIFF.COM INDIA LIMITED  -  रेडिफ़ डॉट कॉम इंडिया लिमिटेड
Skipping:  OMKARNATH THAKUR  -  ओंकार नाथ ठाकुर
Skipping:  OPENTV  -  ओपन टीवी
Skipping:  ENVOY COMMUNICATIONS GROUP  -  एन्वॉय कम्युनिकेशंस
Skipping:  WAR OF THE HOLY LEAGUE  -  वार ऑफ होली लीग
Skipping:  VAPARAISO CHURCH OF CHRIST  -  व्हापरासिओ
Skipping:  PARIS CHARLES DE GAULLE  -  पेरिस रॉसे चार्ल्स डे ग्यूले
Skipping:  PARKWAY APOSTOLIC  -  पार्क वे अपोस्टोलिक
Skipping:  MAUNA LOA  -  मौनालोआ
Skipping:  MASS MUTUAL LIFE  -  मास म्युच्युअल लाइफ़ इंश्योरेंस
Skipping:  STATS CHIPPAC  -  स्टेट्सचिपपैक
Skipping:  NEWFOUNDLAND  -  न्यू फाउंडलैंड
Skipping:  LONDONHEATHROW  -  लंदन हीथ्रो
Skipping:  RETALIX  -  रेटालिक्स लि.
Skipping:  SRISAILAM  -  श्री शैलम
```

Fig. 7 After preprocessing data

Fig. 8 Tensors of word in Hindi and English

```
KAMYAB कामयाब
Hindi representation tensor([[23],
        [64],
        [48],
        [49],
        [64],
        [46],
        [ 1]])
English representation tensor([[12],
        [ 2],
        [14],
        [26],
        [ 2],
        [ 3],
        [ 1]])
```

References

1. Mathew M, Jain M, Jawahar CV (2017) Benchmarking scene text recognition in Devanagari, Telugu and Malayalam. In: 14th IAPR international conference on document analysis and recognition
2. Rosca M, Breuel T (2016) Sequence-to-sequence neural network models for transliteration. Computation and Language
3. Busta M, Neumann L, Matas J (2017) Deep textspotter: an end-to-end trainable scene text localization and recognition framework. In: Proceedings of the IEEE international conference on computer vision, pp 2204–2212
4. Shi B, Bai X, Yao C (2016) An end-to-end trainable neural network for image-based sequence recognition and its application to scene text recognition. IEEE Trans Pattern Anal Mach Intell 39(11):2298–2304
5. Wang F, Zhao L, Li X, Wang X, Tao D (2018) Geometry-aware scene text detection with instance transformation network. In: Proceedings of the IEEE conference on computer vision and pattern recognition, pp 1381–1389
6. Deng D, Liu H, Li X, Cai D (2018) Pixellink: detecting scene text via instance segmentation. Computer Vision and Pattern Recognition
7. Tounsi M, Moalla I, Lebourgeois F, Alimi AM (2018) Multilingual scene character recognition system using sparse auto-encoder for efficient local features representation in bag of features
8. Bhunia AK, Kumar G, Roy PP, Balasubramanian R, Pal U (2018) Text recognition in scene image and video frame using color channel selection. Multimedia Tools Appl 77(7):8551–8678

A UWB Antenna with Circular Polarization Characteristics for Wireless Communications

Aakash Yadav, Madhuri Sahal, Dinesh Yadav, and Deepika Bansal

Abstract The present communication is design and investigation of the performance of a UWB antenna having circular polarization characteristics. The antenna uses low cost and readily available glass epoxy substrate having thickness 1.6 mm and dimensions 40 × 40 mm^2. The circular polarized antenna design in this work is very simple. It consists of an annular circular patch fed by strip line feed with another circular patch connected to the annular patch using a stub inclined at 225º with respect to *x*-axis. The antenna exhibits circular polarization over the frequencies 8.1–8.8 GHz, and good polarization purity. An axial ratio of 0.5 is attained at 8.4 GHz. The return loss characteristics of the antenna demonstrate a −10 dB impedance bandwidth from 2.48–10.94 GHz.

Keywords Ultrawideband · Axial ratio · Circular polarized · Wireless · Single-feed

1 Introduction

Circular polarized (CP) antennas have recently gained a lot of importance for different wireless applications as they offer multiple advantages over the linear polarized antennas. Circular polarized antennas have need not be precisely aligned for signal reception, and they are robust to Faraday rotation issues. They allow for communication in multipath fading scenario and absence of line-of-sight path between transmit and receive antenna. They permit signal reception even if the link is degraded due to adverse weather like rain or snow.

Planar circular polarized antennas are used extensively in different portable wireless devices as they offer multitude of advantages including compact size, low profile, easy fabrication, and integration in compact wireless devices.

A. Yadav · M. Sahal (✉) · D. Yadav · D. Bansal
Department of ECE, Manipal University Jaipur, Jaipur, Rajasthan, India
e-mail: madhuri.sahal@jaipur.manipal.edu

S. Dwivedi et al. (eds.), *Flexible Electronics for Electric Vehicles*, Lecture Notes in Electrical Engineering 863, https://doi.org/10.1007/978-981-19-0588-9_24

Different techniques for generating circular polarized characteristics have been studied in recent decades for generating circular polarized radiation. Several techniques for generating CP are available in literature including chamfering corners of square patch, loading slits to perturb the current distribution for the orthogonal modes [1]. Some of the recent works have proposed circular polarization generation using an asymmetric cross-slot antenna excited with a strip line [2], a square antenna loaded with asymmetrical triangular slits along the diagonals [3], a square antenna loaded with asymmetric length square slot along the diagonals [4], circular annular microstrip antenna fed using dual *L*-shaped probe feeds [5], current perturbation on the edges of patch antenna [6], a circular-slot integrated antenna excited using an offset square shaped monopole [7], circular patch antenna integrated with *e*-shaped slot [8].

In this work, an ultrawideband antenna with circular polarization characteristics in 700 MHz over the frequencies 8.1–8.8 GHz is proposed. The UWB antenna is a circular-shaped annular monopole loaded with a circular stub in the center at an angle of 45° with the vertical to obtain circular polarized radiation. The antenna exhibits impedance matching over the wide frequency range 2.48–10.95 GHz. The antenna dimensions are $40 \times 40 \times 1.6$ mm^3. The antenna exhibits a peak gain of 2.68 dBic at 9.5 GHz. The design of ultrawideband antenna with CP characteristics proposed here is very simple and uses the economical glass–epoxy substrate.

2 Antenna Design

2.1 Design Configuration

The antenna proposed in this work is a monopole designed on a 40×40 mm^2 substrate with permittivity 4.4 (Figs. 1 and 2). The antenna design and simulations are carried out in CST Microwave studio and a series of parametric optimizations are carried to obtain the final dimensions as listed in Table 1.

The reference antenna in step 1 is a circular monopole operating over the UWB band (Fig. 3). The antenna is linearly polarized due to symmetrical current distribution in the ground plane. The next step is introduction of a central slot of radius 7 mm as illustrated in Fig. 2, and introduction of a rectangular centrally placed notch in the antenna ground. The antenna in step 2 is also linearly polarized. The antenna feed is made to be asymmetrical in step 3. Though this leads to lowering of axial ratio but still the axial ratio is greater than 9 dB as in Fig. 4 indicating linear polarization. For circular polarization in the 8 GHz band, a circular stub inductively coupled to the annular monopole using a strip of dimensions 2.7×1.4 mm^2 is introduced. The effect of the circular stub inclined at 45° with the vertical on axial ratio is depicted in Fig. 4.

The surface current of the proposed UWB antenna at 8.4 GHz is indicated in Fig. 5, the vectors indicating the magnitude of current. The rotation sense of the

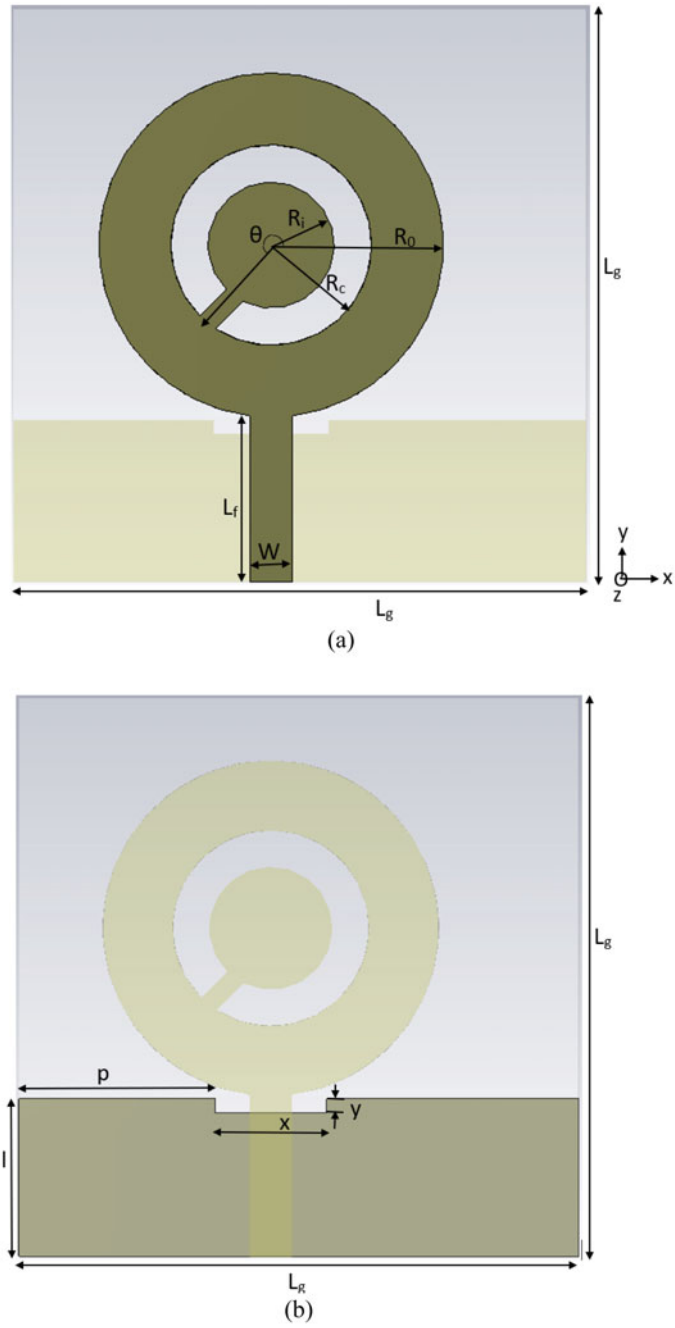

Fig. 1 Proposed UWB monopole antenna design: **a** top view of geometry, **b** bottom view of geometry

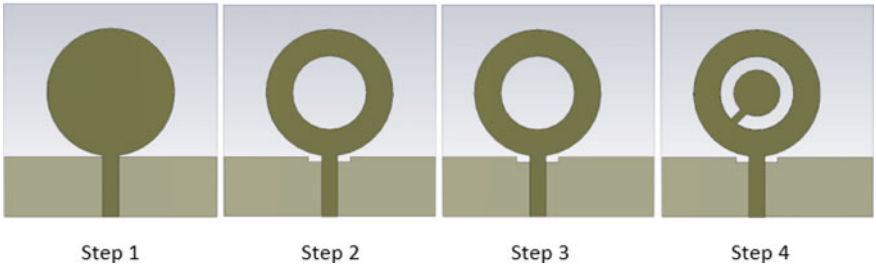

Fig. 2 Evolution of the final design from the reference circular monopole

Table 1 Optimized antenna dimensions

Parameter	Value (mm)	Parameter	Value (mm)
L_g	40	W_f	3
R_o	12	l	11.3
R_i	4.4	p	14
R_c	7	x	8
L_f	11.6	y	1

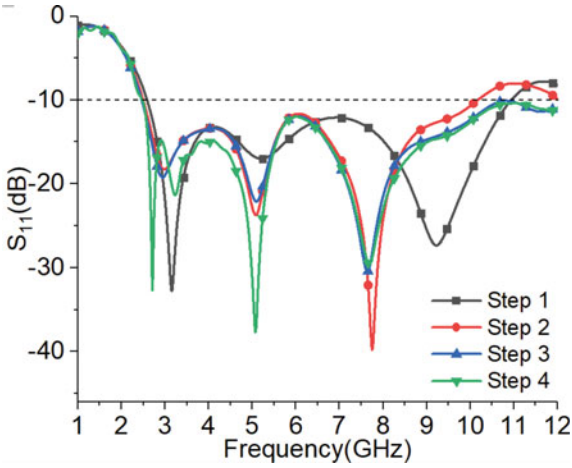

Fig. 3 Reflection coefficient for different steps

current indicates Left hand CP radiation in z direction.

3 Results and Discussion

The return loss coefficients and axial ratio curve of the proposed UWB antenna (Figs. 6 and 7) with CP indicate an impedance bandwidth of 8.46 GHz (2.48–

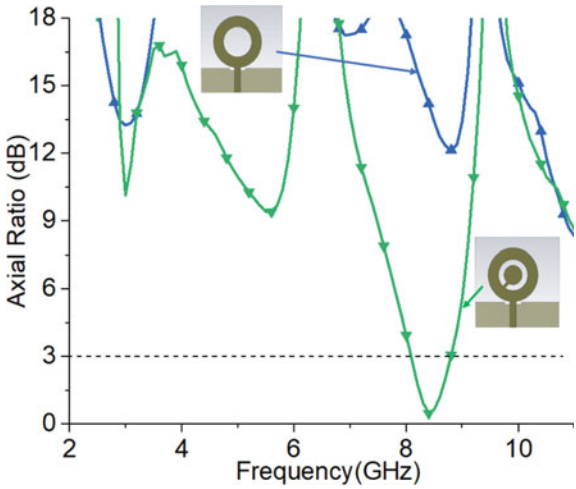

Fig. 4 Effect of circular stub on axial ratio characteristics

10.94 GHz) and axial ratio bandwidth of 700 MHz (8.1–8.8 GHz), respectively. The axial ratio and gain in boresight direction depict a peak simulated gain of 2.68 dBic at 9.5 GHz, whereas the minimum value of axial ratio is 0.5 dB at 8.4 GHz indicating good cross-polar discrimination at the given frequency. The 3 dB gain beamwidth at 8.4 GHz are 107.9º and 127.6º in the phi 0 and phi 90 planes, respectively, and the main lobe directions are 120º and −115º in phi 90 and phi 0 planes, respectively (Fig. 8). The performance of present work is compared with few published works in Table 2.

4 Conclusion

The paper includes the sequential design procedure for the proposed UWB antenna having substrate volume $40 \times 40 \times 1.6\ mm^3$. The antenna is single-fed, compact and circular polarized over 700 MHz, therefore easily integrable into portable wireless devices. The antenna can also be designed on a flexible substrate like PET substrate, this would provide further compactness to the device.

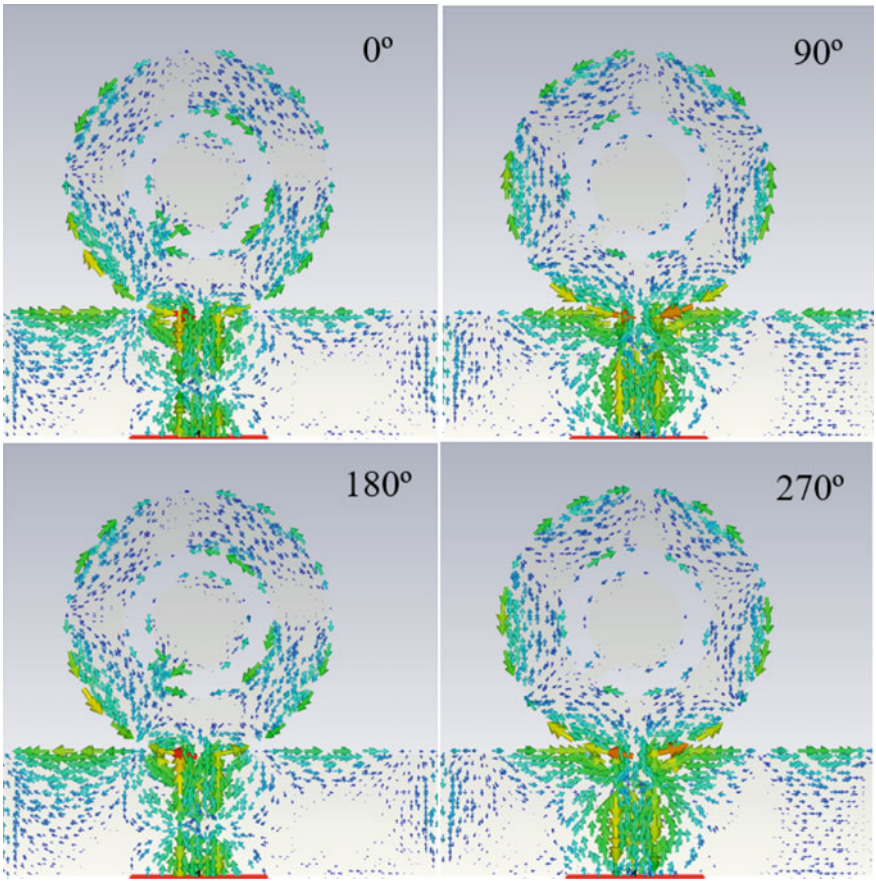

Fig. 5 Surface current of proposed UWB antenna at 8.4 GHz

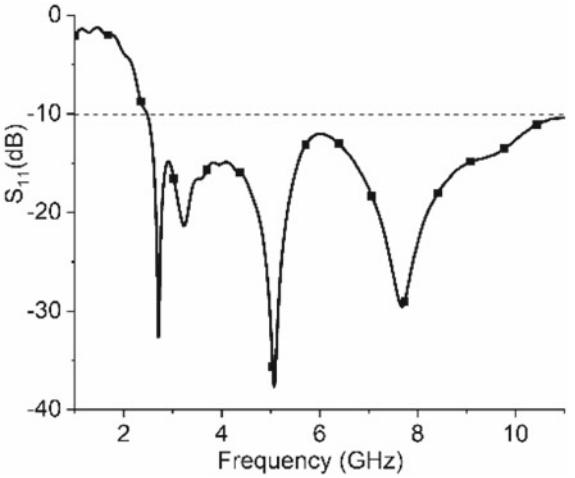

Fig. 6 Simulated return loss coefficients of proposed UWB antenna

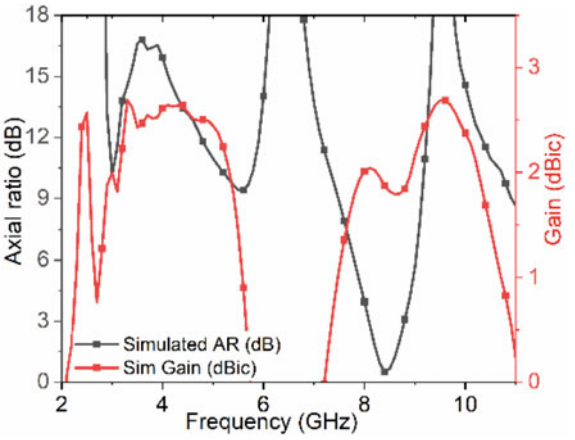

Fig. 7 Simulated axial ratio and boresight gain of proposed UWB antenna

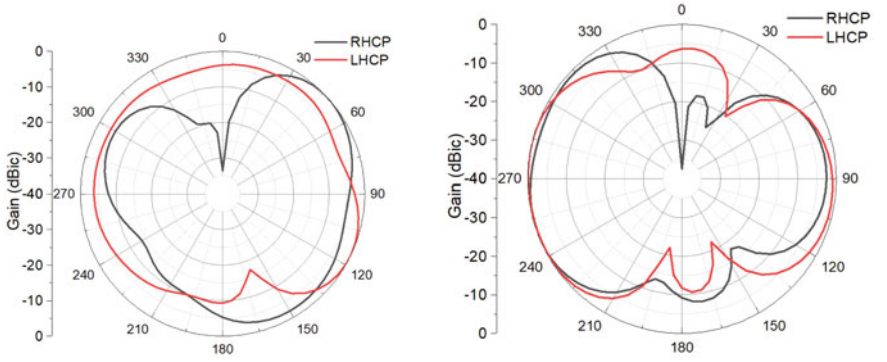

Fig. 8 LHCP and RHCP gains of proposed UWB antenna (phi = 90, phi = 0)

Table 2 Comparison of antenna performance comparison with other reported CP antennas

Reference	Year	Center frequency (GHz)	Absolute Impedance BW*, GHz (fractional impedance*, %)	Axial ratio BW[a], GHz (%)
[7]	2018	2.845	2.03 (71.35)	0.32 (14)
[9]	2015	3.89	0.54 (12.6)	0.13 (3.48)
[10]	2018	2.51	0.155 (6.2)	0.04 (1.6)
[11]	2012	2.45	0.8 (32.65)	0.1 (4.34)
[12]	2014	2.54	0.17 (6.7)	0.05 (1.96)
[13]	2011	2.43	= 0.3 (12.5)	= 0.08 (3.2)
[14]	2018	3.02	0.18 (6)	0.13 (3.3)
[15]	2017	5.7	2.8 (48.27)	0.7,0.45 (11.9, 6.8)
[16]	2018	1.57	0.027 (1.71)	0.01 (0.63)
[17]	2018	0.92	0.05 (5.43)	0.012 (1.3)
[18]	2017	5.8	0.9 (15.5)	0.21 (3.6)
Proposed	**2021**	**6.71**	**8.46 (126)**	**0.7 (8.1–8.8) (8.28)**

(BW is bandwidth, λ_0 is wavelength at center frequency)

References

1. Wong, KL (2004) Compact and broadband microstrip antennas, vol 168, John Wiley and Sons, New York
2. Chen J-M, Row J-S (2015) Broadband slotted patch antennas with circular polarization. Microwave Opt Technol Lett 57(5):1140–1143
3. Nasimuddin N, Qing X, Chen ZN (2010) Slits-loaded microstrip antennas for circular polarization. Microw Opt Technol Lett 52(9):2043–2049
4. Nasimuddin N, Qing X, Chen ZN (2014) A compact circularly polarized slotted patch antenna for GNSS applications. IEEE Trans Antennas Propag 62(12):6506–6509
5. Guo Y, Bian L, Shi XQ (2009) Broadband circularly polarized annular-ring microstrip. Antenna 57(8):2474–2477
6. Kewei Q, Chanjuan F, Bin W (2013) Compact perturbed hexagonal microstrip antenna for dual-band circular polarization. Electromagnetics 33(8):583–590
7. Kurniawan F, Sumantyo JTS, Gao S, Ito K, Santosa CE (2018) Square-shaped feeding truncated circularly polarised slot antenna. IET Microwaves Antennas Propag 12(8):1279–1286
8. Bernard LB, Alphones A (2016) An e-shaped slotted-circular-patch antenna for circularly polarized radiation and radiofrequency energy harvesting. Microw Opt Technol Lett 58(4):868–875
9. Ng KB, Chan CH, Luk KM (2015) Low-cost vertical patch antenna with wide axial-ratio beamwidth for handheld satellite communications terminals. IEEE Trans Antennas Propag 63(4):1417–1424
10. Rangaiah YP, Satyanarayana RVS, Nageswara Rao P (2018) The effect of aspect ratio and fractal dimension of the boundary on the performance of fractal shaped CP microstrip antenna. Prog Electromagnet Res M 64:23–33
11. Ghobadi A, Dehmollaian M (2011) A printed circularly polarized Y-shaped monopole antenna. IEEE Antennas Wirel Propag Lett 11:22–25
12. Reddy VV, Sarma NVSN (2014) Compact circularly polarized asymmetrical fractal boundary microstrip antenna for wireless applications. IEEE Antennas Wirel Propag Lett 13:118–121

13. Row J, Lee T, Chen M (2011) Circularly-polarized ring slot antenna fed by a V-shaped coupling strip. IEEE Trans Antennas Propag (2011).
14. Lin JF, Chu QX (2018) Enhancing bandwidth of CP microstrip antenna by using parasitic patches in annular sector shapes to control electric field components. IEEE Antennas Wirel Propag Lett 17(5):924–927
15. Bui TD, Nguyen QC, Le MT (2017) Novel wideband circularly polarized antenna for wireless applications. In: 2017 IEEE Asia Pacific microwave conference (APMC), Nov 2017, pp 430–433. IEEE
16. Wang MS, Zhu XQ, Guo YX, Wu W (2018) Compact circularly polarized patch antenna with wide axial-ratio beamwidth. IEEE Antennas Wirel Propag Lett 17(4):714–718
17. Yang X, Feng Q, Zheng Z (2018) First-order minkowski fractal circularly polarized slot loop antenna with simple feeding network for UHF RFID reader. Progress Electromagnet Res 77:89–96
18. Maddio S (2016) A compact circularly polarized antenna for 5.8 GHz intelligent transportation system. IEEE Antennas Wirel Propag Lett, 16, 533–536.

Grid Interactive PV System with Advanced Filtering Technique and PV Feed-Forward Loop

Dulichand Jaraniya and Shailendra Kumar

Abstract The controllability and reliability of supply toward distribution side consist of dispatchable and non-dispatchable sources. Renewable source of energy and comply without storage enhanced the reliability and feasibility of the PV systems. The presented article discussed the system consist of photo-voltaic single phase two stage grid connected system with nonlinear load. The current control is used in grid connected mode of the operation. SRF-PLL PI controller is used to design current controller for grid integrated mode of operation. PI integration reduces the error between the sensed and reference signals. The DC link voltage is regulated with the PI controller. PV feed-forward term is used to stabilize the intermittent nature of PV array and boost the generated output. The MPP tracking is done using the P and O MPPT technique which minimizes the oscillations near the MPP. The system is simulated in MATALAB Simulink library.

Keywords PV system · Demand side management · Phase locked loop · Adaptive filter

1 Introduction

Nowadays renewable-based generation is increasing because of their easily availability and environmental friendly as compared to the fossil fuels. Microgrid (MG) based on the renewable generation is increasing day by day because it help in increasing the reliability of the system. It is LV and medium voltage level grids. It is being point of attraction nowadays because of the beauty of the renewable DER integration and continuity of power supply under any deception. It allows the integration of renewable energy sources (RESs) that helps in carbon reduction specially. It can operate in grid connected or islanded mode, so proper controlling is needed to incorporate seamless transition of modes. It is done by incorporating PV with battery storage system. Voltage and frequency is identified by grid and regulated by inverter

D. Jaraniya (✉) · S. Kumar
Department of Electrical Engineering, Maulana Azad National Institute of Technology, Bhopal, India
e-mail: dulichandjaraniya@gmail.com

S. Dwivedi et al. (eds.), *Flexible Electronics for Electric Vehicles*, Lecture Notes in Electrical Engineering 863, https://doi.org/10.1007/978-981-19-0588-9_25

in grid tied and islanded mode, respectively, and also provides ancillary services. At the same time these grids are vulnerable to much deception. These deceptions may under normal condition like intermittent behavior, load fluctuation and under emergency condition it is generation outage and line go out of working. So there is requirement of seamless operation. In grid connected mode frequency is global variable while voltage is local variable, because frequency variation is susceptible only when there is larger load unbalancing or generation outage. Centralized control suffers from lack of redundancy when a single point failure, which can be overcome by the employing hierarchical control approach. In this paper single phase PV-based grid connected system is implemented with SRF-PI controller with angle locking with the help of phase locked loop (PLL).

In [1] the notch filter with PLL in SRF controller is used with PVS for improving the inertia. Compared the presented controller with the conventional PLL-based SRF controller and VSG controller. The advantages of using notch filter are that system behavior under disturbances and harmonics is improved. Pseudo induced voltage improves the inertia of system. Authors used the repetitive learning-based phase locked loop for controlling the distortion in the grid voltage in [2]. Two cascaded control scheme is used for the seamless operation of the MG even under unbalance condition. Proper parameter control is employed [3]. Secondary control is used to complement the behavior of primary control. Developed a model considering the multi DGs connected to the MG [4]. In this paper two layer control using VSI and PQ inverter is implemented. Each inverter take care of particular zone. A thirteen bus system studied considering one as stack bus. Mainly concerning on the secondary control. Load flow analysis is done to estimate the sensitivity of the bus voltage [5]. The system has the seamless transition from the grid tied to islanded mode or vice versa. The operation consist of the mode detection, low voltage ride through, and reactive power injection to support the operations. For this purpose cascaded control loops are presented. SRF controller is used for avoiding complex computations. The both single stage and two stage conversion operated inverters are used in the structure. For front-ended DC-DC boost converter is interfaced for the two stage conversion [6]. SRF-PLL based controller is used to synchronize the system to the grid [7]. Interconnected MGs are presented in [8]. Primary control involves the droop control consist of voltage and current control. Voltage and frequency regulated by secondary control. CCL provides supervisory MG stability. Power management done at global level. The author presented the MGs coupling using small signal modeling, fine parameter search done with particle swarm optimization [9]. Used the adaptive nonlinear control strategy to synchronize the two stage PV system to grid. Improve the dynamic response of PV using FFL [10]. Presented different configuration possible for the generation through MG. The topologies consist of different no. of the RESs. Also mentioned the requirement of the particular generator for the configuration [11]. In [12] PWM Switching pulses for driving VSI generated by new (RWZALMS) algorithm. Controller is provided for the VSI and DC–DC converter, so that maximum utilization of system reaches. The adaptive sliding mode control is used to generate power under islanded mode. ASMC estimated the reference real and reactive power

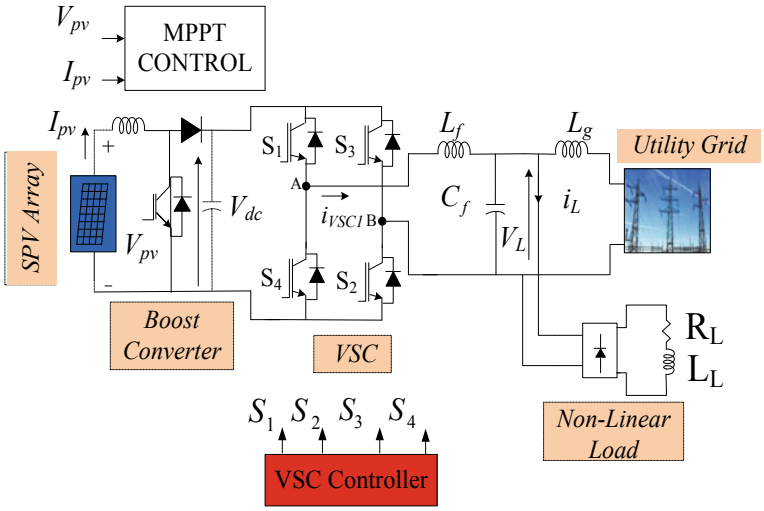

Fig. 1 Schematic representation of system under study

which mitigates the pollution in distorted results. Controller reduce the size of the capacitor required, eliminates dc link voltage undershoot and overshoot [13].

2 System Configuration

Two stage conversion system consist of the solar PV, boost converter, battery via bidirectional converter linear/nonlinear load at point of interconnection (POI) tied to grid via coupling inductor is presented as in Fig. 1. The system assimilated the bidirectional capability, which helps in DSM. MPPT is implemented using the DC–DC boost converter. Voltage source converter provides the coupling between DC–DC converter and grid. System is connected to the grid through a coupling inductor. LC filter is used to filter out the ripples present in current and voltage which leads to make the strong grid operation under grid connected system. Nonlinear load consist of the single phase diode bridge rectifier.

3 Controller Structure

The control structure is done with MPPT control and Current control is implemented using the SRF-PI-PLL controller. Grid voltage, grid current, synchronization angle and load current are sensed for the grid connected operation.

Table 1 Perturb and observe MPPT technique

Region	Perturbation in voltage	Effect on power	Conclusion for next perturbation
First	+ve	+ve	+ve
First	−ve	−ve	+ve
Second	−ve	+ve	−ve
Second	+ve	−ve	−ve

3.1 MPPT Controller

MPPT control is implemented by using *P* and *O* technique. MPPT is used to track global maximum power, helps in maximum utilization of the PV array. This controller identifies the change in power and voltage subtracting old value from new value. The Table 1 shows the basic operation of the MPPT technique and how it is helping in generating the switching signal for the MOSFET switch used to operate DC-DC boost converter. Boost converter provides the MPP tracking in the particular zone of operation, selecting the proper load this zone is reached.

In Table 1 first region indicate the region at left side of the MPP and remaining second region is the right side of the MPP.

3.2 SRF-PLL-Based Grid Side Current Controller

Current controller in grid connected system is designed using the SRF-PLL control. Grid voltage is sensed to calculate the PCC voltage using the alpha and beta component of the grid voltage as shown in Fig. 2. The grid current is sensed to develop the direct component which assimilates the current controller operation for the grid connected system. Feed-forward term is calculated to boost the PV generated power by controlling the dynamic behavior of the intermittent generation (Fig. 2).

4 Simulation Results Discussion

The simulated system consist of 10 kW PV array, boost converter, bidirectional converter, VSI, nonlinear load having single phase diode bridge and utility grid connected to PCC via coupling inductor. The simulated parameters are listed in Table 2.

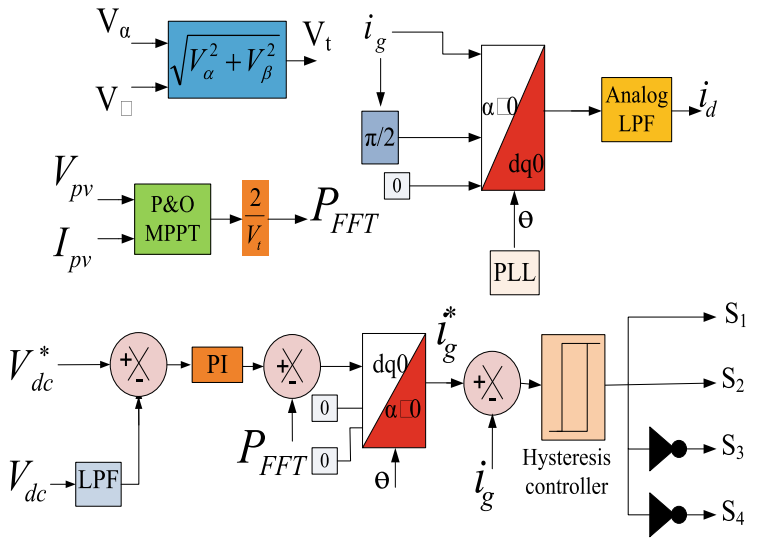

Fig. 2 Development of the grid connected controller

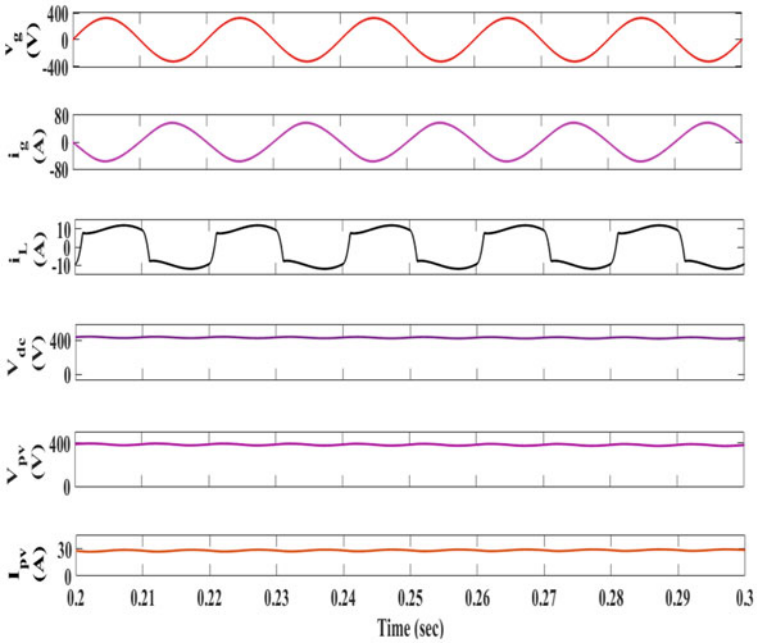

Fig. 3 Grid connected operation while PV array feeding nonlinear load and grid without FFT

Table 2 Parameters used for the system design

Components	Parametric value
Solar module: P_{max}, V_{max}, I_{max}, V_{oc}, I_{oc}	213.15 W, 29 V, 7.35 A, 36.3 V, 7.84 A
Boost inductor, dc link capacitor	3 mH, 5000 μF
LC filter	4 mH, 10 μF
Grid	230 V

4.1 Grid Connected Operation

Under grid connected operation PV supplies the power to battery, nonlinear load and grid. In Fig. 4, the grid current (I_g) and grid voltage (V_g) are out of phase which indicates that the PV array is supplying power to the grid maintaining unit power factor even under nonlinear load.

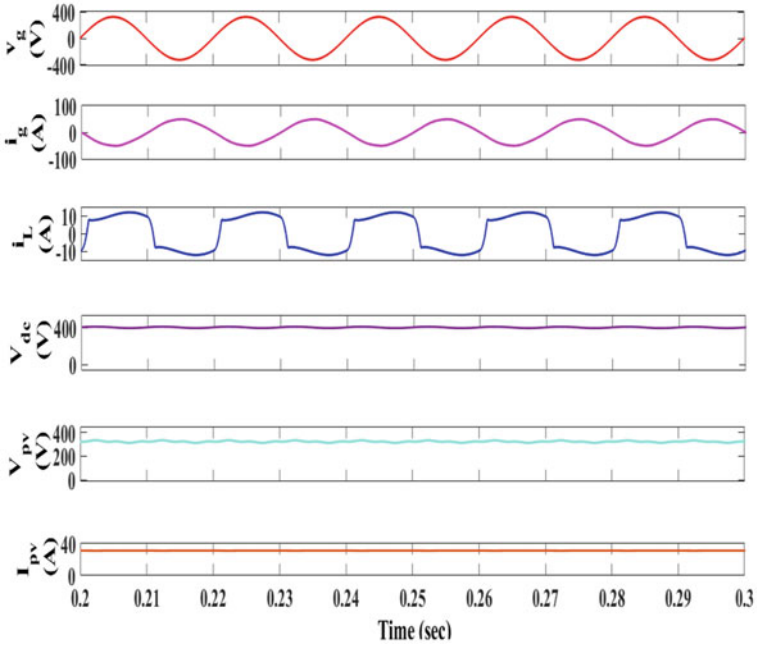

Fig. 4 Grid connected operation while PV array feeding nonlinear load and grid with FFT

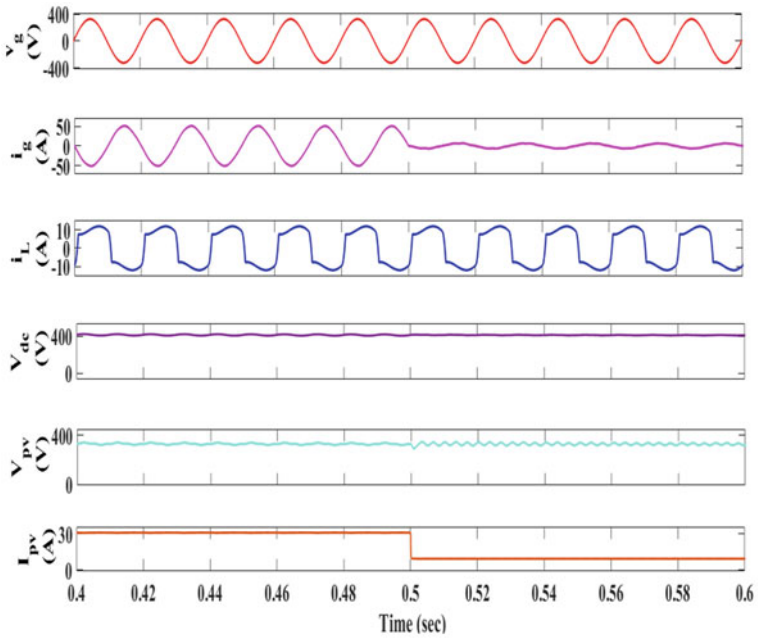

Fig. 5 Grid side parameters under varying insolation condition

4.2 Grid Connection Operation Under Varying Insolation

The behavior of the operation is similar to the grid connected system, only difference is that the insolation is changing according to the cloud crossing in a day. For the system under study the insolation is changed from 1000 to 300 W/m^2 as shown in Fig. 5.

The simulated result shows that as the insolation changed at 0.5 s the grid current and PV current reduces. At the same time the grid voltage, dc link voltage are maintained and ripples in dc link voltage are reduces when operating with 300 W/m^2 insolation. Load current also maintained ensuring DSM at distribution side.

Figures 6 and 7 show the THD analysis of the grid current and load current.

5 Conclusion

System consist of solar PV with grid is studied. System without battery storage is more reliable and increases the efficiency of the system. A renewable source without the storage in comply with power electronic interphase subjected to efficiency improvement. At the same time transition of the mode also help in more reliable system so feasibility of system also enhanced. Demand side management is achieved

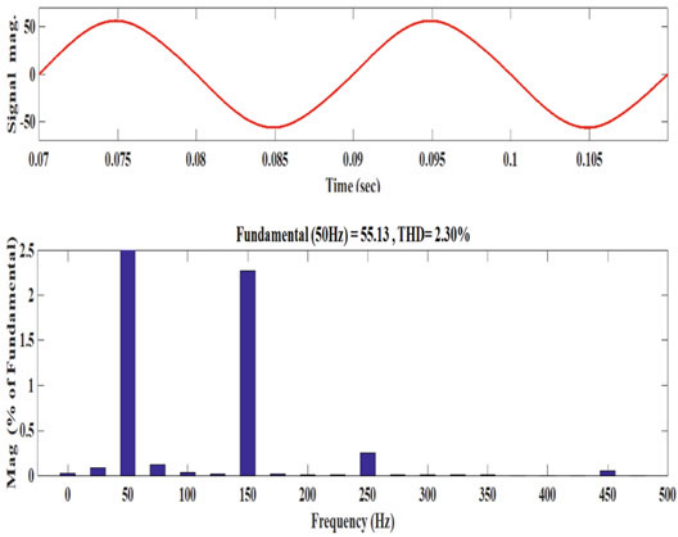

Fig. 6 THD analysis of the grid current

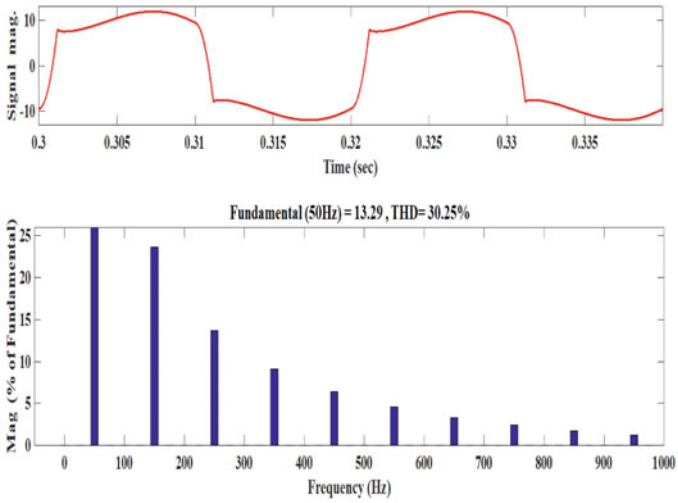

Fig. 7 THD analysis of the load current

under the insolation variation. THD are controlled in accordance with the standard IEEE 519. THD of the grid current is 2.30% even with nonlinear load (30.25%). In future work, battery energy management operation can also be done to improve the reliability of the PV system.

References

1. Panda RK, Mohapatra A, Srivastava SC (2020) Enhancing inertia of solar photovoltaic-based microgrid through notch filter-based PLL in SRF control. IET Gener Transm Distrib 14(3):379–388
2. Sahoo S, Prakash S, Mishra S (2018) Power quality improvement of grid-connected DC microgrids using repetitive learning-based PLL under abnormal grid conditions. IEEE Trans Ind Appl 54(1):82–90
3. Salim OM, Aboraya A, Arafa SI (2020) Cascaded controller for a standalone microgrid-connected inverter based on triple-action controller and particle swarm optimisation. IET Gener Transm Distrib 14(17):3389–3399
4. Wu X, Shen C (2017) Distributed optimal control for stability enhancement of microgrids with multiple distributed generators. IEEE Trans Power Syst 32(5):4045–4059
5. Mohammadi F, Doost Keshtkar H, Dehghan Banadaki A, Feliachi A (2019) A novel cooperative distributed secondary controller for VSI and PQ inverters of AC microgrids. Heliyon 5(6):e01823
6. Ghosh SS, Chattopadhyay S (2020) Three-loop-based universal control architecture for decentralized operation of multiple inverters in an autonomous grid-interactive microgrid. IEEE Trans Ind Appl 56(2):1966–1979
7. Shuvo S, Hossain E, Khan ZR (2020) Fixed point implementation of grid tied inverter in digital signal processing controller. IEEE Access 8:89215–89227
8. Naderi M, Khayat Y, Shafiee Q, Dragicevic T, Bevrani H, Blaabjerg F (2020) Interconnected autonomous AC microgrids via back-to-back converters—Part I: small-signal modeling. IEEE Trans Power Electron 35(5):4728–4740
9. He J, Wu X, Wu X, Xu Y, Guerrero JM (2019) Small-signal stability analysis and optimal parameters design of microgrid clusters. IEEE Access 7(1):36896–36909
10. Srinivas VL, Kumar S, Singh B, Mishra S (2017) A multifunctional GPV system using adaptive observer based harmonic cancellation technique. IEEE Trans Ind Electron 65(2):1347–1357
11. Rezkallah M, Chandra A, Singh B (2019) Microgrid: configurations, control and applications. IEEE Trans Smart Grid 10(2):1290–1302
12. Pathak G, Singh B, Panigrahi BK (2019) Wind-hydro microgrid and its control for rural energy system. IEEE Trans Ind Appl 55(3):3037–3045
13. Kalla UKS, Singh B, Murthy SS, Jain C, Kant K (2018) Adaptive sliding mode control of standalone single-phase microgrid using hydro wind and solar PV array-based generation. IEEE Trans Smart Grid 9(6), 6806–6814

A Probing Study on the Optoelectronic Properties of Flexible-Thin Film $CuGa_{0.89}B_{0.11}Se_2$—A DFT Approach

Karina Khan, Aditi Gaur, Amit Soni, Jagrati Sahariya, and Ushma Ahuja

Abstract The optoelectronic calculations of thin film $CuGa_{0.89}B_{0.11}Se_2$ is made by using first principle investigations that is rooted in the framework of density functional theory and complied with Wien2k code. The complete work is done by using full potential linearized augmented plane wave method. The value of direct band gap is 0.75 eV which is evaluated by exploring the density of state structure and band structure for achieving the electronic properties of the compound that are numerated by Tran-Blaha modified Becke Johnson exchange correlation potential. This exchange correlation functional is also used to find out the optical response of thin film $CuGa_{0.89}B_{0.11}Se_2$.The optical properties are examined through the complex dielectric tensor spectra, spectra of absorption coefficient, reflection and refraction spectra. The integrated absorption coefficient calculated through the absorption spectra is 107.23 ($\times 10^4$ eV/cm) and the percentage of reflectivity at its absolute value is 20%. The notable intensity is observed between 3 and 5 eV which affirms its utility in optoelectronic applications.

Keywords DFT thin film · Optoelectronic properties

K. Khan
Department of Physics, Manipal University Jaipur, Jaipur, Rajasthan 303007, India

A. Gaur · A. Soni (✉)
Department of Electrical Engineering, Manipal University Jaipur, Jaipur, Rajasthan 303007, India
e-mail: amitsoni_17@yahoo.co.in

J. Sahariya
Department of Physics, National Institute of Technology, Srinagar (Garhwal), Uttarakhand 246174, India

U. Ahuja
Department of Electrical Engineering, Mukesh Patel School of Technology Management and Engineering, NMIMS, Mumbai, Maharashtra 400056, India

S. Dwivedi et al. (eds.), *Flexible Electronics for Electric Vehicles*, Lecture Notes in Electrical Engineering 863, https://doi.org/10.1007/978-981-19-0588-9_26

1 Introduction

Chalcopyrites compounds are consider as great interest for the optoelectronic applications because they exhibit the good semiconductor properties and these chalcopyrites are resembling with the diamond and zinc blende compounds in structures. The chalcopyrites compounds of II–IV–V_2 and I–III–VI_2 group are extensively used and explored for optoelectronic devices such as light emitting diode (LED), photocatalyst, sensors, nonlinear optical devices, photovoltaics, due to their varied range in the band gaps from narrow (0.3 eV) to wide (4.0 eV). Chalcopyrites have been investigated by the researchers for energy generation and storage purposes, in order to replace the traditional energy source because most of the elements used in these compounds having good abundance and are eco-friendly too [1–6]. And in the last decades, the scientific communities are showing their zest toward the thin film and flexible technologies for developing the optoelectronic devices such as photovoltaic panels, liquid crystal display (LCD). As the devices based on flexible technologies have many advantages over the bulk form as they are more durable, easy to fold, occupied less area for installation, lightweights and are of lower price [7–10]. $CuGaSe_2$ is a ternary compound of II–IV–V_2 chalcopyrite group that exhibits the direct band gap semiconductor nature and having wide range of applications in visible and infrared areas, linear–nonlinear optical instruments and oscillators, due to which it is calibrated by many explorers experimentally as well computationally [11–13]. The experimental approaches have been used for synthesize the bulk, nanoparticles and thin film of $CuGaSe_2$ are as follow: microwave assisted polyol method, glycol-based solution method, solvothermal method, ion implementation method and many more [14–17]. The computational investigation of the material properties is using through the density functional theory (DFT) through which the thermal, optical and electronic characteristics are observed [12, 13, 18, 19]. The structural, electronic, thermal, magnetic and optical properties of $CuGaSe_2$ can be modify by insertion of different elements. The Zn, Sn and Ge have been doped in $CuGaSe_2$ to alter its photoluminescence and magnetic properties by using experimental techniques [14, 20–22]. The tetragonal $CuGaSe_2$ exhibits wider band gap that is why extrinsic doping (n and p-type) has been performed in order to tuned its properties for making this compound available for more electronic and optical applications [14, 23, 24]. Schon [14] has doped $CuGaSe_2$ by *P*, As, Sb, Na, Li, B, Mg, Cd, Zn, Si, Ge and Sn by using the post growth diffusion and ion implementation method and has calculated electronic and optical properties by adopting the Hall effect and photoluminescence methods. And the $CuGaSe_2$ doping have been performed done by the Mn at Ge site which induced the ferromagnetic character in the formed compound by using the DFT calculations [25, 26]. The doping of the transition metals has been done at Ga site in $CuGaSe_2$ by Dergel et al. [27] which yield the intermediate band gap of the formed compounds. In our previous work we have reported the effect of Al doping in thin film of $CuGaSe_2$ on its structural and optoelectronic properties by using DFT based on FP-LAPW method [28]. The Wien2K has been utilized for computing the uniaxial and bi-axial strain effect on the tetragonal structure of $CuGaSe_2$ [29]. Further

the Sn doping has been performed experimentally on the thin film of $CuGaSe_2$ at Ga site by using ball milling method [30] and observed that formed compound possess intermediate band gap.

By considering above literature survey and previously reported work, we have chosen the boron as dopant in $CuGaSe_2$ in order to report its effect on its structure and optoelectronic response of $CuGaSe_2$.

2 Method of Computations

The computational tool adopted in this work is Wien2k code which is employed in the density functional theory (DFT) and incorporated in full potential linearized augmented plane wave method (FP-LAPW) [31]. The DFT is used well to simulate the structural and optoelectronic properties of the material as this theory computes the ground state energy and electron density which is helpful in determining all materials' properties. And all computational work is executed by using the most trusted exchange correlational potential TB-mBJ which is known for yielding the accuracy in the result.

For proceeding with the doping, first of all we developed the tetragonal structure of $CuGaSe_2$ by using the input parameters of previously reported work [28]. Then by using the tetragonal structure of $CuGaSe_2$, we constructed its thin film by expanding its dimension along x, y and z direction by 2 unit and vacuum of 10 Bohr along z direction. Further, one Ga atom replaced by one B atom which leads to 11.11% doping which deforms its structure into tetragonal primitive with space group 81($P\bar{4}$). The crystal structure along with Brillouin zone of boron doped thin film of $CuGaSe_2$ is presented in Fig. 1a and b. The 100 k points are taken for computations along with this, the values of $R_{MT}K_{max}$, l_{max}, G_{max} and energy are fixed at 7, 10, 12 and −6 Ry, respectively, to obtain the accuracy in the result.

3 Result and Discussion

For describing the electronic properties, we have chosen two parameters the electronic band structure and density of state spectra (DOS spectra) because these parameters are very reliable for putting light on the electronic dealing of the compound. The electronic band structure of thin film $CuGa_{0.89}B_{0.11}Se_2$ is depicted in Fig. 2 which is plotted by using the TB-mBJ exchange correlation functional. In this structure the level of the fermi energy is situated at zero electron-volt and the space between the valence band maximum (VBM) and conduction band minimum (CBM) is 0.75 eV which indicates its energy band gap that proves that compound is semiconductor nature of thin film $CuGa_{0.89}B_{0.11}Se_2$. And we also observed that the VBM and CBM are lies at the $\bar{\Gamma}$–$\bar{\Gamma}$ k points and these different bands at different energy level showing the positions of electrons in VB and CB. According to the previous reported work in

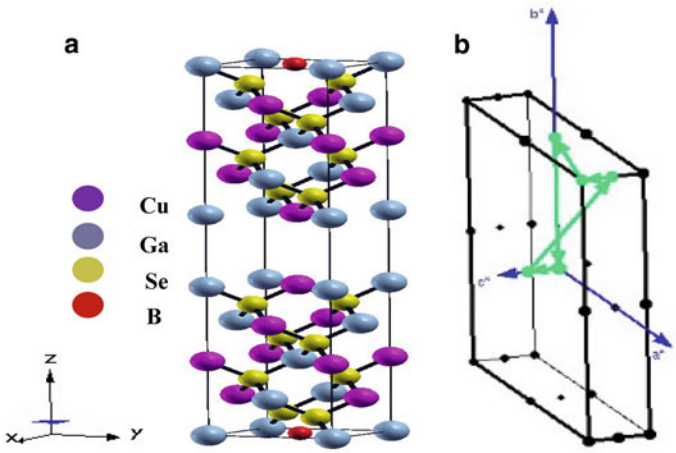

Fig. 1 **a** Lattice structure, **b** Brillouin zone of $CuGa_{0.89}B_{0.11}Se_2$

which the B has been doped in $CuGaSe_2$ by diffusion method shown that the specific resistivity has been increased [14]. The DOS spectra, explain the energy dispensation of electrons and confirms the band gap of the compound and it is depicted in Fig. 3. The VB is present just adjacent to the fermi energy level. We found that three band forms from −8 to 6 eV in which core band is from −8 eV to −3.19 eV, valence band is from −2.14 eV to 0 eV and the conduction band is from 0.75 eV to 6 eV. The main contribution is provided by '*d*' and '*s*' state of Cu and Ga in VB and in core band the contribution is gone to '*p*' and '*s*' state of B and Se. The shifting of the valence band toward the fermi level due to the mixing of the '*s*' and '*p*' state of B and Ga.

The optical characteristics of compounds are important for show casing the compound for optoelectronic devices. Here we explain the optical response of any material by using complex dielectric tensor, absorption coefficient, reflection and refraction produce by the compound. The dielectric tensor spectra explain by two parts one is real dielectric tensor spectra and another is imaginary dielectric tensor spectra which are depicture in the Fig. 4a and b, respectively. The obtained absolute value of real dielectric tensor spectra at 0 eV is 7.17, which is used to explain the capability of compound to polarize the incident electromagnetic wave. The peaks (2.54, 4.54, 5.42 and 7.33 eV) appear in imaginary dielectric tensor spectra tells about the transition performed by free electrons from VB to CB, also it describes the attenuation of light in the compound. The Fig. 5 represents the spectra of absorption coefficient which is used to explain about the extent of absorption of material for the incident photon and the computed value of integrated absorption coefficient is 107.23 ($\times 10^4$ eV/cm), this value indicating the compound is a good absorber for the incident photon. The spectra of reflectivity and refraction are depicturing in Figs. 6a and b which helps us to understand the morphology of the compound. The percentage of reflection at 0 eV is 20% so we concluded that lesser value of reflectivity and higher value of absorption coefficient make the compound suitable for the optoelectronic

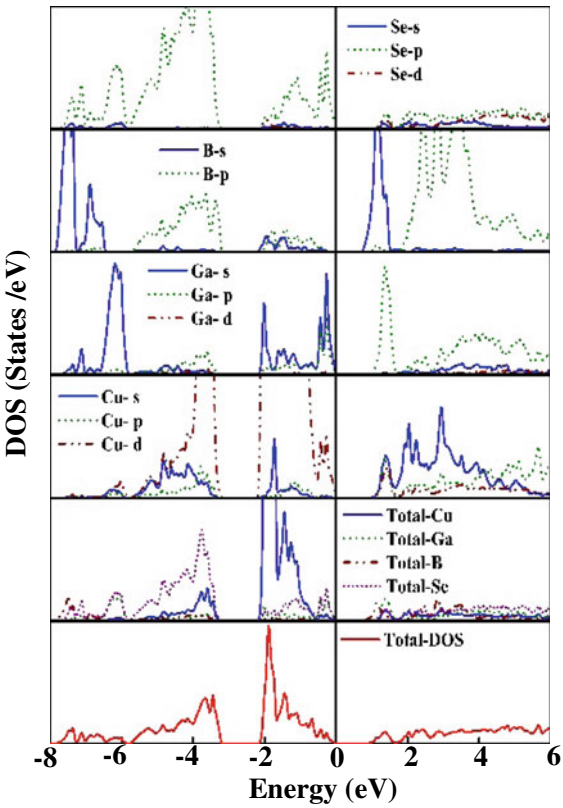

Fig. 2 Density of state (DOS) spectra of $CuGa_{0.89}B_{0.11}Se_2$ by using the TB-mBJ

devices. Also the obtained value of absolute refractivity is 2.68. These two parameters explain the roughness and smoothness of the compound surface. The compound exhibits the anisotropic nature of the compound as the parallel and perpendicular component of all optical parameters do not coincide with each other. The optoelectronic properties of boron doped thin film of $CuGaSe_2$ shows that it is suitable for optoelectronic applications.

4 Remarks of Conclusion

The optoelectronic properties of $CuGa_{0.89}B_{0.11}Se_2$ are successfully simulated through DFT based on FP-LAPW method and operated in Wien2k package. The TB-mBJ exchange correlation potential is utilized for performing the electronic and optical computations. The semiconductor behavior of the compound is affirmed through band structure and DOS spectra which also reveals its direct band gap nature. The higher value of integrated absorption is indicating its utility for optoelectronic devices and also optical spectra proves the anisotropic nature of the compound.

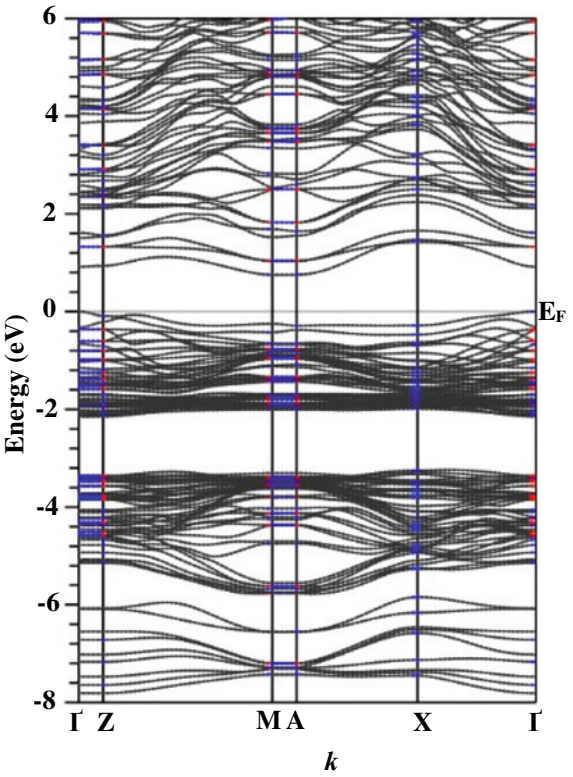

Fig. 3 Electronic Band Structure of $CuGa_{0.89}B_{0.11}Se_2$by using the TB-mBJ

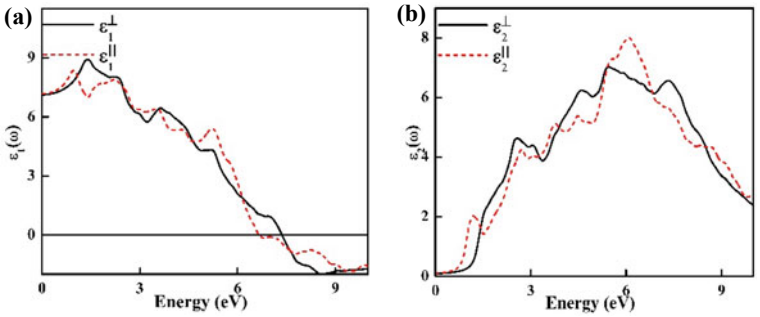

Fig. 4 **a** Real dielectric tensor spectra, **b** imaginary dielectric tensor spectra of $CuGa_{0.89}B_{0.11}Se_2$

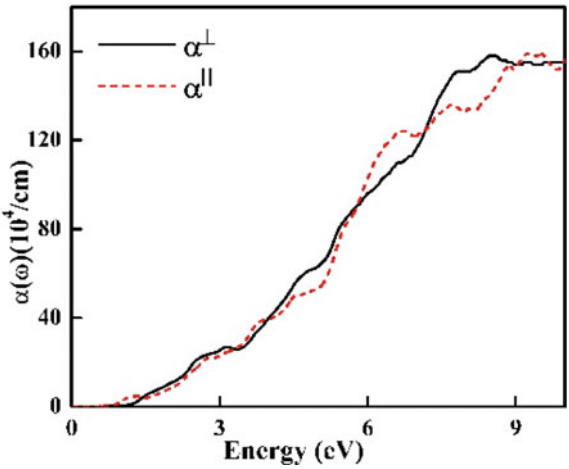

Fig. 5 Absorption spectra of $CuGa_{0.89}B_{0.11}Se_2$

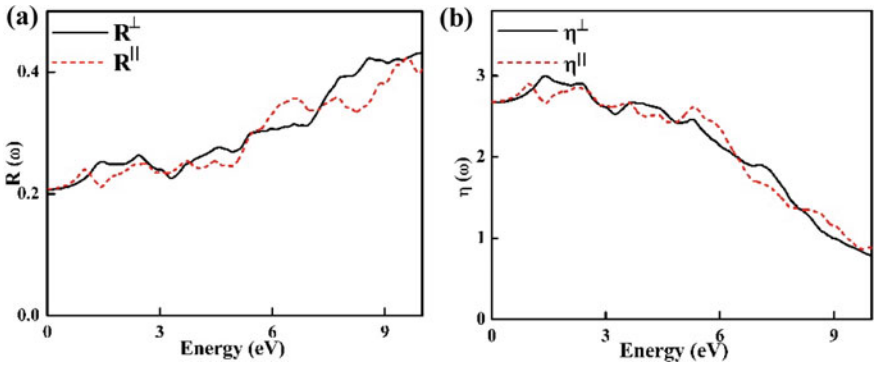

Fig. 6 **a** Reflectivity spectra, **b** refractivity spectra of $CuGa_{0.89}B_{0.11}Se_2$

Acknowledgements All the researchers participated in this work presenting their gratitude toward Prof. P. Blaha for conferring the Wien2k code, a simulation tool. Manipal University Jaipur is highly acknowledged by authors for providing work facilities. The fund for this work given through DST-SERB, New Delhi (India), vide grant number EMR/2017/005534.

References

1. Palacios P, Sánchez K, Conesa JC et al (2006) First principles calculation of isolated intermediate bands formation in a transition metal-doped chalcopyrite-type semiconductor. Phy Status Solidi 203:1395–1401
2. Palacios P, Sánchez K, Wahnón P et al (2007) Characterization by ab initio calculations of an intermediate band material based on chalcopyrite semiconductors substituted by several transition metals. J Sol Energy Eng 129(3):314–318

3. Sahina S, Ciftcia YO Colakoglu K (2012) First principles studies of elastic, electronic and optical properties of chalcopyrite semiconductor $ZnSnP_2$. J Al Comp 529:1–7
4. Moon SH, Park SJ, Hwang YJ et al. (2014) Printable, wide band-gap chalcopyrite thin films for power generating window applications. Sci Rep 4:4408-1-5
5. Omata T, Nagatani H, Suzuki I et al (2014) Wurtzite $CuGaO_2$: A new direct and narrow band gap oxide semiconductor applicable as a solar cell absorber. J Am Chem Soc 136:3378–3381
6. O'Connor GM, Eksteen JJ (2020) A critical review of the passivation and semiconductor mechanisms of chalcopyrite leaching. Min Eng 154:106401-1-12
7. Chen Z, Cotterell B, Wang W et al (2001) A mechanical assessment of flexible optoelectronic devices. Thin Sol Films 394:201–205
8. Romero MJ, Jones KM, Abu Shama J et al (2003) Surface-layer band gap widening in Cu(In, Ga)Se_2 thin films. App Phys Let 83:4731–4733
9. Lincot D, Guillemoles JF, Taunier S et al (2004) Chalcopyrite thin film solar cells by electrodeposition. Sol Energy 77:725–737
10. Liu C, Zhang Q, Wang D et al. (2018) High performance, biocompatible dielectric thin-film optical filters integrated with flexible substrates and microscale optoelectronic devices. Adv Opt Mat 6:1800146–1– 8
11. Alonso MI, Wakita K, Pascual J et al. (2001) Optical functions and electronic structure of $CuInSe_2$, $CuGaSe_2$, $CuInS_2$, and $CuGaS_2$. Phy Rev B 63:075203–1–13
12. Soni A, Dashora A, Gupta V et al (2011) Electronic and optical modeling of solar cell compounds $CuGaSe_2$ and $CuInSe_2$. J Elec Mat 40:2197–2208
13. Soni A, Dashora A, Gupta V et al (2013) Use of chalcopyrite semiconductors $CuXSe_2$ (X=Al, Ga and In) in solar cells: a theoretical study. Int J Sust Ener 32:18–26
14. Schon JH (2000) Extrinsic doping of $CuGaSe_2$ single crystals. J Phys D Appl Phys 33:286–291
15. Tang J, Hinds S, Kelley SO et al (2008) Synthesis of colloidal $CuGaSe_2$, $CuInSe_2$, and Cu(InGa)Se_2 nanoparticles. Chem Mater 20:6906–6910
16. Grevtsev AS, Levin OV, Tverjanovich AS et al. (2017) Microwave assisted polyol synthesis of $CuGaSe_2$ nanoparticles for solar cell application. Funct Mat Let 10:1750050-1-4
17. Wei Y, Zhuang D, Zhao M et al (2018) Fabrication of wide band-gap $CuGaSe_2$ solar cells for tandem device applications by sputtering from a ternary target and post selenization treatment. Mat.Let 230:128–131
18. Hou HJ, Zhang SR, Guan H et al (2015) Investigation of structural, elastic and thermal properties of $CuGaSe_2$: first principles method. Chal Let 10:511–518
19. Bikerouin M, Balli M, Farkous M et al. (2020) Effect of lattice deformation on electronic and optical properties of $CuGaSe_2$: Ab-initio calculations. Thin Solid Films 696:137783-1-8
20. Schön J, Bucher E (2001) Electrical properties of n-type $CuGaSe_2$. Thin Solid Films 387:23–25
21. Schön JH, Baumgartner FP, Arushanov E et al (1996) Photoluminescence and electrical properties of Sn-doped $CuGaSe_2$ single crystals. J App Phys 79:6961–6965
22. Krustok J, Raudoja J, Schon JH (2000) Photoluminescence properties of Ge-implanted $CuGaSe_2$ crystals. Phys Status Solidi (a) 178(2):805–809
23. Schön JH, Kloc C, Arushanov E et al. (2000) On the metal–insulator transition in n-type doped $CuGaSe_2$. J Phys Condens Matter 12:4603–4611
24. Persson C, Zhao YJ, Lany S et al. (2005) n-type doping of $CuInSe_2$ and $CuGaSe_2$. Phys Rev B 72:035211-1-14
25. Zhao YJ, Freeman AJ (2002) First-principles prediction of a new class of ferromagnetic semiconductors. J Mag Mag Mat 246:145–150
26. Erwin SC, Zutic I (2004) Tailoring ferromagnetic chalcopyrites. Nat Mat 3:410–414
27. Dergal M, Faraoun HI, Mahmoudi A et al (2017) First principles study on structural, electronic and optical properties of 3d transition metals-substituted $CuGaSe_2$. Optik 135:346–352
28. Khan K, Gaur A, Soni A, et al. (2020) Revealing the impact of aluminum doping on opto-electronic properties of $CuGaSe_2$ thin films flexible solar cells—A DFT study. Flexible Electron Electric Veh 2294:030004-1-5. AIP Conf Proc
29. Bikerouin M, Balli M, Farkous M et al. (2020) Effect of lattice deformation on electronic and optical properties of $CuGaSe_2$: Ab-initio calculations. Thin Solid Films 696(137783):1–9

30. Fan W, Yao H, Wang Y et al. (2020) Structural and optical characteristics of Sn-doped $CuGaSe_2$ thin films as a new intermediate band material for high-efficiency solar cells. AIP Adv 10(06503):1–6
31. Blaha P et al. (2019). WIEN2k—an augmented plane wave plus local orbitals program for calculating crystal properties. Revised edition WIEN2k19.1, Vienna University of Technology, Vienna, Austria

Enhanced Real-Time Power System Monitoring by Detecting Event Signature

Divya Rishi Shrivastava, Shahbaz Ahmed Siddiqui, and Kusum Verma

Abstract Today, electrical utilities face major challenges in reliable and secure power supply. To overcome the challenges, it is important to continuously monitor and detect not only major but also small events that otherwise may lead system to extreme settings. Real-time information is therefore beneficial and is available from phasor measurements units (PMUs). The paper proposes a real-time event detector (RTED) that accurately and timely detects power system events and therefore enhances situational monitoring. Synchronized frequency measurement-based event projectors (EP) are calculated to apprehend event signatures. To predict an event occurrence in real time, EP are utilized as features to AdaBoost classifier. The performance of proposed RTED to enhance power system situational monitoring is tested on IEEE 39 bus test system. The results highlight that the proposed detector is computationally efficient, robust to event type and topological changes.

Keywords AdaBoost classifier · Power system events · Power system event detection · Synchrophasor measurements

1 Introduction

Modern power systems are unceasingly subjected to wide-ranging operational settings. These widespread operating conditions may cause system failure and decreases reliability of electric grids. Operators are therefore required to incorporate

D. R. Shrivastava
Department of Electrical Engineering, Manipal University Jaipur, Jaipur, Rajasthan 303007, India

S. A. Siddiqui (✉)
Department of Mechatronics Engineering, Manipal University Jaipur, Jaipur, Rajasthan 303007, India
e-mail: shahbazahmed.siddiqui@jaipur.manipal.edu

K. Verma
Department of Electrical Engineering, Malaviya National Institute of Technology Jaipur, Jaipur, Rajasthan 302017, India

S. Dwivedi et al. (eds.), *Flexible Electronics for Electric Vehicles*, Lecture Notes in Electrical Engineering 863, https://doi.org/10.1007/978-981-19-0588-9_27

state-of-art methodology to timely detect events that initiate system towards probable failures. A secure operation ensures power network continuous monitoring and assessment. The network information is continuously available from synchrophasor technology and can be adapted for real-time event monitoring and assessment [1]. Such methodology can detect power system events with nonlinear analysis of PMU measurements [2]. These methods are performed continuously and require more computational efforts. Synchronized voltage and line current-based methods can be utilized for composing impedance indices. These indices calculated for selective bus are applied for event detection [3]. Impedance-based indices needs to be calculated in real-time, in such cases, any missed or erroneous PMU data may raise false alarms. Hybrid methods like wavelet-machine learning approach [4] are also reported in literature to timely detect disturbance. These schemes are often computationally heavy and use larger PMU data length. Literature also suggests Kalman filter and cumulative sum (CUSUM)-based methodology to detect disturbances [5]. This methodology calculates time of fault occurrence and clearance, which is therefore time-consuming and suitable for online applications. Graph theory-based abnormality detections techniques suitable for online applications is suggested in [6]. Event information given to operators in online time frame are sufficient for informatory purpose. But it is limited to less time margin for any control measures that might be required if post disturbance system dynamics attains extreme settings. Recently, Shrivastava et al. [7] recommend centre of frequency–voltage-based event detection. The detection results are available in very less time, but the synchronized data length is large. Assessment with lengthy PMU data may reduce assessment lead time required for developing control measures for events that may lead system in extreme settings.

The literature survey suggests that there is a need to develop a methodology that detects event accurately in real time with minimum network information. The availability of detection results can assist the development of efficient remedial measures and eventually prevent the system from collapse. This paper, therefore, reports fast and accurate event detection methodology using short-synchronized data. The main contributions of the paper are: (i) a new RTED is proposed to timely and accurately detect event occurrence. (ii) Synchronized short frequency data-based EP are proposed to infer event signatures. (iii) An AdaBoost classifier is developed to classify event occurrence in real time. The EP are utilized as features to the developed AdaBoost classifier. The overall summary of proposed work is outlined in Fig. 1.

2 Proposed Real-Time Event Detector (*RTED*)

This section first discusses synchronized frequency-based (EP), subsequently, detection of events in real-time.

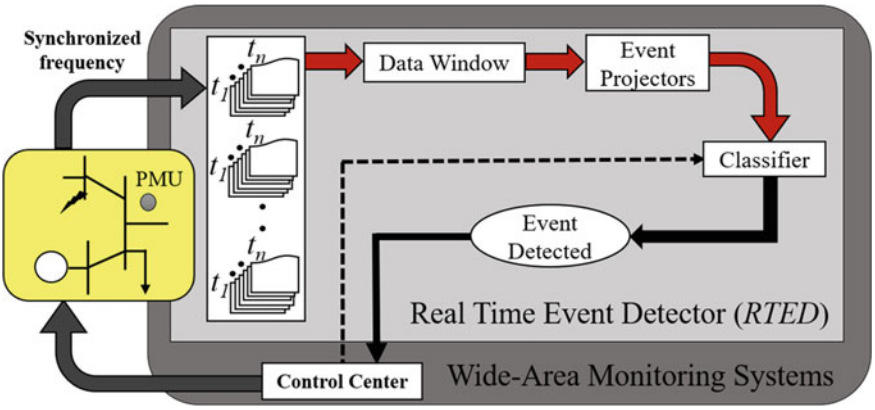

Fig. 1 Overall summary of proposed work

2.1 Event Projectors (EP)

Any event occurrence is realized in terms of generator dynamics; therefore, based on generator bus frequency measurements, a new index, namely EP is calculated. These indices extract event signatures from minimum frequency data and infer power system event occurrence. Let ${f^i}_d$ be the generator bus frequency for i^{th} generator bus and d be the data window length. The corresponding angular speed is, therefore, $\boldsymbol{\omega_i} = 2\pi f_i$ and angular acceleration at any arbitrary tth sample for ith bus is,

$$A_i[t] = \frac{\omega_i[t] - \omega_i[t-1]}{\Delta t} \tag{1}$$

Δt is time difference between two consecutive samples. With inception of any event, generator response to arisen event is calculated with respect to system's overall response. The system overall response can be obtained using centre of inertia (COI) [8]. COI-angular acceleration is calculated as,

$$A_{\mathrm{COI}}[t] = \frac{\omega_{\mathrm{COI}}[t] - \omega_{\mathrm{COI}}[t-1]}{\Delta t} \tag{2}$$

Response to ith generator bus at any tth sample is calculated as relative angular acceleration (RA) as,

$$\mathrm{RA}_i[t] = A_i[t] - A_{\mathrm{COI}}[t] \forall t \in d \tag{3}$$

Signatures of any event occurrence labelled as (*EP*) are obtained as,

$$\mathrm{EP}_i = |\Sigma \mathrm{RA}_i[t]| \forall i \in n_g, t \in d \tag{4}$$

EP are calculated for all generator bus in any power system. For any power network, following pseudocode can be utilized for *EP* calculation.

Pseudocode: calculate event projectors

Calculate A using Eq (1)
Calculate A_{COI} using Eq (2)
for each Generator bus
|Calculate RA using Eq (3)
$|EP = |\sum RA|$ for data Window
end
Record: EP

Under normal conditions, EP for any generator bus at any time will be zero. However, during any event, EP will essentially be non-zero.

2.2 AdaBoost Classifier for Situational Monitoring

AdaBoost classifier a supervised learning algorithm is an ensemble of several decision trees classifiers. A detailed view classifier development, its learning and evaluation metrices can be obtained from [9]. The event projectors calculated from pseudocode is utilized as input features to AdaBoost classifier to predict event occurrence. As event classification problem lies between either "Event occurred" or "Event not occurred", it makes prediction process to be binary in nature. That is, event occurrence is labelled as "1" and event non-occurrence as "0". These binary sets are used as target for AdaBoost classifier model. The features calculated from PMU data available from archived database are utilized to train classifier for associated event occurrence in offline mode.

The trained model is then tested to predict event occurrence in real time for new operating scenarios. In this regard, overall structure of proposed RTED is shown in Fig. 2. The performance of RTED is evaluated by: overall response time of proposed detector and percentage accuracy of true predictions. Percentage true prediction is calculated as correct classifier predictions out of total predictions.

3 Results of Proposed Work

Performance of RTED is demonstrated on IEEE 39 bus system [10] implemented in DIgSILENT PowerFactory and detector is executed in Python [11]. It is assumed that synchronized data from all generator is available. In this regard, generator bus frequency measurements are available with 60 Hz sampling frequency (1 sample/cycle or 60 samples in 1 s). In total, 500 different operating scenarios are used in present study comprising random system loading between 90 and 110% and

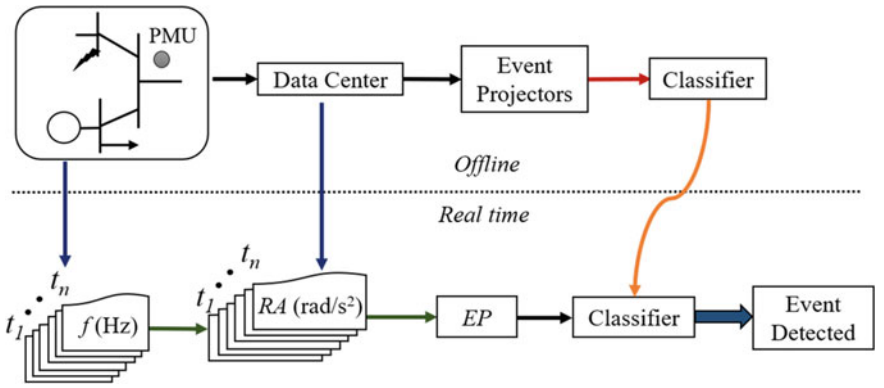

Fig. 2 Structure of real-time event detector (RTED)

system topological changes with events: short circuit cleared with line outage (SC), double line outage leading to bus outage (DL), generator outage (GO), load outage (LO) and no events (NO) as given in Table 1. Out of total cases, 80% used for training and 20% used for testing of proposed detector.

The considered test system comprises ten generators; therefore, ten feature are used to train and test classifier model to predict event occurrence. The synchronized data window is continuously utilized to detect any event. For the present analysis, different short length frequency data window: 3, 6, 12, and 18 cycles are used to assess the suitability of appropriate data window. Table 2 details synchronized data form PMU, features and target for RTED.

The purpose of utilizing different shot data window is to determine the suitable window that can be used to assess event occurrence accurately and in real time. The results for each data window in terms of accuracy and RTED response time are tabulated in Table 3. From the Table, it is evident that 3 cycle frequency window is too short to be utilized for event detection. The accuracy in this case is low, as based on operating conditions, system response to some event is sluggish and raises in due course of time. Further, short data length may give fast response but at the same time it is less precise. Similarly, as the data length is increased form 3 cycle to 18 cycle,

Table 1 Total operating conditions for different events

S. No.	Disturbance type	Operating conditions	Event summery
1	SC	100	Cases with events = 400 Cases with no event = 100 Total case = 500
2	DL	100	
3	GO	100	
4	LO	100	Training = 0.8 * 500 = 400 cases Testing = 0.2 * 500 = 100 cases
5	NO	100	
Total		500	

Table 2 Details of input and output for AdaBoost classifier

Generator bus frequency data from PMU	Features	Target
3 Cycle data window: 10 × 3 = 30	10	Event occurred; Yes: 1, No: 0
6 Cycle data window: 10 × 6 = 60	10	Event occurred; Yes: 1, No: 0
12 Cycle data window: 10 × 12 = 120	10	Event occurred; Yes: 1, No: 0
18 Cycle data window: 10 × 18 = 180	10	Event occurred; Yes: 1, No: 0

Table 3 Performance of RTED with different data window length

Data window (s)	Accuracy (%)		RTED Response time (s)
	Train	Test	
3 cycle (0.05)	69.25	68	(0.3–0.6) × 10^{-3}
6 cycle (0.1)	100	100	(0.6–1.0) × 10^{-3}
12 cycle (0.2)	100	100	(1.0–2.0) × 10^{-3}
18 cycle (0.3)	100	100	(2.0–5.0) × 10^{-3}

the accuracy is enhanced and the overall response time is also very less, making it inefficient for real-time applications.

Thus, 6 cycle data length is providing a better accuracy and satisfactory response time. Noticeably, for larger data length, RTED also performs effectively, but the overall assessment time including fault application time will be more. To further understand overall timeline for proposed RTED from fault application time, an illustration is shown in Fig. 3. The illustration reflects the importing of 6 cycle PMU data and assessment of proposed detector to identify event occurrence.

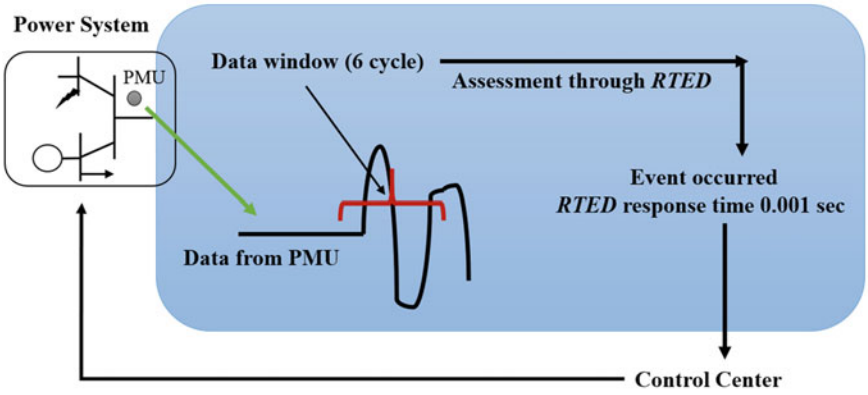

Fig. 3 Timeline for real-time event detector (RTED)

References

1. Jena MK, Panigrahi BK, Samantaray SR (2018) A new approach to power system disturbance assessment using wide-area post disturbance records. IEEE Trans Ind Inform 14(3):1253–1261
2. Liu G, Chen H, Sun X, Quan N, Wan L, Chen R (2018) Low-complexity nonlinear analysis of synchrophasor measurements for events detection and localization. IEEE Access 6:4982–4993
3. Kundu P, Pradhan AK (2018) Real-time event identification using synchrophasor data from selected buses. IET Gener Transm Distrib 12(7):1664–1671
4. Thomas A, Koshy S, Sunitha R (2020) Machine learning based detection and classification of power system events. In: 2020 International conference on power, instrumentation, control and computing (PICC). IEEE, Thrissur, India, pp 1–6
5. Fang K, Huang Y, Huang Q, Yang S, Li Z, Cheng H (2020) An event detection approach based on improved CUSUM algorithm and kalman filter. In: 2020 IEEE 4th conference on energy internet and energy system integration (EI2). IEEE, Wuhan, China pp 3400–3403
6. Shi J, Foggo B, Kong X, Cheng Y, Yu N, Yamashita K (2020) Online event detection in synchrophasor data with graph signal processing. In: 2020 IEEE International conference on communications, control, and computing technologies for smart grids (SmartGridComm). IEEE, Tempe, AZ, USA, pp 1–7
7. Shrivastava DR, Siddiqui SA, Verma,K (2021) Data-driven wide-area situation analyzer for power system event detection and severity assessment. In: Haes Alhelou H, Abdelaziz AY, Siano P (eds) Wide area power systems stability, protection, and security. power systems. Springer, Cham
8. Siddiqui SA, Verma K, Niazi KR, Fozdar M (2018) Real-time monitoring of post—fault scenario for determining generator coherency and transient stability through ANN. IEEE Trans Ind Appl 54(1):685–692
9. YanLing D, Ran D, DongSheng W, RuoYang W, ShaoJun Y, Hui N(2020) Research on Islanding detection method of distributed photovoltaic power supply based on improved adaboost algorithm. In: 2020 IEEE power & energy society general meeting (PESGM). IEEE, Montreal, QC, Canada, pp 1–5
10. Shrivastava DR, Siddiqui SA, Verma K (2017) Optimal PMU placement for coordinated observability of power system under contingencies. 2017 IEEE international conference on circuits and systems (ICCS). IEEE. Thiruvananthapuram, India, pp 334–339
11. Shrivastava DR, Siddiqui SA, Verma K (2020) Interfacing python with DIgSILENT power factory: automation of tasks. In: Kalam A, Niazi K, Soni A, Siddiqui S, Mundra A (eds) Intelligent computing techniques for smart energy systems. LNEE, vol 607. Springer, Singapore

Techniques and Measures for Reduction in Transmission and Distribution Losses

Neeraj Kanwar and Tawish Jain

Abstract This paper talks about the implementation of the best metering practices to reduce the transmission and distribution (T&D) losses. Distribution system is one of the major areas where the distribution companies (DisComs) face huge losses, therefore, reduction of T&D losses may bring profit to the DisComs. In this work, various technical and non-technical losses are identified and tackled accordingly. This paper also discusses the methodology to determine the T&D losses and measures to be taken to reduce the losses and hence increase the overall efficiency of the network.

Keywords Distribution system · Transmission and distribution losses

Abbreviations

B_{eff}	Billing efficiency
C_{Bill}	Bill amount
C_{eff}	Collection efficiency
C_{rev}	Collected revenue
E^{i}_{Bill}	Total energy bill for *i*th month
E_{consp}	Energy consumption in the distribution network
E^{i}_{inp}	Total energy input to the system for *i*th month
$E^{\text{MBC}}_{\text{inp}}$	Input energy in metering billing and collection (MBC) boundary
$E^{\text{HT}}_{\text{consp}}$	Sum of energy sale to HT consumers
$E^{\text{MBC}}_{\text{consp}}$	Energy consumption in the distribution or MBC network
E^{C}_{Bill}	Energy bill to customers
$E^{\text{DisCom}}_{\text{inp}}$	Input energy in the DisCom periphery
E_{S}	Energy sales

N. Kanwar (✉)
Department of Electrical Engineering, Manipal University Jaipur, Jaipur 303007, Rajasthan, India
e-mail: nk12.mnit@gmail.com

T. Jain
Secure Metering and Services Pvt. Ltd., Bhilwara, Rajasthan, India

S. Dwivedi et al. (eds.), *Flexible Electronics for Electric Vehicles*, Lecture Notes in Electrical Engineering 863, https://doi.org/10.1007/978-981-19-0588-9_28

E_{Bill} Energy bill to consumers
E_{coll} Energy collection from consumers
Loss_{dis} Distribution losses (%)
$\text{Loss}_{\text{Tec}}^{\text{LT}}$ LT lines technical losses
K_{Bill}^{n} Bill of nth unit
K_{inp}^{n} Input of nth unit

1 Introduction

In India, the transmission network has been planned and expanded in a really nice manner, but when it comes to distribution network, it looks like it has grown in an unplanned and haphazard manner to meet the growing demands of the consumers. Over the years, this approach had resulted into high-transmission and distribution (T&D) losses or high-aggregated technical and commercial (AT&C) losses. Thus, the focus over the years has been on developing the strategies to reduce the T&D or AT&C losses using the best practices.

2 T&D or AT&C Losses

AT & C Loss is a more accurate measure to calculate the overall efficiency of the distribution system as it measures both technical as well as commercial losses. As the T&D losses were not enough and capable to capture all the losses present in the network, therefore, the concept of AT&C was introduced. The commercial losses are mainly due to low-metering efficiency, defective meters, un-metered supply of energy, theft, and pilferages [1]. This may be eliminated by improving meter efficiency and by appointing a vigilance team. Technical losses contribute to a considerable amount of energy which is lost in the distribution system. These intrinsic losses in transmission and distribution of electrical energy from the generating stations to the end consumers should be reduced by eliminating or minimizing the causes of losses.

T&D loss is calculated as the difference between input in the T&D network and sales to consumers [2]. AT&C loss is calculated as the difference between the input energy units to the system and the units for which the payment is collected. T&D losses and AT&C losses are defined by (1) and (2).

$$\text{Loss}_{T\&D} = \left(1 - \frac{\sum_{i=1}^{i=12} E_{\text{Bill}}^{i}}{\sum_{i=1}^{i=12} E_{\text{inp}}^{i}}\right) \times 100 \tag{1}$$

$$\text{Loss}_{\text{AT\&C}} = [1 - (B_{\text{eff}} \times C_{\text{eff}})] \times 100 \tag{2}$$

Billing efficiency and collection efficiency are calculated using (3) and (4), respectively.

$$B_{\text{eff}} = \frac{\sum_{n=1}^{N} K_{\text{Bill}}^{n}}{\sum_{n=1}^{N} K_{\text{inp}}^{n}} \tag{3}$$

$$C_{\text{eff}} = \frac{C_{\text{rev}}}{C_{\text{Bill}}} \tag{4}$$

To develop a loss reduction strategy, the following framework is adopted:

1. The DisCom defines a detailed loss reduction path for each type of losses, along with the current levels of losses for DisCom.
2. There are two types of losses:
   (a) Technical losses (Loss_{Tec})—Line losses, losses in transformers, losses in service cables and connections, losses due to high-impedance faults, losses in rewired fuses/jumpers, etc.
   (b) Non-technical losses ($\text{Loss}_{\text{Nontec}}$)—Losses at consumer end, tampering/bypassing of meters, theft and pilferage of energy, etc.
3. These losses can be measured as follows:
   (a) Loss_{Tec} is calculated using (5) or (6).

$$\text{Loss}_{\text{Tec}} = \left[E_{\text{inp}}^{\text{MBC}} - E_{\text{consp}}\right] \tag{5}$$

$$\text{Loss}_{\text{Tec}} = \left[E_{\text{inp}}^{\text{MBC}} - (\text{DT}_{\text{consp}} + \sum E_{\text{consp}}^{\text{HT}})\right] + \text{Loss}_{\text{Tec}}^{\text{LT}} \tag{6}$$

(b) $\text{Loss}_{\text{Nontec}}$ that occurs due to incorrect energy accounting is calculated using (7) or (8).

$$\text{Loss}_{\text{Nontec}} = E_{\text{consp}}^{\text{MBC}} - E_{\text{Bill}}^{C} \tag{7}$$

$$\text{Loss}_{\text{Nontec}} = \left[E_{\text{inp}}^{\text{DisCom}} - (\text{Loss}_{\text{Tec}} - E_{S})\right] \tag{8}$$

(c) $\text{Loss}_{\text{Nontec}}$ occurs due to non-recovery is calculated using (9) or (10). Billing efficiency is defined as (11).

$$\text{Loss}_{\text{Nontec}} = E_{\text{Bill}} - E_{\text{coll}} \tag{9}$$

$$\text{Loss}_{\text{Nontec}} = 100 - (B_{\text{eff}} \times C_{\text{eff}}) \tag{10}$$

$$B_{\text{eff}} = 100 - \text{Loss}_{\text{dis}} \tag{11}$$

Some recent developments to reduce the T&D losses that are implemented in current scenario are

(a) LT lines in crowded areas are replaced by aerial bunched cables (AB cables) so that illegal tapping and hooking can be prevented. Because aerial bunched cables are insulated and have thick material coating, and hence, there are very less possibilities for direct hooking.
(b) Vigilance team is appointed to find the thefts and illegal connections.
(c) Installed energy meters are replaced and positioned to outdoor premises so that meter reading process becomes easier.

3 Methodology

The methodology for analyzing and minimizing the AT&C loss level is elaborated in this section. The methodology is divided into three phases [3]:

Phase-1

In this phase, groundwork is laid to carry out the research in the related field, and various strategies are discussed and planned to reduce the level of losses in the distribution network. Various sites are visited to know more about the distribution network in the city. Various elements of AT&C losses are also discussed in this phase.

Phase-2

In this phase, data of various transformers, HT consumers, distribution transformers, feeders, private hospitals, malls, hotels, and cold storages for loss reduction initiatives are collected. Using various tools and techniques, the data from the above-mentioned units are received and analyzed, and accordingly, loss reduction initiatives are taken. Wherever it is not possible to collect the necessary data, data are either collected manually by visiting the site or certain logical and calculative assumptions are formulated for the analysis. In this phase, these initiatives are concisely discussed and analyzed. The loss reduction techniques are discussed further based on the types of losses.

Phase-3

After identifying the different loss reduction techniques based on our complete study and research, a detailed and a comprehensive analysis is carried out to prepare a strategy for loss reduction. Under this strategy, detailed steps for different categories are discussed for conservation of energy and loss reduction techniques.

The detailed loss reduction initiatives which are taken and implemented as mentioned below:

(a) Installation of energy meters on all incoming feeders of 33 and 11 kV sub-stations located inside metering billing and collection (MBC) network area.
(b) Installation of energy meters on all incoming feeders of 33 and 11 kV feeding power to the HT/LT consumers inside MBC network area.
(c) Installation of export/import meters in dedicated feeders connected to sub-stations inside project area but feeding power to outside MBC network area.
(d) Segregation of rural HT (11 kV) feeders according to their categories which includes agricultural, commercial, domestic, etc.
(e) Meter data analysis which includes consumption pattern analysis of household consumers, malls, hospitals, cold storage plants, RO plants, etc.
(f) Phasor diagram study along with the event meter reading instrument (MRI).
(g) Updating all sorts of transformers, poles, and household customers data on GIS.
(h) New DT installation proposal to Nigam (AVVNL) if the conductor length is found to be excessive in length, to reduce the line losses.
(i) Shift the excessive number of DTs to another feeders.
(j) Informing AVVNL if there are any tree touching cases on HT line.

4 Results

The data for various categories which include cold storages, malls, hotels, and private hospitals are recorded and analyzed. The consumption pattern for all customers is shown in Figs. 1, 2, 3, and 4. To obtain these data, the following method is used.

(a) Firstly, the various categories are well segregated to avoid later on problems during analysis.
(b) Then corresponding distribution transformers are inspected, and it is checked whether they are metered or not. If they are metered, their consumption is

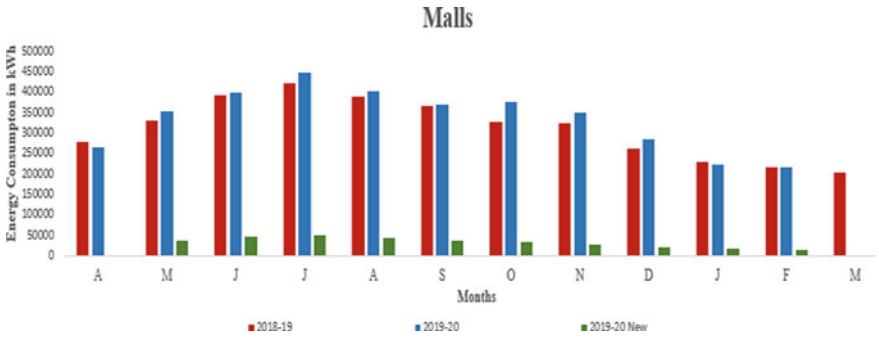

Fig. 1 Consumption analysis for malls

Fig. 2 Consumption analysis for hotels

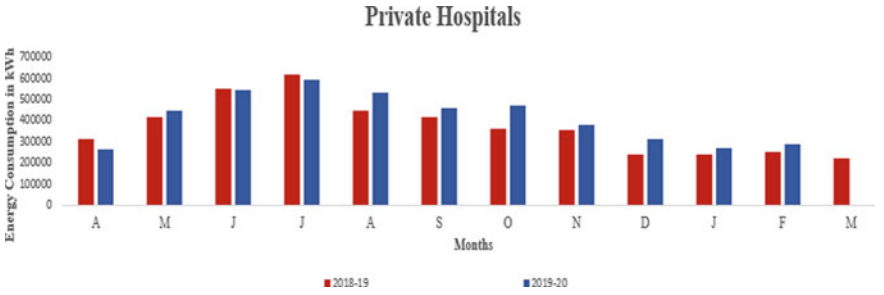

Fig. 3 Consumption analysis for private hospitals

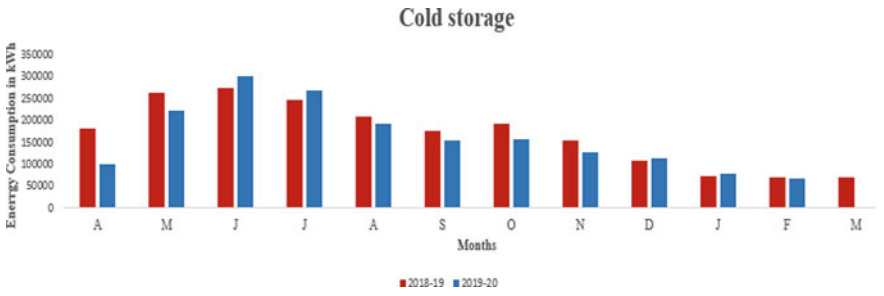

Fig. 4 Consumption analysis for cold storage

recorded using various tools and technologies. If not, then proper groundwork is to be laid, and meter installation is done on them.

(c) The smart meters nowadays also communicate well, and hence, the inbuilt software is used to record the consumption, and using the tools, their consumption analysis is being done.

(d) So, the graphs shown in Figs. 1, 2, 3, and 4 are the result of proper metering and proper strategy. And the graphs are drawn with the help of the data recorded.

After the data are recorded from these distribution transformers, it is matched with the data recorded from their corresponding feeders, and this is how the level of T&D loss is determined in each category.

The following observation is made properly to jump on to the conclusions listed below:

a. The consumption pattern in all categories showed a drastic downfall from October to March. This is because, the usage of air conditioners, coolers, fans, etc., decrease in the winter season.
b. The consumption pattern of cold storages showed the peak demand during summers and the demand drastically falls during October to March period as can be seen from Fig. 4. Also, as cold storages come under the category of seasonal factories, so they only operate for 8 months as per the policy of AVVNL and RERC.
c. Private hospitals also showed an increased number of patients during summers due to the illness caused by the heat strokes, and hence, the analysis showed the increased consumption as can be seen from Fig. 3.
d. A lot of cases are also reported in rainy season as the cases of malaria and dengue are more in this season and hence the increment in the consumption of hospitals.
e. New connections are set up in few malls and hotels. Consumption pattern is shown in Figs. 1 and 2 by green bars.

Finally, based on analysis for the deviation pattern in all the categories, it is concluded that the consumption pattern is more or less the same as the previous year's consumption pattern.

5 Conclusions

There are various factors responsible for T&D losses which need to be eliminated or minimized. The above listed factors and measures are proved to be beneficial in calculating the losses of the consumers whose consumptions are heavy (e.g., malls, private hospitals, etc.) Receiving online data of energy consumption and its analysis saves a lot of time and gives us an edge in execution to control and minimize the losses. Installation of CT/PT set on all the boundary points of MBC area and installation of VCB on all the 33 kV incomers at GSS makes this herculean task easy. Also, as compared to generation and transmission systems, distribution system can be said as the weakest system. Majority of the losses are associated with distribution system, hence reduction of distribution loss is an important task. If the losses are reduced, then the distribution network will become more efficient, more reliable, and more stable. Over the years, a lot of research has been carried out in reducing the T&D losses, but it has also become difficult to eliminate all the losses, strategic, and calculative measures should be taken to reduce or marginalize the major causes of losses. In the present scenario, the T&D system has become the center of attention of the power

sector, and various reforms and strategies for upgrading the T&D system have been carried out to improve its efficiency. Implementation of the planned strategies and calculative measures is the need of the hour. Ultimately, this may contribute in the process and development of our nation.

References

1. Ranganathan V (2005) Determining T&D losses in India: their impact on distribution privatization and regulation. Econ Polit Wkly 40:657–668
2. Mehta VK, Mehta R (2008) Principles of power system. S Chand Publications
3. Ghosh S (2012) Loss reduction and efficiency improvement: a critical appraisal of power distribution sector in India. Int J Mod Eng Res 2(5):3292–3297

Electric Vehicle Regenerative Braking Operation with BLDC Motor Drive

Vishnu Goyal, Ritesh Singh, and Himanshu Priyadarshi

Abstract Electric vehicle (EV) is mainly driven in three different operating modes: accelerating mode, normal operating mode and regenerative braking mode. While driving in accelerating and normal operating modes, the power flows from battery to motor, whereas in regenerative braking mode, electric motor operates as generator and charges the battery through power electronics converter. Three-phase inverter circuit is used as electronics commutator to control the brushless direct-current (BLDC) motor in all required operating modes. A bidirectional DC-DC power converter is used to manage the DC link voltage at the required level as per speed command given by the driver. Bidirectional DC-DC converter is controlled in buck mode to operate the electric vehicle in accelerating and normal operating mode. In other case, the same converter is controlled in boost mode to operate electric vehicle in regenerative braking mode. In this paper, PI controllers are used to maintain required speed of the vehicle, DC link voltage and the battery current for different kind of steady state and transient operation of the vehicle as per road conditions and the driver speed command. Therefore, the performance of the power train can be optimized. In this paper, a closed loop control strategy is demonstrated for bidirectional DC-DC converter and three-phase inverter to operate electric vehicle in different operating mode and recover energy to charge the batter in regenerative braking operation. Control strategy is verified through the simulation using Simulink/MATLAB R2019b package.

Keywords BLDC motor drives · Bi directional DC-DC converter · PI controller · Inverter · Battery · Regenerative braking operation

V. Goyal (✉) · R. Singh · H. Priyadarshi
Manipal University Jaipur, Jaipur, Rajasthan 303007, India
e-mail: vishnu.goyal@jaipur.manipal.edu

R. Singh
e-mail: ritesh.singh@jaipur.manipal.edu

H. Priyadarshi
e-mail: himanshu.priyadarshi@jaipur.manipal.edu

S. Dwivedi et al. (eds.), *Flexible Electronics for Electric Vehicles*, Lecture Notes in Electrical Engineering 863, https://doi.org/10.1007/978-981-19-0588-9_29

1 Introduction

Utilization of internal combustion engine (ICE)-based vehicles in a large number as a public transport becomes a major contributor of the pollution in medium and large cities. Such environmental disastrous is emerging as a big challenge for the automobile industry. As per the new Government policies, automobile industries have taken initiative to provide an eco-friendly solution like electric vehicle. EV can also support to reduce the "green house" gas production and the need of the fossil fuels. For this concern, electric vehicle is considered as a best solution for the transportation [1]. With increasing public awareness about the pollution, recently adoption of electric vehicles is increasing day by day. Although, due to the few limitations of EVs such as the time-consuming charging process and low driving range, till now EVs are not used in a large number [2, 3]. These shortcomes can be removed by applying efficient utilization of battery and modern control of electric motor drives to improve the overall performance of the electric vehicles [4–6].

Electric vehicles mainly consist by three major components: battery pack, electric motor drive and controller. Different types of electric motors are available like induction motor, BLDC motor and switched reluctance machine (SRM) [7]. Within these motors, the BLDC motor has many advantages over other motors like high starting torque, high efficiency, electronic commutating device, soundless operation, low maintenance, more compact construction, fast dynamic response and high speed range, etc. Henceforth, the brushless DC motor has been commonly used in EVs [8, 9].

Kinetic energy is wasted in form of heat while applying conventional mechanical brakes to reduce the speed of the vehicle. Hence, in this paper, regenerative electric braking approach will be discussed and applied using simulation to change the kinetic energy into electrical energy for charging the battery pack. Outcome of regenerative braking can be observed in the form of electric braking and efficient use of battery power [10]. Moreover, PI controller-based closed loop control technique is used to maintain the stable operation of the drives during different operation of the vehicle. In this present work, a brushless DC motor drive is simulated to run the electric vehicle in different operating mode commanded by the driver. Supply voltage level of the BLDC motor drive is controlled by using a bidirectional DC-DC converter, which is also used to control the power flow between motor and the battery. In addition, a bidirectional voltage source inverter (VSI) is used to operate a BLDC motor drive in motoring/braking mode on the basis of Hall effect sensors signals.

2 BLDC Motor Drive

Permanent magnet AC motor is categorized as permanent magnet synchronous motor (PMSM) and BLDC motor. The PMSM develops back emf of sinusoidal waveforms so the stator winding is required to be energized with the sinusoidal currents. In other

hand, BLDC motor develops back emf of trapezoidal waveform, and hence, the stator winding is required to be supplied with the quasi-rectangular shaped currents. BLDC motor stator windings are connected in star, and the rotor is constructed by magnetic material on which permanent magnet poles are mounted. The type of magnetic material used in the rotor depends on the magnitude of magnetic field density required to be develop in the rotor. In addition, Hall effect sensors are implanted on stator to perceive the accurate rotor position to energize the corresponding stator phase winding through three-phase inverter as shown in Fig. 1. A DC link capacitor is used as a momentary energy storage to manage the energy requirement during transient operation of the drives. Three Hall effect sensor signals are decoded to generate the firing pulses for six switches of the inverter and supply the quasi-rectangular shaped of current to the stator windings of the motor. Switching pattern of six switches of three-phase inverter based on Hall effect signals is given in Table 1. BLDC motor controller generates commutation pulses based on the rotor location sensed by Hall sensors and optical encoders.

As per Lenz's law, back emf across the stator winding of the motor opposes the supply voltage. This back emf mainly depends on rotor speed, rotor magnetic field

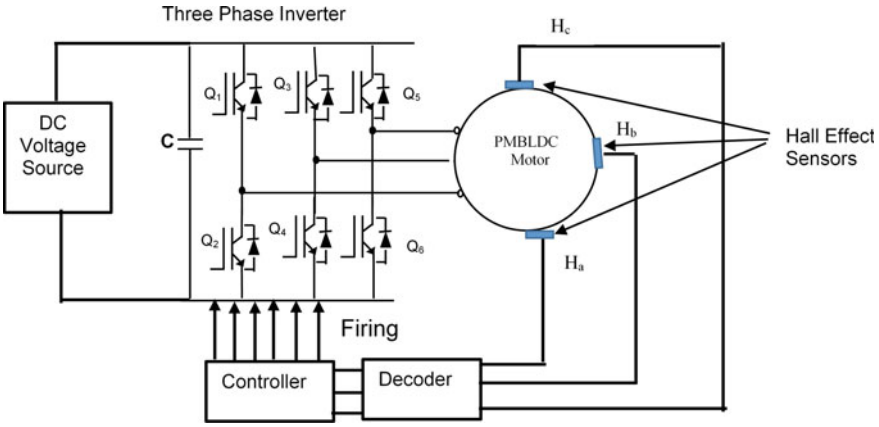

Fig. 1 BLDC motor drives with three-phase inverter

Table 1 Switching pattern for six switches of inverter based on Hall sensors for motoring mode

Ha	Hb	Hc	Ea	Eb	Ec	*Q*1	*Q*2	*Q*3	*Q*4	*Q*5	*Q*6	VL
0	0	1	0	−ve	+ve	0	0	0	1	1	0	Vcb
0	1	0	−ve	+ve	0	0	1	1	0	0	0	Vba
0	1	1	−ve	0	+ve	0	1	0	0	1	0	Vca
1	0	0	+ve	0	−ve	1	0	0	0	0	1	Vac
1	0	1	+ve	−ve	0	1	0	0	1	0	0	Vab
1	1	0	0	+ve	−ve	0	0	1	0	0	1	Vbc

Table 2 Switching pattern for six switches of inverter based on Hall sensors for regenerative braking

H_a	H_b	H_c	Ea	Eb	Ec	Q_1	Q_2	Q_3	Q_4	Q_5	Q_6	VL
0	0	1	0	+ve	−ve	0	0	1	0	0	1	V_{bc}
0	1	0	+ve	−ve	0	1	0	0	1	0	0	V_{ab}
0	1	1	+ve	0	−ve	1	0	0	0	0	1	V_{ac}
1	0	0	−ve	0	+ve	0	1	0	0	1	0	V_{ca}
1	0	1	−ve	+ve	0	0	1	1	0	0	0	V_{ba}
1	1	0	0	−ve	+ve	0	0	0	1	1	0	V_{cb}

and stator winding number of turns. After construction of motor, rotor magnetic field and stator winding number of turns become constant parameter of the motor. Hence, the back emf of the motor will change with the rotor speed.

3 Regenerative Braking Operation

Electric vehicles have one major problem associated with its energy storage device like battery. The battery has limited capacity of storage which becomes the main cause of restriction in the range of EVs. Regenerative braking approach of controlling the speed of the vehicle can be a one of the solutions to increase the range of the EVs. In regenerative braking, BLDC motor operates as generator to convert the kinetic energy of vehicle into electrical that can help to recover energy and recharge the battery during braking [11]. However, the switching pattern of the three-phase voltage source inverter is required to modify for implementation of regenerative braking as shown in Table 2.

Generally regenerative braking is required to be implemented in two different conditions. In first case, the regenerative braking command is given by the driver to decelerate the vehicle speed. And in other case, regenerative braking is also applied while the vehicle is going down from the hill or from the overbridge.

4 Methodology

DC voltage source supplies power to the DC link through the bidirectional DC-DC converter which helps to maintain required voltage level at input terminal of the inverter. This bidirectional converter operates in buck mode during acceleration. But in the regenerative operation this converter operates in boost mode to increase the voltage up to battery voltage for charging the battery. Three-phase inverter supplies power to the BLDC motor from the DC link at the frequency corresponding to driver speed command. Hence, driver speed command has taken reference speed

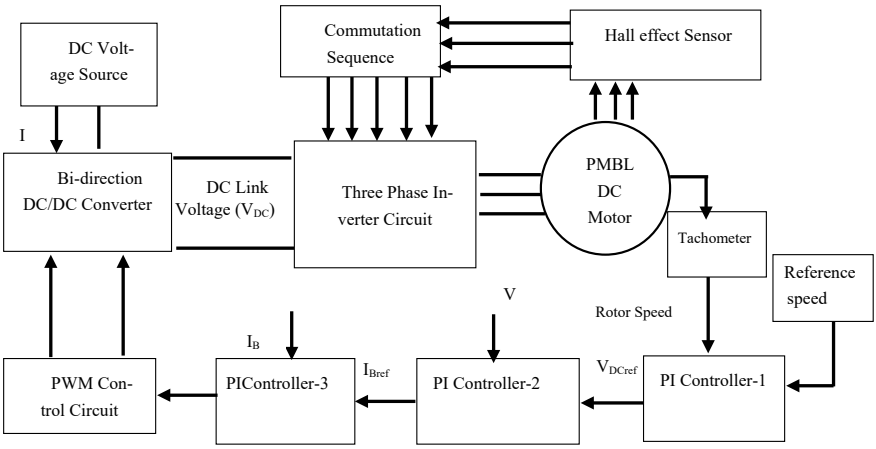

Fig. 2 Block diagram of PMBLDC controller as per driver speed command

for the controller and compared with the rotor speed to generate speed error signal. This speed error signal is minimized through PI controller, and it generates the reference DC link voltage, which is compared with actual DC link voltage. After comparison, DC link voltage error signal is supplied to PI controller and generates the reference signal for the battery current. Likewise, reference of battery current signal is compared with the present battery current and generates the firing pulses for the bidirectional DC-DC converter as shown in Fig. 2.

5 Result and Simulation

Simulation diagram of the complete drive system is shown in Fig. 3. At the starting, accelerating command given by driver is taken as reference speed for the controller. This reference speed is now compared with the present rotor speed and minimizes the speed error as shown in Fig. 4. This speed error is minimized by varying the DC link voltage through bidirectional DC-DC converter and maintaining the DC link voltage as per requirement as shown in Fig. 5. The controller of the DC-DC converter is operating in two different modes to adjust the battery current. In case of higher reference speed, the controller sets the positive value for battery reference current. Thereafter, controller supplies the firing control pulses to the DC-DC converter to operate in the buck mode and supply the required current to accelerate the vehicle as per driver command. In other case, controller sets the negative value of battery reference current and generate the firing pulses for the dc-dc converter to operate the converter in the boost mode to charge the battery.

It can be observed that the regenerative braking operation is implemented in two different ways. In first case, negative torque is suddenly applied on the motor which

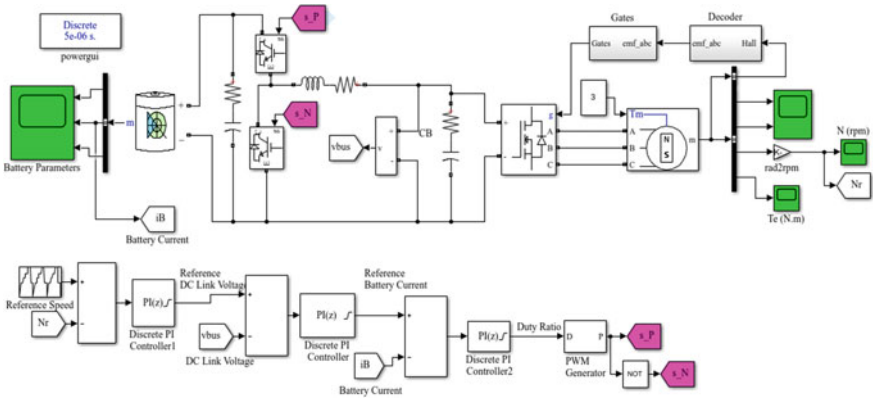

Fig. 3 Simulation model of PMBLDC controller

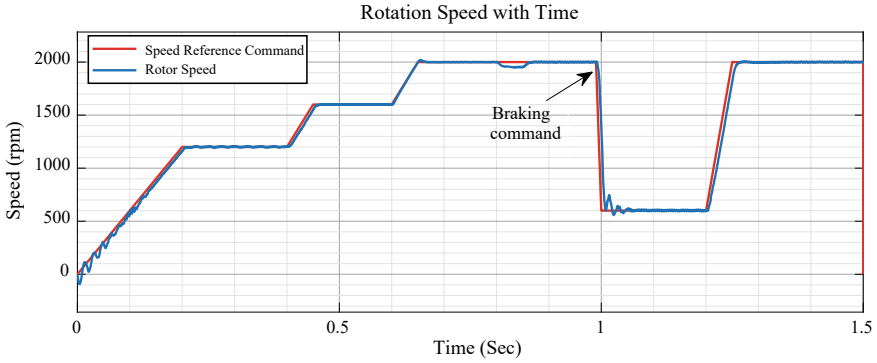

Fig. 4 Speed reference command and rotor speed

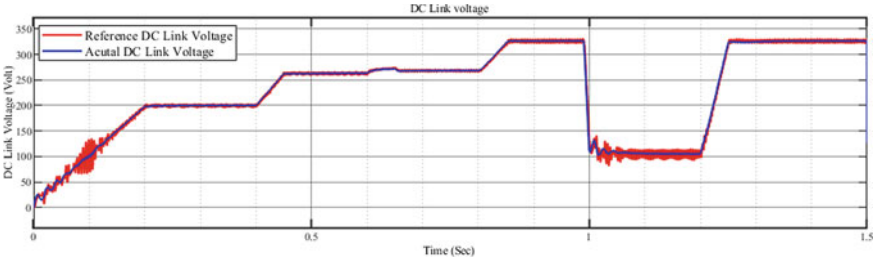

Fig. 5 DC link reference voltage and actual DC link voltage

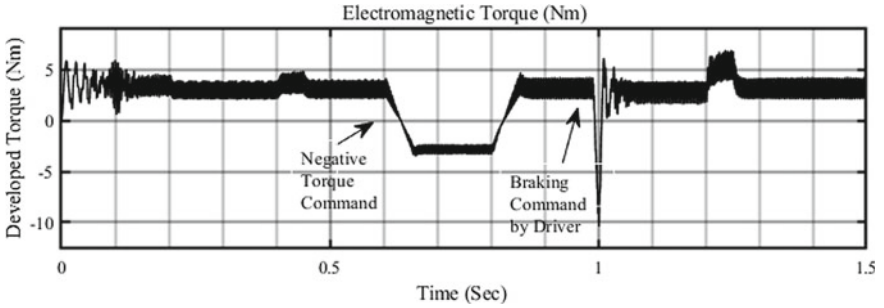

Fig. 6 Electromagnetic torque of the BLDC motor

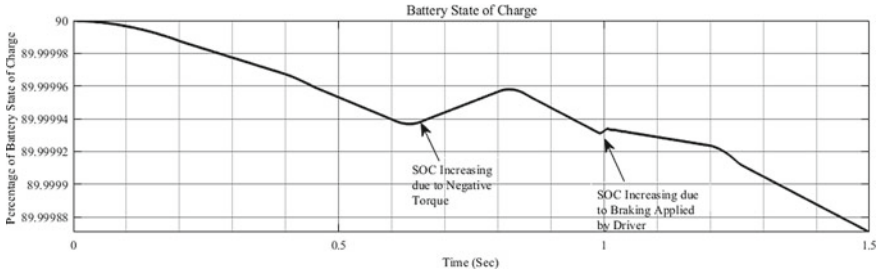

Fig. 7 State of charge of the lithium ion battery pack

shows the vehicle is going downward from the hill or from the overbridge. In that case, regenerative braking is applied to maintain the speed with in a limit. And in other case driver sets the speed reference command for the regenerative braking to reduce the speed of the vehicle, and in that case also, negative torque is developed as shown in Fig. 6. In both the cases, kinetic energy of the vehicle is converted into the electrical energy using regenerative braking and charge the vehicle battery pack, Fig. 7 shows the state of charge of battery pack for both the cases is increasing. Phase A stator current and back emf of the BLDC motor are shown in Fig. 8 in which it is noticed that the magnitude and frequency of the back emf are variable with the speed reference command given by the driver.

6 Conclusion

Simulation model of the lithium ion battery-operated BLDC motor drive using bidirectional DC-DC converter is simulated for electric vehicle application. The DC-DC converter controls the motor as per the speed reference command through the driver for different operation. Simulation is also tested for three different operation of the vehicle like acceleration, normal running in flat road and regenerative

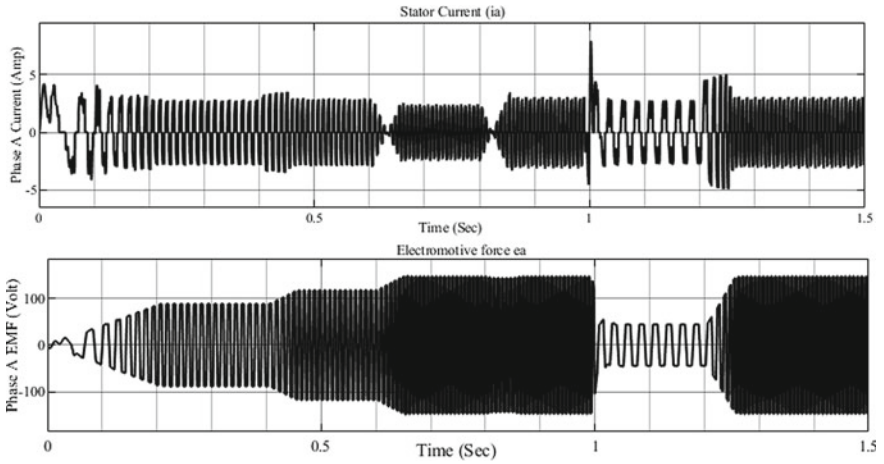

Fig. 8 Stator phase A current and voltage of the BLDC motor

braking. Regenerative controlling approach is developed and implemented to charge the battery during braking operation. It is also observed that the motor is derived stably for different operation of electric vehicle.

References

1. Sneha Angeline PM, Newlin Rajkumar M (2020) Evolution of electric vehicle and its future scope. Mater Today Proc 2214–7853
2. Long B, Lim ST, Ryu JH, Chong KT (2014) Energy regenerative braking control of electric vehicles using three-phase brushless direct-current motors. Energies 7:99–114
3. Mohammad A, Khan ZR (2015) BLDC motor controller for regenerative braking. In: Conference paper, May 2015
4. Wang X, He H, Sun F, Sun X, Tang H (2013) Comparative study on different energy management strategies for plug-in hybrid electric vehicles. Energies 6:5656–5675
5. Zheng P, Wu F, Lei Y, Sui Y, Yu B (2013) Investigation of a novel 24-Slot/14-pole six-phase fault-tolerant modular permanent-magnet in-wheel motor for electric vehicles. Energies 6:4980–5002
6. Khaligh A, Li Z (2010) Battery, ultracapacitor, fuel cell, and hybrid energy storage systems for electric, hybrid electric, fuel cell, and plug-in hybrid electric vehicles: state of the art. IEEE Trans Veh Technol 59:2806–2814
7. Wu H, Cheng S-K, Cui S-M (2005) A controller of brushless dc motor for electric vehicle. IEEE Trans Magnet 41:509–513
8. Wang H-P, Liu Y-T (2006) Integrated design of speed-sensorless and adaptive speed controller for a brushless dc motor. IEEE Trans Power Electron 21:518–523
9. Satyendra Kumar M, Revankar ST (2016) Development scheme and key technology of an electric vehicle: an overview. Renew Sustain Energy Rev 1364–0321
10. Yang M-J, Jhou H-L, Ma B-Y, Shyu K-K (2009) A cost-effective method of electric brake with energy regeneration for electric vehicles. IEEE Trans Ind Electron 56:2203–2212
11. Nian X, Peng F, Zhang H (2014) Regenerative braking system of electric vehicle driven by brushless DC motor. IEEE Trans Veh Technol 61(10):5798–5808

Optimal Selection of Modulation Index and Gain for Nine-Level Symmetric T-Type Cross-Connected Source Inverter Fed EV

Vinay Kumar, Paramjeet Singh Jamwal, Sanjeev Singh, and Shailendra Jain

Abstract The electric vehicles (EVs) operated from induction motor need clean, harmonic free AC supply for efficient operation, also the fault tolerant operation of inverter gives additional reliability to EV system. This paper presents a fault tolerant multilevel inverter for EV application. The harmonic profile of output voltage generated by fault tolerant T-type cross-connected source (TTCCS) inverter depends upon the value of gain for nearest level control (NLC) technique and modulation index for phase opposition disposition sinusoidal pulse width modulation (PODSPWM) technique. This paper presents the application of particle swarm optimization (PSO) algorithm to select the optimal gain for NLC technique and modulation index for PODSPWM technique to operate the nine-level (9L) symmetric fault tolerant TTCCS inverter with better harmonic profile. The presented simulation work is carried out in R2017b version of MATLAB. With the application of PSO, optimal value of gain and modulation index is calculated.

Keywords EV application · Fault tolerant control (FTC) · Nine-level (9L) inverter · Particle swarm optimization (PSO) · T-type cross-connected source (TTCCS) inverter

1 Introduction

T-type cross-connected source (TTCCS) inverter is a reduced device count (RDC) topology which generate nine-level (9L) output voltage with ten IGBT switch (eight unidirectional and two bidirectional) and four symmetric voltage DC sources

V. Kumar (✉) · P. S. Jamwal · S. Jain
Sant Longowal Institute of Engineering and Technology, Longowal, Punjab, India
e-mail: vinay_pei1810@sliet.ac.in

P. S. Jamwal
e-mail: paramjeet_pei1803@sliet.ac.in

S. Singh
Maulana Azad National Institute of Technology, Bhopal, Madhya Pradesh, India
e-mail: sschauhan@manit.ac.in

S. Dwivedi et al. (eds.), *Flexible Electronics for Electric Vehicles*, Lecture Notes in Electrical Engineering 863, https://doi.org/10.1007/978-981-19-0588-9_30

proposed by Saeedian et al. [1]. Fault tolerant control (FTC) of TTCCS inverter topology with single switch open circuit fault along with two control schemes named as phase opposition disposition sinusoidal pulse width modulation (PODSPWM) and nearest level control (NLC) is discussed in [2]. The harmonic profile of output voltage generated by TTCCS inverter topology with FTC depends upon the value of gain (K) for NLC technique and modulation index (M_a) for PODSPWM technique.

To calculate the optimum value of gain and modulation index for better harmonic profile is a tedious task. Similar to this, there are some another problem like identification of optimum value of passive filter, proportional-integral (PI) controller, switching angle, etc., which is resolved by using number of optimization techniques. Particle swarm optimization (PSO) is among popular optimization technique because of its easy implementation and mostly used to calculate the optimum value of passive filter [3], PI controller [4], switching angle [5], etc. PSO was reported 26 years ago by Kennedy and Eberhart and cited by more than 22 K authors till now [6]. In PSO, there is a variation in objective function and inertial weight with variation in application. Therefore, PSO with single objective function at various inertia weight is used in this work, to calculate the optimal value of gain and modulation index to generate output voltage with better harmonic profile. Correa et al. reported single-phase IM operated with vector control scheme [7]. Jahmeerbacus reported the effect of rotor time constant on the performance of single-phase IM operated with vector control [8]. While in this work, 9L-TTCCS inverter fed open-loop single-phase induction motor (IM) is considered which can be used in small electric vehicle (EV) application with vector control.

This paper is discussed in five parts. After discussing introduction in this part, topology is described in second part, PSO algorithm is discussed in third part, performance simulation is discussed in fourth part, and conclusion is given in fifth part.

2 Topology Description

Single-phase IM operated with symmetric configuration of TTCCS inverter as given in Fig. 1 has four DC source with equal DC voltage (V_{DC}), eight bidirectional-conducting-unidirectional-blocking (BCUB) power semiconductor switch (S_{L1}, S_{L2}, S_{R1}, S_{R2}, S_{M1}, S_{M2}, S_{M3}, and S_{M4}), and two bidirectional-conducting-bidirectional-blocking (BCBB) power semiconductor switch (S_{T1}, and S_{T2}).

The 9L topology is split into three segments as left section and right section with T-type configuration and combined with H-type arrangement of switches in central section. Therefore, complete power circuit is named as TTCCS configuration. In healthy condition, TTCCS inverter topology with FTC generates 9L output voltage [2]. When open circuit fault occurs in the switch (S_{T1}, or S_{T2}), the output voltage level remains same at 9L. When open circuit fault occurs in the switch ($\mathrm{S_{L1}}$, $\mathrm{S_{L2}}$, $\mathrm{S_{R1}}$, or $\mathrm{S_{R2}}$), the output voltage level reduced to seven-level (7L). When open circuit

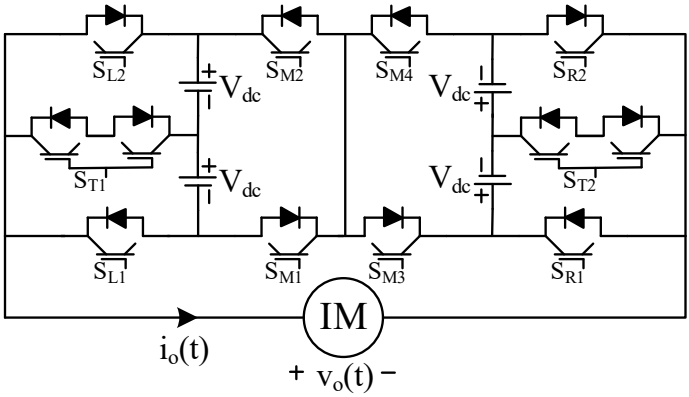

Fig. 1 Circuit diagram of the symmetric TTCCS inverter fed induction motor

fault occurs in the switch (S_{M1}, S_{M2}, S_{M3}, or S_{SM4}), the output voltage level reduced to five-level (5L).

The value of gain for NLC method is calculated manually with the formula given in (1).

$$K = 2 * (\text{Voltage amplitude})/(\text{Number of Levels} - 1) \tag{1}$$

The value of modulation index for PODSPWM method is calculated manually with the formula given in (2).

$$M_a = (\text{Number of levels} - 1)/(\text{Number of maximum Levels} - 1) \tag{2}$$

The PSO algorithm to obtain the value of gain for NLC technique and modulation index for PODSPWM technique is discussed in next section.

3 Optimization Algorithm

Flowchart of PSO to calculate optimum value of modulation index is shown in Fig. 2.

PSO algorithm for modulation index start with the range selection of M_a on the basis of switch conditions. Thereafter, generate initial particles in the selected range along with their velocity in the range (0–1) randomly. Initialize personal THD (THD_p) and global THD (THD_g) value of particle. Now assign first particle value as modulation index in FT-TTCCS inverter topology and run the simulation to evaluate THD. Compare this THD with personal THD (THD_p) of particle, if THD is less than THD_p then replace THD_p with current THD and personal modulation index (M_{ap}) with modulation index (M_a), otherwise, skip this step. Now compare personal THD with global THD (THD_g) of particle, if personal THD is less than global THD then

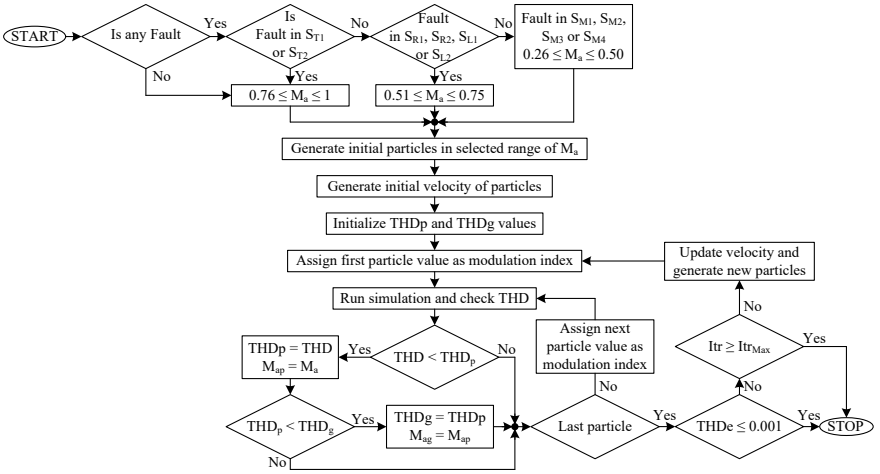

Fig. 2 Flowchart of PSO for modulation index of PODSPWM

replace THD_g with current THD_p and global modulation index (M_{ag}) with personal modulation index, otherwise, skip this step. Now assign next particle as modulation index and repeat same procedure until last particle. Now check whether THD_e is less than equal to 0.001, if yes then stop, otherwise, check whether maximum iteration performed, if yes then stop, otherwise, update velocity and generate new particles. Thereafter, start with first particle and assign first particle value as modulation index and repeat same step until termination criteria is achieved. Flowchart of PSO to calculate optimum value of gain is given in Fig. 3.

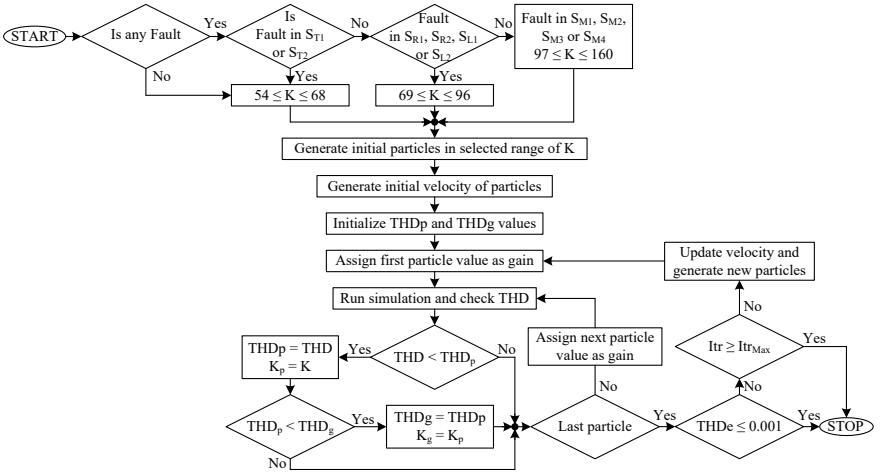

Fig. 3 Flowchart of PSO for gain of NLC

PSO algorithm for gain start with the range selection of K on the basis of switch conditions. Thereafter, generate initial particles in the selected range along with their velocity in the range (0–1) randomly. Initialize personal THD (THD_p) and global THD (THD_g) value of particle. Now assign first particle value as gain in FT-TTCCS inverter topology and run the simulation to evaluate THD. Compare this THD with personal THD (THD_p) of particle, if THD is less than THD_p then replace THD_p with current THD and personal gain (K_p) with gain (K), otherwise, skip this step. Now compare personal THD with global THD (THD_g) of particle, if personal THD is less than global THD then replace THD_g with current THD_p and global gain (K_g) with personal gain, otherwise, skip this step. Now assign next particle as gain and repeat same procedure until last particle. Now check whether THD_e is less than equal to 0.001, if yes then stop, otherwise, check whether maximum iteration performed, if yes then stop, otherwise, update velocity and generate new particles. Thereafter, start with first particle and assign first particle value as gain and repeat same step until termination criteria is achieved.

4 Performance Simulation

Calculated value of gain for NLC method and modulation index for PWM method with both method (manual and PSO) is given in Tables 1 and 2, respectively.

From Table 1, it is clear that the output voltage has lesser THD with the gain value obtained by PSO as compare to gain value obtained manually. From Table 2, it is clear that the output voltage has lesser THD with the modulation index obtained by PSO as compare to modulation index obtained manually. Waveform and harmonic spectrum of 9L, 7L, and 5L output voltage ($v_o(t)$) at gain with manual method are

Table 1 Gain value for NLC method

No. of level	Range of K	Manual		PSO	
		K	THD_v (%)	K	THD_v (%)
9L	$54 \leq K \leq 68$	60	9.3	56.7786	8.9015
7L	$69 \leq K \leq 96$	80	12.20	74.2208	11.5330
5L	$97 \leq K \leq 160$	120	17.51	107.4668	16.4201

Table 2 Modulation index for PWM method

No. of level	Range of M_a	Manual		PSO	
		M_a	THD_v (%)	M_a	THD_v (%)
9L	$0.76 \leq M_a \leq 1$	1	16.77	0.9821	16.3207
7L	$0.51 \leq M_a \leq 0.75$	0.75	21.78	0.7474	21.6337
5L	$0.26 \leq M_a \leq 0.5$	0.5	33.67	0.4934	33.6618

shown in Fig. 4a, c, e, respectively. While waveform and harmonic spectrum of 9L, 7L, and 5L output voltage ($v_o(t)$) at gain with PSO algorithm are shown in Fig. 4b, d, f, respectively.

From the THD comparison shown in Fig. 4, it is clear that output voltage obtained with gain value obtained through PSO algorithm has less THD as compare to the output voltage obtained with gain value manually. Waveform and harmonic spectrum of 9L, 7L, and 5L output voltage ($v_o(t)$) at modulation index with manual method are shown in Fig. 5a, c, e, respectively. While waveform and harmonic spectrum of 9L, 7L, and 5L output voltage ($v_o(t)$) at modulation index with PSO algorithm are shown in Fig. 5b, d, f, respectively.

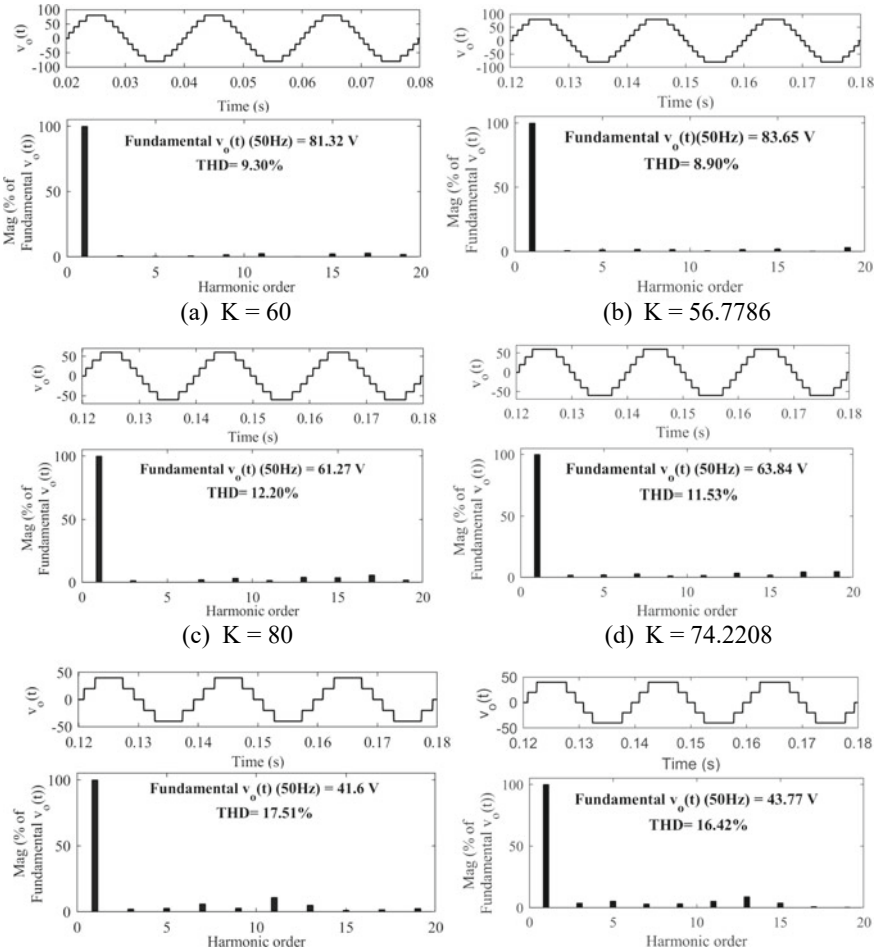

Fig. 4 Voltage THD at gain with manual (**a**, **c**, **e**) and with PSO (**b**, **d**, **f**)

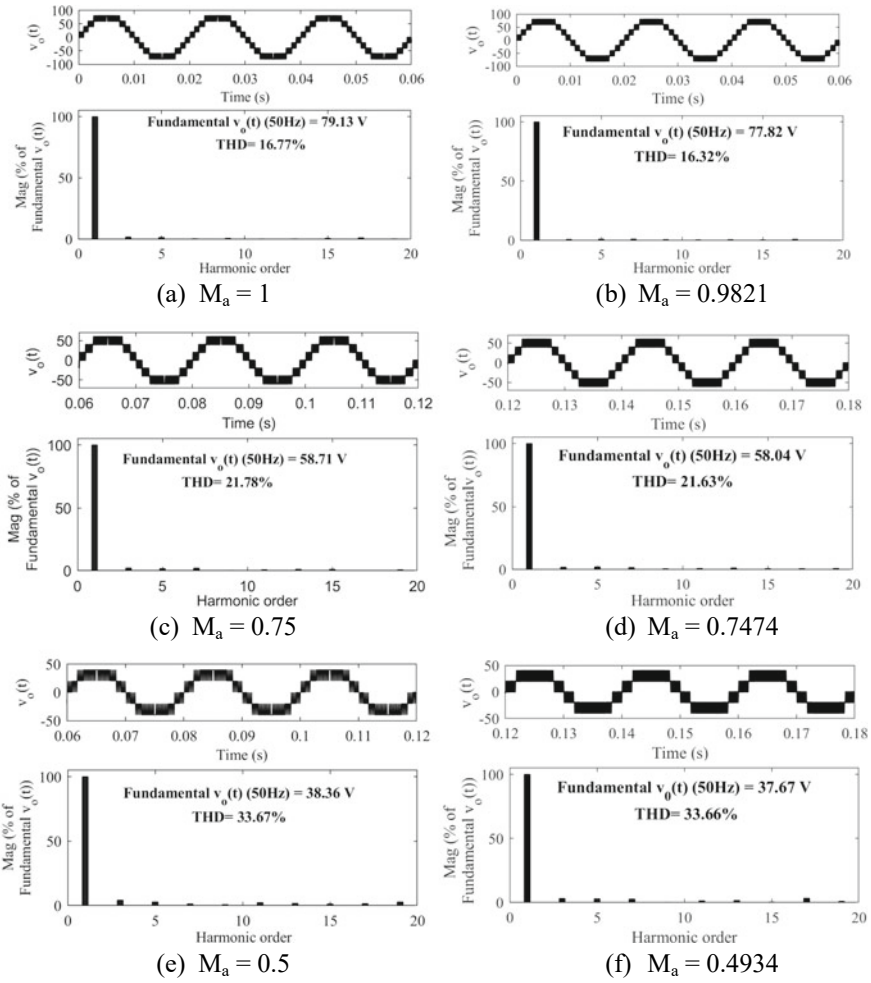

Fig. 5 Voltage THD at modulation index with manual (**a**, **c**, **e**) and with PSO (**b**, **d**, **f**)

From the THD comparison shown in Fig. 5, it is clear that output voltage with modulation index obtained through PSO algorithm has less THD as compare to the output voltage with modulation index obtained manually. Behavior of THD with variation in inertial weight is shown in Fig. 6.

Inertial weight is varied from 0.1 to 1 and it is observed that PSO algorithm find best THD in 6th iteration with all inertial weight. While it obtains best THD in first iteration with w_4 weight. Performance of symmetric TTCCS inverter fed IM with NLC and PODSPWM is shown in Fig. 7 during steady state condition of speed and torque.

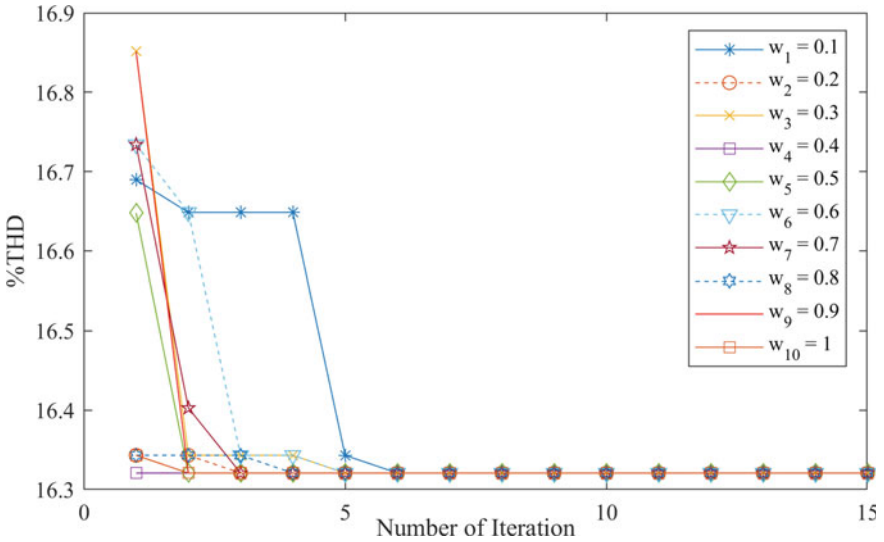

Fig. 6 Behavior of THD with inertial weight variation

5 Conclusion

It is concluded that inverter output voltage has less THDv by NLC with respect to PODSPWM method. PSO took less iteration to obtain best value of gain and modulation index with 0.4 inertia weight. Output voltage with modulation index and gain value obtained through PSO algorithm have less THD as compare to the output voltage with modulation index and gain value obtained manually. Performance of TTCCS inverter fed induction motor is better with PODSPWM as compare to NLC control. Further investigation shall be carried out for reduction of torque ripples in the IM for EV application.

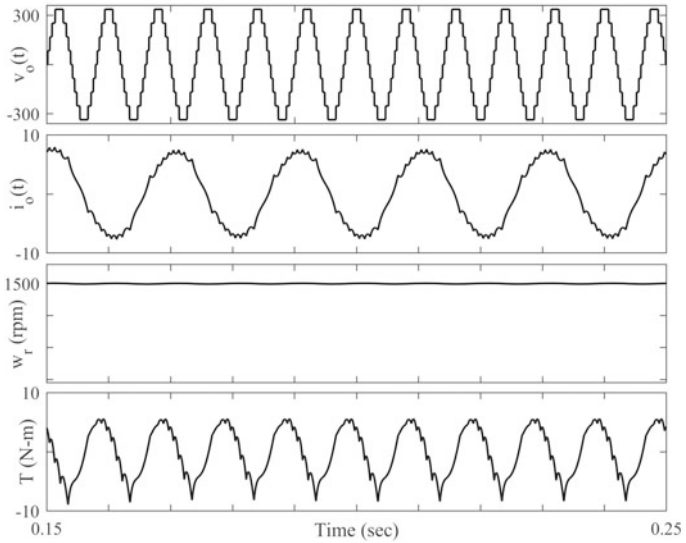

(a) With NLC

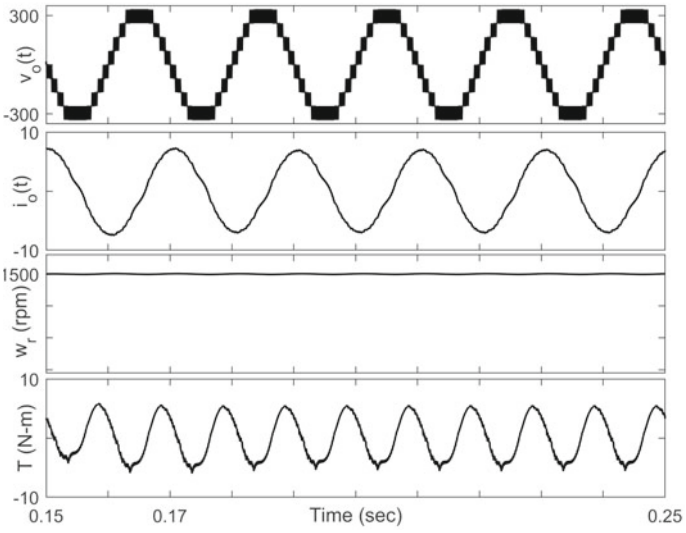

(b) With PODSPWM

Fig. 7 Voltage, current, speed, and torque of symmetric TTCCS inverter fed IM during steady state operation

References

1. Saeedian M, Jafar A, Hosseini SM (2017) Cascaded multilevel inverter based on symmetric–asymmetric DC sources with reduced number of components. IET Power Electronics 10(12):1468–1478
2. Kumar V, Singh S, Jain S (2020) Fault tolerant T-type cross connected source nine level inverter. In: 9th Power India International Conference (PIICON), pp 1–6. IEEE, Sonepat, India
3. Singh S, Singh B (2014) Optimized passive filter design using modified particle swarm optimization algorithm for a 12-pulse converter-fed LCI–synchronous motor drive. IEEE Trans Ind Appl 50(4):2681–2689
4. Jamwal PS, Singh S (2016) Speed controller optimization for PMSM drive using PSO algorithm. In: Pant M, Deep K, Bansal J, Nagar A, Das K (eds) Proceedings of Fifth international conference on soft computing for problem solving. Advances in intelligent systems and computing, vol 436. Springer, pp 989–999
5. Panda KP, Rout S (2017) Swarm optimization based harmonic elimination in improved h-bridge multilevel inverter. In: International conference on inventive systems and control (ICISC), pp 1–6. IEEE
6. Kennedy J, Eberhart R (1995) Particle swarm optimization. In: Proceedings of international conference on neural networks (ICNN), pp 1942–1948. IEEE, USA
7. Correa MBDR, Jacobina CB, Lima AMN, Silva ERCD (2000) Rotor-flux-oriented control of a single-phase induction motor drive. IEEE Trans Industr Electron 47(4):832–841
8. Jahmeerbacus MI (2020) Investigation of performance degradation of vector controlled single-phase induction motor drive under rotor time-constant variations. In: 3rd International conference on emerging trends in electrical, electronic and communications engineering (ELECOM). IEEE, Balaclava, pp 168–172

Remote Monitoring and Control of Irrigation Water Pumping System Using IoT

Mukesh Kumar Kirar

Abstract This paper represents the Android application-based remote monitoring and operation of water pumps through microcontroller ATmega 328P. The Android application has been developed for operating the water pump. Android app is used to provide better user interface, timer-based operation, status of pump and feedback notifications, etc. Android application will communicate with SIM900 GSM module present at the pump terminal, and the commands will be read by the microcontroller. Also feedback of pump status will be sent by GSM module to the App. The current and voltage are continuously sensed by Hall effect current sensor and voltage transformer and are monitored by microcontroller. Power supply for the whole assembly is taken from the main supply.

Keywords Microcontroller · Android application · Induction motor · GSM module · Internet of things

1 Introduction

A major portion of country's electricity is consumed in water pumping loads. There are basically two types of water pumping load: Irrigation pumps used by farmers for irrigating their agricultural fields and water pumps used by Municipal authorities for water supply in cities. In many cases, the irrigation fields are long distance away from the house of the farmers. So a remote operated irrigation pump sets at cost similar to existing systems is a perfect solution for their problems. The squirrel cage induction motors are widely used in water pumps due to their high robustness, reliability, low-cost and maintenance, high efficiency, and long service life. Fully automated SCADA systems are costly so they are not used at small scale. Android app-based operation of water pumps provides the features similar to SCADA system, but at the same time, it ensures the low-cost and reliability of operation.

M. K. Kirar (✉)
Electrical Engineering, MANIT, Bhopal, India
e-mail: mukeshkhaironiya@gmail.com

S. Dwivedi et al. (eds.), *Flexible Electronics for Electric Vehicles*, Lecture Notes in Electrical Engineering 863, https://doi.org/10.1007/978-981-19-0588-9_31

Remote monitoring and operation of the electrical equipment are an important issue which is normally done manually, or using an expensive PLC and SCADA system [1]. Because of low-cost, networkable microcontroller modules, the Internet of things is considered as the key technology to establish a remote monitoring, operation, and control of electrical equipments [2].

Monitoring and control of electrical equipments using IoT are a common approach [3–5]. The remote operation of the pumps using IoT can solve the problem of irregularity in power supply timings and unattained locations. In [6], Web-based automated electric machine test bench with data acquisition and remote control is presented. Automated test bench provides a Web-based and controlled GUI operated platform for IM and DC generator testing. The data can be acquired and stored from the remote location and can be used for performance evaluation and process control [7]. The IoT platform can also be important in condition monitoring of industrial motors [8–13]. Android operating system can be used for remote operation and control of electrical appliances. Android operating system is a mobile operating system (OS) currently developed by Google, based on the Linux kernel and designed primarily for smartphones and tablets. Android Studio is the official integrated development environment (IDE) for developing for the Android platform based on IntelliJ IDEA. The app has been designed to work with Jelly Beans and higher versions.

2 Proposed System

The basic block diagram of the project is shown in Fig. 1. This project is divided into two major sections:

- GSM module with microcontroller
- Android application

Android app will enable the user to communicate with the pump at remote location. Basic start and stop operation of pump along with options like timer mode setting and machine rating are given in the app. According to the options selected by the user, a string will be generated, and the same will be sent to the pump terminal by

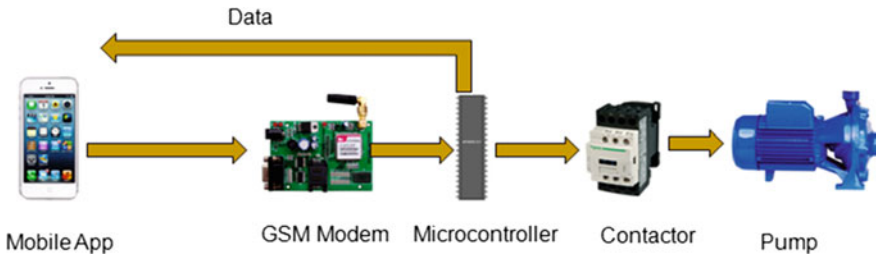

Fig. 1 Basic block diagram of project scheme

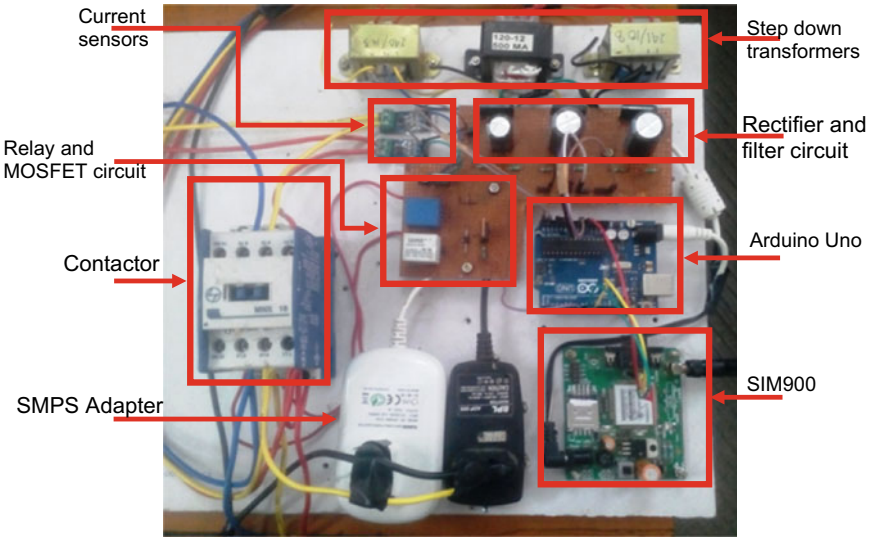

Fig. 2 Final assembly of the module at motor end

SMS. The SMS sent by app will be received by GSM module at pump terminal. The message will be extracted by the microcontroller, and further, actions will be initiated. Microcontroller will provide the necessary signals to the contactor through MOSFET and relay for starting the pump. If the pump is turned on successfully, then microcontroller will feedback this status to the app by generating SMS, which will be sent by GSM modem. The timer options as selected by user will be implemented by the microcontroller, and it will turn on and turn off the pump according to the timer settings. If the power supply is available, then microcontroller will send SMS through GSM modem to inform the user. The currents and voltages of the machine will be sensed by the sensors and microcontroller will read their values. Current (AC) is obtained by sampling while voltage is obtained by directly reading a DC voltage proportional to supply voltage. The power supply for the whole electronic circuitry will be taken from the main supply. SMPS of 12 V is used to power microcontroller, GSM modem, current sensors, and relay.

The final hardware assembly of the proposed system is depicted in Fig. 2. The proposed module will be installed at motor end.

2.1 Current Sensor

The 3-ϕ currents are read by the algorithm shown in Fig. 3. Current sensors (ACS 712) are interfaced with Arduino board. 5 V supply was given to ACS 712 by Arduino board, and output voltage of ACS 712 was taken as an input on the analog pin of

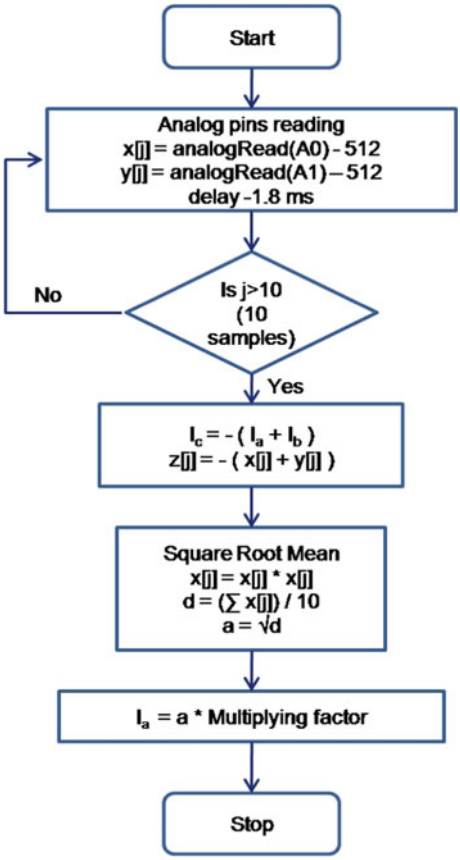

Fig. 3 Current sensing algorithm

the Arduino. Ten samples were taken at interval of 2 ms, and then, the RMS value is calculated using the samples, and then, multiplying factor is used to obtain final value of current. At zero current, output of sensor read by Arduino is 512 due to 2.5 V DC offset.

Ten current samples are taken from the two current sensors present in the two lines, and then, the third line current is obtained by these two line current samples. AnalogRead (AX) function is used by microcontroller to read the analog pin and converts the voltage at analog pin into digital count. Figure 4 shows output of the current sensor at 4 A current. The output voltage of current sensor read by Arduino was displayed by serial monitor and is shown in Fig. 5.

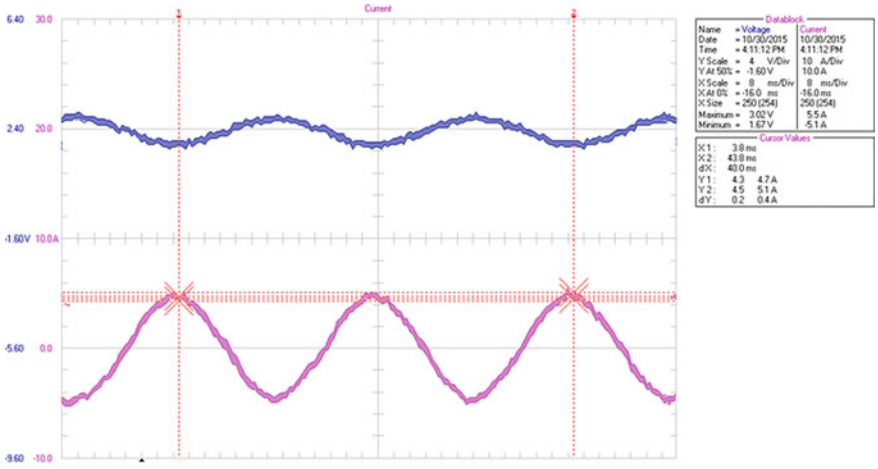

Fig. 4 ACS 712 output voltage at 4 A current

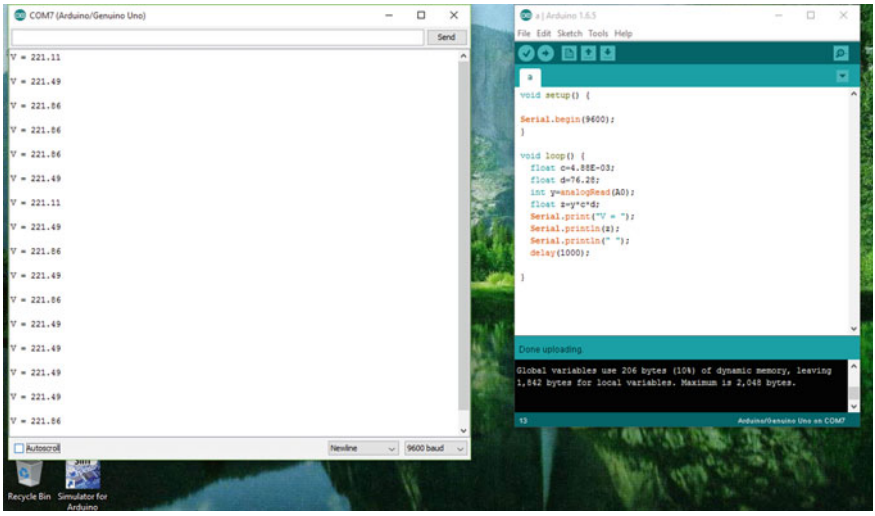

Fig. 5 ACS 712 output read by Arduino

2.2 Voltage Sensor

The supply voltage is stepped down using 230/12 V transformer, and then, the reduced voltage is fed to rectifier IC D2SB40. The output voltage of rectifier IC is unidirectional but pulsating in nature. This pulsating voltage is not suitable for feeding into microcontroller. So the pulsating output voltage after rectifier IC is made constant

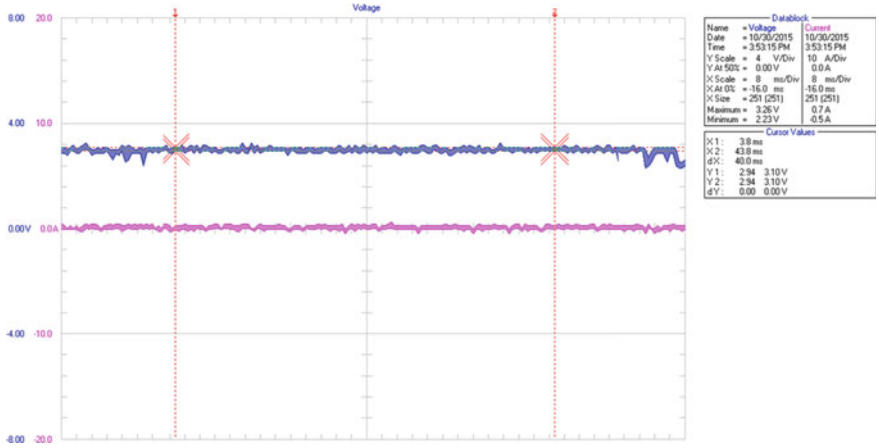

Fig. 6 Sensor output voltage after filter and voltage divider

using a parallel capacitor filter. Since Arduino can read voltages in between 0 and 5 V, so the output voltage has to be reduced for feeding to Arduino.

The voltage sensor voltage is reduced to less than 5 V using voltage divider circuit. Then, the final output is read using Arduino analog input pin. Finally, sensor value is converted into actual value using multiplying factor. The output voltage of transformer secondary terminals is filtered and reduced by voltage divider circuit is shown in Fig. 6. This reduced output voltage is fed to analog pin of Arduino, and the voltage read by Arduino is shown in Fig. 7. The voltage read at analog pin of Arduino is converted into digital count. Also the voltage reaching at analog pin is reduced by voltage divider circuit. Therefore, the readings must be multiplied by a multiplying factor to get original voltage reading.

3 Design of Remote Operation

The SMS is used to send commands from Android app and to receive feedback from pump terminal. The SIM900 modem will receive and send the SMS. The Android app will generate a message according to the options selected by user and will send it to the pump terminal.

The SMS received by SIM900 will be read by the microcontroller, and microcontroller will generate the trip signal to turn the pump on or off through contactor. The SMS received by modem SIM900 is read by microcontroller through the algorithm shown in Fig. 7. Whenever SMS is sent or received, it comes in the format as shown in Fig. 8. The sender mobile number is extracted, and it is compared with the saved mobile number. If these two mobile numbers are matched, then only the message

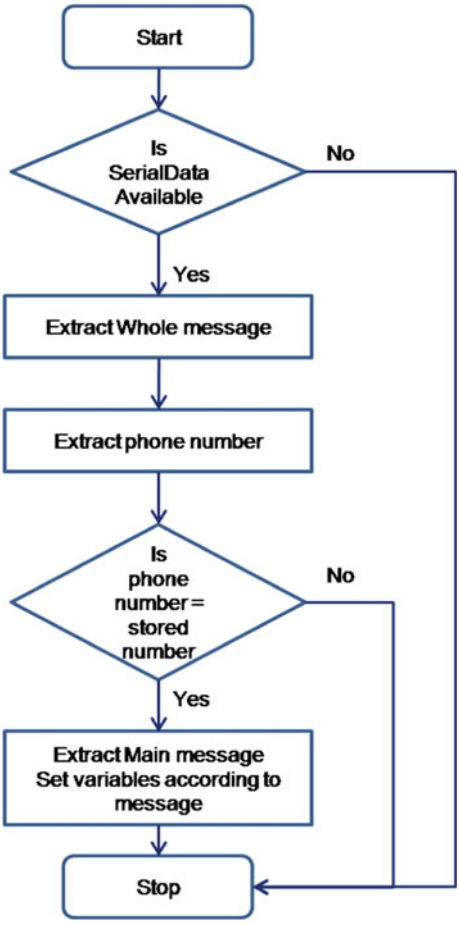

Fig. 7 SMS reading algorithm

will be extracted and read. This number matching will provide security for the entire operation.

AT commands are instructions used to control a modem. AT is the abbreviation of ATtention. Starting "AT" is the prefix that informs the modem about the start of a command line. The AT commands that are used in Arduino program to send and receive SMS are given below:

- AT + CMGF = 1—Set SMS mode to text.
- AT + CMGD = 1,4—Deletes all SMS saved in SIM memory.
- AT + CNMI = 2,2,0,0,0—Alert the GSM to receive SMS.
- AT + CMGS—Used for sending SMS.

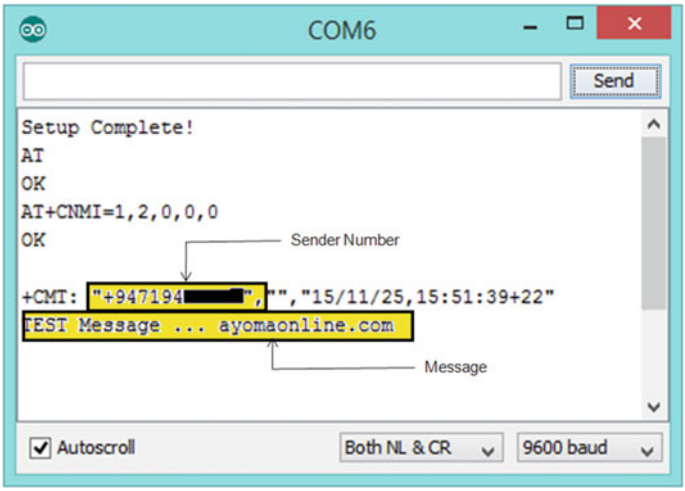

Fig. 8 SMS format

3.1 Android Operating System

It is a mobile operating system (OS) currently developed by Google, based on the Linux kernel and designed primarily for touch screen mobile devices such as smartphones and tablets. Androids' user interface is mainly based on direct manipulation, using touch gestures that loosely correspond to real-world actions, such as swiping, tapping, and pinching, to manipulate on-screen objects, along with a virtual keyboard for text input [12]. Android Studio [13] is the official integrated development environment (IDE) for developing for the Android platform based on IntelliJ IDEA.

First of all, the graphics for the App is created in layout file in XML format. It can be designed either by drag and drop of the components or by writing the code in XML file. The background and other graphics can be set by various commands in XML file. Then, all the buttons and text boxes are assigned identity. Then, the callback functions for the buttons and text boxes are defined in the Java file. All the components are imported in the Java file from the XML file. An activity class is created as an extension of default activity class defined in Android. onCreate() function is called first when the activity begins. In this function, the callback functions for all the components are defined which overrides the default functions defined in default activity class. The events like button press, text box press, etc., are captured by Android, and then, callback function is triggered. A string is being generated in the App which will be sent to the SIM900, and this string will contain all the commands. The structure of string is shown in Table 1.

Figure 9 shows activity life cycle of the general App and Fig. 10 represents flowchart of the Android application which is designed for user interface with motor end controller. The main features of the App are given below:

Table 1 String generated in APP

String	Values	Meaning
FinalMessage[0]	1/0	Start motor/stop motor
FinalMessage[1]	1/0	Timer mode YES/NO
FinalMessage[2]	0–2	Hour input 1
FinalMessage[3]	0–9	Hour input 2
FinalMessage[4]	0–6	Minute input 1
FinalMessage[5]	0–9	Minute input 2
FinalMessage[6]	1/2/3	Pump rating 1—5 HP 2—7.5 HP 3—10 HP

- ***Notification of message sent and delivered***: When user will press the START/STOP button in the main activity, then if SMS is sent and delivered, then notification about sending and delivery of SMS will be notified in notification text box of main activity. This will keep user aware of whether his request has been sent and delivered or not.
- ***Finish() on Pause()***: All the activities other than the main activity are finished as soon as they are kept on hold/pause. This prevents the other activities from staying on the background even after back button is pressed.
- ***App comes to foreground***: As soon as any feedback message comes from the pump terminal, the main activity of the app will come in the foreground if the app is running in background, and the notification panel will be updated according to the message received. This feature makes the user aware of the current notification immediately.
- ***Number check***: As soon as the message is received, first the sender's number is matched with the number saved in the app data. If the number matches only, then notification panel will be updated. This feature provides security from any kind of false/fake notifications.
- ***Timer input boxes***: If the input in the timer hh and mm boxes is left blank, then app will take 8 h as the default input. In Android app, if any ambiguous condition appears, then app will close immediately. So this feature prevents app from crashing down.
- ***Internal timer***: An internal timer will begin if timer mode is selected as soon as START button is pressed. When this timer is finished, then pump status will be changed to OFF. So even if the feedback from pump does not come at right time, the status of the pump in the app will be updated. This feature avoids ambiguity in case of communication delay.
- ***SharedPreferences***: With this, the receiver number and the machine rating will be stored till the time user updates them. This feature reduces the burden of typing the receiver number and machine rating every time when app is opened up.

Figure 11 shows snapshots of Android app on mobile. Figure 11a, b represents

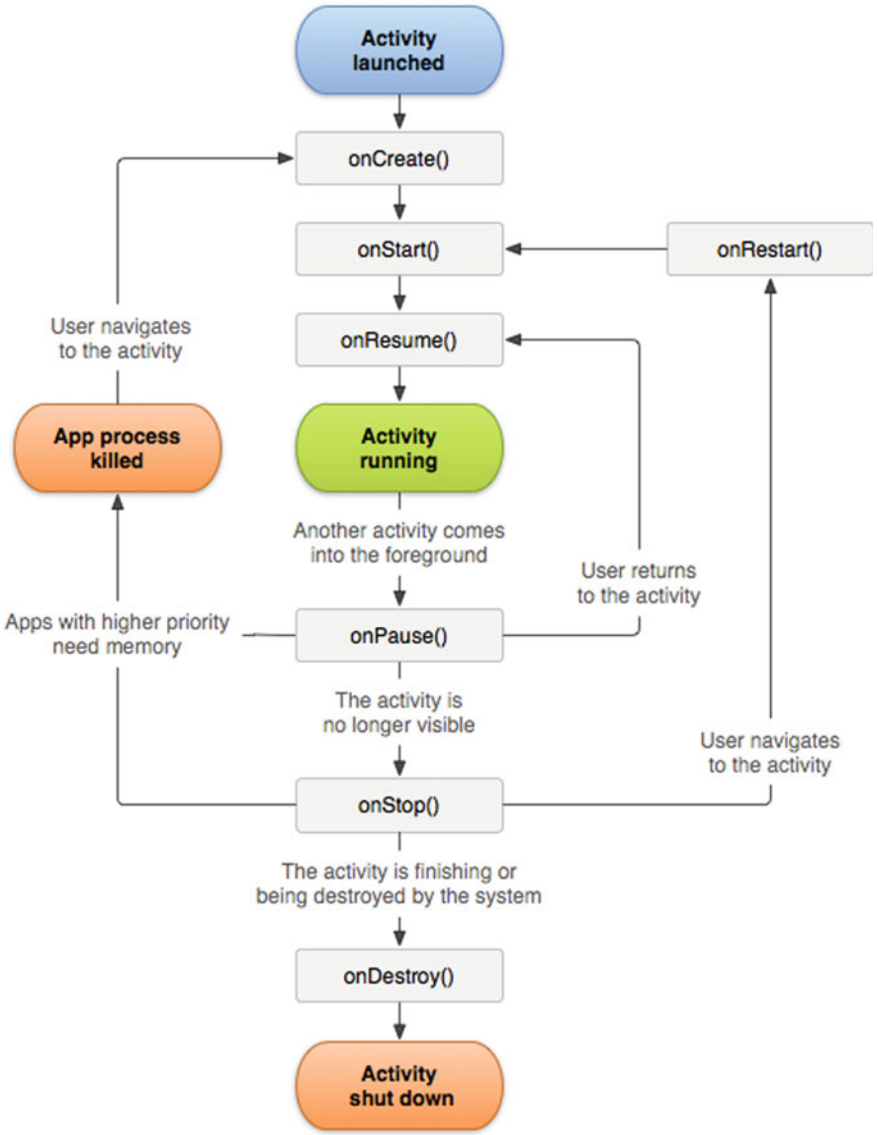

Fig. 9 Activity life cycle

splash screen and main activity page, respectively. Figure 11c shows setting activity page which provides access to the user to change machine rating in the program from the app. Figure 11d shows help activity for user of the app. SharedPreferance is used to store the receiver number and machine rating which removes the need for entering the number and rating every time when app starts. The notifications are updated in

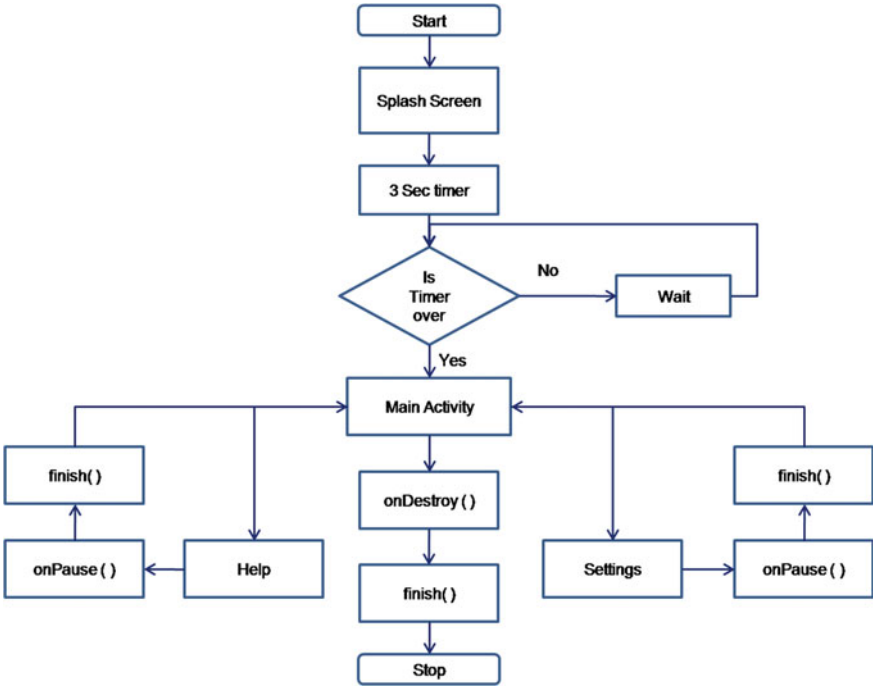

Fig. 10 Activity flowchart of app

the app only if the number from which SMS is coming matches the saved receiver number. This feature provides security to the app. Also a function check () has been provided which acts as a backup in case contactor does not operate when trip signal is given. This function generates the trip signal again and again till the time contactor operates. Comparison of the different technologies is given in Table 2.

4 Conclusion

In this paper, a system for operating water pumps at remote location from Android. The app developed for this project is working satisfactorily. Timer mode, feedback notifications, SMS sending, and receiving functions of the app have shown expected results. All kinds of possible situations have been defined in the app Java file. As a result, the app does not crash it any situation. SharedPreferance is used to store the receiver number and machine rating which removes the need for entering the number and rating every time when app starts. The notifications are updated in the app only if the number from which SMS is coming matches the saved receiver number. This feature provides security to the app. This app provides a simple and effective interface and feedback status to the user.

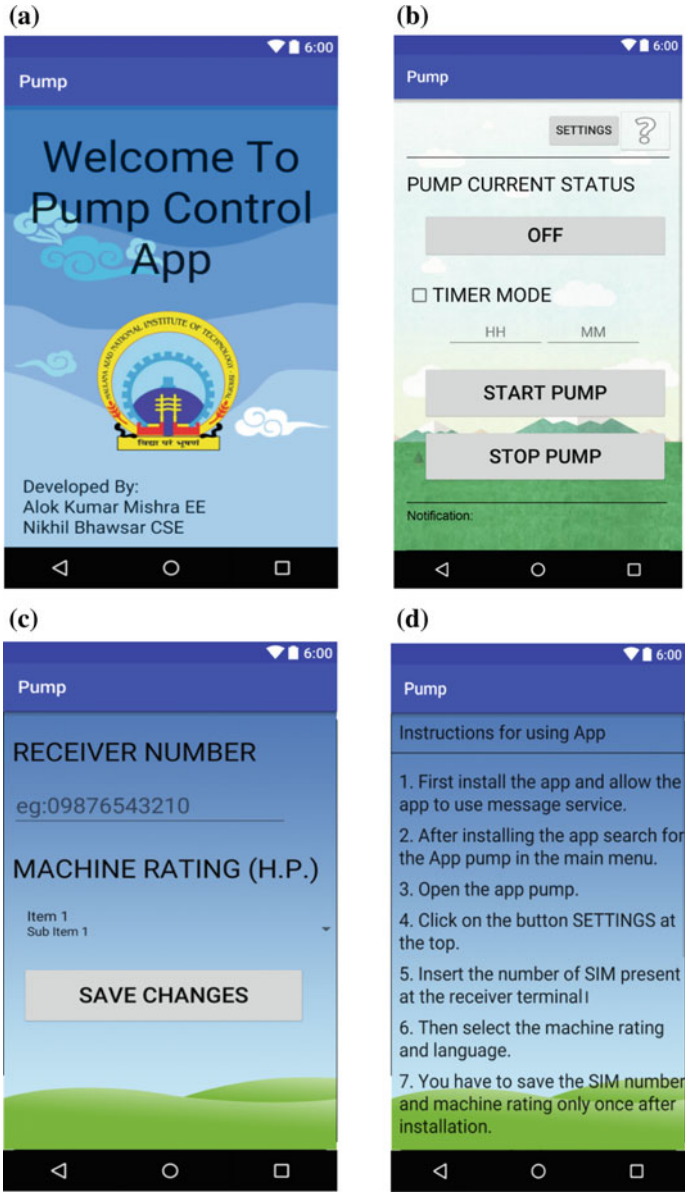

Fig. 11 **a** Splash screen, **b** main activity, **c** settings activity, **d** help activity

Table 2 Comparison of different technologies

	GSM	LTE	eMTC	IoT
Range	< 35 km	< 100 km	< 100 km	< 35 km
Spectrum	Licensed GSM band	Licensed LTE band	Licensed LTE band	Licensed LTE band in band stand alone
Bandwidth	< 200 kHz	LTE carrier (1.4–20 MHz)	1.08 MHz	180 kHz (200 kHz carrier bandwidth)
Max data rate	< 500 kbps	< 10 Mbps < 5 Mbps	1.08 MHz	< 170 kbps (DL) < 250 kbps (UL)

References

1. Giovanni A, Cataliotti A, Cosentino V, Cara DD, Fiorelli R, Guaiana S, Panzavecchia N, Giovanni T (2018) A new PLC-based smart metering architecture for medium/low voltage grids: feasibility and experimental characterization. Measurement 129(2018):479–488
2. Xinlin W, Ha B, Lee GY, Kim H, Yu J, Rhee H, Njau KN, Jande YAC, Sung-Hoon A (2020) Low-cost far-field wireless electrical load monitoring system applied in an off-grid rural area of Tanzania. Sustain Cities Soc 102209
3. Ahmed, Ladhake SA (2011) Innovative cost effective approach for cell phone based remote controlled embedded system for irrigation. In: International conference on communication systems and network technologies, Katra, Jammu, 2011, pp 419–422
4. Hossain SM, Rahman M, Sarker TM, Haque EM, Jahid A (2019) A smart IoT based system for monitoring and controlling the sub-station equipment. Internet of Things 7:100085
5. Singh RR, Yash SM, Shubham SC, Indragandhi V, Vijayakumar V, Saravanan P, Subramaniyaswamy V (2020) IoT embedded cloud-based intelligent power quality monitoring system for industrial drive application. Fut Gener Comput Syst 112 (2020):884–898
6. Ugale RT, Chavhan KB (2016) Web-based automated electric machine test-bench with data acquisition and remote control. In: IEEE International conference on power electronics, drives and energy systems (PEDES), Trivandrum, 2016, pp 1–5
7. Pawar P, Tarun KM (2020) An IoT based Intelligent Smart Energy Management System with accurate forecasting and load strategy for renewable generation. Measurement 152:107187
8. Rahman MS, Masud S, Sultana S, Bari MR (2017) Web based electric home appliance controller and monitoring system. In: 2017 IEEE 8th annual ubiquitous computing, electronics and mobile communication conference (UEMCON), New York City, pp 474–477
9. Thombre AC, Shah S, Thombre AS, Haldankar GT, Kasambe PV (2017) Design of IoT based intelligent AC drive system using space vector algorithm. In: International conference on communication and signal processing (ICCSP), Chennai, pp 2097–2100
10. Shyamala D, Swathi D, Prasanna JL, Ajitha A (2017) IoT platform for condition monitoring of industrial motors. In: 2nd International conference on communication and electronics systems (ICCES), Coimbatore, pp 260–265

11. Li W, Logenthiran T, Phan VT, Woo WL (2018) Implemented IoT-based self-learning home management system (SHMS) for Singapore. IEEE Internet Things J 5(3):2212–2219
12. Johar RA, Fakieh E, Allagani R, Qaisar SM (2018) A smart home appliances control system based on digital electronics and GSM network. In: 15th Learning and technology conference (L&T), Jeddah, 2018, pp 52–58
13. Konstantinos M (2020) A Real-time condition monitoring and maintenance management system for low voltage industrial motors using Internet-of-Things. Procedia Manuf 42:450–456

Comparative Analysis of Speed Control Methods for PMSM Drive Fed Electrical Vehicle

Sanjay Kumar Kakodia, Ashish Kumar Panda, and Giribabu Dyanamina

Abstract In this paper, field-oriented control (FOC), direct torque control (DTC) and space vector modulation-DTC (SVM-DTC) of multi-level inverter (MLI) fed permanent magnet synchronous motor (PMSM) for an electrical vehicle are presented. The FOC, DTC and SVM-DTC are the most frequently used vector control techniques which improve the dynamic response of the PMSM. The FOC technique uses the transformation theory and linear controller to control the fundamental component, and DTC generates the voltage vector with the help of hysteresis band comparator. The vector control of PMSM is simulated with the help of MATLAB/Simulink under different operating conditions, and results are compared.

Keywords Permanent magnet synchronous motor · Multi-level inverter · FOC · DTC and SVM-DTC

1 Introduction

There is a fast-growing interest in electrical vehicles (EVs); it helps to reduce CO_2 emissions and global warming impact on the environment. The electric motor is an integral part of EVs. PMSM has a permanent magnet on the rotor and winding on the stator part, which offers higher-power density, efficiency, high torque to inertia ratio and ease of control. PMSM is more reliable than a DC motor and induction motor because of the absence of a commutator and rotor flux produced by permanent magnets [1]. With the advancement in power electronics devices and microcontrollers, the PMSM has been used tremendously. The PMSM requires a reliable controller scheme. The dynamic response of the PMSM depends upon the control of electromagnetic torque and flux responsible current components. The vector control allows a fast dynamic response for the sudden change in speed and torque. The vector control scheme has two control schemes which are FOC and DTC [2]. In both control schemes, the three-phase machine variable is transformed into two-phase machine

S. K. Kakodia (✉) · A. K. Panda · G. Dyanamina
Department of Electrical Engineering, Maulana Azad National Institute of Technology, Bhopal, India
e-mail: 203113014@stu.manit.ac.in

S. Dwivedi et al. (eds.), *Flexible Electronics for Electric Vehicles*, Lecture Notes in Electrical Engineering 863, https://doi.org/10.1007/978-981-19-0588-9_32

variables, wherein this stator current of the three-phase machine is decomposed into flux and torque responsible components. In FOC, machine variable is transformed in the coordinated system which rotates in synchronism with the rotor flux vector. It requires the position of the rotor which is measured by the hall effect sensors. It requires a complex control scheme. FOC allows PMSM machine torque and flux control using a linear PI regulator [3].

DTC scheme allows the control of torque and flux without transformation and current regulators. In DTC, the desired inverter switching is chosen based on desired stator flux linkage and torque requirement, and the inverter switching frequency is varying. But DTC has higher torque ripples and current ripples in the steady state; however, it improves the speed response [4]. Therefore, SVM-DTC has been implemented to improve the performance of PMSM.

The inverter is an important part of the motor drive application. The inverter output voltage quality improves motor drive performance. The multi-level inverter is the emerging technology for medium voltage and high-power applications. The diode clamped MLI has reduced dv/dt stress across the switch [5]. In this paper, the FOC, DTC and SVM-DTC speed control techniques are simulated, and results are compared.

2 Field-Oriented Control of PMSM

The PMSM machine is similar to the induction machine except permanent magnets are present in the PMSM machine. The stator current produces the flux and torque responsible components together, and it has inherent coupling in speed and torque, which is alleviated by the help of the FOC. In the FOC, machine stator current is decoupled into the flux and torque producing component using a stationary three-phase current to the rotating frame. It produces high torque and low current at the starting of the motor. Figure 1 illustrates the block diagram of the FOC of the PMSM machine [6]. FOC control scheme is based on the Park's transformation. In the FOC scheme, the PMSM stator flux and torque are controlled independently by changing the orientation of field quantity. The mathematical modelling of the PMSM machine is based on the dq synchronous reference frame given by the following equation:

$$v_{qs}^{s} = R_s i_{qs}^{s} + L_{qs}\frac{\mathrm{d}i_{qs}}{\mathrm{d}t} + \omega_r \psi_{ds} \tag{1}$$

$$v_{ds}^{s} = R_s i_{ds}^{s} + L_{ds}\frac{\mathrm{d}i_{qs}}{\mathrm{d}t} - \omega_r \psi_{qs} \tag{2}$$

$$\psi_{qs} = L_{qs} i_{qs} \tag{3}$$

$$\psi_{ds} = L_{ds} i_{ds} + \psi_r \tag{4}$$

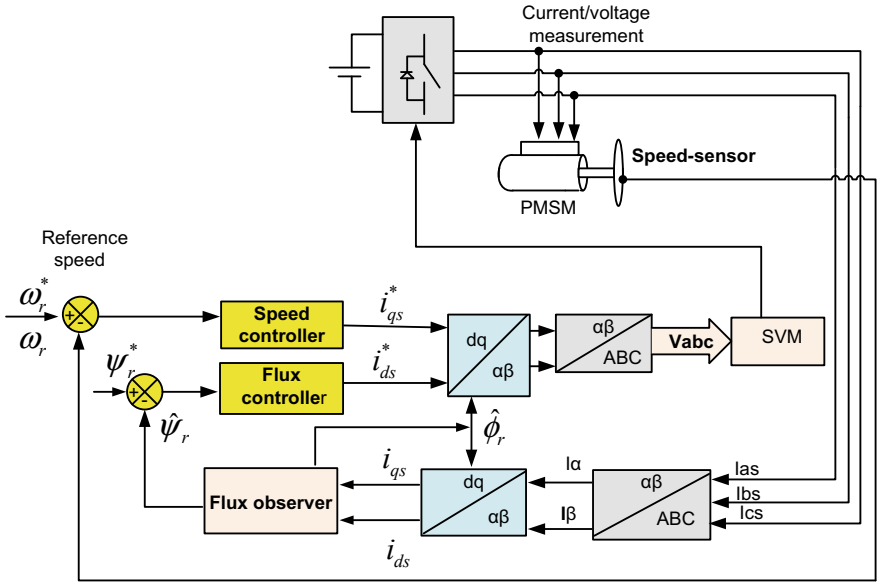

Fig. 1 Block diagram of vector control of PMSM

Solving Eqs. (1) to (4), the electromagnetic torque of the PMSM machine is given by Eq. (5).

$$T_e = \frac{3}{2}\left(\frac{P}{2}\right)(\psi_{ds} i_{qs} - \psi_{qs} i_{ds}) \tag{5}$$

where v_{ds}^s, v_{qs}^s, i_{ds}^s and i_{qs}^s are the stator dq axis voltage and current, respectively, R_s is stator resistance, $L_{ds,}$ L_{qs} are the inductance of machine in dq axis, ψ_{ds}, ψ_{qs} are the stator magnetic flux in dq axis, ψ_r is the rotor flux, ω_r is rotor speed, and T_e is the electromagnetic torque.

From Fig. 1, the stator current is measured and the stator space vector is transformed $\alpha\beta$ using Clarke's transformation. These variables are time variant. So these are transformed into a two-phase time-invariant system using the Park's transformation. This requires a rotor position, which is measured by hall effect sensor, speed enoder etc. [7].

3 Direct Torque Control (DTC) of PMSM

DTC improves the torque performance of the PMSM. FOC has a complex control strategy due to linear regulator and transformation theory. The DTC synthesizes direct voltage vector without linear regulator and transformation. It offers fast dynamic

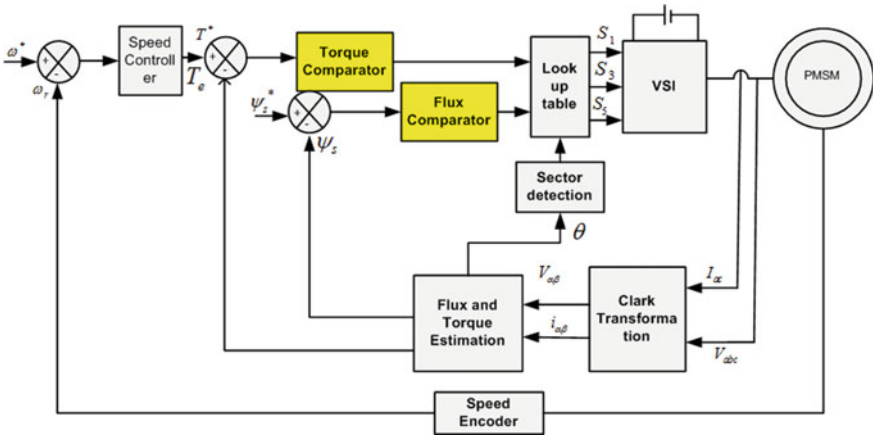

Fig. 2 Block diagram of DTC of PMSM drive

response. In this, the actual PMSM voltage and current are compared with the reference voltage and current respectively, error is passed through a hysteresis controller, and based on the error the appropriate voltage vector is selected using look-up table and fed to PMSM. It has low complexity and requires machine stator resistance only. In Fig. 2, block diagram of DTC is represented. The DTC eliminates the requirement of the dq axis current regulator, modulator and coordinate transformation [1]. The inverter switching signal is generated based on a look-up table and a voltage vector. The stator flux magnitude and angle are estimated from Eqs. 6 and 7; which is used to identify the sector number of inverter operation.

$$|\psi_s| = \sqrt{\psi_{\alpha s}^2 + \psi_{\beta s}^2} \tag{6}$$

$$\theta = sin^{-1}\left(\frac{\psi_{\alpha s}}{\psi_{\beta s}}\right) \tag{7}$$

4 Speed Control of PMSM Using SVM-DTC

In the conventional DTC, the switching frequency is variable which introduces more torque ripples. To minimize the torque ripple, the hysteresis controller is replaced by the PI controller and look-up table with SVM control. The computational time is lesser in SVM-DTC than the conventional DTC because the hysteresis comparator and look-up table are not used. In SVM-DTC, torque and flux responsible components are estimated from the inverter terminal voltage and current, and it is compared with a reference value. The error is passed through the PI controller and reference voltage

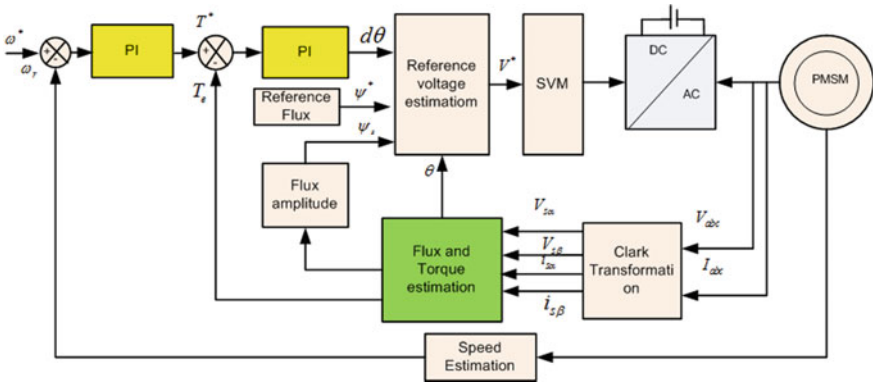

Fig. 3 Block diagram of SVM-DTC for PMSM

vector is estimated and fed to SVM block. It generates the gating pattern for the inverter [8]. The block diagram of the SVM-DTC is presented in Fig. 3. The reference voltage vector equations for SVM-DTC are calculated by the following equation.

$$V_{\alpha\_\text{ref}} = \left(\left|\psi_s^*\right| \cos(\theta + \Delta\theta) - |\psi_s| \cos(\theta)\right) / T_s + R_s i_{s\alpha} \tag{8}$$

$$V_{\beta\_\text{ref}} = \left(\left|\psi_s^*\right| \sin(\theta + \Delta\theta) - |\psi_s| \sin(\theta)\right) / T_s + R_s i_{s\beta} \tag{9}$$

where the magnitude and angle of the reference vector

$$V_{s\_\text{ref}} = \sqrt{V_{s\alpha\_\text{ref}}^2 + V_{s\beta\_\text{ref}}^2} \tag{10}$$

$$\theta = \arctan\left(\frac{V_{s\alpha\_\text{ref}}}{V_{s\beta\_\text{ref}}}\right) \tag{11}$$

where V_{α_ref}, V_{α_ref} are the reference voltage for SVM inverter, T_s is switching time, and $\Delta\theta$ is an increment in load angle.

5 Simulation Results

The FOC, DTC and SVM-DTC are simulated with the help of MATLAB/Simulink. The PMSM machine parameter is given in Table 1. In the FOC using the space vector modulation technique, the gate pulses are obtained for MLI. The step change in speed of 1500 RPM, 1000 RPM and 800 RPM is applied at 0.05, 0.5 and 1 s, respectively. The constant torque of 0.5 N m is applied to the PMSM machine at 0.09 s. Figures 4 & 5 illustrates the speed and torque performance of the PMSM machine under the

Table 1 PMSM parameter

Parameter	Ratings
Pole pair	2
Stator resistance	1.05 Ω
PM flux	0.3 Wb
*dq*_axis inductance	0.02633 mH, 0.026147 mH
Inertia (J)	0.0017 kg m^2
Rated speed	1500 RPM
DC bus voltage	200 V

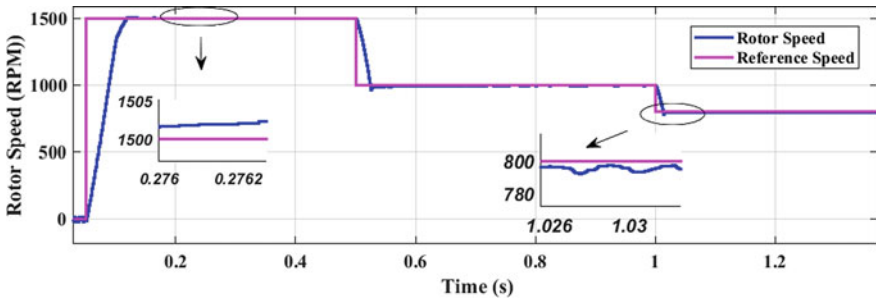

Fig. 4 Speed response of FOC of PMSM during step change in speed

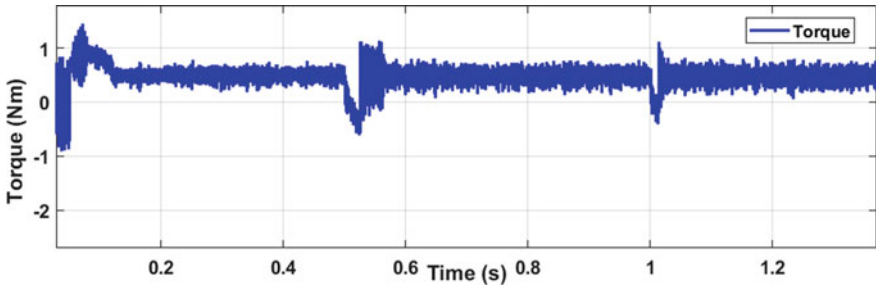

Fig. 5 Torque response of the FOC of PMSM when constant load 0.5 N m is applied at 0.09 s

above operating condition. In this controlling scheme rotor trackthe reference speed but torque has ripples which are not desirable in some specific application. The PI controller tuning requires the mathematical modelling of the PMSM drive but in the practical application, the PMSM drive is highly non-linear and complex and sensitive to parameter variations.

Conventional DTC has better torque response. It has a reduced ripple as compared to FOC, but in the starting, it has a high peak overshoot. In DTC, the speed reversal is applied at 0.5 s and torque of 2Nm is applied at 0.5 s. The DTC has a faster torque response and less settling time. The speed and torque response of the DTC is

presented in Figs. 6 and 7. The DTC can improve the torque response without difficulty. However, the hysteresis controller has a variable switching frequency which is not desirable and it causes higher ripples in the flux and torque that leads to noise in the drive.

Figures 8 and 9 illustrate the performance of the SVM-DTC for PMSM. The conventional DTC has torque ripples and provides some delay. The SVC-DTC improves the setting time and torque ripples. SVM-DTC makes the switching frequency constant and provides a fast dynamic response.

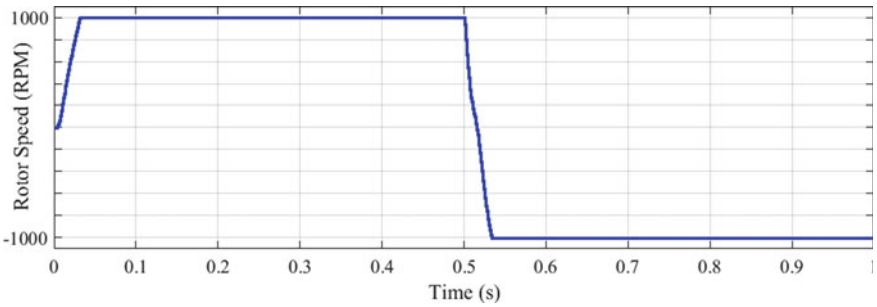

Fig. 6 Speed response of DTC of PMSM when reverse motoring mode is applied at 0.5 s

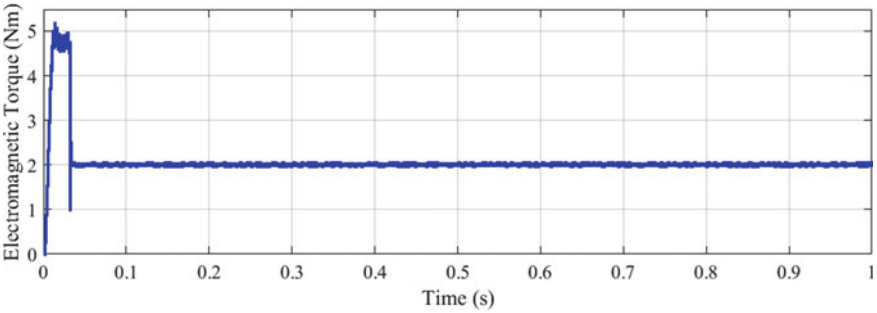

Fig. 7 Torque response of the DTC of PMSM when constant load 2Nm is applied at 0.05 s

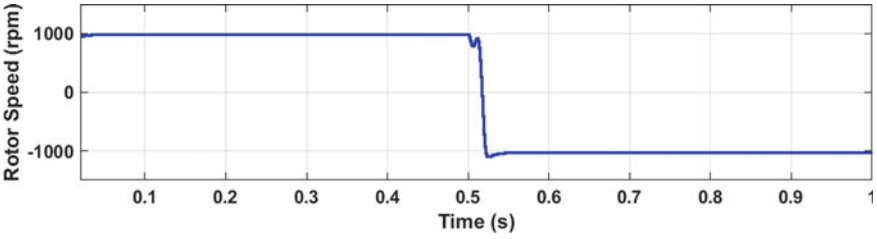

Fig. 8 Speed response of SVM-DTC of PMSM when reverse motoring mode is applied at 0.5 s

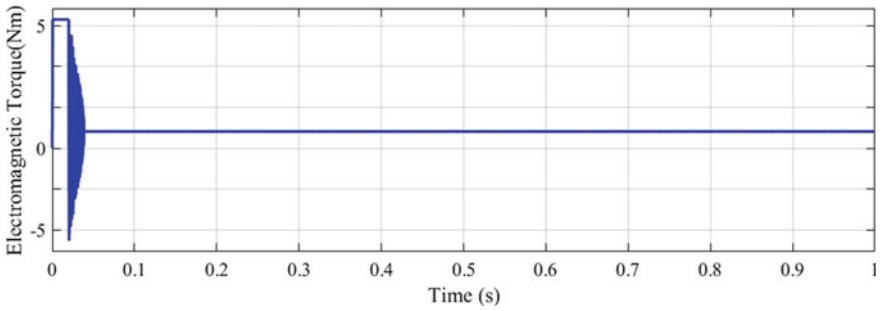

Fig. 9 Torque response of the SVM-DTC of PMSM when constant load is 2 N m

6 Conclusion

This paper compares the speed control methods for the PMSM. The FOC-based speed control method has a steady-state error due to the parameter mismatch and detuning of the PI controller, and the torque response is sluggish. When the step change in speed is applied, the same is reflected in the torque response. The main advantages of DTC are robust, fast torque response, no need for pulse width modulation generation and current regulators. The conventional DTC has fast torque and flux control, and it is robust to drive parameter variation. DTC uses the hysteresis regulator which causes the variable switching frequency, ripples in torque and higher peak overshoot in the staring. DTC drawbacks are alleviated by SVM-DTC, which uses a voltage modulator instead of a look-up table. SVM-DTC inverter has a fixed switching frequency and offers better performance and lower torque ripples. The MATLAB simulation results verify the performance of the PMSM drive.

References

1. Swierczynski D, Kazmierkowski MP (2002) Direct torque control of permanent magnet synchronous motor (PMSM) using space vector modulation (DTC-SVM)-simulation and experimental results. In: IEEE 2002 28th Annual Conference of the Industrial Electronics Society. IECON 02, vol 1, pp 751–755
2. Korkmaz F, Topaloğlu İ, Çakir MF, Gürbüz R (2013) Comparative performance evaluation of FOC and DTC controlled PMSM drives. In: 4th International conference on power engineering, energy and electrical drives, pp 705–708
3. Aguirre M, Calleja C, Lopez-de-Heredia A, Poza J, Aranburu A, Nieva T (2011) FOC and DTC comparison in PMSM for railway traction application. In: Proceedings of the 2011 14th European conference on power electronics and applications, pp 1–10
4. Sandre-Hernandez O, Rangel-Magdaleno J, Morales-Caporal R, Bonilla-Huerta E (2018) HIL simulation of the DTC for a three-level inverter fed a PMSM with neutral-point balancing control based on FPGA. Electr Eng 100(3):1441–1454
5. Kakodia SK, Dyanamina G (2019) Field oriented control of three-level neutral point clamped

inverter fed IM drive. In: IEMECON 2019—9th annual information technology, electromechanical engineering and microelectronics conference, pp 24–29
6. Samar A, Saedin P, Tajudin AI, Adni N (2012) The implementation of field oriented control for PMSM drive based on TMS320F2808 DSP controller. In: 2012 IEEE international conference on control system, computing and engineering, pp 612–616
7. Jayal P, Bhuvaneswari G (2018) Vector control of permanent magnet synchronous motor drive using a reduced switch five-level inverter. In: 2018 IEEMA engineer infinite conference (eTechNxT), pp 1–6
8. Malla SG, Rao MHL, Malla JMR, Sabat RR, Dadi J, Das MM (2013) SVM-DTC Permanent magnet synchronous motor driven electric vehicle with bidirectional converter. In: 2013 International multi-conference on automation, computing, communication, control and compressed sensing (iMac4s), pp 742–747

Emergence of Silicon Photonics in the Field of Biomedical Sensing Applications: A Review

Ravi Mali, Biswajit Sahoo, Nitesh Mudgal, Ankur Saharia, Kamal Kishor Choure, Rahul Pandey, Ghanshyam Singh, and Manish Tiwari

Abstract In the last few decades, the human body is prone to many different types of infectious diseases. This involves making use of technologies for detecting and monitoring the factors responsible for these diseases, and the devices should be free from any kind of harmful radiations. Photonics is considered to be one of the new advancements in the field of technology which can fulfill the need or requirement of biomedical sensing applications. The scope of this review paper summarizes the concept of designing methods and material structures for biomedical applications. These designing methods include plane wave expansion, surface plasmon resonance (SPR), Helium ion lithography, band-gap variations, and refractive index variation of the material. The losses that are incurred or induced during the wave propagation includes adsorption, attenuation, reflection, and diffraction. There are several physical structures of the materials mainly 1D, 2D, 3D, three-layer silicon, five-layer, seven-layer, etc. The above mentioned material structures are used to detect cancer

R. Mali (✉) · B. Sahoo · N. Mudgal · K. K. Choure · R. Pandey · G. Singh
Department of Electronics and Communication Engineering, MNIT Jaipur, Jaipur, Rajasthan, India
e-mail: 2020pwc5588@mnit.ac.in

B. Sahoo
e-mail: 2020pwc5564@mnit.ac.in

N. Mudgal
e-mail: mudgalnitesh@gmail.com

K. K. Choure
e-mail: kamalkishorchore.09@gmail.com

R. Pandey
e-mail: 2020rec9009@mnit.ac.in

G. Singh
e-mail: gsingh.ece@mnit.ac.in

A. Saharia · M. Tiwari
Manipal University Jaipur, Jaipur, India
e-mail: ankursaharia07@gmail.com

M. Tiwari
e-mail: mt.jaipur@gmail.com

S. Dwivedi et al. (eds.), *Flexible Electronics for Electric Vehicles*, Lecture Notes in Electrical Engineering 863, https://doi.org/10.1007/978-981-19-0588-9_33

cell, DNA and protein concentration, identifying different mutation of SARS virus which includes COVID-19, as well as in the field of bio-sensing, bio-screening, and drug delivery system.

Keywords Photonics · Silicon · Plane wave expansion method · Helium · Surface plasmon resonance · Sensors

1 Introduction

The amount of pollution and the radiation levels present in the atmosphere or in the environment are exponentially rising due to continuous development in the field of technologies. This tends to create an adverse effect on the human body and results in different types of harmful diseases like Cancer, Tuberculosis, etc. In order to continuously monitor such circumstances, it needs different types of measurement instruments which have minimal amount of radiation, one such exception is photonics which is used in the field of biomedical sensing which do not emit any kind of radiation. The major features of these kinds of instruments include devices having better sensitivity, smaller in size, and pertaining to low cost. All these types of detections are mainly using two different kinds of methodologies. The first method employs variation of the refractive index variation of the material. The second method includes using of the finite difference time domain (FDTD) method. Whenever the wave propagates through the structure of the material, it is bound to undergo some kinds of losses. These losses mainly include wave propagation loss, attenuation, refraction, and diffraction (PARD losses). These losses are used to measure the proportion of DNA and protein present in the human body and also the angle shift of the wavelength method which is used to measure the concentration of DNA. The number of cancer cells present in the human body is detected using eye-detection technique, which also includes wavelength shift method. The ring resonator is designed using fabrication process variation (FPVs) methodology which is designed for detection purposes, switching, and filtering [1]. Power measurement technique is also used to detect the cancer cells in the human body. The major disadvantages of these kinds of techniques such as X-Ray, chemotherapy, etc., are time-consuming and less accurate. The biomedical sensors have the properties of high sensitivity and high-quality factors. The five-layer Ag-Si3N4-graphene-based sensor which comes under the category of biomedical sensors is used for detection of DNA hybridization. The modeling of this sensor is based on SPR method which has high detection accuracy, high sensitivity, and good quality factor [2]. These types of sensors are fabricated at a low cost. The low-cost cancer cell detection and detection of accurate dehydration are using the concept of reflection and band-gap of the 1D structure [3−5]. The concept of surface plasmon resonance (SPR) is used to generate the decaying evanescent waves at the interface of the metal and dielectric surface is shown in Fig. 1. The input wave is P-polarized which is used to excite the free electrons present at the metal dielectric interface. The electrons which are excited by the P-polarized wave

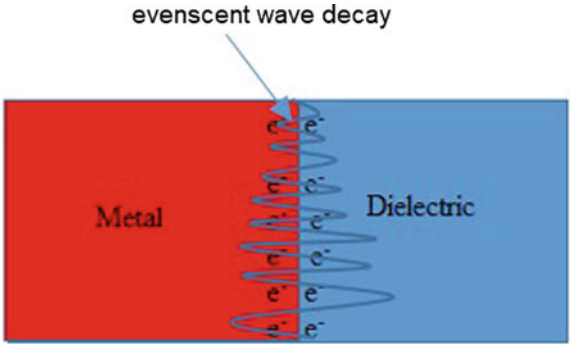

Fig. 1 Concept of surface plasmon resonance. Reproduced from [2]

are used to generate the evanescent decay wave and this wave is generated at the interference of the metal and dielectric. Due to the variation in the refractive index in the sensing medium, the sensing angle also gets shifted. The measurement of DNA hybridization is done by the shift of resonance angle due to the variation of refractive index [6]. The five-layer structure of Ag-Si3N4-graphene-based sensor is used to perform nucleotide-binding between the base pair of adenine, guanine, thymine, and cytosine.

2 Biomedical Applications

2.1 Cancer Cell Detection

Non-radiating devices are used to detect the cancer cells. These devices basically constitute two photonic crystals, a waveguide and a ring resonator. In this, ring resonator is made of GaAs material and the resonant wave shifting takes place due to variation in the refractive index of the ring resonator. Due to the resonant wave shifting process, the 13 nm wavelength will be shifted by the normal cell and basal cancer cell [5, 7]. There are basically two types of cancer detection techniques.

Finite time difference method

Plane wave expansion method: In this method, the transmitted or the reflected wave is received by the variation of refractive index and this received reflected or the transmitted wave is used to measure the amount of time taken for the detection purpose.

This technique is basically used to measure the reflection properties of the material. The reflection properties of the materials basically includes as absorption, attenuation, propagation, reflection, refraction, diffraction, etc. There are basically different types of configurations which are summarized as below. In the arrangement shown in Fig. 2, there is presence of gap coupling between the input waveguide and ring

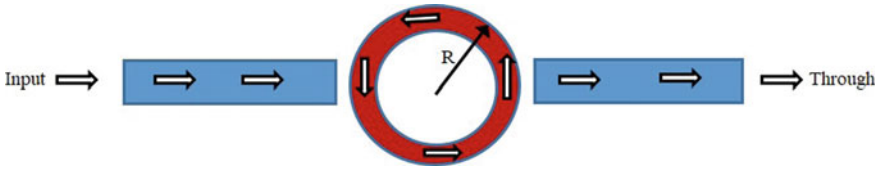

Fig. 2 Waveguide-ring-waveguide resonator Reproduce from [5]

resonator followed by the gap coupling between the ring resonator and output waveguide. The gap coupling has to be done within the waveguide and with the ring resonator. The power is fed through the input port, the power is received at the drop port due to gap coupling [5].

The arrangement shown in Fig. 3 constitutes of the cavity-coupled waveguide and high-quality resonator. The input power is applied through the input port and the output is obtained from the through-port. This arrangement basically makes use FDTD method for the detection purpose.

In the arrangement shown in Fig. 4 the ring resonator is coupled within two rectangular waveguides. A human tissue is basically a combination of small cells which comprises water and organic compounds. The organic compound has protein, cytoplasm, and carbonic compound. The cancer tissue consists of organic compounds which have large amount of cytoplasm as compared to the amount of protein present.

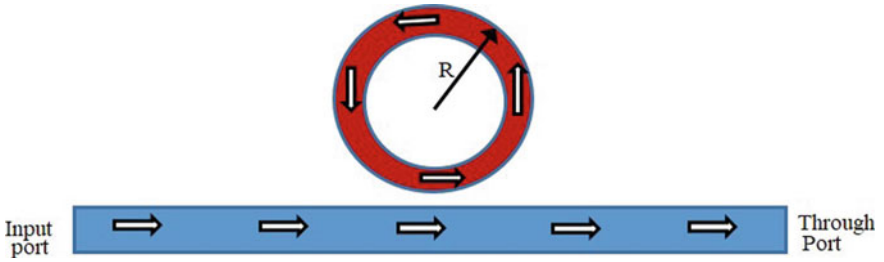

Fig. 3 Single bus waveguide cavity ring resonator reproduce from [5]

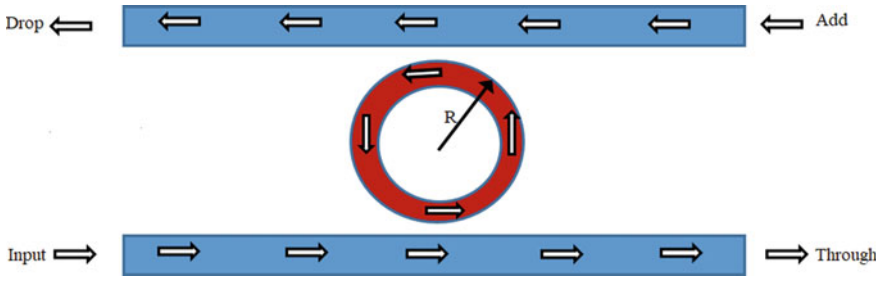

Fig. 4 Double bus waveguide cavity resonator reproduce from [5]

This cytoplasm has a large refractive index, so the wave cannot be transmitted through the cancer cell, but the normal cell constitutes of protein which has lower refractive index, as a result of which the wave can easily transmit through the protein. The measured wave has a resonant shift due to cell reflection or refraction. For example, a wave of 13 nm wavelength can pass through a normal cell but it cannot pass through the cancer cell [5, 7].

2.2 Concentration of DNA and Protein Measurement

In the context of measurement of concentration detection of DNA and protein, silicon photonics is widely used. As shown in Fig. 5, the concentration of DNA and protein is measured by using a 2D crystalline structure of silicon crystal. This crystalline structure is a form of porous material, which absorbs the concentration of DNA and protein. This technique uses plane wave expansion method. In this process, a single wavelength of 400 nm is passed through the 2D silicon crystal, and the output wave is obtained in the form of optical power which gives the result of the concentration of the DNA and protein. The resultant output wave is a mixture of propagation, attenuation, refraction, and diffraction (PARD) losses.

$$\eta = \eta_P \eta_A \eta_R \eta_D \tag{1}$$

$$P_{\text{out}} = \eta P_{\text{in}} \tag{2}$$

The total resultant efficiency is dependent on overall PARD efficiency. The output power for DNA is linearly varied from 0 to 0.025 g/ml, for protein output power varies between 0 to 0.01 g/ml.

From Eqs. (1) and (2), the output power depends on the concentration of the DNA and protein, and it is inversely proportional to the concentration of DNA and protein, and the output power linearly decreases as the concentration of the DNA (in gm/ml)

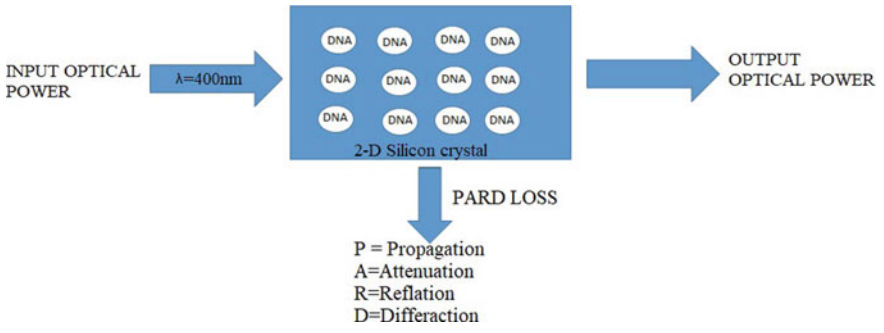

Fig. 5 DNA field in 2D porous silicon crystal reproduced from [8]

protein increases [8]. The silicon and polymer meta-material are also used to be the detection of glucose in human body [3, 9]. The total losses are maximum in the material; however, if the concentration of the DNA is zero, then the resultant output power is maximum [8, 10].

2.3 Cancer Cell Detection by Eye

The cancer cells are detected by the eye-method technique. This method is low cost, and it consumes less time. A lot of other technologies are also being used by researchers for the interest of detection purpose, but such technologies incur higher cost, less accuracy, and consume more amount of time with respect to the abnormal cell increase in our body. The cancer cell detection, by eye method provides high accuracy results, are less time-consuming for detection and also the cost of fabrication is less. In this technology, the air substrate is sandwiched between two silicon substrates. This type of structure is called three-layer structures. The middle layer is called the examine layer [11].

When a light wave of wavelength 740 nm is projected at one end of the silicon layer, it gets reflected by the intermediate layer, i.e., cell. The reflected waves are seen in the form of a spectrum zone by the eye. If the reflected wave is of wavelength less than 740 nm then it is known as red zone. The red color zone shows that the cell is a normal cell. However, if the reflected wave is of wavelength greater than 740 nm, then it is known as black zone. The black zone color shows that the cell is a cancer cell. This crystalline structure device is responsible for moving the cancer cell in our body. As shown in Fig. 6, there will be different kinds of wave reflections because the refractive index will be different for normal cell and the cancer cell. The normal cell will have the lowest refractive index, which results in the reflection of the waves with wavelength less than 740 nm. Human eyes can view this wavelength easily in

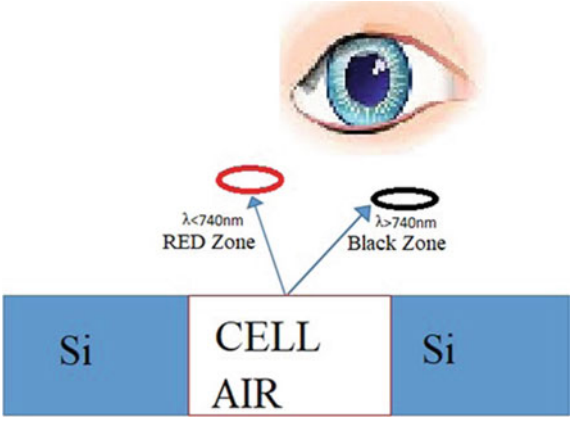

Fig. 6 Three-layer structure of cancer cell detection. Reproduced from [11]

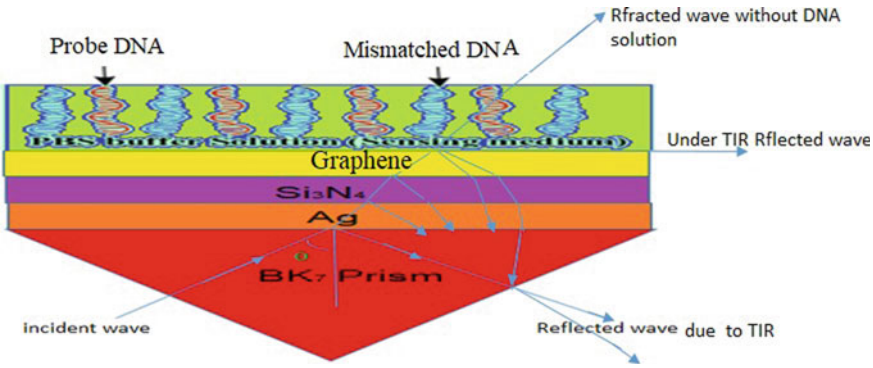

Fig. 7 Five-layer structure for DNA hybridization detection. Reproduce from [6]

the form of the spectrum of the red zone. However, since the refractive index of the cancer cell is large [4]; therefore, reflected wave will have a larger wavelength which is greater than 740 nm. This wavelength can be perceived by the human eyes in the form of black zone and represented by cancer cell [12].

2.4 DNA Hybridization Using SPR

The five-layer structures are used for detection and measurement of the DNA hybridization with non-complementary and complementary [6]. This five-layer structure consists of silver (Ag), silicon nitrate (Si3N4), graphene-coated BK7 glass prism, phosphate-buffer saline (PBS) solution and He–Ne laser which is used for excitation [6].

As shown in Fig. 7, these layers have different refractive index. The refractive index of every layer is varied from bottom to top as a result of which the reflected wave angle will be shifted by every total internal reflection (TIR). This shift produced in the reflected wave angle depends on the thickness of the layer, as well as the refractive index of all layers [6]. The P-polarized wave is excited on the surface of the prism, which are then refracted at the interface of the prism and Ag (silver), this refracted wave further undergoes refraction at the interface of Ag and SI3N4 interface, followed by the refraction through the interface of SI3N4 and graphene. If it is filled in by DNA solution, then during hybridization, single-standard DNA is converted into the double-standard DNA with hydrogen bond. If the PSB is filled with complement and non-complement DNA, then it will reflect the wave and passes through all the layers. The incident angle and reflected angle measure the sensitivity, accuracy, and quality factor [6].

Sensitivity is the ratio of the shifted resonance angle to the shifted refractive index. Unit of sensitivity is degree/RIU-1.Similarly, the detection accuracy also depends on the shift resonance angle. The quality factor is used to represent the performance

of the sensing device. The quality factor (Q) is dependent on the refractive index variation. The quality factor increases due to the small variation in refractive index of the solution. This is measure in RIU-1. If we want to improve the sensitivity of the sensing device in between the refractive index variation from (1.33 to 1.45), the one way to do so is by using the seven-layer structure based on surface plasmon technology [12]. These layers are SF10 glass prism, ZnO, Ag, Au, BaTiO3, graphene, and sensing medium (water). The refractive index is increased from first layer to seven layers. Due to the small variation of refractive index in sensing medium, the angle is shifted near to first angle, as well as there is increase in the sensitivity of the sensor about 14.85% [13]. This is better compared to mos2-graphene-based sensor [13].

3 Conclusion

According to the data provided by the World Health Organization (WHO), four human babies are born in every half a minute, and the measured birth defect is in the ratio of 1:33, which implies that one out of every 33 babies that are born are prone to humanitarian defects. The major source of all these defects includes pollution, consumption of high calorie intake of fast food, and using electronic gadgets which emits very high radiation. It also includes very deadly diseases like Covid-19 which is a kind of SARS virus which indirectly affects the respiratory trac of the human body. Other types of serious body ailments include type-1 diabetes, multiple sclerosis, cancer, and heart disease are increasing in the human body every day. As a result, there is a need to make use of advanced technologies which can continuously monitor and detect these increasing number of diseases, but there needs to trade-off between the new advanced technologies and their emitted radiations, since these radiations can prove to be futile in creating other side effects also. In this review paper, some new technologies are discussed which are used for detection and sensing purpose. In order to measure the amount of glucose, DNA, protein content, etc., presents inside the human body requires real-time measurements. The use of photonic crystals plays a very crucial role in the field of biomedical application for measuring and sensing purpose. There are 1D photonics crystal structures which are being used for cancer cell detection and detection of accurate dehydration [4], as well as 2D crystal structures which are used for DNA concentration and protein detection [8], and 3D crystal structures are used for glucose detection. In this paper, we reviewed some technologies for the molecule detection, sensitivity enhancement, and quality factor enhancement for the different crystal structures. The sensitivity and other parameters are enhanced with the different layer structure using SPR method. This method seems to provide an upper edge in designing of a sensing device with high accuracy and sensitivity. The refractive index variation methods are used for the detection purpose of cancer cell and DNA hybridization with complement or non-complement DNA. This type of configuration is excited by means of P-type polarized wave and accordingly at the interface surface, we obtain an evanescent wave which gives information about the detection and sensing. The sensitivity and the degree of accuracy

detection of the Ag-Graphene affinity layer-based biosensor can be enhanced by the sandwich a layer of BaTiO3 in between silver (Ag) and graphene [12, 13]. This type of sensing device is more accurate in comparison with the electronic device. In other words, we can say that by making use of a single photonic crystal, we can perform 16 different types of detection as well as a single photonic crystal also behaves as a 16 type wavelength generator [14].

References

1. Lin B, Li P, Cunningham BT (2006) A label-free biosensor-based cell attachment assay for characterization of cell surface molecules. Sens Actuat B Chem 559–564. https://doi.org/10.1016/j.snb.2005.04.022
2. Mudgal N, Fasaswal MK, Ismail T, Fahim I, Tiwari M, Singh G (2020) Studyof approaches implemented the prism based surface plasmon resonance sensors. In Optical and wireless technologies. Lecture notes in electrical engineering, vol 648. https://doi.org/10.1007/978-981-15-2926-39
3. Palai G, Kisan S, Das A (2018) A proposal for bio-medical device to measure GUS in human blood using metamaterial. Optik 164:138–142. https://doi.org/10.1016/j.ijleo.2018.03.007
4. Nayak ASC (2016) Early detection of accurate dehydration using one dimensional photonic device. Optik 127:5462–5465. https://doi.org/10.1016/j.ijleo.2016.02.069
5. Danaie M, Kiani B (2018) Design of a label-free photonic crystal refractive index sensor for biomedical applications. Photon Nanostruct Fund Appl 31:89–98. https://doi.org/10.1016/j.photonics.2018.06.004
6. Mudgal N, Saharia A, Choure KK, Agarwal A, Singh G (2020) Sensitivity enhancement with anti-reflection coating of silicon nitride(Si3N4) layer in silver-based surface plasmon resonance (SPR) sensor—for sensing of DNA hybridization. Appl Phys A 126(12). https://doi.org/10.1007/s00339-020-04126-9
7. Wu¨lbern JH, Hampe J, Petrov A, Eich M, Luo J, Jen AKY, Di Falco A, Krauss TF, Bruns J (2009) Electro-optic modulation in slotted resonant photonic crystal heterostructures. Appl Phys Lett 94(24):241107. https://doi.org/10.1063/1.3156033
8. Amiria IS, Yupapina P, Palaic G (2019) Estimation of concentration of DNA and protein through PARD and modified analysis: A realization of an accurate biomedical device Using photonic structure. Optik Int J Light Electron Opt 182:507–511. https://doi.org/10.1016/j.ijleo.2019.01.052
9. Sethi KK, Palai G, Sarkar P (2018) Realization of accurate blood glucose sensor using photonics based metamaterial. Optik 168:296–301. https://doi.org/10.1016/j.ijleo.2018.04.091
10. Palai G, Triparty SK (2012) A novel method for measurement of concentration using two dimensional photonic crystal structures. Opt Commun 285:2765–2768. https://doi.org/10.1016/j.optcom.2012.01.072
11. Amiria IS, Yupapina P, Palaic G, Tripathyd SK (2019) A proposal to identify live cancer cell by naked eye: realization of biomedical application using 1D photonic structure, vol 183, pp 818–821. https://doi.org/10.1016/j.ijleo.2019.02.092
12. Mudgal N, Saharia A, Agarwal A, Singh G (2020) ZnO and Bi-metallic(Ag–Au) layers based surface plasmon resonance (SPR) biosensor with BaTiO3 and graphene for biosensing applications. IETE J Res. https://doi.org/10.1080/03772063.2020.1844074
13. Mudgal N, Yupapin P, Ali J, Singh G (2020) $BaTiO_3$-graphene-affinity layer–based surface plasmon resonance (SPR) biosensor for pseudomonas bacterial detection. Plasmonics 15:1221–1229. https://doi.org/10.1007/s11468-020-01146-2
14. Amiri IS, Sahoo SK, Palai G, Tripathy SK (2019) Generation of '16' type of biomedical laser using a single photonic structure: a new paradigm to operation in medical sciencę. Optik 197:163227. https://doi.org/10.1016/j.ijleo.2019.163227

A Review on Remote Sensing and GIS Technique-Based Morphometric Analysis

Joyita Sinha, B. G. Harshavardhana, Amarendra Kumar Sinha, and Suddhendu Das Mahapathra

Abstract The morphological variations on the surface of the earth are determined to be due to the regular surficial dynamisms. Hence, morphometric studies help in quantifying the change in the different dimensions of the geomorphic features. In view of many methods to characterize the modifications to the geomorphic structures over time, the application of remote sensing (RS) and geographic information system (GIS) has been proved to be an easy, effective, and time-saving approach. This paper attempts to compare and review the evolutionary stages of conventional methods of morphometric analysis with that of remote sensing and GIS techniques for characterizing the drainage basin. The developments in the usage of certain important parameters for the purpose have also been discussed starting from their manual quantification.

Keywords Morphometric analysis · Evolution · Remote sensing and GIS

1 Introduction

Geomorphology is the scientific study of the origin and evaluation of different topographic features formed by physical and chemical processes acting on the surface of the earth. River, wind, ocean waves, ice sheets, tectonism, and volcanism are considered to be the agents that carve the earth surface, resulting in different landforms such as channels, valleys, hills, and plateau [1] . The process of measuring the external shapes and sizes of these different landforms is called morphometry; it is the quantitative description and analysis of the landforms in geomorphology [2]. Morphometric analysis is the measurement and mathematical evaluation of the earth's surface, shape, and dimension of its landform [3–5]. Therefore, the morphometry of a region, indicating the temporal variations, helps in the management of the

J. Sinha · B. G. Harshavardhana · A. K. Sinha · S. Das Mahapathra (✉)
Manipal University Jaipur, Jaipur, Rajasthan 303007, India
e-mail: suddm.kgp@gmail.com

S. Dwivedi et al. (eds.), *Flexible Electronics for Electric Vehicles*, Lecture Notes in Electrical Engineering 863, https://doi.org/10.1007/978-981-19-0588-9_34

natural resources and their sustainable development. In other words, the morphometric studies are also essential to characterize the effect of geomorphological processes such as earthquake, soil erosion, and flooding in a drainage basin [6].

Last a few decades have observed an appreciable usage of remote sensing (RS) and geographical information system (GIS) techniques for the purpose of thematic mapping, morphometric analyses, and quantitative assessment of drainage network systems. The study of Vittala et al. [7] has used RS and GIS for finding a mature stage of geomorphic development within the subwatershed of a South Indian plateau region. With this, they affirmed that RS and GIS as an efficient tool for drainage morphometric analysis. Another recent research work has proved that RS and GIS are efficient in demarcating the groundwater zone as well as the underlying structural pattern of drainage morphometry [8]. Further, Thomas et al. [9] have shown that the RS and GIS can be used successfully to quantify the soil loss while investigating on the hydrological set-up of a mountain environment. Mahala [10] by delineating drainage basin morphometry in two different morpho-climatic settings, recommends the applicability of RS and GIS for obtaining better results compared to any other earlier techniques used. Keeping the stated matter as a base-line information, this paper attempts to compare and review the conventional methods of morphometric analysis with that of RS and GIS-based techniques.

2 Discussion

The early investigations of Horton [2], Thornbury [11], and Strahler [12] were emphasized on the advantages of drainage pattern analysis in characterizing the geomorphic features. In fact, the principle of morphometry for understanding drainage basin characteristics based on geological and geomorphological processes took long time for being developed through the investigations of Hurton [2]; Strahler [13]; Muller [14]; Evans [15]; Chorley et al. [16]; Merritts and Vincent [17]; Ohomori [18]; Cox [19]; Oguchi [20]; Burrough and Mcdonnell [21]; Hurtrez et al. [22].

Their works precisely were pertaining to the inferences of the degree of structural and lithological controls in the evolution of fluvial landforms, when the morphometric parameters were estimated by traditional methods. In other words, the measurements carried out on the toposheets and geological maps were considered to be the base for the determination of morphometric parameters. Thus, the values possibly used to bring in an error factor in all measurements that might have required a long time duration for the extraction of data.

However, in recent times, the RS and GIS techniques are being used to estimate the morphometric parameters as well as to determine the nature of topography/drainage system of a particular basin. The emerging trends in the applications of computers, especially in mapping, development of information systems, and virtual world enabled to integrate a wide range of information about the physical system and to use this digital data for research or to solve practical problems [23]. The advantages of this digital-earth concept over the conventional methods are capable

to create, manipulate, store, and use spatial data much faster and at a rapid rate. In addition, it supports and supplied the mechanism and the data to allow a coupling between the form and process [24]. Moreover, it made the quantitative approach for surface characterization and the mechanism for the interpretation and manipulation of the quantitative datasets easy.

In this context, the applications of RS and GIS by Nag [25] and Vittala et al. [7] on morphometric analysis were notable as they were considered to be the base for the subsequent investigations. The approach has been helpful for the prioritization of micro watersheds [26] and the development of groundwater resources [8, 27]. The arrangement of streams of a particular drainage system was used to identify the drainage pattern that successively reflects structural and lithological controls of underlying rocks. Using remote sensing and GIS, Vijith and Satheesh [28] and Manu and Anirudhan [29] could analyze the drainage characteristics of Meenachil and Achankovil Rivers, Kerala.

Understanding the different morphometric parameters together with all associated contributors is the key advantage of RS and GIS approaches, thus, making it effective for the management of river basin. This feature of overlapping of different maps and simultaneous visualization may be the lacuna in the conventional methods of morphometric analysis. Thus, based on the advantages of RS and GIS techniques over the conventional methods, the usage of the linear(stream order, stream number, bifurcation ratio, and stream length), areal (drainage density, stream frequency, elongation ratio, and circularity ratio) and relief-based morphometric parameters, their indications/interpretations and the step-wise applications for characterizing the drainage basin are explained as below [3, 24].

3 Easy Calculation, Time-Saving and Reduction in Error

3.1 Linear Parameters

3.1.1 Stream Order

It is the primary step in drainage basin analysis. Stream ordering is a method of assigning a numeric order to links in a stream network. This order is a method for identifying and classifying types of streams based on their numbers of tributaries. According to [12], the smallest fingerprint tributaries are numbered as 1st order. The 2nd order stream forms where two 1st-order streams join. A 3rd order stream forms when two 2nd order streams join and so on. First-order streams are dominated by overland flow of water; they have no upstream concentrated flow. Because of this, they are most susceptible to non-point source pollution problems and can derive more benefit from wide riparian buffers than other areas of the watershed. It has been observed that in mature topography there is less number of streams, whereas the

presence of large number of streams is indicative of the topography being susceptible to the erosional processes.

3.1.2 Stream Number

The count of stream segment in a given order is termed as stream number. Further, the stream number is directly proportional to size of contributing basin and the channel dimension. A higher stream number indicates lesser permeability and infiltration. It indicates that several streams usually upsurges in geometric progression as stream order increases [2]. The variation in rock structure in the basin is responsible for disparity in steam frequencies.

Both conventional and the RS and GIS approaches require an appreciable amount of time for demarcating the streams of different orders, as the work for the entire drainage would be done manually. On mapping the streams, their counting in the new approach is done using the digital data analysis by the computer, whereas the earlier method still required manual attempts.

3.1.3 Bifurcation Ratio

Bifurcation ratio is a dimensionless number denoting the ratio between the number of streams of one order and those of the next-higher order in a drainage network. It looks like the relationship between streams of different orders. Horton [2] considered bifurcation ratio as an index of relief and dissection. According to Strahler [13], bifurcation ratio exhibit subtle fluctuation for different region with varied environment except where powerful geological control dominates [13]. According to Schumm [30], bifurcation ratio is the ratio of number of stream segment of given order to the number of segment in the next order. It is dimensionless property and indicates the degree of integration prevailing between streams of various orders in drainage basin [30]. Strahler significantly marked that geological structures do not affect drainage pattern for bifurcation ratio is in between 3.0 and 5.0. When bifurcation ratio is low, there will be high possibilities of flooding as water will tend to accumulate rather than spreading out. The human intervention plays important role to reduce bifurcation ratio which in turn augment the risk of flooding within the basin [31].

3.1.4 Stream Length

It refers to the total length of streams of each consecutive order. It is calculated according to law proposed by Horton [2]. It indicates the successive stage of stream segment development [32]. A direct geomorphic and hydrological sequence can estimated from different order stream lengths. Generally, the total length of streams is

maximum in I-order, and stream length decreases as stream order increases. The irregularities in this trend indicate the discrepancies in lithology [2]. It is the quantification of hydrological characteristics of bedrock and the drainage extent. When bedrock is permeable in character then only subtle number of relatively longer streams are formed in a well-drained basin area. In other words, the less permeable bedrock obtains large number of smaller streams in the basin [33]. Mean stream length reveals the size of component of drainage network and its contributing surface [12]. It's directly proportional to the size and topography of drainage basin.

Usage of opisometer/chartometer to measure the lengths of curved lines of streams on maps was common in earlier days, and hence, estimation of both bifurcation ratio and stream length had required significant time. However, RS and GIS methods have appreciably reduced the time for estimating these parameters.

4 Calculation of Geographical Area for Areal Parameters Is Much Easier Than the Conventional Methods

4.1 Areal Parameters

4.1.1 Drainage Density

This parameter is the computation of the total stream length in a given basin to the total area of the basin [12]. Drainage density is a measure of the texture of the network that indicates the balance between the erosive power of overland flow and the permeability of surfacial soils and rocks. The parameter helps to know the landscape direction and runoff potential of the area. A high drainage density indicates impermeable subsurface material with sparse vegetation and high. Whereas, low drainage density manifests coarse drainage texture, lowered runoff due to an appreciable infiltration and hence, potential erosion in the area [11].

4.1.2 Stream Frequency

It is the total number of channel segments of all stream orders per unit area of the basin; also defined as the ratio between the total number of stream segment cumulative of all orders and the basin area [2]. It may be possible to have different stream frequencies, through the basin has same drainage density. Stream frequency depends on the rainfall, relief, and initial resistivity of rocks as well as drainage density of the basin [11]. The lower value of stream frequency indicates poor drainage network [9]. High slope and greater rainfall increase stream frequency in mountain region, whereas high permeability and less available surface flow decrease the value of stream frequency in plateau environment [34].

4.1.3 Elongation Ratio

It is the ratio of the diameter of a circle having the same area as of basin to the maximum basin length [30]. It is also a significant index of basin shape and the value varies from '0' (maximum elongated) to near '1' (maximum circularity).The maximum value indicates the insignificant geomorphological control on river basin [12]. It also helps to give an idea about hydrological character of a drainage basin. The elongated basin has a low peak discharge. The mountain–plateau front humid environment river basin tends to form less elongated river basin than plateau–plain front river basin of sub-humid environment [35].

4.1.4 Circularity Ratio (Rc)

It is defined as the ratio between the area of the basin to the area of a circle having the same perimeter [12]. Value varies from '0' (minimum circularity) to '1' (Maximum circularity and peak discharge in rainy season). The high, medium, and low value of Rc is indicative of old, mature, and young stages of geomorphological adjustment of any basin. Generally, the mountain–plain front river basin tends to form circular basin due to its young morphological adjustment, whereas plateau–plain front river basin forms elongated basin in response to mature morphological adjustment [7, 9].

4.1.5 Constant Channel Maintenance

The constant of channel maintenance represents the drainage area required to maintain one unit of channel length; hence, it is a measure of watershed erodibility [10]. It is defined as the reciprocal of drainage density as property to define overland flow [30]. The lower value indicates higher flood potentiality and young geomorphological structure. Mountain environment generally has low values due to lower infiltration of bare soil and high overland flow. On the other hand, plateau–plain environment tends to high value due to low drainage density and high infiltration in comparison to hilly environment [10].

5 Better Visualization of the Relief Characteristics with RS and GIS Approach

5.1 Relief Parameters

Basin Relief

Basin relief is the difference in elevation between the highest and lowest elevation of the basin. It determines the slope and so the runoff and sediment transport. Basin relief depends upon the underlain geology, geomorphology, and drainage characteristics of the region. It is the best indicator of erosional stages of any river basin [10].

Relief Ratio

It is the ratio of the difference between elevations at river origin and mouth to the total length of the river. The value depends upon different factors of areal and relief characteristics of basin. The high basin relief, circular basin shape, and small basin area increase the relief ratio value of any basin. The parameter indicates the overall steepness of the drainage basin and related degradation processes [23, 30].

Dissection Index

It is defined as the ratio between relative reliefs to its absolute relief. It indicates the vertical erosion and dissected characteristics of a basin area. The values of the parameter near to '0' indicate maximum denudation stages of evolution and that near '1' indicates minimum denudation stages of geomorphic evolution.

The ruggedness index depends upon underlain geology, geomorphology, slope, steepness, vegetation cover, and climate of the region. The higher value of any area indicates that the area is in primary stage of geomorphic development or denudation activity like in mountain-river basin environment, whereas the values are low for plateau-river basin [36].

Ruggedness Index

Thus, the application of RS and GIS help in proper visualization of the terrain and its characteristics. Through the techniques of overlapping of maps of different themes, the real scenario of the location in terms of geological instability, hydrodynamic variations, and terrain erodability can be deciphered better. Consequently, the temporal changes in the natural environment and human settlements as well as the rate of its variation would be quantified effectively with less efforts.

Combining the effect of all parameters mentioned above, the decision on the actual nature of the drainage basin in terms of the availability of groundwater would be attained automatically through the software. In other words, there is no need of calculating the knowledge-based weightage value for prioritizing the sub-watersheds like before.

6 Conclusion

The following conclusions may be drawn based on the above discussion;

- The morphometric analysis was limited to the types of drainage patterns, sediment yield, and discharge calculations in the conventional practices compared to

the recent approaches namely, RS and GIS techniques to characterize the river morphometry.

- Presently, with the help of computer-aided applications, the groundwater potentiality, subsurface geological structures, soil properties, and corresponding topographic ups and downs (plain, plateau, and mountain) would be understood in much better way.
- The software-based technology helps to demarcate the water-availability in a basin much efficiently compared to the usage of the knowledge-based weightage value for the purpose. Thus, it becomes easy to prioritise the region with respect to the presence of groundwater and its temporal variations that depends on the natural as well as anthropogenic causes.
- Finally, the estimation of morphometric parameters using RS and GIS techniques has become easier as well as time saving. Providing a better visualization of the terrain features, the errors involved in the calculation have been reduced drastically, as the operation of quantification would be taken care by the software itself.
- Thus, the study recommends and upholds the usage of RS and GIS-based operations for characterizing the drainage system as a better tool for the morphometric studies compared to the conventional methods.

References

1. Sapkale JB (2013) Cross sectional and morphological changes after a flood in Bhogawati Channel of Kolhapur, Maharashtra. Indian Geogr Quest
2. Horton RE (1945) Erosional development of streams and their drainage basins. In Horton RE (ed) Hydrophysical approach to quantitative morphology, vol 56, pp 275–370. Geological Society of America Bulletin
3. Clarke JI (1996) Morphometry from Maps. In: Essays in geomorphology. Elsevier Publications, New York, pp 235–274
4. Agrawal CS (1998) Study of drainage pattern through aerial data in Navgarh area of Varanasi district, U.P. Indian Soc Remote Sens 169–175
5. Reddy GP, Maji AK, Gajbhiye KS (2004) Drainage morphometry and its influence on land form characteristics in a basaltic terrain, central India: a remote sensing and GIS approach. Int J Appl Earth Obs Geoinf 4(1):1–16
6. Chavare S, Potdar M (2014) Drainage morphometry of Yerla River Basin using geoinformatics techniques. Neo Geographia 3(3)
7. Vittala SS, Govindaiah S, Gowda HH (2004) Morphometric analysis of sub-watersheds in the Pavagada area of Tumkur district, South India using remote sensing and GIS techniques. J Indian Soc Remote Sens 32(4)
8. Sreedevi PD, Subrahmanyam K, Ahmed S (2005) The significance of morphometric analysis for obtaining groundwater potential zones in a structurally controlled terrain. Environ Geol 47:412–420
9. Thomas J, Joseph S, Thrivikramaji KP (2010) Morphometric Aspects of a small tropical mountain river system, the Southern Western Ghats, India. Int J Digital Earth 3(2):135–156
10. Mahala A (2020) The significance of morphometric analysis to understand the hydrological and morphological characteristics in two different morpho-climatic settings. Appl Water Sci 10(33)

11. Thornbury W (1954) Principles of geomorphology
12. Strahler AN (1964) Quantitative geomorphology of drainage basins and channel networks; Handbook of applied hydrology. McGraw-Hill Book Cooperation, New York
13. Strahler AN (1957) Quantitative analysis of watershed geomorphology. Trans Am Geophys Union 913–920
14. Muller JE (1968) An introduction to the hydraulic and topographic sinuosity indexes. Ann Assoc Am Geogr 58:371–385
15. Evans IS (1984) Correlation structures and factor analysis in the investigation of data dimensionality: statistical properties of the Wessex land surface, England. In: Proceedings of the international symposium on spatial data handling, Zurich., v 1. Geographisches Institut, Universitat Zurich-Irchel, pp 98–116
16. Chorley RJ, Schumm SA, Sugden DE (1984) Geomorphology. Methuen, London
17. Merritts D, Vincent KR (1989) Geomorphic response of coastal streams to low, intermediate, and high rates of uplift, Mendocino junction region, northern California. Geol Soc Am Bull 101:1373–1388
18. Ohmori H (1993) Changes in the hypsometric curve through mountain building resulting from concurrent tectonics and denudation. Geomorphology 8:263–277
19. Cox RT (1994) Analysis of drainage-basin symmetry as a rapid technique to identify areas of possible quaternary tilt-block tectonics: an example from the Mississippi embayment. Geol Soc Am Bull 106:571–581
20. Oguchi T (1997) Drainage density and relative relief in humid steep mountains with frequent slope failure. Earth Surf Process Landf 22:107–120
21. Burrough PA, McDonnell RA (1998) Principles of geographical information systems. Oxford University Press Inc., New York
22. Hurtrez JE, Sol C, Lucazeau F (1999) Effect of drainage area on hypsometry from an analysis of small-scale drainage basins in the Siwalik hills (central Nepal). Earth Surf Process Landform 24:799–808
23. Kulkarni MD (2013) The basic concept to study morphometric analysis of river drainage basin: a review. Int J Sci Res
24. Sukristiyanti S, Maria R, Lestiana H (2018) Watershed-based morphometric analysis: a review. In IOP conference series: earth and environmental science, vol 118, No 1. IOP Publishing, p 012028
25. Nag SK (1998) Morphometric analysis using remote sensing techniques in the Chaka subwatershed, Purulia district, West Bengal. J Indian Soc Remote Sens
26. Ratnam KN, Srivastava YK, Rao VV, Amminedu E, Murthy KS (2005) Check dam positioning by prioritization of micro-watersheds using SYI model and morphometric analysis-remote sensing and GIS perspective. J Indian Soc Remote Sens 33(1)
27. Sreedevi PD, Owais S, Khan HH, Ahmed S (2009) Morphometric analysis of a watershed of South India Using SRTM Data and GIS. Geol Soc India 73:543–552
28. Vijith H, Satheesh R (2006) GIS based morphometric analysis of two major upland subwatersheds of Meenachil river in Kerala. J Indian Soc Remote Sens
29. Manu MS, Anirudhan S (2008) Drainage characteristics of Achankovil River Basin, Kerala. J Geol Soc India
30. Schumm SA (1956) Evolution of drainage systems and slopes in Badlands at Perth Amboy. Geol Soc Am 64:597–646
31. Kelson KI, Wells SG (1989) Geologic influences on fluvial hydrology and bedload transport in small mountainous watersheds, Northern New Mexico. Earth surface processes and landforms, U.S.A
32. Castillo V, Segovia AD, Alonso SG (1988) Quantitative study of fluvial landscapes, case study in Madrid, Spain. Landsc Urb Plan Landsc Urban Plan 16:201–217
33. Miller VC (1953) A quantitative geomorphic study of drainage basin characteristics in the Clinch Mountain area, Virginia and Tennessee. Department of Geology Columbia University, New York

34. Bali R, Agarwa KK, Ali SN, Rastogi SK, Krishna K (2011) Drainage morphometry of Himalayan Glacio-fluvial basin, India: hydrologic and neotectonic implications. Environ Earth Sci 66(4):1163–1174
35. Chen NS, Hu GS, Deng W, Khanal N, Zhu YH, Han D (2013) On the water hazards in the trans-boundary Kosi River basin. Nat Hazards Earth Syst Sci
36. Parveen R, Kumar U, Singh VK (2012) Geomorphometric characterization of Upper South Koel Basin, Jharkhand: a remote sensing & GIS approach. J Water Resour Protect

A TCAD Simulation-Based Study of the Radiation Effects on Ultra-Thin Symmetric Double Gate (SDG) Junctionless Field Effect Nanowire Transistor (JLFENT)

N. Deka, C. Duari, and N. Bora

Abstract This paper presents a TCAD simulation-based study of the radiation effects on an ultra-thin symmetric double gate (SDG) junctionless field effect nanowire transistor (JLFENT). A 3-D model of the nanowire transistor is virtually fabricated by considering the similar parameters as used in actual fabrication by using GENIUS 3-D Visual TCAD software. The JLFENT is exposed to various high irradiative environment from 100 to 500 krad and the effect on the device characteristics like drain current were studied. For comparison we have used different oxide materials namely SiO_2, and high-k dielectric Si_3N_4 and HfO_2 were used. The effect with varying the width of the devices were also studied. Here we found that the use of high-k gate dielectric HfO_2 on the device has shown better response when exposed in different environment of ionizing radiation.

Keywords Radiation effect · Symmetric double gate · Junctionless field effect nanowire transistor · Drain current · Total ionizing dose · 3-D TCAD simulation

1 Introduction

Radiation induced effects have become one of the most important and challenging failure phenomena in modern electronic devices. In past technologies, radiation effects were limited to the hostile environment such as space. However, with the advances in the process technology, the charge stored at the circuit node decreased dramatically due to the shrinking transistor geometries and reduced supply voltages

N. Deka (✉) · N. Bora
Department of Electronics and Communication Engineering, North Eastern Hill University (A Central University of India), Shillong, India
e-mail: nandeka89@gmail.com

N. Bora
e-mail: nbora@nehu.ac.in

C. Duari
Manipal University Jaipur, Jaipur, Rajasthan, India

S. Dwivedi et al. (eds.), *Flexible Electronics for Electric Vehicles*, Lecture Notes in Electrical Engineering 863, https://doi.org/10.1007/978-981-19-0588-9_35

[1–3]. The CMOS technology is nearing the sub 10 nm era due to constant down-scaling and to be remain at per with the Moore's predictions [4, 5]. The single gate MOS devices no longer able to survive beyond 40 nm of technology node and thus multi gate architectures becomes inevitable [6, 7]. The double gate structures both symmetric and asymmetric were extensively studied and were available literatures [8–12]. But due to possible fabrication difficulty to maintain the steep junctions very recently a new device structure without any junctions was proposed [13]. These structures known popularly as junctionless transistors are gaining popularity and is very much likely to replace the existing junction-based transistors in sub 10 nm technology node [14–18]. These device performances to withstand the radiation hardness for potential future space applications is highly desirable. Moreover, as MOS-based technology is nearing the sub-10 nm technology node, with the possibility to adopt the EUV lithography, device fabrication processes could also lead to radiation damages. Further, radiation effects can become increasingly complex to understand as newer technologies are introduced. Technology and design dependence of the radiation effects make analysis and mitigation extremely challenging. This paper shows various radiation effects on different parameters of DG MOSFET and then calculates their impacts on various characteristics of DG MOSFET and we also show the impact of radiation dose on its characteristics.

For the long-term reliability total ionizing dose (TID) effect is especially a concern for MOS-based devices. TID is a permanent damage that occurred in the lattice structure of semiconductor material, which increases gradually with the time of exposer [19]. TID primarily effects the oxide or the insulating layer, which may trap the charges that are produced during exposure which can leads changes in the device performances in long-term, which may cause degradation or failure of the device performance. In irradiated semiconductor devices the total-ionization dose (TID) effect is one of the prominent effects. Conventionally the MOS devices were known to be sensitive to TID effects. With deep-submicron CMOS technologies had become main- stream line in fabrication this view of MOS-based devices has changed drastically. For MOS-based devices with thin gate oxides thicknesses below 10 nm the TID effects in CMOS decreases drastically. However, the thick oxide layer in shallow trench isolation (STI) does not scale down in modern CMOS technologies. As a result, the primary TID concern in deep-submicron CMOS technologies are source-drain and inter-diffusion leakage currents. The gate insulator which is the most sensitive part of a MOS system to radiation effects we must consider the four major physical processes. When high radiation passes through the device gate oxide, it creates electron/hole pairs in the conduction and valence bands of SiO_2. The electrons are swept out of the oxide very quickly as they are more mobile than holes in SiO_2. Small fraction of the electrons and holes produced may recombine. The portion of holes that escapes the initial recombination are relatively immobile and remains near their point of generation. These charges may cause a negative threshold voltage shift in a MOS transistor.

2 Device Structure and Process Parameters

The SOI technology has been used in a similar manner as done in the case of actual hardware fabrication for SDG JLFENT device simulation. The 3-D TCAD simulation diagram of the SDG JLFENT based on SOI technology is shown in Fig. 1. The Lombardi mobility model is employed to include the dependence on doping concentration as well as the transverse and longitudinal electric field values. In simulations the Carrier trapping and DIBL were considered. The Shockley-read-hall (SRH) recombination model is included for leakage currents issues and the *F–D* carrier statistics with impact ionization is utilized in the simulations. The 3-D TCAD simulations for the SDG JLFENT are done by keeping the net doping profile uniform. Si (silicon) is used as the body material and the gate dielectric materials are chosen as HfO_2, Si_3N_4 and SiO_2 for all devices. The structural dimensions and parameters for the SDG JLFENT are given in Table 1.

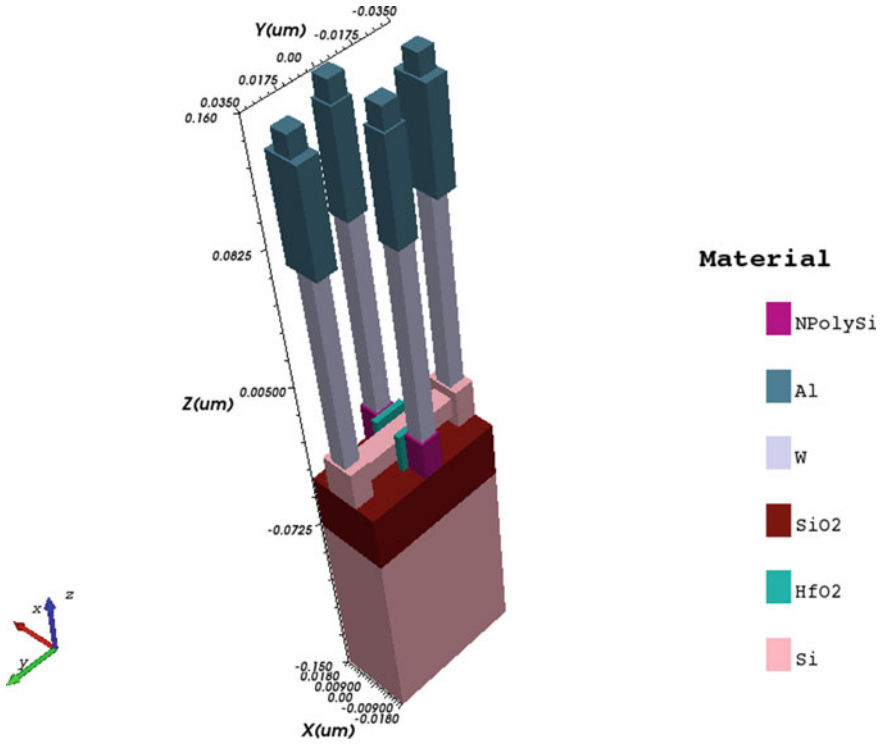

Fig. 1 3-D structure of the SDG JLFENT based on SOI technology

Table 1 Parameters used during TCAD Simulations

Device parameters name	Symbol used	Parameters values
Channel length	L_g	20 nm
Gate width	W	200,150, 100 nm
Si thickness	T_{si}	10 nm
Doping concentration	N_D	1×10^{19} cm^{-3}
Oxide thickness	T_{ox}	2 nm

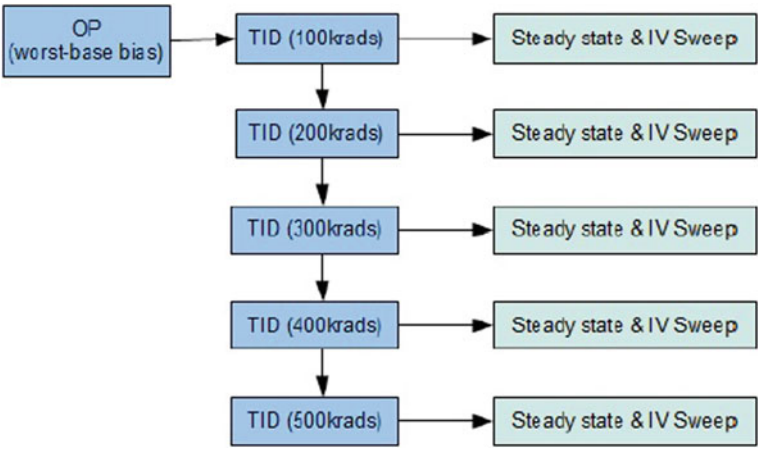

Fig. 2 TID command flowchart [20]

3 Simulation Setup

In order not to underestimate the damage of device, one often biases the device under the worst-condition in the OP simulation before the TID simulation. The worst-case bias for CMOS bulk devices is to have all terminals grounded except gate, which was kept at supply voltage (V_{DD}).

The simulation flow is shown in Fig. 2. We intend to do simulate the SDG JLFENT, I–V curves under various doses. Accordingly, we prepare 5 irradiated device states for the doses of 100 krad–500 krad, respectively, and then start an IV sweep simulation from each state. The simulations have been carried out using 3-D TCAD tool for the SDG JLFENT at different dose rates ranging from 100 to 500 krad [20]. The gate length and the width have been taken per the dimensions mentioned on Table 1.

4 Result and Discussion

Figure 3, shows the transfer characteristics of the SDG JLFENT under different gate

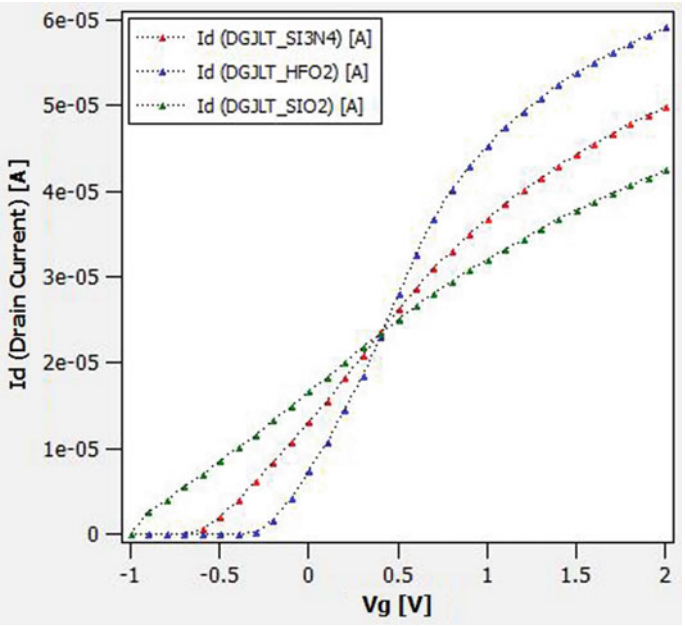

Fig. 3 Transfer characteristics of the SDG JLFENT with different gate oxide (HFO_2, SI_3N_4 and SiO_2) with $V_{ds} = 0.05$ V

dielectric materials, i.e., HFO_2, SI_3N_4 and SiO_2. Due to the reduction in the channel length and the gate oxide thickness it leads to degrade the device performance in terms of the short channel effect and the leakage current. With a thinner gate oxide, more gate tunneling current arises. For gate oxide scaling at the low level 1 nm thickness, high-K dielectric material are required to curtail severe gate leakage. With the use of high-k dielectric in gate oxide, improvement in the device transfer characteristics has been shown in Fig. 3. Though all the three devices show similar type of characteristic, device with HfO_2 gives highest ON current. Further with the use of high-k dielectrics the threshold voltage (Vth) is shifted toward positive value. The Id–Vg characteristics with Copper (Cu) and Aluminum (Al) as conducting materials for Gate, Source and Drain region of the SDG JLFENT are shown in Fig. 4. It is observed that out of the two materials, copper having the higher rate of work function shows better performance as compared to the device with aluminum as the conducting material. As the present CMOS technology has reduced the thickness of the semiconductor layer to the minimum, the off-state leakage current due to lower dimension of T_{si} is the major factor of degradation in the device performance as a whole. Therefore, the material with higher work function (Cu) used in the device design has succeeded to overcome this problem by providing higher ON compared to the device designed with Aluminum (Al) as the conducting material.

Figure 5, shows the I_d-V_g characteristics for a fixed drain voltage of the SDG JLFENT having gate width of 100 nm. Simulations are done both for irradiated and

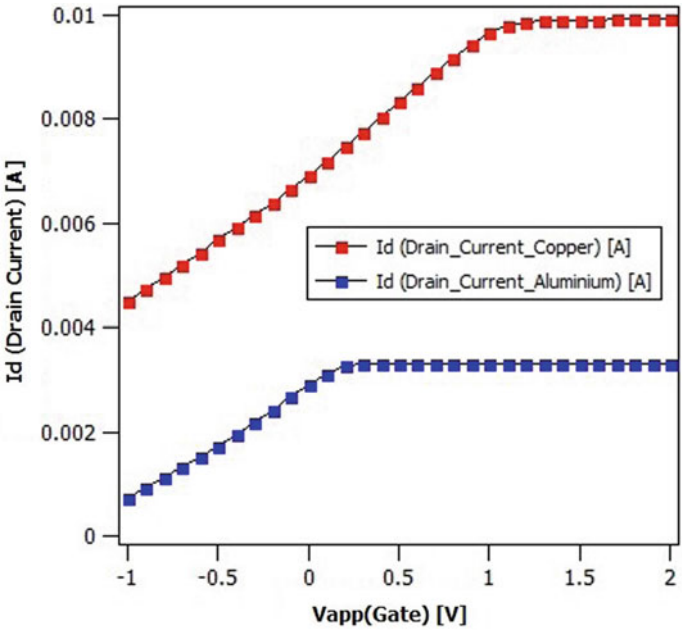

Fig. 4 Drain current (I_{DS}) versus gate voltage (V_{GS}) characteristics of SDG JLFENT at different conducting materials Copper and Aluminu

un-irradiated conditions of the ionizing radiation for the devices with different gate oxide materials (a) HfO_2, (b) Si_3N_4 and (c) SiO_2. The drain voltage has taken to be 1 V. It is observed that for a given gate voltage, the drain current for the irradiated condition is higher than that of the un-irradiated condition. This positive shift is due to the positive charge trapped in both the upper and lower oxides that increase the top-gate surface potential and consequently the lower-gate surface potential by standard vertical coupling effect.

Furthermore, Fig. 6, depicts Id-Vg characteristics for the DG-N-MOSFETs under different irradiative environment of ionizing dose ranging from 100 to 500Krad with different gate widths (W = 300, 200 and 100 nm) and V_{ds} = 1 V. It is observed that the drive current of the narrow gate width device is two orders of magnitude lower than the wider device which is well depicted by Fig. 6. Since the use of high-k gate dielectric material shows better performance in terms of low leakage and higher ON current, the device with HfO_2 as gate dielectric shows better performance as compared to the devices with Si_3N_4 and SiO_2. The effects of radiation dose ranging from 100 to 500 krad are also studied for the devices with different gate oxides and hence changes in the current characteristics have been observed with the change in different irradiative environment provided that the device with HfO_2 as gate dielectric shows better device performance while exposed in different environment of ionizing radiation.

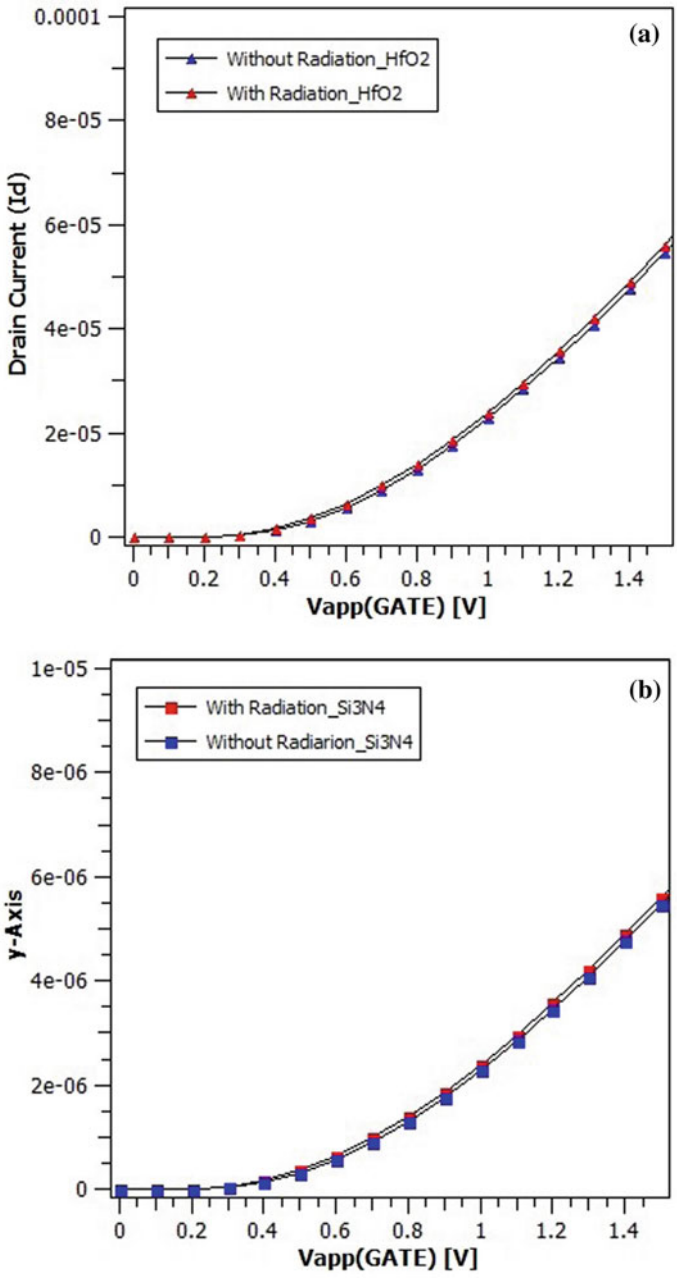

Fig. 5 I_D–V_D characteristics of the Dual Gate Junctionless N-MOSFETs with and without radiation exposure under different Gate Dielectrics $V_{ds} = 1$ V, $W = 100$ nm (a) Hf O_2, (b) Si_3N_4 and (c)SiO_2

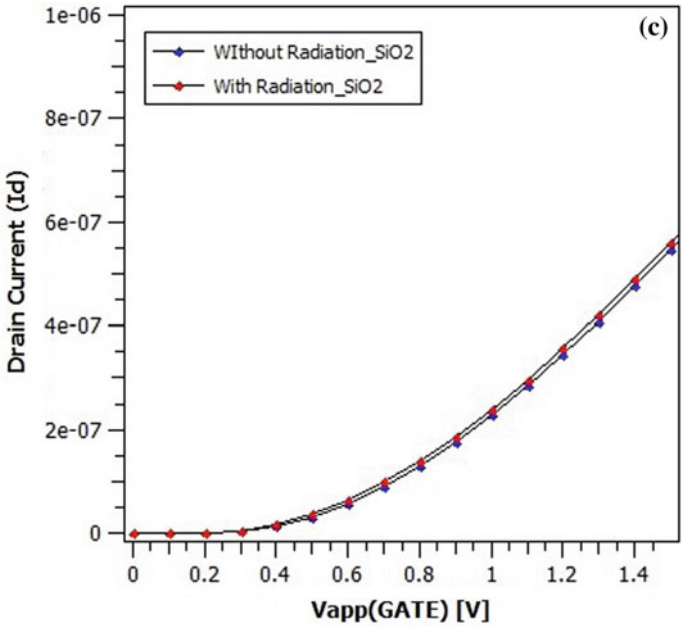

Fig. 5 (continued)

5 Conclusion

In this work, the effect of ionizing radiation on the characteristics of double gate MOSFET has been modeled. This model enables one to estimate quantitatively the change in the device performance when operated in nuclear environment. This model has shown that the use of high-*k* gate dielectric (Hf O_2) on the device has shown better response to the device performance when exposed in different environment of ionizing radiation provided with very less changes in the current characteristics compared to the other gate dielectric material (Si3N4 and SiO_2). Furthermore, it is also observed that lower the gate width of the device lesser the effect of ionizing radiation on the device performance which is because of the drive current of the narrow gate width device is two orders of magnitude lower than the wider device.

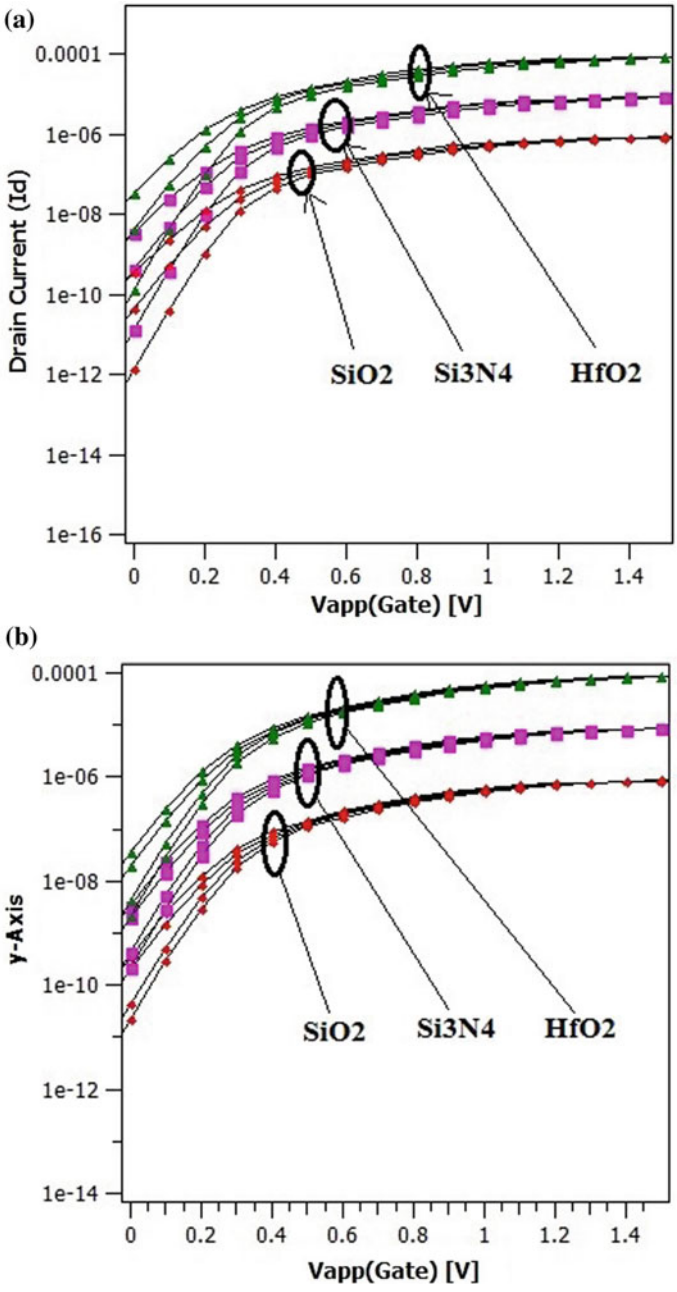

Fig. 6 I_D–V_{tt} characteristics of the dual gate junctionless N-MOSFETs when exposed in various irradiative environment 100Krad-500Krad (Si) with different Gate Dielectrics and Gate widths, V_{ds} = 1 V, **a** W = 300 nm, **b** W = 200 nm and **c** W = 100 nm

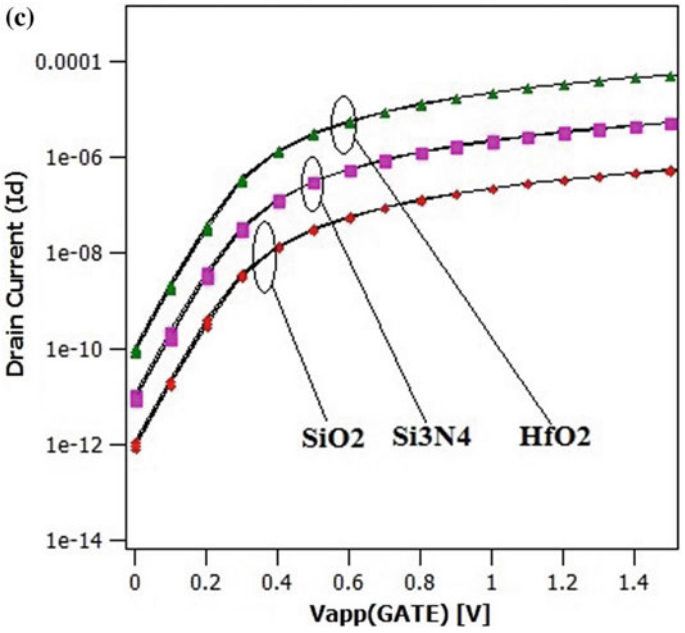

Fig. 6 (continued)

References

1. Gaillardin M, Marcandella C, Martinez M, Andrieu F, Barraud S, Vinet M (2017) Total ionizing dose response of NMOS tri-gate nanowires. In: Proceedings of the European conference on radiation and its effects on components and systems RADECS. https://doi.org/10.1109/RADECS.2016.8093098
2. Dodd PE, Massengill LW (2003) Basic mechanisms and modeling of single-event upset in digital microelectronics. IEEE Trans Nucl Sci 50(III). https://doi.org/10.1109/TNS.2003.813129
3. Oldham TR, McLean FB (2003) Total ionizing dose effects in MOS oxides and devices. IEEE Trans Nucl Sci 50(III). https://doi.org/10.1109/TNS.2003.812927.
4. Yu B, Chang L, Ahmed S, Wang H, Bell S, Yang CY, Tabery C, Ho C, Xiang Q, King TJ, Bokor J, Hu C, Lin MR, Kyser D (2002) FinFET scaling to 10 nm gate length. Tech Dig Int Electron Devices Meet (2002). https://doi.org/10.1109/IEDM.2002.1175825
5. Fleetwood DM (2018) Evolution of total ionizing dose effects in MOS devices with moore's law scaling. IEEE Trans Nucl Sci 65. https://doi.org/10.1109/TNS.2017.2786140.
6. Hisamoto D, Lee WC, Kedzierski J, Takeuchi H, Asano K, Kuo C, Anderson E, King TJ, Jeffrey J, Hu C (2000) FinFET—a self-aligned double-gate MOSFET scalable to 20 nm. IEEE Trans Electron Dev 47. https://doi.org/10.1109/16.887014
7. Colinge JP, Chandrakasan A (2008) FinFETs and other multi-gate transistors. Springer US. https://doi.org/10.1007/978-0-387-71752-4
8. Ernst T, Cristoloveanu S, Ghibaudo G, Ouisse T, Horiguchi S, Ono Y, Takahashi Y, Murase K (2003) Ultimately thin double-gate SOI MOSFETs. IEEE Trans. Electron Devices 50. https://doi.org/10.1109/TED.2003.811371s
9. Baruah RK, Bora N (2011) Analytic solution for symmetric DG MOSFETs with gate-oxide-thickness asymmetry. J Comput Theor Nanosci 8. https://doi.org/10.1166/jctn.2011.1920.

10. Bora N, Baruah RK (2011) Quantum mechanical treatment on modeling of drain current, capacitances and transconductances for thin film undoped symmetric DG MOSFETs. IEEE Int Conf Nanosci Technol Soc Implic NSTSI11, pp 1–6. https://doi.org/10.1109/NSTSI.2011.6111994.
11. Ortiz-Conde A, García Sánchez FJ (2006) Unification of asymmetric DG, symmetric DG and bulk undoped-body MOSFET drain current. Solid State Electron 50:1796–1800. https://doi.org/10.1016/j.sse.2006.10.003
12. Herrera FA, Miura-Mattausch M, Iizuka T, Kikuchihara H, Hirano Y, Mattausch HJ (2020) Modeling of short-channel effect on multi-gate MOSFETs for circuit simulation. In: 3rd International symposium on devices, circuits and systems, ISDCS 2020—Proceedings (2020). https://doi.org/10.1109/ISDCS49393.2020.9263000.
13. Colinge JP, Lee CW, Afzalian A, Akhavan ND, Yan R, Ferain I, Razavi P, O'Neill B, Blake Blake A, White M, Kelleher AM, McCarthy B, Murphy R (2010) Nanowire transistors without junctions. Nat Nanotechnol 5:225–229. https://doi.org/10.1038/nnano.2010.15
14. Akhavan ND, Yan R, Razavi P (2011). Junctionless transistors: physics and properties. https://doi.org/10.1007/978-3-642-15868-1
15. Bora N, Subadar R (2019) A complete analytical model of surface potential and drain current for an ultra short channel double gate asymmetric junctionless transistor. J Nanoelectron Optoelectron 14:1283–1289. https://doi.org/10.1166/jno.2019.2643
16. Jazaeri F, Sallese, J-M (2018) Short-channel effects in symmetric junctionless double-gate FETs. In: Modeling nanowire and double-gate junctionless field-effect transistors. https://doi.org/10.1017/9781316676899.009
17. Bora N, Das P, Subadar R (2016) An analytical universal model for symmetric double gate junctionless transistors. J Nano Electron Phys 8. https://doi.org/10.21272/jnep.8(2).02003
18. Bora N, Deka N, Subadar R (2020) Quantum mechanical analysis on modeling of surface potential and drain current for nanowire jlfet. J Nano Res 64. https://doi.org/10.4028/www.scientific.net/JNanoR.64.123.
19. Ren S, Si M, Ni K, Wan X, Chen J, Chang S, Sun X, Zhang EX, Reed RA, Fleetwood DM, Ye P, Cui S, Ma TP (2015) Total ionizing dose (TID) effects in extremely scaled ultra-thin channel nanowire (NW) gate-all-around (GAA) InGaAs MOSFETs. In: IEEE Trans Nucl Sci. https://doi.org/10.1109/TNS.2015.2497090
20. Cogenda Pte Ltd., Genius, 3-D device simulator, Reference manual. Singapore (2014)

Simulation of Solar-Based Fast Charging Station for Electric Vehicle

Vishnu Goyal, Neeraj Kanwar, and Shubhangi Grover

Abstract Electric vehicles (EVs) are mostly used to charge from the grid but unplanned charging of EVs can be a severe problem for the grid. In today's scenario the charging of electric vehicle from the grid is not an absolute solution for the environment. Hence, green energy is required to extract from the renewable energy sources for charging EVs. Out of many renewable sources the solar energy is found most prominent hence solar-based EVs charging stations become essential to develop for better environment. A boost converter is utilized to increase the generated voltage level up to the dc bus voltage. Moreover, boost converter is controlled through the Maximum Power Point Tracking (MPPT) technique to optimize the power generation from the solar irradiation. However, the solar-based fast charging station is required to maintain constant voltage at the dc bus with the help of Energy Storage System (ESS). A bidirectional dc-dc converter is utilized for maintaining the dc bus voltage through the ESS. Presently, the vehicle manufacturers are developing electric vehicle with different variants in which vehicles have different levels of charging voltage and current. Therefore, decentralized control of individual charger is mandatory to control the power flow from the dc bus to electric vehicle in charging station. Hence, a buck converter is utilized to control the charging of vehicle battery with Constant Voltage Constant Current (CVCC) technique. In this paper solar-based fast charging system and its optimized control technique is presented using Matlab/Simulink/ R2019 b.

Keywords Electric vehicle · Bi directional dc-dc converter · MPPT · Buck converter · CCCV charging technique

V. Goyal (✉) · N. Kanwar · S. Grover
Manipal University Jaipur, Jaipur, Rajasthan 303007, India
e-mail: vishnu.goyal@jaipur.manipal.edu

N. Kanwar
e-mail: nk12.mnit@gmail.com

S. Grover
e-mail: shubhangi.179201052@muj.manipal.edu

S. Dwivedi et al. (eds.), *Flexible Electronics for Electric Vehicles*, Lecture Notes in Electrical Engineering 863, https://doi.org/10.1007/978-981-19-0588-9_36

1 Introduction

For regular activities, the world energy demand is increasing at an alarming rate with growing population, expansion of cities and the modern life style. In addition, electrical power generation by fossil fuel is not environment friendly and future demand of supply become very difficult to fulfil with limited fossil fuel reserves [1]. Hence the utility has to shift towards renewable energy sources for better environment. The solar energy-based Photovoltaic (PV) is widely used renewable energy source for electricity due to it many advantages like clean in nature, sufficient in amount to satisfy the future demand, installation in remote areas and distributed generation [2, 3].

Due to the nonlinear V-I characteristic of PV array, the power generation is drastically affected by solar irradiance and panel temperature. The operating point of PV array can be adjusted to operate at maximum power point with the variation of irradiance and temperature [4]. This operating point adjustment method of extracting maximum power from the available sun light is called Maximum Power Point Tracking (MPPT). This MPPT control technique is implemented by varying the output voltage of the PV panel using DC-DC converter [5]. Some MPPT algorithm techniques like perturb and observe, incremental conductance and constant voltage methods are tested with the variation of irradiance, temperature and load conditions. The outcomes illustrate that the incremental conductance technique delivers the better performance [6]. By using this technique PV panel can track the fast change in the irradiance with desire accuracy.

Now a day's, due to the Govt. policies and public awareness for the environment the acceptance of battery operated electric vehicles is increasing day by day [7]. Although, proper and fast charging infrastructure is required in large number to use EVs without any range anxiety. Presently, three different type of charging methods are applicable [8, 9]: Level 1 single phase alternate current (AC) is used to charge EVs in household outlet with overnight charging time. **Level 2** Three-phase AC outlets are generally used to charge EVs in 4 to 5 h. **Level 3** Direct Current fast charging method is used to charge the EVs up to 80 percent state of charge just in 45 min [10–13]. The lithium-ion battery is generally used in electric vehicles application due to its high life cycle, high energy density and high safety ability [14, 15]. Various charging techniques have been suggested with the growth of utilization of EV like Constant Voltage (CV), Constant Current (CC), Constant Trickle (CTC) and the Constant Current Constant Voltage (CCCV) [16, 17]. In CCCV method the maximum charging current is defined by the charger developers which the battery can endure without any damage. After ensuring that the battery is charged upto to the certain level of SoC, charger will switch the charging method to constant voltage. Hence, CCCV method of charging is able to control the charging current as well as battery voltage also [18, 19].

The sun light is available in the day time only and found it is fluctuating in nature due to the atmospheric conditions. Hence it become essential to use sufficient Energy Storage System (ESS) with the solar power generation for the development reliable

dc fast charging system. Electric vehicle needs constant dc voltage supply irrespective of variation in solar irradiance for proper charging. In this paper, a solar-based fast charging system is implemented and investigated through MATLAB/Simulink using MPPT control technique through boost converter. A bidirectional dc-dc power converter is used to maintain the dc link voltage constant at the desired level through ESS with the variation of solar irradiance. Moreover, a buck converter is used to control the fast charging of the electric vehicle by implementing the CCCV charging method.

2 PV Technology and Maximum Power Point Tracker

Solar energy comes from the sun to the earth in the form of photons, which is called as solar irradiance. Solar cell is an electrical current source energetic by flux of radiation. This technology is basically defined by production of free charge carriers in the solar cell due to the light absorption. With this process, the received power is converted into electrical energy which can be optimized by a boost converter with the help of MPPT technique. This generated power is used to charge the ESS to assist charging operation during clouding weather. *V*-*I* and PV characteristics of PV panel are shown in Fig. 1a and b, respectively.

MPPT technique plays an important role in PV technology. By using MPPT control technique the cost of PV array can be decreased by reducing the number of total PV panels for the same amount of power generation. In this MPPT control algorithm some steps have to be followed for the process of maximize the power generation. In this paper incremental conductance-based algorithm is used for MPPT tracking in which the following objective is to satisfy the condition of dI/dV should be equal to negative of I/V to operate the PV array at the optimized operation point. [6]. In this algorithm, initially PV array voltage and current are constantly measured, which are used to determine the change in voltage and current (ΔV and ΔI). Flow chart of incremental conductance technique is shown in Fig. 2. A MPPT system is primarily consist of firing control circuit of dc-dc boost converter on the basis of solar panel output current and voltage.

3 System Configuration

MPPT control algorithm is implemented to extract the maximum power from the sun light by operating the PV module in the most efficient region. A large battery bank operating as energy storage system is being charged during full sun light and light load condition through bidirectional power converter in charging station. During full sun light, electric vehicles are charged by solar energy only. In the case of low sun light, electric vehicles are charged by power that comes from the PV panel and excess power comes from ESS. Moreover, in other case, if there is no sun light then only

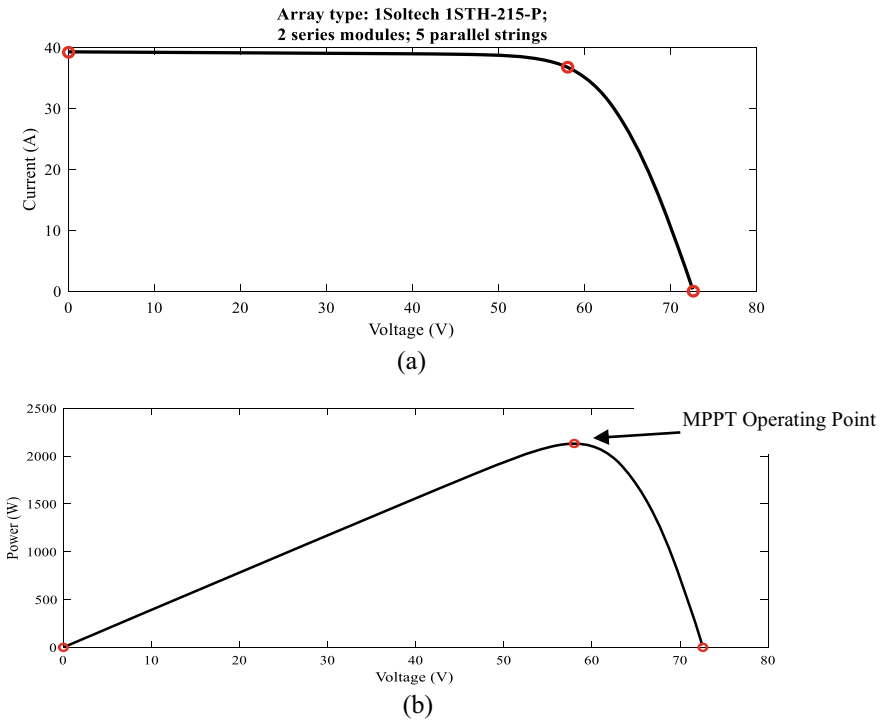

Fig. 1 **a** V-I Characteristic **b** PV Characteristic of PV Panel at 25° C Temperature

ESS will supply total required power for charging the electric vehicles. The complete block diagram of overall system is shown in Fig. 3.

Overall configuration of the system is designed by three different parts, which are performing their task as per present sun light and load on the charging station. First system is defined as PV power generation with its MPPT controlling technique through boost converter. MPPT controller generates the firing pulses through PWM generator for boost converter on the basis of PV voltage, current and change in the duty ratio. This boost converter is maintaining the voltage at it MPPT point for generating maximum power from the available sun light. Second part of the system is used to maintain the dc bus voltage constant at the defined level by controlling the power flow between dc bus and ESS through bidirectional power converter. Third part of the system is presenting electric vehicle charging through buck converter. Buck converter controls the charging voltage and current on the basis of electric vehicle battery parameters.

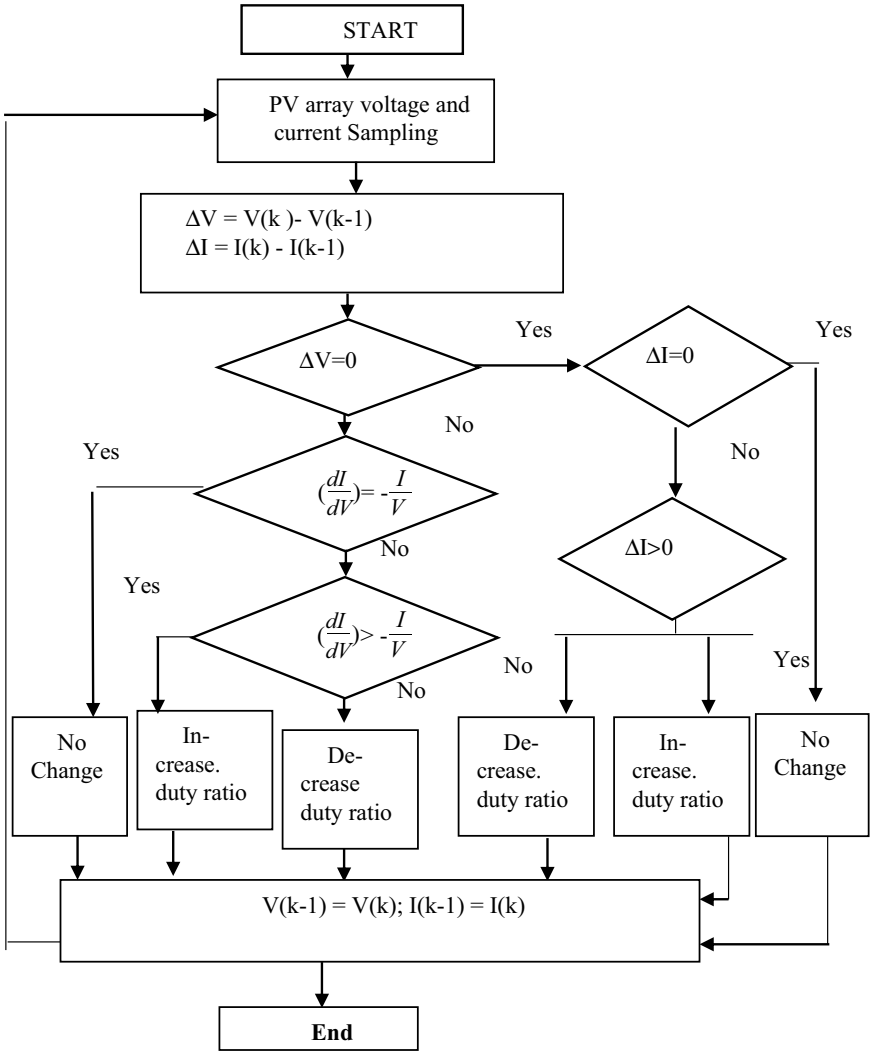

Fig. 2 Flow chart of implementation of incremental conductance MPPT technique

4 Simulation and Results

PV solar-based electric vehicle charging system is developed and simulate in MATLAB/SIMULINK as shown in Fig. 4. In this simulation the effect of variation in solar irradiance is studied with implementation of MPPT control technique. Figure 5 shows the variation of solar irradiance from zero to maximum value with fixed interval of time. Controlled PV output voltage using MPPT technique is shown in Fig. 6. In this figure it is observed that the PV voltage remains constant for the

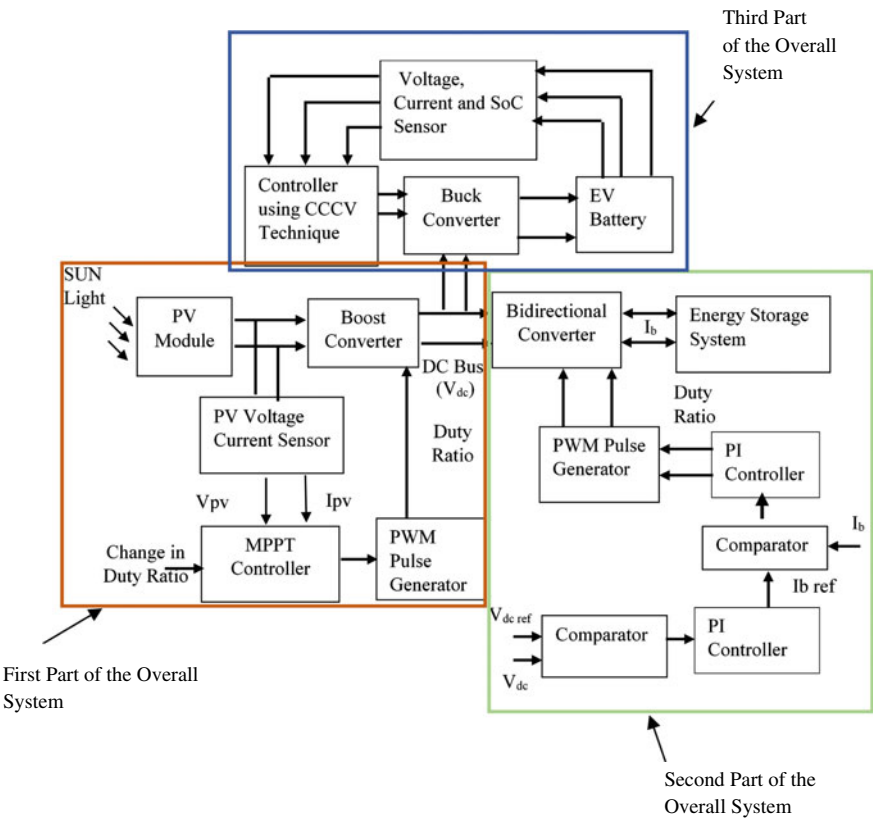

Fig. 3 Block diagram of overall system configuration

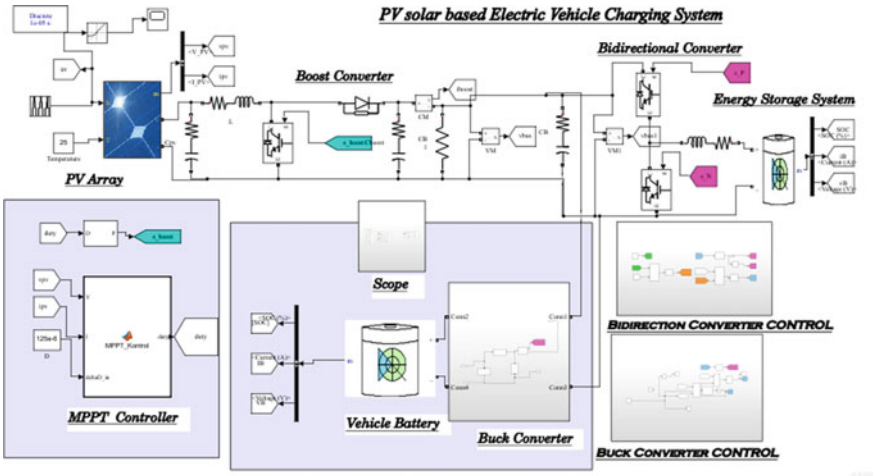

Fig. 4 Simulation of Solar-based Electric Vehicle Charging System

variation in solar irradiance and become zero in the case of no sun light.

Figure 7 shows the variation of PV panel output current with solar irradiance. And total electrical power generation by using MPPT technique is shown in Fig. 8. In this figure it is noticed that the generated power is directly affected by variation of solar irradiance.

Electric vehicle charging process requires constant voltage irrespective of variation in solar irradiance and temperature. Therefore, large backup support is used in the form of ESS in the charging station. This ESS is maintaining the dc bus voltage constant at the desired value through bidirectional power converter. Hence, required dc bus voltage is taken as reference value for the controller of bidirectional converter and compared with the actual value of the dc bus voltage. In case of high irradiance condition, PV panel power generation become higher in that case excess power is used to charge ESS. In other case of poor solar irradiance, required charging power comes from the PV panel as well from ESS. Moreover, for the case of zero irradiance the required charging power comes from the ESS only for charging the vehicle. As per simulation result, it is noticed that the dc bus voltage remains constant at the

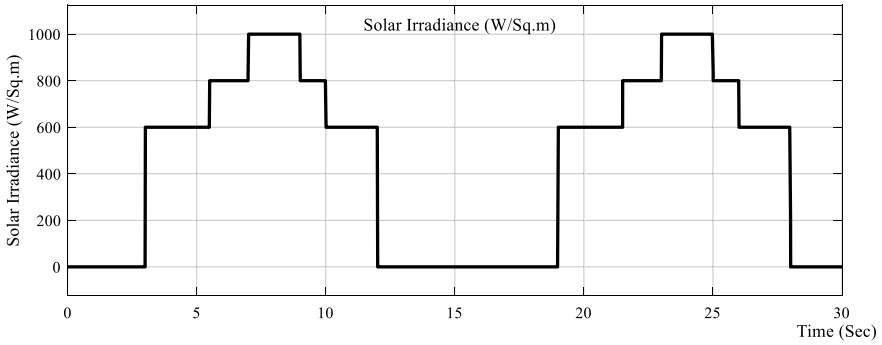

Fig. 5 Solar irradiance in W/m^2

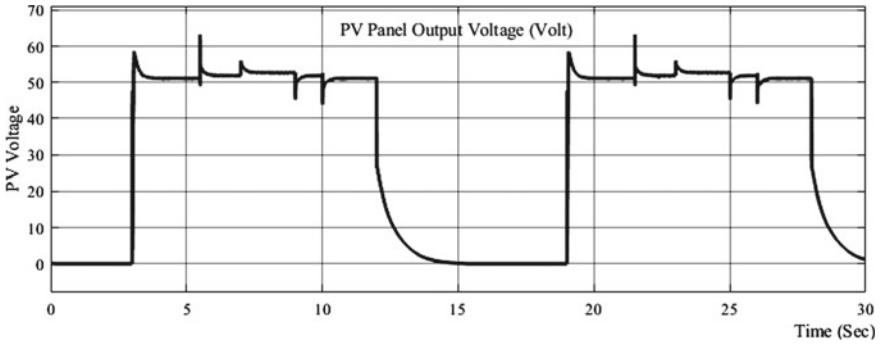

Fig. 6 PV panel output voltage

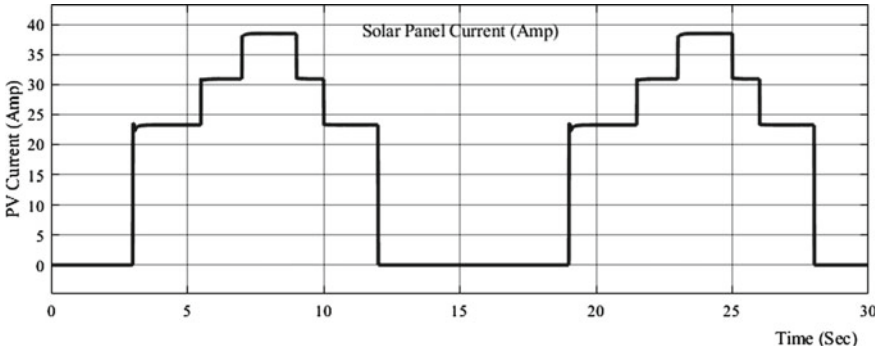

Fig. 7 PV panel current (Amp)

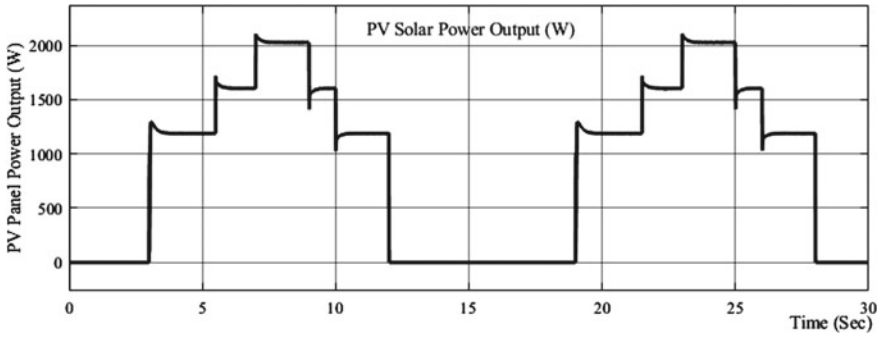

Fig. 8 PV panel power generation

desired value with the variation of solar irradiance or even for zero irradiance also as shown in Fig. 9. Figure 10 shows the state of charge of the ESS of charging station.

It is observed that the initially SoC of ESS is decreasing due to zero solar irradiance thereafter SoC is start to increase with increasing the solar irradiance. This charging

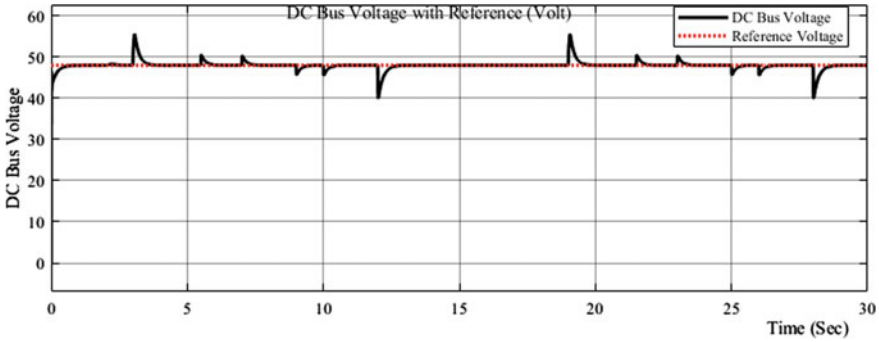

Fig. 9 DC bus voltage with reference value

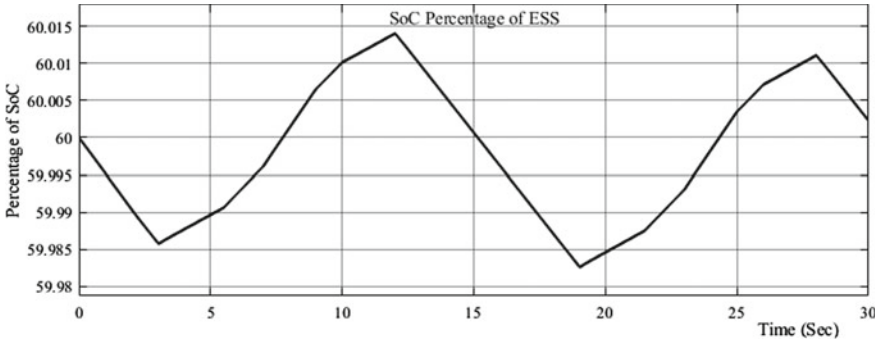

Fig. 10 ESS state of charge level

and discharging current of ESS through bidirectional converter is represented by Fig. 11a by which it is observed that the positive current shows that discharging of ESS and negative current shows the charging of ESS. During discharging process

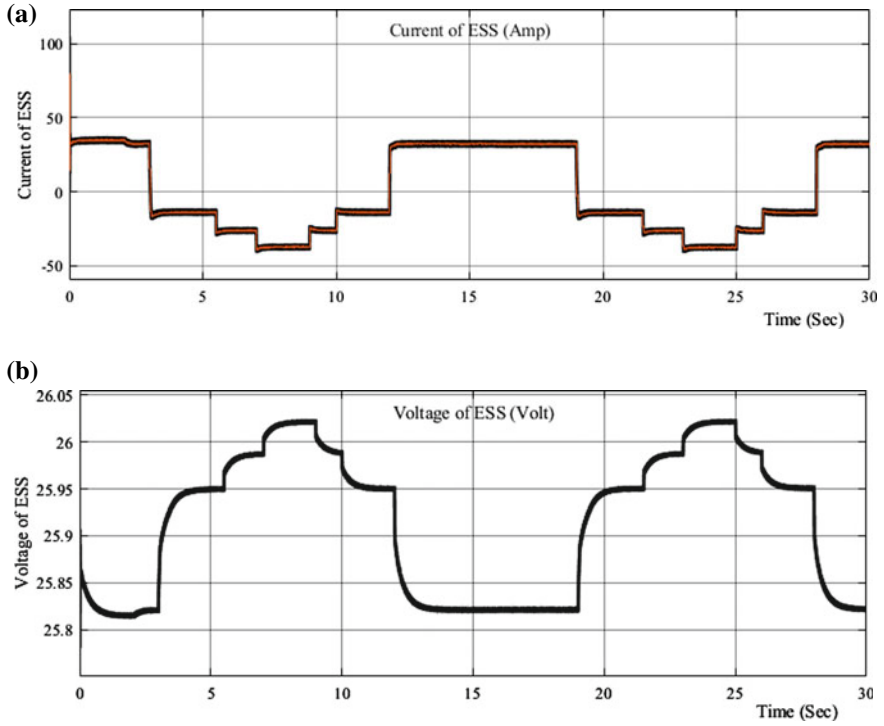

Fig. 11 **a** Current of ESS through bidirectional converter. **b** Voltage level of ESS using bidirectional converter

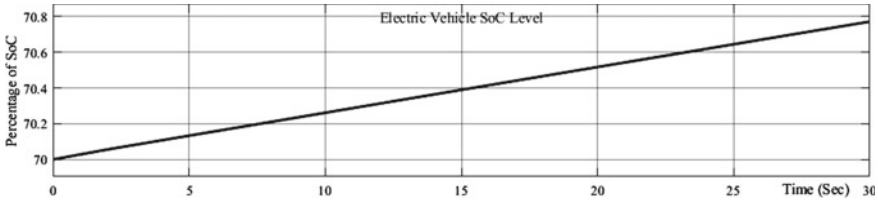

Fig. 12 State of charge of the vehicle battery

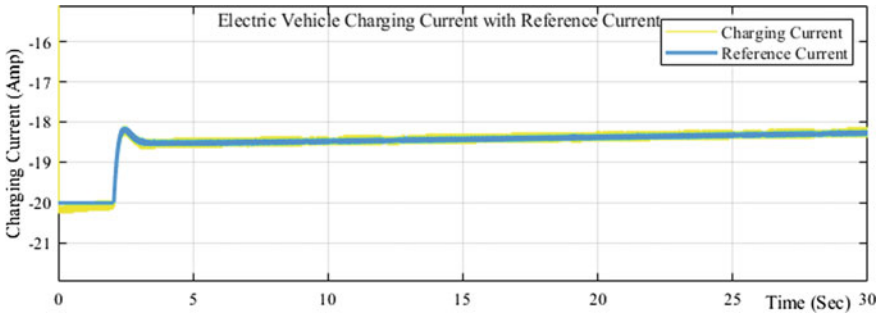

Fig. 13 Electric vehicle charging current with its reference value

the voltages of ESS is decreasing and increasing in the case of charging process as shown in Fig. 11b.

Electric vehicle charging is applied from the dc bus through buck converter using CCCV methodology on the basis of present state of charge as shown in Fig. 12. In this CCCV charging method, battery is started to charge with constant current at the rate of maximum allowable charging current of the battery in the case of low level of SoC. After a predefined SoC level, vehicle battery is now start to charge by applying the constant voltage. It is observed that the battery is start charging with constant current and the charging voltage is increasing in this period. But after achieving a particular level of SoC, constant voltage is applied to charge the battery and the charging current become lower. This transition of charging method from constant current to constant voltage is shown in Figs. 13 and 14. Figure 13 shows the value of charging current with its reference value and Fig. 14 shows the charging voltage with its reference value.

5 Conclusion

In this paper a solar-based electric vehicle charging technique is successfully simulated and verified by various result of the simulation. In overall simulation, three different way of controlling are applied by different power converters for optimize

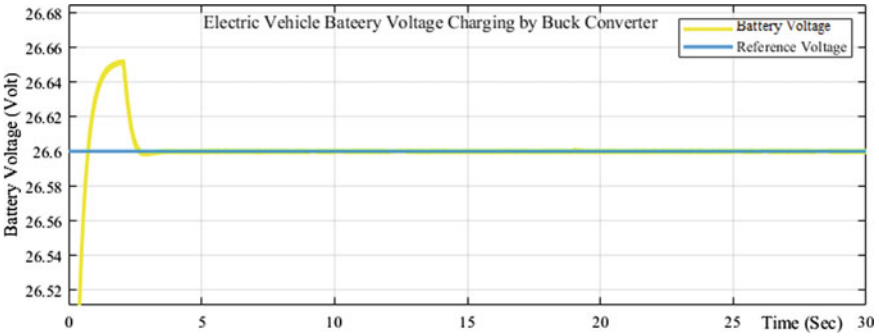

Fig. 14 Electric vehicle charging voltage with its Reference value

the overall performance of the charging station. In first way, MPPT technique is verified to extract maximum power from the available solar irradiance through the boost converter by maintaining the PV voltage at its optimum value. In the second way, it is verified that the bidirectional power converter maintains the dc bus voltage constant at the desire value by controlling the power flow between dc bus and ESS. It is also shown that the dc bus voltage remains constant not only for variable solar irradiance but also for zero irradiance. And in the third way, dc fast charging approach by CCCV methodology is tested and verified through the buck converter. In which, transition of charging method from the constant current to constant voltage is also verified after predefined level of SoC. Hence, it can be concluded that with this charging method charging voltage and current remains with in the safe limit.

References

1. Vinifa R, Kavitha A (2013) Fuzzy based maximum power point tracking on a PV system. In: Energy efficient technologies for sustainability (ICEETS), 2013 International Conference on pp 329–333
2. Huynh D, Dunnigan M (2015) Maximum power point tracking using an adaptive perturbation and observation algorithm for a grid-connected solar photovoltaic system. Int J Grid Distrib Comput 8(3):97–110
3. Arulkumar K, Palanisamy K, Vijayakumar D (2016) Recent advances and control techniques in grid connected PV system—a review. Int J Renew Energy Res 6(3):1028–1049
4. Murtaza AF, Chiaberge M, Spertino F, Tabrez U, Boero D, Giuseppe MD (2017) MPPT technique based on improved evaluation of photovoltaic parameters for uniformly irradiated photovoltaic array. Electr. Power Syst. Res. 145:248–263
5. Eltawil MA, Zhao Z (2013) MPPT techniques for photovoltaic applications. Renew Sustain Energy Rev 25:793–813
6. Christhoper W, Ramesh R (2013) Comparative study of P&O and InC MPPT algorithms. AJER 2(12):402–408
7. Silva C, Sousa DM, Roque A (2017) Charging electric vehicles from photovoltaic generation with intermediate energy storage. In: 2017 6th international conference on clean electrical power (ICCEP), Santa Margherita Ligure, Italy

8. Buchmann I (2017) Ultra-fast Charging. 27 September 2017. Online Available: https://batteryuniversity.com/learn/article/ultra_fast_charging. [Accessed 20 October 2018]
9. Lai CPY, Law KH, Lim KH (2019) Direct fast charging of electric vehicle using solar power. In: 7th international conference on smart computing & communications (ICSCC)
10. Kuperman A, Levy U, Goren J, Zafranski A, Savernin A, Peled I (2010) Modeling and control of a 50KW electric vehicle fast charger. Electr Electron Eng Israel (IEEEI), Eliat 2010:188–192
11. Aggeler D, Canales F, Zelaya-De L Parra H, Coccia A, Butcher N, Apeldoorn O (2010) Ultra-fast DC-charge infrastructures for EV-mobility and future smart grids. In: Innovative Smart Grid Technologies Conference Europe (ISGT Europe). IEEE PES, Gothenburg, Sweden
12. Bauer P, Zhou Y, Doppler J, Stembridge N (2010) Charging of electric vehicles and impact on the grid. In: Mechatronika, 13th international symposium, Teplice, pp 121–127
13. Yilmaz M, Krein PT (2012) Review of charging power levels and infrastructure for plug-in electric and hybrid vehicles. Electr Vehicle Conf (IEVC), Greenville, pp 1–8
14. Ansean D, Gonzalez M, Garcia MV, Viera CJ, Anton CJ, Blanco C (2015) Evaluation of LiFePO4 batteries for electric vehicle applications. IEEE Trans Ind Appl 2:1855–1863
15. Wu X, Hu C, Du J, Sun J (2015) Multistage CC-CV charge method for Li-Ion battery", Hindawi Publishing Corporation mathematical problems in engineering 2015 (294793):10. https://doi.org/10.1155/2015/294793
16. Zhang S, Zhang C, Xiong R, Zhou W (2014) Study on the optimal charging strategy for lithium-ion batteries used in electric vehicles. J Energies 7:6783–6797
17. Wang Z, Wang Y, Rong Y, Li Z, Fantao L (2016) Study on the optimal charging method for lithium-ion batteries used in electric vehicles. Applied energy symposium and summit 2015: low carbon cities and urban energy systems. Energy Procedia 88:1013–1017
18. Norian KH (2013) Measuring electrical components of lithium ion battery at different states of charge. J Power Sources 242:714–717
19. Akira I, Masakazu S, Koji F (2014) Rapid charge and discharge property of high capacity lithium ion battery applying three-dimensionally patterned electrode. J Power Sources 256:244–249

A Multi-Period Load Flow Framework for Active Distribution Network Using DIgSILENT PowerFactory Software

Samarendra Pratap Singh, Neeraj Kanwar, and Amit Saraswat

Abstract Load flow analysis is an effective tool to observe the behaviour of electrical network at a specific point of time. In view of day ahead power system planning and operation, multi-period load flow become even more important tool to capture the image of state variables of electrical network for next 24 h. The paper develops methodology to perform multi-period load flow (MPLF) based on DIgSILENT PowerFactory software. The proposed procedure automize the task for carrying out MPLF. The developed methodology is implemented on modified 33 bus distribution network to analyse the impact of renewable energy sources (RES) in distribution system network in terms of improvement in bus voltage profile and reduction in network power losses.

Keywords DIgSILENT power factory · Distribution network · Multi-period load flow · Renewable energy sources

1 Introduction

DIgSILENT PowerFactory software is an engineering tool which provides platform to perform power system planning and operational studies. The software facilitates environment for modelling of transmission and distribution network. The software has inbuilt programming language, i.e. DIgSILENT programming language (DPL). It enables user to develop operational framework which is not available as an inbuilt function or module in software. This capability attracted many researchers to work on this platform and many research work have been published using this software.

S. P. Singh · N. Kanwar (✉) · A. Saraswat
Manipal University Jaipur, Jaipur, India
e-mail: nk12.mnit@gmail.com

S. P. Singh
e-mail: samarendra.singh@jaipur.manipal.edu

A. Saraswat
e-mail: amit.saraswat@jaipur.manipal.edu

S. Dwivedi et al. (eds.), *Flexible Electronics for Electric Vehicles*, Lecture Notes in Electrical Engineering 863, https://doi.org/10.1007/978-981-19-0588-9_37

In [1], modelling of autonomous microgrid has been developed and steady state analysis has been carried out to observe the bus voltage profile. Framework for modelling of wind farm connected to transmission network is proposed in [2]. Framework for optimal reactive power dispatch to minimize real power loss and voltage deviation for transmission system network has been developed in [3]. Considering wind power uncertainty, a two stage stochastic optimization model for reactive power dispatch has been developed in [4]. Optimal power flow model in presence of FACTS devices to minimize power loss and voltage deviation has been proposed in [5], [6]. To deal with load and RES power output uncertainty, framework for stochastic and probabilistic power flow study has been suggested in [7] and [8], respectively. Above-mentioned works utilize DIgSILENT PowerFactory software for network modelling and use DPL for automation of task and integration with other software. In [9], application of Python with DIgSILENT PowerFactory software is described to automize the process of power system operational studies. Most of the research work mentioned above developed framework for operational studies applicable for a certain point of time.

In this paper, using DIgSILENT PowerFactory software [10] a framework for MPLF is proposed. The modelling part is done on software platform and automation of task has been done using DPL. The next section describes the development of this framework in detail. The developed framework is implemented on modified 33 bus distribution network. Result section describes impact of RES on performance of distribution network. At last, conclusion and future scope of this work is presented.

2 Multi-Period Load Flow Formulation in DPL

This section describes the process of implementing MPLF for active distribution network using DIgSILENT programming language (DPL). The first step is to construct single line diagram with all necessary line data and bus data on grid platform of activated project in DIgSILENT power factory software. Inside Script option under activated project, DPL Command (ComDPL) object named as 'MPLF.ComDpl' is created.

In 'Script' section of this DPL Command object, the main DPL script is written to perform MPLF of distribution network. This DPL script uses syntax similar to C and C++ programming language. The DPL is built with approach quite similar to object oriented programming approach. The main script starts from declaration of local variables. In the next segment of code, AllRelevant() is used to get all classified set of network elements and to load them in locally defined sets. Count() is used to determine number of objects in the set. Refer snippet shown in Fig. 1(a) and (b), respectively.

Now, the code initiates MPLF process. Refer snippet shown in Fig. 2(a). Load flow object 'ComLdf' is called from active study case and loaded into local PF object. PF_Mode is defined as input parameter to the main script and it is made zero to run balanced load flow. In MPLF, load flow is carried out for each time interval for a

```
ClearOutput();
! Defining Variables
int error, timeIV, ii;
int n_bus, n_line, n_load;
int n_WPP, n_PV;
object PF;
object O_load, O_bus, O_line;
object O_WPP, O_PV;
double M1, M2, M3, M4, M5;
double Start_Time, End_Time;
double Exe_Time;
set S_bus, S_line, S_load;
set S_WPP, S_PV;
```

(a)

```
! Loading all the loads (ElmLod) in set S_load
S_load = AllRelevant('*.ElmLod');
n_load = S_load.Count();! number of loads
! Loading all the buses (ElmTerm) in set S_load
S_bus  = AllRelevant('*.ElmTerm');
n_bus  = S_bus.Count();! number of buses
! Loading all the lines (ElmLne) in set S_line
S_line = AllRelevant('*.ElmLne');
n_line = S_line.Count();!Counts number of lines
!Loading all the Wind Power Plants (ElmGenstat) in set !S_WPP
S_WPP = AllRelevant('*.ElmGenstat');
n_wind=S_WPP.Count();!number of Wind Power Plants
!Loading all the Solar Photovoltaic Geneartors in set S_PV
S_PV  = AllRelevant('*.ElmPvsys');
n_PV  = S_PV.Count();number of PV Geneartors
```

(b)

Fig. 1 Snippet MPLF.ComDpl: (**a**) variable definition and (**b**) loading different types of network element in different sets

```
!Multi-period load flow simulation
!Initialising variables for load flow simulations
!Get System Time at start
Start_Time = GetTime(4);
! Load load flow object (ComLdf) of
! active study case in object PF
PF = GetCaseObject('*.ComLdf');
PF:iopt_net = PF_Mode;
! PF_Mode = 0 for balanced load flow
! Start time interval
for (timeIV=1; timeIV<=NOtimeIV;
timeIV+=1)
{
!Adjusting load demand
AdjustLoadDemand: tIV = timeIV;
AdjustLoadDemand: MatrixP = Data_Pl;
AdjustLoadDemand: MatrixQ = Data_Ql;
AdjustLoadDemand:.Execute();
!Adjusting Wind Power Generation
AdjustRESPower: tIV = timeIV;
AdjustRESPower: sRESType = S_WPP;
AdjustRESPower: MatrixP = Data_PWind;
AdjustRESPower: MatrixQ = Data_QWind;
AdjustRESPower.Execute();
!Adjust PV Power plants
AdjustRESPower: tIV = timeIV;
AdjustRESPower: sRESType = S_PV;
AdjustRESPower: MatrixP = Data_PPV;
AdjustRESPower: MatrixQ = Data_QPV;
AdjustRESPower.Execute();
```

(a)

```
EchoOff();!Freezes the user-interface.
error = PF.Execute(); !Perform Load Flow
!Load the first bus in object O_bus
O_bus = S_bus.First();
for (ii = 1; ii <= n_bus; ii+= 1) {
M1 = O_bus:m:u1;
!Storing bus voltage in Vbus
Vbus.Set(timeIV,ii,M1);
O_bus = S_bus.Next(); }
!Load the first line in object O_line
O_line = S_line.First();
for (ii = 1; ii <= n_line; ii+= 1) {
M2 = O_line:m:Ploss:bus1;
!Storing line real power loss in Ploss
Ploss.Set(timeIV,ii,M2);
M3 = O_line:m:Qloss:bus1;
!Stores line reactive power loss in Qloss
Qloss.Set(timeIV,ii,M3);
M4 = O_line:m:P:bus1;
!Stores line real power (from bus)
Pline.Set(timeIV,ii,M4);
M5 = O_line:m:Q:bus1;
!Stores line reactive power(from bus)
Qline.Set(time_iv,ii,M4);
O_line = S_line.Next(); }
 }
End_Time=GetTime(4); ! Get System Time at End
Exe_Time = End_Time - Start_Time;
printf('Execution Time: %g sec',Exe_Time);
```

(b)

Fig. 2 Snippet MPLF.ComDpl: (**a**) adjust setting of load flow, adjust load demand and RES power generation and (**b**) executing load flow and storing results

```
! Subscript Adjusting Load Demand
int jj;
double a, b;
object obj;
set sLoads;
sLoads = AllRelevant('*.ElmLod');
obj = sLoads.First();
jj = 0;
while(obj) {
 jj = jj+1;
 a = MatrixP.Get(tIV,jj);
 obj:plini = a ;
 b = MatrixQ.Get(tIV,jj);
 obj:qlini = b ;
 obj = sLoads.Next();
}
```

(a)

```
! Subscript Adjusting RES Power
Generation

int jj;
double a, b;
object obj;
obj = sRESType.First();
jj = 0;
while(obj) {
 jj = jj+1;
 a = MatrixP.Get(tIV,jj);
 obj:pgini = a ;
 b = MatrixQ.Get(tIV,jj);
 obj:qgini = b ;
 obj = sRESType.Next();
}
```

(b)

Fig. 3 DPL Subscript (**a**) AdjustLoadDemand.ComDpl and (**b**) AdjustRESPower.ComDpl

defined time span. To exhibit this process, time interval based for loop is created. From here onwards, the code enters in time interval loop. Adjustment in loads and RES power generation is done with assistance of subroutine 'AdjustLoadDemand' and 'AdjustRESPower'.

Subroutine 'AdjustLoadDemand' updates the values of active (plini) and reactive power (qlini) of all the loads in network. Subroutine 'AdjustRESPower' updates the values of active (pgini) and reactive power (qgini) of all the RESs. Refer snippet shown in Fig. 3(a) and (b), respectively.

Load active and reactive power data for each time interval are taken from internal matrices Data_Pl and Data_Ql, respectively. RESs active and reactive power data are taken from internal matrices Data_PWind/Data_PPV and Data_QWind/Data_QPV, respectively. Subroutines and internal matrices are defined under the content of MPLF.ComDpl. Refer Fig. 4.

Once the adjustment in load and RESs is done, the load flow is executed and numeric answers are stored in internal matrices. Refer snippet shown in Fig. 2(b). The 'for' loop created for increment of time interval ends here. At the end, execution time of MPLF is calculated.

3 Simulation Results

Modified 33 bus 12.66 kV radial distribution network is used to perform multi-period load flow study. The standard bus data and line data are available in [11]. Photovoltaic generators, PV1 with 845 kW rating and PV2 with 1122 kW rating, are

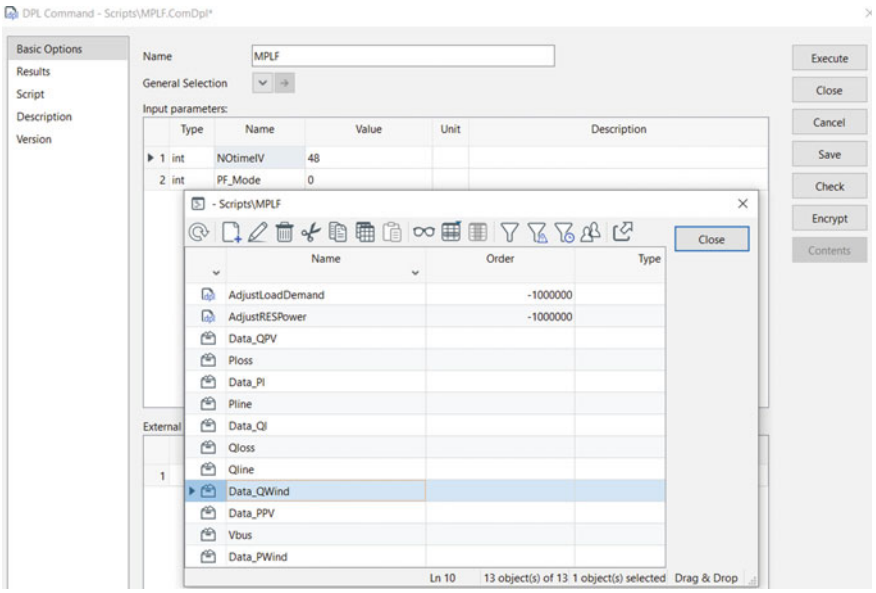

Fig. 4 Subroutines and internal matrices defined under the content of MPLF.ComDpl

connected at bus 14 and bus 24, respectively. Wind power plant WT1 with 1072 kW rating is connected at bus 30. All RES are operated with unity power factor. To study the impact of RES in distribution system network, two scenarios are considered. In scenario1, MPLF is carried out without RES. In scenario2, MPLF is performed with RES. All RES are operated at unity power factor. Load demand curve and RES power generation profile for 24 h are shown in Figs. 5 and 6 , respectively.

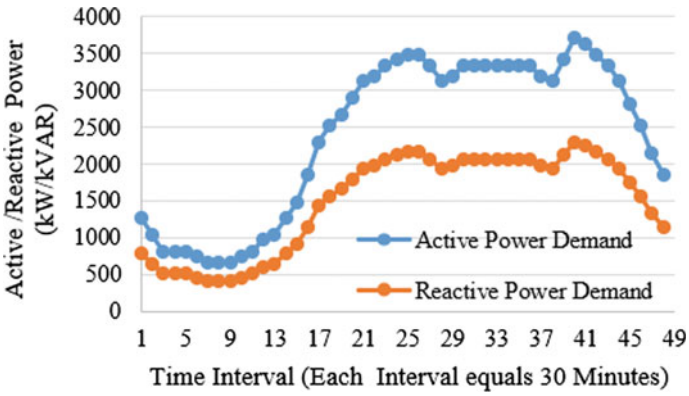

Fig. 5 Total active and reactive power demand profile

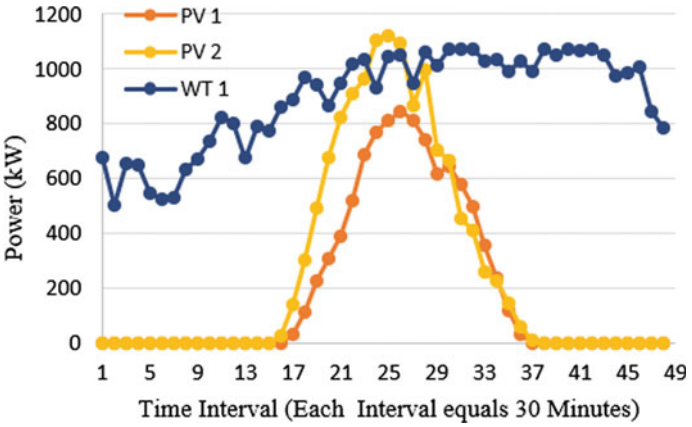

Fig. 6 RES power generation output

The impact of RES in distribution network is observed in terms of improvement in bus voltage magnitude, reduction in power loss and reduced power drawn from external grid. The improvement in bus voltage profile is shown in Fig. 7. In presence of RES, reduction in active and reactive power losses during 24 h is shown in Fig. 8 and Fig. 9, respectively. Without RES, the average active and reactive power losses are 100.13 kW and 66.78 kVAr. With RES, average active and reactive power losses have been reduced to 51.78 kW and 34.22 kVAr. Grid power with and without RES integration is shown in Fig. 10.

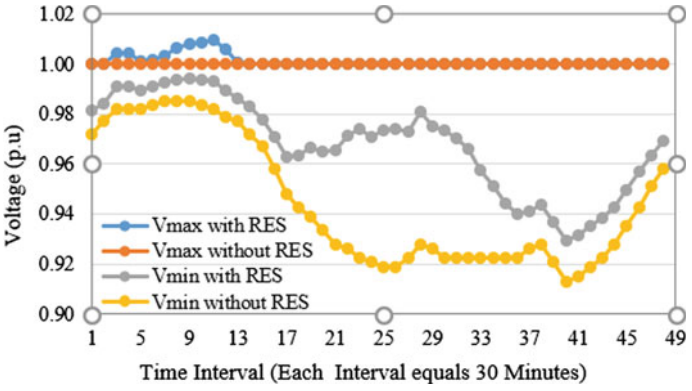

Fig. 7 Maximum bus voltage (Vmax) and minimum bus voltage (Vmin) with and without RES

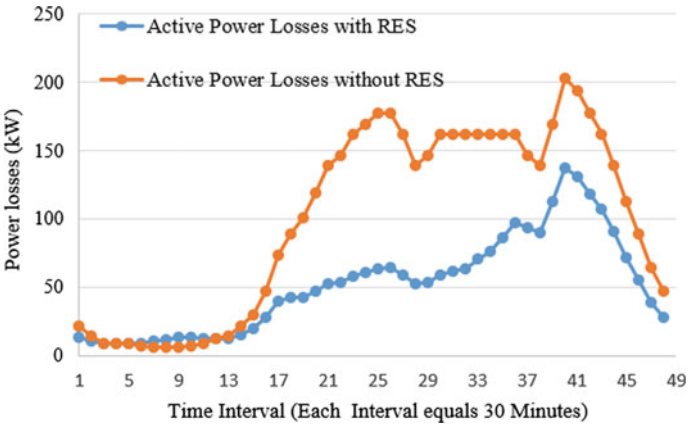

Fig. 8 Active power losses with and without RES

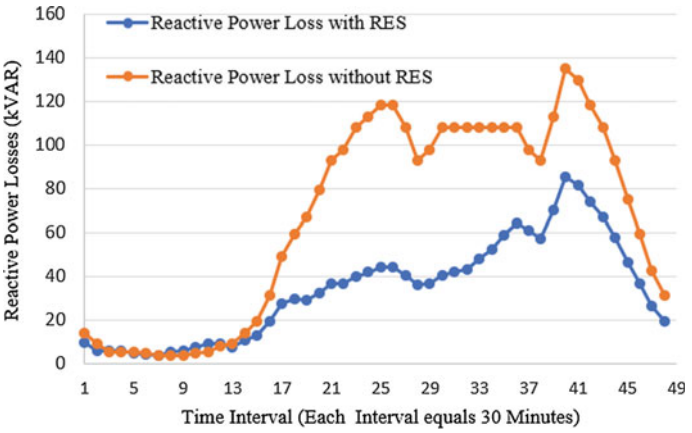

Fig. 9 Reactive power losses with and without RES

4 Conclusions

DPL-based multi-period load flow framework have been developed. The modular programming approach has been implemented and explained with the help of code snippet. The developed framework is successfully tested on modified 33 bus distribution network. It has been observed that presence of RES in distribution network results in improvement in voltage profile and reduction in power losses. The future work includes the development of DPL-based multi-period optimum power flow model for active distribution network.

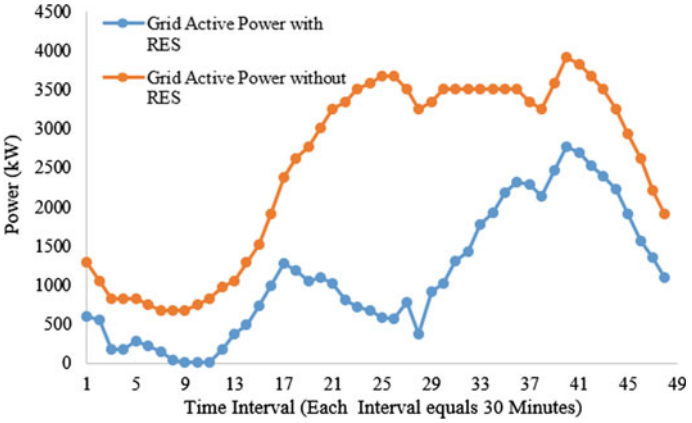

Fig. 10 Grid active and reactive power with and without RES

References

1. Rathore V, Kanwar N (2020) Modelling and analysis of autonomous microgrid with different fault scenarios. In: Conference on flexible electronics for electric vehicles (FlexEV-2020), vol 2294(1), AIP conference proceedings, Jaipur, India
2. Ucheniya R, Saraswat A, Siddiqui SA, Goyal SK, Kanwar N (2020) A wind farm modeling in IEEE-24 bus reliability test system on DIgSILENT power factory. In: 2020 International conference on intelligent engineering and management (ICIEM). IEEE, London, UK pp 477–483
3. Ucheniya R, Saraswat A, Siddiqui SA (2020/19) Optimal reactive power dispatch through minimization of real power loss and voltage deviation. In: Kalam A, Niazi K, Soni A, Siddiqui SA, Mundra A (eds) Intelligent computing techniques for smart energy systems 2018. LNEE, vol 607. Springer, Singapore pp 421–430
4. Saraswat A, Ucheniya R, Gupta Y (2020) Two-stage stochastic optimization for reactive power dispatch with wind power uncertainties. In: 2020 international conference on computation, automation and knowledge management (ICCAKM). IEEE, Dubai, United Arab Emirates, pp 332–337
5. Gaur B, Ucheniya R, Saraswat A (2019) Real power transmission loss minimization and bus voltage improvement using STATCOM. In: 2019 3rd International conference on recent developments in control, automation & power engineering (RDCAPE). IEEE, Noida, India, pp 236–241.
6. Gaur B, Ucheniya R, Saraswat A (2020) Real power transmission loss minimization and bus voltage improvement using UPFC. In: Bera R, Pradhan PC, Liu CM, Dhar S, Sur SN (eds) Advances in communication, devices and networking, ICCDN 2019. LNEE, vol 662. Springer, Singapore, pp 1–9
7. Quan H, Yang D, Khambadkone AM, Srinivasan D (2018) A stochastic power flow study to investigate the effects of renewable energy integration. In: 2018 IEEE innovative smart grid technologies—Asia (ISGT Asia). IEEE, Singapore, pp 19–24
8. Tuinema BW, Rueda Torres JL, Stefanov AI, Gonzalez-Longatt FM, van der Meijden MAMM (2020) Probabilistic power flow analysis. In: Probabilistic reliability analysis of power systems. Springer, Cham

9. Shrivastava DR, Siddiqui SA, Verma K (2020) Interfacing python with DIgSILENT power factory: automation of tasks. In: Kalam A, Niazi K, Soni A, Siddiqui SA, Mundra A (eds) Intelligent computing techniques for smart energy systems. LNEE, vol 607. Springer, Singapore, pp 1033–1037
10. DIgSILENT PowerFactory 2020 [Software], DIgSILENT GmbH
11. Baran ME, Wu FF (1989) Network reconfiguration in distribution systems for loss reduction and load balancing. IEEE Trans Power Delivery 4(2):1401–1407

State of Art and Comprehensive Study on Smart Meter Networking

Aftab Ahmed Ansari and Dyanamina Giribabu

Abstract The considerable increment in power consumption and the quick enhancement of renewables such as wind power and solar power have presented enormous challenges in terms of energy security and the ecosystem, which in the meantime are encouraging the advancement of energy networks in a smarter direction. An advanced grid integrated with two-way power flow ability, inter-device communication, cybersecurity, physical safety, autonomous fault detection, self-healing, and incorporation of renewable energy resources to improve energy efficiency, reliability, quality, and network security can be a potential solution for smarter direction and such type of system is regarded as smart grid (SG). Smart meter is among the key instruments used in the intelligent network. The smart meter is an integrated energy meter that collects data from the load devices of end users and monitors customer energy usage and provides information to the utility provider and/or system controller. A variety of sensors and controls are used in a smart meter, assisted by a specific communication infrastructure. In this context, this paper describes in detail the architecture of the smart meter network, smart meter evolution, various functionalities, and its associated benefits. In addition, it also discusses some security problems and its solution with smart meters.

Keywords Advanced metering infrastructure · Meter data management system · Smart grid · Smart meter · Security issues

1 Introduction

Electricity is prominent in modern world, since it enables daily appliances like computers, televisions, telephones commercial buildings, industrial plants, the Internet, etc. The demand for electricity is growing rapidly, especially the demand for electricity in India will reach the value about 373.43 GW as of January, 31, 2021 [1].

A. A. Ansari (✉) · D. Giribabu
Maulana Azad National Institute of Technology, Bhopal, India
e-mail: aftab786zakir@gmail.com

S. Dwivedi et al. (eds.), *Flexible Electronics for Electric Vehicles*, Lecture Notes in Electrical Engineering 863, https://doi.org/10.1007/978-981-19-0588-9_38

Modern society depends heavily on electricity. Electricity disturbances and failures get a significant adverse effect on life quality. The power supply must therefore be regulated efficiently to provide the customers with high quality and reliability [2]. Smart grid adoption might be a potential way of meeting the rising demand for electricity and the increased usage of intelligent meters. Introducing intelligent metering and algorithms also has the ability to rapidly detect, isolate, and restore power systems at a higher level of precision [3]. Many power measuring equipment and approaches are capable of solving problems related to electricity utilization and control. Currently, the capabilities and configurations of smart meters are extensive to different utilities [4–7]. One of the purposes of this article is to define and review the features and functions of smart meters used commercially.

In India, energy meters are mainly electromechanical but are increasingly being substituted by sophisticated and more reliable digital electronic meters. A significant proportion of energy revenues are lost from electricity theft, inaccurate reading and billing meters, and customers' inability to pay electric payments on time. The use of prepaid energy meters will minimize significant revenue losses.

The market for smart meters has seen the total number of smart meters shipped worldwide for 2019 at around 131.23 million units and is estimated to reach 188.12 million by 2025, with a compound annual growth rate (CAGR) of 6.6% for the forecast period as illustrated in Fig. 1 [8]. The overwhelming acceptance of intelligent meters makes it possible to collect a large amount of fine-grained electricity usage data. Billing is not the only smart meter feature anymore. High-resolution data from smart meters offers a wealth of knowledge on consumer trends of energy use and lifestyles. In the meantime, the de-regulation of the energy industry in several countries around the world, especially on the consumer side, is continuously moving forward. These countries now make little attempt to reform the electricity retail market. Progressively more participants, including suppliers, customers, aggregators, contribute to a more stable, active, and competitive retail sector. How enormous smart meter statistics can be used to encourage and improve the efficiency and stability of the demand side has now become an interesting issue globally.

In several electrical systems worldwide, smart meters will be implemented to provide customer real-time energy consumption and cost statistics. Intelligent meters are electronic measuring mechanisms used by distributors to convey information

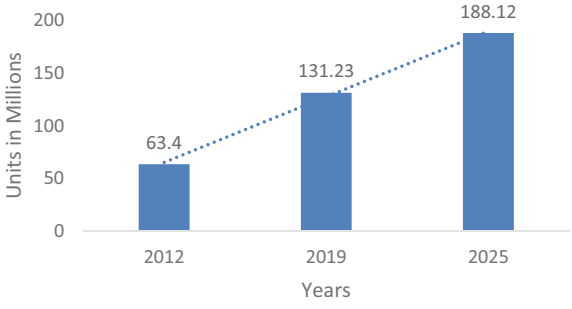

Fig. 1 Smart meter global market size

to billing consumers and to manage their electrical systems. A hybrid electronic measurement system with two-way communication technology is commonly known as advanced metering infrastructure (AMI) for information, monitoring, and control. Prior networks, which used one-way interactions to obtain data from meter, were known as automated meter reading (AMR) mechanism. Over time, AMI has grown from its origins as an AMR to the present two-way interaction and data system [5].

2 The Smart Grid and Smart Metering Concept

The concept 'smart grid' is commonly employed to describe the integration of all supply, grid, and application components linked to a digital power grid upgrade with a reliable, efficient, stable, and manageable open information infrastructure based on standards that could allow two-way communications to provide various advantages for both customers and power suppliers [6].

The smart grid employs smart devices and upgraded power infrastructure for digital communication to increase transmission and distribution grid efficiency. Using this digital technology, smart systems can analyze their health in real-time, adapt them to new environments, monitor distributed resource integrations, and manage end-user smart appliances. Performance and efficiency can be enhanced, and end users can use active positions in the smart grid to save customers' money [6, 7]. Since many years earlier, the installation of automated meter reading (AMR) infrastructure has been setup. Wireless systems or telephone lines were used to transmit data during those years. This device was designed to collect data employing a radio connection mounted in a vehicle passing by the meter, or by telephone lines or wireless networks collecting data from meters.

Intelligent meters must be able to measure simple along with other valuable quantities. Such meters must have a proper communication ports in order to address requests to collect the required information, to turn on or off commands provided by a central access server, and to record incidents and defects in a scenario of any tampering. This meter must have an interface for consumer knowledge to attach an in-home monitor (IHD). A smart meter should be able to illustrate the overall price value of the energy consumed. It should also be able to record customer data every hour, so that subscribers can control their usage.

3 Smart Grid Component

Smart grid's main components are known as follows

- Smart Infrastructure
- Smart Communication
- Smart Management
- Smart Protection Systems.

Meanwhile the smart infrastructure architecture is categorized into two sections.

(1) Smart energy system—The smart energy network is of power generation type, transmission type, and distribution type
(2) Smart information systems—Smart information system will have smart metering, sensors, phasor measurement units, as well as information management.

The first component of the smart energy system is the generation of electricity. Electricity is most commonly generated by power plants that involve the use of flowing water or heat engines powered by chemical combustion or nuclear power. Now, let us see how the generation of power will be improved or how it will take new forms. The form of smart power generation is now offering two-way flow of both data and electricity. Distributed power generation, for example, is a critical component of intelligent grid generation that can certainly play a key and significant role in our intelligent grid. The improvement of the existing transmission system by installing or building intelligent control centers, intelligent power transmission networks, and intelligent substations will also make our transmission system fairly smart. Now, distributed generation facilitates the creation of a new grid model called a microgrid, one of the corner stones of the future intelligent grid distribution. Now, a smarter distribution system would have to be built at different voltage levels so-called smart grid, which will be considered the main corner stone of the future grid.

Another part of smart infrastructure is smart information. Now what's smart information? the smart grid growth is driven by advanced power station technology as well as enhanced computer tracking, analysis, optimization, and control from solely central utilities to the distribution and transmission grid. One important concern is that a distributed system can become smarter only when the data is made available at different nodes at distance through a wireless Internet and for that it needs to have smart meters in place. The smart meter is typically an electrical meter itself which records consumption by an hour or less even at an interval of 5 min, 15 min interval, and half an hour's interval, as per the requirement.

Smart meters are efficient instruments that radically change the function of electricity grids. In contrast to conventional meter features, smart meters could be used as sensors in the whole distribution network [9]. Smart meters can calculate and record the actual electricity usage for a day at a given interval if an advanced metering infrastructure (AMI) is in place [10]. This collected data is transmitted through wireless communication from a secure network to a central data management system. In addition, service providers may use these sensors to detect failures and send alerts of failure or recovery. Using this detail, utilities may provide increasingly reliable electricity. It also allows better strategy, better execution and a more rapid network failure reaction.

4 Smart Metering Evolution

Table 1 illustrates the evolution of electromechanical meters to AMI meters. In the subsection, detailed evolution of smart meter is discussed.

4.1 Manual Meter Reading (MMR)

Meter reading has historically often been performed manually. The meter had to be monitored physically to track the meter readings, normally monthly. This included inspection of remote locations or residences. Sometimes, it is also not possible to track every meter physically or manually. The same was valid not only for the reading of meters but also for the maintenance of meters.

Table 1 Evolution of smart meter technological advances

Meter system	Functionalities/capability/feature
Electromechanical meter	• Electromechanical meter operation is quite simple • As the number of rotations increases, the reading also increases • Environmental factors affect the accuracy of an electromechanical meter
Electronic meter	• Wide range of measurement of electrical parameters • Compared to electromechanical meters, these meters have a high degree of accuracy • Design flexibility • Capacity update
Automated meter reading (AMR)	• Remote meter reading • Detection of a power outage at the meter • Detection of tampering • Profiling of load
AMR plus	• Reading in real time or near real time • Notification of consumer can be read by another commodity
Advanced metering infrastructure (AMI)	• Multiple tariff framework • Remotely programmable • Home area network (HAN) or Local area network (LAN) interface • Remote connection/disconnection of the supply

4.2 Electronic Meter Reading (EMR)

The concept of an electronic meter reading was introduced as a remedy to the issue of being able to recognize or read energy usage more efficiently, and the main step in that direction was an electronic meter reading technology (EMR), adapted and still in use, especially for industrial users. With EMR, meter inspectors do not need to reach consumer premises to receive their monthly usage any more. The majority of EMR technology is a walk-by or a drive-by wherever the meter has it contain a radio frequency transmitter (RF) which helps you by transmitting the receiver reading. The receiver is a portable unit that is mounted in an automobile or employs a radio tower network to capture and transmit the data to the organization and the user. The communications are made through a wireless communication link, for example, by means of ZigBee [11].

4.3 Automated Meter Reading (AMR)

The meter reading techniques with the invention of the automatic meter reading (AMR) was further improved. Automatic meter readings (AMR) are the technology for the automatic processing of data from energy measurement instruments for the automatic acquisition, diagnostics, and status, and pass this information to a centralized billing, troubleshooting, and analytical database system [11]. Over all, this system saves the costs of daily visits to any physical place for meters scanning. Another benefit is that the billing become almost realistic. This timely analysis information helps both customers and suppliers to control better the use and manufacture of electrical energy. AMR systems usually involve handheld mobile and network technologies focused on wired and wireless telephony, radio frequency (RF), or power line transmission platforms.

4.4 Advanced Metering Infrastructure (AMI)

An experience of the advantages of two-way communication among system components such as customers, operators, and resources has resulted in the development of AMR into AMI. It would be no mistake to call AMI rather than AMR an evolutionary move. AMI is an infrastructure of next level that includes smart metering, home area networks, communication networks between utilities and metering, housing management systems, and meter data management systems, etc. Advanced metering infrastructure (AMI) is an integrated smart metering system that facilitates two-way interactions between customers and utilities. The device offers a range of significant features which had not been or should have been carried out manually before, such as the ability to control electricity usage automatically and remotely, to connect

and disconnect service, to detect manipulation, to recognize and isolate faults, and to monitor voltage. Alongside customer innovations such as in-home displays and programmable thermostats, AMI also helps utilities to implement new time-based rate schemes and rewards that enable consumers to cut demand and manage energy use and costs. AMI is a designed network that incorporates a variety of technologies in order to gain its objectives. The network consists of smart meters at the user end, communications systems at various levels of the infrastructure hierarchy to join two ends, Meter Data Management Systems (MDMS), and means for connecting the collected data to software applications and interfaces at the service or head end [12].

The customer is installed with a sophisticated, time-based electronic meter. These meters can transfer the information gathered through generally accessible established networks. The recorded data is received by the host system AMI. They are then forwarded to an MDMS that handles, analyses, and supplies the data to the service provider in a useful format [13, 14]. AMI allows bidirectional communication; thus, it is also possible to communicate or question command or price signals from the service provider to meters or to load controllers.

Coming to this basic block diagram of the AMI as shown in Fig. 2. It consists of three components. The first is the MDMS. This MDMS stands for the meter data management system, and the second is the smart meter, which is essentially located on the consumer's periphery or premises, and this MDMS is essentially present within the data and control center (DCC) utility. And these data control centers are basically located on the periphery or on the premises of the utility. And these two components, MDMS and smart meters, are connected to each other or communicate with each other through a communication infrastructure. So, this is how this very simple block diagram works with regard to the advanced metering infrastructure of the smart grid system.

Data concentrator—The data concentrator is a significant node in the AMI, linked to several smart meters and central servers. It allows data to be shared between MDMS and smart meters and it safely aggregate data.

Meter data management system (MDMS)—MDMS is an AMI heart. This method includes the data collection from concentrators entering the operating center, then proper processing and storage. As a result, the same data form is located at the same address and the data retrieval becomes easier. MDMS provides analytical tools to communicate with the various operating and management systems and collect the appropriate data.

The measurements that are essentially taken from the smart meter are shown in Fig. 3. The first is the RMS voltage, the second is the RMS current, and the third is the calculation of the phase angle. People mainly talk about the angle between the

Fig. 2 Block diagram of AMI

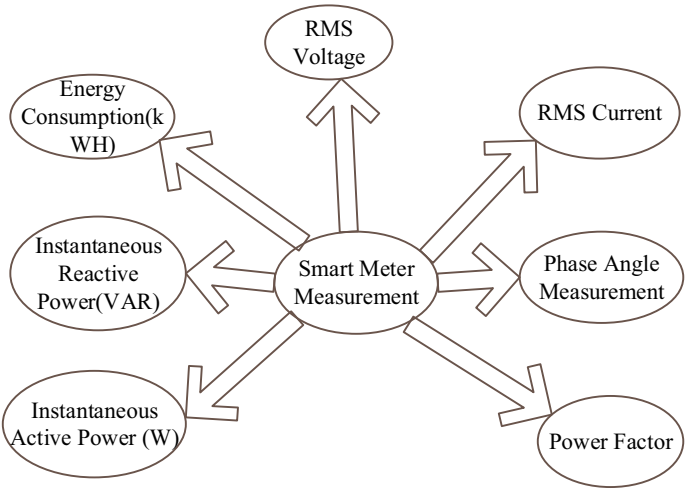

Fig. 3 Measurement from smart meter

voltage and the current of a particular network or customer network through which the load is connected. Even using this smart meter, this phase angle is calculated, and the fourth is a critical power factor for us. The power factor is of great significance to customers. This power factor can also be calculated using the smart meter, and the fifth is instantaneous active power how much power the consumer consumes and can be calculated using this smart meter infrastructure or smart meter unit. And the sixth one is instantaneous power. Power is of two types: one is instantaneous active power, and the other is instantaneous reactive power. These power calculations can be carried out by every individual using smart meter technology, and the last is energy consumption.

5 Smart Meter Network Design

Smart metering, if we see the particular evolution of the electrical metering graph shown in Fig. 4 here before the 1970s, this smart metering idea was zero, with no communication at all until almost 1995. So, basically, this is the time when users started using smart metering technology.

So, after 2000, the smart metering concept was increased and also this smart grid idea is not new which had its existence since last two decades. The 2025 target for smart metering can be achieved through an advanced smart metering facility in the smart grid environment as per above particular graph.

The block diagram shown in Fig. 5 illustrates working of smart meter. The smart meter must first recognize that the signal is either a voltage signal or a current signal, and then move to the next stage known as signal conditioning. It is important to

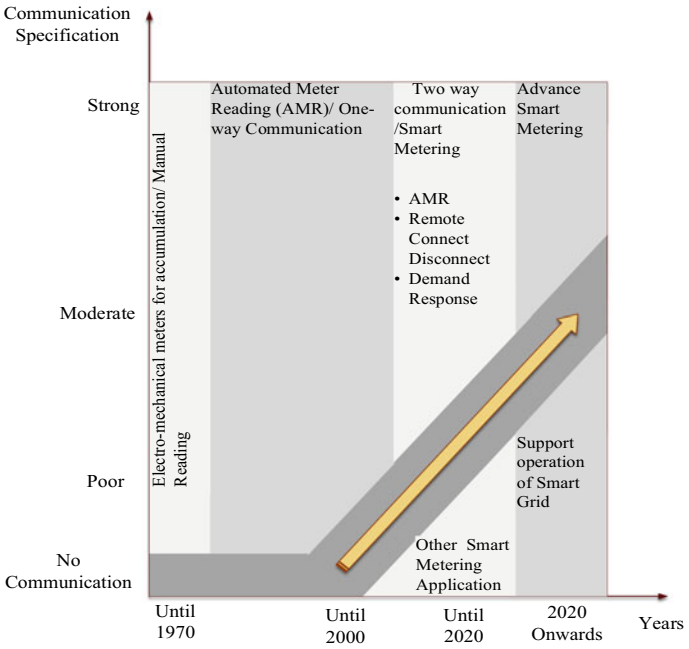

Fig. 4 Evolution of smart metering

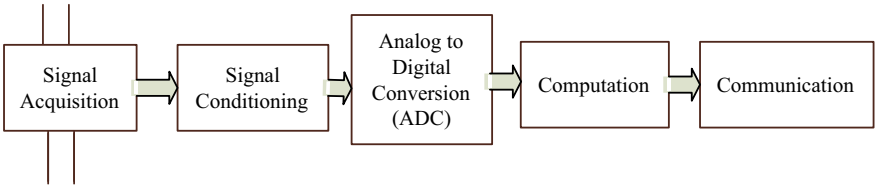

Fig. 5 Smart meter block diagram

control the signal because we must have to stabilize it. Since the signals in the power grid are not strictly sinusoidal, the fundamental frequency part of 50 Hz is not the only one. In this context, high-frequency components and harmonics must ultimately be eliminated. And we also often get aliases within the signal, because the aliasing effect often means that very high-frequency signal components will behave as a fundamental signal component. Consequently, those difficulties which are essentially present on the desired signals which are present within the basic frequency component of the voltage current should be eliminated. Only a simple 50 Hz voltage and a current signal should be allowed for the next block; this is the signal conditioning. An ADC may provide an independent measurement, e.g. an electronic device converting an analog voltage or current to a digital number equal to the voltage or current magnitude. And then it proceeds to the computing block

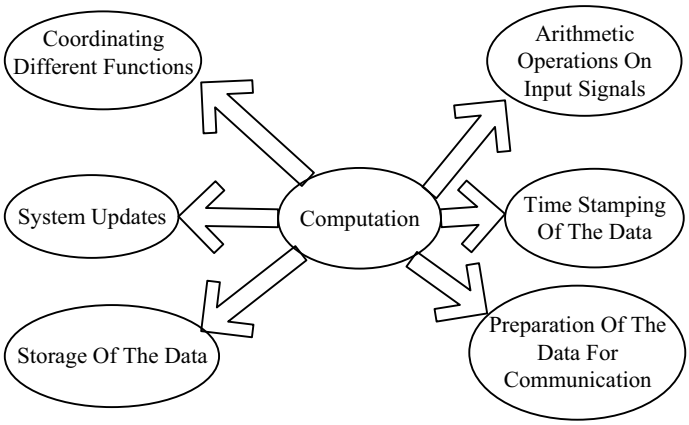

Fig. 6 Measurement using smart meter

where the calculation is done, and this is done essentially by the processor. And the processor helps to calculate whatever components or sub-components it needs from the signal voltage. It will then coordinate for further action.

The measurements that are carried out by smart metres are depicted in Fig. 6. The first is one basically an arithmetic operations of input signals and may be time stamping of the data, and it contains data for communication, storage of the data, updates system, and synchronization of various different functions.

6 Smart Meter Benefits

The introduction of smart metering will have wide range of benefits for the service utility, consumer, and community itself [15–18].

6.1 Benefits for the Consumers

- Customers gain detailed knowledge about their use of electricity. This will provide both customer and company with energy productivity improvements.
- Reduced power outages.
- Improved delivery efficiency awareness and more comprehensive energy use reviews. Bills are based on actual consumption. Pricing is based on current usage.
- The need to estimate the bill is minimized.
- Consumers may change their service behaviors to lower electric bills during peak hours.
- No need to offer permission to utilities for reviewing indoor meters.

- Movement and switching are fast.

6.2 Benefits for Utility Services

- Remote control allows better billing management and other customer issues.
- Remote and automated measurement reading.
- Reduced power outages.
- Existing resource income optimization.
- Reduced operating costs.
- Dynamic pricing enabled.
- Enable more effective use of electricity resources.
- Increased low voltage network information.
- Electrical systems are controlled faster.
- Release experienced staff to serve customers in other high key sectors.

6.3 Benefits for Environmental

- Smart meters minimize greenhouse gas emissions from installed power plants indirectly.
- Smart meters avoid need for new power stations by ensuring that current power consumption is adequately distributed, thus reducing emissions.
- Smart meters interact with the service provider directly, thereby removing the need to place trucks on the lane.

7 Barriers to Smart Metering

There are a variety of challenges to smart metering [15–20].

7.1 Electric Company Challenges

- Transition from old to modern technologies.
- Management of data metering security.
- Carefully handle the consumer to consider the latest technologies and procedure.
- Handle public response with formal introduction to the new meter.
- Dynamic programs and long-term projects.
- Optimizing smart meter rollout.
- More meter and infrastructure costs.

7.2 Challenges for Customers

- Verification of the precision of the data obtained and analyzed by new meter.
- Protection of your confidential data's privacy.
- Additional new meter fees.

7.3 Environmental Challenges

- Old meter destruction.

8 Functionalities of Smart Meters and Smart Metering

The providers might also hope to ensure the highest degree of smart metering functionality and ensure that current levels of technology are used in full by the legislation so that investments are not too quickly redundant [21]. For intelligent meters, the following main functionalities can be considered

- Load data profile
- Access to data metered for consumers and approved third parties on request
- Supply consistency
- Customer price indicator
- Choice of tariffs for variable time of use
- Management of remote meters
- Identification of power outage
- Reduction of remote demand
- Identification of power consumption over particular demand
- Remote login/disconnection
- Competitive pricing and response to demand
- Detection of manipulation and stealing! and rectification.

9 Smart Metering Security Problems

Smart measurement raises a range of security issues and potential security threats [22–28]. Some of these are mentioned here.

9.1 Eavesdropping

Eavesdropping helps the offender to actively listen to information exchanged between an intelligent meter (or an intelligent measuring gateway) and the providers. This attack aims at consumer privacy and can easily be carried out on a wireless communication channel or power line. It is very difficult to detect eavesdropping as it does not interfere with communication.

9.2 Denial of Service (DoS) Attacks

DoS attacks threaten the entire intelligent metering network, the smart grid or sections of the grid. DoS attack can be carried out by an opponent by sending instructions far more than planned to the intelligent metering access points or to the other end of the utility's server. This saturates the network such that it can no longer address the valid requests. The grid or parts of the grid are mostly shut down for essential services.

9.3 Packet Injection Attacks

This threat is initiated by inserting false packets into the system like false requests. The aims of these actions may be to cut the electricity of sections of the intelligent metering system by generating false bills which cause large financial problems or to compromise the billing mechanism.

9.4 Malware Injection Attacks

Malware injection into the system affects information exchange between grid devices and jeopardizes accounting and control process. The grid's demand/consumer status could be manipulated in order to destabilize the grid load.

9.5 Remote Connect/Disconnect Attacks

The smart grid remote connection/disconnection capability can be used to avoid the grid or its parts. This attempt of attack would isolate a large number of users from power, water, and gas supplies.

9.6 Firmware Manipulation Attacks

The configuration of a smart meter or measuring gateway could be manipulated to interrupt the meter's billing and payment system. This involves the management of the prepayment feature or reporting to the remote reader fake usage status. Firmware handling attacks can be rendered via physical access by modifying a smart meter or through the WAN when the gateway promotes remote firmware updates. These attacks usually impact a single person, but can also be massively launched.

9.7 Man-In-The-Middle Attacks

A man-in-the-center attack is a sort of action or attack that the attacker "inserts" himself in the center parties. An attacker connects with both parties, catches and transmits their messages to the other end, and makes everybody think they are talking to explicitly to each other else. The intruder thus has the right to passive elimination or alteration of details exchanged between the partners of communication.

10 Smart Metering Security Solutions

Various safety measures are used to counter security risks and threats on intelligent measurement devices. This involves a combination of security utilities, networks, embedded systems, operating systems, and intrusion detection and protection systems designed for general purposes [27–32].

10.1 Gateway-Based Approach

Gateway is a modern solution suggested by European nations such as Germany and the United Kingdom to smart metering. A gateway allows for secure communications between the intelligent meters and the smart grid. A gateway (or smart metering gateway) serves as a contact system between customers' metering devices and the utility. This gateway acts not just as a contact and control unit between the meters and the service provider, but also to protect the customer's privacy. One gateway is accountable for smart meters and other intelligent devices mounted in a house or building. The gateway interacts regularly with the utility servers via wide area network (WAN). The gateway also offers loading control instructions based on load in the intelligent grid. Therefore, it must be able to help various protocols and standards in communication including wireless MBUS, PLC, RS-485, MBUS, GSM, GPRS, PSTN, Zigbee, etc.

10.2 Encrypted Communication

Interaction should be encrypted between organizations in smart metering systems. Encrypted communication is typically obtained while using existing methods like Transport Layer Security (TLS). However, TLS is no longer considered safe, and therefore, other ways to maintain the security of correspondence need to be coupled with TLS. These involve encryption of the application layer in addition to TLS to boost the overall encrypted communication. An example is the BSI approach to protection profiles (PP) developed in Germany, usually recognized as the BSI PP. They suggest dual encryption and end-to-end encryption on the application layer and also on transport layer.

10.3 Systems for Intrusion Detection and Prevention

Smart metering system networks can be employed for intrusion Detection systems (IDS) and intrusion prevention systems (IPS). This helps to detect intrusions, detect rogue nodes or attacks, and remove these nodes from further network contact.

10.4 Verification of Authenticity

The authenticity of communications participants and the origin of data must be assured. Standard methods, such as digital signatures, may be employed toward this objective.

10.5 Integrity Protection

In order to assure the integrity of the communicated data, security protocols should be employed to facilitate integrity safety. This involves the use of message authentication codes (MAC) to maintain energy usage integrity.

11 Conclusion

Electricity meters in India were primarily electromechanical but are increasingly succeeded by more modern, reliable digital and electronic meters. A significant proportion of energy market share has been lost to power theft, inaccurate meter reading and billing, and customers' inability to pay electricity bills in due course.

In this paper, we analyzed and addressed the modern grid systems and smart metering features and functionalities of smart meters which are sustainably used by different utilities, the operational concepts of smart meters, advanced metering technology, and meter data management system metering. The paper also includes a list of possible security and privacy issues arising from the use of smart metering and possible protection solutions are explored.

References

1. Global Energy Review (2020) IEA 1. https://www.iea.org/reports/global-energy-review-2020)
2. Ali S (2013) Smart grids: opportunities, developments, and trends. Springer
3. Zheng J, Gao DW, Lin L (2013) Smart meters in smart grid: an overview. In: 2013 IEEE green technologies conference (GreenTech)
4. Standard 551-2006 recommended practice for calculating AC short-circuit currents in industrial and commercial power system. Institute of Electrical and Electronics Engineers (IEEE) (2006)
5. Öhrström M (2003) Fast fault detection for power distribution systems. PhD dissertation, El-ektrotekniska System
6. Grid applications stream: fault detection isolation and restoration monitoring and measurement report. Smart Grid Smart City Project (SGSCP) (2012)
7. Tram H (2008) Technical and operation considerations in using smart metering for outage management. In: 2008 IEEE/PES transmission and distribution conference and exposition
8. Markets R (2021) Global smart meters market outlook to 2025—smart electricity meters segment is expected to witness the highest growth. GlobeNewswire News Room. [Online]. Available: https://www.globenewswire.com. Accessed: 29 Jan 2021
9. Yang J, Zhao J, Luo F, Wen F, Dong ZY (2017) Decision-making for electricity retailers: a brief survey. IEEE Trans Smart Grid 9:4140–4153
10. Uribe-Pérez N, Hernández L, De la Vega D, Angulo I (2016) State of the art and trends review of smart metering in electricity grids. Appl Sci 6:68
11. Gao C, Redfern MA (2011) A review of voltage control in smart grid and smart metering technologies on distribution networks. In: 2011 46th international universities' power engineering conference (UPEC)
12. Arif A, Al-Hussain M, Al-Mutairi N, Al-Ammar E, Khan Y, Malik N (2013) Experimental study and design of smart energy meter for the smart grid. In: 2013 international renewable and sustainable energy conference (IRSEC)
13. Ekanayake JB, Jenkins N, Liyanage K, Wu J, Yokoyama A (2012) Smart grid: technology and applications. John Wiley & Sons
14. Živic NS, Ur-Rehman O, Ruland C (2015) Evolution of smart metering systems. In: 2015 23rd telecommunications forum telfor (TELFOR)
15. The European Smart Energy Solution. [Online]. Available: https://esmig.eu
16. Sharma K, Saini LM (2015) Performance analysis of smart metering for smart grid: an overview. Renew Sustain Energy Rev 49:720–735
17. Mohassel RR, Fung A, Mohammadi F, Raahemifar K (2014) A survey on advanced metering infrastructure. Int J Electr Power Energy Syst 63:473–484
18. Steklac I, Tram H (2005) How to maximize the benefits of AMR enterprise-wide. In: Rural electric power conference
19. Depuru SSSR, Wang L, Devabhaktuni V, Gudi N (2011) Smart meters for power grid—challenges, issues, advantages and status. In: 2011 IEEE/PES power systems conference and exposition
20. Cleveland FM (2008) Cyber security issues for advanced metering infrastructure (AMI). In: 2008 IEEE power and energy society general meeting-conversion and delivery of electrical energy in the 21st century

21. Qiao L, Liu X, Jiang B (2014) Design and implementation of the smart meter in vehicle-to-grid. In: 2011 4th international conference on electric utility deregulation and restructuring and power technologies (DRPT)
22. Barai GR, Krishnan S, Venkatesh B (2015) Smart metering and functionalities of smart meters in smart grid—a review. In: 2015 IEEE electrical power and energy conference (EPEC)
23. Kim S, Kwon EY, Kim M, Cheon JH, Ju S-h, Lim Y-h, Choi M-s (2011) A secure smart-metering protocol over power-line communication. IEEE Trans Power Delivery 26:2370–2379
24. Gungor VC, Sahin D, Kocak T, Ergut S, Buccella C, Cecati C, Hancke GP (2011) Smart grid technologies: communication technologies and standards. IEEE Trans Ind Inform 7:529–539
25. Stelte B, Rodosek GD (2013) Thwarting attacks on ZigBee-removal of the KillerBee stinger. In: Proceedings of the 9th international conference on network and service management (CNSM 2013)
26. Chen TM, Sanchez-Aarnoutse JC, Buford J (2011) Petri net modeling of cyber-physical attacks on smart grid. IEEE Trans Smart Grid 2:741–749
27. Vigo R, Yüksel E, Ramli CDPK (2012) Smart grid security a smart meter-centric perspective. In: 2012 20th telecommunications forum (TELFOR)
28. Marah R, El Gabassi I, Larioui S, Yatimi H (2020) Security of smart grid management of smart meter protection. In: 2020 1st international conference on innovative research in applied science, engineering and technology (IRASET)
29. Raciti M, Nadjm-Tehrani S (2013) Embedded cyber-physical anomaly detection in smart meters. In: Critical information infrastructures security. Springer, pp 34–45
30. Lo C-H, Ansari N (2013) CONSUMER: a novel hybrid intrusion detection system for distribution networks in smart grid. IEEE Trans Emerg Top Comput 1:33–44
31. Bohli JM, Sorge C, Ugus O (2010) A privacy model for smart metering. In: 2010 IEEE international conference on communications workshops
32. Rincón AER, Melo WS, de Farias CM, Carmo LFRC (2020) Securing smart meters through physical properties of their components. IEEE Trans Instrum Measure 70:1–11

Realization of Universal Filter Using CCII

Md. Shahbaz Alam, Amit Agrawal, Kulwant Singh, and Ashish Shrivastava

Abstract During the last couple of decades, the trends of current mode approach have followed in the modern applications of analog signal processing, where the electric current is used to represent the information signals. Current conveyors are among the main building block used in current mode circuits. In this chapter, a comparative study of the realization of Universal filters using the realizations of the second generation current conveyor in current as well as voltage modes are presented. As compared to the conventional operational amplifiers, the current conveyor circuit provides high frequency range of operation. Two circuit configurations, current mode having two CCII+ and voltage mode having three CCII+, have been chosen to design Universal filters (LPF, BPF, and HPF). A comparison has been done in respect of input range, bias voltage, and cutoff frequency. PSPICE results of time response and frequency response of all the circuits have been presented.

Keywords Current conveyor · Universal filter · Translinear CCII+

1 Introduction

In this paper, a comparative study of biquad realizations using different realizations of the second generation current conveyor is presented. As compared to the conventional operational amplifiers, the current conveyor circuit provides high frequency range of operation [1–3]. Two circuit configurations have been chosen. One of the

Md. S. Alam · A. Agrawal (✉)
ABES Engineering College, Ghaziabad, UP, India
e-mail: amit.agrawal@abes.ac.in

Md. S. Alam
e-mail: shahbaz.alam@abes.ac.in

K. Singh
Manipal University Jaipur, Rajasthan, India

A. Shrivastava
Skill Faculty of Engineering and Technology, Shri Vishwakarma Skill University Haryana, Gurugram, India

S. Dwivedi et al. (eds.), *Flexible Electronics for Electric Vehicles*, Lecture Notes in Electrical Engineering 863, https://doi.org/10.1007/978-981-19-0588-9_39

configurations belongs to the one input many output type filter category while the other configuration belongs to the many input and many output category. The first Universal filter circuit is having two CCII+ in current mode, and the second circuit is in voltage mode filter having three CCII+s. Both the filters have been simulated with all the realization of the current conveyors presented in below, and a comparison has been done in respect of input range, bias voltage, and cutoff frequency. PSPICE results of time response and frequency response of all the circuits have been presented. The simulation results of various active filters, low pass filter, band pass filter, and high pass filter, in current as well as voltage mode have given below.

2 Introduction to Current Conveyor (CCII)

Current conveyors are the most important building blocks in the field of analog signal processing in current mode as well as in voltage mode, but the current mode current conveyor circuits are widely used due to better performance and better results. In the most fundamental form, the CCII that is second generation of current conveyors are widely used. It is a four terminal device, these terminals are *x*, *y*, *z,* and ground. The *x* is an input terminal having low input impedance, *y* is also an input terminal having high input impedance, on the other hand *z* is an output terminal having high output impedance, and the fourth one grounded. It can perform many useful functions of analog signal processing when they are arranged in particular circuitry with other passive components [4–6]. In CCII, no current flows through terminal *Y*, in order to increase the flexibility of current conveyors. The ideal CCII appeared as an ideal transistor, with the perfect characteristics [1–3]. At the gate or base, no current flows through them, which is represented by terminal *Y*. The emitter or source voltage (appeared at terminal *X*) follows the voltage at terminal *Y*, as there was no base-emitter or gate-source voltage drop. There is infinite input impedance at gate or base (terminal *Y*); whereas, the emitter or source (*X*) has zero input impedance. The current that comes out of the emitter or source (terminal *X*) that reflects as a current in at the collector or drain (*Z*), but with an infinite output impedance (Fig. 1).

The CCII can be expressed as a matrix as shown in Fig. 2 (Table 1):

Fig. 1 Circuit symbol of CCII

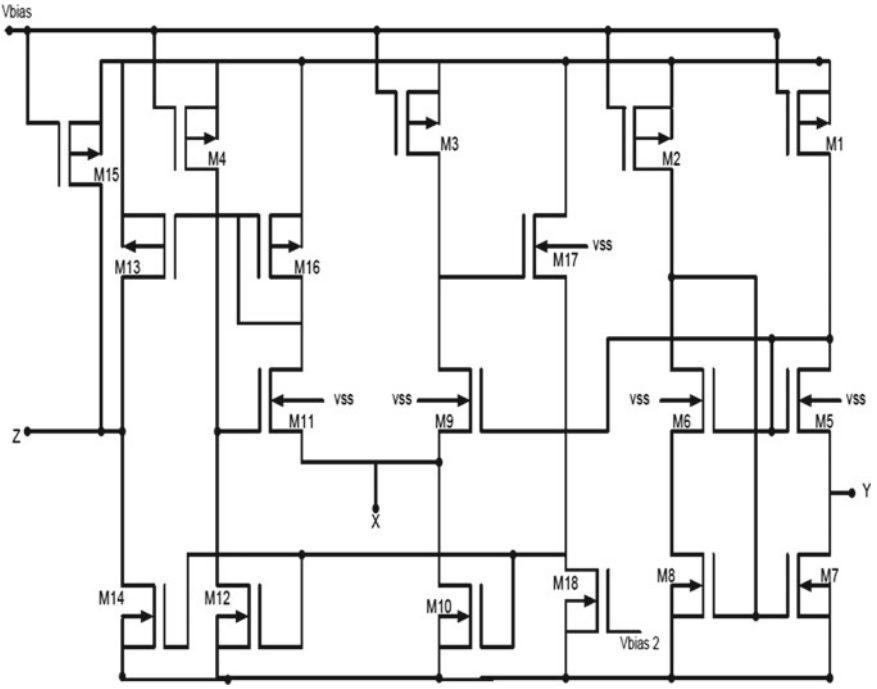

Fig. 2 CMOS realization of CCII

Table 1 Aspect ratio for the CCII+ in transistor mode

Transistors	W (um)	L (um)
All pMOS	100	0.5
All nMOS	50	0.5

$$\begin{bmatrix} I_Y \\ V_X \\ I_Z \end{bmatrix} = \begin{bmatrix} 0 & 0 & 0 \\ 1 & 0 & 0 \\ 0 & \pm 1 & 0 \end{bmatrix} \begin{bmatrix} V_Y \\ I_X \\ V_Z \end{bmatrix}$$

CCII+ that is shown in Fig. 2 uses 0.5 μm CMOS technology. When we apply the input at Y terminal, i.e., $V_{Y,}$ and then we check the voltage at X terminal, i.e., V_X, the relationship between X and Y is shown in Figs. 3, 4, 5, and 6.

3 Filter Designing Using CCII

In this paper, a comparative study of biquad realizations using different realizations of the second generation current conveyor is presented. The current conveyor circuit

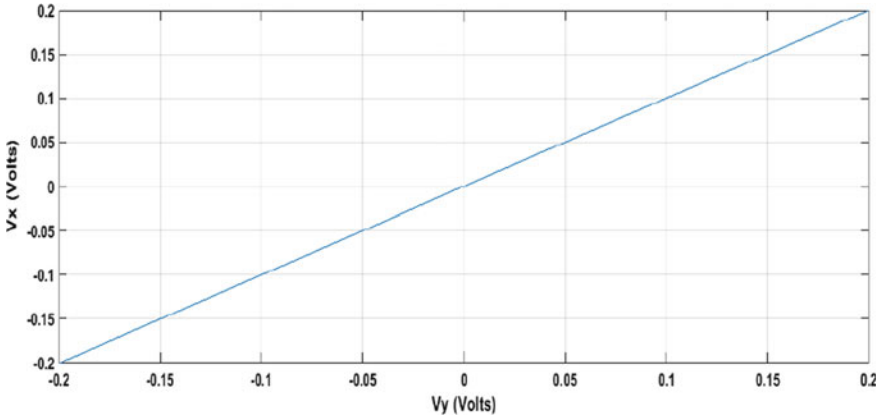

Fig. 3 Port relationship between V_X and V_Y when we applied input DC sweep at Y terminal

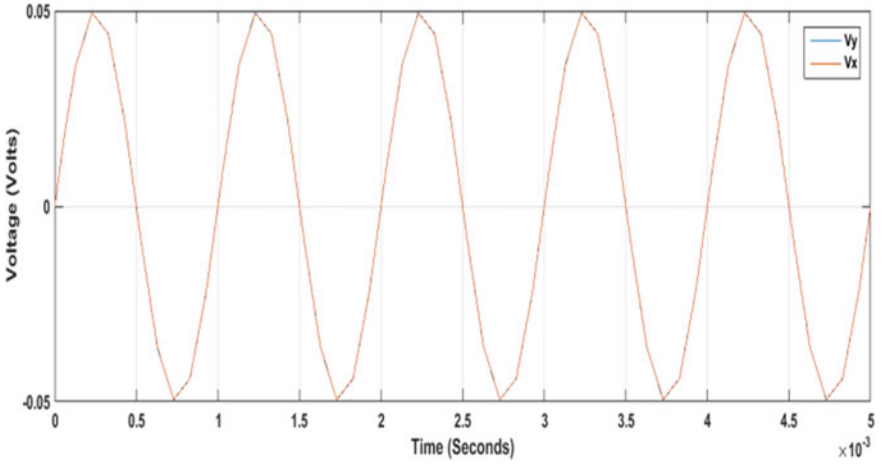

Fig. 4 Port relationship between V_X and V_Y when we applied sinusoidal input voltage at Y terminal

provides high frequency range of operation as compared to conventional operational amplifiers. Two circuit configurations have been chosen. One of the configurations belongs to the single input multiple output type filter category while the other configuration belongs to the multiple input and multiple output category. The first circuit is a current mode universal filter using two CCII+ and the second circuit is a voltage mode filter using three CCII+s. Both the filters have been simulated with the realization of the current conveyor presented above, and a comparison has been done in respect of input range, bias voltage, and cutoff frequency. PSPICE results of time response and frequency response of all the circuits have been presented.

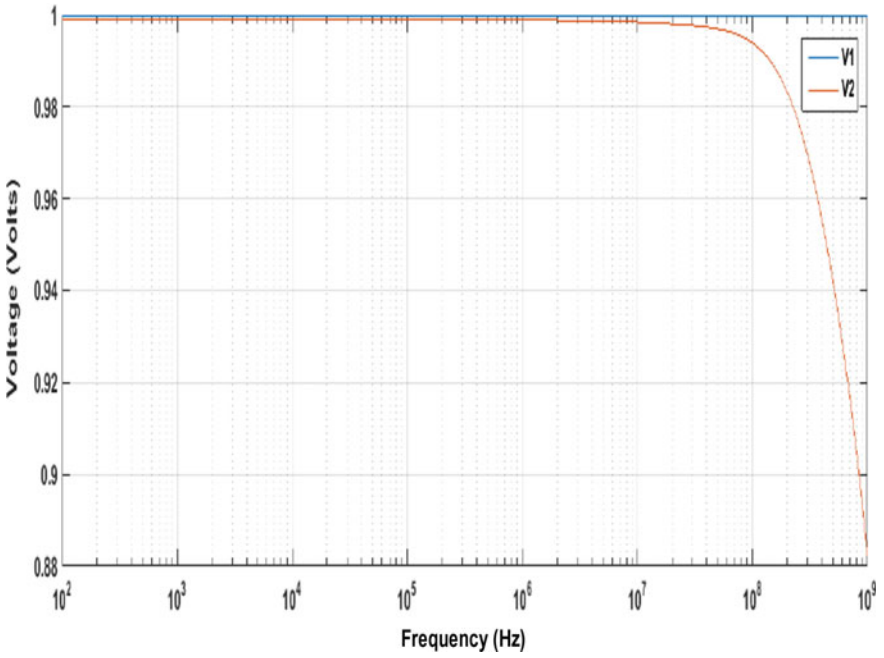

Fig. 5 Port relationship between V_X and V_Y when we applied AC input voltage at Y terminal

3.1 Current Mode Universal Filter

The Circuit shown in Fig. 7 represents the current mode Universal filter using two CCII+.

It may be noted that the three output currents are flowing through grounded elements and additional current followers will be required to drive the loads. The various transfer functions are as given below

$$T_1(s) = \frac{I_{\text{out1}}(s)}{I_{\text{in}}(s)} = -\frac{1}{R_1R_2C_1C_2s^2 + R_2C_2s + 1} \tag{1}$$

$$T_2(s) = \frac{I_{\text{out2}}(s)}{I_{\text{in}}(s)} = -\frac{R_2C_2s}{R_1R_2C_1C_2s^2 + R_2C_2s + 1} \tag{2}$$

$$T_3(s) = \frac{I_{\text{out3}}(s)}{I_{\text{in}}(s)} = \frac{R_1R_2C_1C_2s^2}{R_1R_2C_1C_2s^2 + R_2C_2s + 1} \tag{3}$$

The three transfer functions are, respectively, of low pass filter ($T_1(s)$), band pass filter ($T_2(s)$), and high pass filter ($T_3(s)$) with unity gain. The above universal filter is designed using translinear implementation of CCII+, CCII+ using flipped voltage follower, and CCII+ using AD844. Designed for $f_o = 50$ kHz and $Q = 0.707$, with

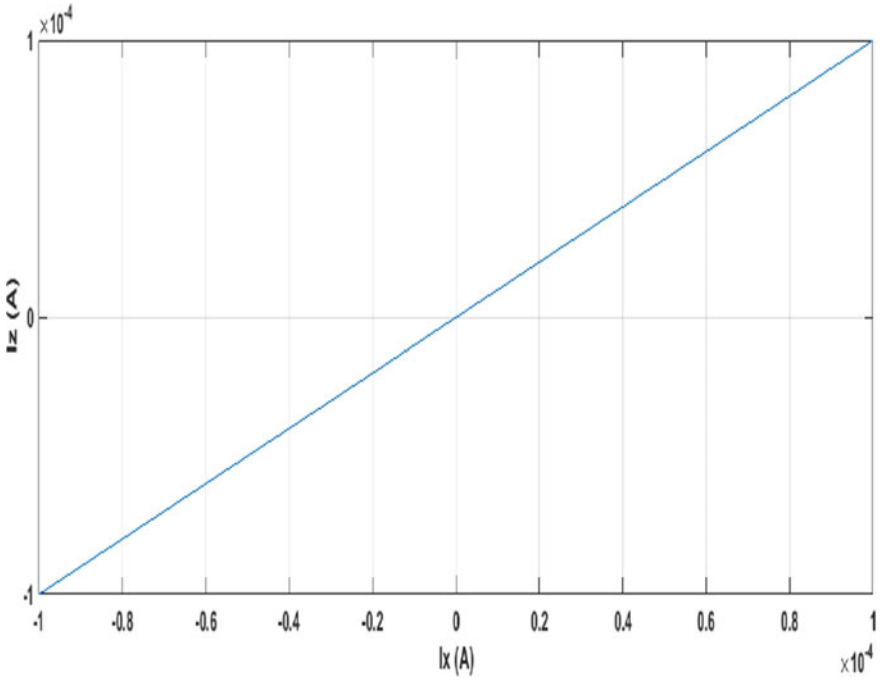

Fig. 6 Port relationship between I_X and I_Z when we applied input DC sweep at X terminal

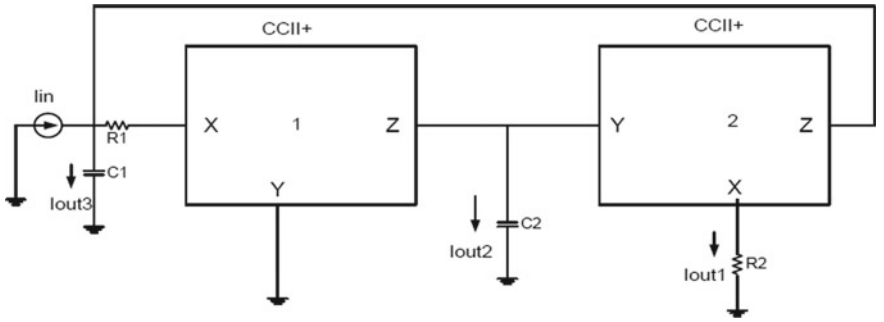

Fig. 7 Current mode universal filter

$R_1 = 10$ kΩ, $R_2 = 20$ kΩ, and $C_1 = C_2 = 0.225$ nF (Figs. 8, 9, 10, 11, 12, 13, 14, and 15).

From the responses, we have analyzed the highest frequency, lowest supply voltage, and lowest input current for low pass filter, band pass filter, and high pass filter. Table 2 summarizes these comparisons for the LP, BP, and HP filters.

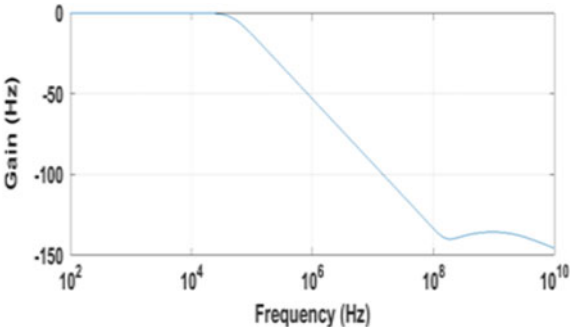

Fig. 8 Low pass filter response with a cutoff frequency of 46.43 kHz

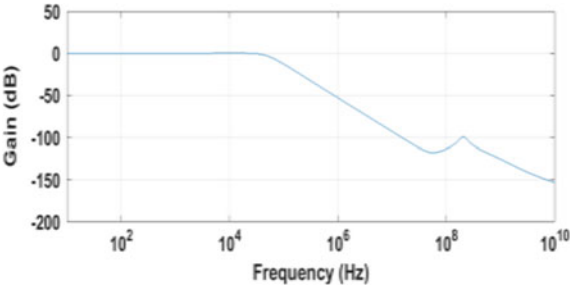

Fig. 9 LPF response with a cutoff frequency of 49 kHz

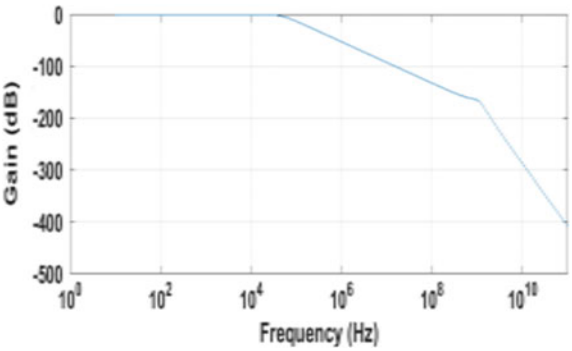

Fig. 10 LPF filter response using cutoff frequency 48.4 kHz

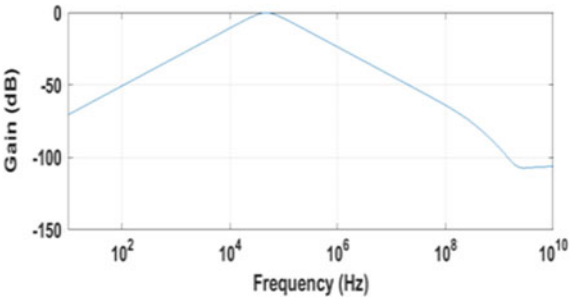

Fig. 11 BPF response using cutoff frequency 46.32 kHz

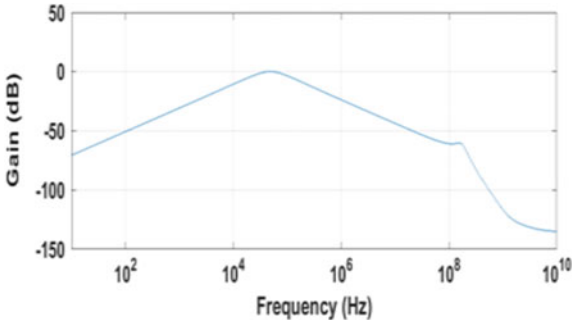

Fig. 12 BPF response with a cutoff frequency of 48.8 kHz

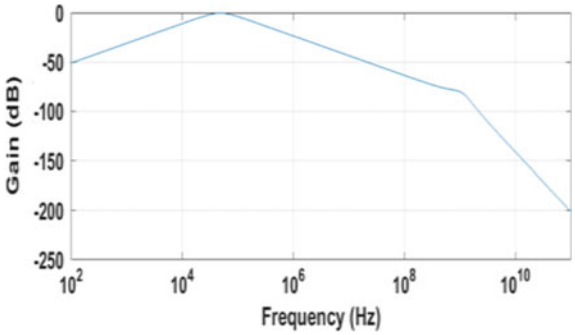

Fig. 13 BPF response with cutoff frequency 50.4 kHz

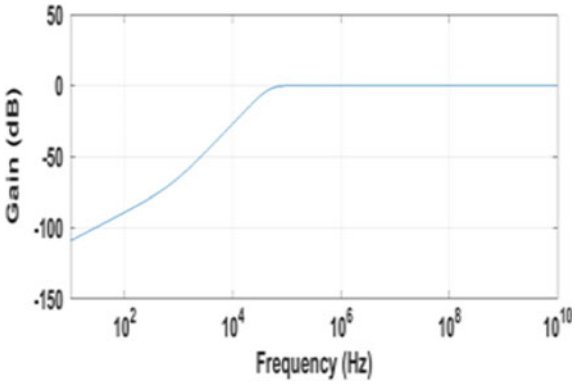

Fig. 14 HPF response with a cutoff frequency of 46.8 kHz

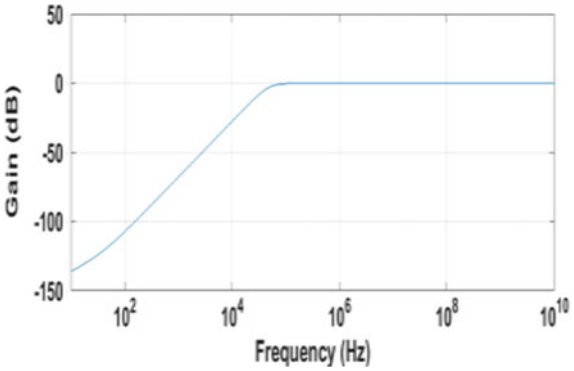

Fig. 15 HPF response with cutoff frequency 47.86 kHz

Table 2 Evaluation of current mode universal filter for LPF, BPF & HPF

Type of filter	Highest frequency (MHz)	Lowest supply voltage (V)	Lowest input current (μA)
LPF	20	±1.2	1
BPF	20	±1.2	0.2
HPF	20	±1.2	0.1

3.2 Voltage Mode Universal Filter

Figure 16 shows a multiple input single output type voltage mode multifunction voltage mode filter and employs three second generation current conveyor [6, 7].

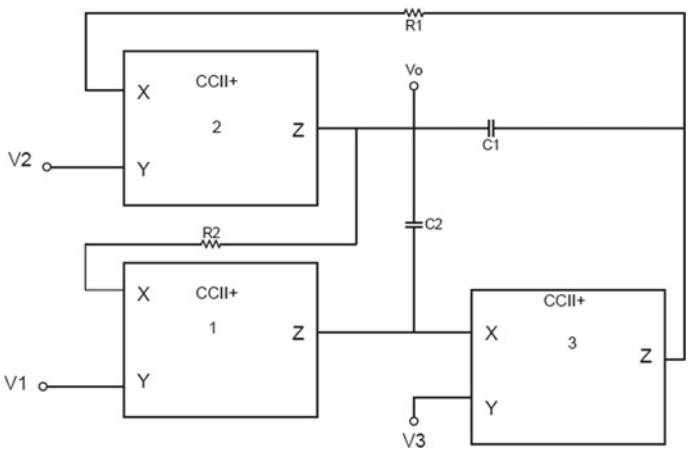

Fig. 16 Voltage mode universal filter

The output voltage V_o can be expressed as

$$V_o = \frac{s^2 C_1 C_2 V_3 + s C_1 G_1 V_2 + G_1 G_2 V_1}{s^2 C_1 C_2 + s C_1 G_1 + G_1 G_2} \tag{4}$$

From Eq. (4), we can see

If V_2 and V_3 are equal (grounded), then second-order LPF can be obtained with the transfer function of V_o/V_1.
If V_1 and V_3 are equal (grounded), then a second-order BPF can be obtained with the transfer function of V_o/V_2.
If V_1 and V_2 are equal (grounded), then a second-order HPF can be obtained with the transfer function of V_o/V_3.

Thus, the circuit is capable of realizing low pass, high pass, and band pass filter.

The transfer functions can realize low pass filter, band pass filter, and high pass filter with unity gain. The above multifunction filter is designed using translinear implementation of CCII+, designed for $f_o = 90$ kHz and $Q = 0.707$, with $R_1 = 20\ \text{k}\Omega$, $R_2 = 40\ \text{k}\Omega$, and $C_1 = C_2 = 0.0625$ nF (Figs. 17, 18, 19, 20, 21, and 22).

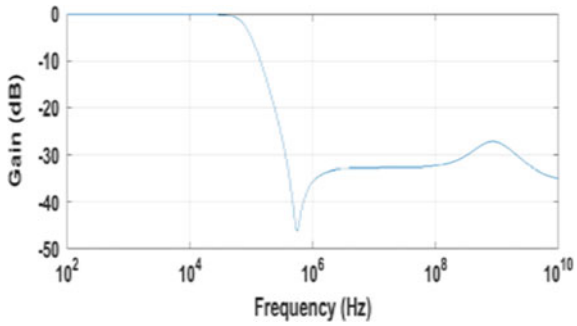

Fig. 17 LPF response with a cutoff frequency of 83.8 kHz

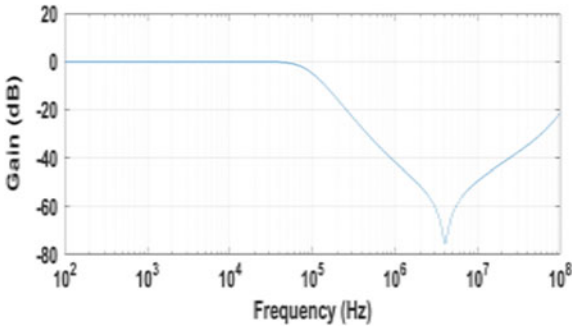

Fig. 18 LPF response with cutoff frequency 82.8 kHz

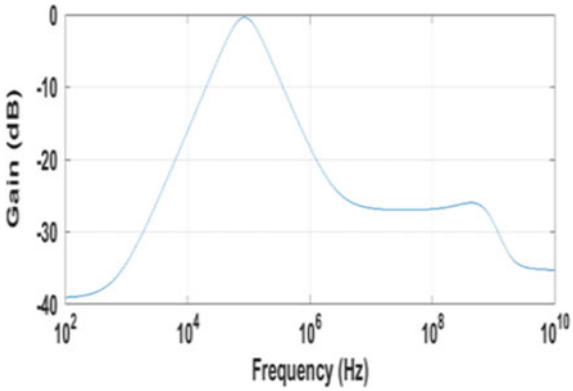

Fig. 19 BPF response with cutoff frequency 85.114 kHz

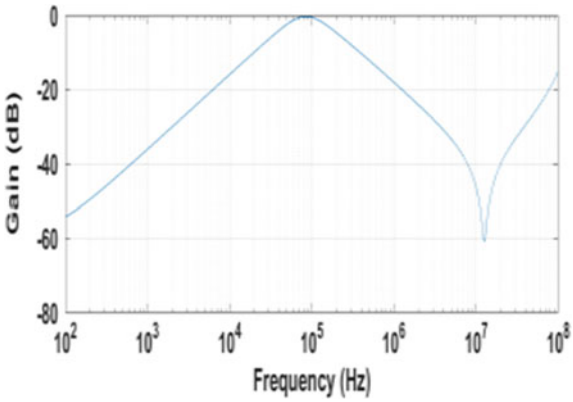

Fig. 20 BPF response with cutoff frequency 85.3 kHz

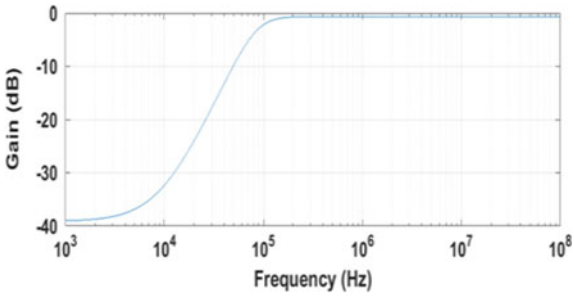

Fig. 21 HPF response with a cutoff frequency of 82.34 kHz

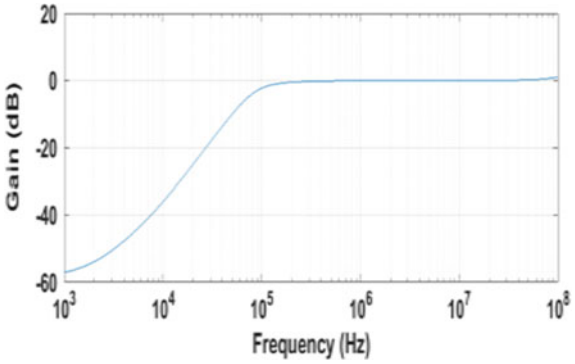

Fig. 22 HPF response with cutoff frequency of 89 kHz

Table 3 Evaluation of voltage mode universal filter for LPF, BPF & HPF

Type of filter	Highest frequency (MHz)	Lowest supply voltage (V)	Lowest input voltage (mV)
LPF	10	±0.5	10
BPF	10	±0.5	15
HPF	10	±0.5	10

From the responses, we have analyzed the highest frequency, lowest supply voltage, and lowest input voltage for low pass filter, band pass filter, and high pass filter, and the results are summarized (Table 3).

4 Conclusion

In this paper, we have carried out a comparative study of different realizations of one current mode and one voltage mode universal filter circuit in respect of input current/voltage range, cutoff frequency, bias voltages. We have used the implementations of the translinear loops and the bipolar current conveyor available in the form of second generation current conveyor (CCII). The cutoff frequency of LPF in current mode realization is lower than that of voltage mode. In current mode, lowest input current is for HPF and highest input current is for LPF, on the other hand, lowest input voltage in voltage mode is for LPF and HPF and highest input voltage is for BPF.

References

1. Eloranta P, Toumazou C (2013) Current conveyors history, theory and application. In: CC.PPT, Mar 2013
2. Sedra A, Smith KC (1970) A second-generation current conveyor and its applications. IEEE Trans Circuit Theory 17(1):132–134
3. Sedra AS, Roberts GW, Gohh F (1990) The current conveyor: history, progress and new results. IEE Proc 137(Pt. G, No. 2):78–87
4. Aseem J, Padaliya J, Savani V (2012) Analysis and characterization of different voltage follower topologies in 90 nm technology. Int J Emerg Technol Adv Eng **2**(12):229–235
5. Saied AB, Masmoudi DS, Salem SB (2013) High frequency CCII based proposed all-pass filter and quadrature oscillator. Int J Sci Adv Technol 3(3):30–34
6. Horng J-W, Wang Z-R, Liu C-C (2011) Voltage-mode low pass, band pass and notch filters using three plus-type CCIIs. Circuits Syst 2:34–37
7. Tonk A, Afzal N (2019) A new low-voltage universal filter realization using bulk-driven second-generation current conveyors. Aust J Electr Electron Eng 16(4)

A Literature Survey on Automated Microgrid

Anu Prakash and Ashish Shrivastava

Abstract In today's fast growing world, meeting energy requirement and its distribution is the most challenging task in rural areas. Due to less reliability and stability of non-renewable sources of energy, controlling, regulating, and distribution of generated energy are most important. The present grid in spite of being smart is unable to fulfill these requirements. So we require microgrid for rural area. Several microgrid which exist use SCADA, power converter for distribution and regulation control, but they are still facing lots of challenges. This paper shows the literature survey on issues and opportunities from the load side in microgrid which helps the researcher to identify the problem for future advancement of microgrid.

Keywords Microgrid · Supply generating unit · SCADA · Controllers · Energies storing system

1 Introduction

When demand increases, more supply is needed. In the case of electricity also, traditional ways of generating electricity are not able to fulfill the demands. It means an evolution is required in whole supply system [1–3]. A big area (rural) can be converted in a no. of regions with centrally connected distributing units that distribute energy to its own region and rest of the unused energy is supplied to other regions. Microgrid is the most suitable form to fulfill electricity demands in rural areas also. Evolutions of conventional power system that can generate, deliver, and monitor

Ashish Shrivastava: Senior Member, IEEE

A. Prakash
Department of Electrical Engineering, Manipal University Jaipur, Jaipur, Rajasthan, India
e-mail: anu.202303041@muj.manipal.edu

A. Shrivastava (✉)
Skill Faculty of Engineering and Technology, Shri Vishwakarma Skill University Haryana, Gurugram, India
e-mail: rewa.ashish@gmail.com

S. Dwivedi et al. (eds.), *Flexible Electronics for Electric Vehicles*, Lecture Notes in Electrical Engineering 863, https://doi.org/10.1007/978-981-19-0588-9_40

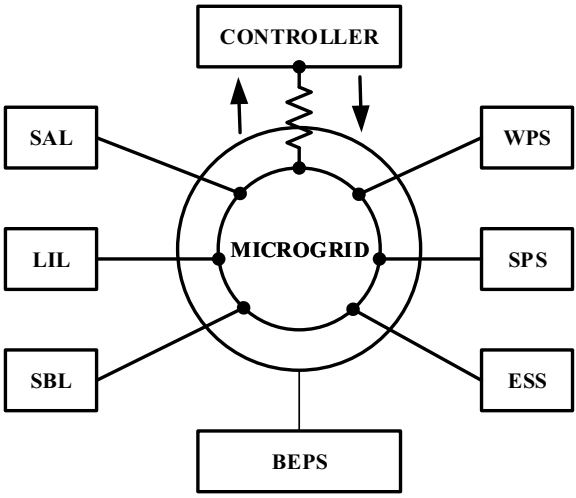

Fig. 1 Concept of microgrid. WPS: wind power station; SPS: solar power station; ESS: energies storing system; BEPS: bioenergy power station; SBL: smart building loads; LIL: local industry loads; SAL: smart area loads

supply for a local region by using non-renewable resources are known as microgrid [2, 3] or a group of supply generating units and loads which shares same distribution networks within same defined electrical boundaries and behaves like a solo controlled unit for power system is known as microgrid. It is a small scaled grid which may be connected with main grid or without grid. It has number of supply generating units (SGUs) which are parallelly connected with a small scaled distribution network that can deliver power to local's demands. It may be ON grid (grid connected), OFF grid, or in hybrid mode. In microgrid, there is no. of supply generating units (SGU) such as solar, diesel, wind, biogas, hydro, etc., which generates energy (SGU) but delivering to loads is based on priority basis. Priority means availability of generating sources. As shown in Fig. 1, all supplies is controlled by microgrid. Supply to loads and loads to supply should must be bidirectional for reducing losses and increasing unused supply.

In today's fast growing world due to reasons such as depletion of natural energy sources, climate change along with a requirement to satisfy both social and economic needs of growing nations, controlling of the use of non-renewable resources is most important. Microgrid can play key role for increasing the uses of renewable energy resources such as solar, wind, biogas, etc. [4].

According to the power transmission and distribution system, there are two types of grids in power system:

a. Conventional grid
b. Microgrid

   (i) Grid connected
   (ii) Islanded—AC and DC.

The consumption of renewable energy resources such as wind and solar energy was done worldwide until year 2009 but because of the reasons of less reliability

and stability of their power generation and load demand, power electronic converters (PEC) and grid systems came into role and it became a good and useful alternative to non-renewable energy resources (NERs) [5]. These PEC and grid system framed the concept of controlling the distributed renewable energy resources by small-scale generating stations which are capable of regulating the generating supply in its area with use of its own control units came into role known as microgrids. Here the methodology of microgrid came into role where it integrates the NERs into distributing system.

There are four major parts in microgrids:

A. SGUs: All types of renewable energies generating systems which generate in different manners but store energies in DC form.
B. Controllers/SCADA: Heart of the automated microgrid having lots of sensors that stores all purposeful data and control supply. It controls all functions of microgrid by using wireless or wired communication protocols [6, 7].
C. Inverters: It converts DC supply in consumption's required form, i.e., AC and takes care of frequency deviations of AC supply [8].
D. Consumptions: The most important part that consume powers.

It means when supply is generated by any types of SGUs, it is directly collected on grid then, microgrid controls these energies according to their types and capacities of generation [8, 9].

For better understanding of the present energy distribution systems, the usage and evolution of microgrids with time to make distribution systems are more effective, and various studies are being done. Various literatures on components, controls, assessments are being written nowadays to find how these microgrids can be best utilized in most effective and efficient ways [4, 5]. Researches are being made to understand adaptive and intelligent control methods to achieve more reliability and stability in microgrid systems. Even government policies are made for microgrid implementation keeping in mind the economic perspective. In spite of all this, there is still not any particular definition, any particular set of advantages or opportunities that can be clearly said for role of microgrid that it plays in the distributing system.

Now continuing particularly with microgrids below, we will be having a review of development of power systems till now and further futuristic approach of researchers on this topic of microgrid.

The microgrid system which is fully fleshed with distributed power generating modules (storage capacity, diagnose loads and supply, and control and monitor demands) is interfaced with non-renewable sources of energy [9]. Microgrid has to operate in both OFF grid and ON grid connected mode with varying load demand so it has energy backup elements. SGU modules are critical and need to have flexible features to work at any load demand. For this purpose, a converter is used in microgrid which can operates in four modes: voltage-controlled source (VCS), current-controlled source (CCS), active rectifier (AR), and active power filter (APF). The purpose of converter is to convert supply energy to in the form of demand's energy and deliver supply to its own region's loads through microgrid scenario [8–10].

- AR mode is mandatory for correction of power factor due to converting DC supply to AC supply or AC supply to DC supply, and for storing generated charges from SGUs. DC supply should be controlled for safety of storing units.
- APF mode is mandatory for harmonics reduction. It produces an AC supply current harmonics for vanishing demand current harmonics frequency. So that it reduces losses on demand side so utilization of energy is increased.
- In VCS mode, power quality of supply is improved and can deliver to loads as per requirement. Voltage and frequency both are improved in this mode by numerous parallel connections of SGUs. Due to this parallel network, microgrid can fulfill high demand with high-power quality and improved frequency [8].

2 Benefits and Challenges

The pros and cons of microgrid having parallel connection of SGUs:

- Reliable and stable supply through renewable resources
- Moderate transmission losses like traditional power system
- Reduce complex network with lower no. of feeders
- Integration of RESs and improve belief in renewable supply sources.

Challenges of implementing of SGUs in microgrid as a distribution system network:

- SGUs are altered power quality
- Quality of generated supply as per demands requirement
- Frequency within appropriate range of demands
- Unpredictable loads/demands
- Energy storing units for uncertainties
- Limited time availability of SGUs
- Bidirectional controller, i.e., supplies to loads and unused energy on load side come back on microgrid for others use.

Challenges of implementing of SCADA in microgrid [6, 7]:

- Converter which convert AC to DC or vice-versa
- Complex electrical network
- Tagging
- Alarming for every uncertainties
- Selection of SGU for delivering supply to loads as per its availability
- Check matching power quality as per requirement of demands
- Control of SGUs which are in remote area
- Energy theft control
- Loads and supply data storing for future study
- Control of storing units
- Supervise unpredictable loads
- Supervise weather and select SGUs for requirements of demands

- Uninterrupted supply to loads/demands
- Connection between two or more microgrid for fulfills the demands to each other
- At the time of uncertainty, selection of other microgrid for help
- Data acquire from no. of microgrids and compare them in hourly basis.

Control System in Microgrid According to Literature Survey

India is very poor in use of renewable energy. The achieved target was 175 GW in 2019 and now 227 GW in 2022 [11].

Computational techniques are doing more improvement in this era. Nowadays, data driven technologies are widely used in several field for appropriate regulation and control. Nowadays, in microgrid, for low cost supervisory and improvement in control, these computational techniques are being used [12]. Usually, control units are connected in center in grid connected or islanded microgrid. The main purposes of this control unit are:

- To monitor power quality, voltage regulation, and frequency in AC microgrid
- To manage utilization of microgrid
- To connect electrical protection circuitry to microgrid
- To detect faults and disturbances at both sides
- To make flexible—plugging and shutting of SGUs
- To make simple connection between SGU and grid for transmission of energies with low losses
- To make flexible to switch any load or SGU from one microgrid to another [13–15].

Protection Issues in Microgrids

Consumers need uninterrupted power supply so that protection system plays a vital role in distribution system. For long life of converters or control system, protection system also plays a vital role in transmission system. When microgrid automatically switches ON grid to OFF grid, there is a big challenge for protection system. In islanded mode microgrid, a leakage current (faulty current) flows in circuit so fault cannot be identified by normal protection circuits. In grid connected microgrid, relay's tripping time is very high. To design smart protection system, it needs implementation of computational techniques for microgrid. AI-based relays play a vital role for overcurrent protection [16, 17].

3 Progression of Microgrid According to Its Uses

Microgrid has no. of SGUs and lots of loads. So for fulfilling demand–supply mechanism, flexibility must be introduced here. Flexibility in selection of SGU, flexibility in selection of demand for fulfilling limited supply, or flexibility in uncertainties, every time life of demand and SGU, both should be taken into account. It means

optimum consumption of SGUs and optimal utilization of storing units are an objective for long lived microgrid. For this purpose, SCADA is the best way to supervise SGUs as well as storing units.

Basically, SCADA controls a microgrid in three manners:

A. Primary control that controls from consumption's side. It means control of voltage, frequency, and active and reactive parts of power. So, it works on stability of microgrid.
B. Secondary control that controls power quality and exhaustion of ESSs when power is supplied by two or more SGUs to a single load. It means controlling of ratio of contribution of SGUs at the time of supply.
C. Tertiary control that control optimization problems of SGUs. It also control scheduling of utilization of SGUs. It controls all alarms and resolves all faults [14, 18].

There are lots of control methods used for losses and power quality control [8, 12, 13]:

(i) Integral Linear Quadratic Gaussian (ILQG) Controller

The main purpose of implementation of the ILQG controller in microgrid distribution network is for tracking the power quality and frequency performance of microgrid as a distribution network. Bandwidth of ILQG controller is larger than other controllers and due to high phase and gain margin microgrid distribution network could become more stable than others.

(ii) Proportional Integral Derivative (PID) Controller

PID controller is used for same type loads configurations or fixed loads type local region like an industry. The algorithm of PID controller is simple and easily implemented due to low order transfer matrices that is easy to design and simple.

(iii) Model Predictive Controller (MPC)

The main purpose of MPC used in microgrid is its ability to control single phase voltage of AC microgrid. Tracking error in the process industry could be minimized by using this controller. Due to dynamic modeling of process, MPC is less effective by harmonics.

(iv) Damping Controller (DC)

The main advantage of damping controller in microgrid is to control supply to grid in negative and imaginary approach. So it is widely used in AC microgrid single phase as well as three-phase supply [19].

Table 1 gives the key points and limitations of different types of controller.

Table 1 Comparison between controllers

Name of the controller	Key points	Limitations
ILQG	• High bandwidth • Highly stable due to large gain and phase margin	Leakage current through parasitic capacitor
PID	• Simple and general algorithm • Simple circuits for implementation • Flexible	Low bandwidth Limited loads qualities and quantities
MPC	• Easily controllable • Low harmonics • Less losses in single phase supply	Less flexible in terms of supply and loads High maintenance cost Costly
DC	• Easily implementation in hybrid grid • Applicable for single and three-phase supply	Very costly Small adaptive power range

4 Future Trends in Microgrids

With the current government policies, renewable energy is still expensive when supplied to grid. Government must come up with new policies for integration of renewable energy sources so that microgrid needs to implement with these rules for delivering supply to demand more efficiently [20].

Considerable research is going on and a few issues with power sharing and inner control have been fixed. Future work is likely to be done on limitation of leakage current in transformer less inverter by using no. of controlling method and topologies.

More research on protection from cyber threats; with increase of cyber hackers and ransomware on rise, this is a much needed line of research [17].

Improved power quality and frequency along with better inertia is also in trend in developing automated microgrid [21].

For reliable and stable power supply system without grid connected is concerned in microgrid. Types of controlling techniques should be improved with wide area covering [22].

A new algorithm should be developed for smart energy storage management.

Comparison among different techniques with smart scheduling of load and supply should give a unique solution which is highly reliable and robust.

5 Conclusion

This paper deals with basic knowledge on automated microgrid having research concerning benefits and challenges. For planning a fully automated microgrid, energy storing management with load forecasting and SGUs scheduling must be driven by

computational techniques. Since a general approach to microgrid planning has been developed, economic feasibility has been taken into account along the paper as a key factor. This survey of mathematical methods applied to microgrid planning can be useful for microgrid planners, or even to introduce power system engineers and young researchers in this field. After this review, some conclusions will be presented.

Basically, the performance of microgrid totally depends on converters. An inverter plays a vital role for improving power quality and frequency in microgrid that delivers to loads. So limitation of losses in inverter should be primary job for better performance of microgrid [23]. In automated microgrid, a transformer less inverter is used.

This paper shows the main objectives of microgrid. The advantages and challenges of microgrid are presented in this paper. In microgrid having SCADA, which types of challenges are seen in supply to distribution network is also written in this paper. Types of controller, its advantages, and limitations will help scholars for buildup of basic knowledge about microgrid.

References

1. Shuai Z, Sun Y, Shen ZJ, Tian W, Tu C, Li Y, Yin X. Microgrid stability: classification and a review. Renew Sustain Energy
2. Shuai Z, Huang W, Shen X, Li Y, Zhang X, Shen J (2018) A maximum power loading factor (MPLF) control strategy for distributed secondary frequency regulation of islanded microgrid. IEEE Trans Power Electron
3. Elsisi M (2019) New design of adaptive model predictive control for energy conversion system with wind torque effect. J Clean Prod 240
4. Hossain MA, Pota HR, Hossain MJ, Haruni AMO (2018) Active power management in a low-voltage islanded microgrid. Int J Electr Power Energy Syst
5. Palma-Behnke R, Ortiz D, Reyes L, Jiménez-Estévez G, Garrido N (2011) A social SCADA approach for a renewable based microgrid—the Huatacondo project. In: Proceedings of the IEEE power and energy society general meeting, Detroit, MI, 24–28 July 2011, p 7
6. Cai L, Erlich I (2003) Coordination between transient and damping controller for series facts devices using ANFIS technology. IFAC Proc Vol 36(20):293–298
7. Awad NH, Ali MZ, Mallipeddi R, Suganthan PN (2019) An efficient differential evolution algorithm for stochastic OPF based active–reactive power dispatch problem considering renewable generators. Appl Soft Comput J 76:445–458
8. Hossain MA, Pota HR, Issa W, Hossain MJ (2017) Overview of AC microgrid controls with inverter interfaced generations. Energies 10(9)
9. Martinot E et al. (2018) Renewables 2018: global status report. Worldwatch Institute, Washington, DC
10. Chen YN, Pei W (2013) Design and implementation of SCADA system for micro-grid. Inf Technol J 12:8049–8057
11. Arunan A, Ravishankar J, Ambikairajah E (2018) Real-time disturbance detection in LV islanded microgrid. In: International conference on harmonics and quality of power (ICHQP), Ljubljana, Slovenia, May 2018
12. Xu Z, Yang P, Zheng C, Zhang Y, Peng J, Zeng Z. Analysis on the organization and development of multi-microgrids. Renew Sustain Energy
13. Mahmoud MS, Alyazidi NM, Abouheaf MI. Adaptive intelligent techniques for microgrid control systems: a survey. Int J Electr Power Energy Syst

14. Martin-Martínez F, Sanchez-Miralles A, Rivier M. A literature review of microgrids: a functional layer based classification. Renew Sustain Energy
15. Planas E, Andreu J, Garate JI, de Alegra IM, Ibarra E. AC and DC technology in microgrids: a review. Renew Sustain Energy
16. CIRED (1999) Dispersed generation. In: Preliminary report of CIRED (international conference on electricity distribution), working group WG04, Brussels
17. Kakran S, Chanana S. Smart operations of smart grids integrated with distributed generation: a review. Renew Sustain Energy
18. Short TA (2014) Electric power distribution handbook. CRC Press
19. Longe OM, Ouahada K, Rimer S, Ferreira HC, Han Vinck A. Distributed optimisation algorithm for demand side management in a grid-connected smart microgrid. Sustainability
20. Jenkins N, Ron A, Peter C, Daniel K, Goran S (2000) Embedded generation, no. 31. IET
21. Adib R, Murdock H, Appavou F, Brown A, Epp B, Leidreiter A, Lins C, Murdock H, Musolino E, Petrichenko K et al (2015) Renewables 2016 global status report
22. Ali JSM, Krishnaswamy V. An assessment of recent multilevel inverter topologies with reduced power electronics components for renewable applications. Renew Sustain Energy
23. Milis K, Peremans H, Van Passel S. The impact of policy on microgrid economics: a review. Renew Sustain Energy

On-Grid Solar Photovoltaic Power Plant Analysis Under PVsyst Simulation Software Platform

Mahipal Bukya, Pancham Kumar, and Rajesh Kumar

Abstract Rajasthan is an enriched solar radiation state with on an average radiation intensity of 6–7 kWh/m^2/day along with more than 300 sunny days per annum. PVsyst simulation software platform is used to design 15.6 kW grid, integrated solar photovoltaic (PV) power plant at Rajasthan district at 25° of latitude. During the investigation, the average global horizontal irradiation and PV plant performance ratio was found to be 5.02 kWh/m^2/day and 74.80%, respectively. In our study, we take all power losses such as irradiation, soiling, temperature, wiring, inverter, power electronics, interconnections, and grid availability into account. The array nominal energy at standard test condition was 29,616 kWh, but after considering all above-mentioned losses in to account only 23,451 kWh of energy is injected into grid, and rest 6165 kWh are lost. This 23,451 kWh grid-injected energy generated by solar PV plant is in clean form and saves the consumer 23,451 units of electricity bill.

Keywords Photovoltaic · Power · PVsyst · Performance ratio · Power loss

1 Introduction

The energy demand in the globe for various developmental activities has increased almost in all the fields. As fossil fuels are deploying day by day due to their limited viability, the time has come to leverage renewable energy sources such as solar, wind, biomass, and small hydropower to address the energy crisis. Various nations have installed solar photovoltaic projects and continuously working to boost the capacity of solar photovoltaic installations to produce electricity and fulfill their

M. Bukya (✉)
Department of Electrical Engineering, Manipal University Jaipur, Jaipur, India
e-mail: mahipalbhukya@gmail.com

P. Kumar
Department of Electrical Engineering, BSDU, Jaipur, Jaipur, India

R. Kumar
Department of Electrical Engineering Jaipur, MNIT Jaipur, Jaipur, India

S. Dwivedi et al. (eds.), *Flexible Electronics for Electric Vehicles*, Lecture Notes in Electrical Engineering 863, https://doi.org/10.1007/978-981-19-0588-9_41

energy requirements, thereby exceeding the total installed capacity in the globe at 583.5 GW.

India receives a very large amount of solar irradiance almost across the year due to its favorable geographical condition. Hence, our nation having enormous potential to produce solar radiated electricity and fulfill the balance energy demand. In India, most areas receive solar irradiance of approximately 4.7 kWh/m^2/day and its land mass is expected to receive approximately 5000 trillion kWh of solar energy per annum [1, 2]. As the PV modules cost decaying day by day and enrich to the hands of common people worldwide, the PV system is expected to become one of the major sources of electricity in the future [3–6]. Most specifically, the simulation system is used for performance analysis as well as a feasibility test of a grid-connected PV generation network.

The current paper measures the grid-connected PV system output over the PVSyst designing software platform. The grid-connected peak plant capacity is 15.4 kWp and the solar photovoltaic plant network consisting of 48 numbers of solar photovoltaic modules, in which 16 modules form a series string and these strings are connected three times in parallel.

2 Methodology

In this work, the performance of a grid-connected PV system with 15.4 kWp was studied using PVSyst simulation software. The plant consisting the modules is free of any shading effects and are fixed at an azimuth angle of 0° with an inclination angle of 25° facing south. The peak output power produced by a single polycrystalline Panasonic makes module is 320 Wp and their various output parameters are tested at standard test condition as mentioned in data sheet Table 1. Three-phase string inverter with 15 kW capacity of "Eversol TLC Solar" make Inverter is used for grid synchronization and their detail specifications are mentioned in Table 2. The grid-connected PV system is ground mounted and covers an area of 93.1 m^2.

All technical data was obtained at standard test condition.

Air mass = 1.5 AM, incoming solar radiation = 1000 W/m^2, and cell temperature (T_c) = 25 °C.

3 Results Analysis

Annual solar radiation data falling on plant site are as shown in Fig. 1.

The projected results of this grid-connected PV system as simulated by PVSyst show that maximum power production is in the month of March, while the minimum is in the month of August (Table 3).

Table 1 320 W Panasonic solar module datasheet

Model number	AE7P320VB4B
Rated maximum power (P_{max})	320 W
Output tolerance	0/+5%
Current at P_{max} (I_{mp})	8.63 A
Voltage at P_{max} (V_{mp})	37.1 V
Short-circuit current (I_{sc})	9.14 A
Open-circuit voltage (V_{oc})	45.6 V
Nominal operating cell temp. (T_{NOCT})	45 °C ± 2 °C
Weight	25.8 kg
Dimension	1956 mm × 992 mm × 40 mm
Maximum system voltage	1000 V
Maximum series fuse rating	20 A
Cell technology	Multi-Si
Application Class A	

Table 2 Eversol TLC solar on-grid inverter

Features of 15 kW Eversol TLC solar inverters
Efficiency 98.3%
Max. input voltage 1000 V
Graphical display
Multiple maximum powerpoint tracking
IP65 protection class
RS485 and Modbus RTU communications
Grid management functions via ZeverCom, ZeverCom WiFi, or ZeverManager
Easy handling for installation and maintenance

In the month of March (2347 kWh), the maximum energy is injected into the grid, while in August a minimum of 1600 kWh is injected. The average horizontal global radiation was 1836 kWh/m^2.

The global incident energy was estimated to be 2041 kWh/m^2 on collector aircraft. It was found that the total annual output energy from the array is 24,632 kWh, while the total energy pumped into the grid is 23,451 kWh. The system's average forecast performance ratio was found to be 74.80%. Figure 2 indicates total loss summary over a year and Fig. 3 indicates performance ratio diagram.

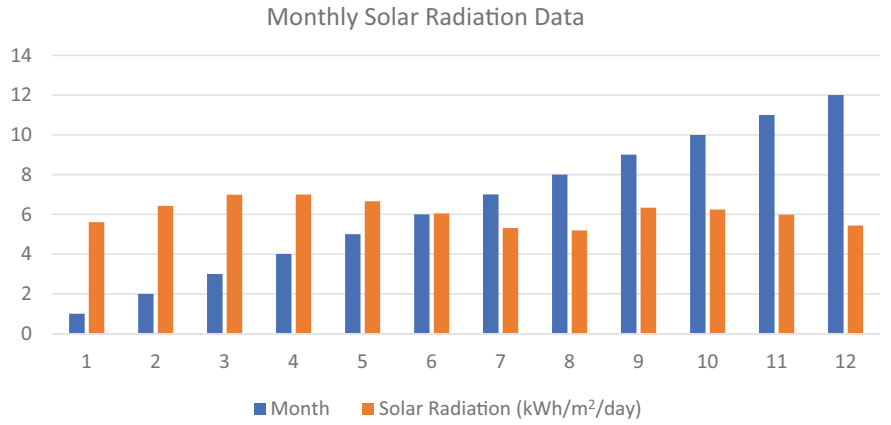

Fig. 1 Monthly solar radiation data

Table 3 Performance evaluation [7–11]

Months	EArray	E_Grid	PR
January	2186	2125	0.794
February	2151	2091	0.776
March	2347 (Max)	2280	0.754
April	2207	1933	0.665
May	2131	2069	0.735
June	1916	1860	0.749
July	1616	1566	0.766
August	1600 (Min)	1550	0.770
September	1955	1907	0.760
October	2236	2172	0.758
November	2131	2070	0.772
December	2146	1827	0.692
Year	24,632	23,451	0.748

Legends EArray—effective energy at the output of the array; E_Grid—energy injected into grid; PR—performance ratio

4 Conclusion

The performance analysis of the 15.4 kWp grid-connected ground-mounted solar PV plant is investigated, and its monthly as well as annual output parameters were measured. Data simulation was carried out with the use of PVSyst software tools. Below are listed the key results from the present studies.

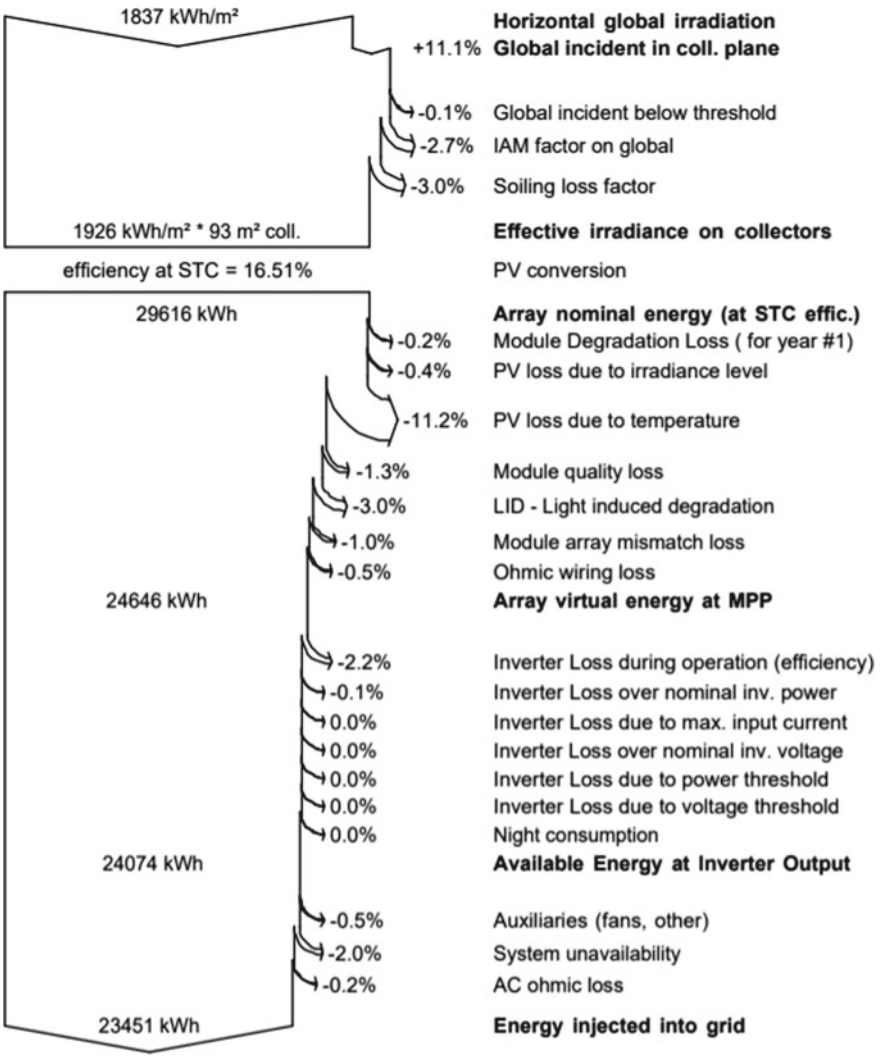

Fig. 2 Loss diagram over the whole year

In the month of March (2347 kWh), the maximum energy is injected into the grid, while in August a minimum of 1600 kWh is injected. The solar PV system of 15.4 kWp displays a healthy 78.1% PR.

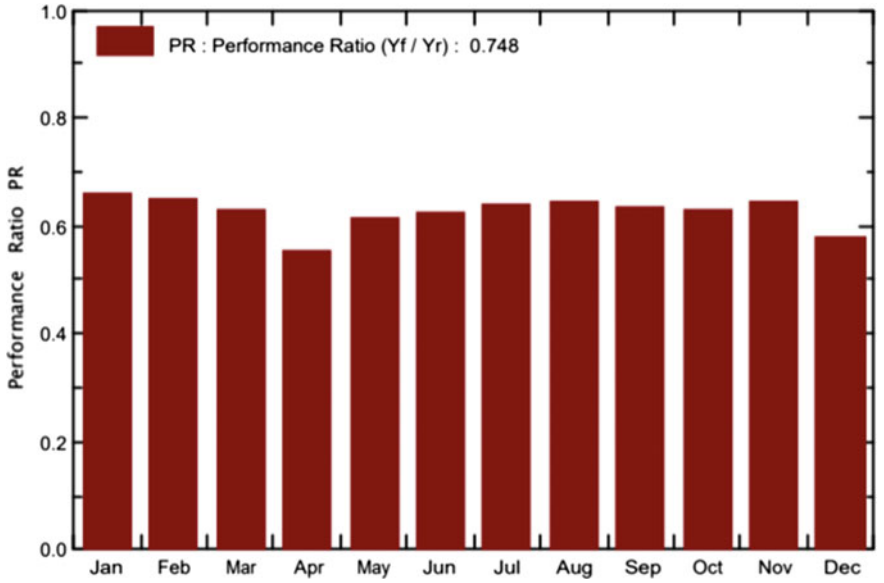

Fig. 3 Performance ratio PR

Acknowledgements The authors would like to thank to Prakhar Mittal (Director Penta Solarex Pvt. Ltd) for providing PVSYSTV6.39 software support from Valkan Engineering PVT Ltd.

References

1. Kumar BS, Sudhakar K (2015) Performance evaluation of 10 MW grid connected solar photovoltaic power plant in India. Energy Rep 1:184–192
2. Adaramola MS (2014) Viability of grid-connected solar PV energy system in Jos, Nigeria. Int J Electr Power Energy Syst 61:64–69
3. Anonymous (2017) Press Information Bureau, Ministry of New and Renewable Energy, Government of India. Retrieved 13 Aug 2017. http://pib.nic.in/newsite/pmreleases.aspx?mincode=28
4. Ayompe LM, Dufy A, McCormack SJ, Conlon M (2011) Measured performance of a 1.72 kW rooftop grid connected photovoltaic system in Ireland. Energy Convers Manage 52(2):816–825
5. Baltus CWA, Eikelboom JA, Van Zolingen RJC (1997) Analytical monitoring of losses in PV systems. In: Proceedings of the 14th European photovoltaic solar energy conference, Barcelona
6. Chaita A, Kluabwang J (2016) Performance evaluation of 3.5 kWp rooftop solar PV plant in Thailand. In: Proceedings of the international multi conference of engineers and computer scientists, IMECS 2016, vol II, Hong Kong, 16–18 Mar 2016
7. Ahmed OA, Habeeb WH, Mahmood DY, Jalal KA, Sayed HK (2019) Design and performance analysis of 250 kW grid-connected photovoltaic system in Iraqi environment using PVsyst software. Indones J Electr Eng Inform (IJEEI). ISSN 2089-3272. https://doi.org/10.11591/ijeei.v7i3.978

8. Aryal A, Bhattrai N (2018) Modeling and simulation of 115.2 kWp grid-connected solar PV system using PVSYST. Kathford J Eng Manag 1:31–34. https://doi.org/10.3126/kjem.v1i1.22020
9. Bouacha S, Hadj Arab A, Belhaouas N, Semaoui S, Haddadi M (2015) Modeling and simulation of 1 MW grid connected photovoltaic system
10. Alsadi S, Khatib T (2018) Photovoltaic power systems optimization research status: a review of criteria, constrains, models, techniques, and software tools. Appl Sci 8:1761. https://doi.org/10.3390/app8101761
11. Ramoliya JV (2015) Performance evaluation of grid-connected solar photovoltaic plant using PVSYST software. JETIR 2(2). ISSN 2349-5162

Design and Modeling of Power Converters to Facilitate Battery Charging/Discharging Harnessed by Stand-Alone PV System

Diksha Tiwari, R. Bharathsrinivas, Minal Salunke, and H. Sumukh

Abstract This paper proposes to design and simulate an efficient battery charging facility for electric vehicles using a stand-alone PV panel. The power conversion stage is designed to get the required voltage level to charge the battery pack. The conversion stage uses two controllers. One controller tracks the maximum power from the PV array and the other regulates the DC voltage for charging the battery pack. Maximum power from the PV array is extracted using the classical method, perturb and observe. A charge controller regulates the voltage level required for charging and discharging battery the pack with a voltage mode control strategy. A closed-loop PID controller with Ziegler–Nichols tuning technique is employed to obtain the control signal. The duty ratio obtained by the PWM and driver circuit is responsible for controlling power switches in the power converters. The regulated voltage delivered by the charge controller is utilized to charge the battery pack. The battery parameters are obtained and analyzed for the charging and discharging cycle.

Keywords PV panel · PID compensator · Battery · P&O technique · MPPT controller · Charge controller

1 Introduction

Today's mild electric vehicles are powered by an internal combustion engine combined with electric motors that use energy stored in batteries. EVs combine the benefits of high fuel economy and low tailpipe emissions with conventional vehicles' power and reach. The EV industry's availability of adequate power has turned from traditional energy sources to renewable energy resources for their development. An electronic DC-DC converter that optimizes the blend between PV panel and the utility network is maximum power point tracker (MPPT). This converts the DC voltage production from solar boards (and a few wind generators) down to the more economical voltage required to charge batteries. In order to accomplish

D. Tiwari (✉) · R. Bharathsrinivas · M. Salunke · H. Sumukh
Department of Electrical and Electronics, KLE Technological University, Hubballi, India
e-mail: dikshatiwari564@gmail.com

S. Dwivedi et al. (eds.), *Flexible Electronics for Electric Vehicles*, Lecture Notes in Electrical Engineering 863, https://doi.org/10.1007/978-981-19-0588-9_42

this, MPPT routines are applied. The P&O algorithm is an MPPT algorithm, also called the "hill-climbing" algorithm. This algorithm comprises a disturbance on the power converter's duty period and a disturbance in the DC link's operation voltage connecting the PV array and the power converter. In this process, the latest disturbance sign and the last increment decide the next perturbation. If there is a gain in power, the change should be held in a similar course, and if the power fails, then the following disturbance should be in the opposite course.

Then the operating point fluctuates near MPP. The features on the consequences of altering insolation values such that the greater the radiation, the more the extracted power using MATLAB Simulink [1]. The novel perturbs and observes algorithm tracks and controls the maximum power point or MPP. Power output can be efficiently maximized and achieved in low-cost microcontrollers that seem to be guaranteed. The battery charging convenience includes a charge controller combined with an MPPT controller. The charge controller is a power converter that regulates the course at which electric current is added to or removed from electric batteries. It prevents overcharging and may guard against overvoltage, which can degrade battery performance or period. A unique scheme and simulation of a DC-DC switching converter system fitting for charging a battery from a solar photovoltaic (SPV) panel and a load control circuit [2] are essential to detach the load from the battery when the voltage of the battery falls underneath a definite value and to reconnect it afresh when the battery charges.

2 System Description

The system underneath consideration is addressed here. This chapter deals with the overall block diagram and control approach of the system considered.

2.1 Block Diagram

To design an efficient battery charging facility, Fig. 1 depicts the overall block diagram and control strategy. To charge lithium-ion battery pack [3] incorporated in EVs from solar energy requires power conversion in several stages. To achieve the same, we are required to design DC-DC converters.

- PV Array: A united combination of collection of solar boards utilized to obtain the necessary voltage level.
- An MPPT controller executes the DC-DC boost converter to obtain the largest energy from the PV panel.
- The battery pack requires a robust charging facility that introduces a charge controller's need, which can neglect the voltage levels. The charge controller is employed with a closed-loop DC-DC buck converter controlled by PWM signals.

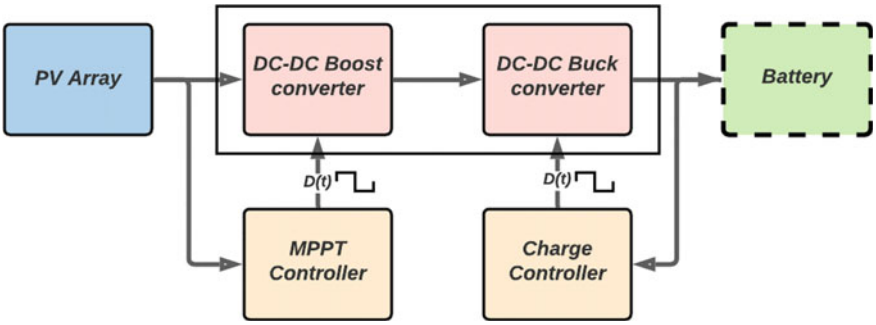

Fig. 1 Block diagram of the system under design

- Load: Lithium-ion battery pack utilizes the DC-voltage levels obtained from the power converter.

To charge the lithium-ion battery pack robust DC voltage level is required. To achieve this DC-DC buck converter working in closed-loop voltage mode control is employed. The P&O MPPT boost converter extracts the maximum power from PV array and is fed to the charge controller.

2.2 PV Array Specification

The specification of the PV array is given as follows

- Open circuit voltage (V_{OC}) = 32.9 V.
- Short circuit current (I_{SC}) = 8.2 A.
- Maximum Power (P) = 200 W.
- Voltage at maximum power (V_{mp}) = 30 V.
- Current at maximum point (I_{mp}) = 6.67 A.
- T is the Temperature in Celsius.
- I and V are the PV Current and Voltage respectively.
- G is the Solar Irradiation.
- Reverse saturation current,

$$I_{rs} = \frac{I_{sc}}{e^{\frac{qV_{oc}}{n \cdot Ns \cdot K \cdot T}} - 1} \tag{1}$$

- Photocurrent,

$$I_{ph} = [I_{sc} + k_i \cdot (T - 298)] \cdot \frac{G}{1000} \tag{2}$$

- Shunt Current,

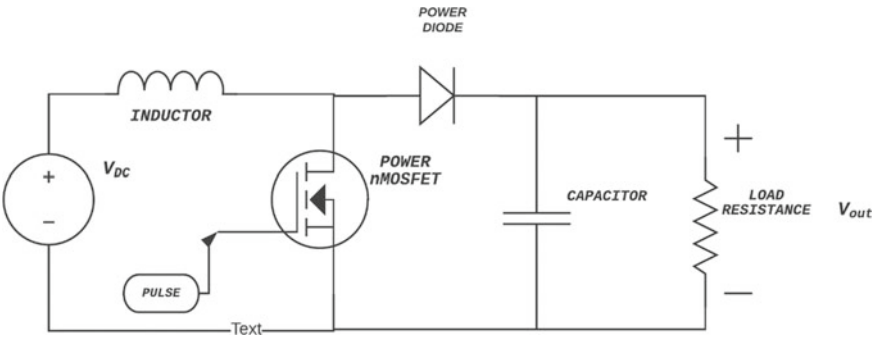

Fig. 2 Circuit diagram of boost converter

Table 1 Boost converter parameters

S. No.	Parameter	Value
Input voltage at MPP	V_{mpp}	32 V
Filter capacitance	C	100 μF
Inductance	L	2 mH

$$I_{\text{sh}} = (V + I \cdot R_{\text{s}})/R_{\text{sh}} \tag{3}$$

- PV Current,

$$I_{\text{pv}} = I_{\text{sc}} - I_0\left[e^{q\frac{(V_{\text{pv}}+I_{\text{pv}}\cdot R_{\text{s}})}{\text{AKT}_j}} - 1\right] \tag{4}$$

2.3 Design of MPPT Boost Converter

The circuit diagram of boost converter is depicted in Fig. 2. The boost converter is designed with the specifications tabulated in Table 1.

2.4 P&O MPPT Algorithm

The P&O approach is based on a repetitive algorithm to trace continuously the MPP by the current and voltage computation of the PV array. This algorithm perturbs the operating voltage to ensure the highest power. The panel voltage is intentionally perturbed (improved or diminished) then the power is associated with the power achieved ere disturbance. If the power is raised due to the disturbance, the subsequent disturbance will be made in the identical course and if the power reduces, the new

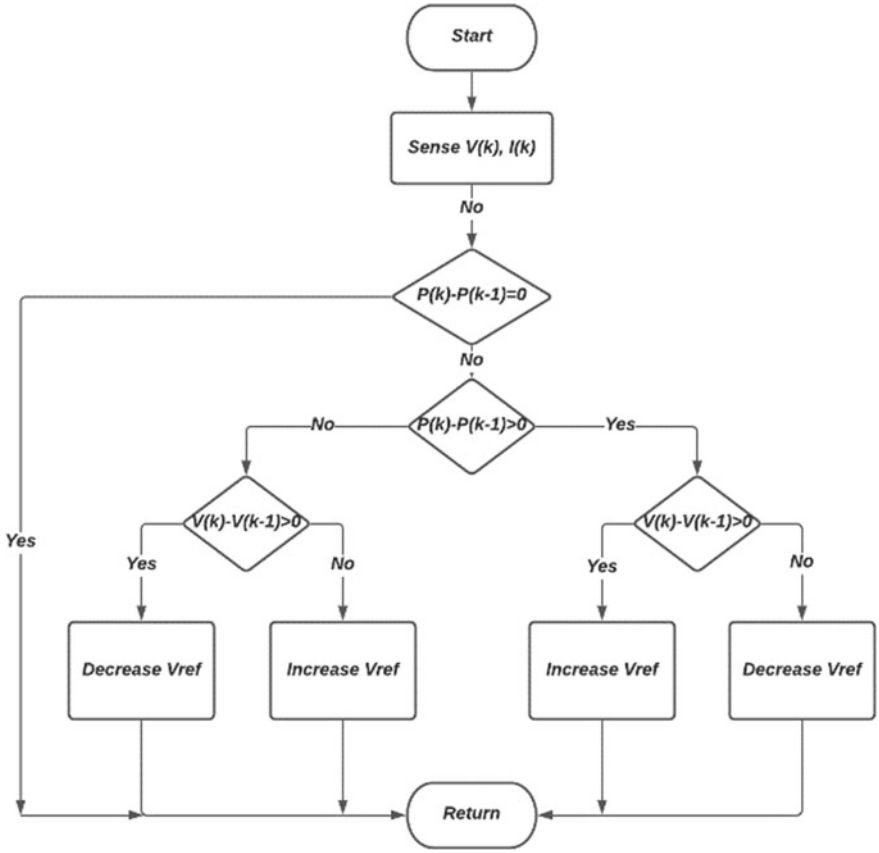

Fig. 3 Flowchart of P&O MPPT algorithm

perturbation is made in the opposing path. Figure 3 describes the algorithm of the P&O MPPT method.

2.5 DC-DC Buck Converter Design

The buck converter is employed as a charge controller to regulate the voltage level obtained from MPPT boost converter. Table 2 describes about the same (Fig. 4).

3 Converter Design

This section depicts the design of charge controller.

Table 2 Buck converter parameters

S. No.	Parameter	Value
Input voltage	V_{in}	Varying due to irradiation function
Filter capacitance	C	100 μF
Inductance	L	2 mH
Switching freq.	f_{sw}	50 kHz
Output voltage	V_o	24 V

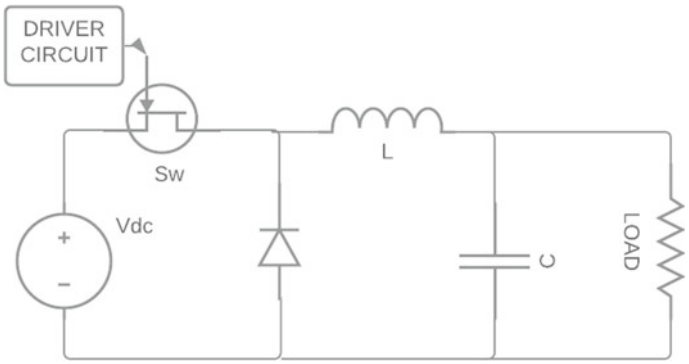

Fig. 4 Circuit diagram of buck converter

3.1 Buck Converter as a Charge Controller

- V_{ref} = Reference Voltage.
- V_c = Control Voltage.
- $D(t)$ = Duty Cycle.
- $V_o(t)$ = Output Voltage.
- $V_s(t)$ = Sensor Voltage.

The error calculated from the converter that functions in negative feedback estimates the duty period and diversifies with time. The output voltage is compared by a reference voltage, and the error is processed by the PID controller. The controller output is the control voltage and is compared with a sawtooth waveform of the PWM circuit to generate the duty period. The output voltage is commonly engaged to a voltage divider circuit with a selective gain before a reference voltage matches it. The output voltage is continuously monitored with the aid of feedback circuit (Fig. 5).

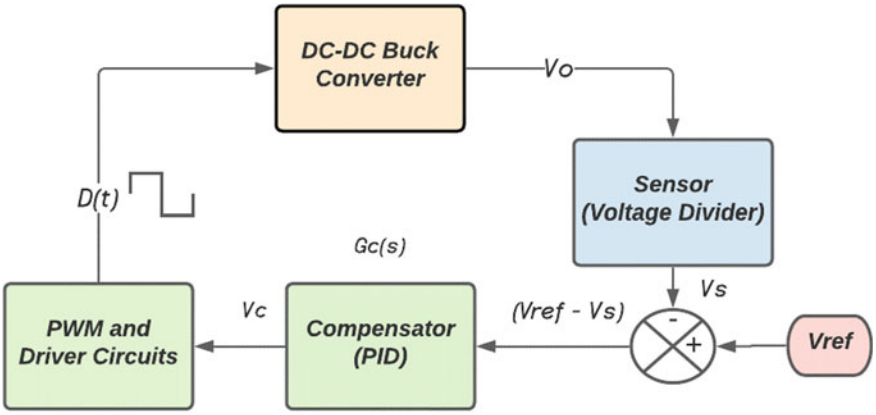

Fig. 5 Block diagram of charge controller

3.2 *Ziegler–Nichols Tuning Technique*

The Ziegler–Nichols tuning technique is applied to tune the controller parameters. This tuning rule is anticipated to give PID loop the most excellent disturbance dismissal. The Converter is regulated by voltage-mode control combined with a PID compensator. This tuning practice exercises the Ultimate gain (K_{cu}) and the Ultimate period (T_{cu}). For the proportional controller, the gain K_p at which the loop swings with consistent amplitude is K_{cu} and the ultimate time period T_{cu}. To obtain K_{cu} and T_{cu}, the controller is set to P-type only by setting $K_i = K_d = 0$. This implies, $G_c(s) = K_p$.

The transfer function for the PID controller is $G_c(s) = K_p + K_i/s + s * K_d$ (Table 3).

- $T_{cu} = 0.02$
- $K_{cu} = 0.001$.

Table 3 PID gains

Gains	Formula	Calculated	Fine tuning
K_p	$0.75 * K_{cu}$	75e−6	25e−6
K_i	$1.2 * K_{cu}/T_{cu}$	0.6	0.5
K_d	$0.075 * K_{cu} * T_{cu}$	1.5e−6	5.5e−6

4 Results

Using the methods and designs mentioned above, required simulations were performed and observations were noted down. The simulation was carried out using MATLAB and Simulink.

4.1 Mathematical Modeling of PV Array

Figure 6 depicts the mathematical modeling of PV array and its implementation in Simulink. The following results are obtained keeping temperature constant of 25 °C and 1000 W/m^2.

Figure 7a, b represent the PV array characteristics. (a) Plots power versus voltage of an PV array and (b) represents voltage versus current of PV array.

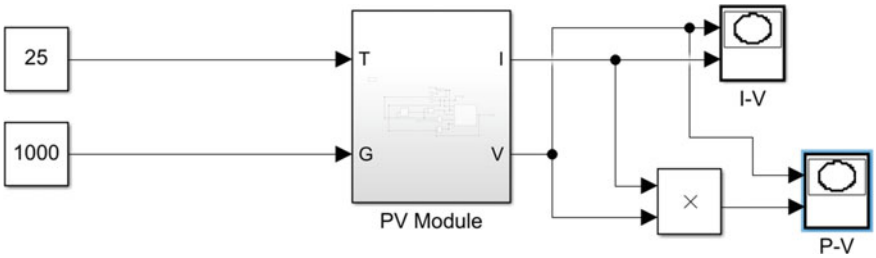

Fig. 6 Mathematical model of PV array

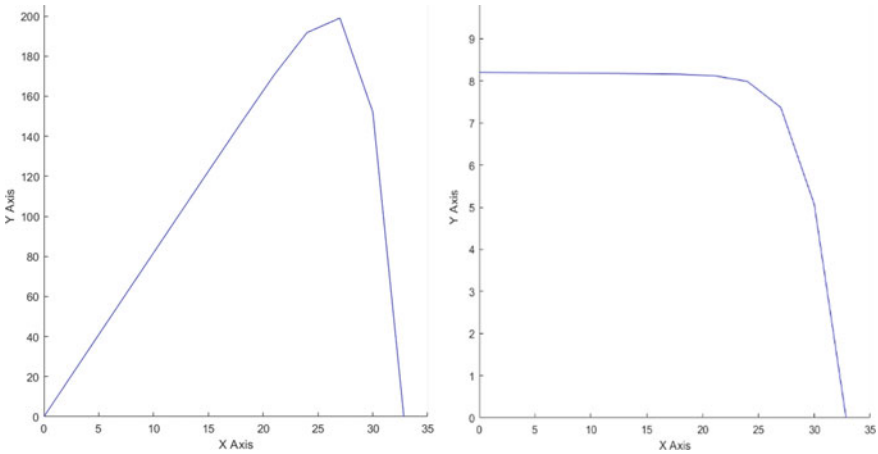

Fig. 7 **a** PV characteristics. **b** IV characteristics

4.2 Boost Converter MPPT

Based on the required specifications, the boost converter is designed and simulated. For a specified irradiation pattern, the converter tracks the maximum power point. The simulation was performed for a temperature of 25° and a specified Irradiation pattern of 1000, 500, 300, and 0 W/m^2 (Fig. 8).

Figure 9 depicts the irradiation pattern imposed on PV array. We can infer that as irradiation pattern changes, PV array's voltage levels vary. This becomes an ideal reference to real-time irradiation pattern. The efficiency of MPPT controller can be calculated as

$$\eta = P_{\mathrm{PV}} / P_{\mathrm{ideal}}$$

From Fig. 10, we infer that ideal power is nearly same as the output power of the

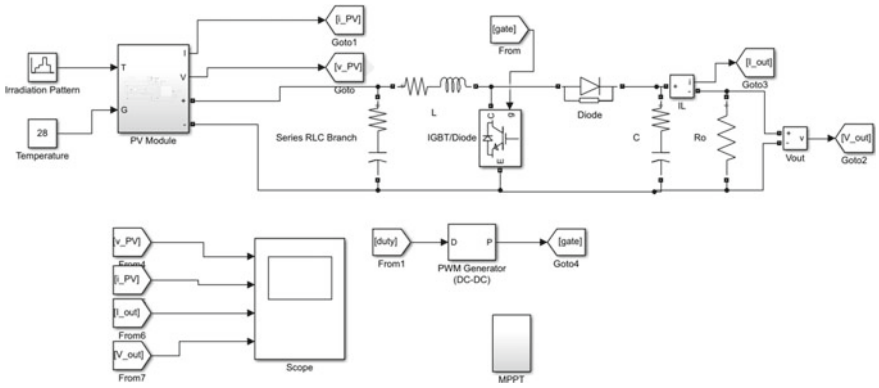

Fig. 8 Circuit diagram of MPPT boost controller

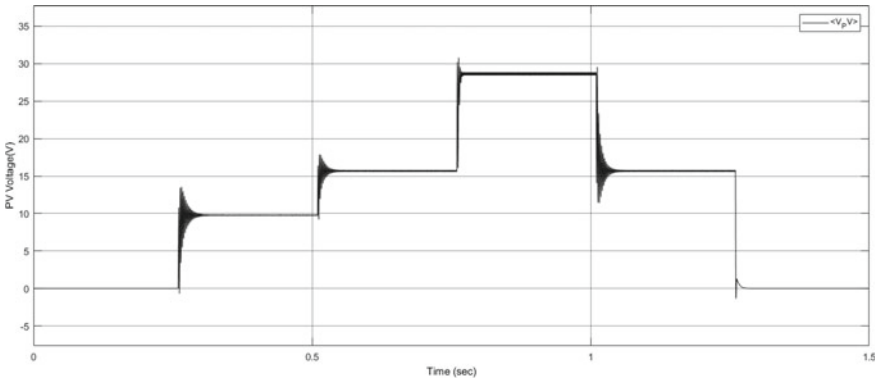

Fig. 9 PV voltage under irradiation pattern

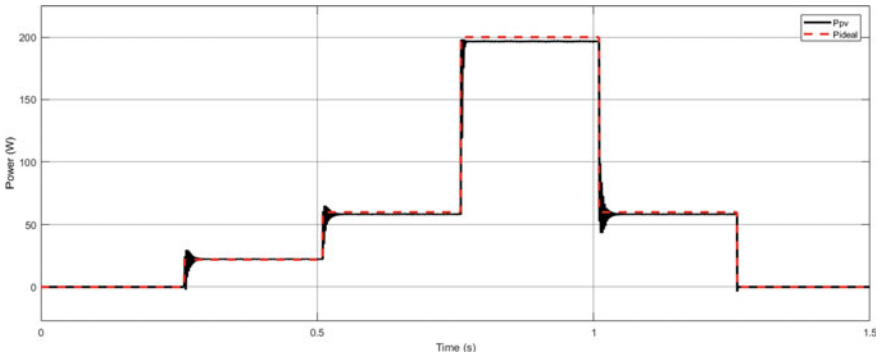

Fig. 10 Ideal maximum power P_{ideal} and PV module power P_{PV}

PV module. The efficiency of the converter is greater than 96% which explains that the tracking algorithm is highly robust and efficient. This maximum power is utilized by charge controller to charge the battery pack.

4.3 Charge Controller

Charge controller circuit is implemented with a closed-loop buck converter operated in voltage-controlled mode. The complete analysis can be inferred from the simulation result as shown in Fig. 11.

As observed in Fig. 12, the output voltage reaches to 24 V with a rise time of around. This voltage level is utilized for charging battery pack. Figure 13 shows the plot of load current of charge controller circuit. It reaches 0.48 A during simulation.

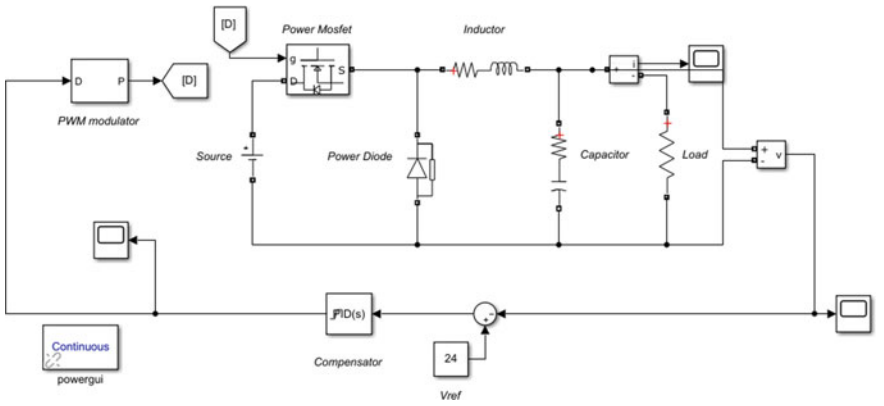

Fig. 11 Charge controller circuit

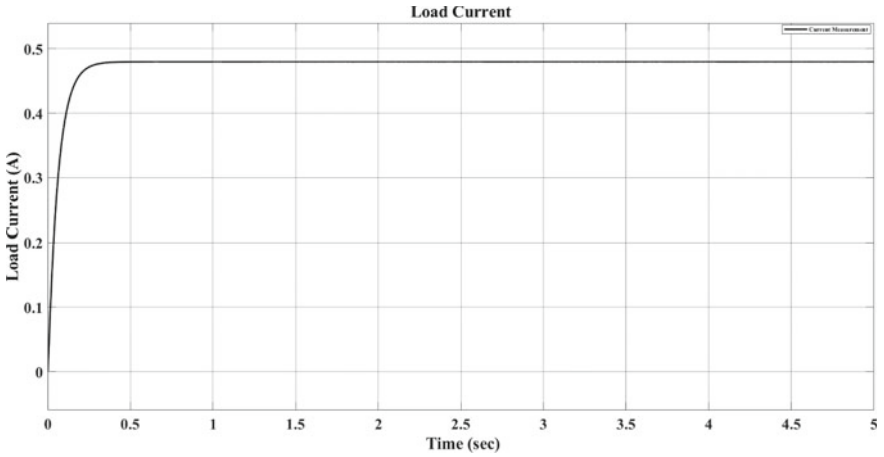

Fig. 12 Output voltage of charge controller

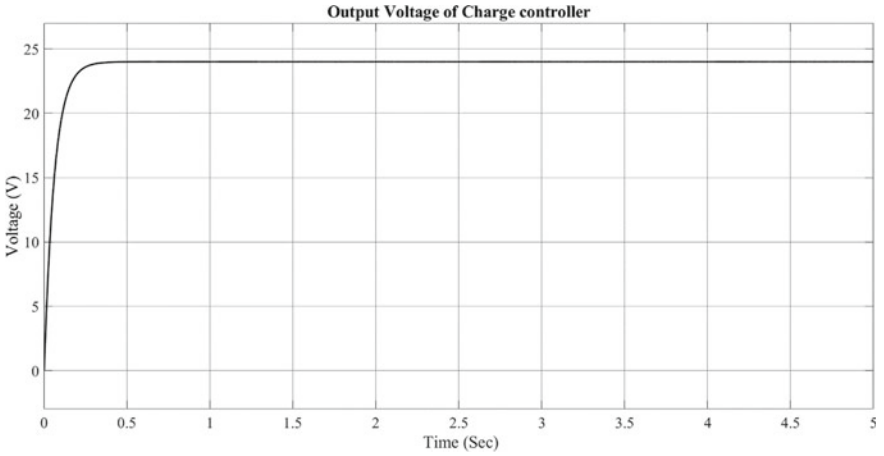

Fig. 13 Load current of the charge controller

As inferred from Table 4, the time-domain performance of the charge controller is highly robust for variations in power. This shows the closed-loop performance is improved by adding a PID controller.

Table 4 Characteristics of output waveform

Parameter	Controller performance
Rise time	0.2 s
Settling time	0.3 s
Peak overshoot	0.1%

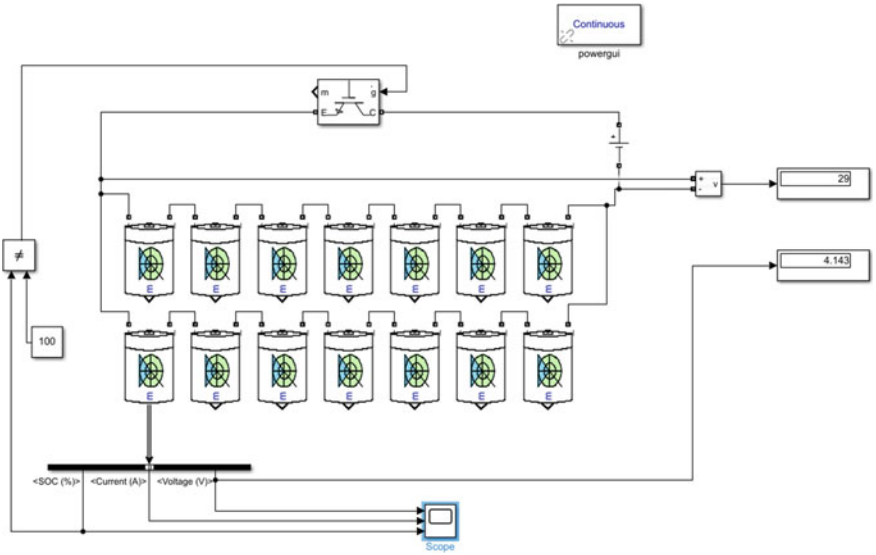

Fig. 14 Charging cycle of battery pack

4.4 Battery Pack Simulation

4.4.1 Charging Cycle

Battery is simulated here which consists of seven cells in series and two such in parallel. This 7SP2 configuration is used for analysis of charging and discharging of the battery. With the help of charge controller, we are able to provide constant voltage level for battery pack. This is utilized to charge the lithium-ion battery pack. This simulation presents the battery characteristics during charging and discharging cycles. The overall SoC and battery pack parameters are represented (Fig. 14).

From Fig. 15, we can infer that the lithium cell's voltage level reaches 4.3 V after charging cycle. Overall voltage level of pack reaches 29 V. The cell's nominal voltage is 3.7 V. The SoC of each cell reaches 100% after charging, and at this point, cell's current reaches zero, which describes the battery pack is completely charged. The Simulink model disconnects the battery from cell when sell's SoC reached 100%.

4.4.2 Discharging Cycle

The charged battery pack is discharged using a 2 Ω resistor across the cell. Figure 16 depicts the same.

From Fig. 17, we can infer that the battery pack's voltage level reaches 0 V after discharging cycle. The SoC of the battery pack reaches 0% after discharging and at this point, cell's current reaches zero, which describes the cell is completely

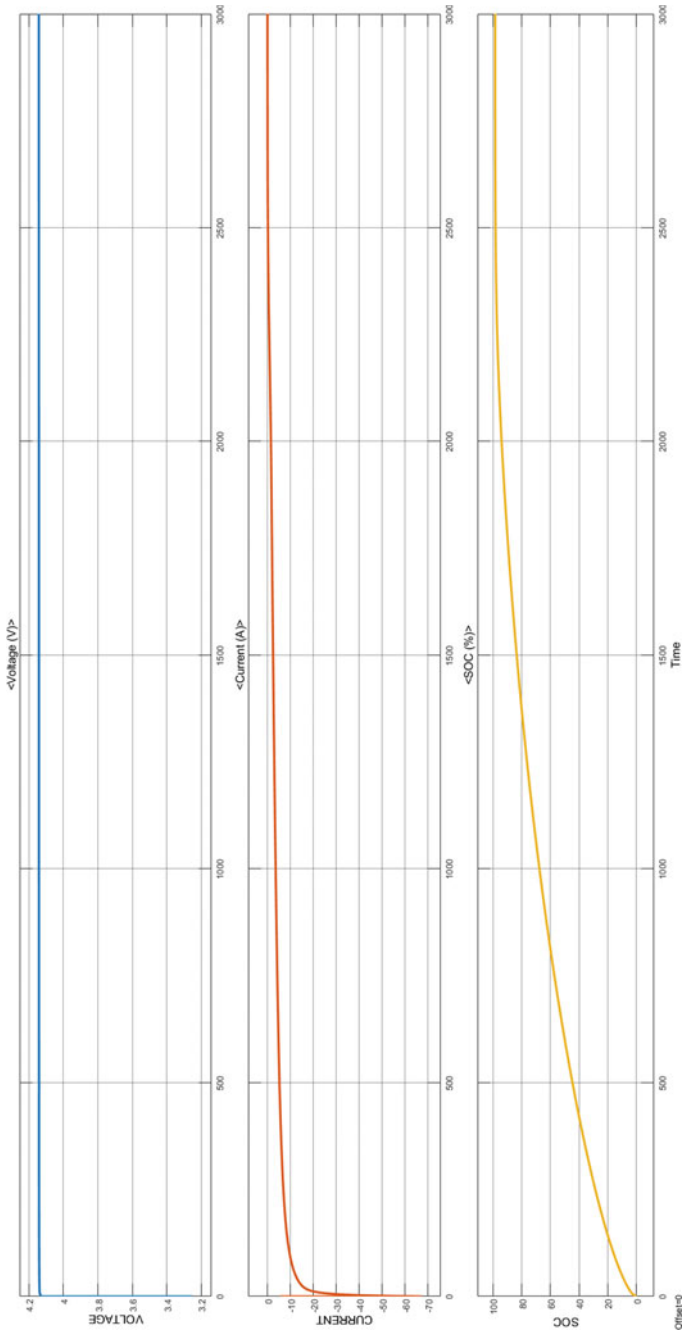

Fig. 15 Voltage, current, and state of charge of the battery pack during charge cycle

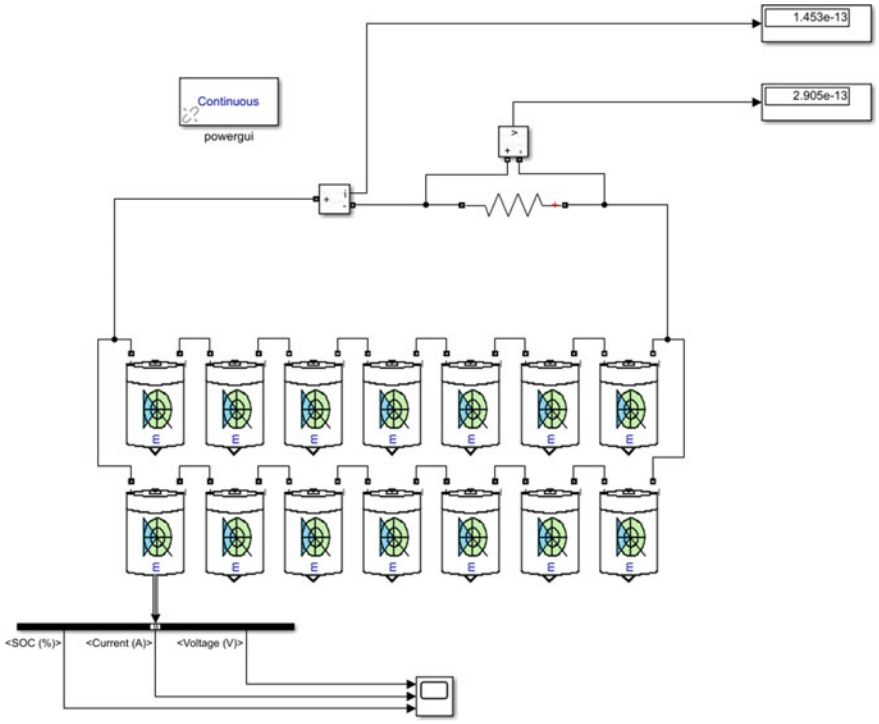

Fig. 16 Discharging cycle of a battery pack

discharged. During discharge cycle, the individual lithium-ion cell provides nominal voltage of 3.7 V without much variation until the SoC reaches zero. This characteristic of lithium-ion cell is highly appreciated.

From the simulation and analysis, we can infer that the charging facility from a stand-alone PV renewable resource for Lithium-ion battery pack incorporated in mild electric vehicles can be realized. The power conversion stages play a vital role in the entire architecture designed. Future works include The hardware realization of entire architecture and cell balancing of battery pack and different kinds of battery pack.

5 Conclusion

- A complete design of PV array sourcing the battery pack with relevant power conversion stages is simulated using MATLAB-Simulink toolbox.
- The PV array is designed with constant temperature and variable solar irradiation. The maximum power from the solar PV array is extracted using the classical perturb and observe algorithm. For a specific irradiation pattern of 1000, 500,

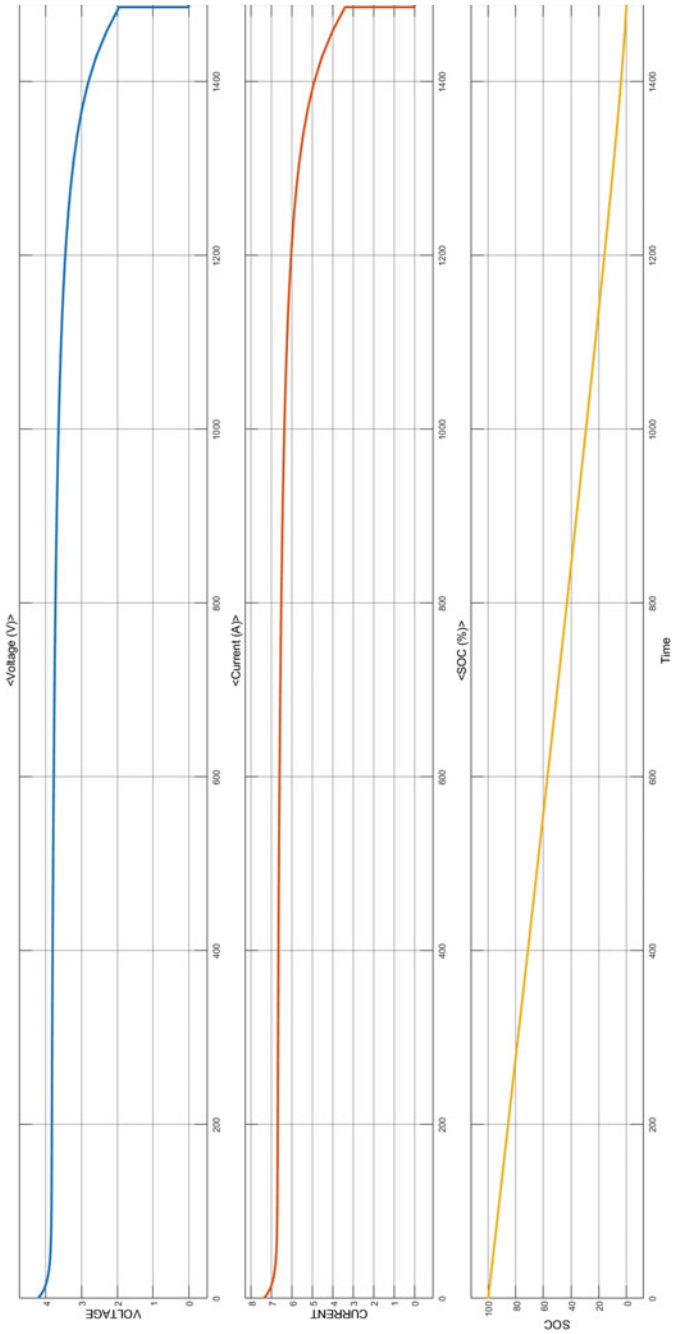

Fig. 17 Voltage, current, and SoC of the battery pack during discharge cycle

300, and 0 W/m^2 maximum power was tracked according to the algorithm with an efficiency of more than 96%.

- The regulated voltage from charge controller is utilized for charging the battery pack. The battery is discharged through a pure resistive load. It is observed from the simulated resulted that the SoC of battery pack reaches 100% on completion of charging cycle.
- During discharging cycle, the SoC drops from 100% to zero percent without affecting the constancy of the voltage. This indicates the robustness of the battery pack.

References

1. Selmi T, Abdul-Niby M, Devis L, Davis A (2014) P&O MPPT implementation using MATLAB/Simulink. In: Ninth international conference on ecological vehicles and renewable energies (EVER), Monte-Carlo, Monaco. IEEE
2. Raghavendra NK, Padmavathi K (2018) Solar charge controller for lithium-ion battery. In: International conference on power electronics, drives and energy systems (PEDES), Chennai, India. IEEE
3. Hsu S-P, Lin C-L, Wu J-Y (2012) Balancing charge/discharge management for series/parallel battery packs. In: 7th IEEE conference on industrial electronics and applications (ICIEA), Singapore
4. Sharma DK, Purohit G (2012) Advanced perturbation and observation (P&O) based maximum power point tracking (MPPT) of a solar photo-voltaic system. In: IEEE 5th India international conference on power electronics (IICPE), Delhi, India
5. Sankaraditya Vikas K, Raviteja Reddy B, Abijith SG, Sindhu MR (2019) Controller for charging electric vehicles at workplaces using solar energy. In: International conference on communication and signal processing (ICCSP), Chennai, India
6. Bharathsrinivas R, Tiwari D, Sumukh H, Salunke M, Hunasimarad M (2020) Design and modeling of photovoltaic based converters for low power AC systems. In: IEEE international conference for innovation in technology (INOCON), Bengaluru, India

Inkjet Printed PEDOT:PSS-based Source/Drain Electrodes for Organic Thin Film Transistors

Sudipta Kumar Sarkar, Mukesh Singh, and Dipti Gupta

Abstract Printed electronics in recent years have attracted considerable attention because fabrication of electronic devices by printing method not only enables large area and volume manufacturing of devices but also reduces the process complexity and fabrication cost quite significantly. Hence, deploying printing method to fabricate organic electronic devices which are crucial for next generation flexible electronics and bio-electronic devices can combine the benefits and attributes of both printing technology and organic electronics. The current research demonstrates inkjet printing of electrically conducting poly (3, 4-ethylenedioxythiphene)-poly(styrenesulfonate) (PEDOT:PSS) to fabricate the source and drain electrodes for pentacene-based organic thin film transistors (OTFTs). The devices were fabricated on a highly doped silicon (n++Si) wafer in top contact bottom gate geometry. The n++Si wafer acted as the bottom gate whereas thermally grown silicon dioxide, vacuum deposited pentacene and inkjet printed PEDFOT:PSS were used as gate insulator, semiconductor and source/drain electrodes, respectively. So, the inkjet printing parameters for the top source/drain electrodes were carefully optimized to obtain a minimum channel length of ∼100 μm and width of ∼600 μm. Thus a channel width to length ratio of 6:1 was achieved. Device performance was tested using source measurement units. The field effect hole mobility, on-off ratio and threshold voltage for these devices were found to be ∼0.02 cm^2 V^{-1} s^{-1}, ∼10^4 and ∼−12 V, respectively.

Keywords Organic electronics · Inkjet printing · PEDOT:PSS · Organic thin film transistor

1 Introduction

Over the past few decades organic thin film transistor (OTFT) has attracted increasing attention because of its promising applications in panel displays, sensors, memory devices, identification tags, etc. [1–3]. In contrast to traditional silicon-based device

S. K. Sarkar · M. Singh · D. Gupta (✉)
Plastic Electronics and Energy Laboratory, Department of Metallurgical Engineering and Materials Science, Indian Institute of Technology Bombay, Mumbai, Maharashtra 400076, India
e-mail: diptig@iitb.ac.in

S. Dwivedi et al. (eds.), *Flexible Electronics for Electric Vehicles*, Lecture Notes in Electrical Engineering 863, https://doi.org/10.1007/978-981-19-0588-9_43

which is mechanically rigid and unsuited for bio-applications, organic electronic device such as OTFT exhibits light weight, superior mechanical flexibility and excellent bio-compatibility. Thus, OTFT shows suitability towards futuristic Internet of things (IoT)-based applications such as portable and implantable sensors, foldable and rollable displays, electronic skins, wearables. So, the fundamental reason behind all these exotic applications of OTFT is that all the organic compounds which are commonly used for device fabrication are inherently light weight, mechanically flexible and bio-compatible. Moreover, since the majority of organic electronic compounds dissolve in routine solvents, the organic devices can potentially be fabricated through easy and cost effective solution based techniques such as inkjet printing, spin coating, spray coating. [4–6]. The solution processing not only significantly reduces the production cost but also enables large area fabrication with easy scale-up opportunity. So, it is always desirable to have each layer of an OTFT made of organic materials as this approach can fully utilize the functionalities and attributes of organic compounds.

As of now numerous efforts have been made both theoretically and experimentally to replace the traditionally used inorganic layers of devices by organic compounds. Organic semiconductors and organic insulators are commonly used in constructing organic devices [7–10]. However, for making the metal contacts or electrodes, traditional metals such as gold, silver and so on are still largely used in the fabrication of OTFTs. Hence, there is a need of significant research to replace the expensive metal-based contact layers (source, drain, gate, etc.) of a thin film transistor with organic compound-based highly conducting electrodes. Although many efforts have recently been put in making organic gate electrode by using electrically conducting carbon nanotube, graphene and several conducting polymers (CPs), very rare efforts have been made to develop the source and drain contacts with these materials [11, 12]. It might be attributed to the fact that few processing challenges such as requirement of patterning, masking and lithography always remain associated with the fabrication of source/drain contacts.

So, the requirement of a mask-free direct patterning method has led the influx of inkjet printed electrodes to the organic devices. Inkjet printing is a high resolution digital printing method in which the target solution is directly printed on the substrate with a digitally entered pattern [13]. Moreover, inkjet printing offers high throughput fabrication of devices on large area substrates which make them suitable for commercial role-to-role (R2R) manufacturing process. As of now the inkjet printing method has been mainly explored to obtain electrodes of metal nanoparticles-based inks [14, 15]. Hence, inkjet printing of CPs to obtain patterned source/drain electrodes for OTFTs can bring a significant impact to this field.

Therefore, in the current work we demonstrate inkjet printing of a poly (3, 4 ethylenedioxythiophene)-poly (styrenesulfonate), PEDOT:PSS-based electrically conducting polymer to obtain the source/drain electrodes of pentacene-based OTFTs. PEDOT:PSS was chosen over other organic conductors due to its excellent air stability, high electrical conductivity and solubility in common solvents such as water.

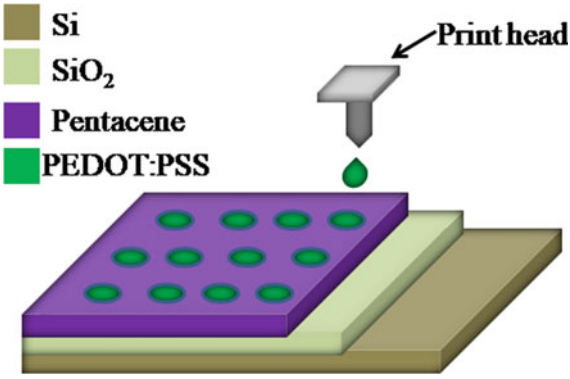

Fig. 1 Schematic representation of inkjet printing of PEDOT:PSS and the device structure of the fabricated OTFT

2 Experimental Details

2.1 Device Fabrication

The OTFTs were fabricated in top contact bottom gate architecture. For this, a highly doped silicon wafer (n++Si) with low resistivity ($\rho \leq 0.005\ \Omega$ cm) was taken as substrate that was also used for the bottom gate contact of the devices. A 300 nm thick silicon dioxide layer (SiO_2) layer was grown on the wafer and it acted as the gate insulator. Then for the organic active layer, pentacene was thermally deposited on the SiO_2 layer with a precise control over the deposition rate. Then finally for the top source/drain contacts, the commercially available PEDOT:PSS was inkjet printed on the pentacene layer and subsequently annealed at 120°C for 10 min. Inkjet printing parameters such as the rise time, fall time, of the applied voltage to the piezoelectric print head was adjusted to obtain better printed patterns with smooth edge, high resolution and continuity. Thus a channel width (W) to length (L) ratio of 6:1 was obtained by printing the source/drain contacts. The inkjet printing process and the device structure are schematically shown in Fig. 1.

3 Results and Discussion

3.1 Optical Microscopic Study

The optical micrographs (Olympus microscope) of the inkjet printed PEDOT:PSS patterns are shown in Fig. 2a and b. The printing parameters such as drop size, step size, print on fly specifications were carefully optimized to obtain contact pads of various shapes. Figure 2a shows a pattern with two long adjacent lines which provides high value of channel width ($W > 1$ mm). However such long pattern was not very useful in making operational devices because of their uniform shape and

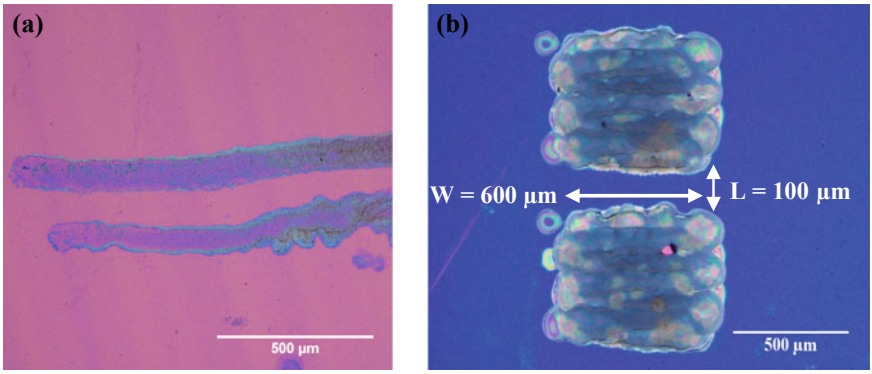

Fig. 2 Optical micrographs of inkjet printed PEDOT:PSS-based **a** electrode lines and **b** rectangular source and drain electrode pads

geometry. On the other hand, a slightly different pattern with rectangular shape and reduced width of—600 µm was obtained and the image is shown in Fig. 2b. The channel length for this pattern was found to be ~100 µm and it has been mentioned in Fig. 2b. This rectangular shaped pattern with *W*/*L* ratio of 6:1 was very useful in terms of providing operational devices. This might be attributed to the low contact resistance and low current loss due to miniaturized size of the contact pads.

3.2 Electrical Characterization

Typical transfer (drain current versus gate voltage) and output (drain current versus drain voltage) characteristics for the OTFT were obtained using a source meter unit-based semiconductor parameter analyzer (Keithley 4200 SCS, Tektronix). The plots are shown in Fig. 3a and b. It is clear from both the plots (transfer plot in Fig. 3a and output plot in Fig. 3b) that the operating voltage of the devices was within the range of −40 V. The output curves in Fig. 3b shows multiple curves corresponding to different gate voltage ranging from 0 to −40 V. It is clear from Fig. 3b that the drain current starts to reach saturation from −30 V for the applied gate voltage of −40 V. Thus the transfer characteristic in saturation Fig. 3a was obtained by acquiring the transfer curve at applied gate voltage of −40 V. The field effect mobility value (μ) of our OTFT was estimated from the transfer curve in Fig. 3a. For this, the following current equation of a metal oxide semiconductor field effect transistor (MOSFET) was used when its source electrode was grounded,

$$I_{\mathrm{D}} = \mu C \left(\frac{W}{L}\right) \frac{1}{2} V_{\mathrm{G}}^2 \tag{1}$$

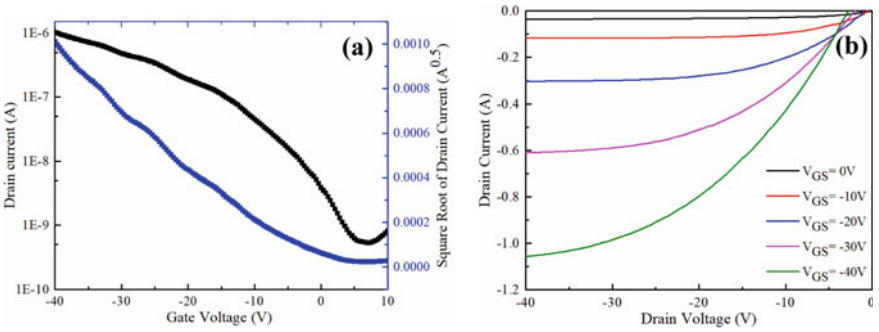

Fig. 3 **a** Transfer characteristics and **b** output characteristics of the fabricated OTFT with inkjet printed PEDOT:PSS-based source/drain electrodes

Table 1 Extracted values of device parameters

μ (cm^2V^{-1} s^{-1})	I_{on}/I_{off}	V_{TH} (V)
~0.02	~10^4	~−12

where I_D, V_G, μ, C, W and L represent drain current, gate voltage, field effect mobility, capacitance of the gate insulator, channel width and channel length, respectively. Other device parameters such as on-off ratio ($I_{on}/_{off}$) and threshold voltage (V_{TH}) were estimated from the transfer curve in Fig. 3a and listed in Table 1. It can be seen from Table 1 that the fabricated OTFTs exhibited excellent performance with high field effect mobility (μ) value of ~0.02 cm^2 V^{-1} s^{-1}, high I_{on}/I_{off} of ~10^4, V_{TH} of −12 V. So, this performance can be attributed to the successful fabrication of every single layer of the device including the successful process optimization for the inkjet printed PEDOT:PSS-based source and drain electrodes. Moreover, the successful operation of our devices indicates an excellent contact behavior of the interface between PEDOT:PSS-based electrodes and the underlying pentacene layer.

4 Conclusion

Inkjet printing of PEDOT:PSS has been demonstrated to successfully obtain the organic source/drain electrodes for an pentacene-based OTFT. With this high resolution printing a channel length of ~100 μm and channel width ~600 μm were obtained. Thus the OTFT with printed organic electrodes and a W/L ratio of 6:1 also exhibited excellent transistor characteristics with high field effect hole mobility value of ~0.02 cm^2 V^{-1} s^{-1}.

Acknowledgements Authors would like to acknowledge Department of Science and Technology (DST), Government of India for financial support and IIT Bombay Nanofabrication Facility (IITBNF), Centre of Excellence in Nanoelectronics (CEN) for providing the microscope facility.

References

1. Chen Q, Yan Y, Wu X, Lan S, Hu D, Fang Y, Lv D, Zhong J, Chen H, Guo T (2019) High-performance quantum-dot light-emitting transistors based on vertical organic thin-film transistors. ACS Appl Mater Interfaces 11(39):35888–35895
2. Li B, Lai P, Tang W (2020) Temperature dependence of sensing characteristics for otft-based hydrogen sensor. IEEE Trans Electron Devices 67(4):1776–1780
3. He W, Xu W, He H, Jing X, Liu C, Feng J, Luo C, Fan Z, Wu S, Gao J (2020) From unipolar, WORM-type to ambipolar, bistable organic electret memory device by controlling minority lateral transport. Adv Electron Mater 6(4):1901320
4. Burke DW, Sun C, Castano I, Flanders NC, Evans AM, Vitaku E, McLeod DC, Lambeth RH, Chen LX, Gianneschi NC (2020) Acid exfoliation of imine-linked covalent organic frameworks enables solution processing into crystalline thin films. Angew Chem Int Ed 59(13):5165–5171
5. Kim JT, Lee J, Jang S, Yu Z, Park JH, Jung ED, Lee S, Song MH, Whang DR, Wu S (2020) Solution processable small molecules as efficient electron transport layers in organic optoelectronic devices. J Mater Chem A 8(27):13501–13508
6. Sarkar SK, Gupta D (2017) Low temperature flash light curing of spray coated zirconium oxide gate dielectric for flexible, fully patterned and low voltage operated organic thin film transistor. MRS Adv 2(23):1273–1278
7. Chen Y, Li C, Xu X, Liu M, He Y, Murtaza I, Zhang D, Yao C, Wang Y, Meng H (2017) Thermal and optical modulation of the carrier mobility in OTFTs based on an azo-anthracene liquid crystal organic semiconductor. ACS Appl Mater Interfaces 9(8):7305–7314
8. Höppner M, Kneppe D, Kleemann H, Leo K (2020) Precise patterning of organic semiconductors by reactive ion etching. Org Electron 76:105357
9. Kang B, Song E, Lee SB, Chae B-G, Ahn H, Cho K (2018) Stretchable polymer gate dielectric with segmented elastomeric network for organic soft electronics. Chem Mater 30(18):6353–6360
10. Rullyani C, Singh M, Li S-H, Sung C-F, Lin H-C, Chu C-W (2020) Stimuli-responsive polymer as gate dielectric for organic transistor sensors. Org Electron 85:105818
11. Darwis D, Sesa E, Elkington D, Sharafutdinova G, Lewis T, Zhou X, Dastoor PC, Belcher WJ (2021) Printing of PEDOT:PSS for top gate organic thin film transistor. J Phys Conf Ser 1 p 012078
12. Yambem SD, Burns S, Arthur JN, Timm J, Woodruff MA, Pandey AK, Marschall R (2019) A highly porous and conductive composite gate electrode for OTFT sensors. RSC Adv 9(13):7278–7284
13. Nayak L, Mohanty S, Nayak SK, Ramadoss A (2019) A review on inkjet printing of nanoparticle inks for flexible electronics. J Mater Chem C 7(29):8771–8795
14. Pajor-Świerzy A, Gaweł D, Drzymała E, Socha R, Parlińska-Wojtan M, Szczepanowicz K, Warszyński P (2018) The optimization of methods of synthesis of nickel–silver core–shell nanoparticles for conductive materials. Nanotechnology 30(1):015601
15. Sarkar SK, Gupta H, Gupta D (2017) Flash light sintering of silver nanoink for inkjet-printed thin-film transistor on flexible substrate. IEEE Trans Nanotechnol 16(3):375–382

Comparative TCO Analysis of Electric and Gasoline Vehicles for Indian Market

Geetanjali and Ashish Shrivastava

Abstract Increasing pollution is a global concern. Emission from combustion vehicle contributes a major share of this pollution. Increasing urbanization has a direct relation with increasing private vehicle demand and further to deteriorating environment and human life. Electrical vehicles are the best solution, as of now, to this global issue. But, higher purchase price of EV is what that is hindering customer to buy EV. Educating the customer about global health concerns of using traditional combustion vehicles and showing the comparison of actual cost of the vehicle that they would incur, called total cost of ownership (TCO) over a period of 5 or 10 years, could influence the customer's decision to opt for electrical vehicle. Various case studies have been done by the authors that can influence customer's decision to adopt electric vehicle. In addition, it also shows that how government can make policies to provide incentives and subsidies to the customers to help the growth of sales of EVs in India.

Keywords Electric vehicle · Pollution · Total cost of ownership

1 Introduction

"Necessity is the mother of invention". A well-known phrase that goes well with the re-emergence of electric vehicles (EVs). Increasing pollution is a global concern now. In 2018, world meteorological organization's (WMO) report stated that global temperature rise by 1.5° due to environmental changes would have concerning effect. This report also suggested that the only solution to above problem is reduction in carbon emission to net zero by 2050. Transportation contributes to almost 27% of this pollution. Humans are the ones who induced drastic changes in the climate and

Geetanjali
Department of Electrical Engineering, Manipal University Jaipur, Jaipur, Rajasthan 303007, India

A. Shrivastava (✉)
Skill Faculty of Engineering and Technology, Shri Vishwakarma Skill University Haryana, Gurugram, India
e-mail: rewa.ashish@gmail.com

S. Dwivedi et al. (eds.), *Flexible Electronics for Electric Vehicles*, Lecture Notes in Electrical Engineering 863, https://doi.org/10.1007/978-981-19-0588-9_44

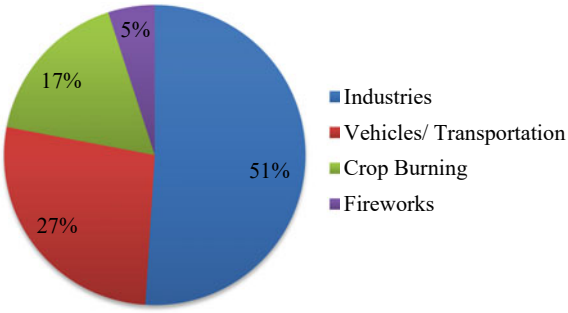

Fig. 1 Major contributors to the pollution [1]

now are the sufferers too. Pollution is also a primary cause of health issues in elderly population and the new generation. As per study, in 2019, 1.67 million premature deaths in India are solely due to air pollution that further reduces GDP by 1.4% [1]. Statistical data shows that three-fourth of transport pollution is caused by combustion vehicles (CVs) (Fig. 1).

In India, urban population is growing at a rate of 3.16% per year, whereas combustion vehicle sale is growing at a rate of 9%. Although, growth in urbanization and CVs sale are the parameters to measure development of a country, but it also accounts for the degradation of air quality. Considering both pros and cons of modernization, re-emergence of EVs is the need of the hour, which was being invented first, in late nineteenth century (1870), but lead was taken by combustion vehicles due to their lower initial cost, higher speed, longer distance covered in one full tank, very less refueling time as compared to electric vehicles.

Besides the enormous advantages of combustion vehicles, the biggest advantage of EVs is that it has zero exhaust emission and hence is environment-friendly. Additional advantages of EVs are listed in Table 1.

Table 1 Comparison of EVs and CVs

Parameter	Electric vehicle	Combustion-based vehicle
Operational cost	1/3rd of combustion engine's operational cost	Significant amount depending on the fuel used
Maintenance	Negligible	At least yearly maintenance is required
Exhaust emission	Zero	Significant
Noise	< 50 db	60–90 db
Energy conversion rate	More than 86% of energy into driving force	Maximum 35% of energy into driving force

2 Literature Review

According to census of India 2011, the urban population has increased exponentially from 17.3% to 31.16% between 1951 and 2011 [2]. This unexpected steep in urban population leads to the increased demand for transportation, which further added up to the air pollution. WHO report says that combustion vehicle emission comprises of those pollutants that can have adverse health effects like ischemic heart disease, stroke, chronic obstructive pulmonary disease, lung cancer and can impact more to the pollution with compromised health conditions like asthmatics, children, and elders. In 2019, India reported 1.67 million deaths due to air pollution, which is 17.8% of total deaths in the country. There are two prime factors for air pollution that cause mortality: household pollution and particulate emission from vehicles. Death rate due to household air pollution has decreased by 64.2% from 1990 to 2019. On the contrary, death rate due to emission from combustion vehicles has increased by 115.3% [1]. Further, these premature deaths decreased the output, and hence, the country had to bear an economic loss of US $28.8 billion in 2019. This loss accounts for 1.4% of India's gross domestic product (GDP). Of all the states of India, Delhi has the highest per capita economic loss due to air pollution [1]. Various studies had been carried out in the past for the adoption of EVs like surveys [3–5], data collected from consumers [6, 7], secondary data analysis [8], optimization techniques [9, 10], and country-wise analysis of people's view for EVs, etc. It was observed that shifting to EVs also depends upon the way a specific country is generating electricity. Like, European countries generate most of their electricity from renewable energy sources and can be best suited for EVs. On the other hand, countries like Germany and the USA should step forward to reduce greenhouse gas (GHG) emission by decarbonizing the process of electricity generation. Other major hindrances to EV adoption in India are EV price, inadequate charging infrastructure [6, 8], driving range [6, 7], and less social awareness of environment [11] among people. Literature has also proved that total cost of analysis (TCO) could be a key factor to understand the economic benefits of EVs that can be a step forward to EVs adoption [5, 8]. A few probability models have also been studied to know the limitation of TCO. A study concluded that total cost of ownership of a private EV is 2.5 times higher than that of combustion vehicle [12]. It is observed that limited driving range of EVs becomes more significant in hilly areas. Inadequate charging stations is another point of concern for the population that drives beyond 150 kms in one go, which is the range of EV in one full charge. And then, the time taken by the EVs to get charged again is 6–8 h [13]. A study conducted in 2014, for more than 25 countries, found that monetary benefits provided to EV customers are a backbone to stimulate public's interest in EVs [14]. Sweden, Norway, and California State are the countries that paid more emphasis on incentive policies and scored the top positions in the sale of EV market [15]. Norway, the Netherlands, and the State of California paid more emphasis on incentive policies and have the highest EV market share.

Table 2 Case study

	Electric vehicle (Mahindra e2o)	Petrol vehicle (Ford free style)
Mileage	120 km [16]	620 km [17]
Electricity/fuel—consumption	12 units (kWh)	40 L [17]
Energy/fuel—usage/km	12/120 = 0.1 units	0.064 L/km
Cost/unit—liter	Rs. 7.30	Rs. 80.43
Cost per km	7.30 × 0.10 = Rs. 0.73	Rs. 5.14
One day expenditure (considering 50 km/day)	50 × 0.73 = Rs. 36.50	Rs. 257.00
Monthly expenditure (25 days travel)	Rs. 912.50	Rs. 6425.00

3 Case Study

This is a case study shown in Table 2 that compares an electric vehicle, Mahindra e2o, and a corresponding petrol vehicle, Ford free style. Petrol prices taken for the analysis are of Delhi. Normally, an EV, once fully charged, can cover a distance of 120 km, while its counterpart petrol car can cover 620 km in one tank full. This case study has considered that an average distance covered by a car owner per day is 50 km. Based on the below analysis, it can be concluded that operational cost of EV per day is Rs. 36.50, which is much lower than the per day operational cost of a petrol car, which is Rs. 257.00. Author has not included maintenance and service charges in this case study, as these charges are not fixed and depend on the spare part charge, labor charge, etc. Even if these charges are added, they would further increase the difference in operational cost of both the vehicles as maintenance of EVs is considered to be negligible. This difference in cost goes on increasing with the usage of EV over the months and further years.

4 Limitations of EV for a Private Consumer

There are various factors that influence the decision of a private consumer to buy an electric vehicle:

- Average cost of electric cars in India is Rs. 13 lakhs as compared to an economical internal combustion engine car of Rs. 5 lakhs.
- Inadequate charging infrastructure is another concern for EVs. India has only 650 charging stations till 2019.
- An electric vehicle battery of 60 kWh takes approx. 6–8 h to get fully charged with a 7 kW charging point.

Fig. 2 TCO calculator

- Once fully charged, EV can cover a distance of 100–150 km, which is very less if compared to traditional combustion vehicles that can cover up to 600 km in one full tank.

5 Key Hindrance to EV

Price of EV is the prime factor for it is not being the choice among private car owners. For a buyer, while buying a car, the purchase price is the total cost of the car, but that is not the actual cost of owning a vehicle. There are number of other expenses like registration fee, road tax, car insurance, monthly fuel expanse, maintenance charges, etc. that a car owner has to incur. So, the total cost of ownership (TCO) is much different from the buying price of a car (Fig. 2).

It is to be noted that TCO is different for every owner. It is difficult to calculate exact TCO for any vehicle as it involves variable costs, but having a rough estimate is a better option than having no calculation of TCO.

6 Adaption of Electric Two and Three Wheelers

On the basis of TCO analysis, as shown in Fig. 3 [18], it is observed that the commercial two wheelers and three wheelers take the edge. On average, commercial two and three wheelers cover a distance of approximately 75 km to 100 km per day, respectively. As shown in Fig. 3, TCO for these EVs is lower as compared to their counterpart, combustion vehicles. The use of two wheelers in private sector, on the assumption that private two wheeler drives for a 25 km per day, electric model takes the edge over its counterpart petrol models, but if the same private consumer opts for higher price range two wheeler, then the TCO per km for this higher-range EV model would be higher compared to a petrol-based combustion vehicle.

Another study, depicted in Fig. 4, reveals that TCO of an electric vehicle is inversely proportional to its usage. As utilization of commercial vehicle is more as compared to private vehicle, hence, the TCO for commercial vehicle is also lower than their petrol/diesel counterparts, as shown in Fig. 4.

Comparison is based on the assumption that private vehicle travels an average of 25 km/day, while a commercial vehicle travels an average of 200 km/day [19].

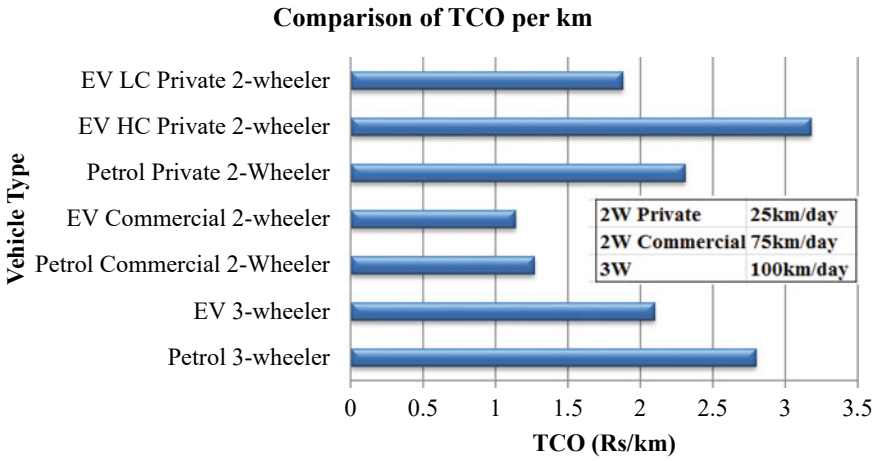

Fig. 3 Comparison of TCO/km

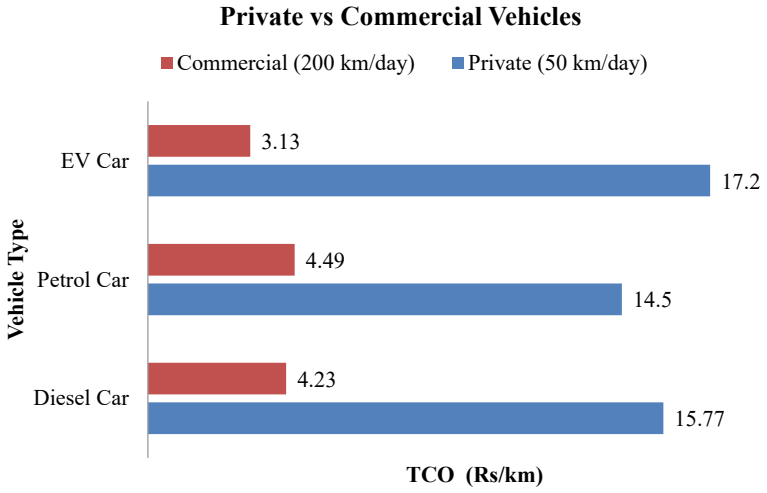

Fig. 4 Private versus commercial vehicles

Above discussion shows that growth and promotion of EVs in India will not be significant unless government makes policies and provides subsidies and other non-financial benefits to the private consumer. TCO analysis can be a key parameter both for policymakers as well as for the consumer [20]. Although Indian government has provided incentives to the EV customers under FAME II Scheme [21], like reduction of GST on electric vehicles from 12 to 5%, road tax, and registration fees of EVs are waived off, interest payment on loan taken for electric vehicle is tax free, and the TCO analysis can further help and provide an insight in estimation of the slab or

range of financial incentives that should be provided to EV customers to boost the interest and sale of EVs among the people. On the other hand, this analysis can help consumer in calculating the actual cost of vehicle that he will incur over a period of 5 or 10 years that can further incline him toward buying electric vehicles.

7 Conclusion

As expected from the trend, in India, demand for private vehicle would be escalating in upcoming years, emphasizing more on developing the policies, schemes that could enhance the EV sales, would benefit the economy and environmental as well. Non-financial incentives such as reserved parking, exemptions from permit restrictions, and exclusive bus lanes can be an additional advantage to financial incentives and drive preference for electric vehicles [22]. Incentives like these would help electric vehicles in overcoming at least one of its limitation of high purchase price and can be a choice among people due to its affordability [23, 24]. As proved above, the TCO/km decreases with the increase in distance covered per day, by providing exclusive bus lanes to the commercial EVs that would help them to avoid traffic jams and can cover more distance in lesser time. EVs are already competing petrol vehicles in two and three wheeler sectors, by providing non-monetary incentives that would help this already competitive sector to boom more.

References

1. Pandey A, Brauer M, Cropper ML, Balakrishnan K, Mathur P, Dey S, Turkgulu B, Kumar GA, Khare M, Beig G, Gupta T (2020) Health and economic impact of air pollution in the states of India: the global burden of disease study 2019. Elsevier Ltd, e25–38
2. Kosankar S, Khandar C (2014) A review of vehicular pollution in urban India and its effects on human health. J Adv Lab Res Biol 5(3):54–61
3. Sovacool BK, Abrahamse W, Zhang L, Ren J (2019) Pleasure or profit? Surveying the purchasing intentions of potential electric vehicle adopters in China. Trasp Res A policy Pract 124:69–81
4. Adnan N, Nordin SM, Rahman I, Rasli AM (2017) A new era of sustainable transport: an experimental examination on forecasting adoption behaviour of EVs among Malaysian consumers. Transp Res A Policy Pract 259–78
5. Leiven T (2015) Policy measures to promote electric mobility—a global perspective. Transp Res A Policy Pract 82:78–93
6. Berkeley N, Jarvis D, Jones A (2018) Analysing the take up of battery electric vehicles: an investigation of barriers amongest drivers in UK. Transp Res D Transp Environ 63:466–81
7. Skippon SM, Kinnear N, Lloyd L, Stannard J (2016) How experience of use influences mass driver's willingeness to consider a battery electric vehicle: a randomised controlled trial. Transp Res A Policy Pract 92:26–42
8. Sierzchula W, Bakker S, Maat K, Van Wee B (2014) The influence of financial incentives and other socio economic factors on electric vehicle adoption. Energy Policy Elsevier, vol 68(C), pp 183–194

9. Onat NC, Kucukvar M, Tatari O (2018) Well to wheel water footprins of conventional versus electric Vehicles in the United States: a state based comparative analysis. J Clean Prod 204:788–802
10. Xiong Y, Wang B, Chu CC, Gadh R (2018) Vehicle grid integration for demand response with mixer user model with decentralized optimization. Appl Energy 231:481–93
11. Committee MA special presentation by centre for science and environment, to the committee on auto fuel policy (nd). Retrieved from www.geospatialworld.net: https://www.geospatialworld.net
12. Mersky AC, Sprei F, Samaras C, Qian ZS (2016) Effectiveness of incentives on electric vehicle adoption in Norway. Transp Environ 46:56–58
13. Kumar RR, Kumar A (2020) Adoption of electric vehicle: a literature review and prospects for sustainability. J Clean Prod 2–2
14. Centre for Environment and Energy Development (2018). http://ceedindia.org/know-whatyou-breathe-air-pollution-statistics-forNothindian-cities. Retrieved from www.ceedindia.org: http://ceedindia.org/know-whatyou-breathe-air-pollution-statistics-forNothindian-cities
15. Arku RE, Birch A, Shupler M, Yusuf S, Hystad P, Brauer M (2018) Charaterizing exposure to household air pollution within the prospective urban rural epidemiology (PURE) Study. Environ Int 144:307–17
16. Mahindra Electric. Mahindra Electric Mobility Limited 2021 (2021). www.mahindraelectric.com. https://www.mahindraelectric.com/vehicles/e2oPlus/
17. Ford India. Ford Motor Company (2020). www.india.ford.com. https://www.india.ford.com/suvs/freestyle/.
18. Kumar P, Kanuri C (2020) Total cost of ownership of electric vehicles: implications for policy and purchase decisions. https://www.wricitiesindia.org/content/total-cost-ownership-electric-vehicles-implications-policy-and-purchase-decisions/
19. Gupta NS (2018) Indian commuters travel 35km/day says survey. The Times of India, 3 Mar 2018. Available at: https://timesofindia.indiatimes.com/business/india-business/indian-commuters-travel-35-km/day-says-survey/
20. Electric Power Research Institute, Total cost of ownership model for current plug-in electric vehicles. (2013)
21. Ministry of Heavy Industries & Public Enterprises FAME India Scheme. Press Information Bureau Government of India (2019)
22. Lebeau K, Lebeau P, Macharis C, Van Mierlo J (2013) How expensive are electric vehicles? A total cost of ownership analysis. In: World electric vehicle symposium and exhibition (EVS27). Barcelona, Spain, pp 1–12. https://doi.org/10.1109/EVS.2013.6914972
23. Pavan AM, Lughi V, Scorrano M (2019) Total cost of ownership of electric vehicles using energy from a renewable-based microgrid. In: 2019 IEEE milan powertech. Milan, Italy, pp 1–6. https://doi.org/10.1109/PTC.2019.8810736
24. Desreveaux A, Hittinger E, Bouscayrol A, Castex E, Sirbu GM (2020) Techno-economic comparison of total cost of ownership of electric and diesel vehicles. IEEE Access 8:195752–195762. https://doi.org/10.1109/ACCESS.2020.3033500

Development of Energy Measurement System for Electrical Vehicle Battery Using Arduino

Peeyush Garg, Deepika Bansal, Souvik Khan, and Siddharth Bhattacharya

Abstract Automobile sectors are shifting toward battery-powered electric vehicles from of fuel-based vehicles. Major drawbacks of fuel based vehicles are air pollution, sound pollution and uneven hike in petrol–diesel's prices. These tend the automobile sector to an alternate solution as electrical vehicles. The battery-based vehicles are free from air and sound pollution. The electric battery supplies energy to electrical motor, tends to move the vehicle. The existing e-bike and e-car are using diverse types of battery as source of power. Varieties of batteries have been used in electrical vehicle. The operating DC voltage and current in EVs are generally high, so an efficient system is required for current, voltage, power, and energy measurement. Present work is to create an electrical energy measurement device, which measures instantaneous voltage, current and power consumed, which is apparently supplied by the electrical battery. The voltage Arduino-based measurement system is used to acquire electrical variables with the help of arrangement of voltage sensor and current sensors. In addition, a temperature measurement sensor is used to measure battery temperature as a safety parameter. All electrical and physical variables are displayed on LCD screen, also can be used for further recording and analysis.

Keywords EV battery · Current sensor · Voltage sensor · Energy measurement · Arduino

1 Introduction

Due to regular uses of petrol and diesel-operated automobile produce a lot of carbon dioxide and other pollutant gasses, these gasses are discharged to the atmosphere, which causes pollution and greenhouse gasses. Also causes various serious health and

P. Garg (✉) · S. Khan · S. Bhattacharya
Department of Electrical Engineering, Manipal University Jaipur, Jaipur, Rajasthan, India
e-mail: peeyush01garg@gmail.com

D. Bansal
Department of Electronics and Communication Engineering, Manipal University Jaipur, Jaipur, Rajasthan, India

S. Dwivedi et al. (eds.), *Flexible Electronics for Electric Vehicles*, Lecture Notes in Electrical Engineering 863, https://doi.org/10.1007/978-981-19-0588-9_45

environment issue. So, electric vehicles are being considered as a best alternative to the traditional IC engine vehicles and an effective measure in the direction of saving our mother earth and creating a pollution free environment for the future generation. The electric vehicles are being developed because they produce zero pollution and are cost-effective as compared to other vehicles and due to advancement of battery technology in past few years and efficiency of motors. Now, EV's are moving toward to become a reliable mean of transportation. Varieties of batteries such as lithium ion (Li-ion), molten salt (Na-$NiCl_2$), nickel metal hydride (Ni–MH), and lithium sulfur (Li-S) used in electric vehicle now a days. Lithium-ion battery is grasping the market due to effective performance and capacity [1, 2].

Electric vehicle generally excited by high-voltage lithium-ion battery sets. These batteries have higher energy density than other batteries, also have some risk factors of catching fire under uncommon situations. It is important to operate the EV batteries in defined safe limits to guarantee the protection of users and the vehicles.

In general, an electrical vehicle comprises different electrical component like battery, power electronics, electric motor, high voltage cable, and integration of on-board charging units [3, 4]. The energy measurement of these component is very crucial for reducing energy losses and can enhance the performance of the battery charging. The electric vehicle battery energy can utilize in best way by digitally monitoring each component energy. The overall performance of the EV is depending on how the vehicle been driven. The EV charging station is not available like petrol, diesel, and gas pumps, so the measurement of the battery energy is especially important for reaching the destination based on energy available in the battery [5].

2 Methodology

The simplified electrical vehicle system comprises the battery unit, motor unit, and wheel arrangement as shown in Fig. 1. The battery unit comprises the battery, electric cables, and integration of on-board charging units. The motor unit has power electronics, electric motor. The wheel arrangement is responsible for the movement of vehicle. The battery unit provides electrical power to the motor unit; motor unit converts electrical energy to mechanical energy. Then, the rotational mechanical energy provides to wheel unit.

The proposed system is energy measurement unit, which is connected after the battery unit and before motor unit as shown in Fig. 2. The proposed system is an additional attachment in between the battery unit and the plug. The system is portable,

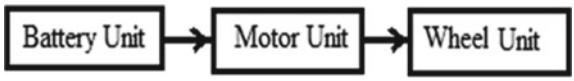

Fig. 1 General block diagram of electrical vehicle system

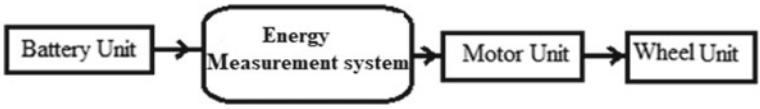

Fig. 2 Block diagram of proposed energy measurement unit

durable, and easy to use. The controller used in measurement system is Arduino Uno. The systematic pin diagram of Arduino Uno board is shown in Fig. 3.

The energy measurement unit is primarily used to measure the current through and voltage across the battery. Further, it is used to calculate the power and energy consumption. The instantaneous power is multiplication of instantaneous current and instantaneous voltage. The instantaneous energy is the accumulative power consumption over a period [6, 7].

$$p(t) = v(t) \times i(t)$$

$$E(t) = \int p(t)\mathrm{d}t$$

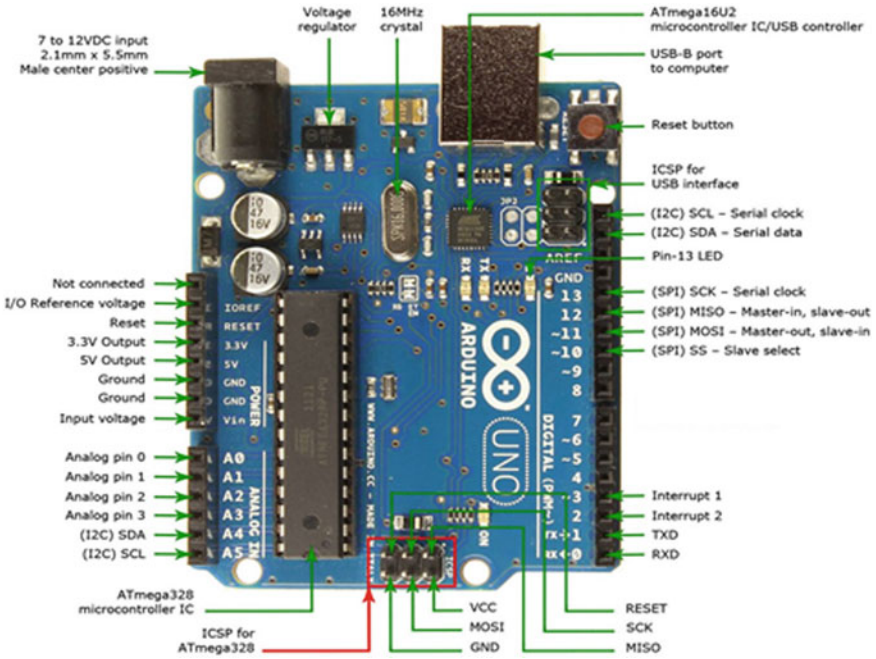

Fig. 3 Systematic pin diagram of Arduino Uno board [8]

The proposed system continuously measures system variables such as voltage, current, and temperature for the EV battery. This system can be further used to ensure the safe operation over the time by adjust cooling and triggering other safety schemes to close down operations and reduce the risk associated to battery or EV.

3 Implementation

The energy measurement unit uses Arduino Uno controller board, LCD panel, two voltage detector sensors, and two and more current sensors [5, 6]. The current sensors and voltage sensors are connected to Arduino Uno for battery current and battery voltage measurement, respectively. The voltage detector sensor is connected in parallel to the battery terminal, and the arrangement of current sensors is connected in series of the battery and motor unit. Along with these sensors, a temperature sensor is connected to measure the temperature of battery outer surface. The measured values or sensors outputs are fetched into Arduino Uno board. An LCD panel is connected to the digital pins of Arduino board to display the sensors outputs, temperature, and energy consumed, etc. A push button switch is connected to the digital pin of the Arduino board for the purpose of system reset and change the display screen of the LCD panel.

3.1 Controller Board—Arduino Uno

Arduino Uno uses ATmega328P, which is a microcontroller board. It comprises total 6 analog inputs, 14 digital input/output pins (of which 6 can be used as PWM outputs), and clock frequency of 16 MHz, one built-in LED and a reset button, etc. Arduino Uno is a perfect choice for various smart application such as data acquisition and home automation [8–10].

Availability of sufficient number of analog pins makes it a perfect choice for energy measurement device for EV battery system.

The four analog pins $A0, A1, A2$, and $A3$ are connected to output of voltage sensor, output of current sensor 1, output of current sensor 2, output of temperature sensor, respectively. These sensors are powered by +5 V, from available supply pins +5 V and GND on Arduino Uno board.

Along with these, a push button switch and LCD panel are connected to Arduino Uno board by mean of digital pins. LCD panel is used to display the measurement results.

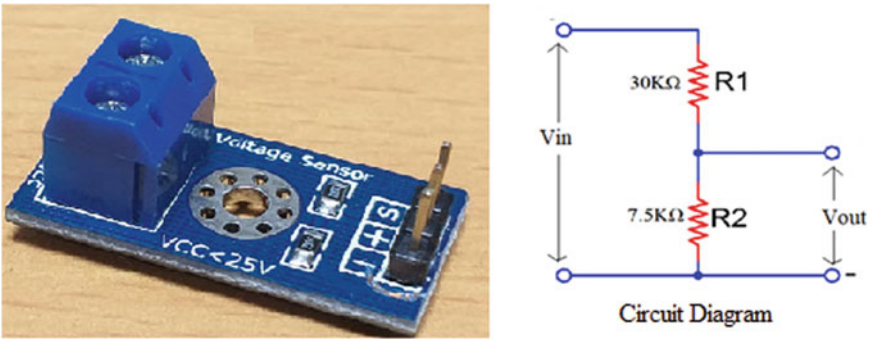

Fig. 4 Voltage detection sensor module

3.2 Voltage Measurement

Generally, existing electrical vehicle battery generates a voltage range of 48 V, and current is in range of 50–60 A for the battery of 3 kW. The battery voltage can be measured using voltage divider method, where the voltage range of 50 V is converted in to in the range of 2.5 V with the help of two voltage sensor of range 25 V. The first voltage sensor is connected in parallel of the battery terminal through plug, which convert the battery output in to divide by 5. Next, voltage sensor again used to measure the output voltage of first voltage sensor, means these two voltage sensor arrangement converts the battery voltage with the gain of 0.04 V/V. Then, the modulated signal of ranging 2 V is fed into analog pin *A*0 of Arduino Uno board. These voltage sensors arrangement also provides the over-voltage circuit protection (Fig. 4).

3.3 Current Measurement

The battery supplied DC current in the range of 50–60 A. In this paper, a parallel arrangement of two current sensors ASC712 of range 30 A is used. The two current sensors are connected in parallel, and the arrangement is connected in series of EV battery. The screw-type terminals of the ASC712 current sensor module are connected in parallel of each other, and arrangement is further cascaded with the motor and power supply unit as shown in Fig. 5.

The Vout pin of the current sensors is connected to analog pin (*A*1 and *A*2) of Arduino board. The maximum possible current in a branch of parallel current sensor arrangement is 30 A, which can effectively measure by a current sensor. The ASC712 works on the principle of Hall Effect and having internal overcurrent protection.

In place of ASC712, non-contact type of current sensor WCS1700 can also use for current measurement. It is an overcurrent detection sensor with short-circuit protection detection module. The current sensor module mainly comprises WCS1700

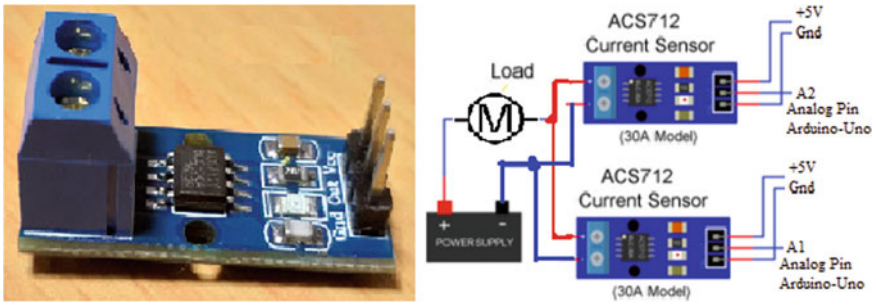

Fig. 5 Current sensor ASC712 and current measurement arrangement

and operational amplifier LM393. The range of current detection is DC $\pm$ 70 A AC: 50 A, and current measured resolution is 32 mV/A.

3.4 Temperature Measurement

The temperature sensor LM35 is place on the outer surface of battery to measure the battery temperature. The V_{out} pin of the sensor is connected on $A4$ port (analog pin) of the Arduino board. The sensor LM35 is powered by $+5$ V, and it is a precision integrated-circuit temperature device.

3.5 Display Unit

A 32×2 LCD is connected to Arduino board to display the results. Register select and enable pins of LCD are connected to the digital pins $D2$ and $D3$, respectively. Digital inputs of the LCD panels are connected from pin $D4$ to pin $D7$ digital I/O pin of Arduino board. A 10 KΩ POT is connected to pin 3 of LCD, and its V_{cc} is connected to $+5$ V, and GND is connected to GND terminal of board.

A digital switch $S1$ is also connected to the digital I/O pin 1 of Arduino board for the purpose of reset the LCD display and change the LCD display screen. The system is programmed in such a way that LCD screen can be changed by pressing digital switch $S1$. The details for the same are given in Table 1.

4 Results Discussion

The designed system is used to measure the real-time current through and voltage across the battery terminal and display on LCD panel initially as shown in Fig. 6. The

Table 1 Display modes on LCD panel

Switch mode	Descriptions
*M*1	Display instantaneous battery voltage and battery current
*M*2	Display time, power consumed, and total energy consumed
*M*3	Display battery temperature

Fig. 6 LCD panel of energy measurement unit

LCD is used to display real-time current, voltage, temperature, power, and energy consumption. The designed energy measurement system is tested on lithium-ion battery, and result displayed on the LCD as shown in Fig. 6.

5 Conclusion

The energy measurement system can be used with any electrical vehicle with suitable sensors selection. The Arduino IDE environment provides a suitable method to acquire the measured values. The measured information can be easily stored and further used to analyze the battery health, alarming, and safety measures. In addition, the proposed system also measures the analog signals like temperature around motor and speed of motor with minor modifications.

References

1. Manzetti S, Mariasiu F (2015) Electric vehicle battery technologies: from present state to future systems. Renew Sustain Energy Rev 51:1004–1012
2. Dhameja S (2001) Electric vehicle battery systems. Elsevier
3. Xingzhe H, Wenli C, Xuedan T, Jie H (2017) Study on on-line detection scheme of DC electric energy metering for electric vehicles. In: 2017 13th IEEE international conference on electronic measurement & instruments (ICEMI), Yangzhou, pp 139–144
4. Bukya M, Kumar R (2020) Safety consideration and design of high voltage cable for electric vehicle. In: International conference on power electronics & IoT applications in renewable energy and its control (PARC-2020), Mathura, India, Feb 28–29
5. Parulekar S, Holmukhe RM, Mehta S, Raj A, Raj R, Karandikar PB (2017) Challenges in transition from internal combustion vehicles to electric vehicles in India by 2030. In: 2017 international conference on energy, communication, data analytics and soft computing (ICECDS). Chennai, pp 779–784

6. Fransiska RW, Septia EMP, Vessabhu WK, Frans W, Abednego W (2013) Electrical power measurement using arduino uno microcontroller and labview. In: 2013 3rd international conference on instrumentation, communications, information technology and biomedical engineering (ICICI-BME), pp 226–229
7. Chung TM, Daniyal H (2015) Arduino based power meter using instantaneous power calculation method. ARPN J Eng Appl Sci 10(21)
8. Arduino CC (2015) Arduino—introduction [Online] Available: http://arduino.cc/en/Guide/Introduction. Accessed 25 Feb 2015
9. Bukya M, Bajaj A, Garg P, Saraswat A (2020) Design and implementation of arduino based control system for power management of household utilities. In: Kalam A, Niazi K, Soni A, Siddiqui S, Mundra A (eds) Intelligent computing techniques for smart energy systems. lecture notes in electrical engineering, vol 607. Springer, Singapore. Print ISBN: 978-981-15-0213-2
10. Garg P, Agrawal S, Yiyang W, Saraswat A (2018) Design and implementation of interactive home automation system using LabVIEW. In: Somani A, Srivastava S, Mundra A, Rawat S (eds) Proceedings of first international conference on smart system, innovations and computing. Smart innovation, systems and technologies, vol 79. Springer, Singapore

A Facile Route for the Synthesis of Pure & Ag-Doped ZnO for Dye-Sensitized Solar Cell Application

Anupam Agrawal, Shahbaz A. Siddiqui, and Amit Soni

Abstract In this work, the synthesis of zinc oxide (ZnO) and silver-doped zinc oxide (Ag-ZnO) and its application in dye-sensitized solar cell (DSSC) have been described. For the synthesis of ZnO and Ag-ZnO, inexpensive and versatile chemical co-precipitation method was used. The X-ray diffraction (XRD), UV–Visible (UV–Vis), and scanning electron microscopy (SEM) were utilized to characterize the synthesized ZnO and Ag-ZnO. These synthesized materials were employed in DSSC as *n*-type layer in conjugation with ruthenium-based dye (N719). The photovoltaic (PV) parameters of ZnO and Ag-ZnO-based DSSC were obtained by current–voltage measurement. The result showed that the power conversion efficiency (PCE) of Ag-ZnO-based (2.77%) DSSC was improved as compared to pure ZnO-based DSSC (2.39%).

Keywords Ag-doped ZnO · Dye-sensitized solar cell · Chemical co-precipitation

1 Introduction

Due to their low cost and relatively good PV efficiency, DSSCs attracted considerable interest [1, 2]. The DSSC includes semiconductor layer, dye, electrolyte, and platinum or graphite-coated counter-electrode. The key component of DSSC is semiconductor oxide having characteristics of wide band gap with a large surface area and high electron mobility [3, 4]. At present, several semiconductor oxides are used such as SnO_2, Nb_2O_5, TiO_2, and ZnO. The highest PCE of 14.3% is obtained with TiO_2 semiconductor oxide sensitized with ruthenium-based dye [5]. Despite this, ZnO is extensively explored due to its distinctive qualities such as low expense,

A. Agrawal (✉) · A. Soni
Department of Electrical Engineering, Manipal University Jaipur, Jaipur, Rajasthan, India

A. Soni
e-mail: amit.soni@jaipur.manipal.edu

S. A. Siddiqui
Department of Mechatronics Engineering, Manipal University Jaipur, Jaipur, Rajasthan, India
e-mail: shahbazahmed.siddiqui@jaipur.manipal.edu

S. Dwivedi et al. (eds.), *Flexible Electronics for Electric Vehicles*, Lecture Notes in Electrical Engineering 863, https://doi.org/10.1007/978-981-19-0588-9_46

suitable band gap (3.2–3.3 eV), low resistance, reduced recombination rate, and high illumination-capturing capabilities [6, 7]. Considering the properties of ZnO thin film, ZnO is employed in several technologies such as PV cell, anti-reflective coating, gas sensing, transparent conductive material, piezo-electric system, and photo-catalyst [8]. Doping of metals and non-metals such as Cu, Co, Ni, Mg, Sn, Al, Pd, Ag, C, S, and N are incorporated in pure ZnO to improve the properties of ZnO thin film [9]. Insertion of Ag in ZnO reduces the recombination rate by creating a new energy level near conduction band of ZnO [10] and enhances PV performance of ZnO thin film [11].

This paper explains the simple synthesis procedure of ZnO and Ag-ZnO with their optical and morphological properties. Detail method of ZnO and Ag-ZnO-based DSSC fabrication via screen-printing method is described. PV performance of different DSSCs is also studied by *I–V* measurement.

2 Experimental Details

2.1 Synthesis of ZnO and Ag-Doped ZnO

We required $Zn(NO_3)_2.6H_2O$ (zinc nitrate hexahydrate) and NaOH (sodium hydroxide), EtOH (ethanol), and DI (distilled) water to proceed the synthesis of ZnO. In the beginning, 7.85 gm of $Zn(NO_3)_2.6H_2O$ (Merck) was dissolved in 125 ml of DI water and called solution 1. Then, 1.12 gm of NaOH (Loba Chemical) was mixed in 125 ml DI water and called solution 2. Now, drop by drop method mix solution 1 into solution 2 under the continuous stirring for six hours. The resulting mixer was centrifuged, and off-white-colored precipitate was extracted. Then, the resultant precipitate was washed with blend of DI water and EtOH (vol. 9:1). After that, precipitate was dried at 80°C for eleven hours. Then, dried product was calcined for two hours at 600°C in order to get ZnO powder. For the synthesis of Ag-ZnO, an additional chemical required was $AgNO_3$ (silver nitrate). 2.375 gm of $AgNO_3$ (Merck) was added in 125 ml of DI water and called solution 3. Now, drop by drop method add solution 1 and 3 in solution 2 under the continuous stirring for six hours. The same process was repeated such as centrifuged, washing, and then calcined at 600°C to get the Ag-ZnO powder.

2.2 DSSC Cell Assembly

By screen-printing technique, ZnO and Ag-ZnO-based electrodes were prepared [12]. This technology involved multiple depositions [13] of the semiconductor oxide film on the fluorine-doped tin oxide (FTO) glass substrate, as per the thickness requirements. Several processes have been followed to make the DSSC: FTO glass

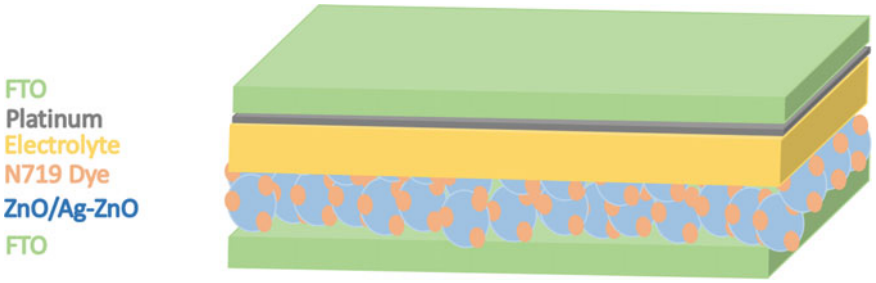

Fig. 1 Detailed structure of DSSC

substrates were cleaned with soap solution, followed by DI water and methanol in ultrasonicator for fifteen minutes each. Now, with help of screen-printing technique ZnO and Ag-ZnO-based paste was deposited on washed FTO substrate. A well-defined protocol was conducted to prepare ZnO and Ag-ZnO paste made from synthesized ZnO and Ag-ZnO powder, DI water, EtOH, terpineol anhydrous (Sigma Aldrich), and ethyl cellulose (Sigma Aldrich) [13]. After each deposition of the semiconductor oxide layer, FTO was held in the ethanol container for five minute proceeded by annealing at a temperature of 110°C for five minutes. After deposition of sixth layer, deposited FTO substrate was calcined at 500°C for thirty minutes. Then, calcined electrode was immersed into *N*719 dye (Sigma Aldrich) solution (tert-butyl alcohol:acetonitrile (vol 1:1)) (Loba Chemical) for approximately twenty hours. Another FTO glass substrate was used as a counter electrode, and the cleaning procedure was similar as discussed above. Now, a thin film of platinum (Pt) was coated on FTO glass substrate through drop casting of H_2PtCl_6 (Rankem Chemical) solution, and a hot-air treatment at 400°C for fifteen minutes was given. The dye-adsorbed electrode and Pt-coated electrode were closed by Bynel polymer (50 micron thick). Then, filling of electrolyte was carried out in vacuum chamber through a 0.6 mm hole in counter-electrode. The liquid electrolyte was prepared from iodine (0.03 M), 4-tert-butylpyridine (0.5 M) (Sigma Aldrich), guanidinium thiocyanate (0.1 M) (Sigma Aldrich), and BMII (0.6 M) (Sigma Aldrich) in a solution of acetonitrile:valeronitrile (vol 85:15) [14]. Finally, ZnO and Ag-ZnO-based DSSCs were fabricated, and complete structure of solar cell is displayed in Fig. 1.

3 Results and Discussion

XRD patterns for synthesized ZnO and Ag-ZnO by chemical co-precipitation method were recorded between the angle range 10 and 90° is displayed in Fig. 2. Phase purity, shape, and crystallite structural parameters of synthesized ZnO and Ag-ZnO were determined by XRD pattern. All the peaks observed in the XRD pattern are synonymous with those mentioned in other research works of ZnO and Ag-ZnO [15, 16]. The hkl planes (100), (002), (101), (102), (110), (103), and (112) are allocated

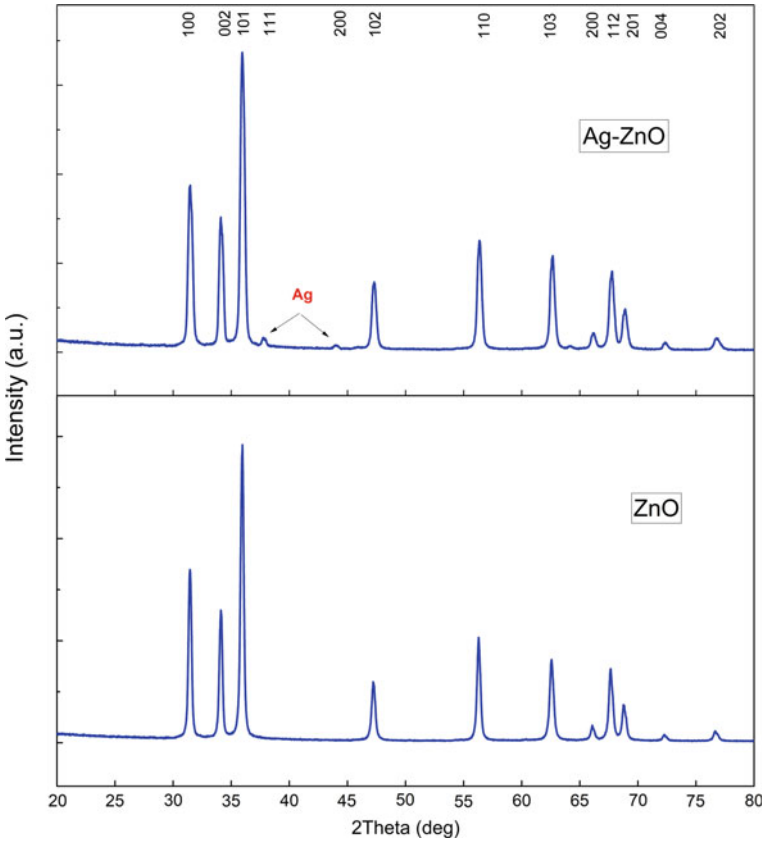

Fig. 2 XRD pattern of ZnO and Ag-ZnO calcined at 600° C

to the peaks that occurred at 2theta (2θ) values of 31.49°, 34.14°, 35.98°, 47.30°, 56.37°, 62.64°, and 67.75°, respectively, for pure ZnO. For Ag-ZnO, XRD patterns display small intensity peaks at 2θ values of 37.81° and 44.02° for hkl planes (111) and (200).

The crystallite size of the synthesized ZnO and Ag-ZnO was determined by Debye Scherer's formula is given by:

$$D = K\lambda/\beta\cos\theta \tag{1}$$

where D signifies the crystallite size of the particles, K represents Debye diffraction constant (0.9), λ signifies the CuK_{α} radiation wavelength (0.1549 nm), β denotes full diffraction width at half intensity maximum measured in radian, θ symbolizes the diffraction angle and calculated from 2θ values.

The 101 plane is the extreme plane that shows the ZnO growth pattern and similarly 111 plane for Ag-ZnO. The crystallite size is 19.527 nm according to 101 plane,

and average crystallite size for Ag-ZnO through all plane is 20.206 nm. Different structural parameters for ZnO and Ag-ZnO calculated by XRD pattern are shown in Table 1.

The SEM used for assessing the morphology of the ZnO and Ag-ZnO powder is displayed in Fig. 3. The SEM image of pure ZnO displays the clusters of small particles that are hexagonal and spherical in shape. The SEM images clearly show the significant growth of size and transition in the shape of the Ag-doped particles. Ag-ZnO samples have rod or capsule-shaped structure.

Optical absorption spectra of ZnO and Ag-ZnO thin film are shown in Figs. 4 and 5, respectively. The optical band gap (E_{opt}) is determined by the Tauc equation:

$$\alpha h\vartheta^n = A\left(h\vartheta - E_{opt}\right) \tag{2}$$

Table 1 Structural parameters for ZnO and Ag-ZnO calculated by XRD

S. No.	2θ (deg)	FWHM (deg)	hkl plane	Crystallite size (nm)
1	31.49	0.4398	100	18.764
2	34.14	0.4034	002	20.597
3	35.98	0.4277	101	19.527
4	37.81	0.4011	111 (Ag-ZnO)	20.940
5	44.02	0.4462	200 (Ag-ZnO)	19.200
6	47.30	0.4392	102	19.747
7	56.37	0.4391	110	20.524
8	62.64	0.4542	103	20.472
9	67.75	0.4616	112	20.728

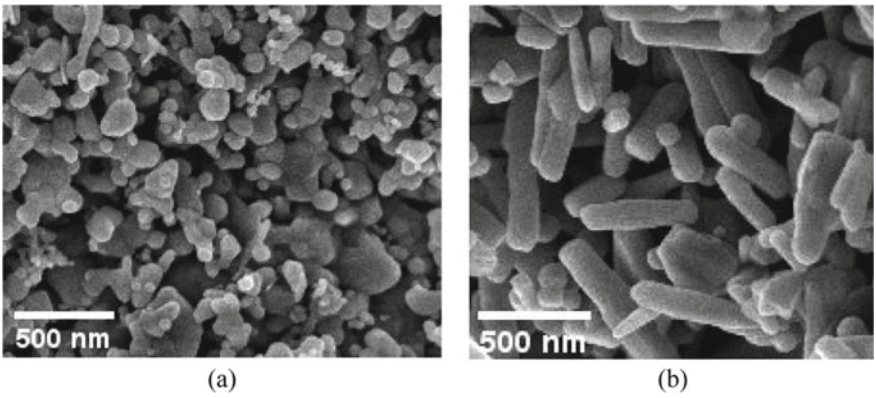

Fig. 3 SEM image of **a** ZnO and **b** Ag-ZnO

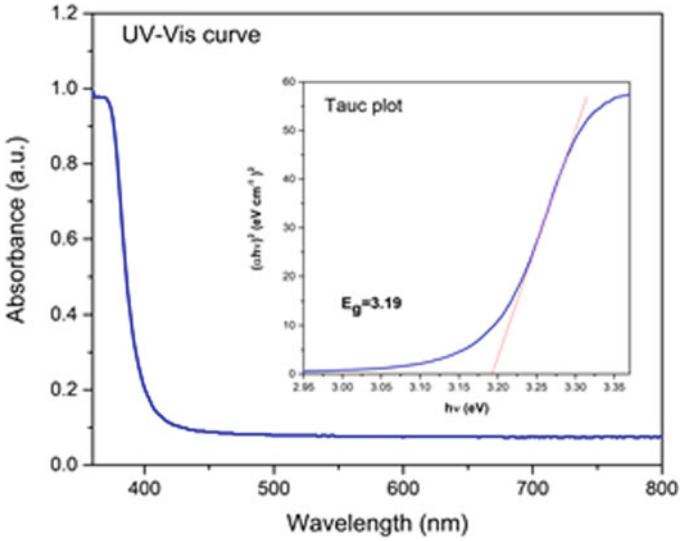

Fig. 4 UV–Vis and Tauc plot for pure ZnO

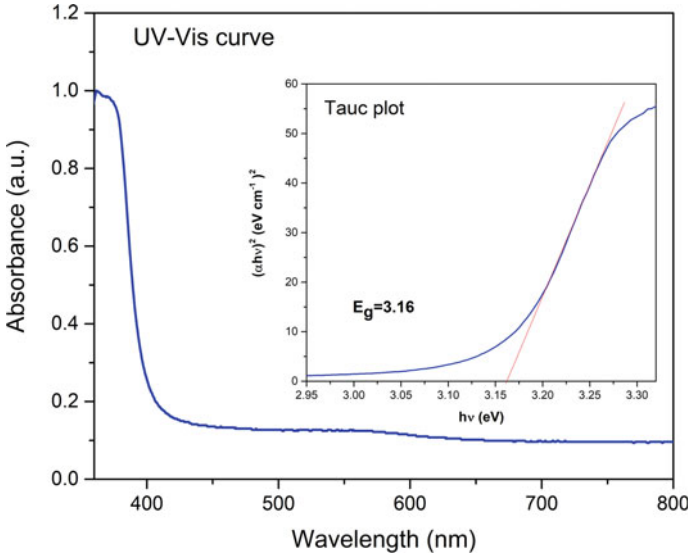

Fig. 5 UV–Vis and Tauc plot for pure Ag-ZnO

where $h\vartheta$ indicates the photon energy and α denotes the absorption coefficient, A is a constant (material transition probability), n is also a constant ($n = 2$ if direct transition or $n = 1/2$ if indirect transition. The Tauc plot between $(\alpha h\vartheta)^n$ and $h\vartheta$ for ZnO and Ag-ZnO thin film is shown in Figs. 4 and 5. Extrapolation of the linear section provides the E_{opt} values of 3.19 eV and 3.16 eV for the ZnO and Ag-ZnO thin film. The obtained E_{opt} values are suitable for the use of PV materials [17].

The PV parameters of ZnO and Ag-ZnO-based DSSCs were estimated via I–V measurement instrument and shown in Table 2. Figure 6 displayed the current density–voltage plots of ZnO and Ag-ZnO-based DSSC. The efficiency of Ag-ZnO-based DSSC is better than ZnO-based DSSC. Here, the area of DSSC is 0.28cm^2. Due to the incorporation of Ag dopant into the crystal lattice of ZnO, which improves the photoanode film quality and reducing the band gap of ZnO film to the visible region. Therefore, it enhances the Ag-ZnO film conductivity resulting in higher current density.

Table 2 PV parameters of different DSSCs

S. No.	DSSC	PCE (%)	J_{SC} (mA/cm^2)	V_{OC} (V)	FF (%)
1	ZnO based	2.39	5.19	0.74	59.89
2	Ag-doped ZnO based	2.78	5.66	0.70	69.49

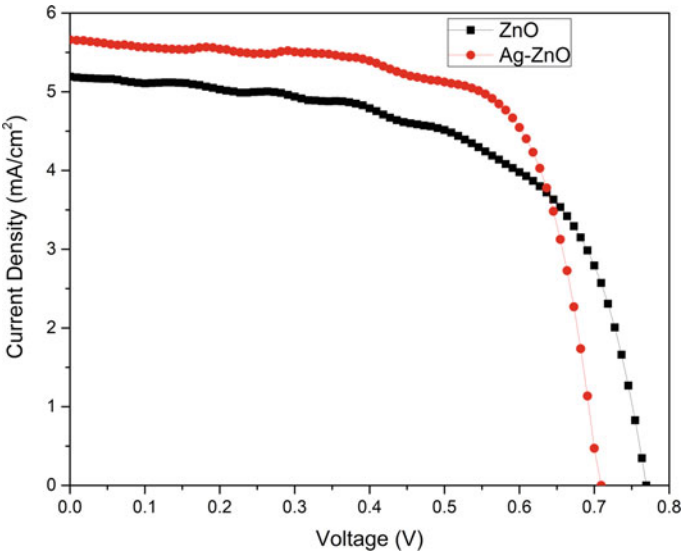

Fig. 6 J–V curve of ZnO and Ag-ZnO-based DSSC

4 Conclusion

ZnO and Ag-ZnO have been synthesized using chemical co-precipitation method. Thin-film UV–Vis absorption spectra of ZnO and Ag-ZnO give the optical band gap of 3.19 eV and 3.16 eV, respectively. Decrement in the band gap of ZnO was observed by doping of Ag which enhance the absorption of visible light for dye. The XRD pattern studies revealed the average crystallite size of around 20 nm for ZnO and Ag-ZnO. The doped Ag material had a significant effect on the shape of the surface morphology which seemed to be rod shaped in SEM analysis. Now, we have successfully designed ZnO and Ag-ZnO-based DSSC by screen-printing technique. PV performance of Ag-ZnO-based DSSC (PCE = 2.78, J_{sc} = 5.66 mA/cm^2, V_{OC} = 0.70 V and FF = 69.49%) is better than the pure ZnO-based DSSC (PCE = 2.39, J_{sc} = 5.19 mA/cm^2, V_{OC} = 0.74 V and FF = 59.89%).

Acknowledgements The authors would like to thank sophisticated analytical instrument facility (SAIF), Manipal University Jaipur, Jaipur, India and Department of Physics, Banasthali Vidhyapeeth, Tonk, India for allowing use of field-emission scanning electron microscope (FESEM) and XRD characterization facilities, respectively.

References

1. O'regan B, Grätzel M (1991) A low-cost, high-efficiency solar cell based on dye-sensitized colloidal TiO_2 films. Nature 353(6346):737–740
2. Shaikh JS, Shaikh NS, Mali SS, Patil JV, Pawar KK, Kanjanaboos P, Hong CK, Kim JH, Patil PS (2018) Nanoarchitectures in dye-sensitized solar cells: metal oxides, oxide perovskites and carbon-based materials. Nanoscale 10(11):4987–5034
3. Fabbiyola S, Kennedy LJ (2019) Bandgap engineering in doped ZnO nanostructures for dye sensitized solar cell applications. J Nanosci Nanotechnol 19(5):2963–2970
4. Zhang Q, Chou TP, Russo B, Jenekhe SA, Cao G (2008) Aggregation of ZnO nanocrystallites for high conversion efficiency in dye-sensitized solar cells. Angew Chem 120(13):2436–2440
5. Kakiage K, Aoyama Y, Yano T, Oya K, Fujisawa J-I, Hanaya M (2015) Highly efficient dye-sensitized solar cells with collaborative sensitization by silyl-anchor and carboxy-anchor dyes. Chem Commun 51(88):15894–15897
6. Vittal R, Ho KC (2017) Zinc oxide based dye-sensitized solar cells: a review. Renew Sustain Energy Rev 70:920–935
7. Agrawal A, Siddiqui SA, Soni A, Sharma GD, Shrivastava DR (2020) ZnO nanoparticles based dye sensitized solar cell: fabrication and characterization. In AIP conference proceedings, AIP Publishing LLC 2294(1), p 030005
8. Lanjewar M, Gohel JV (2017) Enhanced performance of Ag-doped ZnO and pure ZnO thin films DSSCs prepared by sol-gel spin coating. Inorg Nano-Metal Chem 47(7):1090–1096
9. Ong CB, Ng LY, Mohammad AW (2018) A review of ZnO nanoparticles as solar photocatalysts: synthesis, mechanisms and applications. Renew Sustain Energy Rev 81:536–551
10. Padmavathy N, Vijayaraghavan R (2008) Enhanced bioactivity of ZnO nanoparticles an antimicrobial study. Sci Technol Adv Mater 9(3):035004
11. Thongsuriwong K, Amornpitoksuk P, Suwanboon S (2012) Photocatalytic and antibacterial activities of Ag-doped ZnO thin films prepared by a sol–gel dip-coating method. J Sol-Gel Sci Technol 62(3):304–312

12. Kroon JM, Bakker NJ, Smit HJP, Liska P, Thampi KR, Wang P, Zakeeruddin SM, Grätzel M, Hinsch A, Hore S, Würfel U (2007) Nanocrystalline dye-sensitized solar cells having maximum performance. Prog Photovoltaics Res Appl 15(1):1–18
13. Ito S, Chen P, Comte P, Nazeeruddin MK, Liska P, Péchy P, Grätzel M (2007) Fabrication of screen-printing pastes from TiO2 powders for dye-sensitised solar cells. Prog Photovoltaics Res Appl 15(7):603–612
14. Lyons C, Dev P, Maji P, Rathi N, Surolia PK, Byrne O, Xiao X, English NJ, Magner E, MacElroy JMD, Thampi KR (2018) Silicon-bridged triphenylamine-based organic dyes for efficient dye-sensitised solar cells. Sol Energy 160:64–75
15. Dias HB, Bernardi MIB, Marangoni VS, de Abreu Bernardi AC, de Souza Rastelli AN, Hernandes AC (2019) Synthesis, characterization and application of Ag doped ZnO nanoparticles in a composite resin. Mater Sci Eng C 96:391–401
16. Chitradevi T, Lenus AJ, Jaya NV (2019) Structure, morphology and luminescence properties of sol-gel method synthesized pure and Ag-doped ZnO nanoparticles. Mater Res Express 7(1):015011
17. Kumar R, Umar A, Kumar G, Nalwa HS, Kumar A, Akhtar MS (2017) Zinc oxide nanostructure-based dye-sensitized solar cells. J Mater Sci 52(9):4743–4795

Designing and Implementation of a Solar PV Station for Electric Vehicle Charging: PV–EV Charging

Bhuwan Pratap Singh, Sunil Kumar Goyal, Shahbaz Ahmed Siddiqui, and Amit Saraswat

Abstract The green (renewable) energy-based transportation system is adopted worldwide in the past few years. The reason behind this fact is the alarming situation of global warming. However, the sustainable deployment of this new transportation system on a large scale is undeniably a challenging task. Since, the electric vehicles (EVs) are commercialized recently and are available for the consumers. Hence, an interesting option to charge the EVs with the application of solar photovoltaic system (PVS) came out recently, and it offers various economic and technical opportunities. The problem of greenhouse gases due to the internal combustion (IC) engines may be minimized by combining the low-carbon PV power generation with the emission-free EVs. This paper proposed a methodology for charging an EV through PVS (PV–EV charging) with optimized power output. The power generation requirement for charging EV has been estimated on behalf of the technical and performance specifications provided by the manufacturers of various cars (EV-variant) available in the Indian market. The MPPT charge controller is implemented with the DC–DC boost converter to maximize the power output of solar PVS for more effective charging of EVs. The simulation setup is developed in MATLAB/Simulink environment, and the system operations are tested and analyzed under different operating conditions.

Keywords Photovoltaic system (PVS) · PV–EV charging · Stand-alone PVS charging · PV charging station

B. P. Singh · S. K. Goyal (✉) · S. A. Siddiqui · A. Saraswat
Manipal University Jaipur, Jaipur, Rajasthan, India
e-mail: sunilkumar.goyal@jaipur.manipal.edu

B. P. Singh
e-mail: halobhuwan@gmail.com

S. A. Siddiqui
e-mail: shahbazahmed.siddiqui@jaipur.manipal.edu

A. Saraswat
e-mail: amit.saraswat@jaipur.manipal.edu

S. Dwivedi et al. (eds.), *Flexible Electronics for Electric Vehicles*, Lecture Notes in Electrical Engineering 863, https://doi.org/10.1007/978-981-19-0588-9_47

1 Introduction

In the last decade, the result of carbon emission on global warming and running out of limited availability of petroleum are the two fundamental issues emerged in terms of energy throughout the world. The non-renewable sources of energy production are fossil fuels, becoming too environmentally damaging to retrieve and much expensive these days, since, their availability is finite and will eventually disappear. Though, many countries in the world still rely heavily on petroleum, oil, natural gas, and coal for their energy production. On the other hand, solar, wind, and various other renewable energy sources (RES) are abundantly available everywhere and will never vanish out. The energy received from the RES never results in carbon emission, does not pollute the air and water, and hence, it is mostly known as "green energy" or "clean energy" [1].

Most of the RES comes either from the wind or sun, directly or indirectly. Solar energy (energy received from the sun) can be directly used in multiple applications such as lightening homes, heating, cooking, solar irrigation systems, solar power generation systems, solar cooling, electric vehicle charging, street light operations, electricity generation, and in a variety of commercial and industrial uses [2].

The advancements in the battery technologies and the need of a green energy-based sustainable transportation system are the keys to adopt EVs as a most feasible mode of transportation system. The energy storage system (battery) need to be deployed at the charging station to smooth out the fluctuating power output of solar PVS due to their intermittent nature [3]. To make EVs more feasible than IC engine-based vehicles, the leveraging concept for battery pack should be introduced and it would be helpful. Therefore, solar PV-based charging system to be used in charging station of EV charging which is very interesting and effective utilization of solar energy.

In this paper, the power requirement(s) have been identified to charge the EV on behalf of the technical specifications provided for the available electric vehicles in India by their manufacturers. Initially, an assumption has been made regarding the per day average utilization of vehicle, and then the power required per day for its charging is calculated. In the second stage, a stand-alone solar PVS is designed in MATLAB/Simulink to generate the required power and its performance is enhanced with the application of MPPT technique. The most robust and user-friendly technique, i.e., perturb and observe (P and O) is implemented in the PVS which in results maximized the utilization of available solar energy [4]. The solar PVS is not only tested under uniform climatic condition as per standard test conditions (STC); however, its performance is also analyzed in variable climatic conditions. The high-power factor at the sending end and low ripple current at the receiving end is to be maintained by the EVs charger circuit. Hence, a DC–DC boost converter cascaded with a PWM boost rectifier is implemented in the designed system. Finally, results with discussion, conclusions, and suggestions for the future perspectives are presented.

2 EV Technologies

EV is generally referred to the vehicle which has electrically operated engine and uses multiple motors for its torque generation and momentum. However, in this article, the term EVs is utilized only for the battery electric vehicle (BEV), hybrid electric vehicle (HEV), and plug-in hybrid electric vehicle (PHEV). In addition to the replacement of conventional fossil-fuel-based vehicles, zero vibration, ease of gear shifts, no smell, and no noises are the additional advantages of EVs. The EVs can be expected as the serious inroads for the motor industries with technological advancements in power electronics, battery technology, and microelectronics [5].

2.1 Charging Approaches: PV-EV

The charging of EVs through PV can be possible in two ways: (1) charging through PV-grid and (2) charging through stand-alone PV. The advantage of charging through PV-grid is that during unavailability or insufficient availability of solar irradiance, and the charging of EV can be carried out through grid directly [6]. Another benefit of this method is that, the generated power can be supplied to the utility grid when there is no EV available for charging. However, in remote areas, the stand-alone PV charging system is more beneficial where the grid supply is not available or too much expensive [7]. The system configuration is also simpler as there is an involvement of lesser power conversion stages.

Charging through PV-Grid. An additional loading is imposed to the electric utility grid during the charging of EVs as the current is drawn from the grid and it could be very large for fast charging [8]. Moreover, the user has to pay the high tariff premium if the charging of EV takes place during peak hours. A PV-grid charging system is proposed to offset this burden [9, 10]. The spinning reserve capacity is reduced with the availability of generated PV power and in results enhances the grid stability [11]. Apart from this, the PV power can be injected to the grid for monetary gains in the absence of EV to be charged [12].

The state of charge (SOC) of the EV is normally less than 100% when it is plugged in. The priorities of charging in general are sequenced as given below without the energy storage unit (ESU), vehicle to grid (V-G), and vehicle to vehicle (V–V) operations [6, 13]:

Case 1: When the power produced by the PV is higher than the power required to charge the EV then whole generated power would be used to charge the EV. In this case, the charging is not done with the grid power. In case the excess power is still available, then this power would be fed to the utility grid.

Case 2: During the night or in absence of sunlight when the PV generated power is not available, then the charging of EV would be carried out by the utility grid alone. The same process of charging will take place whenever there would be a fault experienced in the PVS.

Case 3: In case, if the generated power through PV is less than the required power to charge the EV due to insufficient irradiation or bad weather conditions, then whatever power is generated by PV in addition to remaining power taken through grid would be utilized to charge the EV.

Case 4: If there is no commitment between PV and the EV, i.e., there is no EV available to be charged, and the PV is continuously generating the power then the whole generated power through PV is fed to the grid. The owner of the PV charging station will get a monetary gain in return of this.

Charging through stand-alone PV. The stand-alone PV charging station stands for the solely charging of EV by whatever power is generated through PV with any involvement of electric utility grid [14]. A lesser number of power conversion stages are involved in this system, and hence, it is more efficient [15, 16]. However, the power generating capacity of the PVS must be sufficiently higher to fulfill the power requirements to charge the desired number of EVs [17]. To achieve the charging requirements through stand-alone PVS, there are two main approaches: (1) direct PV–EV connection and (2) connection of PV–EV through an intermediate ESU. There are several hybrid solutions methods which are also available for the connections [18].

The direct charging method has the one and most important disadvantage, i.e., intermittency and inadequacy of the power generated through PV to charge the desired EV. However, the excess charge whenever available is to be stored in ESU and utilized during unavailability of required power is the advantage of indirect connection [19]. Moreover, the indirect connection is more advantageous, though the initial capital cost of ESU may not be feasible [20]. The crucial component in both the cases is the charge controller. Essentially, the charge controller is a DC–DC converter with an MPPT function block. The main principle of this controller is to regulate the PV voltage which in results ensure that the charging current is optimized.

2.2 Technical Specifications

Electrically operated engines-based vehicles, i.e., EVs are attracting interest all over the world to replace IC engine-based vehicles. The basic reason behind this revolution is that EVs can be roll out as zero-emission vehicles and provides some sake especially to those cities which are struggling with severe air pollution. With the introduction of latest addition by Morris Garages as MG ZS EV, the Indian automobile market now also has a wide range of fully electrically operated vehicles. Moreover, several other car manufacturers are also planning to introduce some more EVs in the Indian market very soon.

The technical and operating specifications of EVs are slightly different from those IC engine-based vehicles like hp, engine displacement, fuel tank capacity, etc. Hence, here an overview of the technical specifications provided by the manufactures of the available electric cars in the Indian market is presented. Table 1 gives the charging characteristics of various available and popular EVs in India on behalf of their battery,

Table 1 Technical specifications and charging details of EVs available in Indian market [21]

S. No.	EV model	Manufacturer	Battery capacity (kWh)	Maximum driving range (km)	Full charge time (rapid 50 kW)	Maximum power (bhp)	Maximum speed (kmph)
1	Tigor EV	Tata motors	21.5	213	2 h (Fast charge)	40.23	80
2	Nexon EV	Tata motors	30.2	312	60 min (0–80%)	127.0	120
3	Kona electric	Hyundai motor company	39.2	452	60 min (0–80%)	134.1	167
4	MG ZS EV	MG Morris Garages	44.5	340	40 min (0–80%)	140.8	140
5	E verito	Mahindra and Mahindra	21.2	110	1.5 h (Fast charge)	41.57	86
6	EQC	Mercedes-Benz	80.0	455–471	1.5 h (10–90%)	402.3	180

maximum driving range, motor capacity, full charge time and type of charging, etc. [21]. The battery specifications vary according to the variation in the car segments and the available features in their interior and driving. The above-mentioned technical specifications and charging characteristics are used to calculate the required power generated through PV for the charging of EV. The Morris Garages (MG) ZS EV electric vehicle has been considered for this calculation as follows:

The energy consumption rate of MG ZS EV is: $\frac{340}{4.5} = 7.64\,\text{km/kWh}$
Average daily running is assumed as: 200 km
Daily energy consumption is: $\frac{200}{7.64} = 26.178\,\text{kWh}$
Available solar insolation during the day: 8 h
Solar PV required to generate desired kWh: $\frac{26.178}{8} = 3.27\,\text{kW}$

Based on the above calculation, the solar PVS designed in this work is having a power generating capacity of 3.2 kW.

3 PV System Design and Simulation

In order to generate the above calculated required power for the charging of electric vehicle, a stand-alone solar PVS of capacity 3.2 kW is designed in MATLAB/Simulink. The characteristic parameters of "Vikram Solar ELDORA 270" PV module are presented in Table 2. The PV array has been formed by taking twelve such modules, and six modules are connected in series per string and two strings are connected in parallel.

Table 2 Parameters of "Vikram Solar ELDORA 270" solar PV module

Parameters	Value
P_{mpp} (W)	270.66
I_{mpp} (A)	07.80
V_{mpp} (V)	34.70
I_{scc} (A)	08.10
V_{ocv} (V)	44.00
R_s (ohms)	0.52303
R_p (ohms)	3126.5623
N_s	72
kV_{OC} (%/°C)	−0.3583
kI_{SC} (%/°C)	0.024975
Parallel strings	2
Series-connected modules per string	6

Hence, the total power generating capacity of the designed stand-alone solar PV system with the aforesaid PV array is 3.2 kW (3247.92 W) which is quite enough to charge the electric vehicle overnight as per the calculated requirement (s).

A DC–DC boost converter is connected between the PV array and the load. It possesses two main purpose here, extract the maximum power from the PV array and boost up the level of generated voltage [22, 23].

The duty cycle to trigger the gate pulse of DC–DC boost converter is generated by the maximum power point technique (MPPT). Perturb and observe (P and O) is the MPPT technique used in this work for this purpose. The main task of this MPPT function is to predict the reference voltage corresponding to the maximum power point (MPP) on P–V curve of the PV array. The I–V and P–V characteristics of PV array vary nonlinearly depending upon the changes in the level of available solar irradiance and temperature [24]. MPPT function continuously tracks the new MPP with the change in inputs to the PV array and predict the reference voltage corresponding to the new MPP at every instant of time. The flowchart of P and O MPPT algorithm is presented in Fig. 1.

The complete simulation setup designed in MATLAB/Simulink R2020a is shown in Fig. 2. The model consists of a PV array of 3.2 kW generating capacity, MPPT function block, DC–DC boost converter and the load. The load here is the approximation of the actual EV which is to be charged during night. During day time when the required power is generated by the PVS is to be stored in the additional battery storage system or can be directly utilized to charge the vehicle.

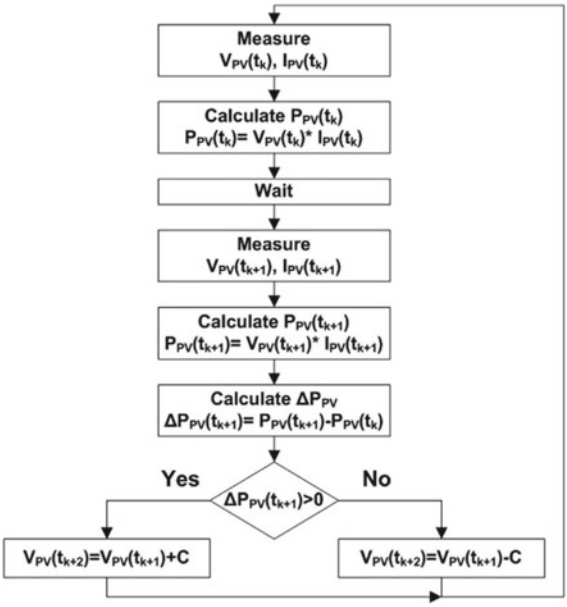

Fig. 1 Flowchart of conventional P and O MPPT algorithm

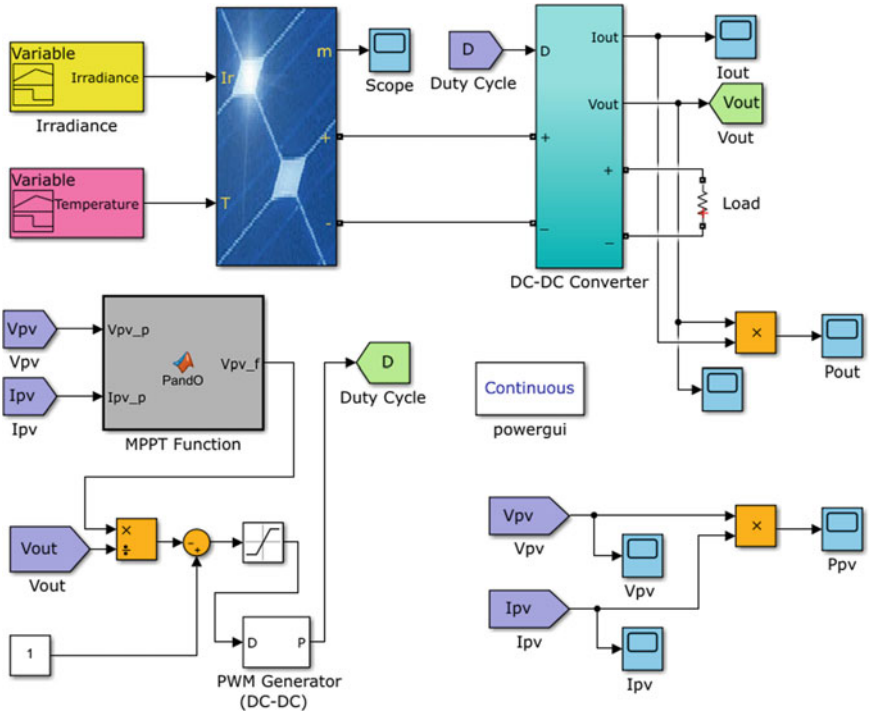

Fig. 2 Simulation setup of 3.2 kW stand-alone solar PVS with MPPT for charging of EV

4 Simulation Results

The designed system is tested and analyzed under standard test conditions (STC) as well as under nonlinearly varying climatic conditions for the extraction of maximum available power from the PV array. The power and voltage delivered to the load are compared with the generated power and voltage at the PV end to calculate the efficiency of PVS and MPPT algorithm.

Case 1: In Case 1, the solar irradiance and temperature both are kept uniform as per STC, i.e., $G = 1000$ W/m^2 and $T = 25°$C. The power output curve at the load end and the voltage generated at the PV end are presented in the Fig. 3 and Fig. 4 respectively.

In Fig. 1, it can be seen that the maximum power delivered to the load after convergence of MPPT algorithm at MPP is 3160 W, and the actual generated power at the PV end at MPP is 3247.92 W. So, the efficiency of tracking algorithm, i.e., P and O here can be defined as 97.29% including power losses in the converter and transmission. The convergence time to stabilize the system at MPP is also quite impressive, i.e., 0.25 s.

The second figure, i.e., Fig. 4 depicts the generated PV voltage at the PV side. The maximum extracted voltage from PV by the MPPT function is near about 204 V which is 97.98% of the rated voltage at MPP, i.e., ($34.7 \times 6 = 208.2$ V). Also, the time taken to extract the maximum voltage from the PV array is just 0.1 s. Therefore, it can be concluded here that the P and O performs well effectively under uniform irradiance and temperature to extract maximum power from the PV array.

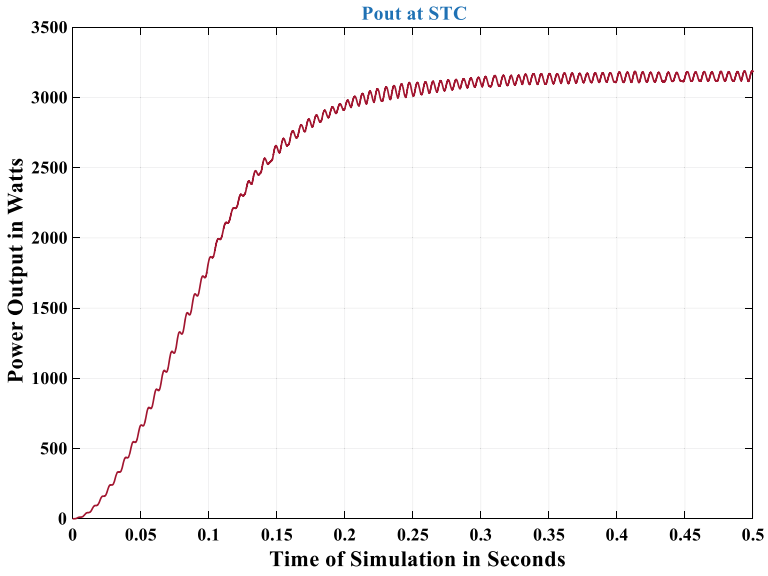

Fig. 3 Power output curve at STC

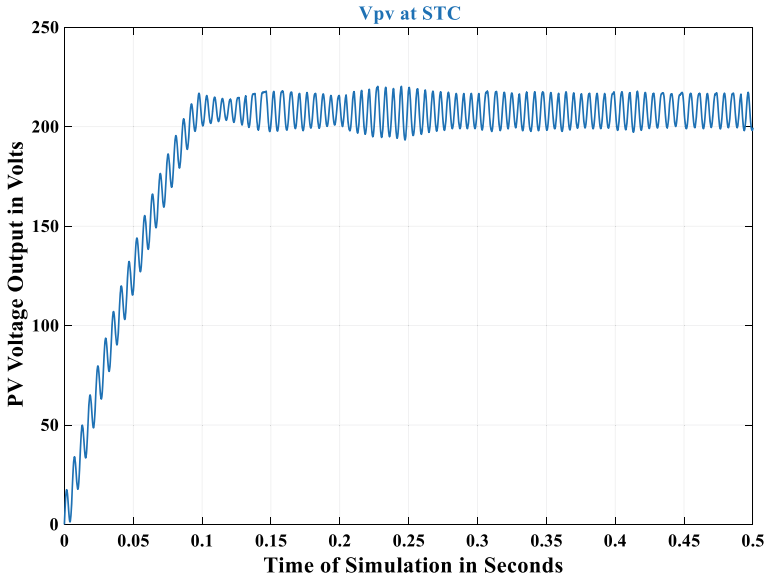

Fig. 4 PV voltage generated curve at STC

Case 2: In Case 2, the continuously variable irradiance is considered on the assumption that the nature of irradiance variation from morning to evening during the day follows almost sinusoidal path. Hence, a sinusoidal varying irradiance pattern is considered as the input to the PV array in this case as shown in Fig. 5.

The variation in temperature also considered on real-time database, the weather data on a mostly sunny day of winters, i.e., on Dec. 23, 2019 at Jaipur, Rajasthan, India, location is taken from accuweather report [25]. The pattern of variable temperature from morning 06:00 a.m. to evening 06:00 p.m. is taken as shown in Fig. 6 and given as the input to the PV array.

The inputs have been given to the PV array as per above description, and the system has been tested with same P and O MPPT algorithm. The power delivered to the load, i.e., P_{out} and the generated PV voltage, i.e., V_{pv} are presented in Figs. 7 and 8, respectively.

It is very clearly visible in the curves of Figs. 7 and 8 that P and O possess some oscillations near MPP at every instant of time when the irradiance and temperature both are nonlinearly varying consistently. It is quite obvious fact about P and O as it is a conventional algorithm which is developed a few decades back when the problem of MPPT was identified. Now, there are several modifications and improvements in the P and O principle which have also been presented in the recent decade. However, from the power output curve of Fig. 7, it is clear that the power delivered to the load at 2.5 s, when the irradiance and temperature values are near about STC values is 3137 W which is 96.58% of the rated generated power. This is due to that fact that the irradiance and temperature both are continuously varying, and it is quite difficult

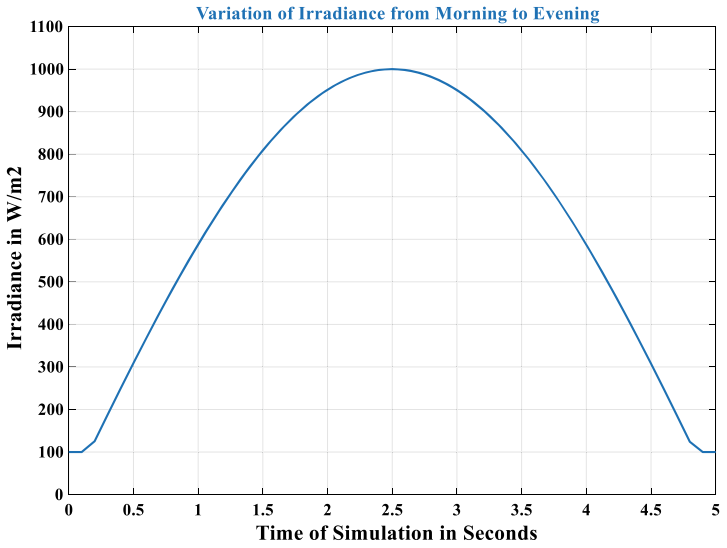

Fig. 5 Sinusoidally varying pattern of solar irradiance from morning to evening

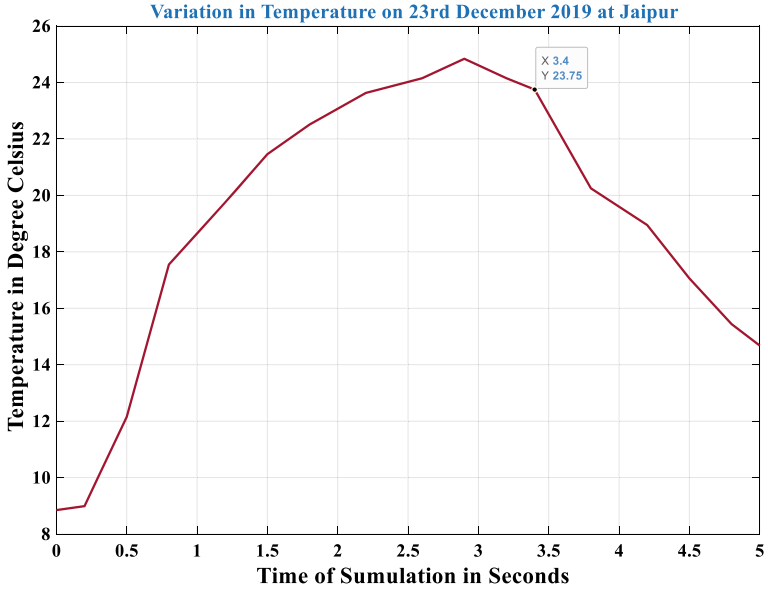

Fig. 6 Temperature variation during 06:00 a.m.–06:00p.m. on Dec. 23, 2019 at Jaipur, India

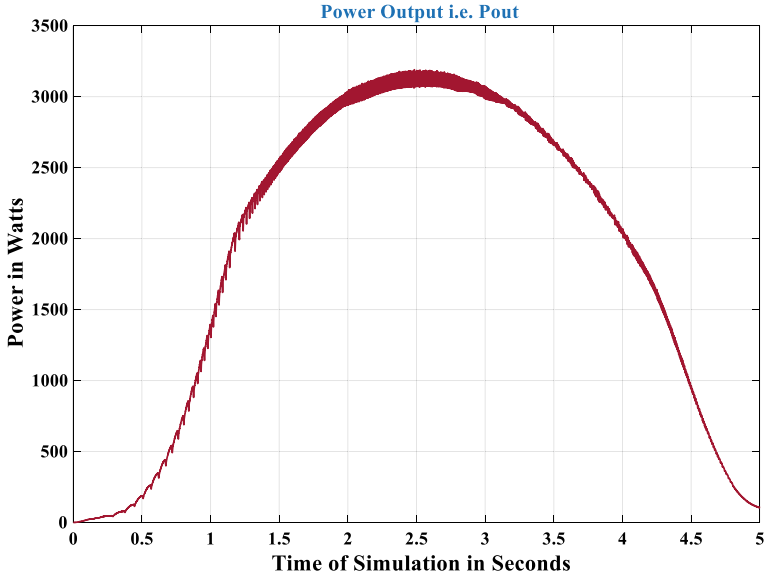

Fig. 7 Power output curve under Case 2

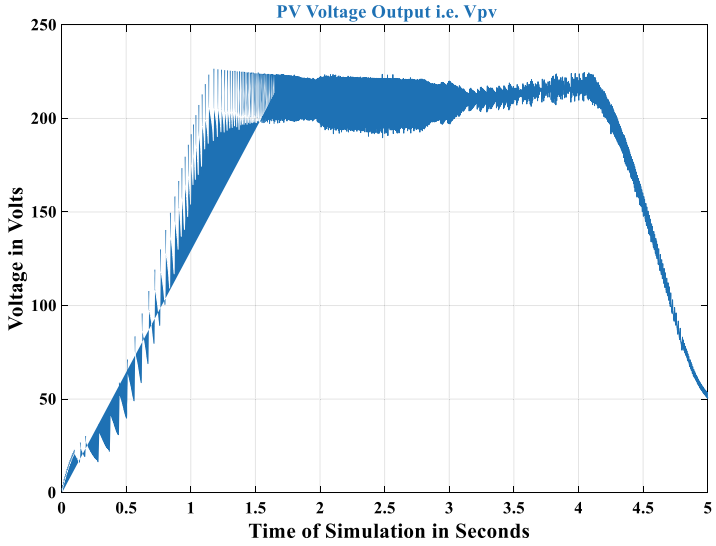

Fig. 8 PV voltage generated curve under Case 2

for the algorithm to predict the desired reference voltage before the actual operating point shifts to new position.

On the other hand, the oscillations can also be seen in the PV side generated voltage. However, the actual generated voltage at 2.5 s is 203.5 V which is 97.74% of the rated generated PV voltage. Though, the efficiency of tracking is satisfactory but the oscillation near MPP are not desirable, and this is the reason why the researchers are still interested in this field to develop such algorithms which should be capable to handle the nonlinear behavior of irradiance and temperature and should not affect the performance of solar PVS.

5 Conclusion

The adoption of green energy-based transportation, i.e., PHEVs and EVs are becoming efficient means of transportation as they are noise free, pollution free, clean and easy to use as compared to the conventional IC engine-based vehicles. The charging or refueling system of these vehicles can easily be fed by the power generated through solar PVS or any other RES. Keeping this in mind, in this work, the technical specifications and charging characteristics of the EVs available in the Indian market for various segments have been identified and studied. On behalf of which the power requirements for the charging of one EV through the PV are estimated. Later, a stand-alone solar PVS is designed and simulated in MATLAB/Simulink to generate the required power for the charging of EV. To ensure the power generated through the designed solar PVS would be maximum, an MPPT function is employed in addition to the DC–DC boost converter. The P and O algorithm of MPPT is used in this work for the tracking of MPP. The designed system is tested and the performance is analyzed under uniform climatic conditions, i.e., at STC as well as under continuously varying climatic conditions. Under STC, the performance of the system is found satisfactory with effective tracking of MPP at 97.98% tracking efficiency. However, under continuously varying input parameters, i.e., irradiance and temperature in case 2, the efficiency of tracking falls down to 96.58% which is not much less than that of the previous efficiency, but the oscillations generated near MPP are quite higher. These power oscillations are generated because of the inefficiency of the tracking algorithm. The MPP shifts to its new position before the prediction of the MPPT algorithm as the irradiance and temperature are continuously varying at every instant of time. Hence, there are some modifications and improvements are still required in the MPPT algorithm to extract maximum power from the solar PVS under these types of continuously variable climatic condition. So that the maximum utilization of solar PVS could be carried out for the more effective charging of EVs.

References

1. Khalil HAEE, Khalil EE (2015) Energy efficiency in the urban environment. CRC press
2. Singh BP, Goyal SK, Siddiqui SA (2019) Grid connected-photovoltaic system (GC-PVS): issues and challenges. In: IOP conference series: materials science and engineering, vol 594, 1 IOP Publishing, p 012032
3. Yan D, Ma C (2020) Stochastic planning of electric vehicle charging station integrated with photovoltaic and battery systems. IET Gener Transm Distrib 14(19):4217–4224
4. Singh BP, Goyal SK, Siddiqui SA (2020) Analysis and classification of maximum power point tracking (MPPT) techniques: a review. Intell Comput Tech Smart Energy Syst 999–1008
5. Mercan MC, Kayalica MÖ, Kayakutlu G, Ercan S (2020) Economic model for an electric vehicle charging station with v ehicle-to-grid functionality. Int J Energy Res 44(8):6697–6708
6. Preetham G, Shireen W (2012) Photovoltaic charging station for plug-in hybrid electric vehicles in a smart grid environment. In: 2012 IEEE PES innovative smart grid technologies (ISGT). IEEE, pp 1–8
7. Tong SJ, Same A, Kootstra MA, Park JW (2013) Off-grid photovoltaic vehicle charge using second life lithium batteries: an experimental and numerical investigation. Appl Energy 104:740–750
8. Benaouadj M, Aboubou A, Becherif M, Ayad MY, Bahri M (2012) Recharging of batteries/supercapacitors hybrid source for electric vehicles application using photovoltaic energy in a stand-alone point. In: 2012 First international conference on renewable energies and vehicular technology. IEEE, pp 161–166
9. Hamilton C, Gamboa G, Elmes J, Kerley R, Arias A, Pepper M, Shen J, Batarseh I (2010) System architecture of a modular direct-DC PV charging station for plug-in electric vehicles. In: IECON 2010–36th annual conference on IEEE industrial electronics society. IEEE, pp 2516–2520
10. Fathabadi H (2017) Novel solar powered electric vehicle charging station with the capability of vehicle-to-grid. Sol Energy 142:136–143
11. Coffman M, Bernstein P, Mann A (2012) Statewide and electricity-sector models for economic assessments of Hawaii clean energy policies. Hawaii Nat Energy Inst Univ Hawaii, USA2012
12. Naghizadeh N, Williamson SS (2013) A comprehensive review of power electronic converter topologies to integrate photovoltaics (PV), AC grid, and electric vehicles. In: 2013 IEEE transportation electrification conference and expo (ITEC). IEEE, pp 1–6
13. Singh B, Verma A, Chandra A, Al-Haddad K (2020) Implementation of solar PV-battery and diesel generator based electric vehicle charging station. IEEE Trans Ind Appl 56(4):4007–4016
14. Abu-Jasser A (2010) A stand-alone photovoltaic system, case study: a residence in gaza. J Appl Sci Environ Sanitation 5(1)
15. Vaidya M, Stefanakos EK, Krakow B, Lamb HC, Arbogast T, Smith T (1996) Direct DC-DC electric vehicle charging with a grid connected photovoltaic system. In Conference record of the twenty fifth IEEE photovoltaic specialists conference-1996. IEEE, pp 1505–1508
16. Kelly NA, Gibson TL (2011) Solar photovoltaic charging of high voltage nickel metal hydride batteries using DC power conversion. J Power Sources 196(23):10430–10441
17. Birnie DP III (2009) Solar-to-vehicle (S2V) systems for powering commuters of the future. J Power Sources 186(2):539–542
18. He F, Fathabadi H (2020) Novel standalone plug-in hybrid electric vehicle charging station fed by solar energy in presence of a fuel cell system used as supporting power source. Renew Energy 156:964–974
19. Mesentean S, Feucht W, Kula HG, Frank H (2010) Smart charging of electric scooters for home to work and home to education transports from grid connected photovoltaic-systems. In: 2010 IEEE international energy conference. IEEE, pp 73–78
20. Mossoba J, Kromer M, Faill P, Katz S, Borowy B, Nichols S, Casey L, Maksimovic D, Traube J, Lu F (2012) Analysis of solar irradiance intermittency mitigation using constant DC voltage PV and EV battery storage. In: 2012 IEEE transportation electrification conference and expo (ITEC). IEEE, pp 1–6

21. https://www.cardekho.com/compare/mg-zs-ev-and-tata-nexon-ev-and-hyundai-kona-and-tata-tigor-ev.html
22. Singh BP, Goyal SK, Siddiqui SA, Kumar P (2020) A study and comprehensive overview of inverter topologies for grid-connected photovoltaic systems (PVS). Intell Comput Tech Smart Energy Syst, 1009–1017
23. Kumar P, Kour M, Goyal SK, Singh BP (2020) Multilevel inverter topologies in renewable energy applications. In: Intelligent computing techniques for smart energy systems. Springer, Singapore, pp 891–902
24. Goyal SK, Sungh BP, Kumar A, Kumar P, Saraswat A (2020) Modelling and simulation of a solar PV system: a comprehensive study. In: 2020 international conference on computation, automation and knowledge management (ICCAKM). IEEE, pp 367–372
25. https://www.accuweather.com/en/in/jaipur/205617/december-weather/205617?year=2019.

Integrated DR and V2G Framework of EV Aggregator Under Low Carbon Paradigm

S. Sharma and P. Jain

Abstract Emerging ambitious and viable scheduling business models for of scheduling of electric vehicles aggregator (EVA) ensures smart electrification of transportation with renewables through coordinated and efficiently deployed V2G driving the transformation of energy services. Proposed work models an integrated DR framework for vehicle-to-grid (V2G) energy management by EVA for efficient use of photovoltaic (PV) generation by smart harmonization among involved entities EV users, grid/system operator (SO) and EVA. EVA regulates V2G (charge/discharge) strategy for dropping vehicle-to-grid (V2G) operational cost and maximizing its revenue through regulation services and modulating charging/discharging rates according to real-time monitored data of self PV generation unit. Battery ageing cost is modelled to compensate EV users against V2G regulation. Different integrated frameworks considered for V2G scheduling case studies are RTP-DR, electricity company TOU DR and Designed TOU DR. Simulation results confirm the effectiveness of anticipated business model from the perspective of V2G operational cost reduction and PV generation utilization.

Keywords Demand response (DR) · Electric vehicles (EVs) · Time-of-Use (TOU) · Grid-to-vehicle-to-grid (G2V2G)

1 Introduction

Massive penetration of PV generation and charging load of EVs in distribution network may lead to adverse impacts such as increased net load (difference of PV generation and total demand) volatility, voltage fluctuations, avalanche effect of additional peaks loads, power loss and module/component overloading [1]. In addition to stress on electrical distribution system or adverse impacts on grid, barriers to EVs massive adoption are steep initial investment, short ranges for driving, long charging time and lack of charging station infrastructure geographically [2].

S. Sharma (✉) · P. Jain
Malviya National Institute of Technology Jaipur, Jaipur, India
e-mail: 2015ree9012@mnit.ac.in

S. Dwivedi et al. (eds.), *Flexible Electronics for Electric Vehicles*, Lecture Notes in Electrical Engineering 863, https://doi.org/10.1007/978-981-19-0588-9_48

Charging station is located at high EV density areas like junction of roads, supermarket and residential area to have availability to maximum EV owner. EVs will have to travel long-distance if charging stations are located in remote areas. In one area, there should not be three charging stations. Therefore, charging stations are distributed zone wise in an area [3]. Deficiency of charging infrastructures is an important hindrance for logistic electrified transportation. Cost-effective charge scheduling for reducing operational cost with limited available chargers turn out to be a burning issue. Therefore, to resolve this issue of serving maximum number of EV users, it necessitates proper scheduling algorithm with maintained power system health. Different aspects for scheduling related to power system distribution network are from perspective of system operator (SO) such as power loss, voltage deviation and limits, branch current and thermal limit and charging/discharging rates. From EV owner's perspective, scheduling attributes are desired state of charge (SOC) at departure time maintaining battery health [4].

Due to market regulations, individual EV cannot participate in electricity market. An EV aggregator (EVA) agent for EV users is a commercial middleman between a SO and plugged-in EVs for their market facilitation [5]. For the SO viewpoint, EVA is perceived as a bulky resource/demand, which may well offer ancillary services such as up and down regulation. An EVA is a charging station operator for charging services to EV users in regulated and efficient manner. EVA efforts to harmonize and achieve a balance between attributes of all involved entities for improved market operations. EVA being commercial entity aim at profit maximization, buy energy from wholesale market at dynamic price and retail it to the EV users with its specially designed tariff. The key factor behind this to earn more profit in energy market dropping the fiscal risk of market participation by G2V2G scheduling frameworks.

G2V is simple charging of EV via distribution network. V2G offers more elasticities and opportunities improving system operation and control [6]. The significant pros are active/reactive power support, power factor control and sustenance for the integration of renewable energy resources. Active power support via V2G can accomplish crest load shaving and load flattening services. These services are attained through G2V mode during valley hours and inoculate surplus EV energy in to distribution system during crest hours.

Figure 1 highlights the categorization of V2G frameworks based on stakeholder's perspective, control, available information and request time [7]. Implementation of price-based demand response programmes in scheduling framework enhances market participation efficiency thereby improving EVA performance parameters, viz. revenue, cost and profit. Time-of-use (TOU) PBDR has potential to reduce the charging cost while satisfying EVs' charging requirements. In the existing literature, integrated DR and V2G scheduling problem aim at individual perspective disregarding other entity attributes.

Offering strategy envisioned for a combined amalgam power plant of wind power suppliers and EVAs with G2V/V2G services rise returns and lessen returns' volatility [8]. Intelligent G2V scheduling plan for EV users in AC microgrids that in tandem minimalizes the power drawn from the upstream electricity company grid to recharge

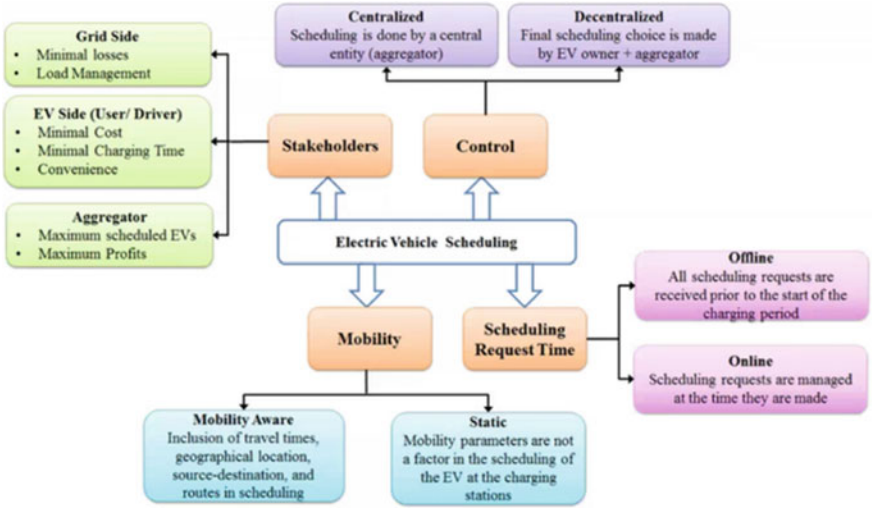

Fig. 1 Classification of V2G/G2V scheduling frameworks

EVs and make the most of their battery lifetime [9]. The effectual amalgamation of demand response, and G2V scheduling decreases emission and operational cost [10].

Willingly partaking in DRP reduces the average charging tariff of EV users and rises the returns as of DR flexibility [11]. DR tool alleviates electricity operating expenses, demand peak and transformer loss of life [12, 13]. In [14], partaking model from the SO's perspective for scheduling of EVs in the smart grid environment executing DR. Applying the EV scheduling and DRP helps microgrid operators to reduce their cost and improve the profit profile [15]. Amalgamated DR operational scheduling framework capitalize on the benefit of distributed generator (DG) owners and distribution network operator (DNO) [16].

Scheduling from EV users' perspective improves lifestyle, service quality, electricity bill and supply electricity demand. Scheduling from SO's perspective reduces operational cost and electricity generation cost while improving system efficiency and reliability [17]. Ref. [18] validates the DR potential in offering improved elasticity services to the distribution system for evaluating optimal generation mix of future distribution systems with a high integration of wind farms.

Table 1 illustrates different stakeholders and their associated attributes in V2G management. Ref. [19] guarantee mutually technoeconomic appropriateness of V2G scheduling in the smart distribution system to minimalize the effect of EV G2V/V2G modes on distribution system while reducing the operational costs associated with EV owner and the electricity company. Ref. [20] reveals that the optimum G2V-V2G operation, associated with TOU rates in a DR programme, and reserve market managing can lessen the electricity and emission costs of the renewable-driven microgrid-EVs parking lot system. Integrated TOU PBDR management and EV charging–discharging operation enabled to attain mutually crest shaving and energy

Table 1 Stakeholders and their attributes in V2G management

	DR tool	EV users	EVA/PL operator/BSS operator/CS operator	System operator
Revenue/charging cost		*	*	
Energy consumed/delivered		*Preferences		*Grid factors
Energy procurement cost/ sale price		*	*	
EV users' satisfaction: desired SOC and bill saving	*	*		
Self-generation RERs: green charging	*	*	*	*

tariff saving through established constraints depending upon the state of charge (SOC) of cars and the corresponding G2V/V2G powers [21]. V2G technology-enabled exploitation of synergies between transportation and power sectors [22]. Integrated energy systems combine different energy conversion technologies and storage and possess the calibre to incorporate distributed renewable energy resources with a least impact on the distribution network [23]. However, DR aspect from EV users' anxiety of charging tariff minimization is disregarded in these works.

The highlights of the anticipated model may be briefed as follows:

(1) Unified DR and V2G scheduling framework of EVA for participation in multiple markets, viz. energy and regulation markets are modelled.
(2) TOU prices are specially designed from EV users' perspective of charging tariff minimization.
(3) Different integrated frameworks considered for V2G scheduling case studies are RTP-DR, electricity company TOU DR and designed TOU DR, for validating the efficacy of the anticipated model.

The continuing part of the paper is systematized as follows: Sect. 2 represents an overview of the anticipated system model of EVA as a service provider to SO. In Sect. 3, the problem formulation of EVA is carried out. Finally, simulation outcomes are analysed and deliberated in Sect. 4, tracked by the inferences provided in Sect. 5.

2 System Model

Figure 2 illustrates typical V2G system architecture of the EVA. Load sharing and grid stability enhancement aspects in G2V/V2G mode are achieved by suitable control algorithms of EVA in coordination with SO. Energy management and power flow between various units such as RE sources, flexible EVs and available grid form an

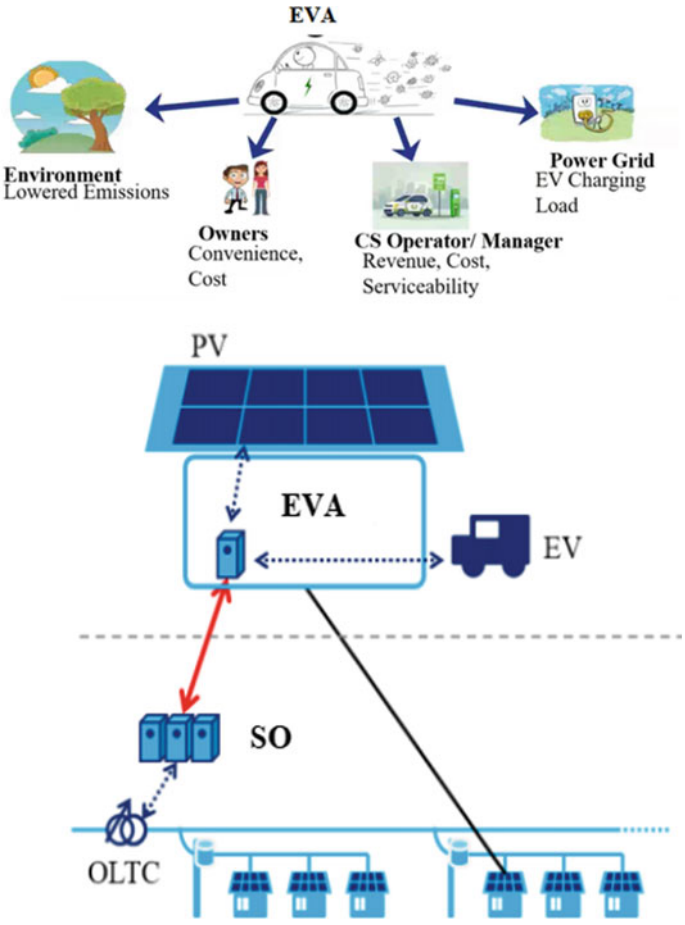

Fig. 2 Schematic of smart coordinated V2G (charge/discharge) scheduling framework of EVA

important aspect of V2G architecture. Daily energy requirement of individual EV is difference SOC percentage of battery capacity.

3 Problem Formulation of EVA

Total charging cost incurred by EVA is total cost of charging process which includes cost of G2V operation and V2G operation. Cost of G2V depends on charging energy required by EV and energy consumption in trip/travel. They are available for limited parking duration and SOC must lie between min and max value. *P* is the preferred/scheduled charging rate, and RTP is the real-time pricing. Battery ageing cost is function of manufacturing cost of battery of individual EV, lifecycle of the

battery, energy capacity of battery, depth of discharge of the battery, labour cost of the battery for installation and total amount of discharged energy by individual EV. Scheduling is subject to different constraints such as charging/discharging rates, energy requirement, battery SOC, etc. EVA manages charge/discharge powers and down/up regulation capacities requirements depending on surplus/deficit generation and efficient utilization of PV generation.

Charging energy required by car is nil for period beforehand entrance otherwise afterwards exit Eqs. (1) and (2). The G2V/V2G powers $P_{i,t}^{\mathrm{G2V}}$ or $P_{i,t}^{\mathrm{V2G}}$ must deference specified charger power limits $P_i^{\min}$ and $P_i^{\max}$ besides the restrictions customized by EV users Eqs. (3) and (4). A binary variable $h_{i,t}$ is employed to specify whether EV is connected to the grid intended for G2V/V2G aimed at regulation services Eq. (5). The further binary variable is unified to settle that at a particular instant simultaneous operation of G2V and V2G is prohibited. This binary variable $u_{i,t}^{\mathrm{G2V}}$ is one for charging and nil intended for discharging. Alteration in SOC from the preceding timeslot is updated from Eq. (6). Earlier entrance SOC set to nil Eq. (7). On entrance to EVA, SOC is EV's primary value Eq. (8). On exit, SOC ought to hold its anticipated value Eq. (9). EVA confines the SOC to be inside bounds $\mathrm{SOC}^{\min}$ and $\mathrm{SOC}^{\max}$ as customized by EV users Eqs (10) and (11). EV SOC is rationalized from its primary value is subject to V2G/ G2V potency ($\eta_{\mathrm{dch}}/\eta_{\mathrm{ch}}$) and power Eq. (12). Equation (13) specifies the extreme likely charging power to charge EV from current to customized SOC in a single time interval. Restraint Eq. (14) indicates congestion managing to alleviate overloading of the transformer.

$$P_{i,t}^{\mathrm{V2G}}, P_{i,t}^{\mathrm{G2V}}, u_{i,t}, d_{i,t}, h_{i,t} = 0 \quad \forall t < t_{a_i} \tag{1}$$

$$P_{i,t}^{\mathrm{V2G}}, P_{i,t}^{\mathrm{G2V}}, u_{i,t}, d_{i,t}, h_{i,t} = 0 \quad \forall t > t_{d_i} \tag{2}$$

$$P_i^{\min} \cdot u_{i,t}^{\mathrm{G2V}} \leq P_{i,t}^{\mathrm{G2V}} \leq P_i^{\max} \cdot u_{i,t}^{\mathrm{G2V}} \, \forall i, t \tag{3}$$

$$P_i^{\min} \cdot \left(1 - u_{i,t}^{\mathrm{G2V}}\right) \leq P_{i,t}^{\mathrm{V2G}} \leq P_i^{\max} \cdot \left(1 - u_{i,t}^{\mathrm{G2V}}\right) \forall i, t \tag{4}$$

$$h_{i,t}, u_{i,t}^{\mathrm{G2V}} \in \{0, 1\} \, \forall i, t \tag{5}$$

$$\mathrm{SOC}_{i,t} - \mathrm{SOC}_{i,t-1} = \left(\mathrm{SOC}_i^{\mathrm{Des}} - \mathrm{SOC}_i^{\mathrm{INI}}\right) \Big/ \left(td_i - ta_i\right) \tag{6}$$

$$\mathrm{SOC}_{i,t} = 0, \quad t < t_{a_i} \tag{7}$$

$$\mathrm{SOC}_{i,t} = \mathrm{SOC}_i^{\mathrm{ini}}, \quad t = t_{a_i} \tag{8}$$

$$\mathrm{SOC}_{i,t} = \mathrm{SOC}_i^{\mathrm{des}}, \quad t = t_{d_i} \tag{9}$$

$$\mathrm{SOC}_{i,t} \geq \mathrm{SOC}_i^{\min}, \quad \forall t \geq t_{a_i} \tag{10}$$

$$\mathrm{SOC}_{i,t} \leq \mathrm{SOC}_i^{\max}, \quad \forall t \geq t_{a_i} \tag{11}$$

$$\mathrm{SOC}_{i,t} = \mathrm{SOC}_{i,t-1} \cdot h_{i,t-1} + P_{i,t}^{\mathrm{G2V}} \cdot u_{i,t}^{\mathrm{G2V}} \cdot \frac{\eta_{\mathrm{ch}}}{\mathrm{BC}_i} - \frac{P_{i,t}^{\mathrm{V2G}} \cdot \left(1 - u_{i,t}^{\mathrm{G2V}}\right)}{\eta_{\mathrm{dch}} \cdot \mathrm{BC}_i} \quad \forall i, t \tag{12}$$

$$Pm \max_{i,t} = \left(\mathrm{SOC}_i^{\mathrm{DES}} - \mathrm{SOC}_{i,t}\right) \cdot h_{i,t} \cdot \frac{\mathrm{BC}_i}{\eta_{\mathrm{ch}}} \tag{13}$$

$$\sum_{i=1}^{N} P_{i,t}^{\mathrm{G2V}} + \mathrm{Load}_t + \sum_{i=1}^{N} d_{i,t} \leq \mathrm{TDC} \tag{14}$$

$$\mathrm{PV}_t + \sum_{i=1}^{N} \left(1 - u_{i,t}^{\mathrm{G2V}}\right) \cdot P_{i,t}^{\mathrm{V2G}} + \sum_{i=1}^{N} u_{i,t} = \mathrm{Load}_t + \sum_{i=1}^{N} u_{i,t}^{\mathrm{G2V}} \cdot P_{i,t}^{\mathrm{G2V}} + \sum_{i=1}^{N} d_{i,t} \tag{15}$$

$$u_{i,t} = P_{i,t}^{\mathrm{V2G}} \cdot \left(1 - u_{i,t}^{\mathrm{G2V}}\right) \tag{16}$$

$$d_{i,t} = \min\left(Pm \max_{i,t},\, P_i^{\max}\right) - P_{i,t}^{\mathrm{G2V}} \cdot u_{i,t}^{\mathrm{G2V}} \tag{17}$$

$$\mathrm{Revenue} = \sum_{i=1}^{N} \sum_{t=1}^{T} \left(dc_{i,t} + uc_{i,t}\right) \cdot \mathrm{RP}_t + \sum_{i=1}^{N} \sum_{t=1}^{T} \left(M_k + \mathrm{EP}_t^{\mathrm{TOU}}\right) \cdot P_{i,t}^{\mathrm{G2V}} \cdot u_{i,t}^{\mathrm{G2V}} \cdot h_{i,t}$$
$$+ \sum_{i=1}^{N} \sum_{t=1}^{T} \mathrm{EP}_t^{RTP} \cdot P_{i,t}^{\mathrm{V2G}} \cdot \left(1 - u_{i,t}^{\mathrm{G2V}}\right) \cdot h_{i,t} \tag{18}$$

$$\mathrm{DC}_{i,t}^{\mathrm{deg}} = \frac{C^{\mathrm{bat}} \cdot C_{\mathrm{Eb}} + C_{\mathrm{labour}}}{L_{\mathrm{cycles}} \cdot C_{\mathrm{Eb}} \cdot \mathrm{DOD}} \tag{19}$$

$$\mathrm{Deg}_{i,t} = \mathrm{DC}_{i,t}^{\mathrm{deg}} \cdot \frac{P_{i,t}^{\mathrm{V2G}} \cdot u_{i,t}^{\mathrm{V2G}}}{\eta^{\mathrm{dch}}} \tag{20}$$

$$\mathrm{Cost} = \left(\sum_{i=1}^{N} \sum_{t=1}^{T} P_{i,t}^{\mathrm{G2V}} \cdot h_{i,t} \cdot \mathrm{EP}_t^{\mathrm{RTP}}\right) + \sum_{i=1}^{N} \sum_{t=1}^{T} \mathrm{Deg}_{i,t} \tag{21}$$

$$Max\ \mathrm{Profit} = \mathrm{Max}(\mathrm{Revenue} - \mathrm{Cost}) \tag{22}$$

$$E_{\mathrm{recharge}}^{\mathrm{daily}} = (\mathrm{SOC}_{\mathrm{Max}} - \mathrm{SOC}_{\mathrm{Ini}}) \times \text{battery capacity}$$

Equation (15) is the power equilibrium equation for demand–supply equivalence. Equations (16) and (17) depicts correspondingly regulation up and down capacities. Equation (18) represents income received by EVA from regulation services, charging and discharging. Battery ageing is a potential factor with V2G from EV users' aspect. It is assumed that V2G behaviour can result in critical battery ageing, and associated value is computed in Eqs. (19) and (20). Equations (21) represents total operating cost as the aggregated procurement charges and battery ageing charges. EVA is targeting its profit maximization Eq. (22) in deliberated model.

The battery ageing cost is as depicted by Eq. (19) is a relation between EV battery storage cost C_{Eb}, the total capacity of the EV battery C^{bat}, labour to replace an EV battery C_{labour} and the number of charge and discharge cycles provided by EV battery L_{cycles} corresponding to a particular depth of discharge (DOD) [24]. Hence, the costs for an EVA are purchase costs of charging energy requirement from EV users and the battery health/performance deterioration/cycle ageing cost paid to them. The cost of cycle ageing is due to discharging electrical energy which is envisioned realizing Eq. (20) from V2G operation of typical EV and at any time t.

Table 2 indicates different charging levels available in charging station. Table 3 illustrates parameters setup in simulation. Table 4 depicts the electricity pricing structure offered by electricity company. Table 5 represents specified electricity rates to EV users designed by EVA from predicted RTP. Table 6 shows pattern of trip behaviour of EVs. It is presumed that 100 electric cars park in the shopping mall/residential parking lot area. Gaussian normal pdfs of periods of entry/evacuation and introductory SOC are produced by National Household Travel Survey (NHTS) statistics [25] per respective averages (7, 19, 0.3) and standard deviations (2, 2, 0.1).

Figure 3 depicts a flowchart of the solution process. Steps of the algorithm are historical data collection, design of TOU price, modelling of EV mobility behaviour

Table 2 EV charging levels based on SAE J1772 (Society of Automobile Engineers) standard [26]

Charging level	Voltage (V)	Current (A)	Power (kW)	Charging time (hour)
AC level I	120 (single phase)	12–16	1.44–1.92	7.0–17.0
AC level II	240 (single or three phase)	Up to 80	Up to 19.20	3.0–7.0
DC level III (fast charging)	200–450 (direct current)	Up to 80	Up to 36	0.5–1.5

Table 3 Simulation setup parameters [27]

Specification of EV	Rated charging rate	3.3, 7.4 kW
	Rated discharging rate	3.3, 7.4 kW
	Rated battery capacity	95 kWh
	Minimum SOC for an unexpected trip	30%
	Energy requirements for the trip	2.95–3.05 kWh/h

Table 4 Electricity pricing structure

Electricity pricing	Electricity company TOU rate ($/MWh)	t_1–t_8	9.23
		t_8–t_{10}	21.43
		t_{10}–t_{18}	31.33
		t_{18}–t_{24}	21.43
	Flat rate ($/MWh)	t_1–t_{24}	31.8

Table 5 Specified electricity rates to EV users designed by EVA using predicted RTP

	Valley	Shoulder valley	Flat	Shoulder crest	Crest
Duration	t_5–t_8	t_2, t_4	t_1, t_9	t_3, t_{10}, t_{24}	t_{11}–t_{22}
TOU rates ($/kWh)	0.013	0.0156	0.017	0.019	0.023

Table 6 Trip behavioural pattern

Pick up	Trip time	7.00–7.15, 7.30–7.45, 18.30–18.45, 19.00–19.15
	Idle parking time	7.15–7.30, 18.45–19.00
Shopping mall	Trip time	13.30–13.45, 14.30–14.45
	Idle parking time	13.45–14.30
Residential parking	Otherwise	

parameters based on historical survey, determination of optimal decision variables through optimization problem considering all time intervals of scheduling horizon.

4 Results and Discussion

The historical energy and regulation up/down market price data from Electric Reliability Council of Texas (ERCOT) market [28] is accessed. EVs' battery operational behaviour regarding V2G/G2V modes are as specified in 2018 eV market [29]. The battery model considered in problem is Tesla model Sedan *S* having replacing value 13,000 $. Harmonized V2G scheduling algorithm is coded employing GAMS 24.2.3 [30].

Figures 4 and 5, respectively, represent weekday base load profile and regulation price of Houston zone in ERCOT market [28]. Figure 6 illustrates energy prices: specially designed TOU price by EVA and weekday real-time prices in Houston zone in ERCOT market [28]. Figure 7 shows PV generation output at car park [31]. Figures 8 and 9, respectively, represent G2V power charged from grid and V2G power injected to grid according to both TOU price and base load at an office parking lot.

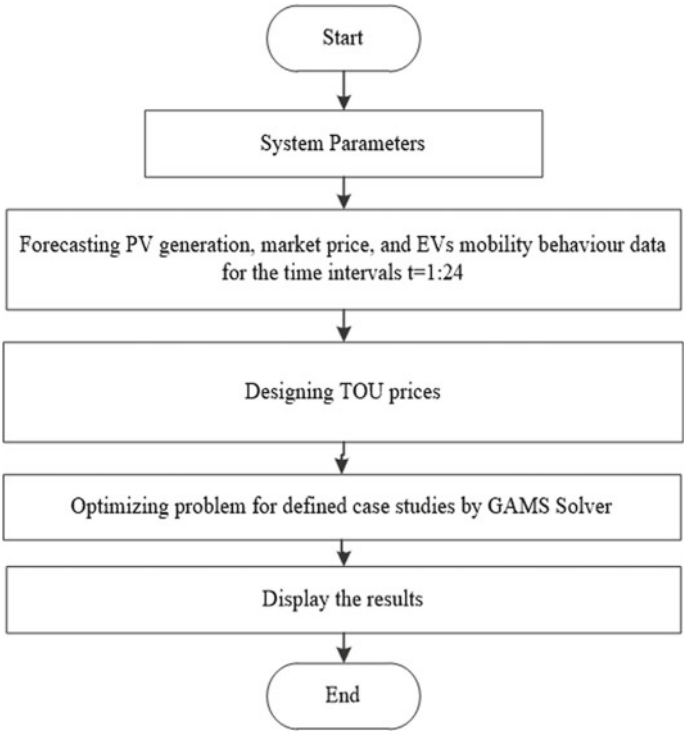

Fig. 3 Flowchart of the solution process

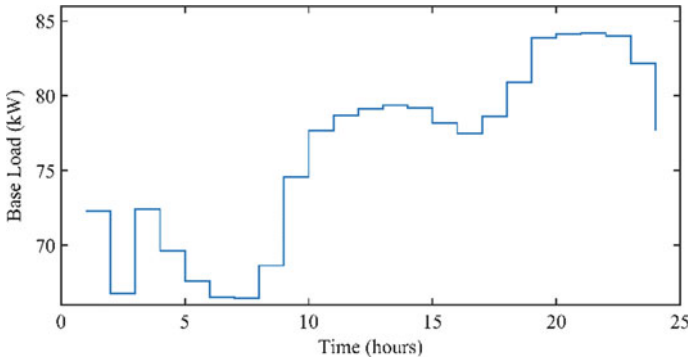

Fig. 4 Weekday base load profile of Houston zone in ERCOT market [28]

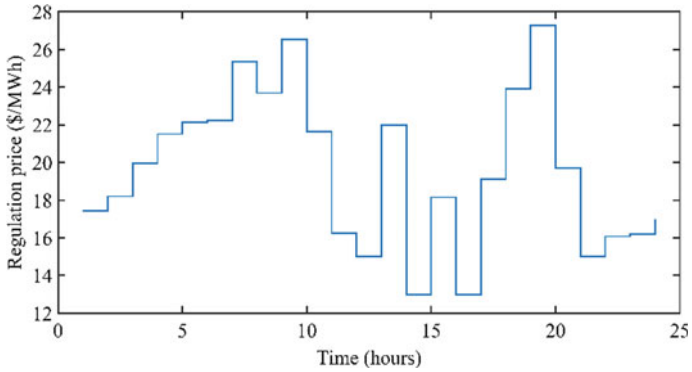

Fig. 5 Weekday regulation price of Houston zone in ERCOT market [28]

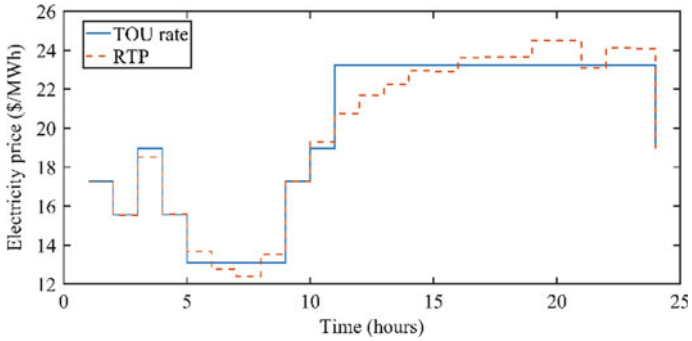

Fig. 6 Specially designed TOU price by EVA and weekday real-time prices in Houston zone in ERCOT market [28]

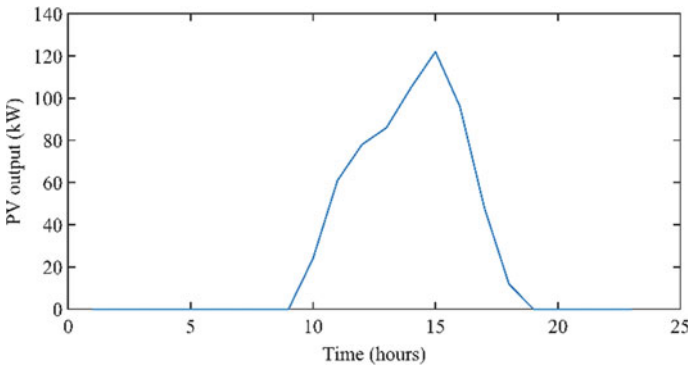

Fig. 7 PV output at car park [31]

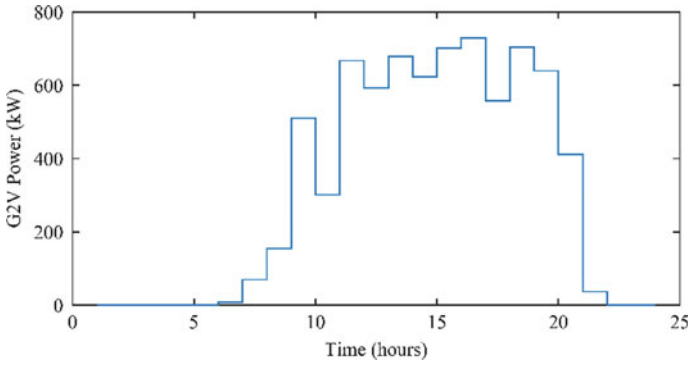

Fig. 8 G2V power charged from the grid

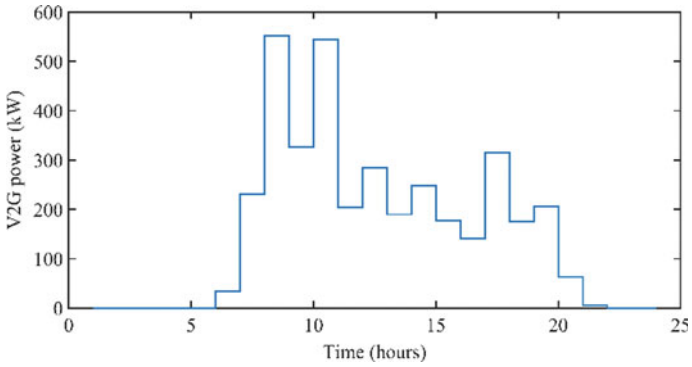

Fig. 9 V2G power injected to the grid

It is clear from these figures that when PV output is available then EVs charge and when there are valley hours, EVs inject power to grid.

Figure 10 shows regulation capacities provided by EVA in response to base load and TOU prices. When TOU rate is lower/higher, regulation down/up capacity is provided by EVA. As detected from Table 7, deviancy of EVA's success parameters is additional for electricity company three-tiered TOU DR as related to RTP and consequently lessens its profit by 29.213% while in case of designed five-tiered TOU, this drop is 16.53%. Accordingly, effectiveness of anticipated technique is confirmed.

5 Conclusion

The proposed model is economically viable concurrently improving revenue of EVA and EV users' charging cost. G2V/V2G rates variation is done by EVA to

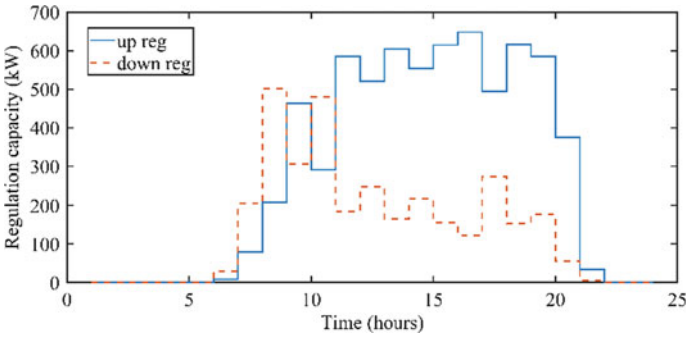

Fig. 10 Regulation capacities provided by EVA to SO

Table 7 Assessment of EVA's success parameters from implemented PBDR

PBDR type	Electricity company TOU	RTP	Designed TOU
EV users' G2V mode charge ($)	1048.33	1090.163	1090.801
EVA's revenue ($)	2441.653	2926.731	2608.311
EVA's profit ($)	1315.583	1758.827	1439.77

reduce the aggregated EVs charging load to sustain network operating limits. V2G power is injected from EVs having higher SOC at crest hours. Table 7 assess EVA's success parameters from implemented PBDR indicating respectively 10.88% and 16.58 % lesser revenue in designed TOU and utility TOU as compared to revenue in RTP. Designed TOU is quite efficient than utility TOU. Slow charging/discharging reduces battery degradation expenses. EVA's effective V2G/G2V scheduling process is certainly supportive to SO accommodating reliability through an escalation of PV incorporation and crest demand managing, balancing technical/fiscal constraints to support large-scale EVs without overloading on the local grid due to V2G power injected into grid during peak hours. Present work considered deterministic model for simplicity and reduce computational cost. It can be further projected for long-term planning problem of EVA considering temporal and spatial uncertainties from EVs, PV output and power market prices using Copula method.

References

1. Irena.org/publications/2020/Sep/Reaching-Zero-with-Renewables
2. https://www.greencarreports.com/news/1126706_cost-remains-the-biggest-barrier-against-ev-adoption-study-finds
3. Cheng S, Gao P (2018) Optimal allocation of charging stations for electric vehicles in the distribution system. In: 2018 3rd international conference on intelligent green building and

smart grid (IGBSG). Yi-Lan, pp 1–5. https://doi.org/10.1109/IGBSG.2018.8393550
4. Basu AK, Bhattacharya A, Chowdhury S, Chowdhury SP (2012) Planned scheduling for economic power sharing in a CHP-based micro-grid. IEEE Trans Power Syst 27(1):30–38. https://doi.org/10.1109/TPWRS.2011.2162754
5. Bessa RJ, Matos MA (2010) The role of an aggregator agent for EV in the electricity market. In: 7th Mediterranean conference and exhibition on power generation, transmission, distribution and energy conversion medpower. Agia Napa 2010:1–9. https://doi.org/10.1049/cp.2010.0866
6. Yilmaz M, Krein PT (2012) Review of benefits and challenges of vehicle-to-grid technology. In: 2012 IEEE energy conversion congress and exposition (ECCE). Raleigh, NC, USA, pp 3082–3089. https://doi.org/10.1109/ECCE.2012.6342356
7. Sovacool BK, Kester J, Noel L, de Rubens GZ (2020, 1) Actors, business models, and innovation activity systems for vehicle-to-grid (V2G) technology: a comprehensive review. Renew Sustain Energy Rev 131:109963
8. Gao X, Chan KW, Xia S, Zhou B, Lu X, Xu D (2019) Risk-constrained offering strategy for a hybrid power plant consisting of wind power producer and electric vehicle aggregator. Energy 177:183–191
9. Fouladi E, Baghaee HR, Bagheri M, Gharehpetian GB (2020) Smart V2G/G2V charging strategy for PHEVs in AC microgrids based on maximizing battery lifetime and RER/DER employment. IEEE Syst J
10. Guo Q, Liang X, Xie D, Jermsittiparsert K (2021) Efficient integration of demand response and plug-in electrical vehicle in microgrid: environmental and economic assessment. J Cleaner Prod 125581
11. Gao J, Yang Y, Ma Z, Gao F (2021) GGlueVaR-based participation of electric vehicles in automatic demand response for two-stage scheduling. Int J Energy Res 45(1):1128–1141
12. Amer A, Shaban K, Gaouda A, Massoud A (2021) Home energy management system embedded with a multi-objective demand response optimization model to benefit customers and operators. Energies 14 (2):257
13. Aghajani GR, Heydari I (2021) Energy management in microgrids containing electric vehicles and renewable energy sources considering demand response. J Oper Autom Power Eng 9(1):34–48
14. Nezamoddini N, Wang Y (2016) Risk management and participation planning of electric vehicles in smart grids for demand response. Energy 116:836–850
15. Rajamand S (2020) Vehicle-to-grid and vehicle-to-load strategies and demand response program with bender decomposition approach in electrical vehicle-based microgrid for profit profile improvement. J Energy Storage 32:101935
16. Hosseinnia H, Modarresi J, Nazarpour D (2020) Optimal eco-emission scheduling of distribution network operator and distributed generator owner under employing demand response program. Energy 191:116553
17. Yazdandoust M, Golkar MA (2020) Participation of aggregated electric vehicles in demand response programs. In: Electric vehicles in energy systems, Springer, Cham, pp 327–357
18. Alhelou HH, Mirjalili SJ, Zamani R, Siano P (2020) Assessing the optimal generation technology mix determination considering demand response and EVs. Int J Electr Power Energy Syst 119:105871
19. Kasturi K, Nayak CK, Nayak MR (2019) Electric vehicles management enabling G2V and V2G in smart distribution system for maximizing profits using MOMVO. Int Trans Electr Energy Syst 29(6): e12013
20. Onishi VC, Antunes CH, Trovão JP (2020) Optimal energy and reserve market management in renewable microgrid-PEVs parking lot systems: V2G, demand response and sustainability costs. Energies 13(8):1884
21. Liu Y, Gao S, Zhao X, Han S, Wang H, Zhang Q (2017) Demand response capability of V2G based electric vehicles in distribution networks. In: IEEE PES innovative smart grid technologies conference Europe (ISGT-Europe), pp 1–6
22. Pfeifer A, Dobravec V, Pavlinek L, Krajačić G, Duić N (2018) Integration of renewable energy and demand response technologies in interconnected energy systems. Energy 161:447–455

23. Timothée C, Perera AT, Scartezzini JL, Mauree D (2017) Optimum dispatch of a multi-storage and multi-energy hub with demand response and restricted grid interactions. Energy Proc 142:2864–9
24. Ahmadian A, Mohammadi-Ivatloo B, Elkamel A (2020) A review on plug-in electric vehicles: introduction, current status, and load modeling techniques. J Mod Power Syst Clean Energy 8(3):412–425
25. https://nhts.ornl.gov/assets/2017UsersGuide.pdf
26. www.sae.org/standards/content/j1772_201001/
27. Tesla Model S (2019) Charging guide pod point. www.Pod-point.com/guides/vehicles/tesla/2019/model-s
28. Market Information-ERCOT.com. Available online at: www.ercot.com.mktinfo
29. https://www.clippercreek.com/wp-content/uploads/2018/06/Time-to-Charge-Chart-20180615_Final_Low-RES.pdf
30. The GAMS software website; 2019 [Online]. Available http://www.gams.com/dd/docs/solvers/ /ipopt.pdf
31. 'Solar anywhere'. Available at https://data.solaranywhere.com/Public/Tutorial.aspx. Accessed 19 Sept 2019

Tri-band Elliptical Patch Antenna for GPS and IRNSS Applications

Ravi Mali, Fateh Lal Lohar, and Sarthak Singhal

Abstract A compact tri-band antenna for Indian Regional Navigation Satellite System (IRNSS) and Global Positioning System (GPS) receiver applications is presented. It consists of slot multiple slot loaded elliptical radiator, microstrip feed line, and conventional ground plane. The antenna is designed on Rogers RT5880 substrate having relative permittivity of 2.2 and loss tangent 0.0009. The volume of this antenna is 250 × 200 × 2.2 mm^3. It operates over three frequency bands L5 (1.1603–1.1686 GHz), L1 (1.5708–1.5804 GHz), and S (2.4816–2.5124 GHz). The reflection coefficient of proposed antenna as −16.739 dB, −13.478 dB, and −34.038 dB at frequencies is of 1.16484 GHz, 1.576 GHz, and 2.496 GHz, respectively.

Keywords GPS · IRNSS · Multiband · Slot · Elliptical patch

1 Introduction

The Global Positioning System (GPS) is an important service which provides by satellite communication. The time and location are provided by GPS in all weather conditions, anywhere on the earth. The GPS carriers use the L-band frequencies from 1 to 2 GHz. The L5 (1.176 GHz) band, L1 (1.576 GHz), and L2 (1.227 GHz) band are used for the civilian and military purposes [1]. At some locations, GPS does not work that, in turn leads to poor navigation and tracking. A system that provides better accuracy is called Indian Regional Navigation Satellite System (IRNSS). This system is developed by Indian Space Research Organization (ISRO). This system required seven satellites. By using this system, an accuracy of 10 m for the Indian land region

R. Mali (✉) · S. Singhal
Malaviya National Institute of Technology Jaipur, Jaipur, India
e-mail: 2020PWC5588@mnit.ac.in

S. Singhal
e-mail: sarthak.ece@mnit.ac.in

F. L. Lohar
Government Engineering College Jhalawar, Jhalawar, India
e-mail: fatehudml@gmail.com

S. Dwivedi et al. (eds.), *Flexible Electronics for Electric Vehicles*, Lecture Notes in Electrical Engineering 863, https://doi.org/10.1007/978-981-19-0588-9_49

and 20 m for the Indian Ocean region can be achieved. The coverage area can be extended up to 1500 km from the primary Indian region. IRNSS has high accuracy in position, time, and velocity of information in real-time applications [2]. IRNSS frequency band is L5 (1.176 GHz) and S (2.4968 GHz) [3, 4]. A compact multiband antenna has played an important role in wireless communication applications. In the last few decades, single-band antennas are replaced by multiband antenna [5, 6]. The methods such as the notch technique [7], slot technique [7], and fractal method [8] are used to design multiband antennas. The proposed antenna provides a three-band resonance by a cut of different types of slots on the patch. The first slot is to provide the GPS-band (1.576 GHz).The second and third slots provided IRNSS-band (1.176 GHz and 2.496 GHz) [9]. The CST software is being used for the analysis and design of the proposed antenna. The simulation result of the designed antenna is carried out by using the CST microwave simulation tool [10].

2 Design Methodology

2.1 Design Consideration

A radiating patch fabricates on the ground substrate. The size of the antenna depends on the resonance frequency and the dielectric constant of the substrate. A low-profile antenna has better efficiency than a high-profile antenna. A large number of miniaturization techniques are being for reducing the size of the antenna like shorting wall shooting pin, slow-wave method, capacitive and inductive feed line load, meandered line, fractal, and Koch structure (Fig. 1).

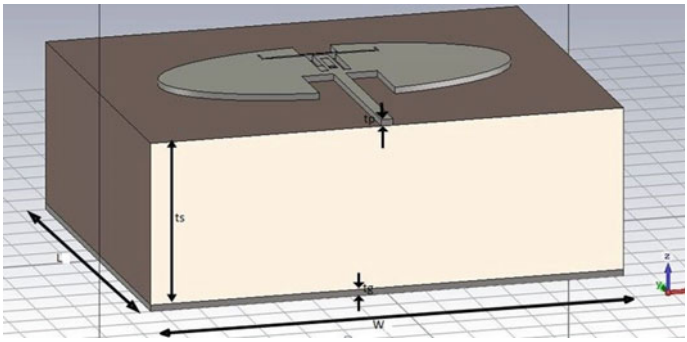

Fig. 1 Side view of proposed antenna

2.2 Design Evolution

Design consideration: The radius of the radiating patch is Rx = 93 mm and Ry = 44.7 mm. The substrate has a relative permittivity of 2.2 and loss tangent 0.0009.The antenna used Rogers RT5880 for substrate and PEC as conductor. The 3 dimensional view of the proposed antenna is shown in Fig.1. As shown in Fig. 2a, inset feed elliptical microstrip patch has dimensions of L1 = 90 mm, W1 = 6.30 mm, L2 = 33.65 mm, W2 = 16.85 mm, Rx = 93 mm, and Ry = 44.7 mm.

Design tri-band antenna: The slot technique has been used to design a multi- band antenna. As shown in Fig. 3, the slot cut in the middle of the patch with the dimension of LL1 and LL2. The slot cut along the desired band. The slot with length L4 has been affected the band of 1.576 GHz; however, the slot LL1 and LL2 has affected the resonant frequency at 1.576 GHz and 2.4976 GHz, respectively.

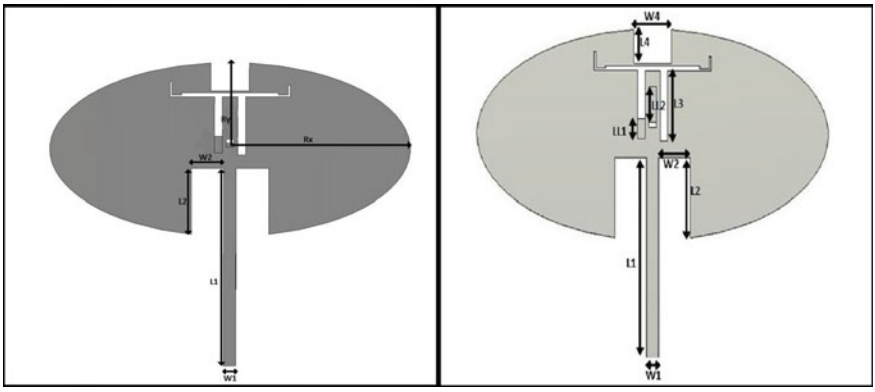

Fig. 2 Front view and structure of proposed antenna

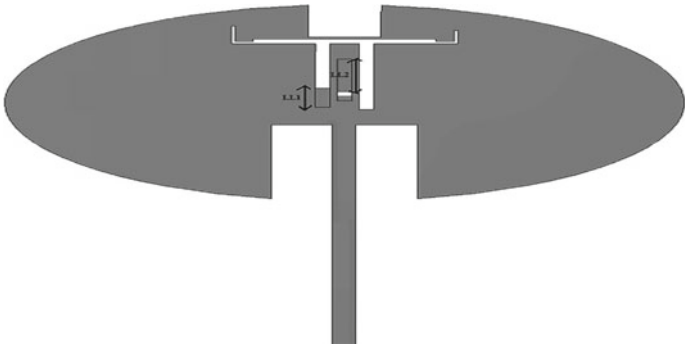

Fig. 3 Variation of slot LL1 and LL2 in proposed antenna patch

3 Result

In Fig. 4, the s11 parameters depicted due to slot length LL1, the length LL1 varied from 0 to 8.75 mm. The first L1-band is less affected but L5-band, and S-band are large affected due to variation of LL1 length, due to parametric analysis finally, we get our requirement band at LL1 = 8.5 mm. The reflection coefficient of these band L1, L5, and S at 1.1616 GHz, 1.576 GHz, and 2.4832 GHz are −20.463, −13.093, and −34.497 dB, respectively.

As shown Fig. 5, the resonant frequency is shifted due to changes in the slot length LL2.The length LL2 is varied from 0–15 mm. The resonant frequency bands are left shifted. There is no effect in L5-band. But if the length LL2 is increased, then both bands L1 and S are left shifted compare to 0 mm; however, at 15 mm, both bands are set at the desired band. The reflection coefficient at LL2 = 0 mm,

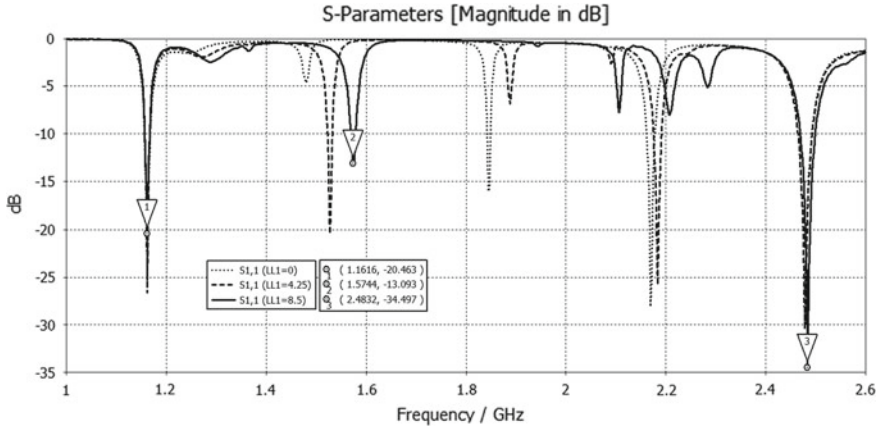

Fig. 4 S11 plot of proposed antenna for three value of LL1 (…) 0 mm, (---) 4.25 mm (—) 8.5 mm

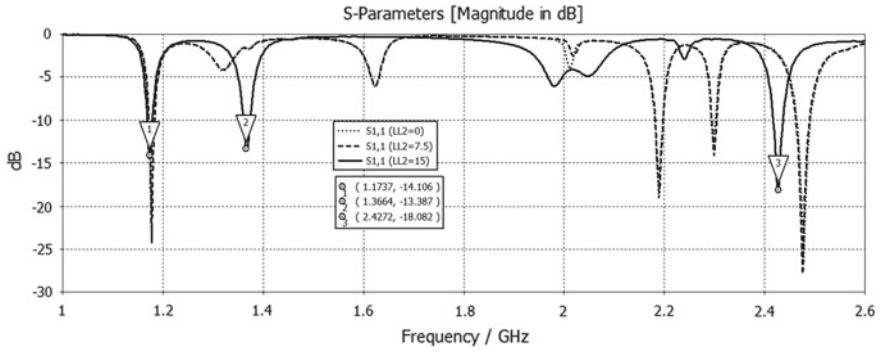

Fig. 5 S11 plot of proposed antenna for three value of LL2 (...) 0 mm, (---) 7.5 mm, (—) 15 mm

7.5 mm, and 15 mm is −14.106 dB at 1.1737 GHz, −13.387 dB at 1.366 GHz, and −18.082 dB at 2.42 GHz. As shown Fig. 6, the final reflection coefficient at 1.1648 GHz is −16.739 dB, 1.576 GHz is −13.478 dB, and 2.4976 is −34.038 dB. The gain, directivity, VSWR, and impedance bandwidth are more effective compare to another design. The L1-Band and L5-Band have narrow bandwidth. The S-band has wide-bandwidth. As shown in Fig. 7, the line impedance of the proposed antenna is 50.82 Ω. The impedance of the patch is match near to the feed line at 1.1648 GHz is 39.11 Ω, 1.576 GHz is 37.73 Ω, and 2.4976 GHz is 49.27 Ω.

In this proposed, the perfect matching impedance with all resonance bands. The real part of the impedance should be equal to line impedance. The imaginary part of impedance should be zero. Both the conditions are fulfilled, then maximum power

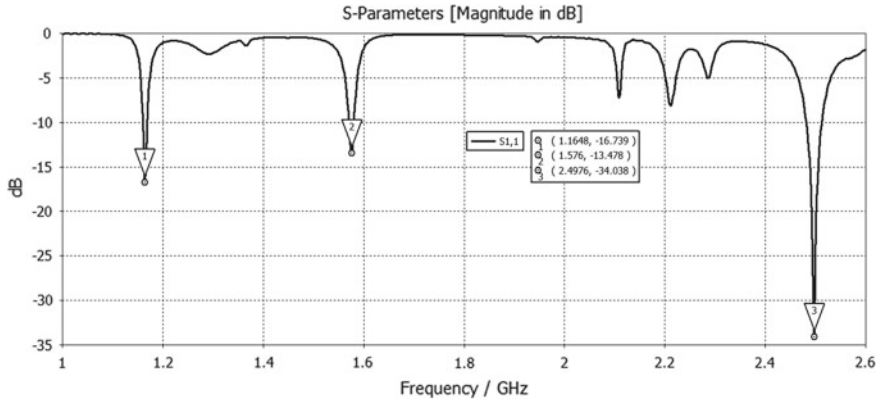

Fig. 6 Reflection coefficient (S11) for the proposed antenna at three resonance frequency 1.1648, 1.576, and 2.4976 GHz

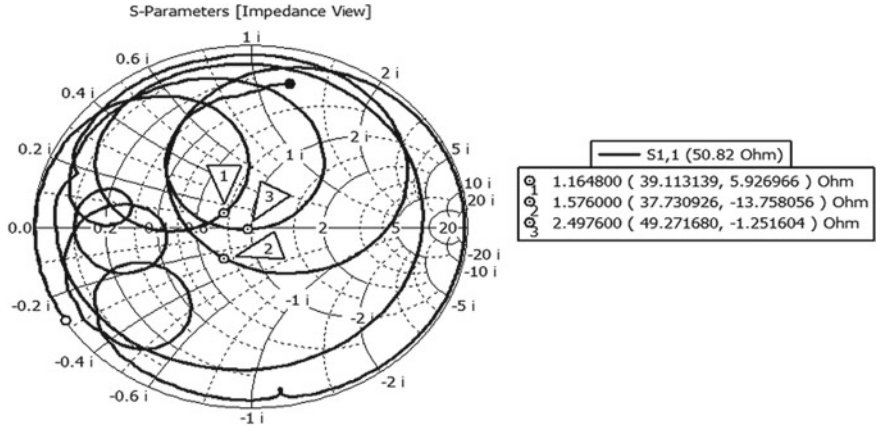

Fig. 7 Input impedance plot at three resonance frequency is 1.1648, 1.576, and 2.4976 GHz

is transferred to the load. The VSWR will be equal to unity for all bands. As shown in Fig. 8, the radiation efficiency at 1.1648, 1.576, and 2.4976 GHz are 89.49%, 86.30%, and 81.16%. In Fig. 9, the VSWR is nearby one which is 1.3407, 1.5377, and 1.0405 on 1.1648 GHz, 1.576 GHz, and 2.4976 GHz, respectively. It is shown that impedance of all tri-band not exactly matched with line impedance, some power reflect, therefore, VSWR not exactly unity.

The gain and direction of this antenna is shown in Figs. 10, 11, and 12, respectively. At 1.1648 gain, direction, side lobe magnitude, and angular width is 7.05 dB, 1.0°, −20.8 dB, and 74.6°. At 1.1648 gain, direction, side lobe magnitude and angular width is 7.83 dB, 6.0°, −16.9 dB, 82.3°. At 1.1648 gain, direction, side lobe magnitude, and angular width is 801 dB, 44.0°, −10.2 dB, and 39.1°. The surface current of the

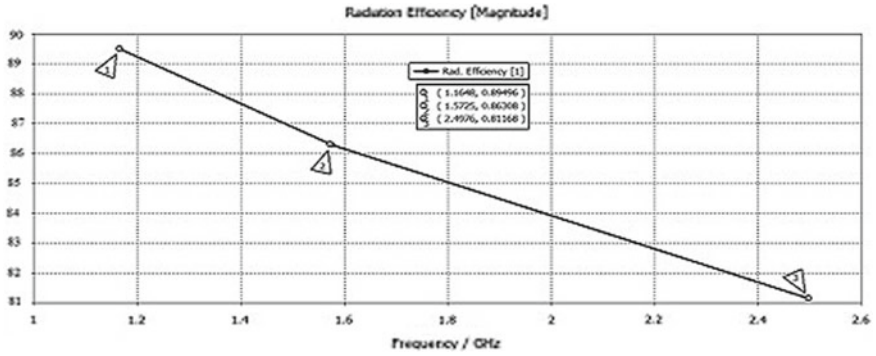

Fig. 8 Radiation efficiency for the proposed antenna at three resonance frequency is 1.1648, 1.576, and 2.4976 GHz

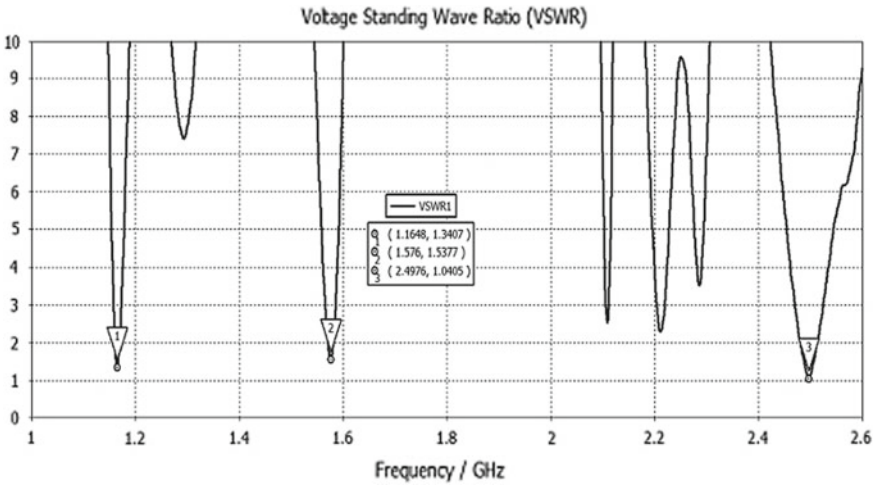

Fig. 9 VSWR proposed for antenna at three resonance frequency is 1.1648, 1.576, and 2.4976 GHz

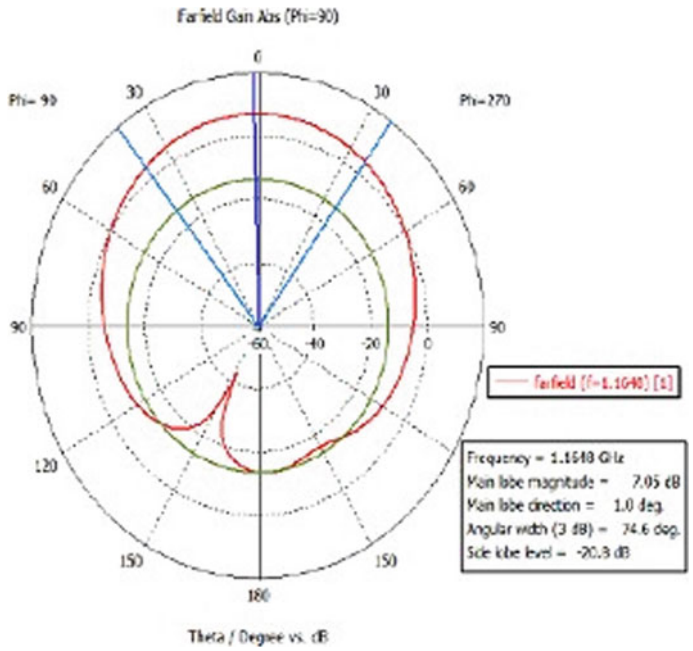

Fig. 10 Gain for proposed antenna at resonance frequency is 1.1648 GHz

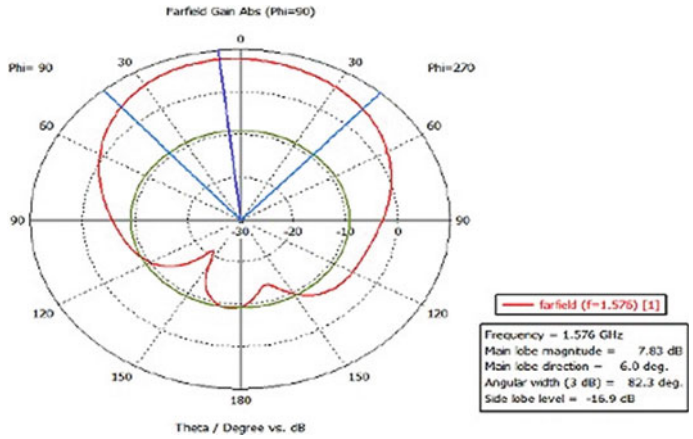

Fig. 11 Gain for proposed antenna at resonance frequency is 1.576 GHz

tri-band antenna is shown in Fig. 3a–c, and for different frequency, different current is flow on the surface of the antenna. Table 2 gives the comparison result of three band L5, L1, and S-band, respectively.

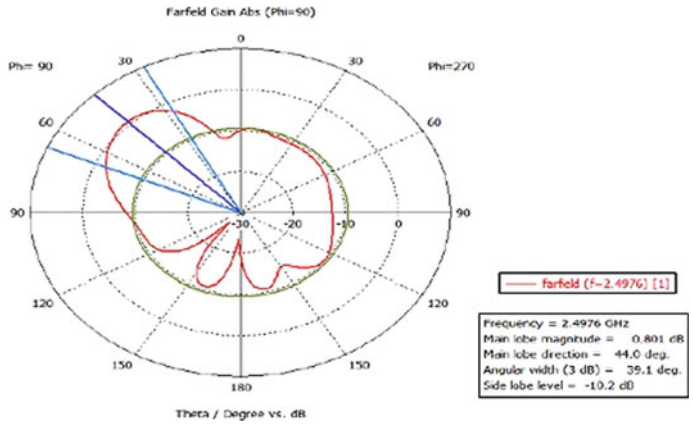

Fig. 12 Gain for proposed antenna at resonance frequency is 2.4976 GHz

4 Conclusion

The elliptical slot tri-band antenna for GPS and IRNSS is designed and simulated successfully on CST microwave studio. The simulation result of the antenna is shown at resonates 1.1648 GHz, 1.576 GHz, and 2.4976 GHz, and return loss is −16.53 dB, −13.247 dB, and −33.89 dB, respectively. The gain produced by the antenna is 7.05, 7.89, and 6.82 dB at 1.1648, 1.576, and 2.4976 GHz. The result in Fig. 4 shows the effect of slot on the patch is generated the multiband frequency characteristics. The multiband characteristics achieved using the changing of rectangular length LL1 and LL2. Table 1 gives all dimension parameter of the antenna and Table 2 gives all antenna performance results like return loss, gain, bandwidth, directivity, VSWR, and other important result which are used to working of antenna perfectly. In the future, we will convert this proposed antenna into tri-band circular polarization characteristics and miniaturization in volume.

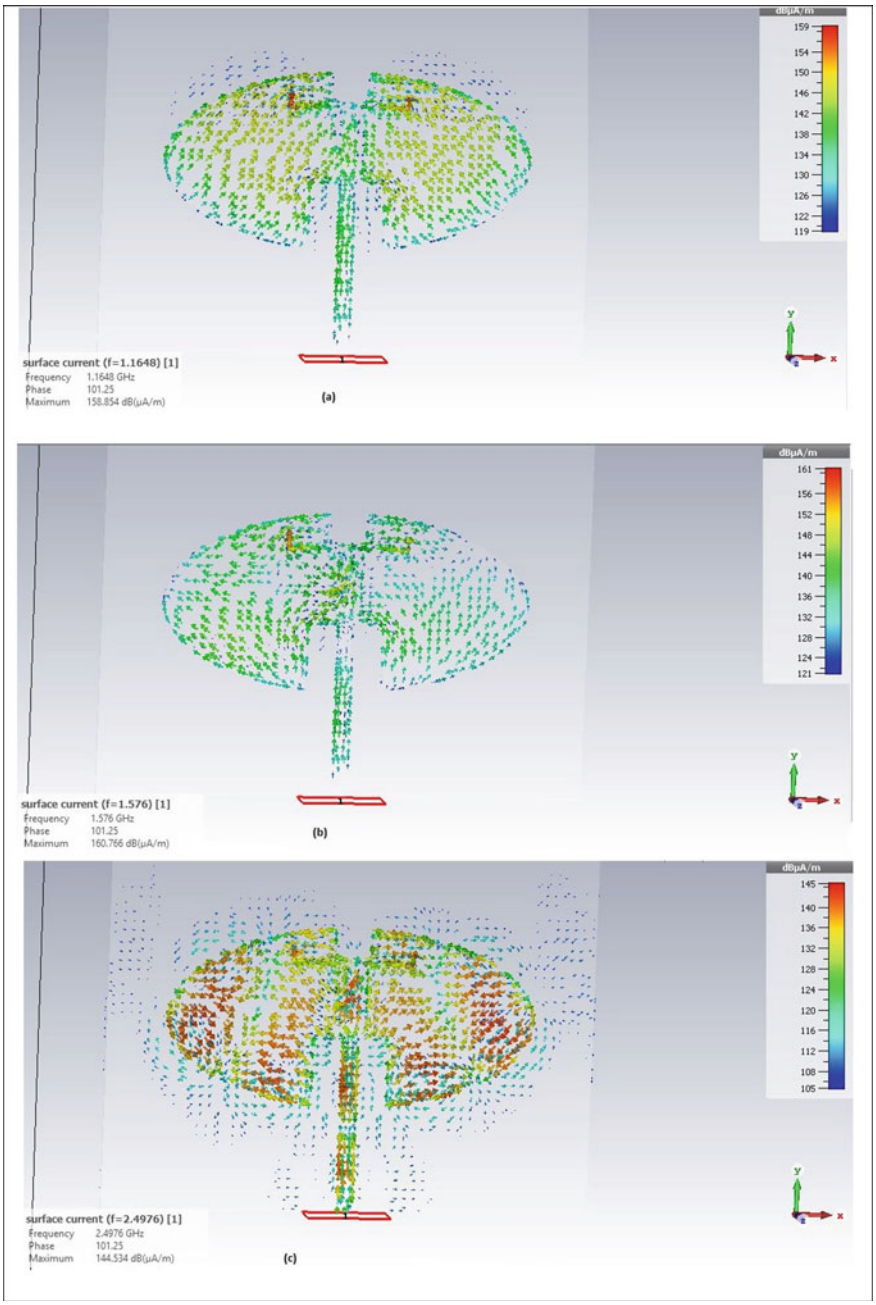

Fig. 13 Surface current proposed for antenna at three resonance frequency is 1.1648, 1.576, and 2.4976 GHz

Table 1 Dimensions of the proposed antenna

Parameter	Value (mm)	Parameter	Value (mm)
L	250	W	n200
RX	93	LL1	8.50
RY	44.7	LL2	15
L1	90	W1	6.30
L2	33.65	W2	16.85
L3	30	W4	20
L4	14.14	Ts	2.2

Table 2 Performance table of proposed antenna

Parameter frequency (GHz)	1.1648	1.576	2.4976
Return loss (dB)	−16.53	−13.247	−33.89
Impedance (Ω)	39.95	36.34	49.21
VSWR	1.3407	1.5377	1.0405
Bandwidth (MHz)	8.3	9.6	30.8
Radiation efficiency (%)	89.49	86.308	81.168
Gain polar plot (dB)	7.05	7.89	6.82
Directivity polar plot (dBi)	7.53	8.48	7.73

References

1. Supriya AS, Rajendra J (2017) A low-cost tri-band microstrip patch antenna for GPS application. In: 2017 Progress in electromagnetics research symposium—fall (PIERS—FALL), Singapore, 19–22 November. https://doi.org/ https://doi.org/10.1109/PIERS-FALL.2017.8293111
2. Naik P, Ruparelia S, Bhatt N, Mahajan M (2017) Review of design strategies of dual/tri-band antennas for GPS and IRNSS applications. ICTACT J Microelectron 3(2):379–384. https://doi.org/ https://doi.org/10.21917/ijme.2017.0067
3. Karthick M, Kashwan KR (2015) Design of IRNSS receiver antenna for smart city applications in India. In: Proceedings of IEEE global conference on communication technologies, pp 277–280. https://doi.org/10.1109/GCCT.2015.7342666
4. Wang L, Guo YX, Sheng W (2012) Tri-band circularly polarized annular slot antenna for GPS and CNSS applications. IEEE Antennas Wirel Propag Lett. https://doi.org/ https://doi.org/10.1109/LAWP.2012.2200869
5. OGUNLADE MA, ZHENG HX (2015) Design of multiband microstrip antenna for mobile wireless communication. In: 3rd international confer ence on management, education, information and control (MEICI 2015), May. https://doi.org/ https://doi.org/10.2991/meici-15.2015.29
6. Sharma V, Patidar DK (2017) Design and analysis of staked multiband microstrip antenna. Int J Adv Res Comput Commun Eng 6(4). https://doi.org/ https://doi.org/10.17148/IJARCCE.2017.6415. ISO 3297:2007 Certified
7. Gogate M, Desai A, Bhujbal M (2017) Multiband patch antenna for wireless devices. In: International conference on emanations in modern technology and engineering (ICEMTE-2017), 5(3)

8. Singh A, Singh GP, Manvendra PCP, Mukesh K, Saxena R (2017) Analysis of V Slot multiband microstrip patch antenna for S, C and X. IJETT J 48(6). https://doi.org/10.14445/22315381/IJETT-V48P259
9. Narayan KGS, Velavikneshwaran V, Baskardas JA (2018) A triband microstrip stacked patch antenna design for GPS and IRNSS application. In: 2018 IEEE Indian conference on the antennas and propagation (InCAP). https://doi.org/10.1109/INCAP.2018.877071
10. Computer simulation tool, CST tool

First Principles-Based Optoelectronic Investigation of B-Doped $CuAlS_2$ Flexible Thin Film Solar Cells

Aditi Gaur, Karina Khan, Amit Soni, Alpa Dashora, and Jagrati Sahariya

Abstract With the upcoming demand for compensating high-cost Si solar cells, low-cost flexible thin films have come to rescue, offering a low-cost electricity solution. These involve a varied collection of inorganic, organic and their hybrid solar cells which are spread over the substrates offering flexible and high-throughput technological solution. Photovoltaic (PV) device designs have explored new dimensions of light weightiness and mechanical technologies of flexible thin film termed as flexible solar cells. These serve as a suitable indoor and outdoor applications' energy source. Integration of flexible PV panels can be made easier with varied dimensions of infrastructure, which in turn aids in formation of innovative energy oriented product designs. CIGS compounds stand out to be the ones that provide highest efficiencies with a value of 18.8% including all thin filmed PV devices. The role of absorbers in thin film solar cells (TFSCs) is majorly played by ternary chalcopyrite samples such as CuAlSe2, $CuGaSe_2$, $CuInS_2$ and $CuInSe_2$ hereby providing high-valued optical absorption coefficient. In this paper, we have presented a density functional theory calculation of B-doped $CuAlS_2$ thin film, whose 10 Å sized vacuum offers an approximate bandgap of 0.7 eV with the exchange correlation as Trans-Blaha modified Becke–Johnson (TB-mBJ) functional. An optoelectronic analysis of this system is presented to investigate the presence of boron in the system as doping element and its effect on the compound's application.

Keywords Absorption coefficient · DFT · Flexible thin film solar cells · Photovoltaic devices

A. Gaur · A. Soni (✉)
Department of Electrical Engineering, Manipal University Jaipur, 303007, Jaipur, India
e-mail: amitsoni_17@yahoo.co.in

K. Khan
Department of Physics, Manipal University Jaipur, 303007, Jaipur, India

A. Dashora (✉)
Department of Physics, The M. S. University of Baroda, 390002, Vadodara, India
e-mail: dashoralpa@gmail.com

J. Sahariya
Department of Physics, NIT Uttrakhand, 246174, Srinagar, Uttarakhand, India

S. Dwivedi et al. (eds.), *Flexible Electronics for Electric Vehicles*, Lecture Notes in Electrical Engineering 863, https://doi.org/10.1007/978-981-19-0588-9_50

1 Introduction

Silicon as an element has been the key basis of photovoltaic (PV) industry due to its abundance in nature [1]. Since more than half a century crystalline silicon solar cells have been utilized but there has been a need of more efficient and cost friendly technology [2]. Traditional solar panels are most likely defeated by thin film flexible solar cell technology which overtakes the renewable energy field. CIGS, CdTe and α-Si:*H* are the compounds among flexible thin film solar cells which have gained interest in today's time. Despite domination of Si solar cells over the photovoltaic market, its high-production cost has aroused everyone's concern [3]. The compensating feature of discovering low-cost flexible substrate as a way to reduce module production cost has been made.

Tremendous growth of thin film solar cells which are flexible and light weighted have made a position in the research field like textile-based wearable electronics, movable chargers, remotely provided power supplies, device displays, etc. [4]. Many organic compounds have also reported light weightiness, flexible nature, low cost, appreciable chemical resistance, heat stability and moisture resistance [5]. These features like lightweight, installation, storage capacity, uninterrupted processing ability, easy process, etc. have made their usage enhanced. Due to these reasons, flexible solar modules stand out to be ideal for membrane roofs (TPO and EPDM low-slope roof systems). Because of these lightweight thin film modules, installation over low-load capacity roofs as presented in an article by Gumm [6]. In one of the articles [7], high conversion efficiencies have been observed in CIGS thin film solar cells with less material requirement and easier procedural steps in comparison to crystalline silicon solar cells. But for better environmental-friendly cost-efficient options, building integrated photovoltaics (BIPV) has been adopted. To meet such requirements, conventional hard and heavy glass substrates of CIGS thin film solar cells must be replaced with negligible efficiency loss and flexible lightweight substrates. Authors in [8] have depicted the optoelectronic investigation of $CuAlS_2$ and $CuAlSe_2$ with better optical absorption reported for the later sample. $CuAlS_2$ showed a bandgap of about 1.77 eV with PBE exchange correlation. This is a suitable material for optoelectronic application. In a work by Jaffe and Zunger [9], the experimental bandgap of $CuAlS_2$ is quoted to be around 3.49 eV categorizing it as wideband semiconductor. Authors in their work [10] depicts the theoretical as well as experimental investigation of $CuAlS_2$ thin film-doped with Sn. Results have shown better photoelectron chemical performance (PEC) in Sn-doped $CuAlS_2$ films due to wide absorption spectrum caused by the intermediate band [11]. In another work by Naveena [12], earth abundant and non-toxic quaternary thin film system of $CuAl_{1-x}Fe_xS_2$ have been created. With the insertion of Fe, the optical absorption of the film has increased in comparison to bulk $CuAlS_2$. Authors in [13] have used low-cost dopants, i.e. Fe and Sn in $CuAlS_2$ (CAS) thin film and their insertions report better absorption as compared to bulk and thin film. The Sn-doped CAS film has by far reported higher effective mass of charge carrier and thus provide improvised performance. The optical and structural parameters of $CuAlS_2$ thin films have been

studied through chemical bath deposition technique. Its X-ray diffraction (XRD) reveals the effect of annealing temperature and simple calculation of optical parameters like refraction, optical bandgap, etc. have been done through transmission and absorption spectra [14].

2 Computational Details

Wien2k tool has been used with first principle linear augmented plane wave (FP-LAPW) methodology as the guiding force in investigating the electronic, structural and optical aspects of the thin film compound. Tran-Blaha modified Becke–Johnson (TB-mBJ) as the exchange and correlation functional is used to obtain the bandgap for $CuAl_{0.89}B_{0.11}S_2$ system for an accurate calculation. The lattice dimensions and several other internal parameters of the structure are taken as follows: $a = b =$ 5.33 Å and $c = 10.57$ Å [15] with product of R^*K_{max} that decides the accuracy and computational speed of system valued as 6; G_{max} which helps in calculation of certain parameters like density gradient is valued as 12; k-points valued as 20 and l_{max} which decides the maximum value of angular momentum provided to the wave function expansion is set as 10. The RMT sphere values for Cu are valued 2.38 a.u., for Al is valued 2.22 a.u. and for S is valued as 1.95 a.u. Following the procedural steps, a thin film of $CuAlS_2$ doped with boron has been prepared by a $2 \times 2 \times 2$ dimensional supercell with a vacuum sized 10 Å. Boron has been added to the compound with a 11.11% value at Al (Aluminium) site which has yielded a bandgap of about 0.7 eV(=0.67 eV). The initial bulk structure belongs to the tetragonal space group numbered as #122–I42d which later on gets transformed into primitive tetragonal category numbered as 81–P4.

3 Results and Discussion

3.1 Structural and Electronic Analysis

Depending upon the pictorial representation, boron in $CuAlS_2$-doped system is observed to have created a two atomic layer separation of about 10 Å with the creation of thin film. The doping element in the created film can be observed stacked in the upper and lower atomic layers of primitive tetragonal structure as shown in diagrammatic representation of doped thin film structure in Fig. 1a. Figure 1b depicts tetragonal structure of Brillouin zone with the space group turned to 81–P4 through supercell formation. This system's thin film offers a bandgap of about 0.7 eV with the TB-mBJ functional. In this paper, we have gathered the electronic analysis of the doped system's thin film based on its structure, and the slab inserted becomes the deciding factor which tells us the resemblance between film and bulk material

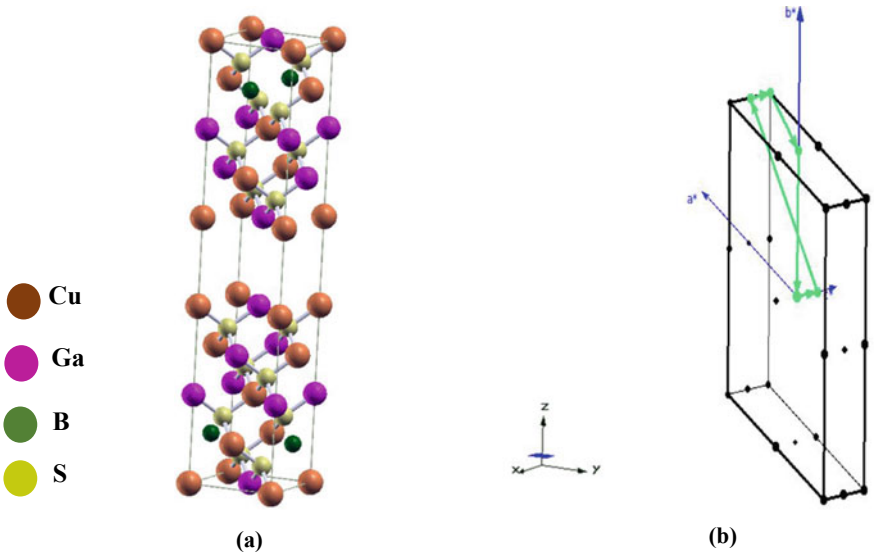

Fig. 1 **a** Crystal structure and, **b** Brillouin zone of $CuAl_{0.89}B_{0.11}S_2$

based on respective bandgaps. The diagrammatic representation of band structure and density of states (DOS) spectra [16] can be correlated on the energy axis. The science behind the electronic transitions between the different bands of a system is revealed by the analysis of band structure. DOS and PDOS reveal the science behind the state densities of different element through their orbital effect and their total contributions done to a system. For CuAl0.89B0.11S2, we set the interpolations in between each of the k-points (Γ, *Z*, *M*, *A*, *X*, Γ) forming the band structure as in Fig. 2a. In this figure, we can see the formation of 0.7 eV band, with the conduction band and valence band formed around the fermi energy. The figure reports a direct band formed between these bands. The configuration of this thin film compound presents a combinational result of s, p and d orbitals which acts as the deciding factor in positioning of upper valence band exactly underneath the fermi energy's slot (EF = 0). DOS spectra observes major contributions by 4 s orbitals of Cu, 3*p* orbitals of Al and 3*p* orbitals of *S* along with the dopant element *B*'s contribution being 2*p*. The density of states and partial density of states for $CuAl_{0.89}B_{0.11}S_2$ has been presented in Fig. 2b.

3.2 Optical Analysis

The optical analysis of a system is defined by parameters like absorption, refraction, reflectivity and dielectric tensor. With a brief description, area under the curve for a system depicts the absorption aspect and is attained through integrated absorption

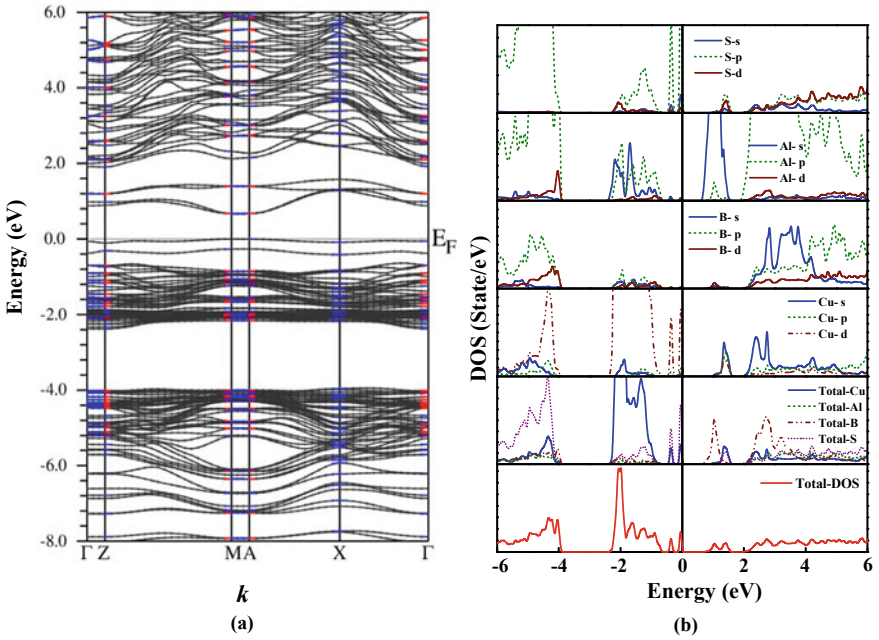

Fig. 2 **a** Band Structure and, **b** DOS of $CuAl_{0.89}B_{0.11}S_2$ system

coefficient (IAC) value. In our work, the value of IAC is reported to be 87.92 for that particular area under curve. Initially, the absorption coefficient shows isotropic nature with anisotropy shown in the later optical range (2–5 eV). The absorption curve for $CuAl_{0.89}B_{0.11}S_2$ compound is shown in Fig. 3a.

The interband electronic transitions correlating to the band structure is expressed in terms of imaginary dielectric tensor [17]. Kramers–Kronig relation is used to attain a high-frequency dielectric constant which is known as real dielectric tensor [18]. In the present work, all the optical properties are depicted in the form of two polarizations, i.e. perpendicular while plotting along x and y values ($E \perp c$) termed as ordinary and perpendicular for plotting with z values termed as extraordinary ($E \| c$). The imaginary and real dielectric part shows anisotropy which means there is difference in the parallel and perpendicular components of system. The dielectric tensor plot for imaginary component of $CuAl_{0.89}B_{0.11}S_2$ system is depicted in Fig. 3b along with real component of dielectric tensor plot as shown in Fig. 3c. The dielectric function $\varepsilon(\omega)$ provides help in determining the absorption coefficient of a system along with other optical aspects like refraction and reflectivity [19]. The absolute refractivity value $\eta(0)$ valued as 2.53 is shown in Fig. 4a for the compound $CuAl_{0.89}B_{0.11}S_2$. Reflectivity of the system is depicted in Fig. 4b with a percentage value of 18.7%. To improve the efficiency of system, the optical losses in it must be

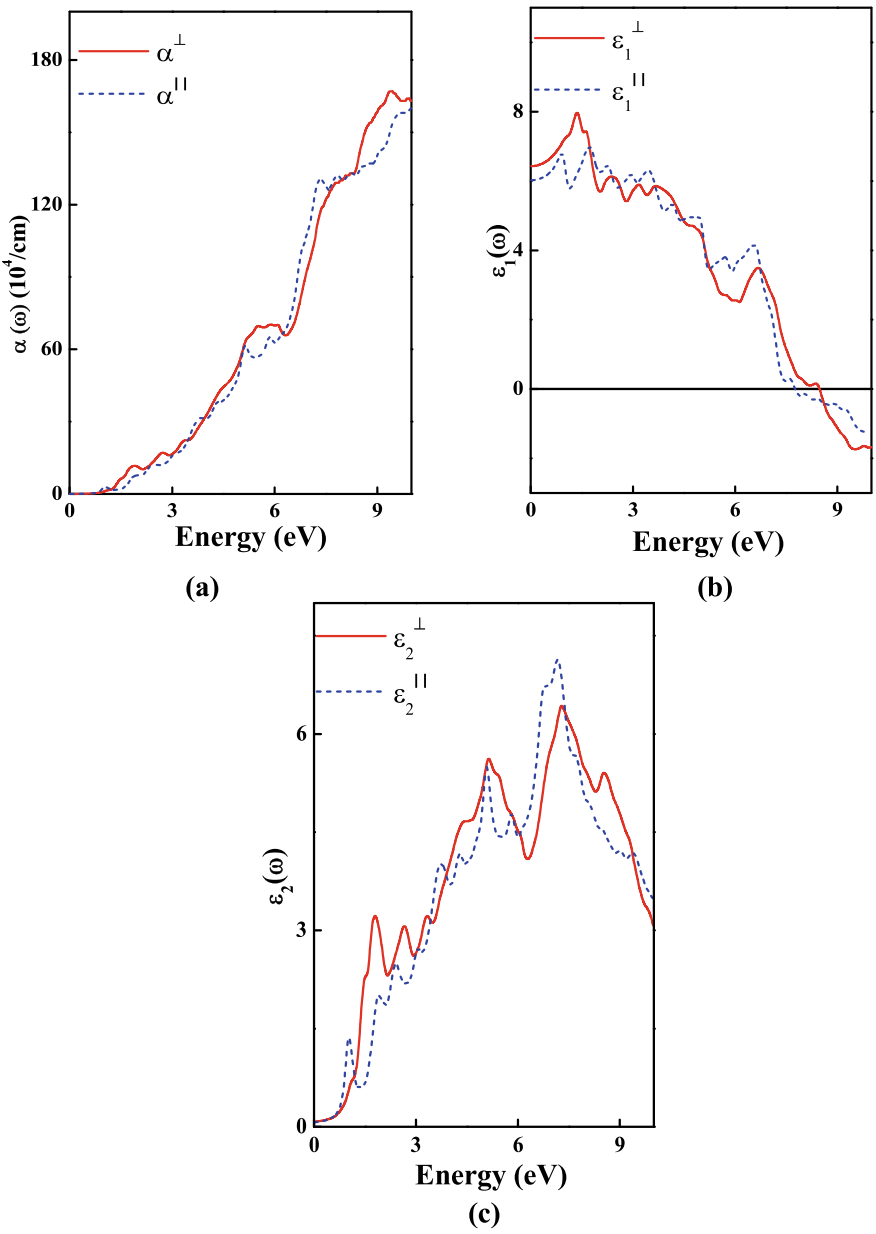

Fig. 3 **a** Absorption curve plot, **b** imaginary dielectric tensor, **c** real dielectric tensor plot of $CuAl_{0.89}B_{0.11}S_2$

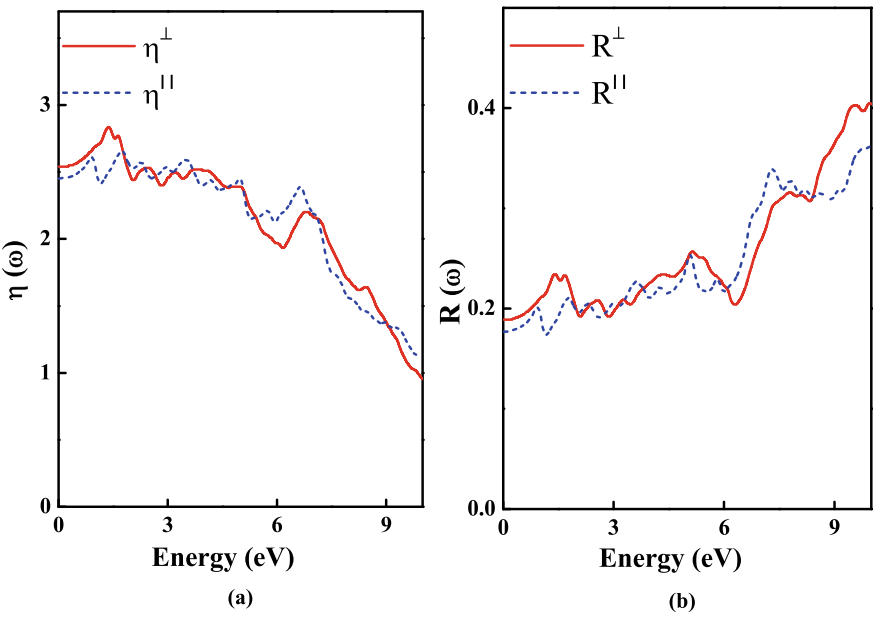

Fig. 4 **a** Refractivity, **b** reflectivity curve of $CuAl_{0.89}B_{0.11}S_2$

reduced and this analysis is provided by studying the optical properties [17]. Reflectivity and refractivity plots also clearly report anisotropic nature in the system due to doping of boron.

4 Conclusion

The bandgap calculation of doped thin film $CuAl_{0.89}B_{0.11}S_2$ has been made through TB-mBJ-based exchange correlation. The process of thin film was accomplished by the insertion of about 10 Å vacuum slab. Optical properties have shown anisotropy between the ordinary and extraordinary components, i.e. the perpendicular and parallel components. The doped film has shown a direct bandgap nature similar to the bulk material with low value of reflection serving as a boon. The optoelectronic investigation of system aids in exploring the new technology of flexible thin film solar cells in the optoelectronic category. This type of flexible thin film solar cell can produce an interesting candidature in the optoelectronic application field. In future, we can explore more features of this film by investigating the increased doping percentage of boron in $CuAl_{0.89}B_{0.11}S_2$ thin film. Also, we can alter the different vacuum sizes to check its effect on the bandgap of the system and choose accordingly. Flexible thin film solar cells are the current technological advancement

in the optoelectronic field of application, by taking up the wideband semiconductors and using the bandgap engineering technique on it, we can provide more such feasible solutions to its existence.

Acknowledgements We would like to thank Prof. P. Blaha for his rigorous efforts in the proper utilization of wien2k code in obtaining a fruitful product for material science. A theoretical approach has been created through this platform for achieving material investigation. Our sincere gratitude to the organization DST-SERB, New Delhi, under the project vide grant number EMR/2017/005534 along with Manipal University, Jaipur, to provide a platform for carrying out all possible theoretical research work.

References

1. Yamaguchi M (2001) Renew Sustain Energy Rev 5:113–135
2. Choubey PC, Oudhia A, Dewangan R (2012) Recent Res Sci Technol 4:99–101
3. Ramanujam J, Bishop DM, Todorov TK, et al. (2019) Progress in material science 110(100619):1–60
4. Giacomo FD, Fakhruddin A, Jose R, Brown TM (2016) Energy Environ Sci 9:3007–3035
5. Get R, Islam SM, Singh S (2019) Microelectronic Engineering 222(111200):(1–23)
6. Gumm M (2021) https://www.miasole.com/the-advantages-of-flexible-thin-film-solar-modules/
7. https://www.printedelectronicsworld.com/journal/print-articles.asp?articleids=20011 (2021)
8. Soni A, Arora CM, Gupta V (2012) Electronic structure and optical properties of solar cell materials $CuAlX_2$ (X=S, Se). In: Asia-Pacific power and energy engineering conference 2012, IEEE, pp 1–4
9. Jaffe JE, Zunger A (1983) Phys Rev B 28:5822
10. Guo C, Yang C, Xie Y, Chen, P Qin M, Huang R, Huang F (2016) RSC Adv 1–6
11. Naveena D, Thirumalaisamy L, Dhanabal R, Sethuraman K, Bose AC (2020) ACS Appl Energy Mater 3(11):10550–10559
12. Gaur A, Khan K, Bhagat BR, Sahariya J, Soni A, Dashora A (2021) Sol Energy 215:144–150
13. Alwan TJ, Jabbar MA (2010) Turk J Phys 34(2):107–116
14. Verma UP, Jensen P, Sharma M, Singh P (2011) Theor Comput Chem 975:122–127
15. Omar A (1999) Elementary solid state physics. Addison-Wesley Publishing Company, USA
16. Terzzas EY et al (2009) Adv Mater Res 68:89–95
17. Chen R, Persson C (2014) Adv Mater Res 894:254–258
18. Hadjab M, Ibrir M, Berrah S et al (2018) Optik—Int J Light Electron Opt 169:69–76
19. Elanzeery H, Daif OE, Buffiere M et al (2015) Phys Status Solidi A 1–7

Versatile Gaming by Neurological and Behavioral Analysis

Krishna Soni, Arjun Singh, and Punit Gupta

Abstract Neurological and behavioral assessment, which is the depiction of the ability of an individual's brain to adapt to certain aspects and situations. Typically, the human brain is of the highest neuroplasticity among all living beings, i.e. the adaption quotient of their brain is the fastest and the most efficient, yet still most of the individuals repel changes and are more comfortable in static environment rather than dynamic and unpredictable. In this work, we have proposed a model for behavior analysis a human being using VR and unity using its decision and choices.

Keywords AR · VR · Unity · Neuroplasticity

1 Introduction

NBA here stands for neurological and behavioral assessment, which is the depiction of the ability of an individual's brain to adapt to certain aspects and situations. Typically, the human brain is of the highest neuroplasticity among all living beings, i.e., the adaption quotient of their brain is the fastest and the most efficient, yet still most of the individuals repel changes and are more comfortable in static environment rather than dynamic and unpredictable. This trait of the human brain can be classified as the triggering of various brain forms. Namely reptilian, paleo-limbic, neo-limbic and prefrontal. All these forms are responsible for various patterns of understanding for the brain. There are different types of VR glasses, starting from simple ones such as Google cardboard and VR box, to more sophisticated ones such as PS VR, HTC Vive. With the help of these glasses only, one can indulge in the experience, which remains as the downside of the technology, a version of virtual reality is

K. Soni · A. Singh (✉) · P. Gupta
Department of Computer and Communication, Manipal University Jaipur, Jaipur, India
e-mail: vitarjun@gmail.com

K. Soni
e-mail: infinitebuster@gmail.com

P. Gupta
e-mail: punitg07@gmail.com

S. Dwivedi et al. (eds.), *Flexible Electronics for Electric Vehicles*, Lecture Notes in Electrical Engineering 863, https://doi.org/10.1007/978-981-19-0588-9_51

also in the form of AR or augmented reality which does not require the use of glasses, but it is currently limited to the use to screen overlays and not immersive experience. The game provided will attempt to determine the dominance of which form of brain an individual has. Digital reality is now the most prevailing form of collective technology, and it describes the use of digital products such as mobile phones, computers, laptops and smart devices; most of the time, people are indulged in one or the other form of technology, making it their own reality. Virtual reality, which originated originally as level up for gaming is now becoming a whole new field of technology by enabling us to create a digital world and to immerse in.

1.1 Theme of the Assessment

The theme of the assessment is one, which is generally used, i.e., outer space. The process takes place amidst the orbit of Earth, surrounded by satellite and planets. The story itself of the assessment is chosen and tailored in such a way that it coincides with the setup to make the user feel more immersed in the assessment. This has direct effect over the efficiency of the process as the user can indulge in what they are witnessing in front of them. Based on scientific research, it is proven that the most engaging type of experience is one which is experienced by all the senses. Overall understanding of the movement of planets and their satellites were taken place when the assessment was being created to provide maximum preciseness possible.

While experiencing VR Fig. 1, some people may find it nauseous or have a feeling of vertigo, which is completely normal, though prolonged usage of VR glasses is not recommended. If the symptoms present itself, it is best to sit in an upright position with head straight with the back, this will gradually rectify the feeling of vertigo.

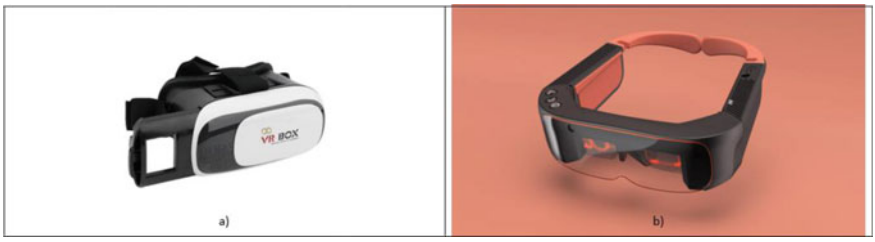

Fig. 1 Equipment used in virtual reality (left) and augmented reality (right)

1.2 Pros and Cons of Assessment

It is true that every individual is different and has varying traits, which proves the fact that one's strengths are other's weakness. So, to determine which dominance an individual has, it is required for him or her to undergo NBA.

1.3 The Game Plot

The total game plan from starting to all the respective ending is shown Fig. 2. There

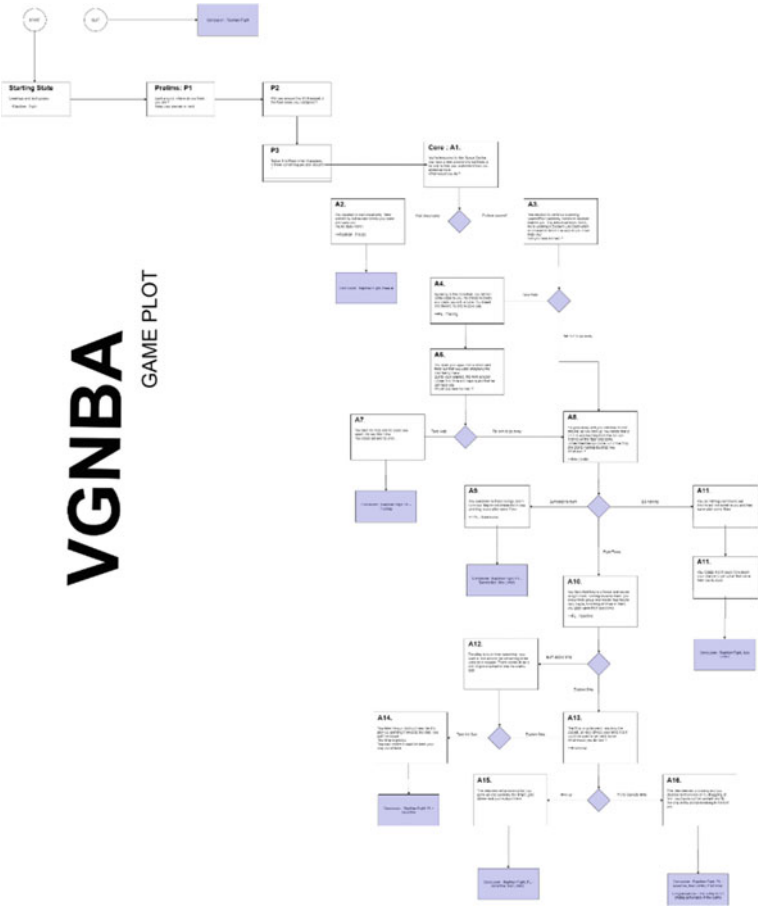

Fig. 2 VGNBA game plot

are numerous possible endings achievable in the game and all this depends upon the selection/choices made by the user inside the game premises.

2 Proposed Model

There are various modules, incorporated, which together makes it work. These modules are:

Reptilian (limbic amygdala): This is the most common category to be found in individuals; it consists of three different sub-categories which are fight, flight or freeze (Fig. 3).

Fight: The autonomous response of the brain to resist or "fight" a certain and sudden situation; this is the most primitive of the brain functions. Example—the urge to sway off an insect if it lands on your body.

Flight: The response which triggers when a potential threat is witnessed by the brain. It results in the individual running away or "taking a flight" from the situation. Example—running to a side when a vehicle is approaching swiftly.

Freeze: This is less common and means that the brain is not able to properly assess the situation and ends up "freezing" in the situation. Example—how an individual might freeze when seeing a lion in the forest.

Paleo-limbic: This category defines how an individual is from the core, i.e., what "general nature" they possess. There are various terms in this category, a person can be one of them or a combination of them (Fig. 4).

Dominant: Individuals who have a dominating nature or confidence about them. They believe that their successes are their doings and are high motivated to do things.

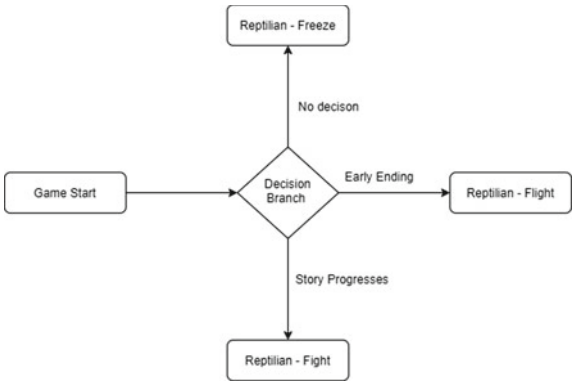

Fig. 3 Reptilian module

Fig. 4 Paleo-limbic module

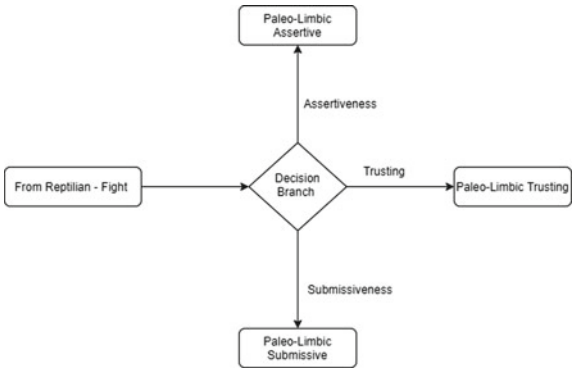

Submissive: People with fragile personalities who are more reliant on others and the environment for the completion of their tasks.

Assertive: People who have a tendency to balance the above two. They can say Yes to what they want, and No to what they do not.

Trusting: This trait signifies that the individual will easily trust someone, rather than doing a keen observation first. This leads to mental and physical deterioration when she/he faces distrust.

Doubtful: People with a sense of self-doubt when it comes to taking up challenges up front.

Neo-limbic: This is where our brain is most of the time. It is also responsible for memories and experiences, i.e., whenever an individual is faced with a situation, she/he looks into its past experience as to what would be most acceptable or "correct" in that situation. (Fig. 5). An individual's preference/liking/disliking is formed here on the basis of their experiences and past decisions. Apart from this, neo-limbic also define drives or what makes people do things.

Fig. 5 Neo-limbic module

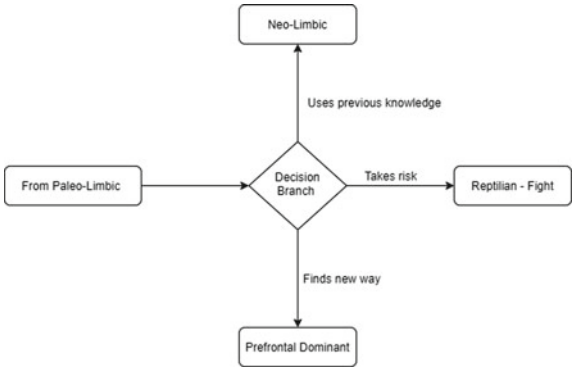

Intrinsic Drive: The individual in internally motivated to do something such as cleaning the house if she/he likes clean places (Fig. 6).

Extrinsic Drive: The individual needs to be pushed or forced to do something out of their "comfort zone" which might be a result of a past experience (Fig. 7).

Obsessions: All of the people without exception are obsessed/addicted with something and that something shapes their lives directly or indirectly. These obsessions could be temporary or permanent. An example of this would be obsession/addiction of drugs, alcohol, etc. (Fig. 8).

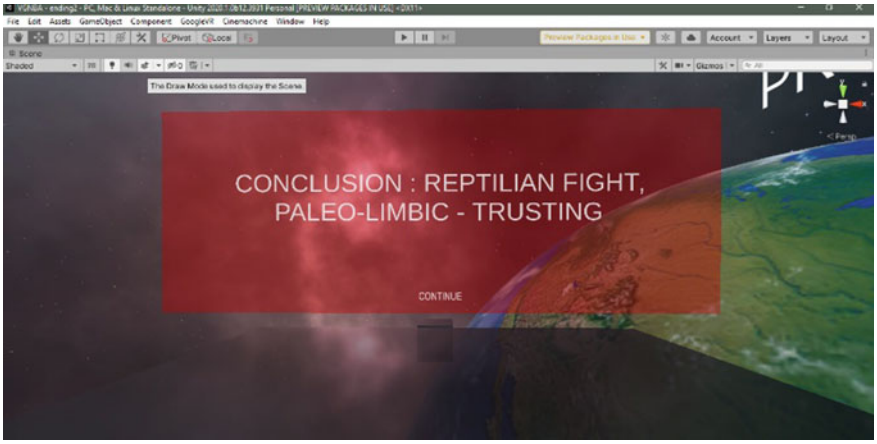

Fig. 6 Ending 1x

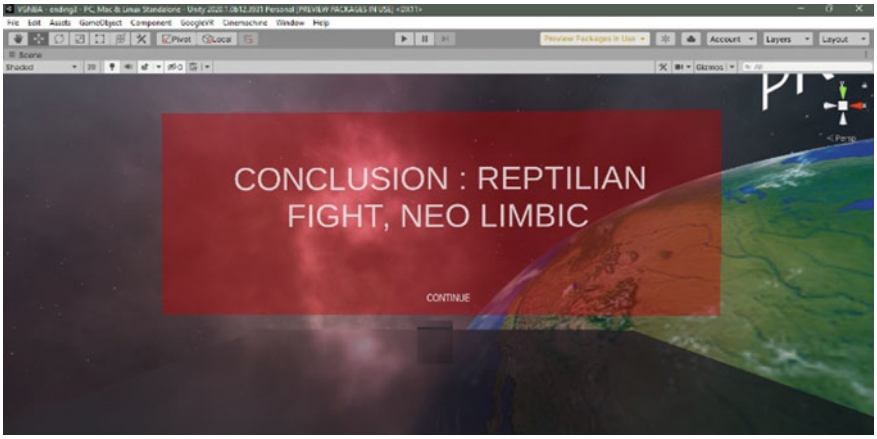

Fig. 7 Ending 2x

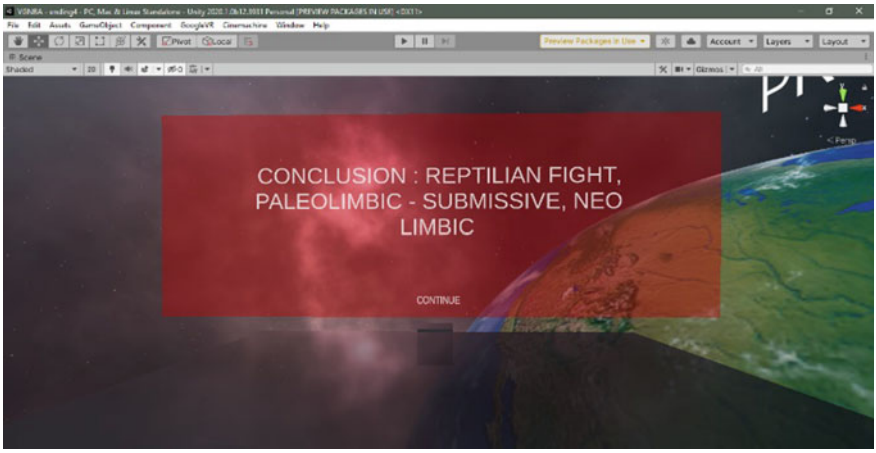

Fig. 8 Ending 3x

2.1 Multiple Endings of the Assessment

These endings are achieved with the choices that the user makes inside the game in VR environment with the help of glasses. Though, these results are not absolute, there are a good initial source of insight over one's own decision-making patterns. Unlike most game, this one is designed with the base of a neurological assessment, and focus has been majorly given to that concept. Keeping that in priority, there were multiple, a total of seven endings, created in the game. The user will achieve only one single ending in one go, depending on their mindset and choices they make throughout the assessment.

Though there is only one ending per assessment cycle, the ending has more than one trait as dominant in the result, this is due to the fact that every individual is different and will act differently when in similar situations. The dynamic property of the assessment in not its structure but the complex virtues of the user's brain structure, hence, the assessment will be targeting a large spectrum of individuals and not a restricted group. The core technology used here is the Unity Engine for creating the assessment game and its structure. Unity has been used by major firms in the field of gaming for the creation of basic games as well as ones with photo-realistic graphics which uses a very developed artificial intelligence in the game characters. Unity Engine was developed by Unity Tech initially for the Apple Mac OS, later it was also released for Windows. Uses of Unity vary from interactive experiences, architectural visualization, animation, simulations and most importantly, virtual reality. The user will end up in one the endings by progressing thorough the game, each of these endings are based on one or more of the brain traits, i.e., the user is definite to get at least one ending. The result will help the user/player to backtrack their decision to understand why they ended up in that place, and this can be used as a standard to improve the individual's overall behavioral understanding. Moreover, at any of the

endings, the user/player will be presented by a printed info-card corresponding to the trait they received as result. The card will contain detailed information over the trait, the places of its origination and if required, how to improve it.

2.2 Neuroplasticity

The term neuroplasticity refers to the structuring and re-structuring of the brain and how it handles the information, given to it through different bodily senses. It points towards the ability of the brain to adapt to certain conditions and to create patterns about that condition, with increased repetition, and these patterns are reinforced and the overall efficiency of the particular individual, in that particular domain increases significantly.

An instance where neuroplasticity takes charge is when an individual is indulging in an activity for the first time, she/he may find it difficult to do so, for example, writing with a non-dominant hand, riding a bicycle, playing a musical instrument, etc., but with repetition and increased level of focus in that particular domain, that activity seems to happen effortlessly as the subconscious mind has taken charge of the activity. The development from a rank of novice to a master in a particular field is thanks to our brain's ability to adapt to changes, i.e., neuroplasticity brain processes sensory information and works on strengthening synapses, and these synapses are what plays a vital role in the development of the skill, which is consistently repeated by the individual (Fig. 9).

Fig. 9 Brain as a connection of neurons

2.3 There Are Different Types of Neuroplasticity

(i) **Structural neuroplasticity**
The process of changing of brain's neural connections. Neurons are consistently made and they contribute to the central nervous system throughout the life. There are various stimuli which can affect the nervous system such as caffeine, alcohol and other stimulants, and these also have a long-term effect on the neuroplasticity.

(ii) **Functional neuroplasticity**
The alteration of the properties of neurons that are functional in nature. This is procedural event, i.e., it depends upon the previous activities and stacks upon them to create more synaptic connections. It contributes a little to the encoding of memories into the brain. VR has the potential to provide an affordable and conveniently generated 3D environment as per the requirement at hand, this gives rise to creation and manifestation to all the scenarios that are imagined by an individual, a team or even a whole organization. Keeping that in mind, it also gives a platform for the articulation of ideas from one to many, by creating the scenario in the virtual environment, ready to be interacted by the creator, as well as everyone else. Neuropsychology is the domain where the patterns of an individual are observed and evaluated for specific activities, under proper conditions. It is a key component in scientific treatment and rectification of many nervous-related disorders. VR is an apt platform for the overall development of neuropsychology. A tool, which can enable ecological and modifiable testing conditions tailored to the individual's requirements. Both hardware and software move forward with the increase in the efficiency of products and services that are available to us. VR and its related concepts are at a crucial point of escalation and has a very high potential for the coming times and technologies.

(iii) **Decisive Game Flow**
Here, "states" refer to the in-game situations. Some of these are compulsory, while others are presented depending upon the player's decisions. With respect to the states, the results are reached, which will define the final result of the assessment. The transitions from state to state is designed in such a way that the user is presented with different options at each of the state, though these different options are much more varying in nature and are sued to backtrack and evaluate the patterns by which the user made those decisions and reached a certain ending by going through various states. Scenes are the core display components of the game; they display the current progress of the game as a frame. This frame transitions from start to end by the movement and interactions with the in-game sprites. A scene is in 3D representation, which can be configured as needed through the functionality of the camera, which is a major component of Unity.

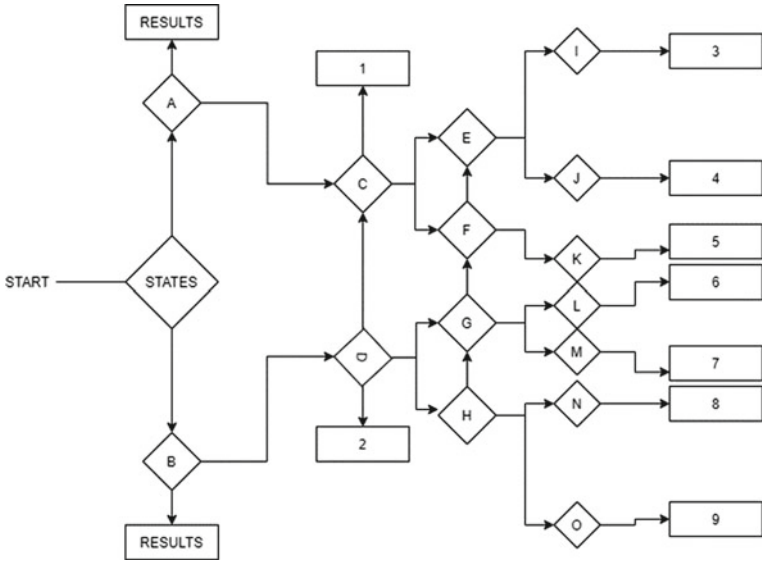

Fig. 10 Flow of game from states to endings

2.4 General Methodology

The application strives to provide the following functionalities, when required.

a. The application is started, for the first time, it should display the user to with information about the game and its plot (Fig. 10).
b. The user should be able to proceed with the game by providing appropriate input and it will progress the user towards the completion of the assessment.
c. Mostly, the user will be presented with informative scenarios with choices and problem solving (Fig. 11).
d. Upon the completion of the assessment, the user will be explicitly notified about the same and the result will be shown on the game page (Fig. 12).
e. The user can know the current progress of the game progress tracker and is welcome to quit the game in between when required to do so (Fig. 13).

3 Results and Discussion

The main objective of this assessment is to provide the player/user with an approximate analysis of its neurological behavior by proving one or more dominant brain trait to the player to create the scope of improvement in that aspect. The user will end up in one the endings by progressing thorough the game, each of these endings are based on one or more of the brain traits, i.e. the user is definite to get at least one ending. The result will help the user/player to backtrack their decision to understand why they ended up in that place, this can be used as a standard to improve the

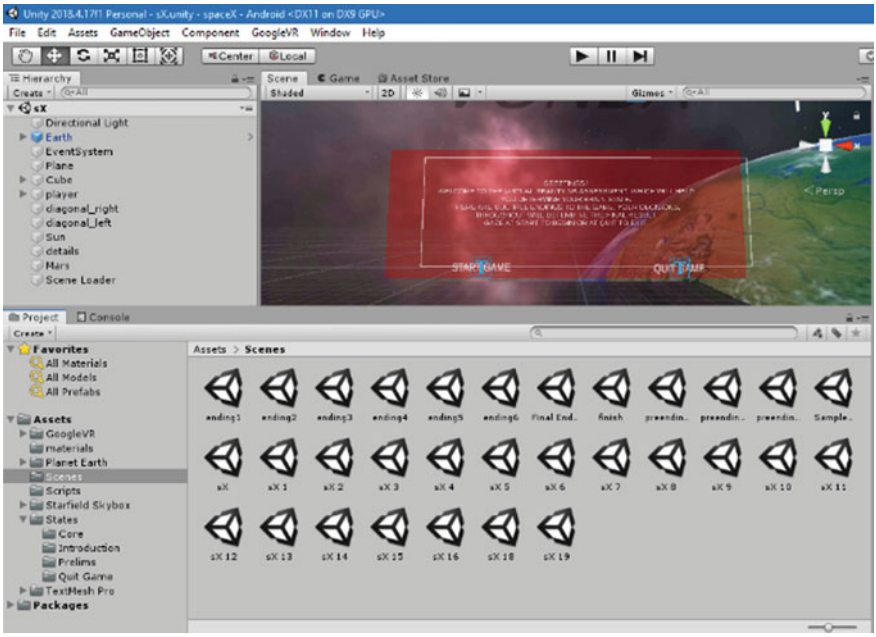

Fig. 11 All the scenes, presented in the game

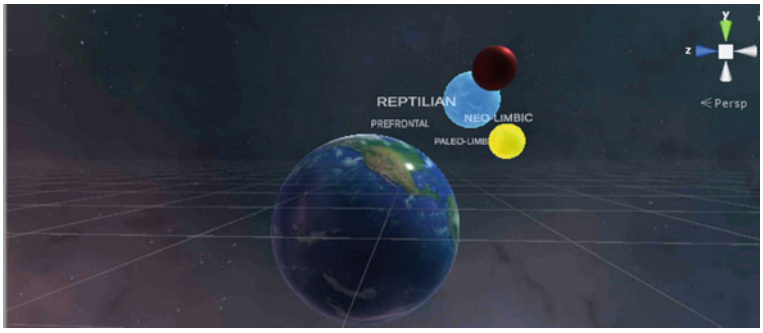

Fig. 12 Actual in-game overview of the assessment

individual's overall behavioral understanding. Moreover, at any of the endings, the user/player will be presented by a printed info-card corresponding to the trait they received as result. The card will contain detailed information over the trait, the places of its origination and if required, how to improve it.

The assessment requires one essential property to be most potent, that being the awareness of the user, i.e. the user should take the assessment with such a mindset that she/he is not aware of it, this induces an effect of realism and helps the user to take

Fig. 13 Assessment screen as seen from VR glasses

more realistic choices in the assessment. Since this assessment is majorly dependent on the user's own decisions throughout, this property needs to be addressed.

4 Conclusion

The game in its initial stages will provide with an approximate result but with gradual help through time, the assessment's accuracy will increase and the concept used here is the same one which is applied in industries such as medical and science to achieve what cannot be appropriately achieved by the use of traditional techniques. Gaming promises to induce certain signals to the brain which are scientifically proven to be beneficial w.r.t. neuroplasticity and for proper growth of the brain. Conclusions drawn from the assessment are of verifiable nature as the game plot is provide and the user can backtrack her/his decisions to understand why they arrived at the condition or result which was displayed to them. Medical VR is the field, which utilizes the potential of virtual reality in the domain of medical sciences to create virtual simulations of real-life conditions as well as for educating, rising aspirants in the medical field. Various medical equipment is also being made with the integration of VR to enhance the overall scope of its application and to increase its efficiency. It is a certainty that the field of VR will be integrated to many other domains in the coming Time and that integration will bring about a great change in terms of efficiency, application and overall development.

References

1. Virtual reality and neuropsychology, Maria T Scultheis, Drexel University: https://www.researchgate.net/publication/10712577_Virtual_reality_and_neuropsychology_upgrading_the_current_tools
2. Understanding various brain structures: https://www.limbix.com/research
3. Dayan E, Cohen LG (2011) Neuroplasticity Subserving motor skill learning. https://www.sciencedirect.com/science/article/pii/S0896627311009184
4. Concepts of Neurology: https://en.wikipedia.org/wiki/Neurology
5. Google AR/VR: https://arvr.google.com/cardboard/
6. Concepts of VR: https://en.wikipedia.org/wiki/Virtual_reality
7. VR detail: https://www.vrs.org.uk/virtual-reality/what-is-virtual-reality.html
8. Digital Reality: https://www.deloitte.com/ch/en/pages/innovation/articles/digital-reality-explained.html
9. MR/VR/VR variances: www.lane4performance.com/insight/blog/vrarmr-the-different-realities-driving-digital-transformation/
10. Creating 3D unity interfaces: https://www.learn.unity.com/tutorial/11-user-interface
11. Neuroscience course: https://www.udemy.com/course/my-brain-and-i/
12. Unity game dev course 2D: https://www.udemy.com/course/unitycourse/
13. Unity game dev course 3D: https://www.udemy.com/course/unitycourse2/
14. Google SDK: https://www.developers.google.com/vr/develop/unity/get-started-android
15. Applications of digital reality: https://www.toptal.com/designers/product-design/vr-ar-mr-the-future-of-design
16. Chen et al. W (2019) AgriTalk: IoT for precision soil farming of turmeric cultivation. IEEE Internet Things J (6)3:5209–5223
17. Misra NN, Dixit Y, Al-Mallahi A, Bhullar MS, Upadhyay R, Martynenko A (2020) IoT, big data and artificial intelligence in agriculture and food industry. IEEE Internet Things J
18. Varghese, R, Sharma S (2018) Affordable smart farming using IoT and machine learning, In: 2018 second international conference on intelligent computing and control systems (ICICCS), Madurai, India, pp 645–650
19. Syed F. K, Paul A, Kumar A, Cherukuri J (2019) Low-cost IoT+ML design for smart farming with multiple applications. In: 2019 10th international conference on computing, communication and networking technologies (ICCCNT), Kanpur, India, pp 1–5
20. Dolci R (2017) IoT solutions for precision farming and food manufacturing: artificial intelligence applications in digital food. In: 2017 IEEE 41st annual computer software and applications conference (COMPSAC), Turin, pp 384–385

A Study on Electronic Properties of Tetragonal $CuAlSe_2$ Thin Film by a DFT Method

Shikha Sharma, Karina Khan, Amit Soni, and Jagrati Sahariya

Abstract This study reports the results of the formation of $CuAlSe_2$ tetragonal ternary thin film by using a computational approach and consider the density functional theory (DFT) method. The calculations that we performed are employed in the method full potential linear augmented plane wave (FP-LAPW) method. The main properties of a compound such as optoelectronic and structural are investigated by considering approximation technique Tran-Blaha modified Becke–Johnson potential approximation (TB-mBJ) for obtaining more accurate results. $CuAlSe_2$ thin film is made up of dimension $2 \times 2 \times 2$ and along with this, we insert a vacuum of 10 Bohr along the z-axis. By using the energy band structure, refractivity, reflectivity, and real dielectric nature, we will investigate the electronic and optical properties. We obtained a 1.16 eV energy band gap of thin film of $CuAlSe_2$. The calculated results confirmed that the thin film of $CuAlSe_2$ can be used for the photovoltaic devices.

Keywords Thin film · $CuAlSe_2$ · First principles calculation

1 Introduction

In the present situation, with the increasing consumption of energy, we needed more and more power or energy. But unfortunately, fossil fuels which we are using for the last few decades are very limited amount as a source of non-renewable resources. Now, we have to focus on renewable energy for long-term use. Solar energy is one of the important renewable energy sources. Thin film solar cells are fabricated by

S. Sharma · K. Khan
Department of Physics, Manipal University Jaipur, Jaipur, Rajasthan 303007, India

A. Soni (✉)
Department of Electrical Engineering, Manipal University Jaipur, Jaipur, Rajasthan 303007, India
e-mail: amitsoni_17@yahoo.co.in

J. Sahariya
Department of Physics, National Institute of Technology, Srinagar Garhwal, Uttarakhand 246174, India
e-mail: jagrati.sahariya@gmail.com

S. Dwivedi et al. (eds.), *Flexible Electronics for Electric Vehicles*, Lecture Notes in Electrical Engineering 863, https://doi.org/10.1007/978-981-19-0588-9_52

thin layers with a thickness of a few micrometers on a substrate. Only fewer materials are needed for the fabrication of the solar cells. Due to this, the cost of these types of solar cells can be potentially reduced. In the early 1970s, the development started in the fabrication of thin films. Science has recently grown a large scale into various major research areas of thin film formation. For industries, the coating of thin film technologies growing very rapidly and this growth breakthrough in the field of microelectronics, optics and nanotechnology [1, 2]. Since the quantity of the material used is limited only to the surface of thin film layer, so these materials and devices are useful for minimizing toxicity. The applications are growing in areas like thin films for optical devices, magnetic devices, solar cells and their buffer layers, electrochemistry, protective coatings and catalyst [3, 4, 5 and 6]. Pure $CuAlSe_2$ and its doped thin film have been prepared experimentally in various ways. There are different methods for thin film synthetization like chalcogenization of thin Cu and Al layers deposited by evaporation under the vacuum method [7]. Lopez et.al. [8] have grown the thin film of $CuAlSe_2$ on the oxide which is in transparent form and develops substrates through salinization technique [8]. Doped thin films have been prepared by the deposition on antimony tin oxide substrates [9]. Marsenic et al. [10] have measured the optical behavior by reflection spectra of $CuAlSe_2$ and $CuAlS_2$ crystals. The electronic behavior of $CuGaSe_2$ and $CuInSe_2$ have been examined by theoretical approach study (DFT) and provided the details of its band gap and absorption which proper for solar cell applications [11, 12]. Beraich et al. [13] prepared and characterized Cu_2FeGeS_4 thin film synthesized via spray method and confirmed with a theoretical study by DFT. Gudelli et al. [14] discussed transport properties of Cu-based chalcopyrite materials using FP-LAPW method. A copper-rich ternary chalcogenide semiconductor with direct band gap for photovoltaic applications [15]. Gupta et al. [16] represent stability and optoelectronic properties of $Cu(Sb/Bi)(S/Se)_2$ ternary chalcogenides compounds. Khan et al. [17] studied the optoelectronic properties of copper-rich ternary compound by DFT. The electronic and optical properties of $CuGaS_2$ by first principles of calculations [18].

2 Computational Details

In this paper, the investigation of the optoelectronic properties of $CuAlSe_2$ has been performed. We used the simulation technique Wien2k code in the frame of DFT [19]. For more accurate results for the properties of $CuAlSe_2$ materials, the exchange correlation function we prefer here is TB-mBJ potential [20].

The computation of the thin film of $CuAlSe_2$ is initiated by developing the body-centered tetragonal structure of the space group,122 ($I\bar{4}2d$), for this purpose, we have taken the lattice constant a=b=5.596 Å, c=11.004Å from the already reported work of $CuAlSe_2$ [11]. By using the standard structure of $CuAlSe_2$, we constructed a thin film of dimensions$2 \times 2 \times 2$, which alter the structure into tetragonal primitive having 81 ($P4$) space group. The lattice structure of $CuAlSe_2$ is represented in Fig. 1. For

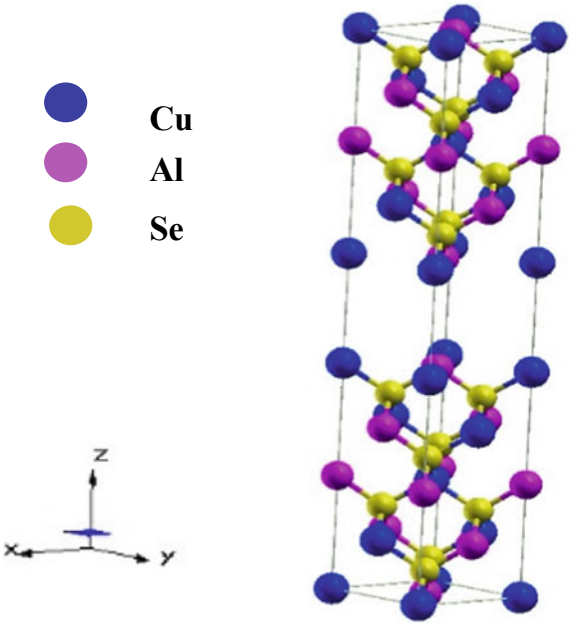

Fig. 1 Lattice structure of $CuAlSe_2$

achieving the maximum accuracy in the calculations, we also consider some other parameters as a input, $R_{\mathrm{MT}} \times R_{MAX} = 7$, k points $= 100$, $G_{\max} = 12$ and $l_{\max} = 10$.

3 Discussion on Calculated Results

3.1 Electronic Behavior

In this section, we have calculated the electronic band structure for $CuAlSe_2$ using TB-mBJ exchange correlation potential. Figure 2(i) gives a detailed explanation of energy band structure at highly symmetrical direction. On observing the structure of energy band structure, we concluded that $CuAlSe_2$ has a direct energy band gap because the peak point of valence band maximum (VB_{max}) and conduction band minimum (CB_{min}) is at the same M momentum point, which is useful for optoelectronic materials. The evaluated energy band gap of $CuAlSe_2$ is 1.16 eV.

In Fig. 2 we represents the density of state (DOS) spectra, which shows and confirmed the semiconductor nature of the compound. We lay the DOS spectra, for the explanation of the distribution of energy of occupied electrons at each energy level, which describes the band formation. On observing the DOS spectra, we observed that upper most part of valence band is placed at bottom of fermi energy (E_F) at 0 eV. This is due to the mixing of the Cu-'s' and Al-'p' energy state. The gap between the E_F and conduction band is equivalent to the calculated band gap through Fig. 1. The

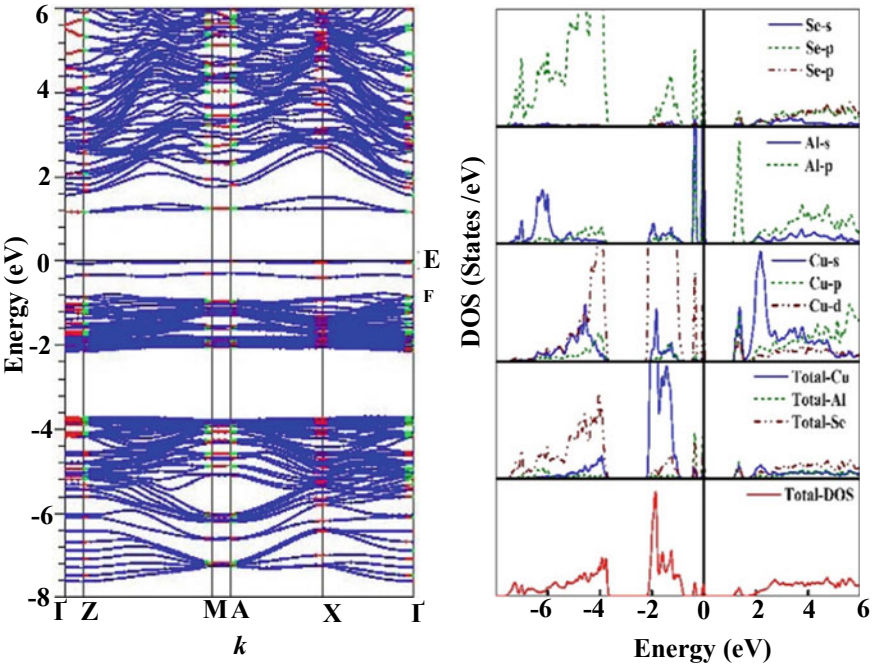

Fig. 2 Band structure of thin film $CuAlSe_2$ at the extremely symmetry direction and thin film DOS spectra

achieved band gap of thin film of $CuAlSe_2$ semiconductor depicts that the compound is acceptable for the solar cells.

3.2 Optical Behavior

The plotting of the curve for dielectric tensor, absorption, reflection and refraction has been done for the illustration of the optical properties of the thin film of $CuAlSe_2$ which are represented in Fig.3(i–v). It is understandable from the plots of optical properties that the parallel and perpendicular components of each curve are matches between 3–5 eV with one another which giving the compound isotropic nature but after that they are displaying the anisotropic behavior. Figure 3(i) presents frequency dependent real (dispersive) dielectric tensor spectra through which we observed the extent of polarization of thin film of $CuAlSe_2$ and its absolute value is 5.91 at zero frequency. The obtained peaks of the imaginary (absorptive) dielectric tensor spectra are presented in Fig. 3(ii) which specifies the inter band transitions of the electrons from the valence to conduction band. It is clear from the absorption spectra that is shown in Fig. 3(iii) that the most notable intensity of the electromagnetic wave of thin film of $CuAlSe_2$ is lying in the range of (0–5) eV, that signifies and

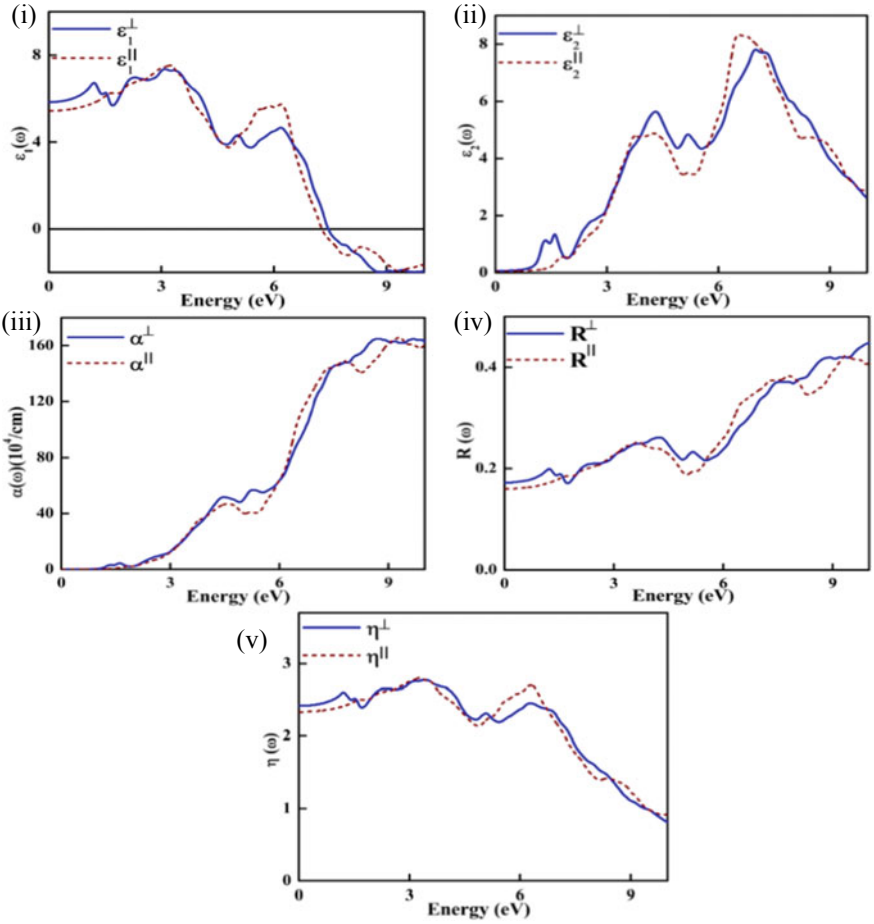

Fig. 3 Represent in **(i)** Curve of real dielectric tensor; **(ii)** Curve of imaginary dielectric; **(iii)** Absorption curve; $CuAlSe_2$ curve; **(iv)** Curve of reflectivity; **(v)** Curve of refractivity of $CuAlSe_2$

confirmed the photovoltaic nature of thin film of $CuAlSe_2$ and we computed the integrated absorption coefficient through absorption spectra for measuring the extent of absorption of photon by thin film of $CuAlSe_2$ and its value is 83.690 ($\times 10^4$ eV/cm). This value is an important parameter for optoelectronic devices. Figure. 3 (iv, v) represents the reflectivity and refractivity of the compound and their values are at 0 eV is 0.17 and 2.43, respectively which is lower as compared to absorbance, so it is indicating that thin film of $CuAlSe_2$ can be termed as photovoltaic material. The peaks in reflectivity are result of inter band transition (Table 1).

Table 1 Energy band gap of $CuAlSe_2$ by using different methods

Methods	Values (eV)
EV-GGA	1.92 [21]
LDA	1.09 [22]
GGA(PBE)	1.26 [23]
TB-mBJ(Our work)	1.16

4 Conclusion

The complete DFT calculations are done by using FP-LAPW method that is embodied in Wien2k code. By implementing TB-mBJ exchange–correlation potential, we analyzed the properties like structural, electronic and optical of thin film of $CuAlSe_2$. The obtained value of band gap signed that the thin film of $CuAlSe_2$ exhibits a semiconductor nature. The optical spectra certify the anisotropic nature of $CuAlSe_2$ thin film. The spectra of absorption prove the utility of compound's in thin film flexible photovoltaic cells.

Acknowledgements We all are highly bounden to Prof. P. Blaha, Vienna University Group for indulging with us the Wien2k package. Also thankful to Manipal University, Jaipur, India, for their all feasible support. The financial help is contributing by the DST-SERB, New Delhi, India, vide grant number EMR/2017/005534.

References

1. Gordillo G (2002) New materials used as optical window in thin film solar cells surface review and letters 9:1675–1680
2. Dharmadassa IM (2018) Advances in thin film solar cells, 2nd edn. Pan Stanford Publishing Pte. Ltd., Singapore
3. Cabral C, Lavoie C (2020) Thin film deposition research and its impact on microelectronics scaling. Vac Sci Technol A 38(4):1–14
4. Fthenakis V (2009) Sustainability of photovoltaic, the case for thin-film solar cells. Renewable and sustainability energy reviews. Elsevier Ltd 13(9):2746–2750
5. Lee TD, Ebong AU (2017) Renewable and Sustainable Energy Reviews. Elsevier Ltd 70:1286–1297
6. Mahmoudn WE, AL-Ghamdi AA (2010) Opt Las Tech (42):1134–1138
7. Marsillac S, Benchouk K (1997) $CuAlSe_2$ thin films obtained by chalcogenization, de physics III 7(11):2165–2169
8. Lopez-Garcia J, Guillen C (2011) Formation of semitransparent $CuAlSe_2$ thin films grown on transparent conducting oxide substrates by selenization. Mater Sci 46(23):7603–7610
9. Lopez-Garcıa J, Montero J (2015) Crystallization of wide-band gap $CuAlSe_2$ thin films deposited on antimony doped tin oxide substrates. J Alloy compd 648:104–110
10. Masnic A (2020) Birefringence and exciton spectra of $CuAlSe_2$ and $CuAlS_2$ crystals. J Eng Sci XXVII 1:23–27
11. Soni A, Dashora A (2011) Electronic and optical modeling of solar cell compounds $CuGaSe_2$ and $CuInSe_2$. J Electron Mater 40(11):2197–2208

12. Khan K (2020) Revealing the impact of aluminium doping on optoelectronic properties of $CuGaSe_2$ thin flexible solar cells-DFT .In: AIP conference proceedings 2294
13. Beraich M (2020) Preparation and characterization of Cu_2FeGeS_4 thin-film synthesized via spray ultrasonic method (DFT study). Mat Lett 275:12807
14. Gudelli VK, Kanchana V et al (2015) CuAlTe2: A promising bulk thermoelectric material. J Alloy Compd 648:958–965
15. Xia J, Fang H et al (2018) CsCu5Se3: A Copper-Rich Ternary Chalcogenide Semiconductor with Nearly Direct Band Gap for Photovoltaic Application. Chem Mater 30(3):1121–1126
16. Gupta Gk, Chaurasiya R et al (2019) Thermodynamic stability and optoelectronic properties of Cu(Sb/Bi)(S/Se)2 ternary chalcogenides. Promising ultrathin photo absorber semiconductors, Solar Energy177:679–689
17. Khan MS, Khan G et al (2020) A combined density functional study about the optoelectronic properties of copper rich ternary chalcogenide materials. Int J light electron opt 221:1–11
18. Xu B, Li X, Qin Z (2011) Electronic and optical properties of CuGaS2: First principles of calculations. Physica B 406(4):946–951
19. Blaha P (2019) WIEN2k—an augmented plane wave plus local orbitals program for calculating crystal properties, revised edition WIEN2k19.1, Vienna University of Technology, Vienna, Austria
20. Tran F, Blaha P (2009) Phys Rev Lett 102:226401–226404
21. Shirakata S, Chichibu SJ (1997) Appl Phys 36:7160
22. Reshak AH, Auluck S (2008) Solid State Commun 145:571
23. Ghosh A, Thangavel R (2015) J Mater Sci 50:1710

Optoelectronic Analysis of $CuGaS_2$-Based Flexible Thin Film Solar Cell: First Principle Investigation

Hansraj Karwasara, Karina Khan, Aditi Gaur, Amit Soni, K. C. Bhamu, and Jagrati Sahariya

Abstract We studied structural and optoelectronic properties by using first principle calculation of flexible thin film of $CuGaS_2$ using Tran Blaha-modified Becke Johnson (TB-mBJ) within density functional theory (DFT). This computational work is performed under full potential linearized augmented plane wave (FP-LAPW) method for finding the solution of the Kohn–Sham equations and it is based on Wein2k code. The density of states and band structure calculated for analyzing the electronic behavior of the flexible thin film of $CuGaS_2$ by utilizing the TB-mBJ exchange–correlation potential. The direct band gap is 1.42 eV which is investigated through band structure that indicates its semiconductor response for the photovoltaic applications. The flexible thin film of $CuGaS_2$ constructed with $2 \times 2 \times 2$ dimension and vacuum of 10 Bohr along z-direction. We report optical properties like complex dielectric tensor at zero eV is 5.12 and integrated absorption coefficient is 64.868 ($\times 10^4$ eV/cm) of $CuGaS_2$ thin film. The reflectivity of material is 15% which showing its usefulness in optoelectronic devices.

Keywords Thin-film · TB-mBJ · Optical properties

1 Introduction

Copper gallium sulfide ($CuGaS_2$) is a member of I-III-IV_2 ternary chalcopyrite semiconductors which is widely useful in optical appliances like solar cells and nonlinear

H. Karwasara · K. Khan
Department of Physics, Manipal University Jaipur, Jaipur, Rajasthan 303007, India

A. Gaur · A. Soni (✉)
Department of Electrical Engineering, Manipal University Jaipur, Jaipur, Rajasthan 303007, India
e-mail: eamitsoni_17@yahoo.co.in

K. C. Bhamu
Department of Physics, Gramin Mahila P.G. College, Sikar, Rajasthan 332024, India

J. Sahariya
Department of Physics, National Institute of Technology, Uttarakhand, Srinagar (Garhwal) 246174, India

S. Dwivedi et al. (eds.), *Flexible Electronics for Electric Vehicles*, Lecture Notes in Electrical Engineering 863, https://doi.org/10.1007/978-981-19-0588-9_53

optical instruments because of its direct bandgap and high absorption coefficient [1–3]. Over the last few decades' properties of $CuGaS_2$ have been investigated by experimentally and theoretically by many different group of researchers. At ambient condition, $CuGaS_2$ material possess wider band gap [4, 5], and it is considered as a suitable material for light emitting diodes and stable perovskite solar cells [6, 7]. Beside that many experimental methods used to make thin film of $CuGaS_2$ such as modulated flux deposition method (MFD) [8], chemical deposition, spray pyrolysis, flash evaporation [9, 10], and electron beam evaporation [11]. A. Soni et al. [12] have discussed density of states (DOS) and optoelectronic properties of $CuGaS_2$ by linear combination of atomic orbitals (LCAO) and FP-LAPW method of density function theory (DFT). Doping of Mn, Ti, Mo, and Al in $CuGaS_2$ material is also studied by various groups in last decade [13–16].

The above mentioned work on $CuGaS_2$ motivated us to study the properties of thin film of $CuGaS_2$ by using Wien2k code [17].

2 Details of Computation

To calculate the optical and electronic properties of thin film of $CuGaS_2$, we use Tran Blaha-modified Becke Johnson (TB-mBJ) exchange correlation functional which is used in density functional theory (DFT) and embodied in Wien2k code. The lattice constants for this calculation are taken to be a=b=5.3375Å and c=10.5834Å, and atomic positions are taken as: Cu (0,0,0), Ga (0,0,0.5), and S (0.29,0.25,0.125). The value radii of muffin tin (MT) sphere is 2.50 Å, 2.21 Å, and 1.90 Å for Cu, Ga, and *S,* respectively. A plane wave expansion with $R_{MT} \times K_{Max}$ equal to 7 and G_{MAX}, l_{MAX}, number of k points are 12, 10, and 100, respectively. We used $2 \times 2 \times 2$ dimension and gap of 10 Bohr in z-direction for construction of $CuGaS_2$ thin film which produce tetragonal primitive crystal structure having 81 ($P4$) space group and its crystal structure is shown in Fig. 1.

3 Results and Discussion

3.1 Electronic Properties

The electronic response of $CuGaS_2$ thin film is firstly shown by band structure which is presented in Fig. 2a. The highest point of valence band curve (below 0 eV) and lowest point of the conduction band curve (above 0 eV) lie on the same k point value, which showing the direct band gap and its value is 1.42 eV. The theoretical band gap of $CuGaS_2$ thin film is smaller than experimental value because of an intrinsic feature of TB-mBJ [6].

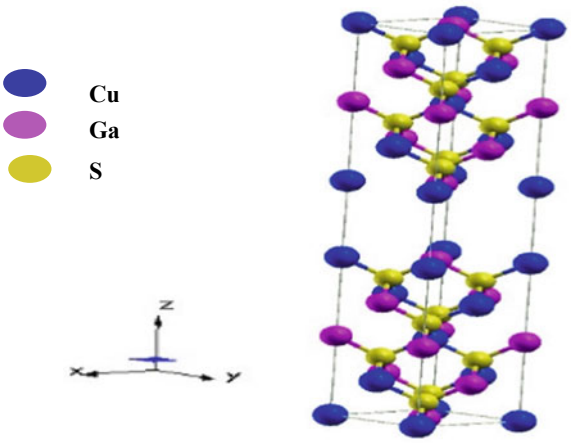

Fig. 1 Crystal structure of $CuGaS_2$

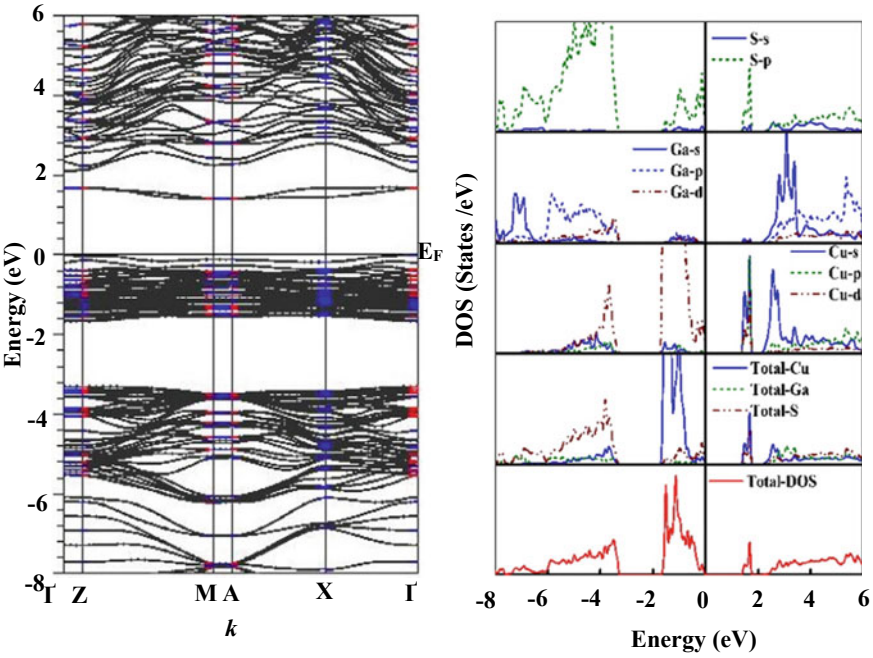

Fig. 2 **a** Band structure and **b** density of states (DOS) of $CuGaS_2$

Figure 2b shows the total density and s, p, and d projected densities of states in Cu, Ga, and S. The upper valence band is situated just below the Fermi energy, and conduction band is originated from hybridization of 4 s states of Cu, 3d states of Ga, and 3 s states of S. The band gap is calculated from the difference the value of upper valence band and lower conduction band value.

3.2 Optical Properties

The optical properties are given by $\varepsilon(\omega) = \varepsilon_1(\omega) + \varepsilon_2(\omega)$ where $\varepsilon_1(\omega)$ and $\varepsilon_2(\omega)$ are real and imaginary part, respectively. We plot the spectra along the parallel and perpendicular directions of $\varepsilon_1(\omega)$ and $\varepsilon_2(\omega)$ shown in Fig. 3a, b and obtained that compound is anisotropic in nature. We obtained the absolute value of real dielectric tensor is 5.12 which is indicating the polarization power of the compound. The absorption curve is shown in Fig. 3c which indicates the photovoltaic nature of thin film of $CuGaS_2$ and the computed value of integrated absorption coefficient is 64.868 ($\times 10^4$ eV/cm). Further, we plot the reflectivity spectra in Fig. 3d through which we analyzed the surface morphology of the material and value of absolute reflectivity is 0.15 that tells about the energy loss during the interface of electromagnetic waves. The Fig. 3e shows the refractivity spectra which is used to tell about the nature of the surface on the material and its value used for the designing purpose of the optoelectronic devices and value of refractivity is 2.27 at zero eV.

All the computed parameters reflect that the thin film of $CuGaS_2$ is appropriate for the optoelectronic applications.

4 Conclusion

Our work shows a sequential study of structural and optoelectronic response of $CuGaS_2$ thin film by using TB-mBJ exchange correlational potential of Wien2k code. From electronic properties, we concluded that the thin film of $CuGaS_2$ have direct band gap with value 1.42 eV is investigated by FP-LAPW method. Optical properties confirmed the isotropic nature of $CuGaS_2$ thin film.

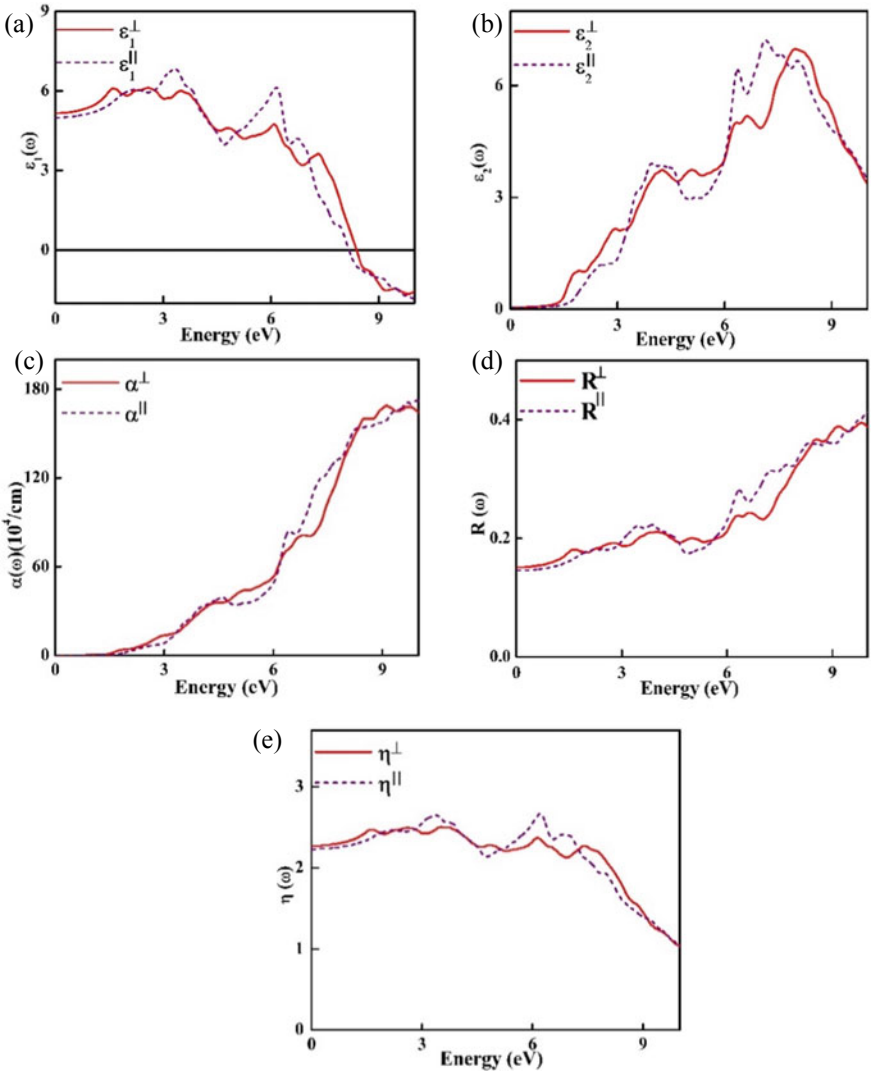

Fig. 3 **a** Real dielectric tensor curve, **b** imaginary dielectric tensor curve, **c** absorption curve, **d** reflectivity curve, and **e** refractivity curve of thin film $CuGaS_2$

Acknowledgements We are obliged to the Prof. P. Blaha of Vienna University for their Wien2k Software. We also grateful to DST- SERB, New Delhi for financial help of vide grant number EMR/2017/005534 and Manipal University Jaipur for their research facility.

References

1. Gaber AM, Tuttle JR, Albin DS, Tennant AL, Contreras MA (1994) High efficiency polycrystalline Cu(In, Ga)Se_2-based solar cells. In: R Noufi (ed) 12th NREL photovoltaic program review (AIP Conf Proc) vol 306 p 59
2. Birkmire RW, Eser E (1997) First-principles calculations on vibrational and dielectric properties of chalcopyrite $CuGaS_2$. Annu Rev Mater Sci 27:625
3. Branch MS, Berndt PR, Botha JR, Leitch AWR, Weber J (2003) Structure and morphology of $CuGaS_2$ thin films. Thin Solid Films 431–432:94–98
4. Birkmire RW (2001) Compound polycrystalline solar cells: recent progress and Y2 K perspective. Sol Energy Mater Sol Cells 65:17
5. Jäger-Waldau A (2004) Electrodeposition of Cu-Ga precursor layer from deep eutectic solvent for $CuGaS_2$ Solar energy thin film. Sol Energy 77:667
6. Laksari S, Chahed A, Abbouni N, Benhelal O, Abbar B (2006) First-principles calculations of the structural, electronic and optical properties of $CuGaS_2$ and $AgGaS_2$. Comput Mater Sci 38:223–230
7. Ma W, Zhang Z, Mengen M, Liu Y, Gencai P, Gao H, Mao Y (2020) $CuGaS_2$ quantum dots with controlled surface defects as an hole-transport material for high-efficient and stable perovskite solar cells. Sol Energy 211:55–61
8. Guillén C, Herrero J (2006) $CuInS_2$ and $CuGaS_2$ thin films grown by modulated flux deposition with various Cu content. phys stat sol (a) 203(10):2438–2443
9. Donglin X, Jangzhuang L, Man X, Xiujian Z (2008) Electro deposited and selenized CIGS thin films for solar cells. J Non-Cryst Solids 354:1447–1450
10. Araujo J, Ortíz R, López-Rivera A, Ortega JM, Montilla M, Alarcón D (2007) Electrochemical growth of $CuInSe_2$thin film on different substrates from alkaline medium. Charact films J Solid State Electroch 11(3):407–412
11. Jeong W, Park G (2003) Structural and electrical properties of $CuGaS_2$ thin films by electron beam evaporation. Sol Energy Mater Sol Cells 75:93–100
12. Soni A, Gupta V, Arora CM, Dashora A, Ahuja BL (2010) Electronic structure and optical properties of $CuGaS_2$ and $CuInS_2$ solar cell materials. Sol Energy 84:1481–1489
13. Picozzi S, Zhao Y, Freeman A, Delley B (2002) Mn-doped CuGaS2 chalcopyrites: An ab initio study of ferromagnetic semiconductors. Phys Rev B 66:205206
14. Lv X, Yang S, Li M, Li H, Yi J, Wang M, Niu G, Zhong J (2014) Investigation of a novel intermediate band photovoltaic material with wide spectrum solar absorption based on Ti-substituted $CuGaS_2$. Sol Energy 103:480–487
15. Thirumalaisamya L, Ahsan N, Sivaperuman K, Kim M, Kunjithapatham S, Okada Y (2020) Engineering of sub-band in $CuGaS_2$ thin films via Mo doping by chemical spray pyrolysis route. Thin Solid Films 709:138252
16. Khan K, Gaur A, Soni A, Sahariya J (2020) Revealing the impact of aluminum doping on opto-electronic properties of $CuGaSe_2$ thin films flexible solar cells—a DFT study. AIP Conf Proc 2294:030004
17. Blaha P, Schwarz K, Luitz JC (1997) Wien 97—an augmented plane wave + local orbitals program for calculating crystal properties, Springer, Berlin. Comput Phys Commun 59:1–287

Design and Implementation of Android-Based Digital Dashboard for Electric Car

Shopan Dey, Aniruddha Mukherjee, and Amit Soni

Abstract This paper discusses the design and implementation of an android-based digital dashboard system for the electric car. In this system, there is a CAN-based controller and an android application. The controller needs to be connected with the motor controller through the CAN. And the android device needs to be connected with the controller using Bluetooth communication. Then, the android device will work as the dashboard of a car. By using this dashboard, user can monitor the real-time data like car speed, rev, brake, battery voltage, current and power consumption, motor and controller temperature and error. User can also control peripheral devices from the dashboard. During the research, the authors have developed a controller that can collect the real-time data from the motor controller then processed and send it to an android device. The author also implemented this system in a converted electric car. Based on the experiment and testing, it is proved that the designed system can work accurately and reliably.

Keywords Digital dashboard · CAN · Arduino Nano · HC05 · Android

1 Introduction

Nowadays, electric car is getting popular day by day due to high vehicular pollution created from conventional vehicles. Conversion of conventional fuel vehicle to an electric vehicle is one of the best solutions for fulfillments of electric vehicle demand. And the digital dashboard is the one of important modules for the electric car even it is a new electric car or converted electric car.

However, there are some existing CAN and LCD display based electric car dashboard are available. Benedetti and his co-author develop a digital dashboard with Raspberry Pi 3. In their system, they used USB OBD-II to collect real-time data

S. Dey · A. Mukherjee (✉)
University of Engineering and Management, Jaipur, Rajasthan, India
e-mail: mukherjeeanirudh73@gmail.com

A. Soni
Manipal University Jaipur, Jaipur, Rajasthan, India

S. Dwivedi et al. (eds.), *Flexible Electronics for Electric Vehicles*, Lecture Notes in Electrical Engineering 863, https://doi.org/10.1007/978-981-19-0588-9_54

from the vehicle's ECUs. Then, collected data is analyzed by the GUI application which is written by QT5 framework and generates real-time gauges and indicators are displayed on a 7-in. HDMI display [1]. In another paper, system on module (SoM) and Qt framework are used to collect real-time data from the vehicle's ECUs using CAN protocol [2]. Chakraborty presented in his paper an android-based vehicle monitoring and controlling system using the Arduino and different kind of sensor [3]. A graphical user interface was created for calculating the energy performance of an electric car using the MATLAB-GUI. In their paper authors, have done a mathematical analysis of vehicle movement [4]. An analysis of Bluetooth in intra-car sensor implementation was done with the help of the HC05 Bluetooth module. This module can acquire receive signal strength indicator (RSSI) that is useful for deep analysis and simulates the network architecture [5]. An intelligent electric vehicle control system was developed, where real-time date is showed in front of the driver and passengers' seat. The real-time data includes battery voltage, battery level, current and energy consumption, temperature monitoring, vehicle speed, rpm meter, online and offline global position system (GPS). The infotainment system consists of different kind of android game and social networking application [6]. In another paper, a car black box is implemented using the embedded system. In this system, the black box collects real-time data including vehicle speed, tire presser, rev, brake, light, card door, light, lay-up and life belt from vehicle ECUs. Then, process the data and store in RAM [7]. Martinus and his team have presented a modular concept for electric car development [8]. PIC microcontroller and graphic programmable LCD display are used to design a CAN-based digital dashboard unit for car [9]. Valov and his team member developed a module for taximeter which can collect vehicular movement data from the electric car using the CAN interface [10]. ZigBee-based multi-smart car control system is designed by using distributed control architecture. In this system, the wireless communication, motor driver, the magnetic field sensors and other hardware module are developed [11]. Another CAN-based distributed module for an electric car was developed by Jianfeng and teams. In this system, the main communication board communicates with other electrical expansion board using the CAN bus [12]. LCD display system for an electric vehicle is designed based on the CAN bus. In this system, the interface and data acquisition circuit collect the data from different module then processed and showed on LCD display [13].

Based on the literature survey, in this paper, we present the design and implementation of android-based digital dashboard for the electric car. In our system, the main control unit which was designed with the Arduino NANO collects the vehicular data from the motor controller using the CAN bus. Then, processed the data and send it back to the android device by using Bluetooth communication. For the android device, we have developed an android application to collect the processed data and display the gauges and data to the GUI. In Fig. 1, the block diagram of the system is presented. In the block diagram, CAN module will communicate with motor controller and Bluetooth module will communicate with android device. And Arduino Nano will drive both modules and process the real-time data.

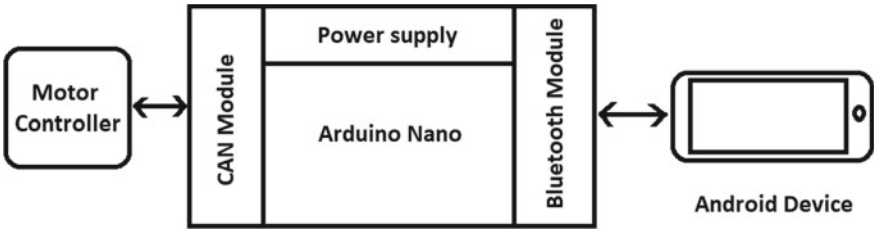

Fig. 1 Block diagram of android-based digital dashboard for electric car

2 Methodology and Setup

In our design, we used different open-source module including Arduino Nano, HC05 Bluetooth module and MCP2515 CAN module. MCP2515 CAN module is used to collect raw data from the motor controller and Arduino Nano is the main control unit for the device. It processed the data and sent it to the android device using the Bluetooth module. We used a 5 V power supply for our hardware device which is available from the CAN bus of the motor controller. And the power switch of the motor controller is connected to the ignition key. After turn on the ignition key, it will turn on the digital dashboard. If the android device of a user is connected to the dashboard, it will show all informative data and gauges on the android device. In the software part, we have developed an android application using the Android Developer IDE. This application collects the data from the hardware device using the Bluetooth and also generates the gauges. The hardware device needs to be connected to a motor controller using the CAN port. Then, the hardware device collects the data every 100 ms. The hardware device is showing in Fig. 2.

In Fig. 2, MCP2515 CAN module is connected with Arduino Nano using SPI communication and HC05 Bluetooth module using UART communication. A four-channel relay module is connected with Arduino Nano for controlling electrical peripherals from the dashboard. Arduino Nano is programmed by Arduino IDE using C language. Then, the whole circuit is implemented on a PCB. +5 V, GND, H, L pins need to be connected with the motor controller for power supply and CAN interface.

3 Results and Discussion

Once completing the setup, the digital dashboard can be powered on by the ignition key. Then, need to open the android application (My CAR) and connect the android device with the dashboard controller. After the connection established, all data will be visible on the application like Fig. 3a. The screenshots of android application are presented in Fig. 3. In Fig. 3a, left side four toggle buttons are included for controlling four different channels of the relay module. And on the right side, three

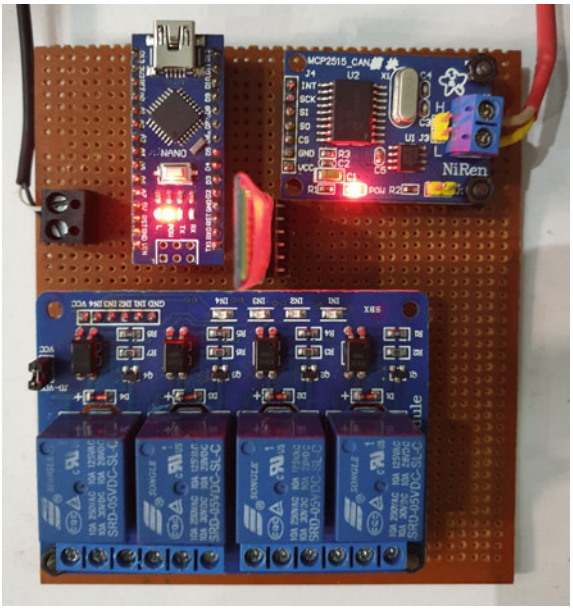

Fig. 2 Hardware unit of android-based digital dashboard for electric car

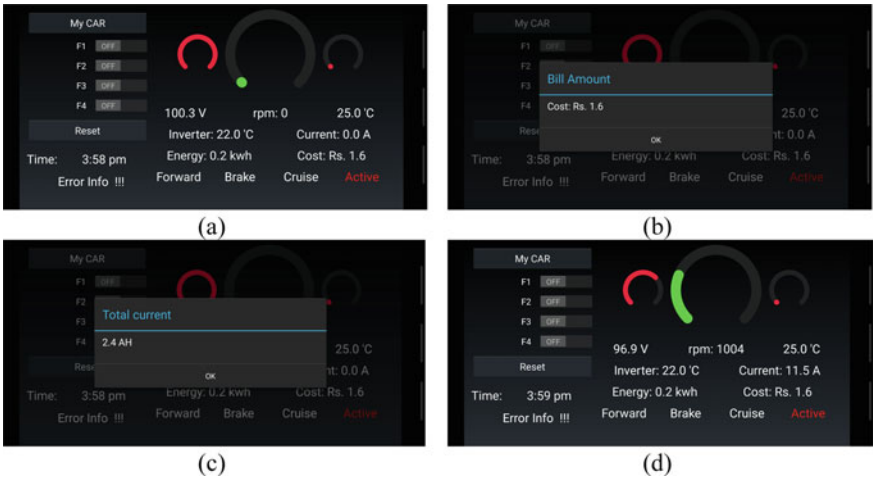

Fig. 3 Screenshot of android application: **a** dashboard, **b** electricity costing, **c** battery consumption, **d** motor speed

different gauges are included for battery voltage, motor speed and motor temperature. By clicking on Error Info !!! it will show all error log if available. Total current consumption will pop-up by clicking on current. Bill amount will pop-up by clicking on energy. Bill amount is calculated from total consumed unit multiplied by per unit electric costing in Rajasthan. Per unit electric costing can be set by the user. Using this system, users' android device will become a remote dashboard of his/her car. User can remotely access the car dashboard function within the Bluetooth range. This dashboard system can also be used as a car remote key.

4 Conclusion

The design and implementation of an android-based digital dashboard for electric car were presented in this paper. Our designed digital dashboard was implemented on a converted electric car and performed laboratory testing and on-road testing. In both testings, it has shown good performance in the aspect of accuracy and reliability. The proposed controller is tested on EV in different power condition also. The proposed controller is tested on EV in different power condition also. All services are performed well in full battery running test, low-battery running test, critical battery shutdown test and charging condition testing. In the future work, we will implement a global position system (GPS) and the Internet of Things for the higher aspect of electric car fleet management system. And fully remote access of car management system and vehicle dashboard.

References

1. Benedetti D, Agnelli J, Gagliardi A, Dini P, Saponara S (2020) Design of a digital dashboard on low-cost embedded platform in a fully electric vehicle. In: 2020 IEEE international conference on environment and electrical engineering and 2020 IEEE industrial and commercial power systems Europe (EEEIC/I&CPS Europe), Madrid, Spain, pp 1–5. https://doi.org/10.1109/EEEIC/ICPSEurope49358.2020.9160509
2. Patil RM, Chethan KP, Ramaprasad R, Nithin HK, Rangayyan S (2021) Infotainment system using CAN protocol and system on module with Qt application for formula-style electric vehicles. In: Gupta D, Khanna A, Bhattacharyya S, Hassanien AE, Anand S, Jaiswal A (eds) International conference on innovative computing and communications. Advances in intelligent systems and computing, vol 1165. Springer, Singapore. https://doi.org/10.1007/978-981-15-5113-0_16
3. Chakraborty D, Sharma K, Roy RK, Singh H, Bezboruah T (2016) Android application based monitoring and controlling of movement of a remotely controlled robotic car mounted with various sensors via Bluetooth. In: 2016 international conference on advances in electrical, electronic and systems engineering (ICAEES), Putrajaya, 14–16 Nov 2016
4. Cubon P, Sedo J, Radvan R, Stancek J, Spanik P, Uricek J (2014) Calculation of demand of electric power of small electric vehicle using Matlab GUI. In: 2014 ELEKTRO, Rajecke Teplice, Slovakia, pp 149–153. https://doi.org/10.1109/ELEKTRO.2014.6847891

5. Firmansyah E, Grezelda L, Iswandi (2014) RSSI based analysis of Bluetooth implementation for intra-car sensor monitoring. In: 2014 6th international conference on information technology and electrical engineering (ICITEE), Yogyakarta, Indonesia, pp 1–5. https://doi.org/10.1109/ICITEED.2014.7007930
6. Han GY, Ken LC, Wai CK (2012) Electric vehicle intelligent control system-hardware modules configurations. In: 2012 IEEE conference on sustainable utilization and development in engineering and technology (STUDENT), Kuala Lumpur, Malaysia, pp 187–191. https://doi.org/10.1109/STUDENT.2012.6408401
7. Jiang L, Yu C (2010) Design and implementation of car black box based on embedded system. In: 2010 international conference on electrical and control engineering, Wuhan, China, pp 3537–3539. https://doi.org/10.1109/iCECE.2010.860
8. Martinus PY, Bagus SA (2014) The modular concept design development of national electric car: case study at Institute of Technology Bandung. In: 2014 international conference on electrical engineering and computer science (ICEECS), Kuta, Bali, pp 127–135. https://doi.org/10.1109/ICEECS.2014.7045232
9. Pawlenka T, Kulhánek J, Tomčík P, Zapletal R (2019) Design of digital CAN based car dashboard unit. In: 2019 20th international Carpathian control conference (ICCC), Krakow-Wieliczka, Poland, pp 1–4. https://doi.org/10.1109/CarpathianCC.2019.8766024
10. Valov N, Valova I, Ivanova D, Chervenski D (2019) Module for taximeter use of CAN interface in car. In: 2019 16th conference on electrical machines, drives and power systems (ELMA), Varna, Bulgaria, pp 1–5. https://doi.org/10.1109/ELMA.2019.8771677
11. Wang C, Shen Z, Tian E, Zheng Q (2014) Multi-smart car control system design and research based on ZigBee. In: The 26th Chinese control and decision conference (2014 CCDC), Changsha, China, pp 1490–1494. https://doi.org/10.1109/CCDC.2014.6852402
12. Jianfeng W, Dafang W, Jie X (2009) The design of electric motor car's body network based on CAN-bus distributed control. In: 2009 Chinese control and decision conference, Guilin, China, pp 3712–3717. https://doi.org/10.1109/CCDC.2009.5191511
13. Zhilong Y, Dongsheng L, Long H, Haiying W (2011) Hardware design on electric vehicle LCD display system based on CAN bus. In: Proceedings of 2011 6th international forum on strategic technology, Harbin, China, pp 283–286. https://doi.org/10.1109/IFOST.2011.6021023

Design of Adaptive Artificial Vehicle Acoustic System (AVAS) for an Electric Vehicle

D. Sivaraj, Shivam Dutta, S. Hemanth Kumar, and D. Venkata Sai Jogarao

Abstract One of the emerging technologies in the automobile sector is replacing an internal combustion engine with an electric motor to decrease the share of environmental pollution caused by automobiles. India is one of the countries which is adapting this technology intending to see all 150 cc two-wheelers and three-wheelers with IC engines replaced by electric vehicle by 2025 and 2023, respectively. One of the challenging tasks with the introduction of electric vehicles is its acoustic feature. As electric motors are silent in operation, it is difficult for pedestrians to notice the arrival and existence of vehicles near them. There is a need for technology that produces artificial sound as of internal combustion engine in electric vehicles to solve this problem. This project is one of the methods to solve the problem, as mentioned earlier. New technology is designed using an embedded system to produce the required and specific sound in electric vehicles.

Keywords Noise · Artificial acoustic · Embedded system · Electric vehicle · Proximity

1 Introduction

The contribution of electric vehicles to society has brought new trends in the environment, including a drastic elimination of internal combustion engines in cars and two-wheeler vehicles [1]. The benefits of an electric vehicle over conventional vehicle include zero-emission property and silent in operation, thus reducing both air pollution and sound pollution. Electric vehicles, in general, do not produce any sound,

D. Sivaraj · S. Hemanth Kumar · D. Venkata Sai Jogarao
PSG College of Technology, Coimbatore, India
e-mail: dsr.ece@psgtech.ac.in

S. Hemanth Kumar
e-mail: hemanthkumarsundaraju@gmail.com

S. Dutta (✉)
Assam College of Engineering, Guwahati, Assam, India
e-mail: shivamduttasd1@gmail.com

S. Dwivedi et al. (eds.), *Flexible Electronics for Electric Vehicles*, Lecture Notes in Electrical Engineering 863, https://doi.org/10.1007/978-981-19-0588-9_55

while it is moving at a slower speed [2]. Silence in operation has side effects too. The side effects are increasing chances for the unpredictability of vehicles by pedestrians, which may affect the safety of the pedestrians.

A pedestrian, being not able to hear these sounds, cannot evaluate the electric vehicle [3]. These people can probably be future consumer and may want to purchase or hear the vehicle pass by. So, manufacturers want sounds to promote positive impressions of the vehicle model. But, it would not be profitable for the vehicle to make noise, which does not suit any future transportation. Hence, this quietness of an electric vehicle also has some positive sides. The sound produced externally must not add any noise to the current traffic scenario, which is annoying and creates noise pollution.

An embedded system can be programmed for generating acoustic. Analog audio signals can either be generated or can be edited from recorded audio. A microcontroller can be used for producing sound. Acoustic should be musical, and these must be vibrations that are strongly regular. Whereas, noise is a complex mix of different frequencies, which are constantly changing concerning time. Audacity is an open-source software, which can be used for generating, recording, and editing audio. This software application has proved to be indispensable to many for more basic audio generating, editing, and recording tasks, and different sampling and digital modulation techniques are also available on the software.

The electric automotive sector is lacking in the good acoustic system while driving at the lower speed. In this paper, a process for the generation of acoustic from an embedded system is discussed with step by step evaluation. An experiment is to be performed, which uses the proposed methodology to assess the detection of the pedestrian and car based on the proximity sensor. On detection, the acoustic is generated from the system. Then, the proposed methodology is reviewed for the results of the experiment.

2 Necessity of AVAS (Acoustic Vehicle Alerting System) in Electric and Hybrid Vehicles

Zeitler et al. conducted some tests to analyze the distance at which pedestrian recognizes the approaching vehicles with different propulsion systems like the internal combustion engine, hybrid vehicles running using both engines and electric motors, electric vehicles [4]. The conclusions made from the experiment are as follows:

Most of the pedestrians couldn't be able to recognize the approaching of electric vehicles and hybrid vehicles (moving on motor) at lower speeds (below speed 10 km/h) until the vehicle reaches the position of the pedestrians [5]. On the other hand, pedestrians recognized the approach of IC engines quickly, thus, ensuring safety toward the lives of pedestrians.

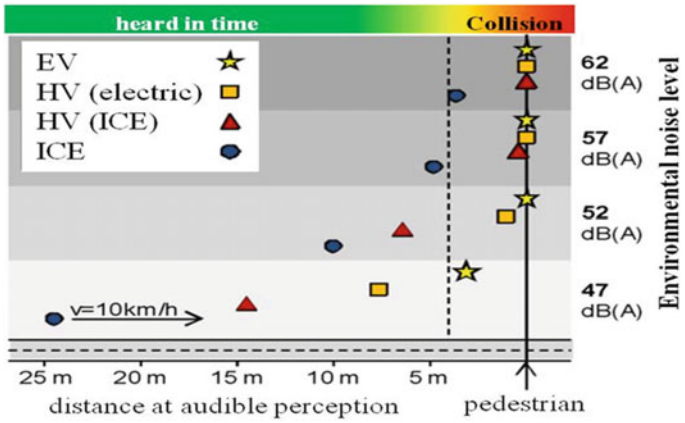

Fig. 1 Distance to the vehicle when detecting it [4]. Based on the above experimental results, it mandates the need for an artificial sound generation system that makes pedestrians identify the approach of the electric vehicle at low speeds comfortably

3 Comparison Between IC Vehicle and E-Vehicle

One of the main differences between internal combustion engine vehicle and electric vehicle is the synthesis of sound during operation (Fig. 1).

The absence of sound in the electric vehicles during their operation may create pedestrians as it is hard to identify the presence of a vehicle when it is approaching the pedestrians [6]. So, there is a need for a technology that synthesizes sound artificially based on government rules.

4 Parameters for Generation of Artificial Acoustic

Artificial synthesis of sound can be done by taking the inputs based on

A. Motor speed
B. Speed of the vehicle
C. Acceleration of the vehicle
D. Presence of pedestrian.

5 Regulations

According to the amending Regulation (EU) No 540/2014 of the European Parliament and the Council as regards the acoustic vehicle alerting system requirements for vehicle EU-type approval, the AVAS must be installed in any new vehicle on or after

July 1, 2021 [7]. According to the above regulations, a vehicle should automatically generate a sound in the minimum range of its speed starting from 0 to 20 km/h and also during reversing (in case, the vehicle is not fitted with any warning sound). A switch is provided for the vehicle driver to halt the function of AVAS. But, when the vehicle is restarted, the system should be switched back to its default position. The amplitude of the sound can be attenuated during the operational time. The sound generated by the AVAS should synchronize with vehicle speed and behavior. The sound should not exceed the sound level of M1 vehicles, which are driven by an IC engine. According to UNECE Regulation No 138, vehicles having overall sounds with a margin of +3 dB need not be equipped with AVAS. A manufacturer can offer choices for the vehicle driver to switch different sounds. Each component in the AVAS shall have a mark of the manufacturer and a valid identification number.

6 Block Diagram of Embedded System

The dynamic inputs for the embedded system (Arduino Uno) are taken from potentiometer, HC-SR04 ultrasonic sensor, and wheel speed sensor such as Hall effect sensor as shown in Fig. 2. The throttle position of the electric vehicles is sensed using a potentiometer. The drop or increase in the potentiometer's voltage occurs as the result of varying resistance by the angular displacement of the wiper. This

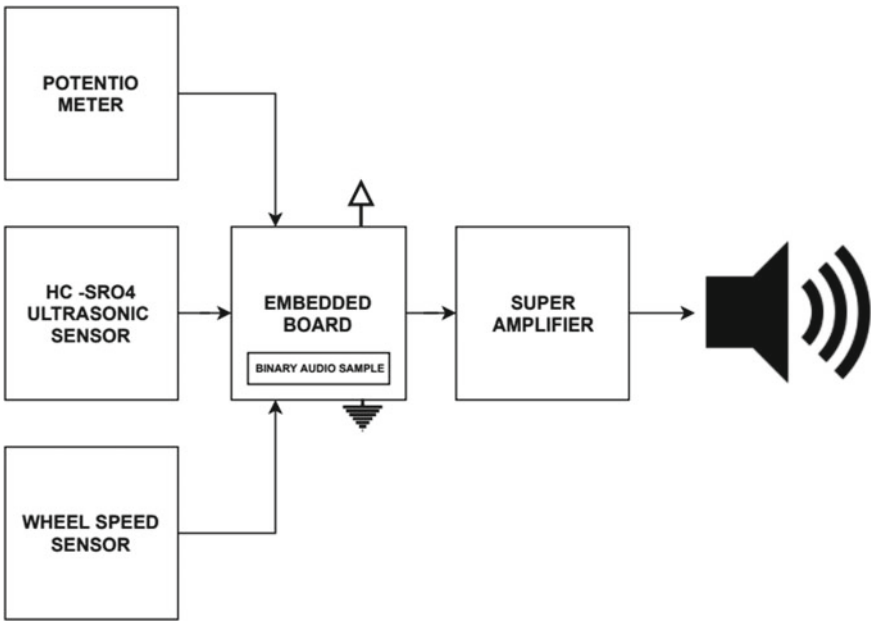

Fig. 2 Process of generation

signal is carried out to the Arduino board [8] as a primary input that regulates the frequency of the acoustic system. The HC-SR04 ultrasonic sensor [9] detects the presence of pedestrians and another vehicle's path within the threshold distance. This RADAR setup has an operation frequency and a sensing range of 40 kHz and 45 m, respectively. The vehicle's current speed is measured by a wheel speed sensor such as opto-coupler or Hall effect sensors.

The embedded system receives the signals from all three devices and regulates the tuned audio frequency as an output. The signal from the embedded systems is amplified using a super amplifier such as the Darlington pair and fed to the input terminals of the speakers.

7 Waveform Results

Artificial sound is a synthetic vibration generated, modulated and transmitted as an audio wave of pressure through a matter. Amplitude and frequency are the two significant parameters of the sound as mentioned earlier wave. Amplitude is the maximum displacement that a wave can undulate from its equilibrium. In other terms, it is the measure of the loudness of the sound propagated. The frequency of the wave determines the tone of the sound. The wavelength displacement of two nearby crests of the wave is indirectly proportional to the sound wave frequency.

When two or more waves propagate at an identical time, waves interfere, furthermore resulting in a single wave. If the frequencies of the waves are incredibly close to each other, it bombards the amplitude. Humans hear this as a beat or a loud sound [10]. Else, it leads to a soft or low amplitude sound. The frequency ranges that a human can hear stretches between 20 and 20,000 Hz. Sounds owning frequency higher than 20,000 Hz are called ultrasonic, and they have high-speed propagation properties, which are used to detecting the presence of pedestrians in this work.

In this work, the sample sound is modulated using audacity, an open-source software that provides solution for audio [11]. Figure 3 represents the wave form of the modulated sound. The resolution of the sound sample is set to 8000 Hz. Figure 4 represents the frequency analysis of the desired sound sample. Spectrum algorithm and Hann window function is employed in the analysis. At 3739 Hz, −53 dB is coordinated in Fig. 4. The output audio shall be selected from the range of 20 to 2000 Hz which is having an average sound level of −50 dB. The magnitude of the sound can be set to the desired value with an amplifier mentioned earlier.

8 Analysis of Amplifier

A Darlington pair is a single transistor obtained by a combination of two PNP or NPN transistors [12]. The emitter of the input transistor is connected to the collector of the output transistor. Therefore, the input transistor amplifies the current, which is further

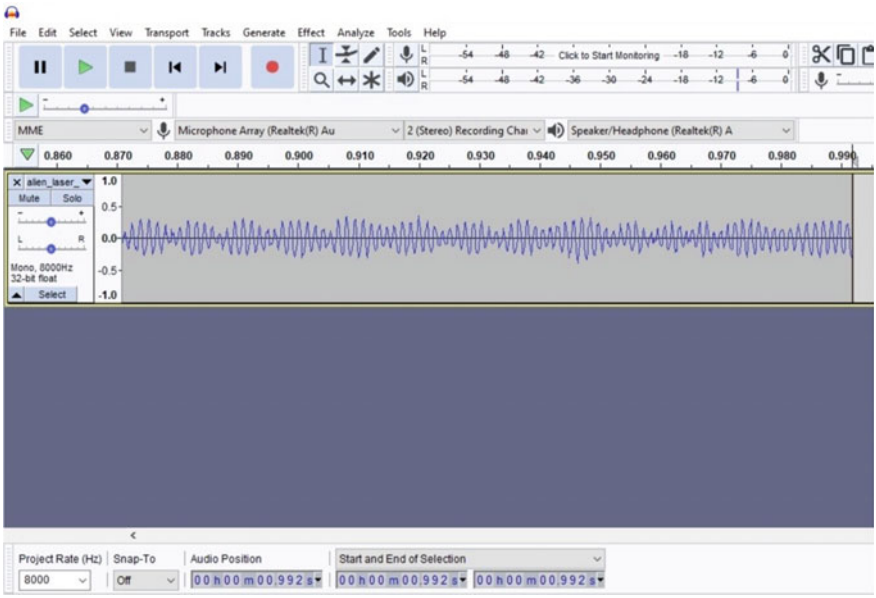

Fig. 3 Wave analysis

amplified by the output transistor. This transistors arrangement enables high current gain from a low base current, so using a small amount of large current load can be operated. In the proposed work, NPN type of transistors is used as the electron-based devices are faster than hole-based devices due to the mass difference of electron and positive charge. Electrons are less in mass compared to positive charge due to which its mobility is good comparatively (Fig. 5).

9 Conclusion and Future Scope

An artificial acoustic system for an electric vehicle which is adaptive is developed using an embedded system, and need for AVAS is highlighted. This work can be continued by making this system a part of CAN bus communication for diagnostic and system synchronization. An option can be given to the driver to change the vehicle sound. Additionally, a sound generating system inside the driver cabin can be developed to alert him when he encounters an obstacle. The ultrasonic inputs from the adaptive cruise control can alert the driver inside a cabin about the pedestrian presence.

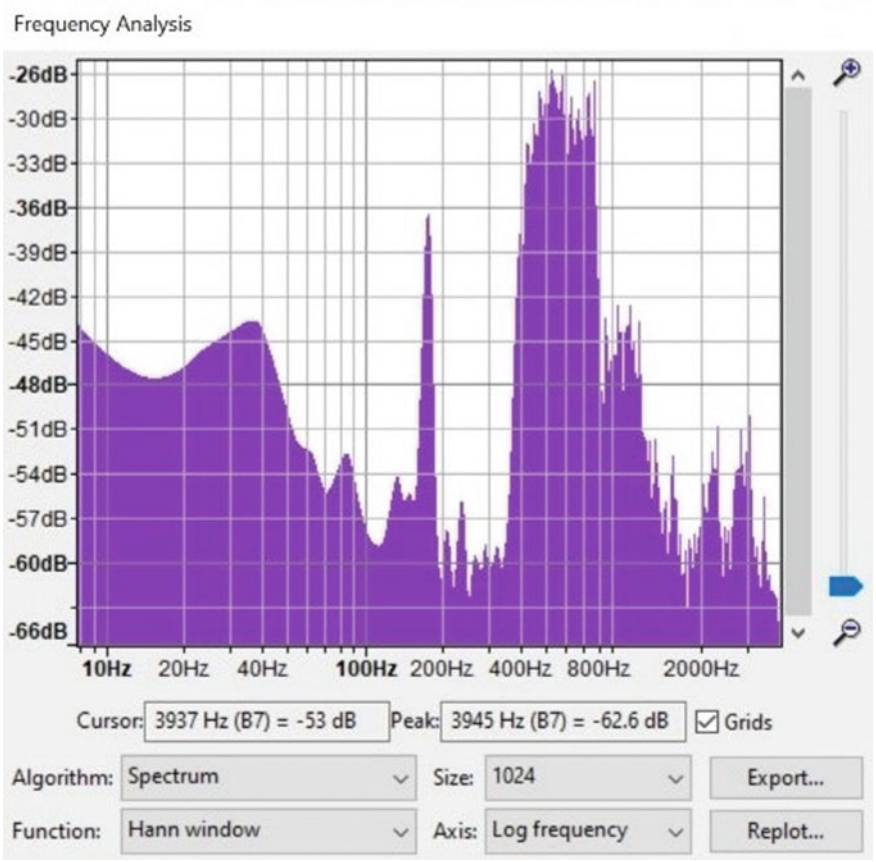

Fig. 4 Frequency analysis

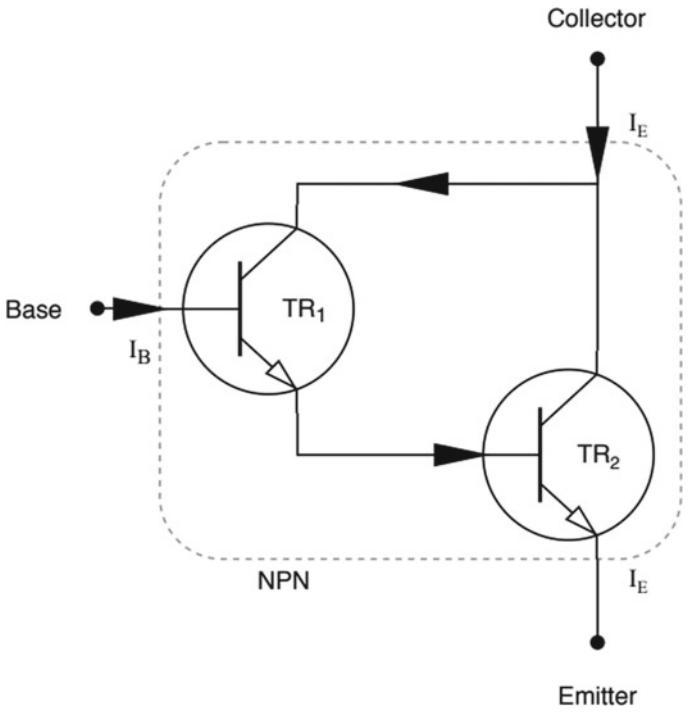

Fig. 5 Circuit diagram of Darlington pair

References

1. Johannsen H, Müller G. Effects of low noise emissions of electrical vehicles for pedestrian accident risks. Paper number 13-0394. Verein für Fahrzeugsicherheit Berlin e.V, Germany
2. SAE (2012) Measurement of minimum noise emitted by road vehicles. SAE standard; Product code: J2889/1; Revision number: A; Date published: 2012-05-14
3. Pardo-Ferreira MC, Torrecilla-García JA, Heras-Rosas CL, Rubio-Romero JC (2020) New risk situations related to low noise from electric vehicles: perception of workers as pedestrians and other vehicle drivers. Int J Environ Res Public Health 17(18):6701. Published 14 Sept 2020. https://doi.org/10.3390/ijerph17186701
4. Zeitler A, Liebing R, Kerber S (2010) Sounddesign im Dienste der Wahrnehmbarkeit von leisen Fahrzeugen. In: 36. Deutsche Jahrestagung für Akustik—DAGA 2010, Berlin (in German)
5. Brand S, Petri M, Haas P, Krettek C, Haasper C (2013) Hybrid and electric low-noise cars cause an increase in traffic accidents involving vulnerable road users in urban areas. Int J Inj Contr Saf Promot 20(4):339–341. https://doi.org/10.1080/17457300.2012.733714. Epub 2012 Oct 19. PMID: 23083396
6. Yamauchi K, Menzel D, Fastl H, Takada M, Nagahata K, Iwamiya S (2011) Cross-cultural study on feasible sound levels of possible warning signals for quiet vehicles. In: INTERNOISE 2011, Osaka, Japan, 4–7 Sept 2011
7. Regulation (EU) No 540/2014 of the European Parliament and of the Council of 16 April 2014 on the sound level of motor vehicles and of replacement silencing systems, and amending Directive 2007/46/EC and repealing Directive 70/157/EEC Text with EEA relevance

8. Louis L (2018) Working principle of Arduino and using it as a tool for study and research. Int J Control Autom Commun Syst 1. https://doi.org/10.5121/ijcacs.2016.1203
9. Kamal AM, Hemel SH, Ahmad MU (2019) Comparison of linear displacement measurements between a MEMS accelerometer and Hc-Sr04 low-cost ultrasonic sensor. In: 2019 1st international conference on advances in science, engineering and robotics technology (ICASERT), Dhaka, Bangladesh, pp 1–6. https://doi.org/10.1109/ICASERT.2019.8934569
10. Nyeste P, Wogalter MS (2008) On adding sound to quiet vehicles. Proc Hum Factors Ergon Soc Annu Meet 1747–1750
11. Audacity® software is copyright © 1999–2021 Audacity Team. The name Audacity® is a registered trademark
12. Pandey A, Chakraborty S, Saw SK, Nath V (2015) A Darlington pair transistor-based operational amplifier. In: 2015 global conference on communication technologies (GCCT), Thuckalay, India, pp 273–276. https://doi.org/10.1109/GCCT.2015.7342665

Optical Response in Strained Type-II AlInAs/AlSb Ultrathin QW Heterostructure

Amit Kumar Singh, Rohit Singh, Dibyendu Chowdhury, and Amit Rathi

Abstract AlSb/InAs heterostructure has a unique band alignment with a large conduction band offset finding application in a range of electronic devices. AlSb-based heterostructures have very recently been utilized for the fabrication of HEMTs, FETs, memories, and photodetectors. In this paper, the band structure, wave functions, dispersion curve, and optical gain of AlSb/AlInAs heterostructure have been reported. Kane 8×8 model with self-consistent calculations has been used to obtain the optical gain in type-II AlInAs/AlSb heterostructure as a function of 2D carrier injection. The peak TM optical gain at an energy of 0.652 eV is observed to be 1662 cm^{-1}, while the peak TE optical gain is found to be 1271 cm^{-1} at an energy of 0.649 eV for a 2D charge carrier injection of 5×10^{12} cm^{-2}. Further, a gradual blueshift is observed in the optical gain spectra as the 2D charge carrier injection is increased. The heterostructure has been found to operate in NIR, IR-B range with a high optical gain.

Keywords Type-II · Optical properties · AlInAs/AlSb · Kane model · Quantum well · Heterostructure

1 Introduction

Optical response in various type-II M and W quantum well heterostructures is being examined for infrared applications several recent works. AlSb/InAs hetrostructure has a unique band alignment with a large conduction band offset finding application

A. K. Singh · A. Rathi (✉)
Department of Electronics and Communication Engineering, Manipal University Jaipur, Jaipur 303007, India
e-mail: amitrathi1978@gmail.com

R. Singh
Department of Electrical Engineering, Shiv Nadar University, G. B. Nagar, Greater Noida 201314, India

D. Chowdhury
Department of Electronics and Communication Engineering, Haldia Institute of Technology, Haldia, West Bengal, India

S. Dwivedi et al. (eds.), *Flexible Electronics for Electric Vehicles*, Lecture Notes in Electrical Engineering 863, https://doi.org/10.1007/978-981-19-0588-9_56

in a range of electronic devices. AlSb/InAs heterostructure has very recently been utilized for the fabrication of HEMTs and FETs [1, 2]. AlSb/InAs heterostructure has also been used for the development of efficient memory cells with low-voltage switching and photodetectors [3, 4]. Further, the conduction band in these type-II heterostructures can be tuned remarkably by varying the thickness of the component layers [5]. k·p theory has been used for the study of optical gain tuning in the infrared range [6, 7]. 8-band k·p theory has been used to show that by modulation doping in type-II InAs/AlSb quantum well structures can lead to type-I transitions [8]. Kolokolov and Ning have reported a high TM mode optical gain in AlSb/InAs quantum wells [9]. Wave function behavior on doping in AlSb/InAs heterostructure has been studied using k·p theory [10, 11]. Intersubband transitions and its effect on physical properties in InAs/AlSb heterostructures have been investigated based on the multiband k·p theory [12–14]. AlInAs layer has been used for surface smoothing in AlSb-based heterostructures fabricated using molecular beam epitaxy, and electronic properties have been examined [15]. AlInAs/AlSb material system has been used in the development of high electron mobility transistors in several works [16–19]. Optical properties of InAs/AlSb quantum well heterostructures have analyzed for infrared applications [20, 21].

2 Device Structure and Specifications

The type-II heterostructure examined here has an AlInAs quantum well with composition $Al_{0.2}In_{0.8}As$ and AlSb barrier layers grown on AlSb substrate. The $Al_{0.2}In_{0.8}As$ layer has a thickness of 8 nm. The initial 2 nm of AlSb layer is undoped; then, the next 10 nm is p-type uniformly doped, and then, the next 6 nm is undoped. Further, after the AlInAs quantum well layer, the initial 6 nm is undoped; the next 10 nm is p-type uniformly doped, and finally, the last 2 nm is undoped. Figure 1 shows the band structure of $Al_{0.2}In_{0.8}As$/AlSb heterostructure with heavy-hole and light-hole bands. The type-II band alignment is evident form Fig. 1 as the conduction band of AlSb layer lies above the conduction band of AlInAs layer, and at the same time, the valence band of AlSb layer lies above the valence band of AlInAs layer.

3 Results and Discussion

Kane 8×8 Hamiltonian model has been widely studied recently for the study of nanodimension semiconductors [22, 23]. In this work, the wave function confinement in the barrier (AlSb) and well (AlInAs) regions has been computed using the Kane 8×8 Hamiltonian model with the effective-mass approximation [24, 25]. Electronic properties of $Al_xIn_{1-x}As$ alloys have been studied using the density functional theory, and the bandgaps have been reported [26]. The physical parameters of compound semiconductors and their alloys required in the computation have been discussed in

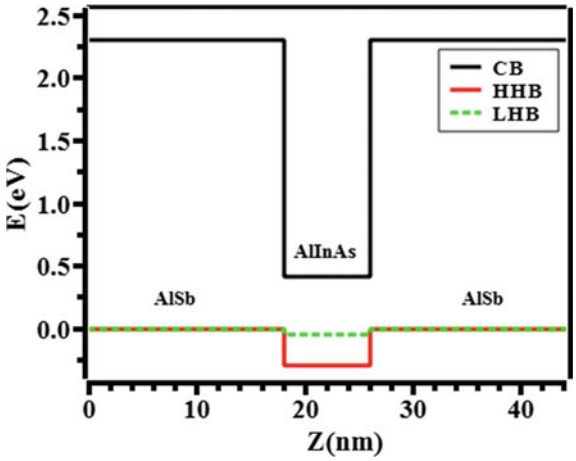

Fig. 1 Band structure of $Al_{0.2}In_{0.8}As/AlSb$ heterostructure

detail [27]. Figure 2a shows the net wave functions, while Fig. 2b shows the e1up, h1up, e1down, and h1down wave functions in the AlInAs/AlSb heterostructure grown on AlSb substrate at 300 K. It is evident that the electrons are confined in the AlInAs layer, while the hole confinement can be observed in the AlInAs layer as well as at the interface of InAs and AlSb layers.

Figure 3 shows the k·p dispersion in $Al_{0.2}In_{0.8}As/AlSb$ heterostructure at a 2D carrier density of 5×10^{12} cm^{-2}. A near parabolic nature in the conduction band is observed. The hole states h2up and h3up are placed closely with the energy gap at $k = 0$ (e1up − h1up) being ~0.6 eV.

Figure 4 shows the TE mode optical gain in $Al_{0.2}In_{0.8}As/AlSb$ heterostructure as the 2D carrier density is gradually increased from 1×10^{12} to 5×10^{12} cm^{-2}. The peak TM optical gain at an energy of 0.652 eV is observed to be 1662 cm^{-1}, while the peak TE optical gain is found to be 1271 cm^{-1} at an energy of 0.649 eV for a

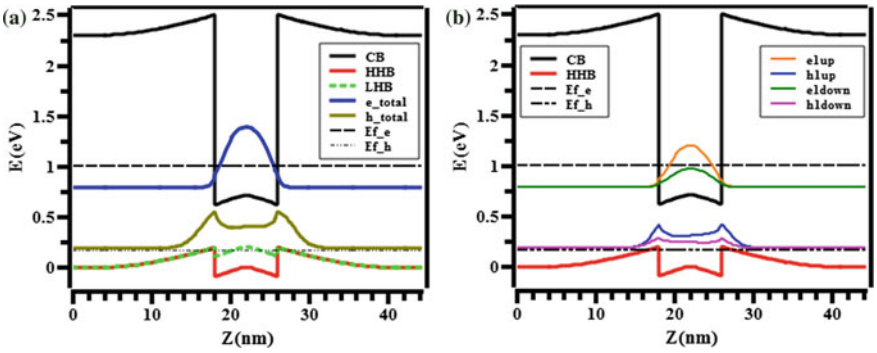

Fig. 2 **a** Net wave functions—$Al_{0.2}In_{0.8}As/AlSb$ heterostructure. **b** Wave functions—$Al_{0.2}In_{0.8}As/AlSb$ heterostructure

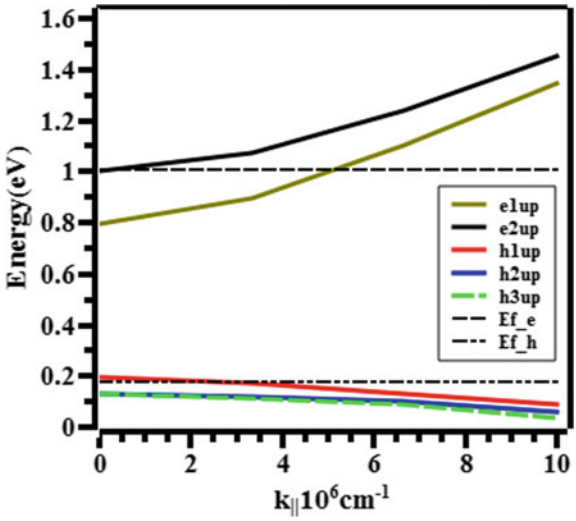

Fig. 3 Dispersion—$Al_{0.2}In_{0.8}As/AlSb$ heterostructure

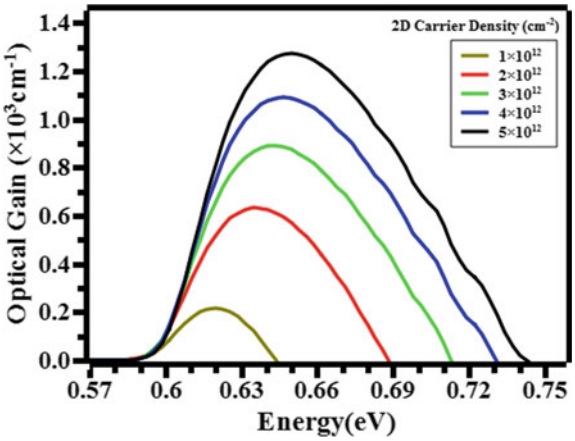

Fig. 4 Optical gain—AlInAs/AlSb heterostructure TE mode—2D carrier density

2D charge carrier injection of 5×10^{12} cm^{-2}. A steady blueshift is observed in the optical gain spectra as the 2D charge carrier injection is increased (Fig. 5).

4 Conclusion

A type-II AlInAs/AlSb ultrathin QW heterostructure with the AlInAs layer thickness 8 nm has been designed. The quantum well has been has been optimized for increased hole and electron wave function overlap. The band structure, wave functions, dispersion curve, and optical gain of AlSb/AlInAs heterostructure computed using Kane

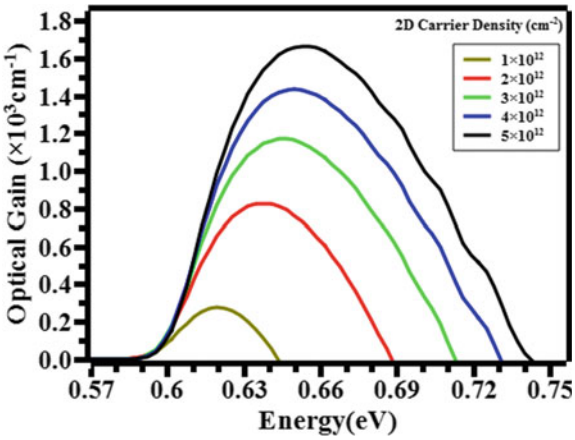

Fig. 5 Optical gain—$Al_{0.2}In_{0.8}As$/AlSb heterostructure TM mode 2D carrier density

8 × 8 model show the response of the heterostructure in NIR, IR-B range with a high optical gain. A gradual blueshift in the optical gain spectra with 2D charge carrier injection is observed in the range ~0.6 to 0.74 eV (2.066 − 1.675 μm).

Acknowledgements Authors are obliged to Dr. Konstantin I. Kolokolov (F/o Physics, M. V. Lomonosov Moscow State University, Moscow, Russia) for his technical help with the heterostructure design studio software.

References

1. Chou YC, Yang JM, Lin CH, Lee J, Lange M, Tsai R, Nam P, Nishimoto M, Gutierrez A, Quach H, Lai R, Farkas D, Wojtowicz M, Chin P, Barsky M, Oki A, Boos JB, Bennett BR (2007) Manufacturable and reliable 0.1 μm AlSb/InAs HEMT MMIC technology for ultra-low power applications. In: IEEE MTT-S international microwave symposium digest. https://doi.org/10.1109/MWSYM.2007.380488
2. Grillet C, Cresti A, Pala MG (2018) Vertical GaSb/AlSb/InAs heterojunction tunnel-FETs: a full quantum study. IEEE Trans Electron Devices. https://doi.org/10.1109/TED.2018.2834307
3. Tizno O, Marshall ARJ, Fernández-Delgado N, Herrera M, Molina SI, Hayne M (2019) Room-temperature operation of low-voltage, non-volatile, compound-semiconductor memory cells. Sci Rep. https://doi.org/10.1038/s41598-019-45370-1
4. Li H, Alradhi H, Jin Z, Anyebe EA, Sanchez AM, Linhart WM, Kudrawiec R, Fang H, Wang Z, Hu W, Zhuang Q (2018) Novel type-II InAs/AlSb core-shell nanowires and their enhanced negative photocurrent for efficient photodetection. Adv Funct Mater. https://doi.org/10.1002/adfm.201705382
5. Razeghi M, Nguyen BM (2010) Band gap tunability of type II antimonide-based superlattices. Phys Procedia. https://doi.org/10.1016/j.phpro.2010.01.164
6. Singh AK, Rathi A, Riyaj M, Bhardwaj G, Alvi PA (2017) Optical gain tuning within IR region in type-II $In_{0.5}Ga_{0.5}As_{0.8}P_{0.2}$/$GaAs_{0.5}Sb_{0.5}$ nano-scale heterostructure under external uniaxial strain. Superlattices Microstruct. https://doi.org/10.1016/j.spmi.2017.07.014

7. Dolia R, Bhardwaj G, Singh AK, Kumar S, Alvi PA (2017) Optimization of type-II 'W' shaped InGaAsP/GaAsSb nanoscale-heterostructure under electric field and temperature. Superlattices Microstruct. https://doi.org/10.1016/j.spmi.2017.10.007
8. Kolokolov KI, Ning C-Z (2004) Doping-induced type-II to type-I transition and mid-IR optical gain in InAs/AlSb quantum wells. In: Novel in-plane semiconductor lasers III. https://doi.org/10.1117/12.530465
9. Kolokolov KI, Ning CZ (2003) Doping-induced type-II to type-I transition and interband optical gain in InAs/AISb quantum wells. Appl Phys Lett. https://doi.org/10.1063/1.1605236
10. Alvi PA (2017) Transformation of type-II InAs/AlSb nanoscale heterostructure into type-I structure and improving interband optical gain. Phys Status Solidi Basic Res. https://doi.org/10.1002/pssb.201600572
11. Rathi A, Singh AK (2018) Optical response computations in type-II doped AlSb/InAs nano-heterostructure under external uniaxial strain in SWIR range. In: 2017 IEEE 3rd international conference on engineering technologies and social sciences. ICETSS 2017. https://doi.org/10.1109/ICETSS.2017.8324153
12. Larrabee DC, Khodaparast GA, Kono J, Ueda K, Nakajima Y, Nakai M, Sasa S, Inoue M, Kolokolov KI, Li J, Ning CZ (2003) Temperature dependence of intersubband transitions in InAs/AiSb quantum wells. Appl Phys Lett. https://doi.org/10.1063/1.1626264
13. Li J, Kolokolov K, Ning CZ, Larraber DC, Khodaparast GA, Kono J, Ueda K, Nakajima Y, Sasa S, Inoue M (2002) Intersubband transitions in InAs/AISb quantum wells. Mater Res Soc Symp Proc. https://doi.org/10.1557/proc-744-m9.2
14. Larrabee DC, Tang J, Liang M, Khodaparast GA, Kono J, Ueda K, Nakajima Y, Suekane O, Sasa S, Inoue M, Kolokolov KI, Li J, Ning CZ (2002) Intersubband transitions in narrow InAs/AlSb quantum wells. In: Proceedings IEEE Lester Eastman conference on high performance devices. https://doi.org/10.1109/lechpd.2002.1146771
15. Desplanque L, Vignaud D, Godey S, Cadio E, Plissard S, Wallart X, Liu P, Sellier H (2010) Electronic properties of the high electron mobility $Al_{0.56}In_{0.44}Sb/Ga_{0.5}In_{0.5}Sb$ heterostructure. J Appl Phys. https://doi.org/10.1063/1.3475709
16. Vasallo BG, Rodilla H, González T, Lefebvre E, Moschetti G, Grahn J, Mateos J (2011) Monte Carlo analysis of impact ionization in isolated-gate InAs/AlSb high electron mobility transistors. Acta Phys Pol A. https://doi.org/10.12693/APhysPolA.119.222
17. Boos JB, Bennett BR, Kruppa W, Park D, Mittereder J, Bass R, Twigg ME (1999) Ohmic contacts in AlSb/InAs high electron mobility transistors for low-voltage operation. J Vac Sci Technol B Microelectron Nanometer Struct. https://doi.org/10.1116/1.590687
18. Wu B (2003) Sb-based high electron mobility transistors: processing and device characterization. M.Sc. thesis, University of Notre Dame, p 71
19. Moschetti G (2012) Ultra-low power InAs/AlSb HEMTs for cryogenic low-noise applications. Thesis for Chalmers University of Technology, Sweden
20. Li J, Kolokolov KI, Ning CZ, Larrabee DC, Khodaparast GA, Kono J, Ueda K, Nakajima Y, Sasa S, Inoue M (2004) Microscopic modeling of intersubband resonances in InAs/AlSb quantum wells. Phys E Low-Dimens Syst Nanostruct. https://doi.org/10.1016/j.physe.2003.08.016
21. Fuchs F, Schmitz J, Ralston JD, Koidl P (1994) Spatially direct and indirect photoluminescence from InAs/AlSb heterostructures. Phys Rev B. https://doi.org/10.1103/PhysRevB.49.13638
22. Glinskii GF, Mironova MS (2014) An 8-band Kane model for quantum-sized heterostructures based on cubic semiconductors A^3B^5. J Phys Conf Ser. https://doi.org/10.1088/1742-6596/572/1/012052
23. Gravesen J, Willatzen M (2019) The four-band spin-less Kane model in curvilinear coordinates. Phys Status Solidi Rapid Res Lett. https://doi.org/10.1002/pssr.201800305
24. Trebin HR, Rössler U, Ranvaud R (1979) Quantum resonances in the valence bands of zinc-blende semiconductors. I. Theoretical aspects. Phys Rev B. https://doi.org/10.1103/PhysRevB.20.686
25. Kolokolov KI, Savin AM, Beneslavski SD, Minina NY, Hansen OP (1999) Energy spectrum and topology evolution of the fermi surface of two-dimensional holes in $GaAs/Al_{0.5}Ga_{0.5}As$

heterostructures under uniaxial compression: theory and experiment. Phys Rev B Condens Matter Mater Phys 59:7537–7545. https://doi.org/10.1103/PhysRevB.59.7537

26. Ameri M, Boufadi F, Touia A, Faudil M, Hachemane D, Boudia K, Slamani A, Aze-Eddine A (2012) Ab initio calculations study of structural and electronic properties of ternary alloy $Al_xIn_{1-x}As$. Mater Sci Appl. https://doi.org/10.4236/msa.2012.310099
27. Vurgaftman I, Meyer JR, Ram-Mohan LR (2001) Band parameters for III–V compound semiconductors and their alloys. J Appl Phys 89:5815–5875. https://doi.org/10.1063/1.1368156

Analysis and Design of Microstrip Patch Antenna with Two Different Metamaterial Unit Cells

Nameeta Sharma, Kirti Vyas, and Rahul Srivastava

Abstract In this paper, we design and fabricate a metamaterial-inspired antenna with size reduction and multiband resonant frequencies. Here, we analyze the metamaterial unit cell with conventional split ring resonator and complementary split ring resonators. We incorporate the MM unit cell with a conventional microstrip patch antenna to get multi-bands. Antenna is resonant on three frequency bands 2.3, 4.5, and 7.4 GHz.

Keywords Complementary split ring resonator (CSRR) · Metamaterial · Negative permeability · Negative permittivity · Negative refractive index · Split ring resonator (SRR)

1 Introduction

Microstrip patch antennas are very popular in the present era of wireless communication technology because of its characteristics like less weight, compact, small size moderate gain, and bandwidth [1]. Mobile handsets are in demand because new applications. New frequency bands and compact miniaturized system are required for recent wireless devices. Therefore, the antenna that covers the multiband characteristics with compact size is found to be more useful in present electronics wireless devices.

In twenty-first century, electromagnetics play a vital role in the designing of microwave devices. In the twenty-first century, electromagnetic double-negative materials are key component; they are also known as metamaterials (MMs). Veselago first proposed the medium with negative refractive index [2]; Pendry reported a split ring resonator (SRR) with negative capabilities [3], and Smith extracted the different parameters of MM from reflection and transmission coefficients [4–7]. Some other methods are also defined for extracting the parameters of MM [8, 9]. In different studies, metamaterials are used for directivity enhancement [10, 11], size

N. Sharma (✉) · K. Vyas · R. Srivastava
Department of Electronics and Communication Engineering, ACEIT, Jaipur, Rajasthan, India
e-mail: rattlenameeta@gmail.com

S. Dwivedi et al. (eds.), *Flexible Electronics for Electric Vehicles*, Lecture Notes in Electrical Engineering 863, https://doi.org/10.1007/978-981-19-0588-9_57

miniaturization [12], gain enhancement [10, 13], and used to generate multiband [14] antenna. Other applications of metamaterials are microwave filter [15] design, MIMO antennas [16], phased array antenna [17].

In this research work, we have designed a traditional split ring resonator and a complementary split ring resonator (CSRR) with the same MM unit cell. We keep the dimension and substrate material same for both designs. We analyze the variation in the resonant frequency and double-negative characteristics of the MM unit cell.

In the next part of the research, we choose a conventional microstrip patch antenna (MPA) designed at 2.34 GHz frequency and incorporate (conventional) MM unit cell with the antenna and found that MPA is showing multiband with miniaturization of dimension of MPA. Physical size of the patch antenna is $0.23\lambda_0 \times 0.29\lambda_0 \times 0.00625\lambda_0$. Fabricated and tested results of MM-inspired antenna are also present here.

In the last part of the paper, we reduce the ground plane size and make its dimension equal to the dimension of the antenna and found that antenna is still resonant at the same frequency band.

2 Design and Analysis of Metamaterial Unit Cell

2.1 Analysis of Conventional SRR

The conventional split ring resonator unit cell (Fig. 1) having the dimensions of the

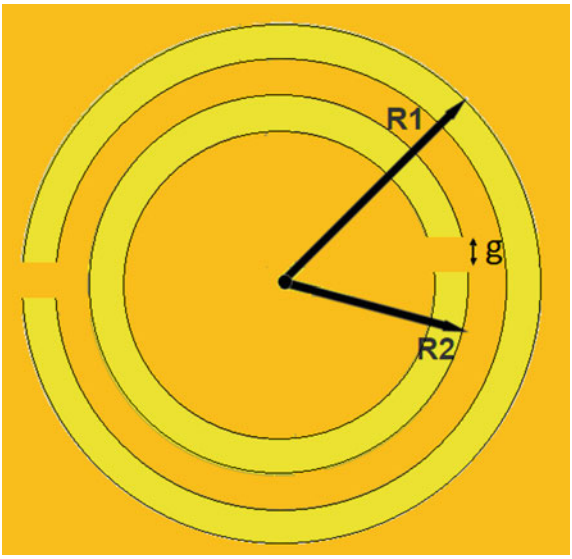

Fig. 1 Proposed SRR metamaterial unit cell where $R1 = 5.2$ mm, $R2 = 4.5$ mm, and $g = 0.5$ mm

proposed MM unit cell are '$R1$' is 5.2 mm, and '$R2$' is 4.5 mm, $w = g = 0.5$ mm. FR4 dielectric substrate is used with thickness 0.8 mm.

Equivalent circuit of the general SRR structure is shown in Fig. 2, where we are using parallel combination of L_{eq} and C_{eq}. After simulation in ADS software, we found $L_{eq} = 0.8$ nH and $C_{eq} = 38$ pF.

Resonant frequency can be calculated by following formula.

$$f = \frac{1}{2\pi\sqrt{L_{eq}C_{eq}}}$$

We have $L_{eq} = 0.8$ nH and $C_{eq} = 38$ pF. Substituting these values in above equation and we found

$$f = \frac{1}{2\pi\sqrt{0.8 \times 10^{-9} \times 38 \times 10^{-12}}}$$

$$f = \frac{1}{2\pi\sqrt{3.04 \times 10^{-12}}}$$

$$f = 9.12\,\text{GHz}$$

So, the resonance frequency of the above structure is 9.12 GHz. Simulation result of generalize SRR is shown in Fig. 3, where we are getting the S21 below −10 dB from 8.6 to 10.4 GHz, and S11 is 0 dB in this bandwidth. Numerically, computed result (9.1 GHz) is also belongs to the same band.

At 9 GHz frequency, real value of effective permittivity is negative, and permeability is zero at that frequency (Fig. 4a). The imaginary part of the permittivity and permeability is zero at 9 GHz frequency (Fig. 4b). So, this structure has the same characteristics, i.e., ENG material, as the proposed SRR.

The proposed and generalize SRR structure have different value of equivalent inductance and capacitance values. Due to this difference, their resonant frequencies are differing, while they have same physical area of unit cell.

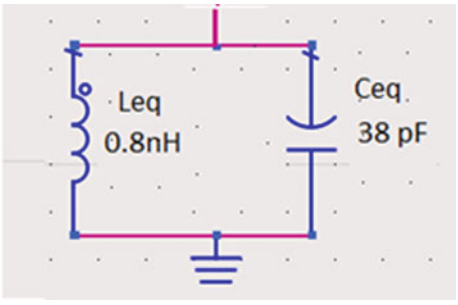

Fig. 2 Equivalent circuit generalize SRR

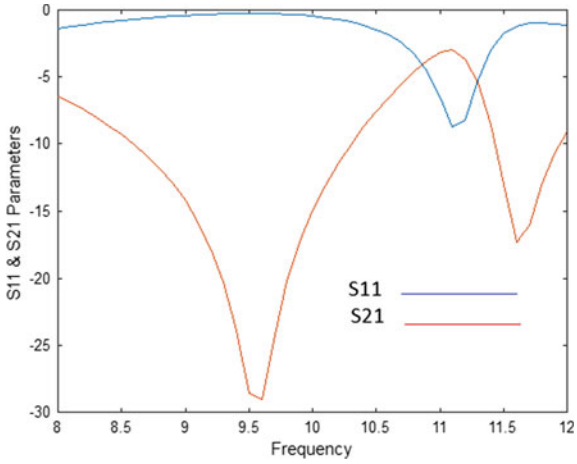

Fig. 3 S11 and S21 parameters of generalize SRR

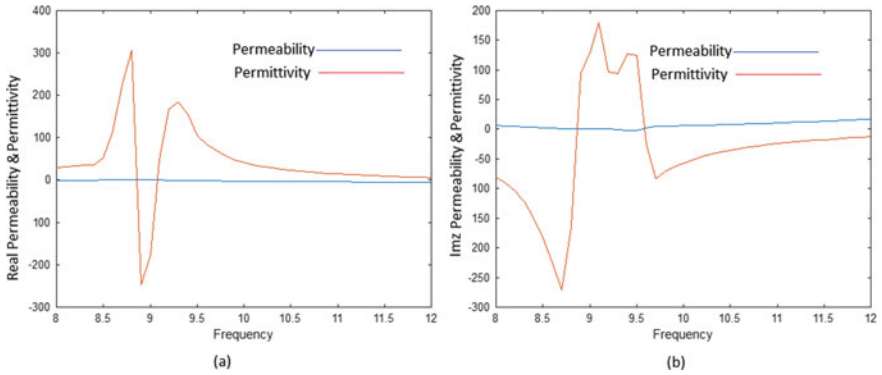

Fig. 4 Effective permittivity and permeability of generalize SRR **a** real part of ε and μ, **b** imaginary part of ε and μ

2.2 Analysis of Conventional CSRR Unit Cell

In complimentary split ring resonator (CSRR), the split rings are etched from the conducting surface. In this work, the same geometry is used (same as Sect. 2.1), with only difference is that rings are non-conducting and surface is conducting (Fig. 5).

Simulation results are shown in Figs. 6 and 7. By the results, reflection parameters are below −10 dB from 6.1 to 6.3 GHz band and 7.9 to 8.8 GHz, and transmission parameters are below −10 dB from 6.6 to 6.8 GHz. Permittivity and permeability both are negative from 8.2 to 10 GHz frequency band.

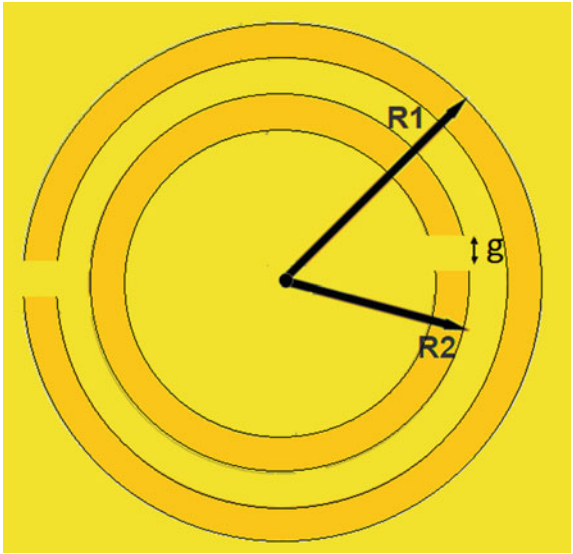

Fig. 5 Proposed CSRR metamaterial unit cell where $R1 = 5.2$ mm, $R2 = 4.5$ mm, and $g = 0.5$ mm

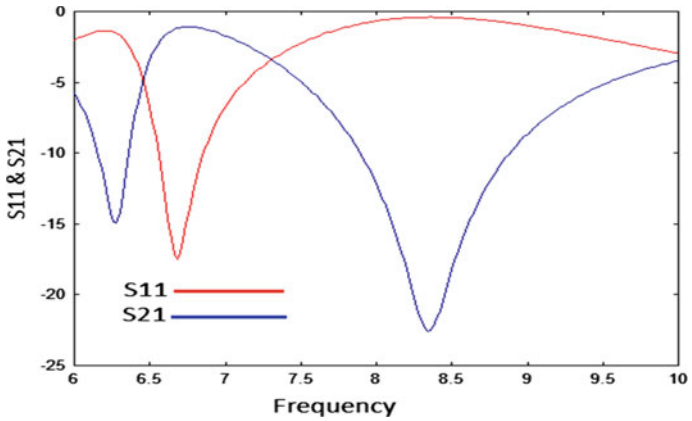

Fig. 6 S11 and S21 parameters of generalize CSRR

3 Antenna Design with MM Unit Cell

In the previous section, we have seen two MM unit cells of same dimension but with slightly changed geometry. In this section, a simple microstrip patch antenna (MPA) is used, designed on 2.3 GHz frequency, and both kind of MM unit cell is embedded with the antenna for miniaturization and multibanding. Patch antenna and its reflection parameters are shown in Figs. 8 and 9, respectively. MPA is having the

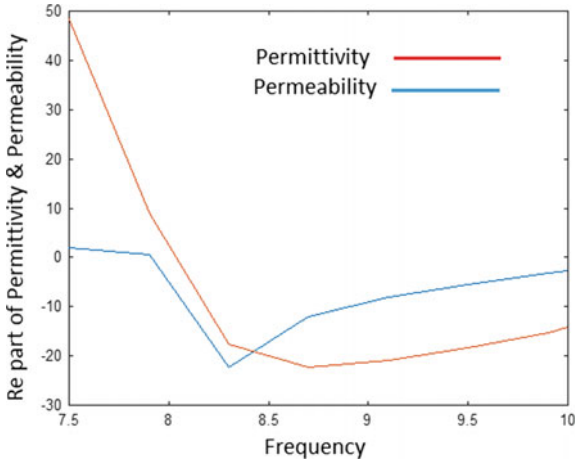

Fig. 7 Real part of permeability and permittivity

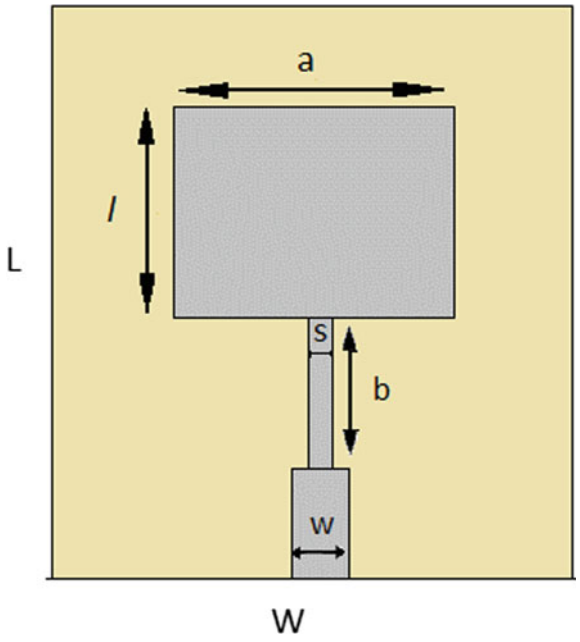

Fig. 8 Microstrip patch antenna with $a = 29.66$ mm, $l = 38.1$ mm, $b = 24.05$ mm, $s = 1.5$ mm, $w = 5$ mm, $L = 98.5$ mm, and $W = 100$ mm

dimension 29.66 mm × 38.1 mm. Quarter wave transformer is 24.05 mm long and 1.5 mm wide, and feed is 15 mm long and 5 mm wide. FR4 dielectric substrate is used having the dimension 110 mm × 98.5 mm. Thickness of the substrate is 0.8 mm. Over all dimension of the antenna is also 110 mm × 98.5 mm with the same ground size.

Simulation of microstrip antenna was done on HFSS software.

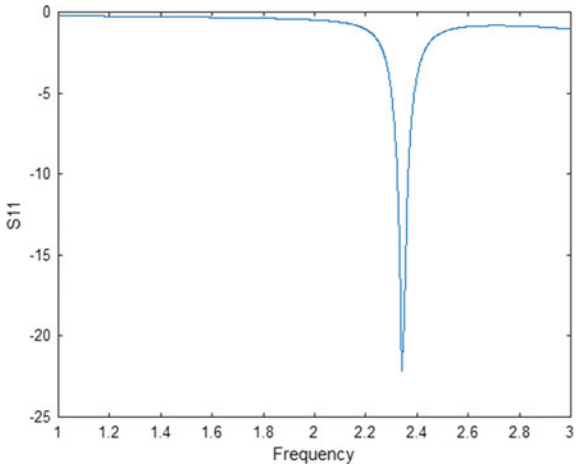

Fig. 9 S11 parameter versus frequency plot of MPA

MPA is resonant at 2.34 GHz frequency, and gain of the antenna is 15.8 dB. We coupled both of the unit cells (proposed SRR and generalize SRR) with the MPA. MM unit cell is placed on MPA where the electric field has moderate intensity. When we embedded the MM unit cell with an antenna, then electric field of the unit cell disturbs the electric field of the antenna. It also disturbs the other parameters of the antenna; hence, we insert the MM unit cell carefully on antenna.

3.1 Patch Antenna with SRR Metamaterial Unit Cell

In this experimental work, patch antenna was loaded with generalize SRR MM unit cell field distribution, and surface current on antenna is shown in Fig. 10, and reflection coefficient curve is shown in Fig. 11.

MPA with SRR loading is resonant on two frequencies, i.e., 2.27 and 4.45 GHz frequencies.

Simulation of same antenna with two different unit cells (having the same dimension) makes the antenna resonant at different frequencies. When MPA is loaded with proposed MM unit cell, it gives three resonant frequencies. As we have seen that the MPA is resonant at 2.34 GHz frequency, and MPA-loaded antenna has lowest frequency was 2.1 GHz. So, miniaturization is also obtaining with multibanding using MM with antenna. Reduction in the size of antenna can be calculated as

$$\frac{2.34 - 2.16}{2.34} \times 100 \approx 8\%$$

We are getting approximately 8% reduction in the size of the antenna.

In the next experiment, we reduce the antenna size by keeping the ground, substrate, and patch width of same dimension as shown in Fig. 12. Figure 12 shows

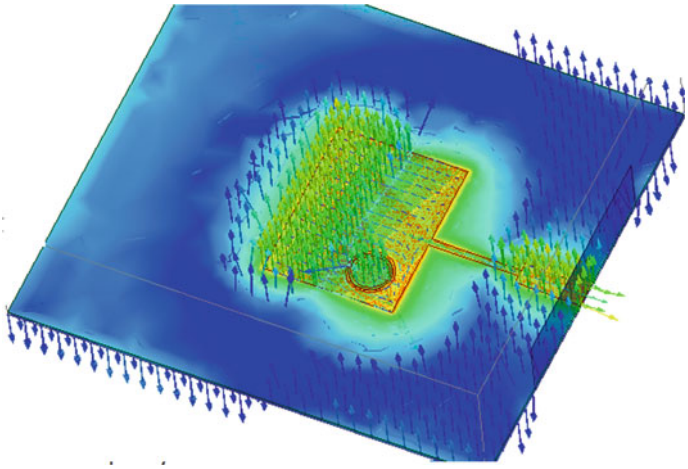

Fig. 10 Surface current on MPA

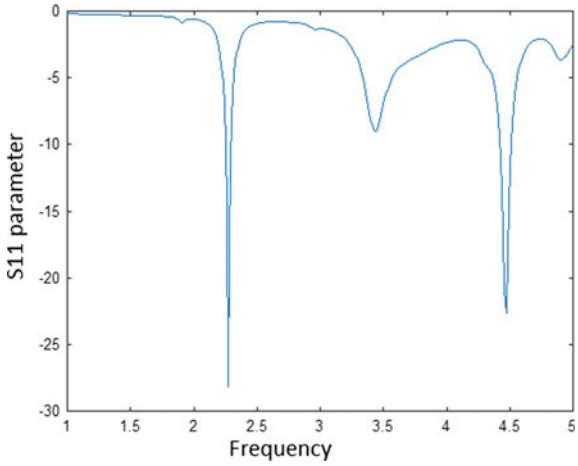

Fig. 11 S11 versus frequency

the magnitude of E-field and wave propagation through the surface.

We have fabricated the above antenna and tested it on Agilent Technologies vector analyzer Model No. N5234 from 1 to 8 GHz frequency range. The fabricated antenna is shown in Fig. 13, and S-parameters of both simulated and fabricated antenna are shown in Fig. 14.

By Fig. 14, the antenna is resonant on three frequency bands 2.3, 4.5, and 7.4 GHz. The fabricated results are reflecting the simulated results. The Figs. 15 and 16 show the radiation pattern with and without antenna and Fig. 17 shows the antenna gain.

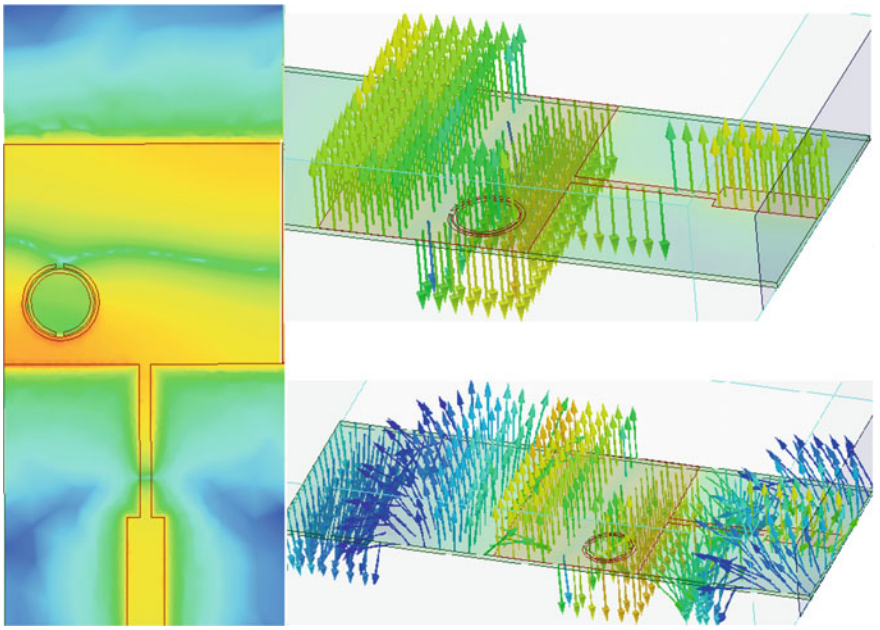

Fig. 12 Magnitude of E-field and wave propagation through the antenna

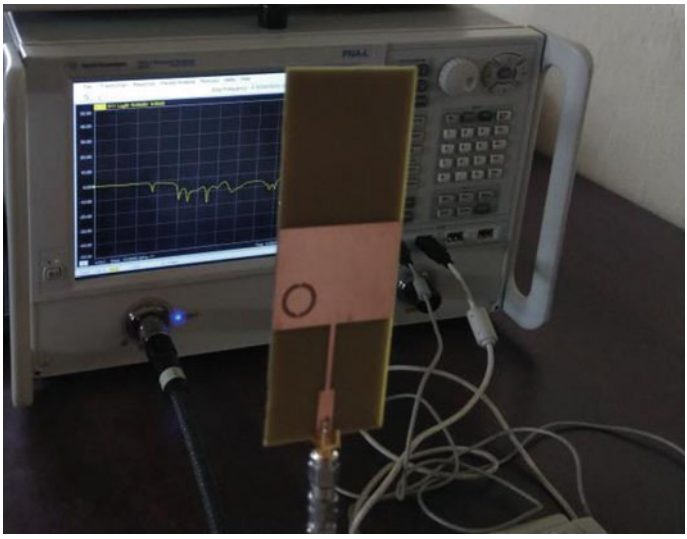

Fig. 13 Fabricated antenna

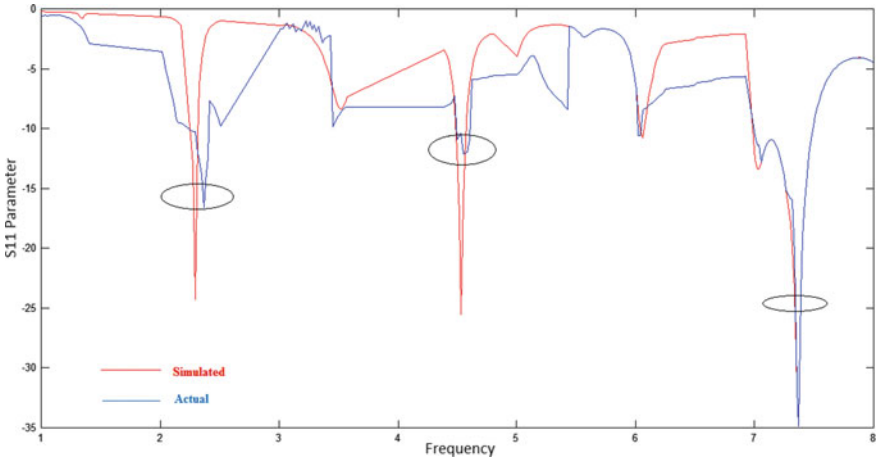

Fig. 14 Simulated and actual results of antenna

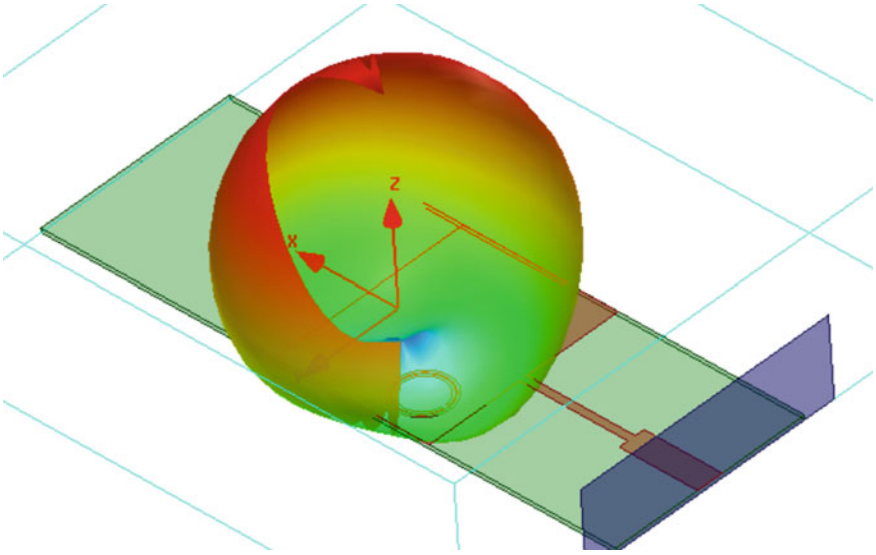

Fig. 15 Simulation of radiation on antenna surface

4 Conclusion

We have demonstrated the configurations of metamaterial unit cells and their behavior with antenna. MM slab can be used for miniaturization of antenna or for design a multiband antenna. We miniaturized the antenna with generating multiband. This technique can be used in wireless communication or in mobile communication.

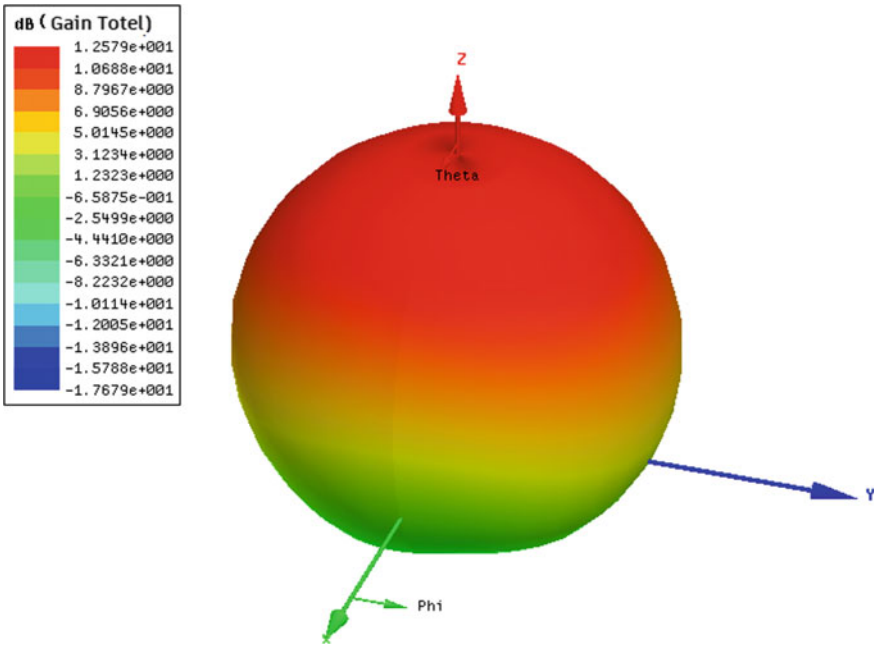

Fig. 16 Radiation pattern of antenna

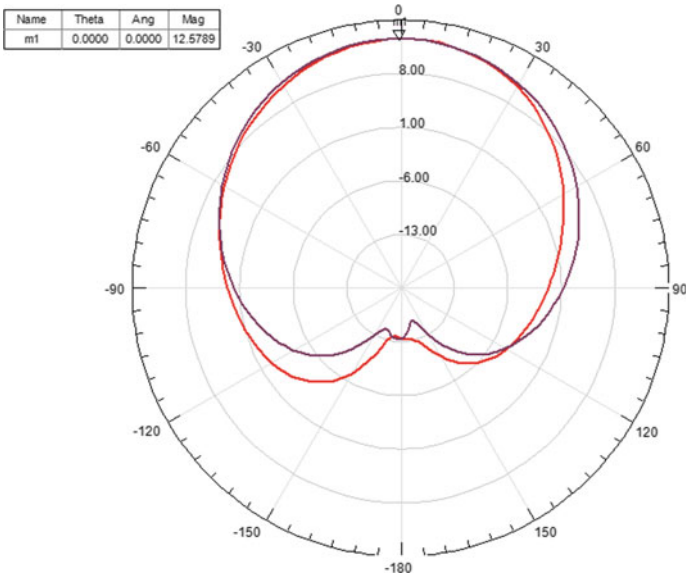

Fig. 17 Gain of the antenna

References

1. Veselago VG (1968) The electrodynamics of substances with simultaneously negative values of e and μ. Sov Phys Usp 10:509
2. Pendry JB, Holden AJ, Robbins DJ et al (1999) Magnetism form conductors and enhanced nonlinear phenomena. IEEE Trans Microw Theory Techn 47:2075
3. Shelby RA, Smith DR, Schultz S (2001) Experimental verification of a negative index of refraction. Science 292:77
4. Smith DR, Padilla WJ, Vier DC et al (2000) Composite medium with simultaneously negative permeability and permittivity. Phys Rev Lett 84:4184
5. Smith DR, Vier DC, Koschny T et al (2005) Electromagnetic parameter retrieval from inhomogeneous metamaterials. Phys Rev E 71:036617
6. Smith DR, Schultz S, Markos P et al (2002) Determination of effective permittivity and permeability of metamaterials from reflection and transmission coefficients. Phys Rev B 65:195104
7. Chen X, Grzegorczyk TM, Wu B et al (2004) Robust method to retrieve the constitutive effective parameters of metamaterials. Phys Rev E 70:016608
8. Falcone F, Lopetegi T, Laso MAG et al (2004) Babinet principle applied to the design of metasurfaces and metamaterials. Phys Rev Lett 93:197401
9. Markos P, Soukoulis CM (2003) Transmission properties and effective electromagnetic parameters of double negative metamaterials. Opt Express 11:649
10. Wu S, Yi Y, Yu Z, Huang X, Yang H (2016) A zero-index metamaterial for gain and directivity enhancement of tapered slot antenna. J Electromagn Waves Appl 30(15):1236510
11. Dawar P, Raghava NS, De A (2016) High gain, directive and miniaturized metamaterial C-band antenna. Cogent Phys 3(1):714–720
12. Xiong H, Li D, Yang C, Li XM, Ou X (2016) Miniaturization of monopole antenna by metamaterial loading technique. IETE J Res 62(5):714–720
13. Awan ZA (2017) Gain characteristics of a metamaterial coated slotted sphere. J Mod Opt 64(8):807–818
14. Mulla SS, Deshpande SS (2018) Miniaturization of multiband annular slot ring antenna using reactive loading. J Electromagn Waves Appl 32(14):1779–1790
15. Kumar A, Verma AK (2013) DGS-based Chebyshev low-pass filter for wireless communication. IETE J Res 59(4):433–437
16. Torabi Y, Bahri A, Sharifi A-R (2016) A novel metamaterial MIMO antenna with improved isolation and compact size based on lSRR resonator. IETE J Res 62(1):106–112
17. Dadashzadeh G, Torabi Y, Kargar M, Rahmati B (2016) Widescan phased antenna array based on cavity-backed ELC-slot microstrip patch antenna element. IETE J Res 62(5):557–563

An Inimitable Control Strategy for Micro-Grid with Fast Voltage Regulation and Voltage Disturbances Mitigation

Sweeka Meshram

Abstract This paper presents a control strategy for grid-integrated PV/Pico-hydro hybrid system. The PV and Pico-hydro systems are considered in this paper as DG system, which are hybridized for injecting generated power to main grid. As the islanding situation occurs, the DG system is cut off from the main grid, and then, there will be power difference between generation and load demand. This will cause the unstable voltage operation of the system. Hence, a smart load shedding algorithm for islanding is developed in this paper featuring fast load voltage regulation and successful mitigation of unbalanced voltage disturbances. An algorithm for synchronization and grid reconnection is also developed, when the fault is recovered. The transient and steady-state analysis, stability analysis of the proposed grid-integrated hybrid system are performed under the grid disconnection and reconnection to realize that the proposed system, and its control strategies are working well. The harmonic analysis is also performed to indicate the improved power quality of the system.

Keywords PV system · Hydro system · SEIG · Islanding · Smart load shedding

1 Introduction

Renewable energy sources (RESs) are gaining more attention because of threatened limitations of the conventional sources such as production of harmful emissions, causes global warming, greenhouse effects, and acid rain and future shortage in fossil fuels [1]. The bottleneck of renewable energy is that it is difficult to generate large quantities of electricity as produced by traditional fossil fuel generators and reliability of supply as these systems often rely on the weather for its source of power. To defeat these difficulties of RES system, either RES system can be integrated with the power grid or two or more RES systems can be hybridized to provide continuous power supply and to fulfill demanded power supply. Hybridization of renewable sources via common DC bus of a power converter has been prevalent because of

S. Meshram (✉)
MANIT, Bhopal, Madhya Pradesh 462003, India
e-mail: kirarmk@gmail.com

S. Dwivedi et al. (eds.), *Flexible Electronics for Electric Vehicles*, Lecture Notes in Electrical Engineering 863, https://doi.org/10.1007/978-981-19-0588-9_58

easy integration monitoring and control as compared with a common AC bus. There are some related works on common DC bus-based hybrid systems [2].

As the penetration level of distribution generation (DG) into the grid is increasing day by day, concern about undetected islanding operation has been raised [3, 4]. Islanding is a phenomenon in which a part of micro-grid containing both load and DG unit is disconnected from rest of the grid and persists to work normally [4, 5]. During grid-connected mode, each DG system is generally operated to supply or to inject predetermined power to grid, which is obtained by current controller synchronized with grid. When islanding situation occurs, each DG system must detect islanding situation and must be switched from current control to voltage control mode to maintain constant voltage for local-connected load based on priorities. During the grid-connected mode, the DG system is operated to inject optimum power to the grid. As the islanding occurs, the grid will be disconnected, and DG is supposed to fulfill the power requirement of the local consumer load. The power generated by local DG system is either less or greater than the local load demand, and this will cause voltage and frequency disturbance at the point of common coupling (PCC). These voltage and frequency disturbances are stochastic in nature, and their recovery time varies from a fraction of cycles to few cycles. Some controlled reactive power sources such as distribution static synchronous compensators (DSTATCOMs) [6, 7], active power filters (APFs) [8], and inverter-based DG [9] are developed for load voltage regulation at PCC. However, these existing techniques have slow regulation performance. The range of voltage recovery time is 0.005–0.006 s with voltage dip of about 0.1–0.4 p.u. reported. Hence, for fast voltage regulation, a smart load shedding is required to secure energy delivery to sensitive load. Load shedding is a process, in which a portion of the load is disconnected from the system based on some priorities for protecting the electrical power system from potential hazard [10–12].

In this paper, performance of the grid-integrated advanced PV/Pico-hydro hybrid system is analyzed under the grid connected or islanding mode of operation. For the Pico-hydro system, self-excited induction generator (SEIG) preferred as it is more advantageous over the synchronous generator. The PV system and Pico-hydro hybrid system is hybridized via common DC bus for reducing control complexity and cost of the system. In this paper, a new control strategy is described and implemented for grid connected and islanding mode of operation. During grid-connected mode, the control strategy will work as constant current controller [13] to inject the preset amount of power to grid, and in islanding mode, the control strategy will work as constant voltage controller [14] to maintain constant voltage at PCC to connected local sensitive load. This paper proposes a smart load shedding algorithm for disconnecting the load based on priorities during islanding mode. The algorithm for synchronization and resynchronization during grid reconnection has also been described in this paper.

2 System Configuration

Figure 1 depicts the configuration of proposed advanced PV/Pico-hydro hybrid

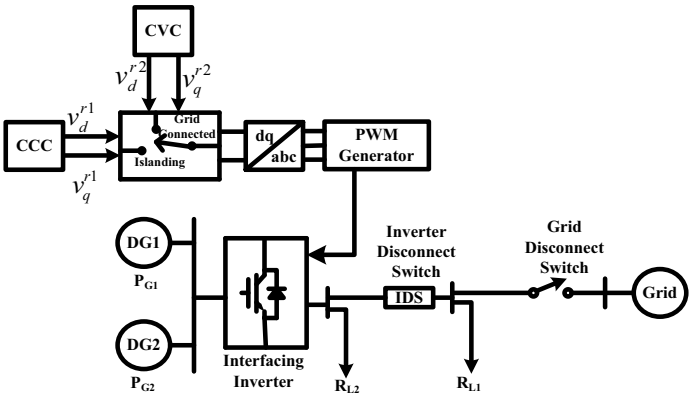

Fig. 1 Configuration of the proposed system

system integrated with power grid. Figure 2 shows MATLAB Simulink model of the grid-connected AC-linked PV/Hydro hybrid system. The DG_1 and DG_2 represent PV system and Pico-hydro system, respectively. To integrate hybrid system with power grid, a voltage source inverter (VSI) is used as an interfacing device. To control this interfacing inverter for grid-connected DGs, a smart controller is required that can maintain the constant output voltage at the point of common coupling (PCC) under different possible conditions such as connection/disconnection of grid, solar irradiance/hydro energy variation, and load variation. For grid-connected mode, the controller will be operated as a constant current control mode for supplying specified power to the grid. When hybrid system is cut off from the main grid, controller must detect this islanding situation and change to voltage control mode, and hybrid system will provide constant voltage to a part of consumer load as per the capability. Hence, for controlling the interfacing inverter to operate either in grid-connected mode or islanding mode, the controller needs to switch either to constant current controller (CCC) or to constant voltage controller (CVC).

3 Smart Load Shedding

Load shedding is a method, in which a fraction of the electrical load is detached from the system based on certain priority to protect the power system from potential dangers [11, 12]. During grid-connected mode, the power grid will supply or absorb power, which is power difference between power generated by hybrid system and total load demand. When the voltage at PCC has reached between 0.88 and 1.1 p.u. and frequency between 49.3 and 50.5 Hz, then power grid must be disconnected from hybrid system to avoid electrical hazard according to IEEE Std. 1547 [15]. But, when grid is disconnected from the hybrid system, the hybrid system must supply the power to the consumer load (P_L) which is greater than the power generated by

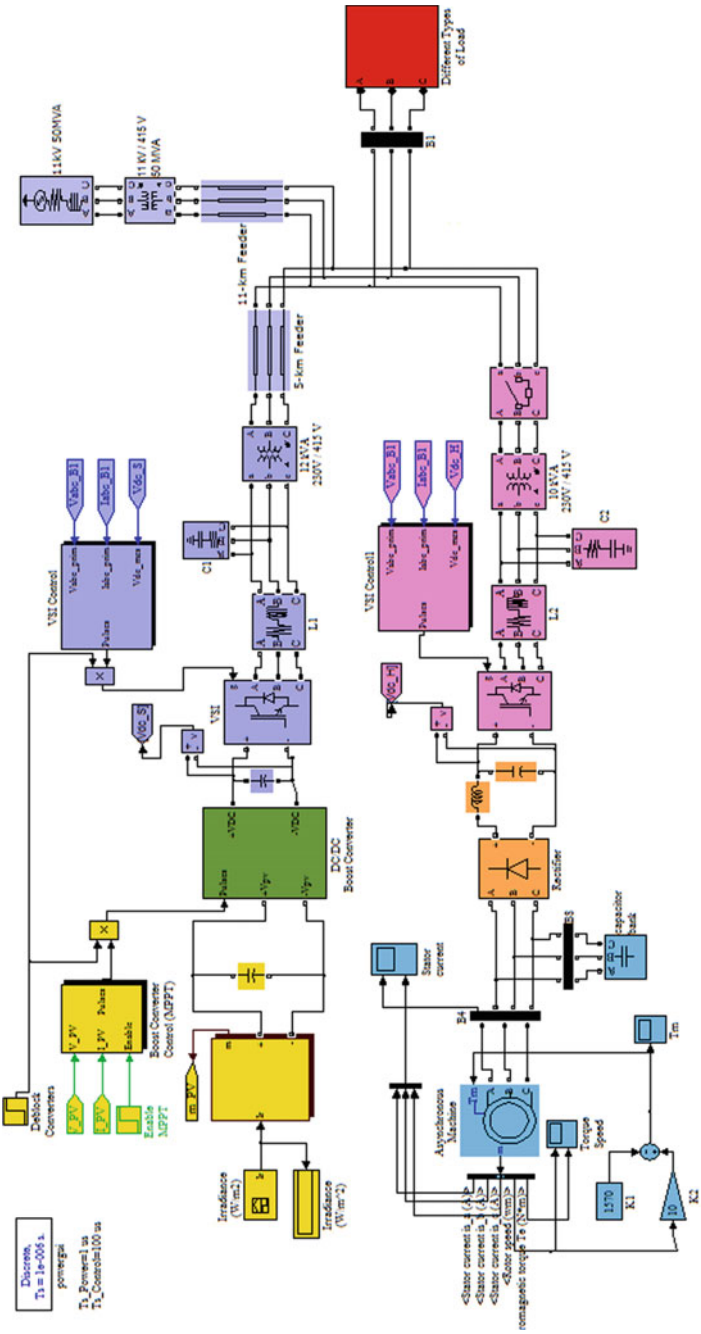

Fig. 2 MATLAB Simulink model of the grid-connected AC-linked PV/hydro hybrid system

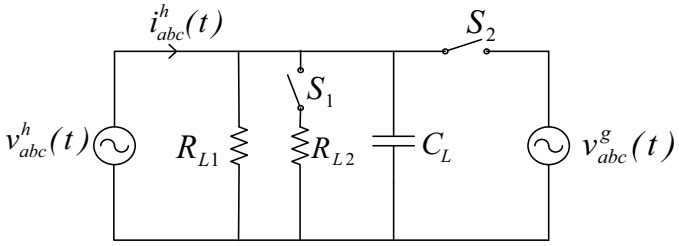

Fig. 3 Equivalent circuit diagram of system for implementing smart load shedding

the hybrid system. This will cause the voltage and frequency floating from the rated values [16]. For protecting the system from such situation, a smart load shedding is required.

A constant impedance load is considered for developing smart load shedding method (SLSM). The SLSM is proposed here to detect voltage and frequency change rate after grid disconnection and to determine how much load is to be shed before going system to the islanding mode. Figure 3 shows the equivalent circuit of the system for implementation of smart load shedding.

Following method is developed to identify the quantity of load to be disconnected,

Step-1: The load voltages $V_a^L(t)$, $V_b^L(t)$, $V_c^L(t)$ can be calculated before load shedding using Fig. 3.

$$V_a^L(t) = \frac{I_{Ld}(t) \cdot R_{L1} \cdot Z_{LC}}{\sqrt{R_{L1}^2 + Z_{LC}^2}} \cdot \sin \omega t \tag{1}$$

$$\begin{aligned} V_b^L(t) = &\left(\frac{\sqrt{3}/2 I_{Ld}(t) \cdot R_{L1} \cdot Z_{LC}}{\sqrt{R_{L1}^2 + Z_{LC}^2}} \cdot \mathrm{e}^{-\frac{Z_{LC}}{R_{L1}} \omega t} \right) \\ &+ \left(\frac{-1/2 I_{Ld}(t) \cdot R_{L1} \cdot Z_{LC}}{\sqrt{R_{L1}^2 + Z_{LC}^2}} \cdot \sin \omega t \right) \\ &+ \left(\frac{-\sqrt{3}/2 I_{Ld}(t) \cdot R_{L1} \cdot Z_{LC}}{\sqrt{R_{L1}^2 + Z_{LC}^2}} \cdot \cos \omega t \right) \end{aligned} \tag{2}$$

$$\begin{aligned} V_c^L(t) = &\left(\frac{-\sqrt{3}/2 I_{Ld}(t) \cdot R_{L1} \cdot Z_{LC}}{\sqrt{R_{L1}^2 + Z_{LC}^2}} \cdot \mathrm{e}^{-\frac{Z_{LC}}{R_{L1}} \omega t} \right) \\ &+ \left(\frac{-1/2 I_{Ld}(t) \cdot R_{L1} \cdot Z_{LC}}{\sqrt{R_{L1}^2 + Z_{LC}^2}} \cdot \sin \omega t \right) \end{aligned}$$

$$+\left(\frac{\sqrt{3}/2 I_{Ld}(t)\cdot R_{L1}\cdot Z_{LC}}{\sqrt{R_{L1}^2+Z_{LC}^2}}\cdot\cos\omega t\right) \tag{3}$$

Step-2: The magnitude of the voltage can be expressed as,

$$V_{Ld}(t)=1+\Delta V_{Ld}(t) \tag{4}$$

where

$$\Delta V_{Ld}(t)=I_{Ld}(t)R_{L1}Z_{LC}\sqrt{\frac{\mathrm{e}^{-\frac{2\omega t Z_{LC}}{R_{L1}}}\left(1+\mathrm{e}^{\frac{2\omega t Z_{LC}}{R_{L1}}}-2\mathrm{e}^{-\frac{\omega t Z_{LC}}{R_{L1}}}\cdot\cos\omega t\right)}{R_{L1}^2+Z_{LC}^2}}$$

Hence, if $N=\frac{\omega t Z_{LC}}{R_{L1}}$, then Eq. (4) can be written as,

$$V_{Ld}(t)=1+I_{Ld}(t)R_{L1}Z_{LC}\sqrt{\frac{\mathrm{e}^{-2N}\left(1+\mathrm{e}^{2N}-2\mathrm{e}^{-N}\cdot\cos\omega t\right)}{R_{L1}^2+Z_{LC}^2}}$$

Step-3: The slope of load voltage magnitude can be expressed as,

$$\begin{aligned}s&=\frac{\mathrm{d}V_{Ld}(t)}{\mathrm{d}t}=\frac{\mathrm{d}\Delta V_{Ld}(t)}{\mathrm{d}t}\\&=\frac{\mathrm{e}^{-2N}\omega I_{Ld}(t)Z_{LC}\left(\mathrm{e}^{N}\sin\omega t R_{L1}+\left(-1+\mathrm{e}^{N}\cos\omega t\right)\right)Z_{LC}}{\sqrt{\left(1+\mathrm{e}^{-2N}-2\mathrm{e}^{-N}\cos\omega t\right)\left(R_{L1}^2+Z_{LC}^2\right)}}\end{aligned} \tag{5}$$

Step-4: The magnitude of the current can be calculated from Eq. (6),

$$I_{Ld}(t)=\frac{s\sqrt{\left(1+\mathrm{e}^{2N}-2\mathrm{e}^{-N}\cdot\cos\omega t\right)\left(R_{L1}^2+Z_{LC}^2\right)}}{\mathrm{e}^{-2N}\omega Z_{LC}\left(\mathrm{e}^{N}\sin\omega t R_{L1}+\left(-1+\mathrm{e}^{N}\cos\omega t\right)Z_{LC}\right)} \tag{6}$$

Step-5: The amount of load to be disconnected can be calculated as,

$$R_{L1}=\frac{1}{\sqrt{I_{Ld}^2(t)-\frac{1}{Z_{LC}^2}}}\quad R_{L2}=\frac{R_{LT}R_{L1}}{R_{L1}-R_{LT}}$$

where $R_{LT}=\frac{R_{L1}\cdot R_{L2}}{R_{L1}+R_{L2}}$. R_{L2} is a part of load, which is to be disconnected for safe islanding operation of the system, and R_{L1} is the amount of load, which will be fed by the hybrid system.

4 Algorithm for Reconnection of Grid to Hybrid System

When fault in the power grid disappears, there must be transition from islanded mode to grid-connected mode. During reconnection period, there will be large transient. Therefore, hybrid system must be well synchronized with the power grid before switching to grid-connected mode from islanded mode. Until hybrid system is not synchronized with power grid, system must be operated on islanded mode. Once the hybrid system is synchronized with grid, then grid can be reconnected to hybrid system, and controller will work as constant current controller. To realize this goal, following algorithm is developed,

Step-1 Calculate the phase difference between power grid voltage and interfacing inverter voltage using following Eq. (7)

$$\phi = \angle v^g_{abc}(t) - \angle v^h_{abc}(t) \tag{7}$$

Step-2 The ϕ can be obtained using Eq. (8)

$$\phi = \sin^{-1} \frac{\frac{4}{3}m + \frac{2}{3}n}{\sqrt{3}} \tag{8}$$

where

$$\begin{aligned} m &= v^g_a(t) \cdot v^h_a(t) + v^g_b(t) \cdot v^h_b(t) + v^g_c(t) \cdot v^h_v(t) \\ &= \frac{3}{2}\cos\phi \\ n &= v^g_b(t) \cdot v^h_a(t) + v^g_c(t) \cdot v^h_b(t) + v^g_a(t) \cdot v^h_v(t) \\ &= \frac{3}{4}\left[-\cos\phi + \sqrt{3}\sin\phi\right] \end{aligned}$$

The algorithm for the grid reconnection can be achieved using the PI controller and PLL. The signal $\sin\phi$ is given to the PI controller to generate $\Delta\phi$, which is compared with the ϕ_{old} and comparison generates ϕ_{new}. The ϕ_{new} is fed to PLL for synchronization.

5 Results and Discussion

A simulation model of proposed hybrid system with smart load shedding has been developed using the MATLAB Simulink toolbox. The proposed system is modeled with a 10 kW PV system, which is hybridized with 7.5 kW advanced SEIG-based hydro system and this hybrid system. This RES hybrid system is integrated with the power grid to insure continuous electrical power supply.

Table 1 Specifications and parameters for PV system

Quantity	Symbol	Value
PV panel parameter		
Output power of PV panel	P_{pv}	10 kW
DC output voltage	V_{pv}	275–321 V
DC output current	I_{pv}	10.9–33.02 A
Boost converter parameters		
Switching frequency	f_{Bs}	5 kHz
Capacitor	C_B	15 μF
Inductor	L_B	170 mH
MPPT controller gain	k_{MPP}	7.2

The specifications and parameters of PV system, hydro system, and interfacing inverter are given in Tables 1, 2, and 3, respectively.

Table 2 Specifications and parameters for SEIG-based hydro system

Quantity	Symbol	Value
Output power	P_h	7.5 kW
Capacitor bank	C_h	3 kVAr
Rated voltage	V_h	415 V
Rated current	I_h	10.4 A
Rated speed	N_h	1500 rpm
No. of pole	P	4
Frequency	f_h	50 Hz

Table 3 Specifications and parameters for interfacing inverter

Quantity	Symbol	Value
Output capacity	P_{inv}	20 kW
Switching frequency	f_s	10 kHz
Output frequency	f	50 Hz
Filter inductance	L_f	8 mH
Filter capacitor	C_f	56 μF
DC link voltage	V_{DC}	500 V
DC link capacitor	C_{DC}	1200 μF
Grid voltage	$v^g_{abc}(t)$	230 V
Grid frequency	f_g	50 Hz

5.1 Interfacing Inverter

The solar irradiance is variable. Hence, a space vector pulse width-modulated (SVPWM) VSI has been used in this paper with 10 kHz switching frequency with output voltage has rating 230 V, 50 Hz. A low-pass filter with LC element (250 mH, 36 μF) is connected between interfacing inverter and isolation transformer for smooth and clean power injection. The control strategy for interfacing VSI discussed before is utilized for simulation. At first, the hybrid system is operated in islanding mode to test either the control strategy is performing the synchronization or not.

It can be concluded from Fig. 4 that proposed control strategy is able to perform feature of synchronization, and its response time is 0.00125 s. Hence, control strategy is able to generate VSI output voltage synchronized with grid voltage with 0.00125 s delay, which is very less, and there will be no problem during grid integration. The in-phase supplied current by the system is also shown in Fig. 4.

The voltage and current harmonic spectrum analysis of the complete hybrid system with LC filter has been done as shown in Fig. 5. The THD% of the output voltage

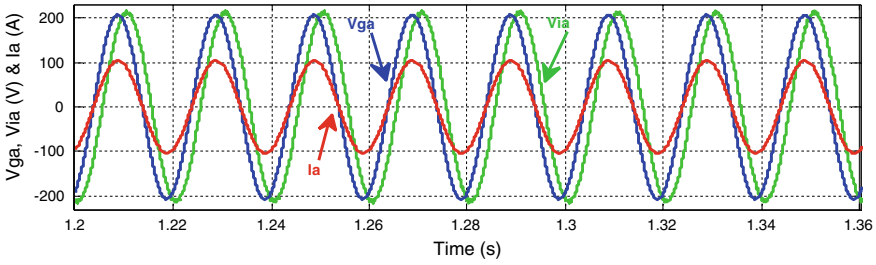

Fig. 4 VSI response (V_{ia}) with proposed control strategy for grid voltage (V_{ga}) with injected current (I_a)

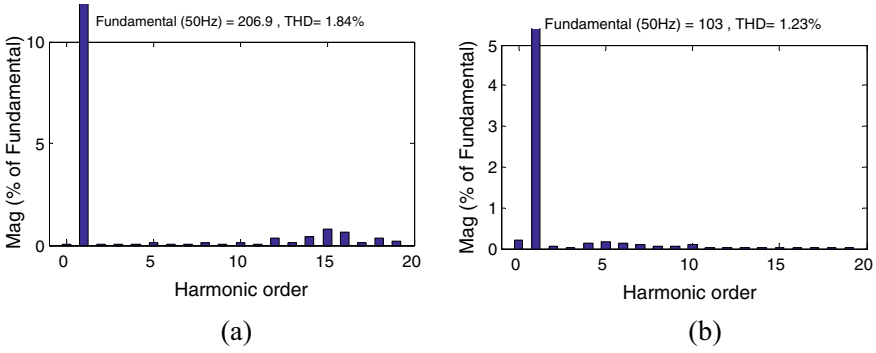

Fig. 5 Harmonic spectrum analysis with LC filter. **a** Harmonic content of voltage of hybrid system. **b** Harmonic content of supplied current by hybrid system

and current of hybrid system is 1.84 and 1.23%, which is less than 5% limit imposed by IEEE-519 standard [16].

5.2 Grid Connected to Islanded Mode

The *RLC* load is maintained to be resonant at 50 Hz, and load consumes 25 kW initially. The PV system and hydro system are designed to supply 10 kW and 7.5 kW, respectively. Hence, the hybrid system is able to supply approximate 17 kW and zero reactive power. Initially, hybrid system is operated in grid-connected mode.

The grid is disconnected at 0.42 s, and the system will be operated in islanding mode at 0.425 s as can be seen in Fig. 6. During grid-connected mode, VSI and grid voltages (V_{ia} and V_{ga}) are in phase till 0.42 s. As islanding occurs, phase difference between V_{ia} and V_{ga} starts increasing from 0.425 s. Just after, mode switching (i.e., from grid-connected to islanding), the phase difference between V_{ia} and V_{ga} is minimum, but with time, this phase difference will increase up to 0.0225°.

Figure 7 shows the voltages and currents at the PCC before and after grid disconnection from hybrid system. At 0.42 s, the power grid is disconnected, and control strategy changes from constant current controller to constant voltage controller for smooth transition. Hence, little transients appear during transition and removed very quickly within 0.0115 s at 0.4315 s. The hybrid system is designed to supply 17 kW; therefore, a part of load has been disconnected to avoid the mismatch of power between generation and load demand implementing smart load shedding algorithm. Based on the certain priorities, a constant impedance load of 15 kW is fed by the islanded hybrid system, which can be seen from variation in currents waveform (I_{abc}).

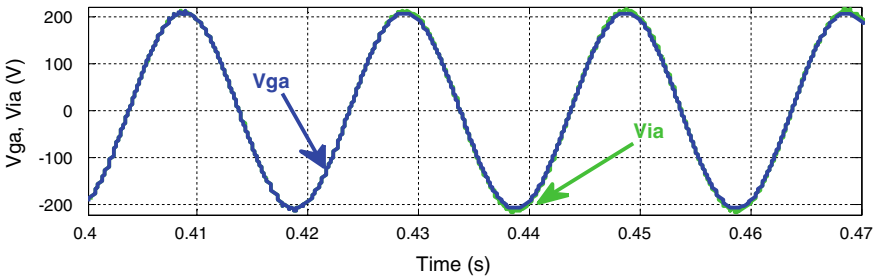

Fig. 6 VSI and grid voltage, when system is switching from grid connected to islanding mode

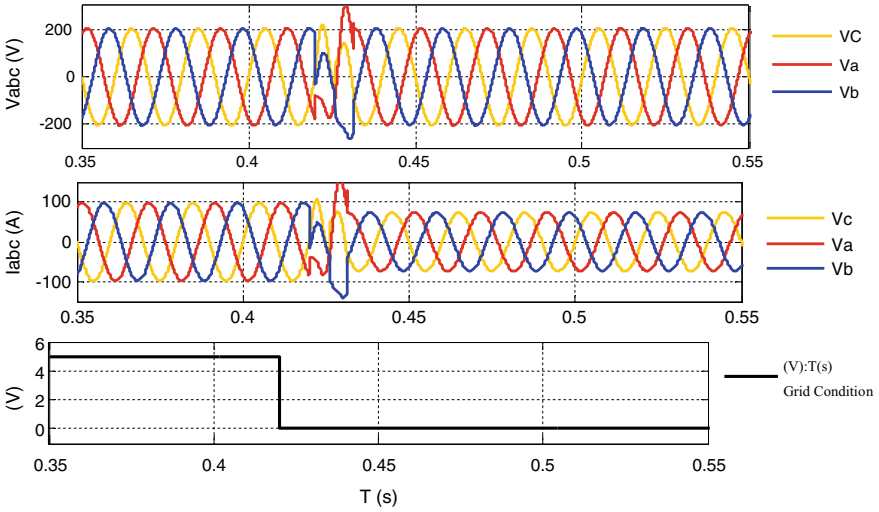

Fig. 7 Voltage and current at PCC during transition from grid connected to islanding mode

5.3 Islanded to Grid-Connected Mode

The power grid is reconnected at 0.8 s, and control strategy will changes from constant voltage controller to constant current controller. The hybrid system is operated in synchronous islanding mode until both hybrid system and grid are resynchronized.

Figure 8 shows the synchronization of the of phase voltages of interfacing VSI and grid at both ends of PCC, when synchronization process starts working for transition of islanded to grid-connected mode. It can be seen from Fig. 8, the synchronization algorithm is successful for tracking grid voltage and forces the hybrid system voltage to be synchronized with the grid voltage.

After completion of synchronization, the power grid will be reconnected to hybrid system. Figure 9 shows voltages (V_{abc}) and currents (I_{abc}) at the PCC before and after grid reconnection. As the load shedding algorithm is also implemented with control

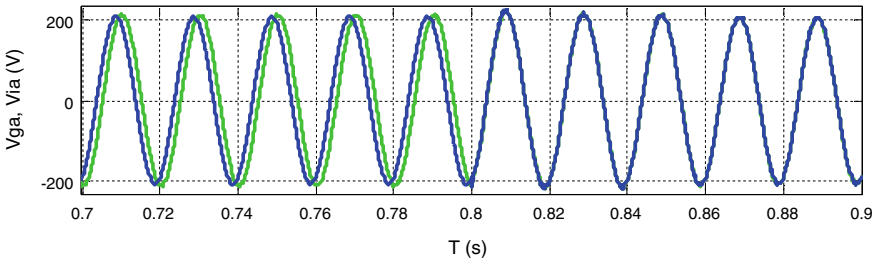

Fig. 8 VSI and grid voltage, when system is switching from islanding to grid-connected mode

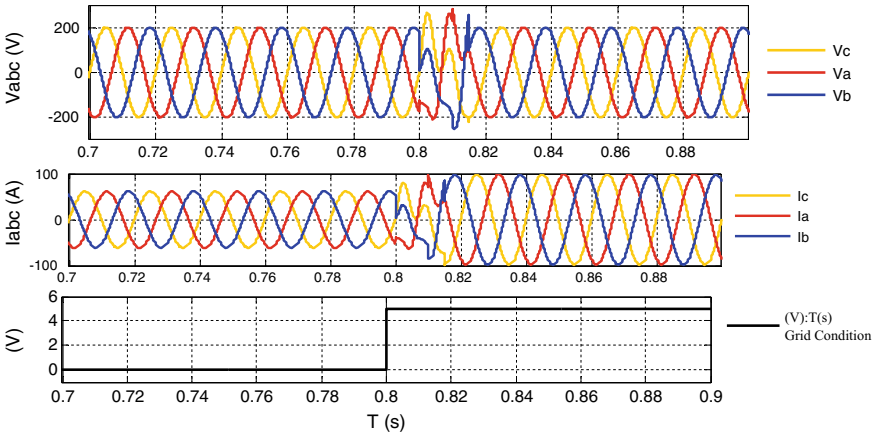

Fig. 9 Voltage and current at PCC during transition from islanding to grid-connected mode

strategy and synchronization algorithm, therefore, transients occur during connection/disconnection of the grid. These transients will be removed within 0.015 s, and after 0.815 s, clean and smooth voltage at PCC will be available.

In islanding mode, 15 kW is only fed by the hybrid system. As the grid is reconnected to the hybrid system at 0.8 s, the addition of 10 kW load is also fed by the system using smart load shedding algorithm, which can be seen from variation in current waveform.

5.4 Smart Load Shedding

For avoiding the power mismatch between generation and load demand in case of islanding mode and to maintain the magnitude of voltage at PCC in its normal operating range during load variation, a smart load shedding algorithm is proposed and implemented. Due to variation of solar irradiance, generated power of PV system and hybrid system during islanding mode is changed, i.e., from 0.42 to 0.82 s. During islanding mode, constant impedance load of about 15 kW is fed by the hybrid system. For hydro system, constant speed-driven SEIG is used. Hence, power generated by the hydro system is constant, i.e., 7.5 kW. The load demand is constant but the load generation balance may disturb due to the intermittent nature of PV system.

With solar irradiance variation, there will be power mismatch, and the voltage magnitude at PCC will reduce with reduction in power generation. For avoiding above explained situation, smart load shedding algorithm is developed in this paper.

Figure 10 shows the voltages and current at PCC during islanding mode with implementation of smart load shedding algorithm. Using the load shedding algorithm, the voltage magnitude at PCC is maintained to be constant with variation in P_h as the P_h decreases; the magnitude of voltage at PCC also reduces because of power

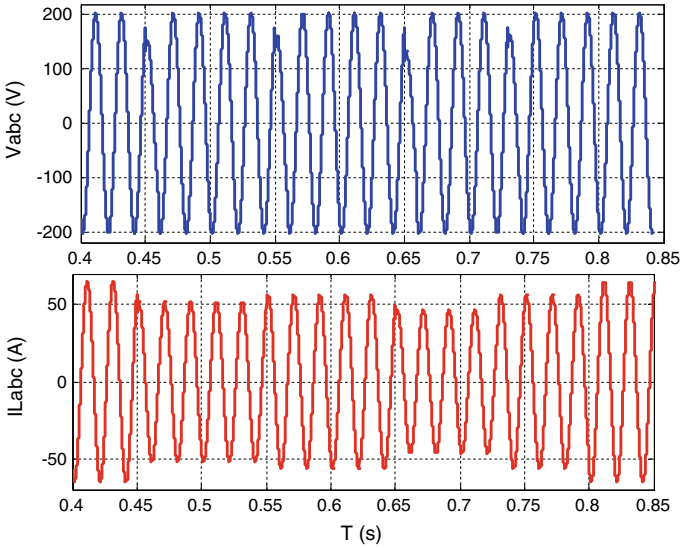

Fig. 10 Voltages and currents at PCC during islanding mode with load shedding

mismatch, but the load shedding algorithm cuts off the load as per requirement and keeps voltage within its normal operating range.

6 Conclusion

In this paper, islanding detection, smart load shedding, synchronization and resynchronization algorithm during grid reconnection is developed for grid connected and islanding mode of operation of PV/hydro hybrid system. The presented results clearly show that control strategy is efficient and can differentiate islanding condition and variation in load and as per requirement can implement load shedding algorithm. The resynchronization algorithm can easily synchronize the hybrid system during grid reconnection. The control strategy is able to remove transients during grid-connection and islanding in 0.0115 s and 0.015 s, respectively. Proposed smart load shedding algorithm is capable for fast voltage regulation and unbalanced voltage disturbances elimination. Load shedding algorithm has voltage recovery time 0.0012 s with the voltage dip of about 0.8–0.9 p.u. reported in results, which is in permissible levels.

References

1. Ramakumar R, Chiradeja P (2002) Distributed generation and renewable energy systems. In: 2002 37th intersociety energy conversion engineering conference, 2002. IECEC'02, 29–31 July 2002, pp 716, 724
2. Giraud F, Salameh ZM (2001) Steady-state performance of a grid-connected rooftop hybrid wind–photovoltaic power system with battery storage. IEEE Trans Energy Convers 16(1):1–7
3. Du P, Ye Z, Aponte E, Nelson J, Fan L (2010) Positive-feedback-based active anti-islanding schemes for inverter-based distributed generators: basic principle, design guideline, and performance analysis. IEEE Trans Power Electron 25(12):2941–2948
4. Kim J-H, Kim J-G, Ji Y-H, Jung Y-C, Won C-Y (2011) An islanding detection method for a grid-connected system based on the Goertzel algorithm. IEEE Trans Power Electron 26(4):1049–1055
5. Jayaweera D, Galloway S, Burt G, McDonald JR (2007) A sampling approach for intentional islanding of distributed generation. IEEE Trans Power Syst 22(2):514–521
6. Jain A, Joshi K, Behal A, Mohan N (2006) Voltage regulation with STATCOMs: modeling, control and results. IEEE Trans Power Delivery 21(2):726–735
7. Lehn PW, Iravani MR (1998) Experimental evaluation of STATCOM closed loop dynamics. IEEE Trans Power Delivery 13(4):1378–1384
8. Fujita H, Akagi H (2007) Voltage-regulation performance of a shunt active filter intended for installation on a power distribution system. IEEE Trans Power Electron 22(3):1046–1053
9. Marei M, El-Saadany E, Salama M (2004) A novel control algorithm for the DG interface to mitigate power quality problems. IEEE Trans Power Delivery 19(3):1384–1392
10. Abou El Ela AA, El-Din AZ, Spea SR (2007) Optimal corrective actions for power systems using multi-objective genetic algorithms. In: Proceedings of 42nd international UPEC, pp 365–376
11. Liu J, Liu Z, Li L (2009) An efficient method for under voltage load shedding. In: Proceedings of APPEEC, pp 1–4
12. Malekpour AR, Seifi AR, Hesamzadeh MR, Hosseinzadeh N (2008) An optimal load shedding approach for distribution networks with DGs considering capacity deficiency modelling of bulked power supply. In: Proceedings of AUPEC, pp 1–7
13. Qi C, MingJian S, LinGao W (2015) The constant current control of anti-scaling descaling device based on incremental digital PID controller. In: The 27th Chinese control and decision conference (2015 CCDC), Qingdao, China, pp 4948–4952. https://doi.org/10.1109/CCDC.2015.7162810
14. Mohammed SAQ, Rafaq MS, Choi HH, Jung J (2020) A robust adaptive PI voltage controller to eliminate impact of disturbances and distorted model parameters for 3-phase CVCF inverters. IEEE Trans Ind Inform 16(4):2168–2176. https://doi.org/10.1109/TII.2019.2891243
15. IEEE Standard 1547-2003 (2003) IEEE standard for interconnecting distributed resources with electric power systems, pp 0_1–16
16. IEEE Standard 519-1992. IEEE guide for harmonic control and reactive compensation of static power converters

Comparative Study of Battery Charging Methods in Electric Vehicles

H. B. Chandana, Vinay Kumar Jadoun, N. S. Jayalakshmi, and Neeraj Kanwar

Abstract Electrical vehicles are one of the major contributions with respect to global energy conservation and in prevention of greenhouse effect. In electric vehicles, battery is one of the important components. Various methods of charging are being introduced. According to the study on this, charging of battery can affect factors like battery life cycle and charging time. This work gives relative study of different battery charging methods of electrical vehicle like constant voltage, constant current, and other intelligent battery charging methods. Various factors that are considered in charging methods such as temperature, battery capacity, and charging time are also studied.

Keywords Electric vehicles · Battery · Charging methods · Temperature · Battery capacity · Charging time

1 Introduction

In recent years, there has been increasing in development of electric vehicle-related studies. Different charging algorithms vary in charging efficiency, charging time, battery life cycles, and cost [1]. All this are significant parameter. It is still cannot be defined which is the most appropriate one for the application, as many algorithms have been developed [2]. Considering the pros and cons of each algorithm, the goal is to match each one with its appropriate application. There are different charging methods: constant voltage, constant current, variation of constant current/constant voltage charging algorithms, multistage current charging, non-contact charging method, battery swap, on-board solar charging [3].

H. B. Chandana · V. K. Jadoun (✉) · N. S. Jayalakshmi
Department of Electrical and Electronics Engineering, Manipal Institute of Technology, Manipal Academy of Higher Education, Manipal, Karnataka 576104, India
e-mail: vjadounmnit@gmail.com

N. Kanwar
Department of Electrical and Electronics Engineering, Manipal University Jaipur, Jaipur 303007, India

S. Dwivedi et al. (eds.), *Flexible Electronics for Electric Vehicles*, Lecture Notes in Electrical Engineering 863, https://doi.org/10.1007/978-981-19-0588-9_59

Constant current is most used method of charging [4]. By varying internal resistance, battery efficiency of constant current charging can be improved [5]. Fast charging can be done using cascaded H-bridge charging for CC/CV charging [6]. Multistage charging methods contain more advantages. Multistage constant current charging can be done [7]. For the optimal charging of multistage, constant current pattern is being developed [8]. Solar energy is renewable source of energy; it is a vast resource. Solar-powered batteries are more economical. In this case, solar module collects the charge and stores the charge in the batteries. This is through charge controller of MPPT [9]. Maximum power extraction from modules can be done using different charging circuits [10].

Transportation has highest importance in our daily life. Because of which, the consumption of fuel is increasing exponentially with increasing population [11]. Thus, ultimately causing adverse effects on the environment. India includes more than four extremely polluted cities [12]. The consumption of fossil fuels like petrol and diesel is increasing in an exponential manner which causing depletion of the same [13]. Thus, electric vehicles are needed to create better environment and future. The efficiency of electric vehicles is four times better than internal combustion engine (ICE) [14]. That is ICE has efficiency of 22–23%, while EVs have 90% [15]. ICEs have 50% more moving parts than EVs which make EVs more reliable and long lasting compared to ICE. The main problem in adapting electric vehicles is the battery [16]. Battery has drawbacks when it comes to weight, volume, and cost. It is a hazardous and highly important when it comes to EVs [17]. The most commonly used battery is Li ion because of its increasing energy density and decreasing in cost from past few years. By increasing energy density, the drawbacks can be reduced [18]. The commonly used materials for battery are nickel, cobalt, graphite, lithium, and manganese. The energy density of petrol is 12,500 Wh/kg, which is 40 times greater than energy density of battery, i.e., 300 Wh/kg [19]. Battery weight is 10 times higher than petrol for every km traveled, and size is 5–6 times higher. To overcome the drawbacks of battery, the efficiency of EVs needs to be improved [20]. It can be improved by improving the motors and controllers, wheels, and other parameters.

The battery life of EVs depends on multiple factors [21]. Increasing life cycle leads to decrease in cost [22]. Performance of degradation in second life batteries is not known [23]. The number of charge and discharge cycle is the key parameter [24]. Li-ion battery is best behaved in 25 °C temperature [25]. Decreasing the temperature minimizes the working of battery, and increasing the temperature causes the battery to deteriorate [26]. This will decrease batteries performance [27]. Depth of discharge or DoD, i.e., operation region of charge and discharge. State of health (SoH) is a measure of capacity of battery remaining as the battery is used [28]. The end of life (EoL) of battery is when the battery capacity reaches to 75–80% of its initial capacity [29]. Battery life depends on charging of battery [30]. Slow charging increases the battery life, while fast charging effects the battery.

In this paper, different battery charging methods are compared. A study on the charging parameters like charging time, charging efficiency, reliability, and cost is carried out.

2 Parameters

2.1 Charging Time

It can be defined as the time required to charge the battery to its full capacity.

$$\text{charging time (h)} = \frac{\text{battery capacity (kWh)}}{\text{charging power (kW)}}$$

2.2 Charging Efficiency

It can be defined as the amount of energy that is discharged by a battery to the amount of energy used to charge the battery considering the losses dissipated. Different batteries have different charging efficiency.

$$\text{charging efficiency} = \frac{\text{amount of energy discharged}}{\text{energy used for charging}}$$

2.3 Reliability

Reliability in case of battery charging method is its ability to limit various parameters under all possible conditions and to give same performance over period of time.

2.4 Cost

The amount of investment is required to adapt a particular charging strategy.

3 Charging Methods

Charging of electric vehicle is a process of high importance. The voltage and current are controlled while charging to have highly effective, efficient, and safe charging. If the charging current is too high, it can damage the battery. Conversely, if it is too low, then it requires more time to charge. There are various methods in charging of a battery; it can be classified into three: conductive charging, inductive charging, and swapping.

3.1 Conductive Charging

It is most common method of charging batteries in electric vehicles. In user point of view, it gives the user the choice of charging the EV at home, at workplace, or at public charging stations. Conductive charging can be AC/DC.

In AC charging, the EV can be charged anywhere with standard electrical outlet. It can easily communicate with the battery management system because of internal wiring network. This leads to higher performance and economically beneficial. But, this is only suitable for the PHEV applications, where the specific energy is low. There is limitation in power output because AC power should be converted into DC power in the vehicles. This takes relatively more charging time. DC charging is usually used for high power designs. The power intake is only limited by the capacity of the battery to intake the energy. Generally, DC is used for fast charging, and it takes less time that is 1 h or less. This requires high investment, and the charging can only be done at the charging stations. The limitations of DC charging are it effects the grid due to the harmonics, and there is restriction on the supply network.

Some of charging methods in conductive charging:

Constant Current Charging

In this type of charging, the current is maintained constant by varying the voltage over a period, until the gassing voltage is reached. This method is safe, but it takes more charging time to complete.

Figure 1 shows the simulation of constant current charging method. A 24 V

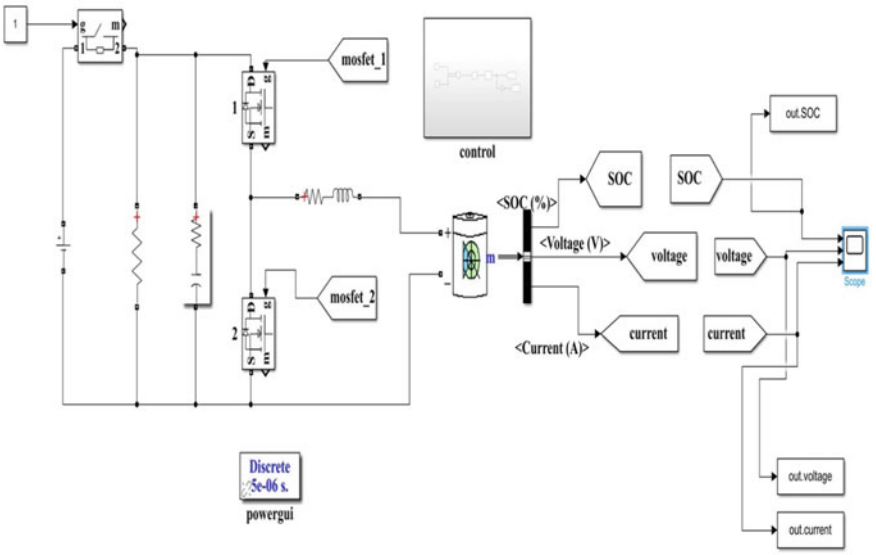

Fig. 1 Simulation of constant current charging

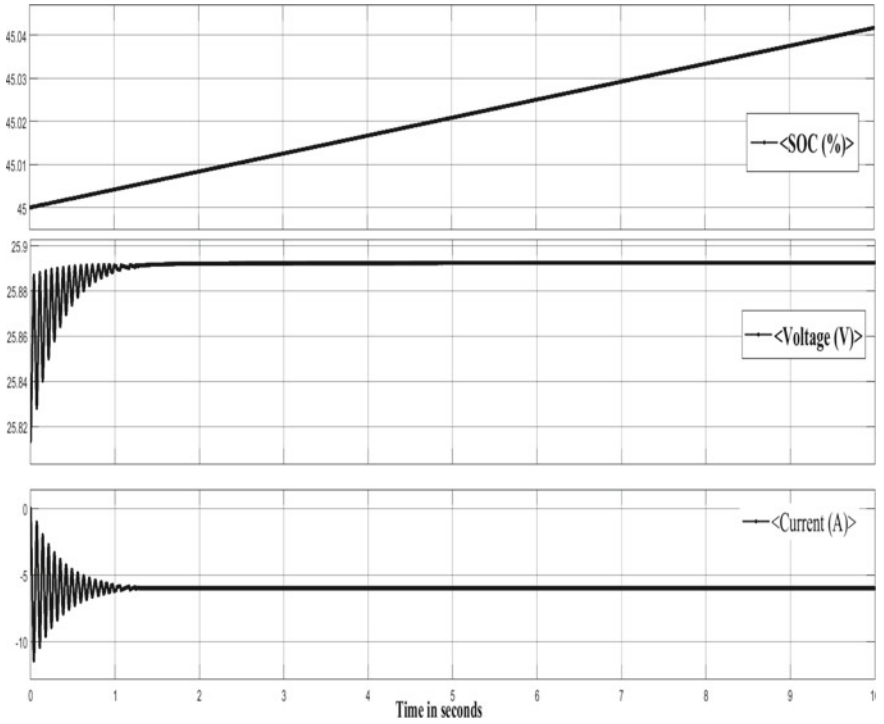

Fig. 2 Waveforms of constant current simulation

nominal voltage is given with a battery of 40% initial SOC. The reference current is taken as −6. The obtained waveforms are shown in Fig. 2.

Constant Voltage Charging

In this method of charging, the voltage is kept constant to charge a battery. This method is not recommended because the high current damages the deeply discharged battery. In a battery with 80% SOC, the current becomes zero as it state of charge increases. A deeply discharged battery requires a high starting current to charge, which causes serious damage to the battery.

Figure 3 shows the simulation of constant voltage charging method. A nominal voltage of 24 V is applied to the battery with 40% initial state of charge. The voltage at 80% SOC is taken as the reference voltage. The waveforms obtained are shown in Fig. 4.

Multi-Step Constant Current Charging

In this method, the battery is charged at maximum allowable charging rate by slowly decreasing the current in steps as the state of charge increases. This method is fast but requires a complex charger. Initially, the voltage is increased up to gassing voltage. By observing the limit of gassing voltage, the voltage being applied to the battery

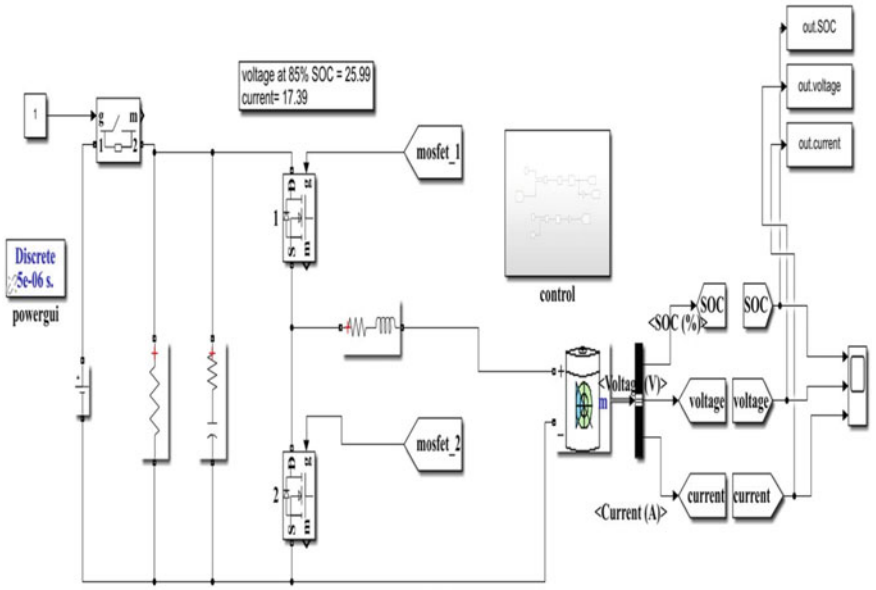

Fig. 3 Simulation of constant voltage

is decreased to its second lowest voltage. This process repeats for every step of charging. This method takes much less charging time.

Modified Constant Voltage

This type of charging contains three stages; first stage is constant current charging stage where charging current is limited to maximum allowable safe current recommended by the manufacturers. This stage requires half time of total charging time. Once the battery reaches the gassing voltage, it shifts to the constant voltage charging stage. Here, the current decreases with the voltage maintained constant near the gassing voltage. When current reaches saturation, it goes to next stage that is floating stage, where a specific voltage is applied to the battery to compensate for the lost charge.

There are various others methods which are listed in Table 1 along with principle and application.

3.2 Inductive Charging

In this type of charging, the energy is transferred to the electric vehicles from the power source by magnetic induction coupling. This is based on electromagnetic induction and high frequency charging. This process contains two coils primary and secondary coil. These two coils are linked electromagnetically. The primary coil is

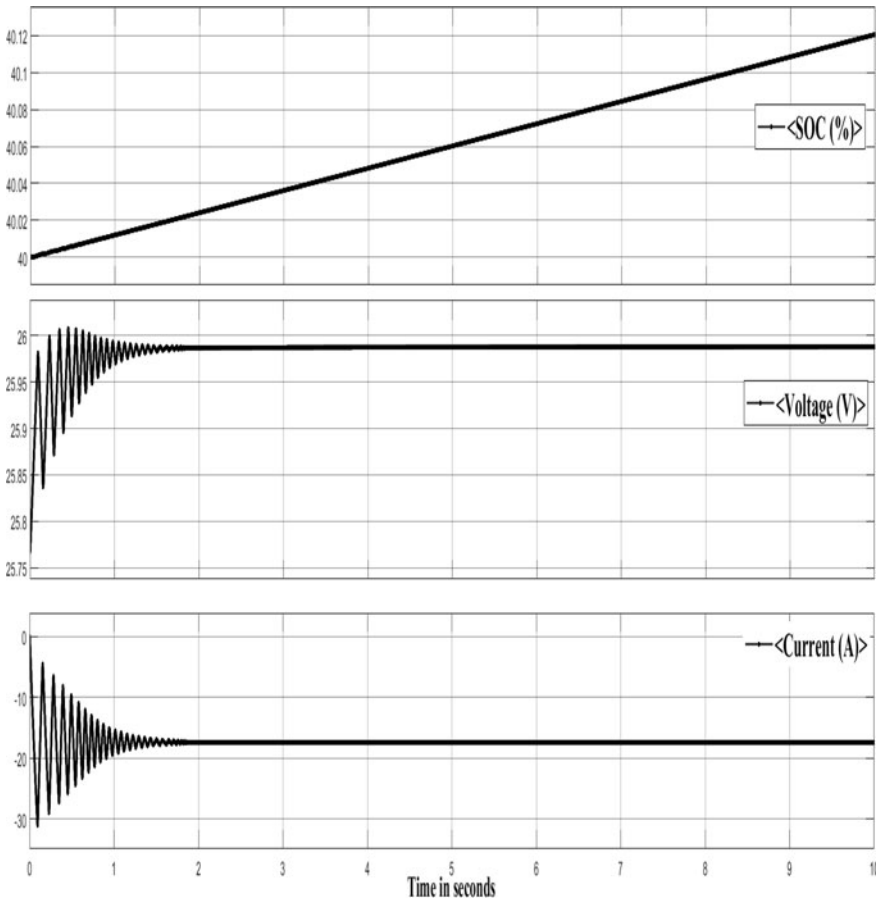

Fig. 4 Waveforms of constant voltage simulation

placed on the rod-like construction linked to the source, and secondary coil is placed at the bottom of the car with a safe distance from the traveler. The AC power is rectified and transferred to the vehicle in the form of high-frequency AC.

Wireless charging is more favorable than the conductive charging because of less cables. It is safe and suitable for all weather conditions. But, there are many disadvantages like high investment, less space, high weight, exposure to radiation, induction losses, and misalignment tolerance.

Dynamic charging can also be used in inductive charging. Here, the vehicle is charged through the coils buried in the road. Electromagnetic field is emitted by the buried coil and picked up by the car riding over them, hence charging the vehicle. This leads to low stand in time for the customers, increase in battery life because of frequent charging, and smaller battery size is enough. Limitations are related to

Table 1 Different charging methods

Charging methods	Principle	Application
Constant voltage	Constant charging voltage, diminishing current	Lead–acid batteries: automobile batteries, backup power lithium-ion cells
Constant current	Variable terminal voltage to remain current constant	Nickel-cadmium and nickel metal hydride cells and batteries
Taper current	Unregulated constant current	SLA (sealed lead–acid) batteries only
Pulse charge	Voltage or current PWM on/rest/on: 1 s/20–30 ms/1 s	Constant current and constant voltage with better stabilization
Negative pulse charge	Additional negative discharging pulses during rest period	Further improvement in stabilization over pulsed voltage
IUI charging	Constant *I*, constant *V*, equalize	Optimizing the charging duration, not suitable for lead–acid batteries
IUO charging	Constant *I*, constant *V*, float	Same
Trickle charging	Compensate for self-discharge, in standby mode	Not suitable for some battery chemistries, e.g., NiMH and lithium
Float charging	Constant voltage below gassing *V*	Mainly used with lead–acid batteries
Random charging	Random bursts of charging	Solar panel, EV braking, etc.

power transfer efficiency and cost. The coil structure may change, and there may be unwanted objects on the road.

3.3 Batter Swapping

It is changing the depleted battery with a fully charged battery in battery switching bay. This method is quite convenient because it is quick and easy process. The depleted batteries are collected and charged for the later uses. This is similar as refilling the tank. To accept this type of charging, batteries need to be standardized for different vehicles; SOH estimation should be done to ensure the battery life each time after swapping, and as high current connection is done between the battery and the vehicle, cutting off the connection for replacing the battery is to be made safer.

4 Conclusion

Batteries are one of the important components in electric vehicles. In this paper, different battery charging methods of electric vehicles are studied. And their advantages and limitations in case of efficiency, charging time, cost, and other parameters are studied.

It can be concluded that constant charging method is safe, but it takes large charging time to complete. Constant voltage method is not recommended because the high current damages the deeply discharged battery. Multistage current charging method takes much less charging time. The wireless charging is more favorable than the conductive charging and is cableless; it is safe and suitable for all weather conditions.

All charging methods cannot be used for the charging of every battery. Every method has its advantages and limitations. Charging methods can be combined to get a more efficient charging method. Swapping is considered has the best method if it can overcome some drawbacks.

References

1. Qarebagh AJ, Sabahi F, Nazarpour D (2019) Optimized scheduling for solving position allocation problem in electric vehicle charging stations
2. Stojkovic J (2019) Multi-objective optimal charging control of electric vehicles in PV charging station
3. Li H, Wen L, Chen W, Gong X, Zeng X (2018) The rapid and coordinated charging strategy for private electric vehicles
4. Ahn J-H, Lee BK (2018) High efficiency adaptive-current charging strategy for electric-vehicles considering variation of internal resistance of lithium-ion battery
5. Moeini A, Wang S (2018) Design of fast charging technique for electrical vehicle charging stations with grid-tied cascaded H-bridge multilevel converter
6. Thomson SJ, Thomas P, Anjali R, Rajan E (2018) Design and prototype modelling of a CC/CV electric vehicle battery charging circuit
7. Zhu X, Han H, Gao S, Shi Q, Cui H, Zu G (2018) A multi-stage optimization approach for active distribution network scheduling considering coordinated electrical vehicle charging strategy
8. Khan AB, Choi W (2018) Optimal charge pattern for the high performance multi-stage constant current charge method for the Li-ion batteries
9. Sahu D, Srinivasa Rao Nayak P (2020) Design and analysis of solar e-rickshaw charging system
10. Premchand M, Gudey SK (2020) Solar based electric vehicle charging circuit in G2V and V2G modes of operation
11. Typaldos P, Papamichail I, Papageorgiou M (2020) Minimization of fuel consumption for vehicle trajectories
12. Amin AB, Patel HP, Vaghela SP, Patel RR (2019) IOT based vehicle anti-collision and pollution control system
13. Fathabadi H (2018) Internal combustion engine vehicles: converting the waste heat of the engine into electric energy to be stored in the battery
14. Ferraz V, Tavares J, Llerena-Pizarro O, Silveira J (2019) Internal combustion engine fueled with biogas: energetic, economic and environmental analyses
15. Wang C, Liang M, Chai Y (2019) Finite-time identification algorithm for volumetric efficiency map in SI gasoline engines

16. Rebai M, Kelouwani S, Dubé Y, Agbossou K (2018) Low-emission maximum-efficiency tracking of an intelligent bi-fuel hydrogen-gasoline generator for HEV applications
17. Fathabadi H (2018) Plug-in hybrid electric vehicles (PHEVs): replacing internal combustion engine with clean and renewable energy based auxiliary power sources
18. Santos G, Grandinetti F, Alves R, Lamas W (2020) Design and simulation of an energy storage system with batteries lead acid and lithium-ion for an electric vehicle: battery vs. conduction cycle efficiency analysis
19. Xu Q, Wang F, Zhang X, Cui S (2019) Research on the efficiency optimization control of the regenerative braking system of hybrid electrical vehicle based on electrical variable transmission
20. Grunditz EA, Thiringer T, Saadat N (2020) Acceleration, drive cycle efficiency, and cost tradeoffs for scaled electric vehicle drive system
21. Gharibeh HF, Khiavi LM, Farrokhifar M (2019) Life cycle cost analysis of electric vehicles based on critical price and critical distance
22. Bai Y, Li J, He H, Dos Santos RC, Yang Q (2020) Optimal design of a hybrid energy storage system in a plug-in hybrid electric vehicle for battery lifetime improvement
23. Martinez-Laserna E, Sarasketa-Zabala E, Villarreal I, Stroe D-I, Swierczynski M, Warnecke A (2018) Technical viability of battery second life: a study from the ageing perspective
24. Shen D, Xu T, Wu L, Guan Y (2019) Research on degradation modeling and life prediction method of lithium-ion battery in dynamic environment
25. Ali H, Khan HA, Pecht MG (2020) Evaluation of Li-based battery current, voltage, and temperature profiles for in-service mobile phones
26. Hussein AA, Pise A, Chen X, Batarseh I (2018) Enhancement of Li-ion battery performance at low temperatures by DC-DC converter duty-cycle autotuning
27. Xintian L, Guojian Z, Yao H, Bo D (2018) Research on the capacity fading characteristics of a Li-ion battery based on an equivalent thermal model
28. Xiang M, He Y, Zhang H, Zhang C, Wang L, Wang C, Sui C (2020) State-of-health prognosis for lithium-ion batteries considering the limitations in measurements via maximal information entropy and collective sparse variational Gaussian process
29. El Mejdoubi A, Chaoui H, Gualous H, Van Den Bossche P, Omar N, Van Mierlo J (2018) Lithium-ion batteries health prognosis considering aging conditions
30. Qaisar SM (2020) Li-ion battery SoH estimation based on the event-driven sampling of cell voltage

Inductive Power Transfer Modelling for Wireless Charging of Electric Vehicles

C. S. Arpitha, Vinay Kumar Jadoun, N. S. Jayalakshmi, and Neeraj Kanwar

Abstract Increase in the emission of greenhouse gases and depletion of fossil fuels paved the way for developing a more appropriate transportation. Electric vehicle is one such electrified transportation which helps to overcome these problems. Since the market for electric vehicles is growing rapidly, it is important to overcome the drawbacks associated with it. Therefore, the wireless charging methods were developed replacing fossil fuels. This automatically reduces the cost of the batteries and weight and also reduces the environmental pollution. Hence, this work mainly concentrates on designing of a static wireless electric vehicle charging system. It works on inductive power transfer method using cascaded H-bridge multilevel inverter along with dual LC compensation network. The effectiveness of the system is determined through simulation using MATLAB/Simulink.

Keywords Electric vehicles (EVs) · Wireless charging system (WCS) · Inductive power transfer

1 Introduction

For many years, the vehicles are being electrified for conservation of environment, preserving energy resources and so on. With the increase in population, use of automobiles are also increased [1]. This automatically resulted in increasing the demand for electrified vehicles such as electric vehicles, plug-in vehicles, and so on [2]. Since for the past few years, electric vehicles have gained wide popularity as they require less maintenance, reduces the overall weight and replacing the need for fossil fuels [3]. Adoption of electric vehicles is associated with some disadvantages like

C. S. Arpitha · V. K. Jadoun (✉) · N. S. Jayalakshmi
Department of Electrical and Electronics Engineering, Manipal Institute of Technology, Manipal Academy of Higher Education, Manipal, Karnataka 576104, India
e-mail: vjadounmnit@gmail.com

N. Kanwar
Department of Electrical Engineering, Manipal University Jaipur, Jaipur 303007, India

S. Dwivedi et al. (eds.), *Flexible Electronics for Electric Vehicles*, Lecture Notes in Electrical Engineering 863, https://doi.org/10.1007/978-981-19-0588-9_60

longer charging time, higher cost and so on [4]. Hence, the charging of electric vehicles associated with cables/wires were replaced by wireless charging medium. The wireless charging of electric vehicles takes place by transferring the energy through electromagnetic waves [5]. But here, the increase of distance results in the decrease of electromagnetic field strength [6]. Wireless charging systems are flexible, are capable of fully automated charging and convenient [7]. The wireless charging of electric vehicles is possible in two ways, viz static and dynamic [8]. These wireless charging systems are easily accessible due to their architecture, their strategies for maintaining safety and so on [9].

Many wireless charging methods are available for charging of electric vehicles, viz capacitive power transfer, magnetic gear wireless power transfer, inductive power transfer, and resonance inductive power transfer [10]. Inductive and capacitive power transfer actions can be combined to form a hybrid power transfer system [11]. Inductive wireless power transfer is one of the oldest power transfer techniques that is being used [12]. It was discovered by Tesla in 1914. Inductive power transfer systems are appropriate for all kinds of situations as they are not affected by the environmental conditions [13]. In inductive power transfer technique, the primary and secondary side coils must be in close range of one another to make the system more efficient [14]. There are few compensation techniques [15] to improve the performance of the system which operates on inductive power transfer techniques such as series–series (SS), series–parallel (SP), parallel–series (PS), parallel–parallel (PP) and many more [16]. Even some of the topologies give more efficiency than the given techniques [17]. The performances can be compared to get the more suitable topology [18]. The characteristics of this WCS can be examined using magnetic coupling theory [19].

AC/DC rectifier is nothing but a bridge rectifier which converts alternating current to direct current [20]. This direct current is of high frequency [21]. A capacitor of large value can be used to reduce the ripple of the DC voltage obtained [22]. However, the efficiency can be affected if the diode switches are used [23]. H-Bridge multilevel inverters are more attracted these days due to increase in the use of power electronic devices [24]. These multilevel inverters have some advantages over the normally available inverters such as many voltage level generations are possible, higher efficiency, and so on [25]. The main aim of this inverter is to produce required AC level output voltage from the DC input voltage [26]. The input voltage can be a single source or multisource [27]. In case of breakdown of any one of the power grids [28], the other grid operates normal to provide required DC input through AC/DC rectifier system [29].

This paper mainly concentrates on designing and developing a model for charging of electric vehicles wirelessly. The compensation topology considered in this system is series–series (SS). Here specifically, a cascaded H-bridge multilevel inverter [30] is considered for DC to AC conversion. The proposed model is simulated using MATLAB/Simulink. The output voltage, current and power waveforms are analysed.

2 Modelling of Wireless Charging System

Any wireless charging system normally consists of two sections/sides, viz transmission side and receiver side. In this model, the transmission side consists of AC/DC Rectifier and cascaded H-bridge inverter, whereas receiver side consists of AC/DC rectifier only. Since the receiver section is to installed in electric vehicle, it should weigh less. The transmission section can be installed in any charging compatible areas such as parking lots, petrol bunks and garages. The system should operate in the frequency of resonance due to which the receiver side can withdraw maximum power from the transmission side.

Figure 1 shows the circuit diagram for the proposed wireless charging system. The capacitors C_p and C_s are used in order to obtain the required condition for resonance. These capacitors can also remunerate the losses in the primary and secondary sides.

According to the principle of magnetic coupling [24–26], the resonant frequency ω_0 between the two coils can be given as follows;

$$\omega_0 = \frac{1}{\sqrt{L_p C_p}} = \frac{1}{\sqrt{L_s C_s}} \tag{1}$$

where L_p and L_s are the self-inductances of primary and secondary coil, respectively.

C_p and C_s are primary and secondary side capacitances. In this model, $C_p = C_s$ and $L_p = L_s$. 'M' is the mutual inductance between the primary and secondary inductance.

The magnetic coupling coefficient between the two coils can be given as

$$k = \frac{M}{\sqrt{L_p L_s}} \tag{2}$$

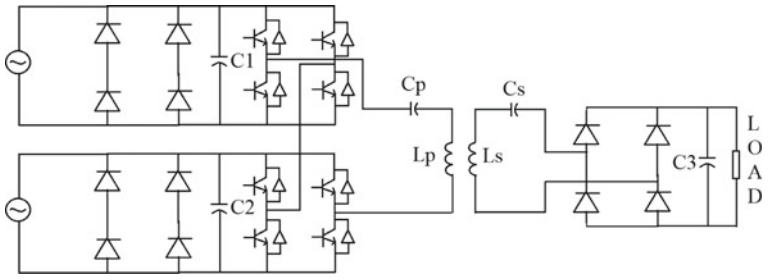

Fig. 1 Circuit diagram of the inductive WCS

3 Simulation and Results

The circuit diagram shown in Fig. 1 is simulated in MATLAB/Simulink whose simulation model is shown in Fig. 2.

This model consists of AC/DC rectifier and DC/AC inverter subsystems which are shown in Figs. 3 and 4. For a load of 100 Ω connected across the capacitor C_3, the output voltage, current and power waveforms are observed.

In Fig. 2, there are two AC/DC rectifiers in the transmission side as two supplies are taken from the grid.

The supplies from the grid are rectified by the rectifiers, and the rectified power is given to the inverter. Here, a cascaded H-bridge multilevel inverter is used. It is formed using MOSFETs.

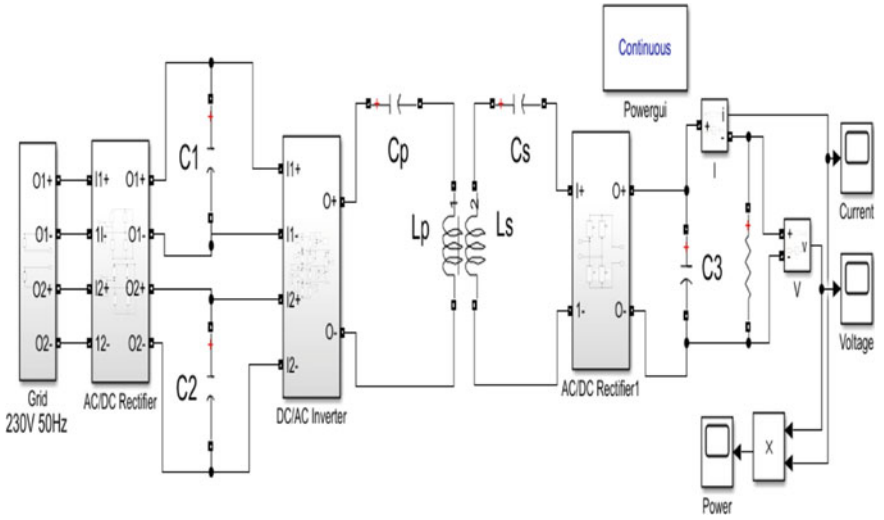

Fig. 2 Simulink model of the system

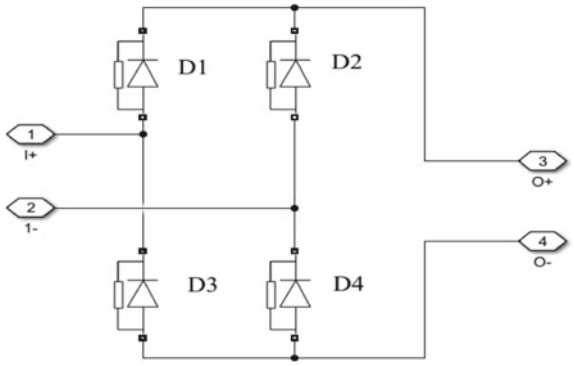

Fig. 3 AD/DC rectifier subsystem

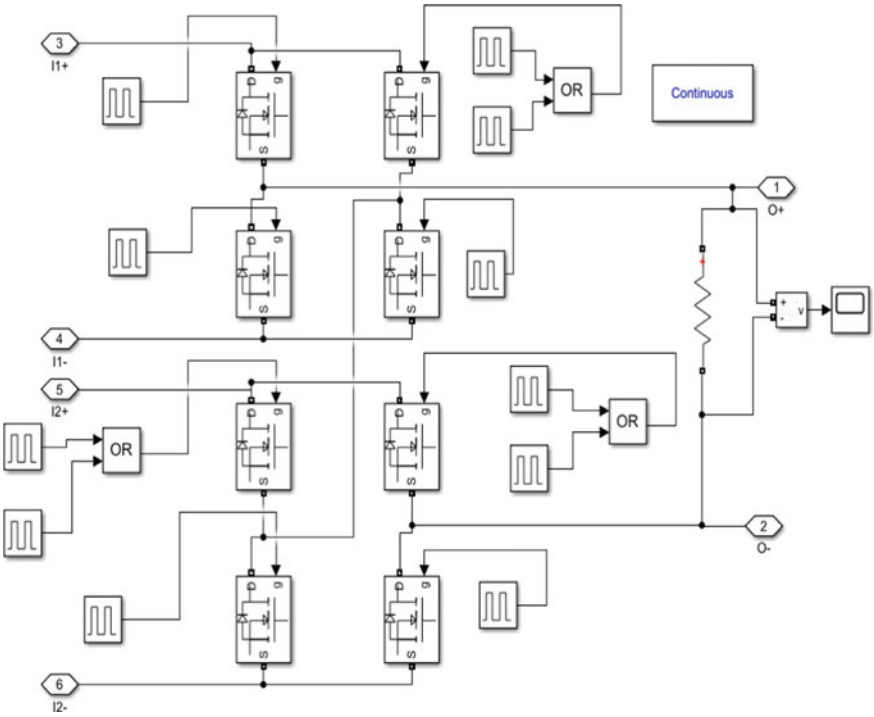

Fig. 4 Cascaded H-bridge multilevel inverter subsystem

MOSFETs which can be observed in Fig. 4. A resistive load is connected across the cascaded inverter system to obtain the required output. Then the inverted output is again given to the AC/DC rectifier in the receiver side through LC compensation network. Here, the rectifier rectifies the inverted input. Then output (voltage, current and power) is measured across the resistor of 100 Ω which is connected across the capacitor C_3.

Figure 5 shows the output voltage waveform of the cascaded H-bridge multilevel inverter with different gate pulses at eight different MOSFETs. The switching sequence of the all the switches and simulation parameters are given in Tables 1 and 2, respectively.

From Fig. 6, it can be observed that the output voltage is initially high and later settle at constant voltage. Similarly, the output current and power are also initially high as can be observed from Figs. 7 and 8, respectively.

By observing the output waveforms, it is understood that the waveforms are not completely smooth. In order to obtain a complete smooth waveform, a buck converter can be implemented in the system. However, this converter reduces the obtained output power.

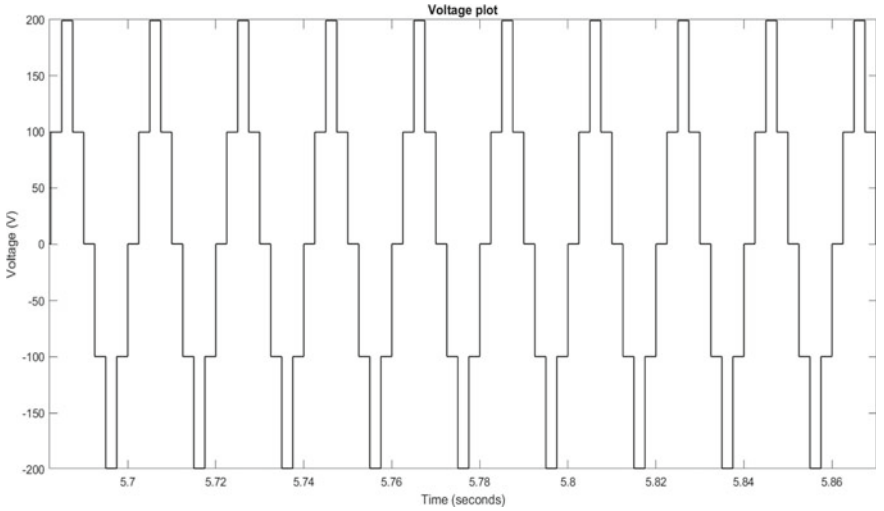

Fig. 5 Output voltage of the cascaded H-bridge multilevel inverter for an input of 100 V DC

Table 1 Switching sequence of cascaded H-bridge multilevel inverter

	0	V	2 V	V	0	−V	−2 V	−V
$S1$	1	1	1	1	1	0	0	0
$S2$	1	0	0	0	1	1	1	1
$S3$	0	0	0	0	0	1	1	1
$S4$	0	1	1	1	0	0	0	0
$S5$	1	1	1	1	1	1	0	1
$S6$	1	1	0	1	1	1	1	1
$S7$	0	0	0	0	0	0	1	0
$S8$	0	0	1	0	0	0	0	0

Table 2 Simulation parameters

Parameters	Design values
Input voltage	230 V
Frequency	50 Hz
C_1	1000 μF
C_2	1000 μF
C_3	1000 μF
C_P	5 mF
C_s	5 mF
L_P	15 mH
L_s	15 mH
M	7.5 mH

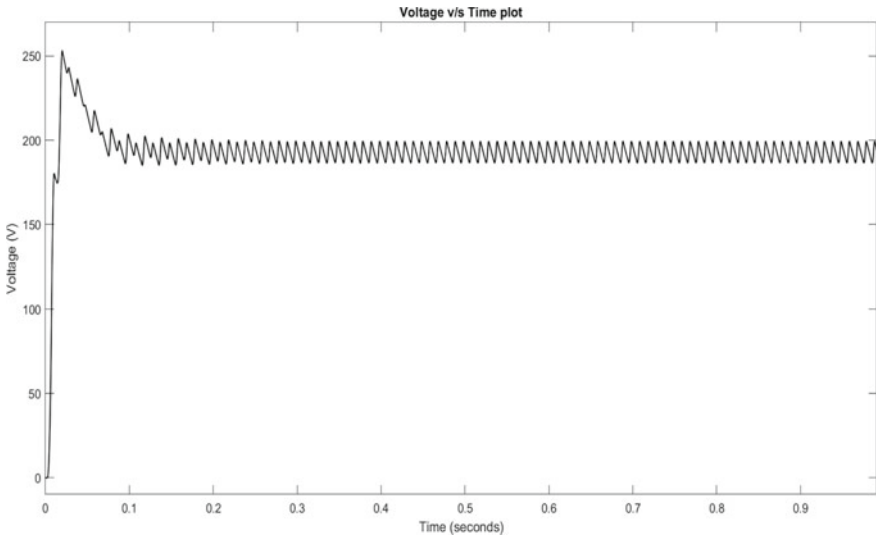

Fig. 6 Output voltage of the proposed wireless charging system

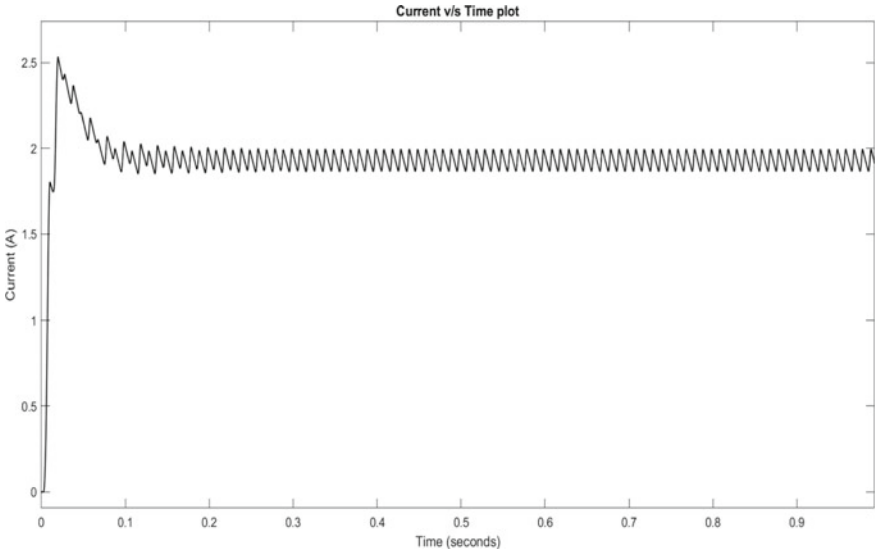

Fig. 7 Output current of the proposed WCS

4 Conclusion

In this paper, a wireless charging system using inductive power transfer is designed and its effectiveness is determined through simulation using MATLAB/Simulink.

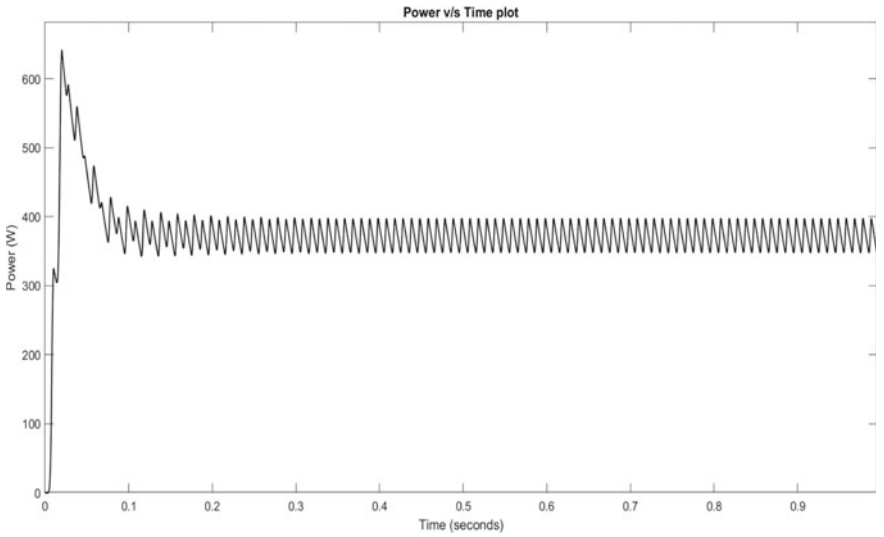

Fig. 8 Output power of the proposed WCS

The procedure carried out for simulation has been explained briefly, and the output waveforms under loaded condition are observed. This proposed model may have many disadvantages. Further research is required for reducing the power loss, cost, distortion in the waveforms and so on.

References

1. Ajith MA (2019) Switched amplifier resonant inductive wireless charging setup for electric vehicles. In: IEEE second international conference on smart systems and inventive technology, pp 1051–1055
2. Regensburger B (2018) High-performance 13.56 MHz large air-gap capacitive wireless power transfer system for electric vehicle charging. In: IEEE 19th workshop on control and modeling for power electronics. Italy
3. Li J (2019) Electromagnetic induction position sensor applied to anti-misalignment wireless charging for UAVs. IEEE Sens J
4. Jian H-S (2018) Adaptive wireless power charging system. In: 13th IEEE conference on industrial electronics and applications (ICIEA)
5. Ouyang H (2020) Development of wireless charging system with improved energy efficiency for electric vehicles. In: IECON 2020 the 46th annual conference of the IEEE Industrial Electronics Society. IEEE
6. Al-Saadi M (2019) Analysis and comparison of resonance topologies in 6.6 kW inductive wireless charging for electric vehicles batteries. Proc Manuf 32:426–433
7. Debbou M (2016) Inductive wireless power transfer for electric vehicle dynamic charging. In: IEEE PELS workshop on emerging technologies: wireless power transfer (WoW), USA, pp 118–122
8. Niculae D (2019) A review of electric vehicles charging technologies stationary and dynamic. In: IEEE 11th international symposium on advanced topics in electrical engineering, Romania

9. Zhang B (2019) Challenges of future high power wireless power transfer for light-duty electric vehicles—technology and risk management. J eTransportation 2
10. Chirag Panchal F (2018) Review of static and dynamic wireless electric vehicle charging system. Eng Sci Technol Int J 21:922–937
11. Zhang X (2018) Influence of misalignment of electric vehicle wireless charging system coupling structure on magnetic field distribution. In: IEEE 2nd international electrical and energy conference, China, pp 553–556
12. Mohamed N (2018) Wireless charging system for a mobile hybrid electric vehicle. In: IEEE international symposium on advanced electrical and communication technologies (ISAECT)
13. Vincent D (2019) A novel three leg inverter for high power hybrid inductive and capacitive wireless power transfer system. In: 45th annual conference of the IEEE Industrial Electronics Society, pp 1544–1548
14. Adel El-Shahat F (2019) Electric vehicles wireless power transfer state-of-the-art. Energy Proc 162:24–37
15. Baroi S (2017) Design and simulation of a wireless charging system for electric vehicles. In: IEEE, 2nd international conference on electrical & electronic engineering, Bangladesh
16. Ayisire E (2018) Magnetic resonance coupling modelling for electric vehicles wireless charging. In: IEEE global humanitarian technology conference, USA
17. Nguyen VT (2017) Optimizing compensation topologies for inductive power transfer at different mutual inductances. In: IEEE PELS workshop on emerging technologies: wireless power transfer (WoW), pp 153–156
18. Chen Y (2019) A comparative study of S–S and LCC-S compensation topology of inductive power transfer systems for EV chargers. In: IEEE 10th international symposium on power electronics for distributed generation systems (PEDG), pp 99–104
19. Shi L (2020) Design and experiment of a reconfigurable magnetic resonance coupling wireless power transmission system. IEEE Microw Wirel Compon Lett
20. Song K (2018) Magnetic coupled resonant wireless power transfer system characteristics with orientation. In: IEEE eighth international conference on instrumentation and measurement, computer, communication and control, pp 1749–1752
21. Gal-Katziri M (2019) Analysis and design of coupled inductive bridges for magnetic sensing applications. IEEE J Solid-State Circ
22. Garinto D (2019) Three-phase AC–DC converter with asymmetrical Vienna rectifier. In: IEEE conference on energy conversion (CENCON), pp 177–181
23. Alam MD (2018) Flyback AC–DC rectifier with active power factor correction. In: IEEE 10th international conference on electrical and computer engineering
24. Rasoulinezhad R (2018) An interleaved AC–DC ZCS-PWM boost rectifier. In: IEEE international telecommunications energy conference
25. Jang Y (2018) A two-switch, isolated, three-phase AC–DC converter. IEEE Trans Power Electron
26. Yarlagadda AK (2018) A modified seven level cascaded H bridge inverter. In: 5th IEEE Uttar Pradesh section international conference on electrical, electronics and computer engineering (UPCON)
27. Aalami M (2018) Design of a new combined cascaded multilevel inverter based on developed H-bridge with reduced number of IGBTs and and DC voltage sources. In: IEEE 12th international conference on compatibility, power electronics and power engineering
28. Chakraborty TK (2018) Generation of 13-level output voltage from single phase multilevel inverter consisting of cascaded three H-bridge units. In: 2nd IEEE international conference on power electronics, intelligent control and energy systems, pp 361–364
29. Maurya S (2019) An efficient technique to reduce total harmonics distortion in cascaded H-bridge multilevel inverter. In: IEEE international conference on electrical, computer and communication technologies (ICECCT)
30. Gu L (2019) A single-stage isolated three-phase bidirectional AC/DC converter for high power applications. In: IEEE energy conversion congress and exposition (ECCE), pp 2850–2855

Wine Quality Prediction Based on Machine Learning Techniques

Yogesh Gupta and Amit Saraswat

Abstract Nowadays, it is extremely difficult to choose wines as there are numerous wine manufacturers. In response to the increase in customer base of wine, wine companies need to improve their quality and sales. There have been many attempts to develop a methodological approach for assessment of wine quality. In this paper, machine learning methods such as decision tree, random forest and support vector are used to check the quality of two types of wine: red and white. This work takes into account various ingredients of wine to predict its quality. The experiments show the superiority of random forest over decision tree and support vector classifiers.

Keywords Red wine · White wine · Decision tree · Random forest · Support vector

1 Introduction

Nowadays, all the industries are improving the quality of their products due to the huge competition in market. They use various technologies to enhance the production and to smooth the whole process. But, it becomes more expensive due to the increase in demands of product. This work explores the role of machine learning techniques to check the quality of wine. It is extremely difficult to choose wines as there are numerous wine manufacturers. In response to the increase in customer base of wine, wine companies need to improve their quality and sales. We have developed a method that considers various ingredients of wine to predict its quality using decision tree, random forest and support vector classifiers. We predict wine quality on a scale of 0–10. The main reason behind this is that the traditional methods involved in wine quality prediction are extremely time consuming and do not give a good accuracy;

Y. Gupta
Department of Computer Science, BML Munjal University, Gurugram, India
e-mail: yogesh.gupta@bmu.edu.in

A. Saraswat (✉)
Department of Electrical Engineering, Manipal University Jaipur, Jaipur, Rajasthan, India
e-mail: amit.saraswat@jaipur.manipal.edu

S. Dwivedi et al. (eds.), *Flexible Electronics for Electric Vehicles*, Lecture Notes in Electrical Engineering 863, https://doi.org/10.1007/978-981-19-0588-9_61

hence, there have been several attempts at reducing time and improving the accuracy. However, a trained and experienced wine quality tester (human) would provide better results but that is time consuming and costly.

In recent years, ingesting of wine has increased basically because it makes a positive impact on our health as it helps in keeping our heart rate in check. Consumption of wine in small amounts can prevent us from strokes. Increased consumption of wine has resulted in companies going for quality assessment tests. The main objective of this work is to forecast the wine quality taking some features as inputs. Higher the score out of 10, better is the quality. There are 12 input variables in total and one output, i.e. quality of wine.

The paper is planned as follows: Sect. 2 presents the existing work related to wine quality prediction. Section 3 discusses the methodology in detail. Experimental results and analysis are done in Sect. 4. At the last, conclusion and future directions are drawn in Sect. 5.

2 Related Work

There have been few works present in literature based on machine learning to predict wine quality. The main reason is that the traditional methods involved in wine quality prediction are extremely time consuming and do not give a good accuracy; hence, there have been several attempts at reducing time and improving the accuracy. After back propagation algorithm came into existence in 1974 [1], neural networks became very popular. Recently, support vector machine is introduced [2, 3], and it is gaining more attention nowadays. *SVM* and neural network are used in predictions due to their flexibility and learning capabilities. But, model selection and variable selection are the critical issues in applying these machine learning techniques. The selection of suitable variable [4] plays an important role not only in discarding irrelevant inputs, but it leads to a simpler model also. This simpler model can be easily interpreted and gives better performance. Although a simpler model has limited learning capabilities, complex models may over-fit the data.

Cortez et al. [5] assessed the wine quality using a regression approach which preserved the order of grades. Sensitivity analysis was given as knowledge to measure changes in response for variations in input variable. Moreover, Cortez et al. considered all features to predict wine quality. Cortez et al. [6] proposed an approach for predicting wine taste preferences of human being. They used three machine learning techniques: support vector machine, neural network and regression. Yin et al. [7] used soft measurement based on multivariate methods to evaluate wine quality. They included principal component regression, partial least squares regression, ordinary least squares regression and modified partial least squares regression in their approach. Ribeiro et al. [8] presented a model to predict organoleptic parameters from chemical parameters of the vinification process using machine learning techniques.

Gupta [9] developed neural network and support vector machine and evaluated the performances on wine data sets. Malik [10] proposed a prediction method based on the reviews of the customers. They created a database based on that information collected from reviewers. Further, they identified the parameters to perform classification based on that information. Pawar et al. [11] predicted the wine quality using regression and support vector classifiers. Reddy and Govindarajulu [12] presented a new prediction model for wine quality based on a centric clustering approach. They used red wine data set for performing classification. Further, they assigned different weights to all attributes using Gaussian distribution process. The obtained results were satisfactory.

3 Methodology

In this work, white and red wine data sets [13] are used containing a total of 6497 records. The data includes values of 12 input variables and one output variable quality (on a scale of 1–10).

Figure 1 shows the processes adopted in methodology. First the collected data is pre-processed. Data pre-processing includes two different stages: data cleaning and data transformation. In data cleaning process, missing data and noisy data are handled, whereas normalization is done in data transformation process. Subsequently, some of the important features are selected. Further, the quality of wine is predicted, and accuracy is computed for all developed models.

In this work, decision tree, random forest and support vector classifiers are used. These classifiers are supervised learning algorithm and use labelled data. Decision tree is a tool which is used in determining what result will be obtained if a certain decision is made. Each decision will lead to another set of options and the option we choose will determine what result we will obtain. An example where the logic of decision trees can be seen in coding would be if–else, switch statements. In a decision tree, classification is based on different procedures such as recursive binary splitting and then identifying the cost of a split.

Random forest classifier is an extension of the decision tree. Every single decision tree would be producing a class prediction. The idea which governs the working of

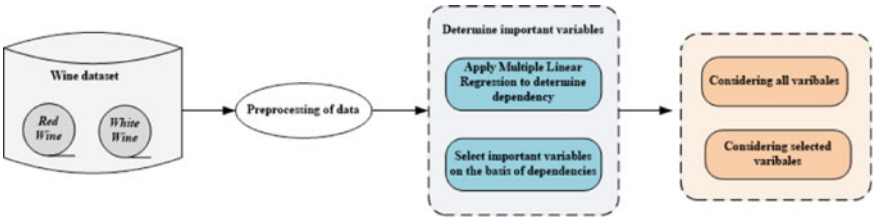

Fig. 1 Block diagram of used methodology

a random forest classifier is that if a large number of uncorrelated models start operating as a committee, then it would always outperform any of the individual constituent models. Support vector classifier is used to classify different classes of data points in any data set. The objective of support vector is to find a hyperplane on an N-dimensional space. The hyperplane should have a maximum margin, so we can easily classify additional data which we might add in our data at some point of time in future with convenience.

4 Result Analysis and Discussion

The performances of used algorithms are evaluated in terms of accuracy at certain error tolerances (ACC_t) and mean absolute deviation (*MAD*). First, data is divided into test and training data. In this work, 20% of the data is used as testing data. After that, normalization is performed on data as algorithms may perform poorly if individual inputs, i.e. features do not look like normally distributed. Normalization fits the values in a specific range. Further, decision tree, random forest and support vector classifier are applied and obtained accuracy and MAD values as given in Tables 1 and 2 for both types of wine.

Table 1 summarizes the values of *MAD* and ACC_t for *decision tree, random forest* and *support vector* in case of red wine data set. It is clear from this table that *random forest* outperforms other algorithms. Similarly, Table 2 presents the results of both the metrics *MAD and* ACC_t for white wine data set. This table clearly shows that

Table 1 Performance of red wine quality prediction models. Estimation metrics include (ACC_t) and (*MAD*)

	Decision tree	Random forest	Support vector machine
MAD	0.537	0.513	0.583
$ACC_t = 0.25$	0.286	0.302	0.206
$ACC_t = 0.50$	0.363	0.481	0.317
$ACC_t = 1.0$	0.525	0.677	0.489
$ACC_t = 2.0$	0.682	0.769	0.615

Table 2 Performance of white wine quality prediction models. Estimation metrics include (ACC_t) and (*MAD*)

	Decision tree	Random forest	Support vector machine
MAD	0.583	0.571	0.618
$ACC_t = 0.25$	0.237	0.275	0.196
$ACC_t = 0.50$	0.428	0.491	0.386
$ACC_t = 1.0$	0.549	0.657	0.512
$ACC_t = 2.0$	0.688	0.778	0.635

random forest outperforms decision tree and support vector with higher accuracy at low error tolerance values and less mean absolute deviation.

5 Conclusions and Future Work

In the last few years, the usage of machine learning has been increased in wine industry for quality prediction. In this direction, wine quality certification plays a very important role. This paper explores the usage of three different types of machine learning techniques to predict the quality. The experiments show the superiority of random forest over decision tree and support vector classifiers. The reason of this superiority of random forest is the differences in training phases. The training in random forest always guarantees an optimum fit the data. In future, large data set can be taken for experiments, and other machine learning techniques may be explored.

References

1. Werbos P (1974) Beyond regression: new tools for prediction and analysis in the behavioral sciences. PhD thesis, Harvard University, Cambridge, MA
2. Boser B, Guyon I, Vapnik V (1992) A training algorithm for optimal margin classifiers. In: Proceedings of the fifth annual workshop on computational learning theory, pp 144–152
3. Smola A, Schölkopf B (2004) A tutorial on support vector regression. Stat Comput 14:199–222
4. Guyon I, Elisseeff A (2003) An introduction to variable and feature selection. J Mach Learn Res 3(7):1157–1182
5. Cortez P, Teixeira J, Cerdeira A, Almeida F, Matos T, Reis J (2009) Using data mining for wine quality assessment. In: Proceeding of international conference of discovery science. Lecture notes on artificial intelligence, pp 66–79
6. Cortez P, Cerdeira A, Almeida F, Matos T, Reis J (2009) Modeling wine preferences by data mining from physicochemical properties. Decis Support Syst 47:547–553
7. Yin S, Liu L, Gao X, Karimi H (2014) Multivariate methods based soft measurement for wine quality evaluation. Abstr Appl Anal 2014:1–7
8. Ribeiro J, Neves J, Sanchez J, Delgado M, Machado J, Novais P (2009) Wine vinification prediction using data mining tools. Comput Comput Intell 78–85
9. Gupta Y (2018) Selection of important features and predicting wine quality using machine learning techniques. Proc Comput Sci 125:305–312
10. Malik MSI (2020) Predicting users' review helpfulness: the role of significant review and reviewer characteristics. Soft Comput 24:13913–13928
11. Pawar D, Mahajan A, Boithe S (2019) Wine quality prediction using machine learning. Int J Comput Appl Technol Res 8(9):385–388
12. Reddy YS, Govindarajulu P (2017) An efficient user centric clustering approach for product recommendation based on majority voting: a case study on wine data set. Int J Comput Sci Netw Secur 17(10):103–111
13. https://archive.ics.uci.edu/ml/machine-learning-databases/wine/

Microgrid Energy Management Using Electric Vehicles

Kiran Chaurasia and H. Ravishankar Kamath

Abstract The increasing angst to reduce global pollution and to meet the generated energy demand of the increasing global population has encouraged nations to explore opportunities present in clean energy sources. This increased concern for environmental awareness has revived the inclination to develop renewable energy power generation strategies and to utilize potential present in electric vehicles. The issues present in renewable energy power generation: intermittent nature, distributed generation, lack of effective energy storage system is a concern. Similarly, electric vehicles which are predicted as the major player in upcoming vehicle market sales need an effective charging network to support their energy demand. For the present traditional grid to meet the electric vehicle's energy demand and to sustain synchronization during peak demands can be a challenge. Are there possibilities that these two problems, have one common solution? Microgrids can be the answer. But how? With this intent, the present review covers the opportunities, challenges, and latest applied energy management strategies for a renewable energy integrated microgrid assisted with electric vehicles.

Keywords Microgrid · Renewable energy · Energy scheduling · Electric vehicles · Energy management

1 Introduction

To combat harmful carbon emissions, electric vehicles (EVs) can be a beneficial alternative. The automobile industry is alternating its focus on electric vehicle markets. However, large integration of EV with the traditional grid poses technical challenges: increased energy demand, low power quality due to induced harmonics,

K. Chaurasia (✉)
Department of Electrical Engineering, Manipal University Jaipur, Jaipur, Rajasthan 303007, India
e-mail: kiranchaurasia314@gmail.com

H. Ravishankar Kamath
SEEC, Manipal University Jaipur, Jaipur, Rajathan 303007, India
e-mail: ravi.kamath@jaipur.manipal.edu

S. Dwivedi et al. (eds.), *Flexible Electronics for Electric Vehicles*, Lecture Notes in Electrical Engineering 863, https://doi.org/10.1007/978-981-19-0588-9_62

voltage disturbances, etc. EVs can be an asset to renewable energy microgrid [1–3]. Therefore effective energy coordination between renewable energy and EVs is a research challenge. Typical microgrid (MG) aids in the integration of different types of EVs, supports the inclusion of multiple distributed energy sources (DERs), reduced carbon emission, minimizes line losses, encourages consumer participation, supports the prosumer concept, enables energy market participation. Based on their operational characteristics: a microgrid can be grid-connected, can be a part of a networked grid, or in isolated mode. A microgrid needs an energy management system to maximize its benefits [4, 5]. Several research papers have proposed approaches to maximize the energy management system of microgrids. The literature review examined observed energy management strategies, regulation, techniques, and control methods being proposed to maximize energy utilization and increase reliability. The following section is divided as follows: The challenges of EVs-assisted renewable energy microgrids are discussed in Sect. 2. Section 3 outlines a review of strategies carried for energy management of electric vehicle-assisted renewable energy microgrids. The conclusion of the paper is sketched in Sect. 4.

2 Electric Vehicles Assisted Renewable Energy Microgrids

A typical microgrid encompasses energy balance and demand-side management while addressing constraints such as economic viability, sustainability, and operations accuracy. Figure 1 shares the challenge for an effective energy management system of electric vehicle-assisted renewable energy microgrid.

Higher-level renewable energy integration can reduce non-renewable source dependence but the intermittent nature of renewable source adds uncertainty in its generation. Imbalance can cause blackouts, severe voltage drops [5]. Thus renewable energy integration is a huge technical challenge for a microgrid. Microgrids support multiple energy forms such as chemical energy, thermal energy, distributed generation (solar energy, wind energy), generators, electric chillers, fuel cells, thermal-solar collectors, combined cooling heating and power, etc. Similarly, energy storage preferences such as electric vehicles, flywheel energy storage, compressed air energy

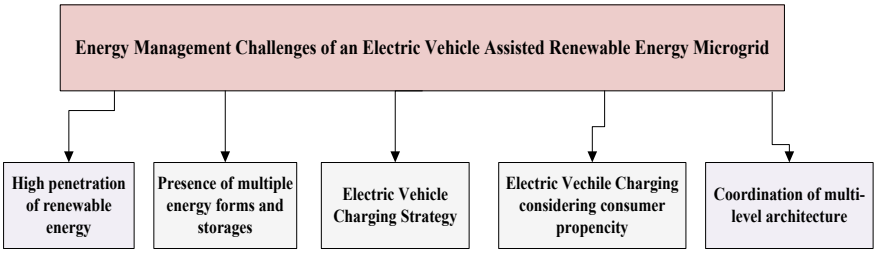

Fig. 1 Energy management challenges

storage, and super-capacitor can help in maximising renewable energy usage [6, 7]. But for a microgrid considering multiple energy generation options need to carry a thorough analysis to understand the coordination aspects amongst its entities [8].

Coordination of the multi-level architecture of a microgrid is important because it enhances the reliability and efficiency of the grid. Consumers play important role in the intelligent microgrid. There is a need for grid infrastructure that encourages active consumer participation. The next section reviews the latest energy management strategies carried across [9, 10].

3 Analysis of Related Work

The energy management system (EMS) of a microgrid is focused on optimizing the available energy resources, participating in the energy market, conducting analysis to depict loopholes in an energy management system, forecasting distributed energy resources, energy scheduling. These functions help the microgrid realize its optimal functions. A critical analysis of EMS strategies for Electric vehicle-assisted renewable energy microgrid has been present in Table 1.

4 Conclusion

The renewable energy and electric vehicle integration to microgrid is both a boon and bane for energy management of a microgrid. Availability of large-scale renewable discourages usage of non-renewable energy sources similarly participation of EVs in microgrid energy management encourages maximizing available energy usage. In the coming years, the electric vehicle market is bound to outgrow. This will induce reliability and sustainability challenges on the present grid. Hence, the grid should evolve as per energy needs. The literature survey carried observed the importance of demand-side management (DSM) for EVs-assisted microgrids. The DSM enables: consumer-direct participation in decision making, encourages load management, energy market participation, and establishes effective co-ordination between centralized entity, utilities, and consumer. The microgrid system design major concern is stability which requires interconnection strategies, power flow plan, and reliability analysis, power quality maintenance. In this aspect evolution of modeling, methodologies, and evaluation indices using DSM related to integration of EV in renewable energy based microgrid is the most crucial aspects of planning and estimation which can be considered for future research directions.

Table 1 Energy management strategies of EV assisted renewable energy MG

Refs.	Entities	Energy management strategy	Contribution
[11]	V2G, grid-connected microgrid, solar, wind, thermal units, parking lot	Built an optimization model providing energy balance and storage using EVs. Objective function of model was to reduce operational costs including generation cost participation in day-ahead market with real-time 24 h cost balance	The presence of the ambiguities in demand, available EVs, varying renewable characteristic addressed. By using the storage and energy of the EVs reduced the microgrid total operational cost
[12]	EVs, wind energy, grid-connected microgrid, battery storage	Developed a scenario-based stochastic optimization using the Monte-Carlo simulation. Objective function of the model was to reduce operational cost using a modified shuffled frog leaping algorithm	Addresses the problem of optimal day-ahead scheduling considering wind, EVs charging pattern, storage. The proposed optimization model results outperformed when compared
[13]	Integrated microgrid, wind, solar, battery storage, EV station	Modified the traditional simulated annealing algorithm to build a disturbance system to optimize charging, energy scheduling and joint optimization	Output depicted the electric vehicle charging station (EVCS) and energy storage capacity were decreased by 50%, and microgrid investors profit surged by7%
[14]	plug-in electric vehicles (PEV), multiple renewable sources, microgrid	The developed strategy focused on proposed scenario for year 2025 of California state. A high grade mobility grid dispatch planning was carried. Aimed to use 50% of renewable energy capacity of grid to charge 5 million PEV	The proposed strategy considers grid constraints, expected PEV (0.95 to 5 million), grid operation cost ($120 to $690 million). The strategy showed a RE curtailment of 40% relative to unmanaged PEV
[15]	Hybrid AC/DC microgrids, electric vehicle, wind, solar, fuel cell	Modeled three charging patterns for a hybrid AC/DC microgrid consisting of plugin hybrid electric vehicles: for coordinated, for uncoordinated and for smart charging depending on type of charging strategy, capacity and market participation. Flower pollination algorithm was used to solve the optimal problem	To reduce uncertainty effects a data-driven model was built. Using point estimate method and support vector machine (SVM) which helped in extracting standard deviation of uncertain parameters. IEEE standard test system verified the performance of developed model

(continued)

Table 1 (continued)

Refs.	Entities	Energy management strategy	Contribution
[16]	Industrial microgrid, solar, wind, electric vehicle	EV aggregator developed to work on four charging schemes of EV and to analyze the impact of EVs on industrial microgrid. Demand side management, time of use applied at three levels: off-peak, mid-peak, on-peak. The aggregator decreased the computational time and enhanced renewable penetration and EVs	Uncertainties of renewable energy and EV behavior were modelled using probability distribution function taking account of historical data. Simulation results supported the aim to maximize renewable energy integration and lower the operation cost
[17]	Multi-microgrids, electric vehicles	Two stage strategy represented. First, method proposed to forecast expected EV loads using back propagation neural network using long short-term memory deep learning. Second, an adaptive evolutionary algorithm using decomposition and differential evolution for fast economic energy scheduling of MGs	To reduce transmission losses, microgrid operating cost, enhance renewable energy management in presence of uncertainty associated with EV. Simulations carried supported global search performance, convergence performance of the discussed algorithm
[18]	Grid microgrid, multiple renewable energy sources, PEVs, Battery storage system	A stochastic programming framework was developed to optimize renewable energy integrated MG assisted with plug-in electric vehicles (PEVs). The framework addressed a single-objective optimization problem to reduce microgrid operating cost and scheduling periods of PEVs	The uncertainty of renewable intermittency generated by wind energy power outputs and solar energy units, uncertain behavior of EV consumers uses a modified harmony search algorithm to optimize the problem
[19]	Fuel cell, solar, wind, electric vehicle, grid connected microgrid	A scenario-based stochastic optimization problem using the Monte-Carlo simulation developed. Objective function includes reducing operating cost and a single-objective optimization problem sorted using modified shuffled frog leaping algorithm	Addresses optimal day-ahead scheduling, considers charging patterns of EV, renewable and storage units. Simulated and compared with a test MG to compare the performance with other algorithms

References

1. Haidar AMA, Muttaqi KM, Sutanto D (2014) Technical challenges for electric power industries due to grid-integrated electric vehicles in low voltage distributions: a review. Energy Convers Manage 86:689–700
2. Wang R, Hsu S-C, Zheng S, Chen JH, Li XI (2020) Renewable energy microgrids: economic evaluation and decision making for government policies to contribute to affordable and clean energy. Appl Energy 274
3. Mwasilu F, Justo JJ, Kim EK, Do TD, Jung JW (2014) Electric vehicles and smart grid interaction: a review on vehicle to grid and renewable energy sources integration. Renew Sustain Energy Rev 34:501–516
4. Hirsch A, Parag Y, Guerrero J (2018) Microgrids: a review of technologies, key drivers, and outstanding issues. Renew Sustain Energy Rev 90:402–411
5. Khan MdSA, Kadir KM, Mahmod KS, Alam MdII, Kamal A, Bashir MdMA (2019) Technical investigation on V2G, S2V, and V2I for next generation smart city planning. J Electron Sci Technol 17
6. Badal FR, Das P, Sarker SK (2019) A survey on control issues in renewable energy integration and microgrid. Prot Control Mod Power Syst 4:8
7. Amleh N, AlMuhaini M, Khalid M (2020) Impact of smart restoration and energy storage systems on the reliability of electric microgrid. Arab J Sci Eng 45:1911–1925
8. Wang Z, Lu Z, Tan C, Zhang X (2021) Multi-objective load dispatch of microgrid based on electric vehicle. In: Liu Q, Liu X, Shen T, Qiu X (eds) The 10th international conference on computer engineering and networks. CENet 2020. Advances in intelligent systems and computing, vol 1274. Springer, Singapore
9. Hardman S, Jenn A, Tal G, Axsen J, Beard G, Daina N, Figenbaum E, Jakobsson N, Jochem P, Kinnear N, Plötz P, Pontes J, Refa N, Sprei F, Turrentine T, Witkamp B (2018) A review of consumer preferences of and interactions with electric vehicle charging infrastructure. Transp Res Part D Transp Environ 62:508–523
10. Moshi GG, Berizzi A, Bovo C (2013) Grid connected systems for access to electricity: from microgrid to grid extension. In: Colombo E, Bologna S, Masera D (eds) Renewable energy for unleashing sustainable development. Springer
11. Mortaz E, Valenzuela J (2017) Microgrid energy scheduling using storage from electric vehicles. Electr Power Syst Res 143:554–562
12. Yang H, Pan H, Luo F, Qiu J, Deng Y, Lai M, Dong ZY (2017) Operational planning of electric vehicles for balancing wind power and load fluctuations in a microgrid. IEEE Trans Sustain Energy 8(2):592–604
13. Yi T, Cheng X, Chen Y, Liu J (2020) Joint optimization of charging station and energy storage economic capacity based on the effect of alternative energy storage of electric vehicle. Energy 208
14. Szinai JK, Sheppard JR, Abhyankar N, Gopal AR (2020) Reduced grid operating costs and renewable energy curtailment with electric vehicle charge management. Energy Policy 136
15. Wang P, Wang D, Zhu C, Yang Y, Abdullah HM, Mohamed MA (2020) Stochastic management of hybrid AC/DC microgrids considering electric vehicles charging demands. Energy Rep 6:1338–1352
16. Noorollahi Y, Golshanfard A, Aligholian A, Mohammadi-ivatloo B, Nielsen S, Hajinezhad A (2020) Sustainable energy system planning for an industrial zone by integrating electric vehicles as energy storage. J Energy Storage 30
17. Tan B, Chen H (2020) Multi-objective energy management of multiple microgrids under random electric vehicle charging. Energy 208
18. Liu C, Abdulkareem SS, Rezvani A, Samad S, Aljojo N, Foong LK, Nishihara K (2020) Stochastic scheduling of a renewable-based microgrid in the presence of electric vehicles using modified harmony search algorithm with control policies. Sustain Cities Soc 59

19. Li H, Rezvani A, Hu J, Ohshima K (2021) Optimal day-ahead scheduling of microgrid with hybrid electric vehicles using MSFLA algorithm considering control strategies. Sustain Cities Soc 66

Ecofriendly Multi-Agent-Based Smart MicroGrid Architecture Simulation and Analysis Using HOMER Grid

Gouri Shankar Gurjar, Prabhat Kumar, Bhwani Partap Singh, Dalip Singh, and Virendra Sharma

Abstract CO_2 emission is the major challenge for any developing country, it is because of increasing demand of industries, vehicles and electric power grids. Generally, conventional source and method of electric generation produce more CO_2. In this research, to reduce CO_2 emission and to improve fuel efficiency of different smart microgrid architecture were developed and evaluated by using advance HOMER grid software. These architectures were designed in reference to Sushantloak city Jaipur for residential load and commercial load. Architecture used multi-agent-based control system to make control and monitoring more efficient. The comparative and simulation analyses using HOMER grid software identified most suitable architecture that consume less fuel and emit less CO_2.

Keywords Smart microgrid · Architecture of smart microgrid · HOMER grid · Solar panel

1 Introduction

Smart grid is a latest technology for grid management and control system but due to high cost of instruments, it is taking time in implementation. Still most hybrid grid is using smart microgrid [1]. Smart microgrid is a similar technology to smart grid. It can be better used for industries, intuitions where DER is available for energy fulfillment [2]. Research to modify it for better efficiency and lower cost as well as CO_2 emission reduction [3]. Smart microgrid involves millions of consumers, generators and a large number of service providers with a variety of energy resources with varying controllability. This system requires deal in intelligence, two-way communication, automation distributed and local control system, self-configuring and self-healing capabilities to be built in the grid [4]. Most smart microgrid architecture uses

G. S. Gurjar · P. Kumar · V. Sharma
Arya College of Engineering and IT, Jaipur 303704, India

B. P. Singh · D. Singh (✉)
Department of Automobile Engineering, Manipal University Jaipur, Jaipur 303007, India
e-mail: dalip08784@gmail.com

S. Dwivedi et al. (eds.), *Flexible Electronics for Electric Vehicles*, Lecture Notes in Electrical Engineering 863, https://doi.org/10.1007/978-981-19-0588-9_63

technologies for energy resource management [5]. The common understanding of the term smart grid in research works encompasses the development of new power control strategies and communication systems to face the challenges which arise from the expansion of renewable source of energies (e.g., photovoltaic PV systems, wind turbine systems and combined heat) [6–8]. Multi-agent-based smart microgrid is a technology, where all function for controlling and monitoring are categorized according to agents [9]. And it can be integrated with different architectures of smart microgrid and it can improve efficiency of microgrid [10]. Renewable energy could be used for a substantial proportion of the global energy demands to reduce gas emissions and increase the carbon credit as well. Carbon credit analysis is used to mitigate the emission of carbon dioxide. Some work done in that area like carbon reduction and the earned carbon credit was calculated for a solar park and wind energy park in India. They calculated the reduction of CO_2 of a domestic system in India. Moreover, they studied CO_2 mitigation per annum for different fixed cases of PV coverage area under warm climate [11–13]. HOMER grid is a powerful tool for design and simulation of grid with renewable and non-renewable energy with load demand. It simulates fuel consumption and CO_2 emission analysis [14]. HOMER simulates grid economic with a complete varying load behavior. In this paper, CO_2 emission and fuel efficiency are analyzed using HOMER grid software and plot different PV coverage area ratios over one year.

1.1 Gaps in Published Research

The researcher used many technologies and system for optimization of energy and to reduce CO_2 but paper was with some gaps as listed.

- Most systems were simulated on HOMER but did not mention any real-time performance.
- Few of researchers considered some hypothetical data.
- Performance parameters were not clearly defined or referred.
- Multi-agent-based control system was not used before as it is a programming method.

1.2 Objectives

- To implement multi-agent-based smart microgrid.
- To compare different architecture available to reduced CO_2 emission and to save fossil fuel.
- To compare simulated architecture to real-time application and check result.

2 Material and Methods

To meet objective, the methods of multi-agent system were divided all functions and command in three major agents as and the agent relation and work domain shown in Fig. 1 [15–18].

DER agent (slave agent):

It handles responsibility for power generation, renewable source priority set, respond to master agent, alarm generate and fault diagnose.

Load agents (slave agent):

It handles responsibility for load dispatch, load management, fault diagnose, alarm generation and responds to master agent.

Control agent (master agent):

It handles all smart microgrid functions like self-healing, self-configurable and two-way communications, command to slave agent.

VI System Architecture

Above discussed methodology is integrated as per developed architecture and classified as follows

- System #1: Solar + Generator + 011
- System #2: Solar + 011
- System #3: Solar + Storage: 100LI + 011
- System #4: Solar + Generator + Storage: 100LI + 011
- System #5: Generator + 011

For the above system configuration, the data collected for a site real-time smart microgrid which geographical location is situated at.

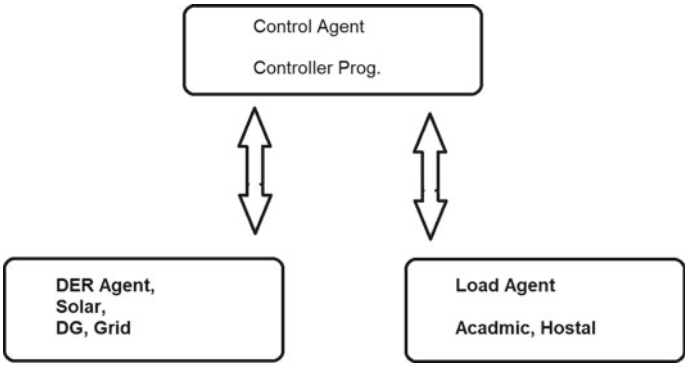

Fig. 1 Agent relation and work domain

Location	*191, Sushantloak city, Sirsi, Jaipur, Rajasthan 302,021, India*
Latitude	*26 °54.75 min N*
Longitude	*75 °47.24 min E*
Time zone	*Asia/Kolkata*

Load agent performed a detailed study of load behavior. At the site, there are two type of load one is residential load (hostel load) and another is commercial load (academic load). The load behavior is shown in Tables 1 and 2. Load is described according to day, month and season. Residential load is given in Table 2, and in this table, we can see load is in kW in X axis month is given and in Y axis hour is given [19–21].

Table 1 Load consumed in academic block

Hr	Jan	Feb	March	April	may	June	July	Aug	Sep	Oct	Nov	Dec
0	2.00	2.00	2.00	2.00	2.00	2.00	2.00	2.00	2.00	2.00	2.00	2.00
1	2.00	2.00	2.00	2.00	2.00	2.00	2.00	2.00	2.00	2.00	2.00	2.00
2	2.00	2.00	2.00	2.00	2.00	2.00	2.00	2.00	2.00	2.00	2.00	2.00
3	2.00	2.00	2.00	2.00	2.00	2.00	2.00	2.00	2.00	2.00	2.00	2.00
4	2.00	2.00	2.00	2.00	2.00	2.00	2.00	2.00	2.00	2.00	2.00	2.00
5	2.00	2.00	2.00	2.00	2.00	2.00	2.00	2.00	2.00	2.00	2.00	2.00
6	2.00	2.00	2.00	2.00	2.00	2.00	2.00	2.00	2.00	2.00	2.00	2.00
7	10.00	10.00	10.00	10.00	10.00	10.00	10.00	10.00	10.00	10.00	10.00	10.00
8	30.00	30.00	30.00	30.00	30.00	5.00	15.00	15.00	15.00	15.00	15.00	15.00
9	30.00	30.00	30.00	30.00	30.00	5.00	20.00	20.00	20.00	20.00	20.00	20.00
10	30.00	30.00	30.00	30.00	30.00	5.00	20.00	20.00	20.00	20.00	20.00	20.00
11	30.00	30.00	30.00	30.00	30.00	5.00	20.00	20.00	20.00	20.00	20.00	20.00
12	30.00	30.00	30.00	30.00	30.00	5.00	20.00	20.00	20.00	20.00	20.00	20.00
13	30.00	30.00	30.00	30.00	30.00	5.00	20.00	20.00	20.00	20.00	20.00	20.00
14	25.00	25.00	25.00	25.00	25.00	5.00	20.00	20.00	20.00	20.00	20.00	20.00
15	25.00	25.00	25.00	25.00	25.00	5.00	20.00	20.00	20.00	20.00	20.00	20.00
16	25.00	25.00	25.00	25.00	25.00	5.00	20.00	20.00	20.00	20.00	20.00	20.00
17	20.00	20.00	20.00	20.00	20.00	5.00	20.00	20.00	20.00	20.00	20.00	20.00
18	10.00	10.00	10.00	10.00	10.00	2.00	2.00	2.00	2.00	2.00	2.00	2.00
19	5.00	5.00	5.00	5.00	5.00	2.00	2.00	2.00	2.00	2.00	2.00	2.00
20	5.00	5.00	5.00	5.00	5.00	2.00	2.00	2.00	2.00	2.00	2.00	2.00
21	2.00	2.00	2.00	2.00	2.00	2.00	2.00	2.00	2.00	2.00	2.00	2.00
22	2.00	2.00	2.00	2.00	2.00	2.00	2.00	2.00	2.00	2.00	2.00	2.00
23	2.00	2.00	2.00	2.00	2.00	2.00	2.00	2.00	2.00	2.00	2.00	2.00
24	2.00	2.00	2.00	2.00	2.00	2.00	2.00	2.00	2.00	2.00	2.00	2.00

Table 2 Load consumed in hostel block

Hr	Jan	Feb	March	April	May	June	July	Aug	Sep	Oct	Nov	Dec
0	8.00	8.00	8.00	30.00	30.00	30.00	30.00	30.00	30.00	30.00	30.00	10.00
1	8.00	8.00	8.00	30.00	30.00	30.00	30.00	30.00	30.00	30.00	30.00	10.00
2	8.00	8.00	8.00	30.00	30.00	30.00	30.00	30.00	30.00	30.00	30.00	10.00
3	8.00	8.00	8.00	30.00	30.00	30.00	30.00	30.00	30.00	30.00	30.00	10.00
4	30.00	30.00	8.00	30.00	30.00	30.00	30.00	30.00	30.00	30.00	30.00	30.00
5	35.00	35.00	8.00	30.00	30.00	30.00	30.00	30.00	30.00	30.00	30.00	30.00
6	35.00	35.00	8.00	30.00	30.00	30.00	30.00	30.00	30.00	30.00	30.00	30.00
7	10.00	10.00	10.00	10.00	10.00	10.00	10.00	10.00	10.00	10.00	10.00	10.00
8	10.00	10.00	10.00	10.00	10.00	10.00	10.00	10.00	10.00	10.00	10.00	10.00
9	10.00	10.00	10.00	10.00	10.00	10.00	10.00	10.00	10.00	10.00	10.00	10.00
10	10.00	10.00	10.00	10.00	10.00	10.00	10.00	10.00	10.00	10.00	10.00	10.00
11	10.00	10.00	10.00	10.00	10.00	10.00	10.00	10.00	10.00	10.00	10.00	10.00
12	10.00	10.00	10.00	10.00	10.00	10.00	10.00	10.00	10.00	10.00	10.00	10.00
13	10.00	10.00	10.00	10.00	10.00	10.00	10.00	10.00	10.00	10.00	10.00	10.00
14	10.00	10.00	10.00	10.00	10.00	10.00	10.00	10.00	10.00	10.00	10.00	10.00
15	10.00	10.00	10.00	10.00	10.00	10.00	10.00	10.00	10.00	10.00	10.00	10.00
16	10.00	10.00	10.00	10.00	10.00	10.00	10.00	10.00	10.00	10.00	10.00	10.00
17	20.00	20.00	20.00	20.00	20.00	20.00	20.00	20.00	20.00	20.00	20.00	20.00
18	20.00	20.00	20.00	20.00	20.00	20.00	20.00	20.00	20.00	20.00	20.00	20.00
19	20.00	20.00	20.00	20.00	20.00	20.00	20.00	15.00	15.00	15.00	12.00	10.00
20	20.00	20.00	20.00	20.00	20.00	20.00	20.00	15.00	15.00	15.00	12.00	12.00
21	20.00	20.00	20.00	20.00	20.00	20.00	20.00	15.00	15.00	15.00	12.00	12.00
22	20.00	20.00	20.00	20.00	20.00	20.00	20.00	15.00	15.00	15.00	12.00	12.00
23	20.00	20.00	20.00	20.00	20.00	20.00	20.00	15.00	15.00	15.00	12.00	12.00
24	20.00	20.00	20.00	20.00	20.00	20.00	20.00	15.00	15.00	15.00	12.00	12.00

For week days, Table1 is of academic load. In Table 1, it can be seen that load is running least from 9 PM to 6 AM. And from 6 to 8 AM, it increase gradually. At 12 PM, load is at its peak. From 12 to 4 PM, it remains high and from 4 to 8 PM it decreases. During the year in the month of June and in the last days of December, load is at its least because of holidays. This load behavior represents to a commercial load. And it can be better optimized with preferred renewable energy resource solar. Similar to commercial load, residential load is also given at site, and in the table, X axis represents month and Y axis to hours in table [22–24].

Table 2 shows hostel load data from January, February, march and December month are showing minimum energy consumption as in hostel no Air-conditioners is running during night hours and in day hours all students are at academic block so average load is 10 kW in the day for water heating from 4 to 7 AM consumption of

electricity is 30 kW similarly from April to November air-cooler and air-conditioners are running so during night hour 30 kW is average consumption. And duration of 6 PM to 11 PM load is slightly increase due to lights is on in hostel and load is slightly decrease after 11 pm to 4 am due to lights is off. Both loads are further demonstrated according to season. It means the range of varying load for one period to other.

Figure 2 shows the seasonal load profile; the graph is plotted in kW and month in the seasonal load peak load is 30 kW and minimum load is in month June is 7 kW. The average load is 20 kW. Heat map is derived from HOMER for academic and hostel load shown in Figs. 3 and 4. Its color from dark blue to red is showing in ascending order of energy consumption and *X* axis for days of year and *Y* axis for hours of day. So first heat maps for academic load where energy consumption is from 8 AM to 4 PM as indicate in image and dark blue shows less energy consumption and in second heat map for hostel load where consumption is from 0 to 6 h and 18 to 24 h of day and during 8 to 16 it is less.

For described loads, we identified that average electric consumption for a day is 1638 kWh/day, and yearly, it is 597.9 MWh and CO_2 released to generate this much of electricity is 140 ton in environment; so, we compared few architecture and we designed and simulated list of these architecture are explained earlier. On

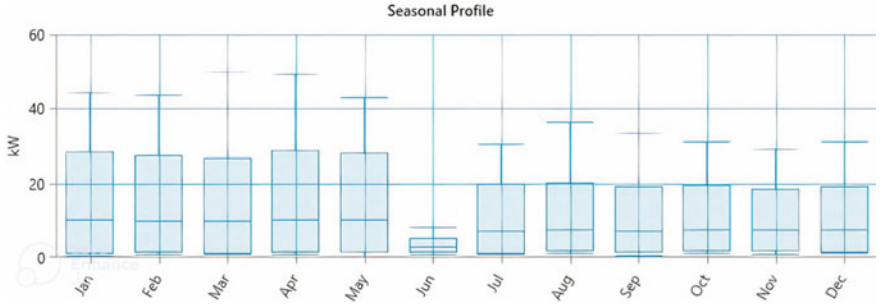

Fig. 2 Seasonal load profile of academic block

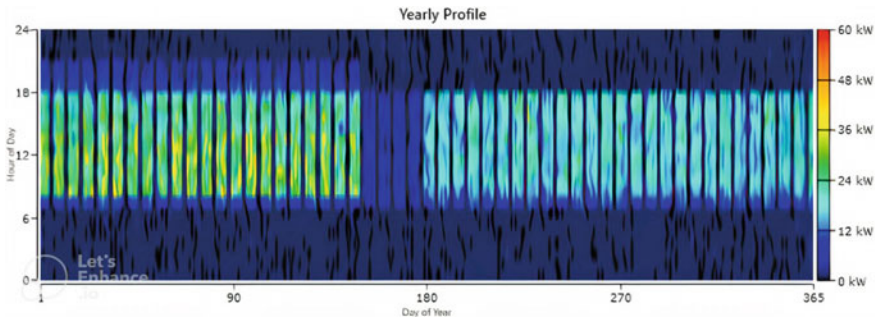

Fig. 3 Yearly load profile of academic block

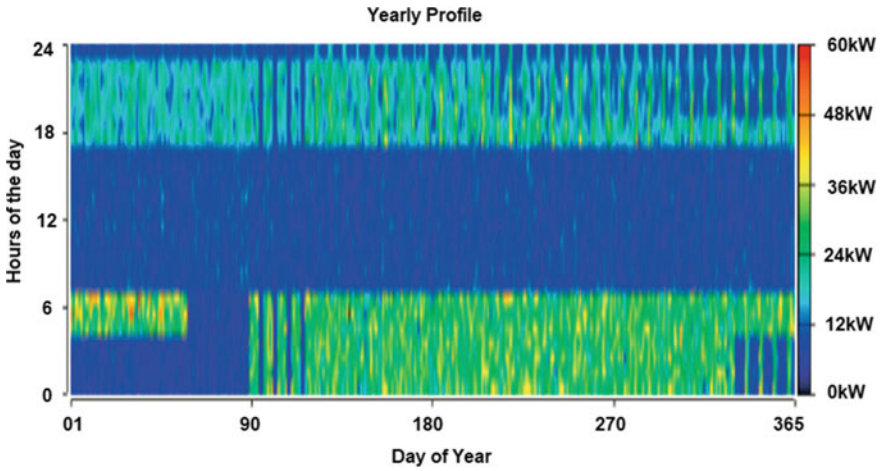

Fig. 4 Yearly load profile of hostel block

simulation from HOMER on comparing all architecture, we found these results are given in comparative Table 3 and parameters like CAPEX, OPEX, annual total saving, annual demand charges, fuel consumption and CO_2 emission are compared. This table indicates a result data on simulation on HOMER. It is not only about financial values parallel it gives a social impact as CO_2 emission and fuel burning both has direct impact on society so it is well tuned tool for simulation of grid with renewable and non-renewable sources.

3 Result

See Table 4.

In the result, we found that architecture which has solar, diesel generator and storage were economically and socially found to be best suitable for the given load. Architecture is shown in Fig. 5.

4 Conclusion

It is concluded from the all experimental setup and data available that solar with generator and battery is more suitable option. Even it can be more explored with biogas and other renewable source. And to identify best system architecture, we can simply simulate that against load.

Table 3 Comparative table of architecture and performance parameters

	Base case	Solar + Generator + 011	Solar + 011	Solar + Storage: 100LI + 011	Solar + Generator + Storage: 100LI + 011	Generator + 011
CAPEX	₹ 0	₹ 9,512,500	₹ 9,500,000	₹ 9,570,000	₹ 9,582,500	₹ 12,500
OPEX	₹ 1,696,797	₹ −2,222,828	₹ −2,216,423	₹ −2,221,359	₹ −2,217,764	₹ 1,694,419
Annual total savings (₹)	₹ 0	₹ 3,919,624	₹ 3,913,220	₹ 3,918,155	₹ 3,914,561	₹ 2378
Annual utility bill savings (₹)	₹ 0	₹ 3,991,814	₹ 3,976,849	₹ 3,986,814	₹ 3,986,670	₹ 6156
Annual demand charges (₹/yr)	₹ 76,046/yr	₹ 39,147/yr	₹ 50,854/yr	₹ 18,092/yr	₹ 19,653/yr	₹ 71,353/yr
Annual energy charges (₹/yr)	₹ 1,620,750/yr	₹ −2,334,164/yr	₹ −2,330,908/yr	₹ −2,308,110/yr	₹ −2,309,527/yr	₹ 1,619,288/yr
Discounted payback time (yrs)		2.7	2.7	2.7	2.7	7.3
Simple payback time (yrs)		2.4	2.4	2.4	2.4	5.8
IRR %		41.52	41.51	41.29	41.19	17.20
Net present cost (₹)	₹ 21,935,360	₹ −19,223,140	₹ −19,152,850	₹ −19,146,650	₹ −19,087,680	₹ 21,917,130
CO_2 emissions* (metric ton/yr)	115.3	44.8	44.9	27.8	27.8	115.3
Annual fuel consumption (L/yr)	n/a	97	n/a	n/a	41	44

Table 4 The lowest net present cost system architecture is: Solar + Battery + Generator + 011

The lowest net present cost system architecture is:	Solar + Battery + Generator + 011
Your annual savings can be	₹3,991,814
System capital cost	₹9,512,500
Over the project lifetime of 25 years your savings can be	₹ 99,795,350
Your IRR	42%
Your payback time can be	2.4 years

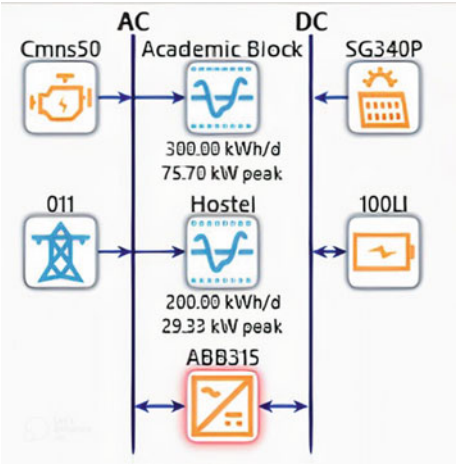

Fig. 5 Result from simulation is shown in tabular format for best suitable architecture

From the experimental setup, it is found that 140 ton of CO_2 released is reduced within a year for the given load, and these multi-agent-based architectures are designed with reference to type of load.

References

1. Aste N, Chiesa G, Verri F (2008) Design, development and performance monitoring of a photovoltaic-thermal (PVT) air collector. Renew Energy 33:914–992
2. Kern J, Russell M (1978) Combined photovoltaic and thermal hybrid collector systems. In: 13th IEEE photovoltaic specialists, Washington, DC, USA: Massachusetts Institute of Technology, Lexington (USA). Lincoln Lab.; COO—4577-3; CONF—780619-24
3. Widyolar BK, Abdelhamid M, Jiang L (2017) Design, simulation and experimental characterization of a novel parabolic trough hybrid solar photovoltaic/thermal (PV/T) collector. Renew Energy 101:1379–1389
4. Joe J, Iniyan S, Goic R (2015) Flat plate solar photovoltaic—thermal (PVT) systems: a reference guide. Renew Sustain Energy Rev 51:62–88
5. Kumar A, Baredar P, Qureshi U (2015) Historical and recent development of photovoltaic thermal (PVT) technologies. Renew Sustain Energy Rev 42:1428–1436

6. Amori KE, Abd-AlRaheem M (2014) Field study of various air based photovoltaic/thermal hybrid solar collectors. Renew Energy 63:402–414
7. Othman M, Tabook M, Sopian K, Roslan MH, Ibarahim Z (2016) Performance analysis of PVT Combi with water and air heating system: an experimental study. Renew Energy 86:716–722
8. Rejeb O, Dhaou H, Jemni A (2015) A numerical investigation of a photovoltaic thermal (PVT) collector. Renew Energy 77:43–50
9. Coventry JS (2005) Performance of a concentrating photovoltaic/thermal solar collector. Sol Energy 78:211–222
10. Abdelhamid M, Singh R, Qattawi A, Omar M, Haque I (2014) Evaluation of on-board photovoltaic modules options for electric vehicles. IEEE J Photovoltaics 04:1576–1584
11. Aste N, Del Pero C, Leonforte F (2014) Water flat plate PV-thermal collectors: a review. Sol Energy 102:98–115
12. Sharma H, Mishra S (2019) Hybrid optimization model for smart grid distributed generation using HOMER. In: 3rd international conference on recent developments in control, automation and power engineering. IEEE, ISBN 978-1-7281-2068-3/19
13. Singh G, Tiwari AN (2019) Optimization of a smart grid distributed generation: designing of a hybrid solar system for a building. IEEE, ISBN 978-1-5386-1703-8/17
14. Reiman AP, Homer JS (2019) Quantifying technical diversity benefits of wind as a distributed energy resource. IEEE, 978-1-7281-3103-0/20
15. Purser MS (2015) A technical and economical study of implementing a micro-grid system at an educational institution. In: IEEE power & energy society innovative smart grid technologies conference. IEEE, ISBN 978-1-4799-1785-3/15
16. Li F, Li Q, Zhang J, Kou J, Ye J, Mantooth A (2021) Detection and diagnosis of data integrity attacks in solar farms based on multi-layer long short-term memory network. IEEE Trans Power Electron. https://doi.org/10.1100/TPEL_2020.3017935
17. Lazaroiu C (2018) New approach for smart community grid through blockchain and smart charging infrastructure of EVs. In: 8th international conference on renewable energy research and applications (ICRERA). IEEE, ISBN 978-1-7281-3587-8/19
18. Raisa H, Taskin J (2015) Smart management of PREY and renewable energy sources for grid peak demand energy supply. In: International conference on electrical engineering and information communication technology (ICEEICT). IEEE, ISBN 978-1-4673-6672-2/15
19. Golub V (2018) Optimization of anoff-grid PV system in respect to the capacity shortage value. In: IEEE PES innovative smart grid technologies conference Europe (ISGT-Europe). IEEE, ISBN 978-1-5386-4505-5/18
20. Farias HEO (2019) Battery energy storage systems: impact analysis on different loads with distributed generation. IEEE, 978-1-5386-8218-0/19
21. Reyasudin Basir Khan M, Pasupuleti J (2019) PV-battery system design for an indigenous people school in Malaysia. In: Proceedings of the IEEE 6th international conference on smart instrumentation, measurement and application ICSIMA
22. Baharozu E, Soykan G (2016) Economic and environmental evaluation of a designed smart micro-grid system in Turkey. In: 4th international Istanbul smart grid congress and fair (ICSG). 978-1-5090-0866-7/16
23. Liu X, Shahidehpour M, Cao Y, Wu L, Wei W, Liu X (2016) Microgrid risk analysis considering the impact of cyber attacks on solar PV and ESS control systems. IEEE Trans Smart Grid 08(3):1330–1339
24. Yang B, Guo L, Li F, Ye J, Song W (2019) Vulnerability assessments of electric drive systems due to sensor data integrity attacks. IEEE Trans Ind Inform